Star Formation in Galaxies: From the Epoch of Reionisation to the Present Day

Samantha Hickey

Submitted to the University of Hertfordshire in partial fulfilment of the requirements of the degree of Doctor of Philosophy.

July 2012

Abstract

In this thesis, I explore both obscured and unobscured star formation over a large fraction of cosmic time. I use the HAWK-I Y-band science verification data over GOODS-South, in conjunction with optical and infrared data to search for Lyman-break galaxies at $z \gtrsim 6.5$ (i.e. within the first billion years of the Universe). I find four possible (two robust) z'-drop candidates ($z \gtrsim 6.5$) and four possible (but no robust) Y-drop candidates ($z \gtrsim 7$). I use my results to place constraints on the luminosity function at $z \sim 6.5$ and find significant evolution in the population of Lyman-break galaxies between $3 < z \lesssim 6.5$.

I also explore obscured star formation with a population of 70μm selected galaxies over the COSMOS field. I use AAT spectroscopy in conjunction with other available spectroscopic redshifts for my sample, and photometric redshifts otherwise, to calculate the total infrared luminosity of each galaxy. Two libraries of spectral energy distributions are considered; Siebenmorgen & Krügel (2007) templates and Chary & Elbaz (2001) models. We have supplemented our data with that of Huynh et al. (2007) collected over the GOODS-North field and adapted it to directly compare with the results of this work. The far-infrared luminosity function is then determined using the

$1/V_{max}$ technique. A double power law parameterisation is found to provide the best fit to the data. The far-infrared luminosity function was fitted for all parameters and the evolution was measured out to $z \sim 1$. Three different types of evolution were allowed, pure luminosity, pure density and luminosity dependent density evolution. In all cases strong positive evolution was evident with the best-fit case being pure luminosity evolution where $p = 2.4^{+0.6}_{-0.7}$. Due to the larger volume surveyed compared to previous studies, this work provides better constraints on the bright end of the far-infrared luminosity function displaying a shallower bright end slope ($\alpha_2 \sim -1.6$) than previously determined, implying a higher number density of the most luminous objects and thereby a greater contribution from these objects to the total infrared energy density. However the shallower slope determined here can be reconciled with other work if the Chary & Elbaz (2001) models are used instead of the Siebenmorgen & Krügel templates; demonstrating that spectral energy distribution model selection is a key component in determining luminosity functions at far-infrared wavelengths.

The far-infrared–radio correlation (FIRC; $q_{\rm IR}$) was determined for the sample of 70μm selected star-forming galaxies using 1.4 GHz radio data over the COSMOS field, and no evolution was found out to $z \sim 2$. The 70μm monochromatic evolution in the FIRC was also examined (q_{70}) and no evolution was found in this parameter with redshift.

Supervisors

Dr Matt J. Jarvis

Centre for Astrophysics Research

University of Hertfordshire

&

Dr Andrew Bunker

Department of Physics

University of Oxford

Acknowledgements

I would like to thank the following people for their help and support over the course of my PhD. Firstly, I would like to thank Matt Jarvis for his patience, perseverance and dedication to his students despite his busy schedule. I would also like to thank him for the opportunities he has provided me with and for always having time to answer my questions, no matter how trivial.

I would also like to thank Andy Bunker for providing me with the opportunity of working at the Anglo-Australian Observatory in my first year and for sharing his expertise with me, particularly in the field of Lyman-break galaxies.

Special thanks go to my family who have supported me through, not only my PhD but my entire education. I would like to thank my dad for all of the 'dinner time' conversations about science and for providing an example for me to aspire to. I would like to thank my mum for her love, support and understanding and for always being there for me. I would also like to thank Harry and Tadgh.

I would especially like to thank James, without whom, this thesis may never have been finished. I am grateful for his enduring patience, effort, thoughtfulness and above all, his love.

Finally, I would like to thank all of the people I have met in the department who create such a friendly environment, furthermore, I am grateful for the friendships that have made my PhD so enjoyable.

Contents

Chapter 1

Introduction

1.1 Star Formation History

Observations of the star formation history of the Universe have shown a peak in the star formation rate between $z \sim 1 - 2$ (see Figure 1.1 and Lilly et al. 1996; Madau et al. 1996; 1998). They also show that the star formation rate of the Universe has been declining since this epoch. The star formation rate history is important as it can tell us about galaxy formation and evolution. It can differentiate between different types of galaxy evolution such as monolithic collapse and hierarchical evolution. It can also tell us if the star formation rate density was high enough in the past to be responsible for reionisation: the epoch when there were enough ultraviolet (UV) photons to ionise the neutral hydrogen in the intergalactic medium, resulting in the Universe becoming transparent to all electromagnetic radiation. The star formation rate density of the early Universe is highly dependent on the star formation rate of the early galaxies and their co-moving number density.

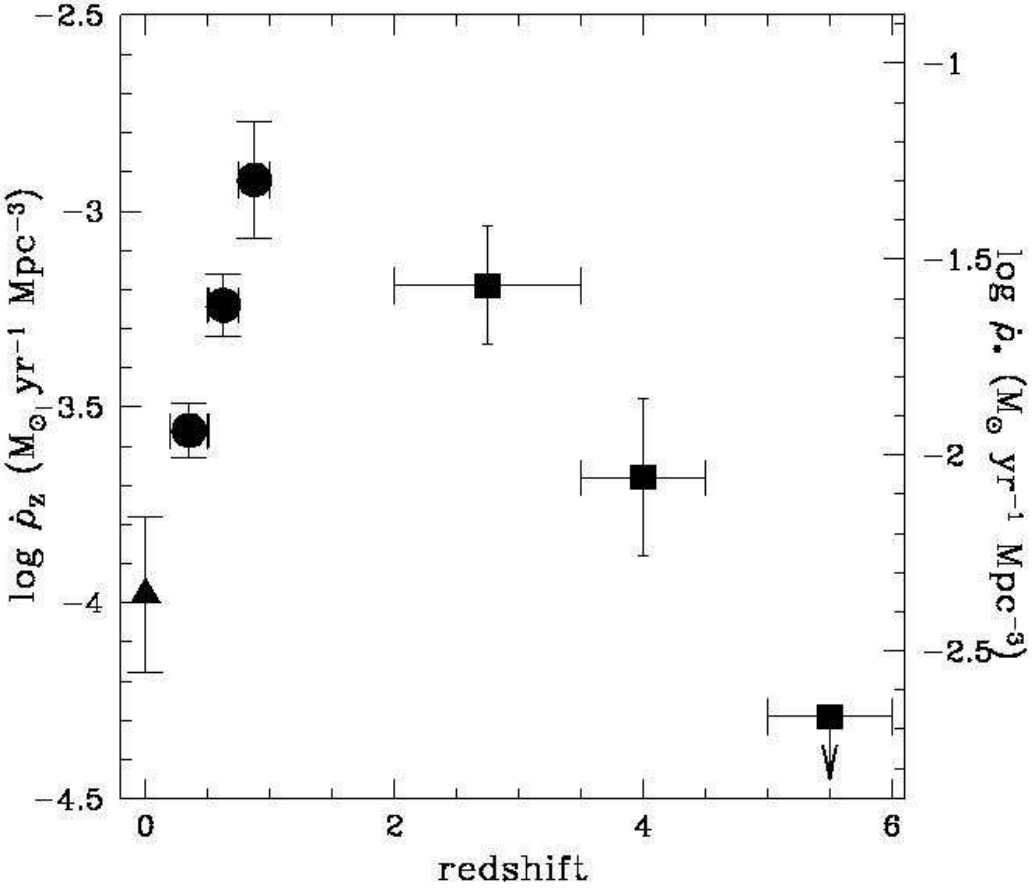

Figure 1.1: Figure from Madau (1998) showing the star formation rate density as a function of redshift. It is clear that the peak of the star formation rate density is around $z \sim 1$ and that there is a sharp decline towards lower redshifts. Although there also appears to be a drop towards higher redshift, this is uncertain due to the effect of dust obscuration. This Figure has since populated with further observations extending to higher redshift (e.g. Bunker et al. 2004)

In this chapter, I will provide a general introduction to the observational work that has provided the bulk of our knowledge on the star formation history of the Universe.

1.1.1 The Schmidt-Kennicutt law

The Schmidt-Kennicutt law is an empirical one relating the observable surface density of gas to star formation rate. The following relation $\Sigma_{\rm SFR} = \epsilon_{\rm SF}\Sigma_{\rm gas}^{N}$ was proposed by Schmidt (1959) where $\Sigma_{\rm SFR}$ represents the star formation rate surface density, $\epsilon_{\rm SF}$ represents the star formation efficiency, $\Sigma_{\rm gas}$ represents the surface density of gas and N denotes the index of the power law relation. The initial findings of Schmidt (1959) pointed to a value of $N = 2 \pm 1$ based on measurements of our galaxy. Kennicutt (1998a) extended the study of the Schmidt law to include data taken from 61 normal spiral galaxies and a sample of starburst galaxies demonstrating that the Schmidt law holds over 5 orders of magnitude in gas density and 6 orders of magnitude in SFR (see Figure 1.2).

If the density of gas is a strong determinant in the likelihood of a star being formed then it is natural to assume that the star formation rate should be proportional to the gas density as given by the Schmidt law. It would also be natural to assume that as the gas density increased so should the star formation rate, if this occured in a linear fashion, that would result in $N = 1$. However if we have a cloud of gas with density $\rho_{\rm gas}$ and assume that the star formation rate of that cloud will then be determined by the free-fall timescale of the cloud ($\tau_{\rm ff}$) which is proportional to the inverse square of the mean

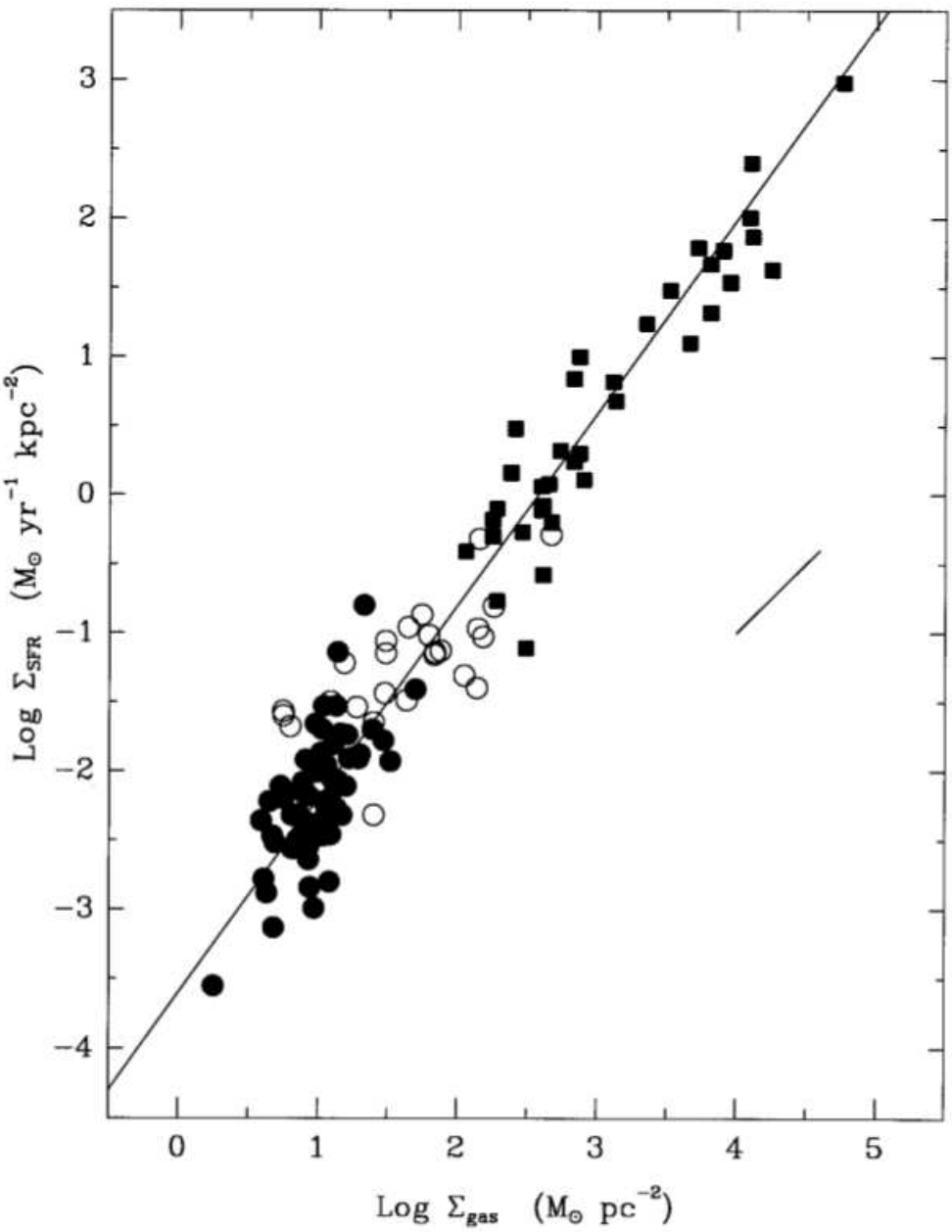

Figure 1.2: Figure from Kennicutt (1998a) showing the Schmidt-Kennicutt law relating the gas surface density to the star formation rate surface density. Filled circles represent normal disk galaxies, filled squares denote starburst galaxies and open circles represent the centres of normal disk galaxies. The solid line represents the least squares fit resulting in $n = 1.4$.

density of the cloud ($\tau_{\rm ff} \propto 1/\sqrt(\rho)$) then we obtain the following equation relating the star formation rate and the density of the cloud $\rho_{\rm SFR} \propto \rho_{\rm gas}/\tau_{\rm ff} \propto \rho_{\rm gas}^{1.5}$. Thus an index of $N \sim 1.5$ is logical if the timescale of the collapse of the cloud is approximately the free-fall timescale. However there are many processes that hinder star formation such as feedback from supernovae or AGN, metallicity and magnetic fields but they can be accounted for within the star formation efficiency factor which is generally $<< 1$.

1.1.2 The UV continuum

The star formation rate of high redshift galaxies ($z \sim 6$) is typically determined through measurements of their UV continuum. The UV continuum is defined as being between $1250 - 2500\,\text{Å}$ in the rest-frame and is mainly produced by young massive stars. It is bordered by the Lyman-α break (where Lyman-α is the first atomic hydrogen transition from n=2 to n=1) short ward of $1216\,\text{Å}$ and significant contamination from the lower mass older population long ward of $2500\,\text{Å}$. The strength of the UV continuum as an indicator, lies in the fact that it is a direct tracer of young, massive and short-lived stars, and therefore provides information on the recent star formation history. The UV continuum is a direct tracer of the recent star formation rate (SFR), and it should scale linearly with SFR (Kennicutt 1998b).

The main drawback of this method is the high efficiency with which dust absorbs the UV, resulting in a potential underestimate of the SFR. In order to account for this, a good idea of the dust extinction is required, however this is hampered by the inherent clumpiness associated with star forming regions

(Calzetti et al. 1994). Another drawback is the difficulty of observations from the ground due to the absorption of UV flux by the atmosphere. However, it becomes possible for galaxies at $z > 0.5$, where the UV light is redshifted in to the optical waveband. Spectral synthesis models (Searle et al. 1973; Larson & Tinsley et al. 1978; Bruzual & Charlot 1993) are used to calibrate the UV continuum flux, however this introduces assumptions with inherent uncertainties such as the length of the star formation episode. Normally a constant SFR is assumed, and this results in an underestimate of the SFR if the galaxy is undergoing a starburst. Another important assumption is the shape of the initial mass function (IMF), which is usually assumed to be a Salpeter IMF (Salpeter 1955), although other forms are regularly used (e.g. Scalo 1986; Kroupa et al. 1990; Chabrier 2003)

1.1.3 Nebular recombination Lines

If optical spectra are available it is possible to use nebular recombination lines to obtain an estimate of the SFR. Photons with wavelengths shorter than 912 Å (the Lyman limit) will be absorbed by hydrogen, as 912 Å represents the ionising potential of neutral hydrogen. The absorption of radiation short-ward of this limit causes the hydrogen atoms to become ionised. As they recombine and the electron falls through the energy levels, a photon will be released with energy equal to the energy level difference. These emission lines are therefore a direct tracer of the UV emission short-ward of the Lyman limit of which, the majority is generated by young (< 20 Myr) and massive ($> 10\,M_{\odot}$) stars and hence, traces the SFR.

Hydrogen emission lines

Hydrogen, being the most abundant element in the Universe can be expected to be the main component of this absorbing matter. Due to its abundance and low ionisation potential it typically produces the brightest rest-frame optical emission line Hα at $\lambda = 6563\,\text{Å}$ which represents the first line in the Balmer series (i.e. the transition from the $n = 3$ to $n = 2$ energy level). The main advantage of this indicator is that it traces only young massive stars and is therefore a measure of the current star formation rate (Kennicutt 1998b). It does not suffer from contributions from older stars and therefore provides an estimate of the SFR irrespective of a previous star formation history. This is particularly useful for measuring the SFR in starburst galaxies where the typically assumed constant SFR is not applicable.

One of the main disadvantages of this method is its sensitivity to dust extinction which is an intrinsic property of a young star forming region. However owing to its longer wavelength, it is less affected by dust attenuation than bluer (shorter wavelength) emission lines. Extinction corrected Hα is still a reliable SFR tracer even in highly obscured star-forming galaxies (Moustakas et al. 2006). It is also only observable from the ground below $z \sim 0.4$ before it is redshifted to the near infrared where it can be observed through the atmospheric window at $0.7 \lesssim z \lesssim 2.5$. Although not dependent on a star formation history, this method still relies on assumptions about the IMF to determine the ratio of high to low mass stars being formed. It also assumes that wherever there is star formation, we will be able to detect the ionised gas. However this is not necessarily the case in highly obscured star

forming regions.

Hβ represents the second transition in the Balmer sequence (from $n = 4$ to $n = 2$), although it is generated from the same processes as Hα, it is significantly weaker and more easily absorbed. Hence, the main uncertainty in using Hβ is dust absorption, however it does lie at a shorter wavelength $\lambda = 4861\,\text{Å}$ and is therefore visible beyond $z = 0.5$ in optical spectra. The other higher order hydrogen emission lines suffer much the same problem as Hβ, in that they are significantly weaker than Hα and lie at shorter wavelengths and are thus, more susceptible to dust obscuration.

1.1.4 [OII]

Another nebular emission line commonly used as a SFR tracer is the forbidden [OII] $\lambda \approx 3727\,\text{Å}$ line doublet. [OII] is an effective emission line for measuring SFR due to its intensity, however is not directly coupled to the ionising flux and is thus typically calibrated using the more reliable Hα flux. The [OII] doublet arises when temperatures of 10,000-20,000K (common for star-forming regions) are reached, this results in the thermal electron energy kT being approximately equal to the excitation energy between the S level and the two upper D levels (Kennicutt 1998b).

[OII] is a shorter wavelength line and as such is visible in optical spectra out to higher redshift than Hα, however owing to its shorter wavelength it is more easily attenuated by dust, and is sensitive to metallicity (e.g. Kewley et al. 2004).

1.1.5 Far-Infrared Luminosity

Measurements of the UV continuum and nebular emission lines without corrections for reddening (which can introduce large uncertainties) provide an estimate of the unobscured star-formation in a galaxy, however star formation is often obscured and as a result much of the UV and optical light may be attenuated. This dust and gas absorbing the UV and optical light will re-emit this radiation at infrared wavelengths radiating as a greybody spectrum. A measurement of the far-infrared luminosity of a galaxy can provide a complementary star formation rate indicator to direct measurements of the UV continuum and optical emission lines. In fact, the combination of infrared luminosity and Hα derived star formation rates have been found to be the most robust indicator (Kennicutt et al. 2009).

The main drawback associated with infrared luminosity as a tracer is that some of the starlight will not be absorbed by dust, resulting in the infrared luminosity under predicting the total star formation rate (Kennicutt et al. 2009). However for dusty galaxies, far-infrared emission has been found to linearly correlate with SFR (Kennicutt 1998b) and is therefore a particularly applicable tracer for dusty infrared galaxies (Calzetti et al. 2011).

The star formation rates estimated from total infrared luminosities for a sample of 250μm selected galaxies at $z < 1$ with $L_{IR} > 10^{10} L_{\odot}$ have been found to account for $\sim$90 per cent of the total SFR (Buat et al. 2010). This indicates that for galaxies with bright infrared luminosities, the total infrared luminosity is an accurate tracer. For those galaxies with $L_{\rm IR} < 10^{11} {\rm L}_{\odot}$ or $SFR < 1 {\rm M}_{\odot} {\rm yr}^{-1}$, the L_{IR} only accounts for $\sim$ 70 per cent of the total SFR

indicating a need for another method to supplement this tracer at the lower infrared luminosities (Buat et al. 2010). The total infrared luminosity may also be used to estimate the dust attenuation in the optical and UV through arguments based on energy balance (da Cunha et al. 2010; Smith et al. 2011 submitted).

The Infrared Astronomical Satellite (IRAS; Neugebauer et al. 1984) was launched in 1983, with the aim of imaging the entire sky in four wavebands, namely 12, 25, 60 and 100μm. The IRAS all sky survey imaged over 96 per cent of the sky, at best, in the point source catalogue, down to 0.5 Jy in the first three bands and 1.5Jy at 100μm, detecting objects with L_{IR} between $10^6 L_\odot$ and $10^{13} L_\odot$. It was the first space based telescope to cover nearly the entire sky at infrared wavelengths and it revolutionised extra-galactic infrared astronomy. IRAS increased the number of extra-galactic infrared sources by 3 orders of magnitude and heralded the discovery of a new class of objects that emitted > 95 per cent of their bolometric luminosity at infrared wavelengths (Soifer et al. 1984). IRAS being sensitive to emission from warm dust, detected the prevalence of obscured starbursts in the local Universe and invited the systematic study of infrared emission from galaxies (see Soifer et al. 1987b for a review).

IRAS was followed by the Infrared Space Observatory (ISO; Kessler et al. 1996) in 1995 with the aim of revealing the role of star formation in the activity and evolution of galaxies. By extending infrared observations out to 200μm, ISO was able to uncover a cooler dust component (T$\sim$ 20K) associated with star formation. Utilising its greater sensitivity, ISO was able to confirm the duality of starbursts and AGN components in many of the

most infrared luminous objects, first proposed from work with IRAS (Genzel & Cesarsky 2000).

In 2003 the *Spitzer* Space Telescope was launched and owing to its improved sensitivity, it was able to extend the study of infrared emission out to $z \sim 6$ (Eyles et al. 2005, 2007). *Spitzer* has been used to infer the stellar mass of some of the highest redshift objects, and has been used to detect dust obscured star formation out to high redshift (see Soifer et al. 2008 for a review). The recently launched *Herschel* Space Observatory (Pilbratt et al. 2010) is currently extending these observations to longer wavelengths probing from $70 - 500\mu$m.

1.2 Radio Luminosity

Radio emission has been found to correlate with far-infrared luminosity (de Jong et al. 1985; Helou et al. 1985), this allows it be be exploited as yet another star formation rate indicator. Typical radio emission in normal galaxies (i.e. those not containing a significant contribution from an AGN) occurs in two forms. The first being free-free emission in HII regions. This emission is typically flat spectrum and provides a radio background for the galaxy. The second type is non-thermal radio emission as a result of relativistic electrons releasing synchrotron radiation as they are accelerated by supernovae. Only massive stars ($\mathrm{M} > 8\,\mathrm{M}_{\odot}$) with short lifetimes result in supernovae and therefore, this type of radio emission traces recent massive star formation. This component is often characterised with a steep spectral index of $\alpha = -0.8$ (where $\mathrm{S}_{\nu} \propto \nu^{\alpha}$) and dominates the radio emission below $\nu \sim 30\,\mathrm{GHz}$. Radio

emission, like infrared emission is unobscured by dust. Through the far-infrared–radio correlation (e.g. de Jong et al. 1985; Helou et al. 1985), radio luminosity can be calibrated and utilised as a star formation rate indicator. Radio luminosity in conjunction with optical emission lines, has also been used, instead of infrared luminosity to estimate attenuation corrected star formation rates (Kennicutt et al. 2009).

1.2.1 The Far Infrared - Radio Correlation

As described in Section 1.2, a tight correlation has been found between far-infrared and radio luminosity (de Jong et al. 1985; Helou et al. 1985; see Figure 1.3). The calorimeter theory (Völk 1989) proposes that galaxies are 'calorimeters' in the sense that the accelerated electrons lose all of their energy before escaping from the galaxy. The UV light emitted by massive stars is efficiently absorbed by dust and remitted in the infrared, such that the energy from both processes is a consistent fraction of the total. This results in a constant far-infrared–radio correlation (FIRC). The intricacies of the correlation however, are not well understood and often 'conspiracies' have to be invoked in order to maintain the FIRC. Lacki et al. (2010a & b) find that 'calorimetry' holds and only imply 'conspiracies' in cases of low or high column densities, while allowing the magnetic field strength to vary significantly.

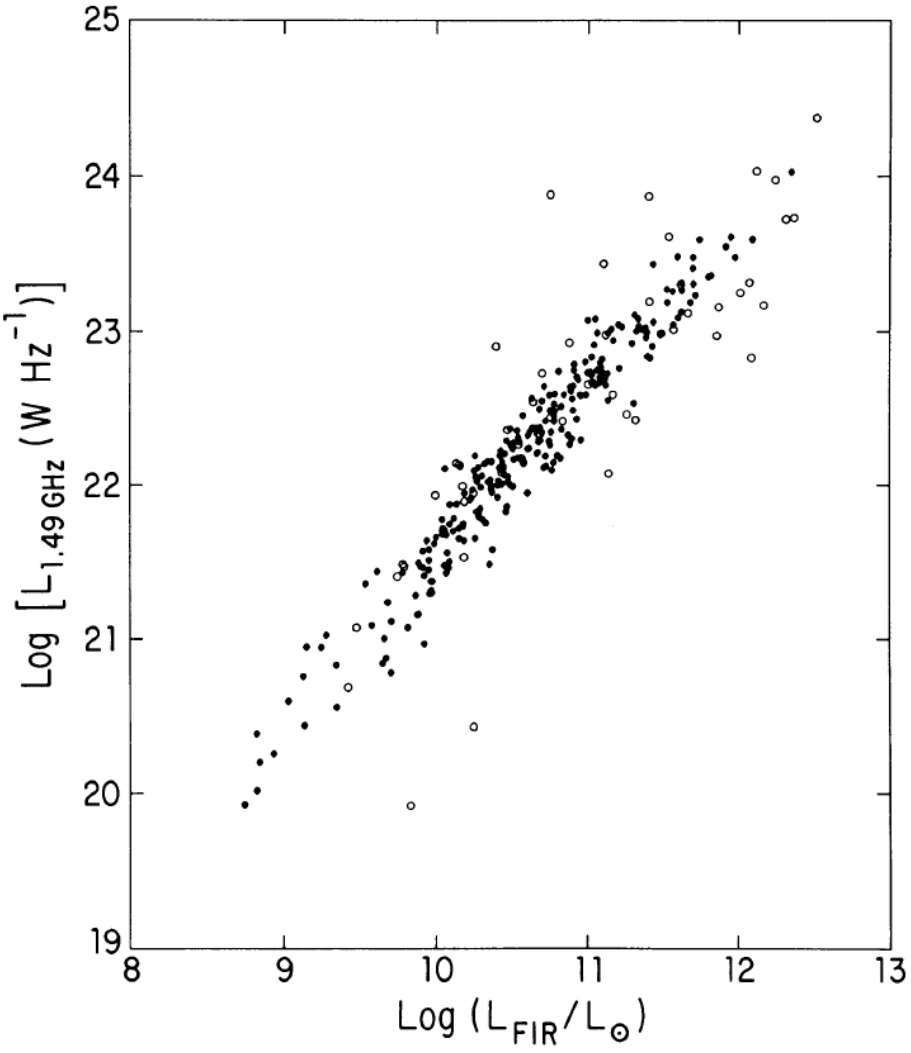

Figure 1.3: Figure taken from Condon et al. (2002). The correlation of far-infrared luminosities versus 1.49 GHz radio flux densities for a sample of 258 60μm selected galaxies (filled circles) with 55 AGN also shown (open circles).

1.2.2 Evolution of the Far Infrared - Radio Correlation

Evolution of the FIRC with redshift could provide clues about different conditions under which star formation takes place at higher redshift. Lacki et al. (2010a) predict evolution in the FIRC at high redshift from inverse Compton cooling loses due to the cosmic microwave background in galaxies with low average column densities resulting in a dimming of the radio flux density and therefore a change in the FIRC.

The FIRC has been studied with respect to redshift to determine if and how it evolves, and varying results have been found. Some claim evolution whereby the correlation may decrease slightly towards higher redshift (e.g. Seymour et al. 2009; Ivison et al. 2010a & b). However the majority find a constant correlation with redshift (Appleton et al. 2004; Jarvis et al. 2010; Michalowski et al. 2010; Sargent et al. 2010; Bourne et al. 2011).

1.3 UV Searches for High Redshift Galaxies

The identification of high-redshift galaxies is crucial to developing our understanding of the early Universe, galaxy evolution and the epoch of reionisation. Luminosity functions and star formation rate indicators are some of the tools used to characterise these early galaxies. Searches for the first galaxies began circa 1975 looking for spectroscopic features in the UV (see Giavalisco 2002 for a review).

1.3.1 The Lyman Break

The Lyman break is a discontinuity in the spectrum of star-forming galaxies. At low redshift, when the Universe is ionised (i.e. without a significant fraction of neutral hydrogen) it occurs at the Lyman limit (912 Å). It is located in the UV regime which is dominated by emission from massive stars. It forms as a result of the absorption by neutral hydrogen in the stellar atmospheres of massive stars short-ward of the Lyman limit ($\lambda = 912$ Å). As the light from the galaxy is redshifted and passes through clouds of neutral hydrogen, absorption will occur for photons that have been redshifted to 1216 Å. This results in a line blanketing due to absorption from neutral hydrogen at multiple redshift epochs known as the Lyman-α forest (see Figure 1.4 for a representation of the Lyman-α forest in the spectrum of a quasi-stellar object). Towards higher redshift and in to the epoch of reionisation, the amount of neutral hydrogen in the Universe increases, resulting in more severe absorption approaching total absorption by the Lyα forest at these epochs, as shown by the complete absorption of the Gunn-Peterson trough in Quasi-Stellar Object (QSO) spectra at $z > 6.2$ (Becker et al. 2001; Fan et al. 2002). This shifts the Lyman discontinuity or break to the rest-frame wavelength of 1216 Å.

1.3.2 The Lyman-Break Technique

Based on population synthesis models it was first proposed by Meier (1976a & b) that high redshift galaxies could be selected by searching for the Lyman-Break between two short wavelength filters (e.g. U and B). This has become

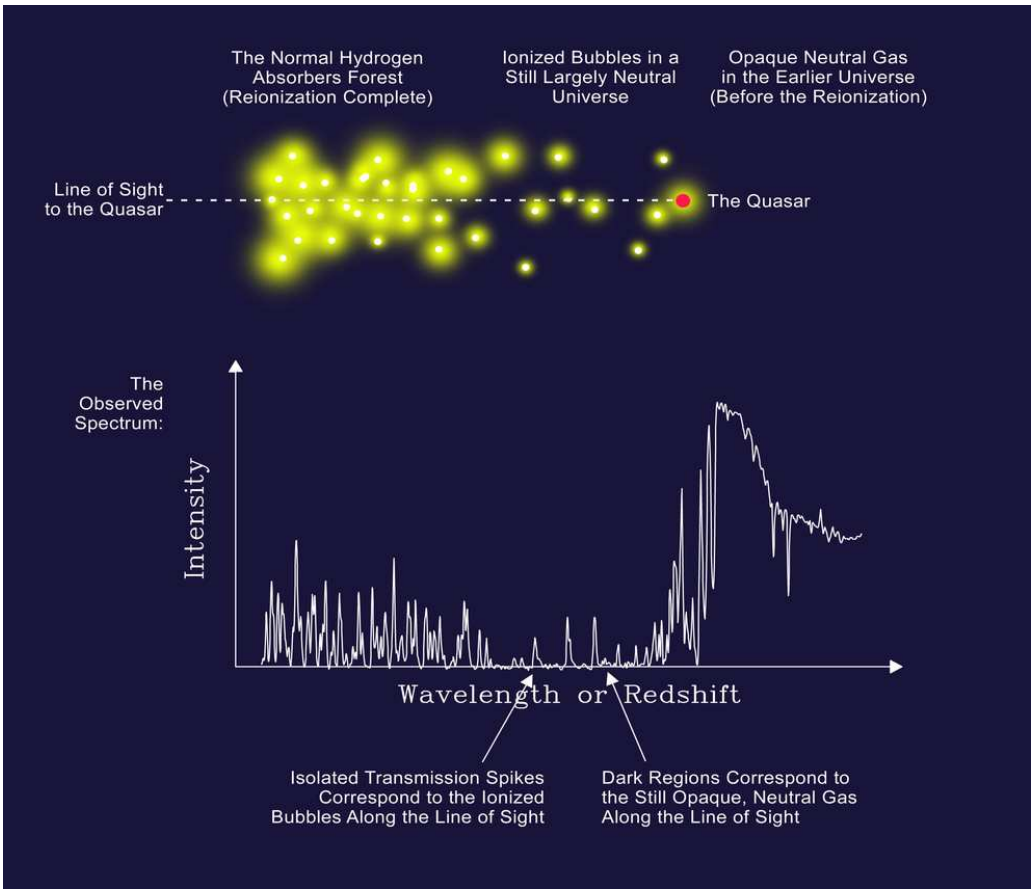

Figure 1.4: Figure showing the Lyman-α forest in the spectrum of a QSO as a result of absorption from intervening clouds of neutral hydrogen. Figure credit Djorgovski (http://www.astro.caltech.edu/∼george/reion/)

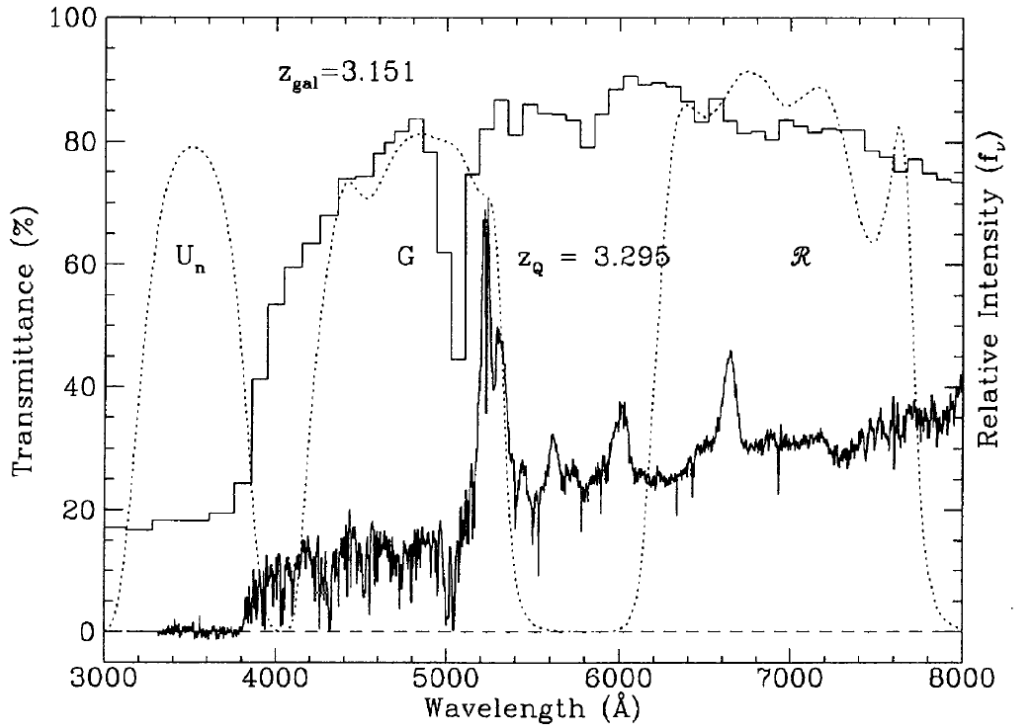

Figure 1.5: Figure from Steidel et al. (1995) showing the $z \sim 3$ Lyman break selection technique with U_n, G and R filters and a star-forming galaxy spectrum over-plotted. Also shown is the spectrum of a QSO also at $z \sim 3$.

known as the Lyman-Break technique (Guhathakurta et al. 1990; Steidel et al. 1995; Steidel et al. 1996) and is universal and adaptable, as it can be applied to both low and high redshift galaxies. The technique relies on finding a significant flux decrement between two broadband filters indicating a spectral break short-ward of Lyman-α at 1216 Å or the Lyman limit at 912 Å in the rest frame of the galaxy, attributable to absorption from neutral hydrogen. In higher-redshift galaxies this "Lyman break" is redshifted to longer wavelengths, therefore the choice of filters dictates the range of redshifts the survey probes.

The initial large surveys of Lyman-break galaxies primarily employed the U (3650Å), G (4750 Å) and R (6580 Å) filters which searched between $2.5 \lesssim z \lesssim 3.5$. The galaxies found in these initial surveys were coined U-drops due to their flux "dropping out" in the U-band. The U–drops with $R \sim 25.5$ proved to be an impressively reliable sample, with a 90 per cent success rate when confirmed from spectroscopic observations. The typical contaminants to this population are G- and K-type stars due their red $G-R$ colours (Steidel et al. 1996).

The technique was extended to $z \sim 4$ (Steidel et al. 1999) to search for the G-drop population, typically using G (4750 Å), R (6580 Å) and I (8060 Å) filters. However with increasing redshift, the accuracy with which these galaxies can be selected, decreases ($\approx$ 40 per cent success rate). The main contaminants to this selection arise from early type galaxies at $0.5 < z < 1$ (Steidel et al. 1999). This decrease in accuracy is partly due to the objects being fainter and the features moving to wavelengths where the sky is brighter.

More recently, the technique was successfully applied to $z \sim 6$ galaxies (the i'-drop population) with data from the *Hubble Ultra deep field* (H-UDF) (Beckwith et al. 2006) using *The Hubble Space Telescope* (HST). A significant number of $z \sim 6$ i'-drop galaxies were identified and spectroscopically confirmed by several authors (e.g. Bunker et al. 2003, 2004; Stanway et al. 2004; Bouwens et al. 2007).

1.3.3 Very High Redshift Lyman Break Galaxies at $z \sim 7-8$

Until recently, only a handful of galaxies were known at $z > 6.5$, selected through Lyman-break broad-band imaging (e.g. Bouwens et al. 2005, 2008) and also narrow-band imaging (e.g. Ota et al. 2008; Ouchi et al. 2010) for Lyman-α line emitting galaxies (see Section 1.3.6). The Wide Field Camera 3 (WFC3) is the latest addition to HST and with its two detectors covers UV through to the near infrared wavelengths. Due to its superior sensitivity and provision of access to longer wavelength data, it has already greatly increased our knowledge of the high redshift Universe ($z > 6$) and many authors have already used this instrument to push our knowledge to even higher redshift.

A number of z'- and Y-drops have been identified and the luminosity function at $z \sim 7-8$ has been determined (e.g. Bunker et al. 2010; Bouwens et al. 2010a & b; McLure et al. 2010). Bunker et al. (2010) have used the identification of 10 robust z-drops to provide a lower limit on the star formation rate density at $z \sim 7$ of $0.004 \mathrm{M}_{\odot} \mathrm{yr}^{-1} \mathrm{Mpc}^{-3}$. They find this density at $z \sim 7$ to be a factor of 10 (and 2) lower than that estimated at $z = 3-4$

(and $z = 6$). Vanzella et al. (2011) presented spectroscopic confirmation of two $z-$drop Lyman-break galaxies at $z \sim 7$ with SFRs of $\sim 8.9 M_{\odot} yr^{-1}$ and $\sim 9.4 M_{\odot} yr^{-1}$. The typical specific star formation rates (defined as the SFR per unit galaxy stellar mass) for Lyman-break galaxies at $z \sim 6.5$ are 1.9 ± 0.8 Gyr^{-1} (McLure et al. 2011).

A number of $Y-$drops ($z \sim 8-9$) over the H-UDF have also been identified (e.g. Bunker et al. 2010; Lorenzoni et al. 2011). Three bright $Y-$drops have been identified from a shallow wide-field parallel time survey by Yan et al. (2011) with $L > 2L^*$ and it is proposed that these galaxies could be the progenitors of massive Lyman-break galaxies found below $z \sim 5$.

The morphologies of $z \sim 7-8$ galaxies over the H-UDF have been found to be extremely compact, with little size evolution taking place from $z = 7$ to $z = 6$, indicating larger galaxies are built up over time towards lower redshift (Oesch et al. 2010). The $z \sim 7$ and $z \sim 8$ luminosity functions have been determined (e.g. Wilkins et al. 2010; Oesch et al. 2010) from a sample of 73 z'-drops and 59 Y-drops with indications for an extremely steep faint end slope ($\alpha \lesssim -1.7$) (Bouwens et al. 2011a). This steep faint end slope would imply that faint galaxies make a significant contribution to the total luminosity density at this epoch.

Spectral Slope

An important result from the recent WFC3 observations has been the increasingly blue spectral slopes observed for high redshift galaxies. Typically at $z \lesssim 6$, the spectral slope is $\beta \sim -2.2 \pm 0.2$ (Stanway et al. 2005) or $\beta \sim -2$ (Bouwens et al. 2008). Bouwens et al. (2011b) find blue slopes

($\beta \lesssim -2.5$), indicative of young ages, low to no dust attenuation and low metallicities. Finkelstein et al. (2010) studied a population of star forming galaxies between $6.3 < z < 8.6$ in the HUDF and also found bluer UV colours for $z \sim 7$ galaxies compared to local galaxies. Labbé et al. (2010) studied the infrared properties of a sample of 36 z'drops and three Y-drops in the HUDF. Using fitted spectral energy distributions (SEDs) and stellar synthesis population models, typical ages of > 100 Myr were determined. They also find a steepening of the blue Far-UV slope ($\beta \sim -2.5$) with decreasing luminosity possibly as a result of low metallicity. Indications of low metallicity in the highest redshift galaxies implies that there is little dust and that these galaxies reside in an epoch without significant enrichment from supernovae or stellar winds, this implies young ages, and that the galaxy may be mostly composed of hydrogen. However McLure et al. (2011) found no evidence for a significant steepening of the spectral slope ($\beta = -2.05 \pm 0.09$) using a robust sample of Lyman-break galaxies between $6.7 < z < 8$.

1.3.4 Evolution in the Lyman-Break Galaxy population

Initial indications for evolution in the Lyman-break galaxy population with redshift came from studies of the *Hubble Deep Field*, where the number density of Lyman-break galaxies at $z \sim 4$ was found to be lower than the number density at $z \sim 3$ (e.g. Madau et al. 1996; Madau et al. 1998). However owing to the small area covered by the *Hubble Deep Field* (≈ 5 square arcmin), this field only probed faint galaxies. Contradictory evidence was found from

larger area (0.23 square degree) ground based observations, where no evidence for evolution was found (e.g. Steidel et al. 1999). The luminosity functions determined from the $z \sim 3-4$ population allowed for the comparison of the number density of Lyman-break galaxies found at higher redshift epochs. There is now strong evidence for significant evolution in the population from $z \sim 3-4$ to $z \sim 6$ (Bunker et al. 2004; Stanway et al. 2004; 2007). Bunker et al. (2004) find that the SFR at $z \approx 6$ was six times less than at $z \approx 3$. Consistent with a decrease in the star formation rate with redshift, typical stellar masses and ages of Lyman break galaxies have also been shown to decrease with redshift from $M^*/M_\odot \sim 10^{10}$ at $z \sim 3$ to $M^*/M_\odot \sim 10^9$ at $z \sim 5-6.5$ (Papovich et al. 2001; Shapley et al. 2001; Eyles et al. 2005, 2007; Verma et al. 2007; Finkelstein et al. 2010; McLure et al. 2011).

As discussed above, the recent availability of WFC3 has enabled studies of galaxy populations beyond $z \sim 6$ out to $z \sim 8$. Evidence for significant evolution in the co-moving number density of Lyman-break galaxies from $z \sim 6$ to $z \sim 7$ has been found in the sense that the number density has decreased from $z \sim 6$ to $z \sim 7$ (e.g. Wilkins et al. 2010; Finkelstein et al. 2010). WFC3 observations also show evidence for evolution in the Lyman-break galaxy population from $z = 6-7$ to $z = 8-9$ (e.g. Lorenzoni et al. 2011). McLure et al. (2010) find evidence for evolution in the UV luminosity function with the comoving number density of galaxies reducing by a factor of ~ 2.5 between $z \sim 6-7$ and again by a further factor of ~ 2 between $z \sim 7-8$. Recent ground based studies have also shown a decrement in the number density of Lyman-break galaxies beyond $z = 6$ (Castellano et al. 2009; Hickey et al. 2010 - see Chapter 3).

1.3.5 Reionisation

$z > 6$ has been shown to be a crucial transition epoch in the history of the Universe. The discovery of complete absorption of the Lyman-α forest (the Gunn-Peterson trough) in the spectra of (QSOs) at $z > 6.2$ (Becker et al. 2001, Fan et al. 2002; Willott et al. 2005) indicates a large neutral fraction of hydrogen, and the Wilkinson Microwave Anisotropy Probe (WMAP) results suggest that the Universe was entirely neutral at $z > 10$ (Kogut et al. 2003) with a protracted period of reionisation (Dunkley et al. 2009). Hence, exploring the epoch $6 < z < 10$ is crucial if we are to understand what reionised the Universe, and thus set the stage for galaxy formation at the end of the "Dark Ages". Specifically, UV light from star forming galaxies during this era has been proposed as the most likely reionisation mechanism, as the number density of high-redshift active galactic nuclei (AGN) appears too low to be solely responsible (e.g. Dijkstra et al. 2004).

In Section 1.3.4, I discussed the evolution in the Lyman-break galaxy population, such that the comoving number density of galaxies decreases with redshift. Therefore the number density of these galaxies in the epoch $6 < z < 10$ needs to be quantified in order to determine if they were capable of reionising the Universe.

There is however, mounting evidence that star forming galaxies do not provide enough ionising flux beyond $z = 6$ to reionise the Universe without invoking a significant population of star-forming galaxies below the flux limit (i.e. a steep faint end slope), a top heavy IMF, low metallicities, and/or a high escape fraction of ionising photons (e.g. Bunker et al. 2010; Lorenzoni

et al. 2011; McLure et al. 2010).

Evidence for very low metallicities has been found in the extremely blue spectral slopes of the $z \gtrsim 7$ galaxies (see Section 1.3.3). Indications of a significantly steeper faint end slope of the luminosity function have also been found (Bouwens et al. 2011a; Oesch et al. 2010) whose gradient generally increases with redshift, 1.79 ± 0.12 ($z \sim 5$), 1.73 ± 0.20 ($z \sim 6$), 2.01 ± 0.21 ($z \sim 7$) and 1.91 ± 0.32 ($z \sim 8$). Although there is significant uncertainty on the slopes, the authors find it possible for the abundant low luminosity galaxies, implied by the steep slope, in conjunction with the less abundant more luminous galaxies to be responsible for reionisation.

1.3.6 Lyman-α Emitters

The first surveys that carried out searches for high redshift galaxies based on their UV spectral features were surveys searching for the Lyman-α (Lyα) emission line at 1216 Å using narrow band filters. Lyα emitters are galaxies identified through their strong Lyα emission. Lyman-break galaxies and Lyα galaxies are thought to be part of the same population. It has been proposed that the large equivalent widths (EW) found in the Lyα emitters of EW$\gg$ 100 Å (rest-frame) may be an early stage of evolution in a starburst galaxy where the stars have a low to no metal content (therefore no absorption from dust) and a top heavy IMF resulting in extremely bright UV emission (Malhotra & Rhoads 2002).

The first surveys for Lyα emitters searched around QSOs, due to the assumed increased probability of finding a galaxy near another galaxy due to

enhanced clustering (Djorgovski et al. 1985). Searching in this environment was also advantageous in that, the wavelength of the narrow band filter could be adjusted given the redshift of the QSO. The technique consisted of combining both a broadband and narrow band filter. The broadband filter would measure the continuum close to Lyα in order to establish a base line from which any excess could be measured. The narrow band filter would then sample the wavelengths covering the potential Lyα and any excess in this filter above the continuum derived from the broadband filter could be attributed to Lyα emission. The first galaxy detected using this technique was around a QSO at $z \sim 3.2$ (Djorgovski et al. 1985). A number of high redshift galaxies have since been detected in this manner (e.g. Steidel et al. 1991; Hu & Cowie 1987; Cowie et al. 1998; Rhoads et al. 2000; Hu et al. 2002; Ajiki et al. 2003; Ouchi et al. 2010; Kashikawa et al. 2011).

Shimasaku et al. (2006) find that Lyman-break galaxies with fainter UV continua have larger Lyα equivalent widths (EWs). They find that almost all star-forming galaxies at $z \sim 6$ have Lyα emission with rest-frame EWs$>$ 20 Å and also $\sim$ 80 per cent of Lyman-break galaxies at $z \sim 6$ have Lyα rest-frame EW$\gtrsim$ 100 Å. This is very different to the lower redshift picture implying drastic evolution in the Lyα properties. Metal-free populations or top-heavy IMFs are required to explain Lyman-α emitters with EWs$\gtrsim$ 200 Å (Shimasaku et al. 2006).

1.4 Infrared Luminous Galaxies

In this section, I discuss the information that has been gleaned from studying infrared luminous galaxies.

1.4.1 The Cosmic Infrared Background Radiation

The cosmic background radiation of the Universe is composed of unresolved sources and spans the entire electromagnetic spectrum, from gamma rays all the way to radio waves. The most significant peak in this background is due to the cosmic microwave background (CMB; Penzias & Wilson 1965; Smoot et al. 1992; see Figure 1.6). This is followed by the cosmic ultraviolet /optical background (COB) and the cosmic infrared background (CIB). Until NASA's Cosmic Background Explorer (COBE) satellite was launched in 1989, and even for some time after that, only upper limits on the CIB were available. COBE hosted two instruments: the Far Infrared Absolute Spectrometer (FIRAS) covering wavelengths between 100 and 10,000μm and the Diffuse Infrared Background Experiment (DIRBE) covering wavelengths between $1.25-240\mu$m. Puget et al. (1996) claimed the first tentative detection of the CIB from COBE using FIRAS and the first tentative detection of the CIB from the DIRBE data was claimed by Schlegel et al. (1998). Since then the CIB has been characterised with observations using many facilities such as The Infrared Space Observatory (ISO; Kessler et al. 1996) at 2.4-197μm, the Submillimetre Common-User Bolometer Array (SCUBA; Holland et al. 1999) at $350-2000\mu$m and the *Spitzer* Space Telescope (Werner et al. 2004) at 3.6-160μm.

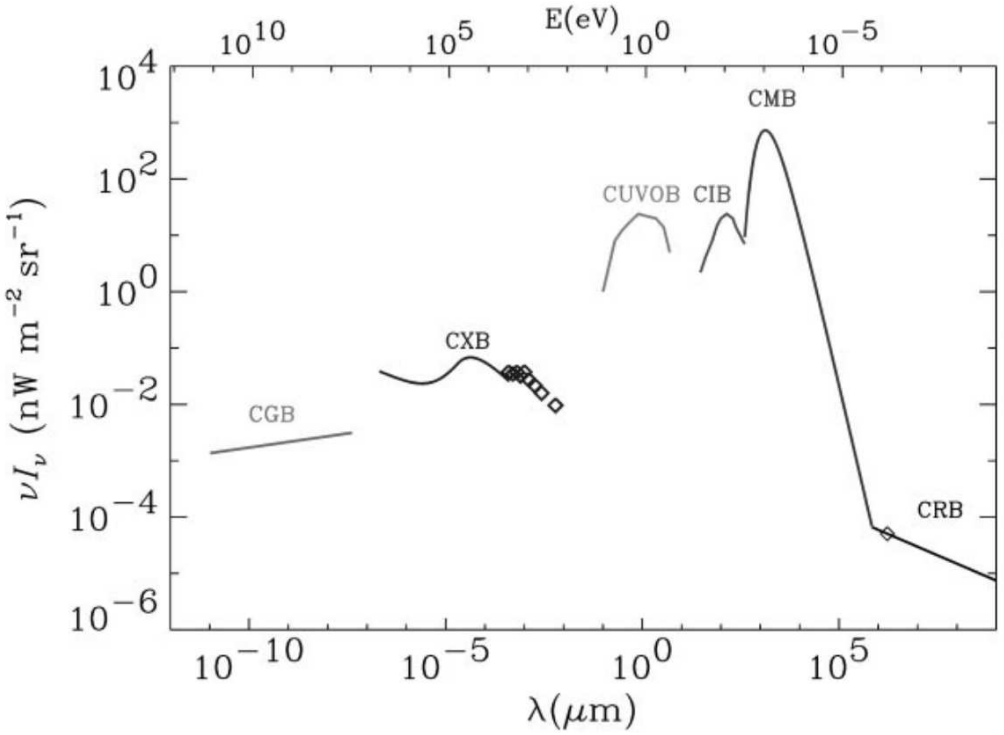

Figure 1.6: Figure and caption from Hauser & Dweck (2001). Spectrum of the cosmic background radiations. The radio background (CRB) is represented by a $\nu I_\nu \propto \nu^{0.3}$ spectrum, normalised to the Bridle (1967) value at 170cm. The cosmic microwave background (CMB) is represented by a blackbody spectrum at 2.75K. The UV-optical (CUVOB) and infrared (CIB) backgrounds are schematic representations of the work summarised in the review by Hauser & Dweck (2001). The data for the X-ray background (CXB) are taken from Wu et al. (1991), and the curves are analytical representations summarised by Fabian & Barcons (1992). The γ-ray background (CGB) is represented by the power law given by Sreekumar et al. (1998).

The CIB is composed of all of the emitted UV-optical light, associated with galaxy formation, that has been absorbed by dust and re-emitted in the infrared. This makes it fundamentally important if we are to understand the formation and evolution of galaxies over cosmic time. The CIB is just as bright as the COB and both have brightnesses of $24\text{nWm}^{-2}\text{s}r^{-1}$ (Dole et al. 2006). This implies that over cosmic time, galaxies emit equal amounts of their bolometric luminosity at optical and infrared wavelengths (see Figures 1.6 & 1.7). This was first established by Low & Tucker (1968) and Kleinmann & Low (1970a,b) who looked at extragalactic sources in the mid-infrared.

1.4.2 Luminous and Ultra-Luminous Infrared Galaxies

When Dole et al. (2006) examined the contributions of infrared galaxies to the far-infrared background it was discovered that the galaxies with the singular greatest contribution to the total CIB are Luminous Infrared Galaxies (LIRGS) at $z \approx 1$. This implies that these galaxies can tell us a great deal about the star formation history of the Universe.

Luminous Infrared Galaxies (LIRGs) and Ultra-Luminous Infrared Galaxies (ULIRGS) are defined as having total infrared luminosities from $10^{11} - 10^{12} L_{\odot}$ and $10^{12} - 10^{13} L_{\odot}$ respectively. As their name implies, LIRGS and ULIRGS are extremely bright at infrared wavelengths. This is due to dust absorbing ultra-violet (UV) light, from star formation and/or Active Galactic Nuclei (AGN) and re-emitting it at the longer infrared wavelengths. The dust that gives rise to these extremely bright infrared luminosities is produced and introduced to the interstellar medium (ISM) via stellar winds, the

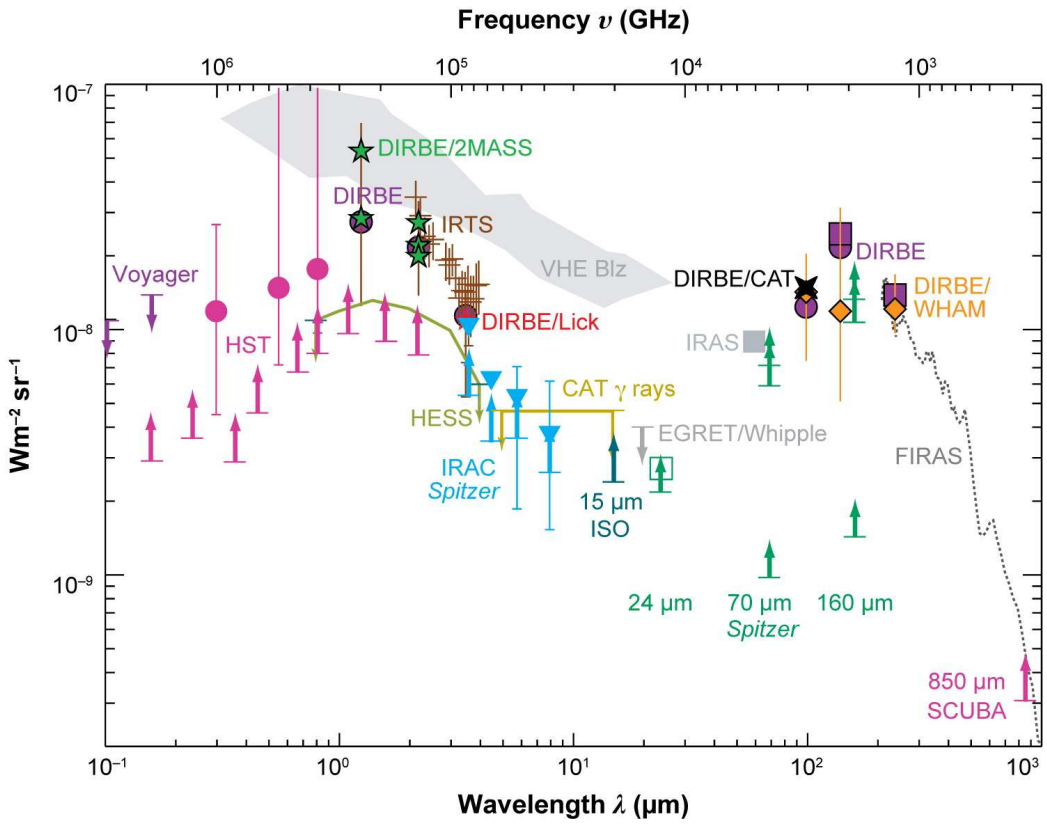

Figure 1.7: Figure and caption from Soifer et al. (2008): The extragalactic background light spectral energy distribution from 0.1 to 1000μm, adapted from Dole et al. (2006). At Spitzer wavelengths from 24 to 160μm, the green arrows are lower limits based on directly observed sources. The higher green arrows at 70 and 160μm are based on stacking numerous 24μm detections, as discussed in Dole et al. whereas the highest green arrows at these wavelengths reflect the estimated contribution of all 24μm sources, including those beyond the sensitivity limit of the stacking analysis. The green open square is the estimated 24μm background when these faint sources are included. Note that the corrected 70 and 160μm background estimates from the MIPS data are essentially equal to the backgrounds estimated at these wavelengths by other techniques. See Dole et al. (2006) for identification of the other data sets and background estimates included in this figure.

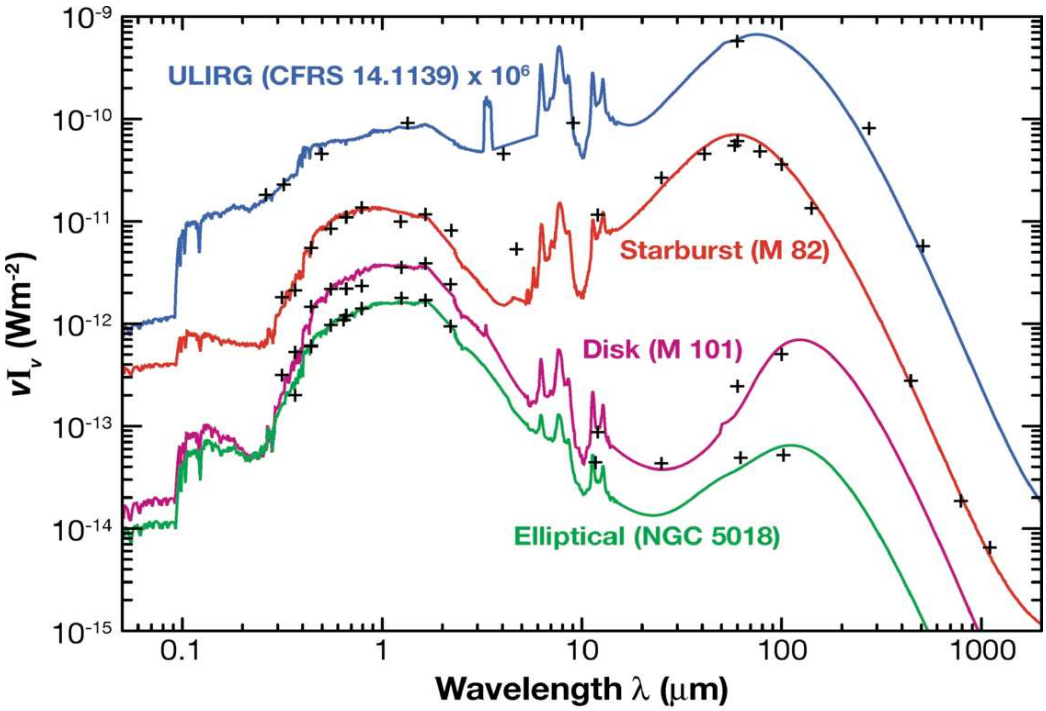

Figure 1.8: Figure taken from Lagache et al. (2005) showing the spectral energy distributions of an elliptical, disk, starburst and ULIRG type galaxy and their increasing far-infrared contribution to bolometric luminosity with increasing star formation rate.

supernovae of massive stars and outflows from AGN.

By the 1980's it was already known that some late-type galaxies could produce as much and sometimes even more of their luminosity in the infrared. The source of this emission was accepted as thermal emission from dust (Rieke & Lebofsky 1978; Telesco & Harper 1980; Scoville et al. 1982). These infrared bright galaxies were first identified by Kleinmann & Low (1970) using ground-based telescopes and observations between 1 and 25μm, and in large numbers using IRAS (Soifer et al. 1987b) (see section 1.1.5).

Numerous studies have contributed to our understanding of these bright galaxies such as Sanders et al. (2003) and Soifer et al. (1987a & b) who showed that the infrared luminous galaxies discovered by IRAS are the most numerous objects at $L_{\rm IR} > 10^{11} L_{\odot}$ in the local Universe and that these galaxies emit most of their bolometric luminosities at infrared wavelengths as a result of dust obscured star formation (See Figure 1.8 for a comparison of the increase in far-infrared emission to the total bolometric luminosity of a galaxy with increasing star formation rate). Locally, LIRGs and ULIRGs contribute $\sim 9 \pm 1$ per cent and $\sim 0.6 \pm 0.2$ per cent respectively to the star formation rate distribution function (Bothwell et al. 2011; Goto et al. 2010). Soifer et al. (1984) examined 86 galaxies from the IRAS mini-survey and found that up to 25 per cent were interacting galaxies and suggested that the galaxy interactions may be important in triggering the star bursts.

Galaxies in the local Universe emit roughly a third of their bolometric flux in the far infrared. In order for the magnitude of the COB and the CIB to be approximately equal, galaxies at higher redshift ($0 < z < 2$) must be emitting a larger percentage of their flux at infrared wavelengths. Strikingly, in some cases, more than 95 per cent of the energy of ULIRGs is emitted in the far-infrared. Schiminovich et al. (2005), and more recently Magnelli et al. (2009) found the UV luminosity density is five times smaller than the infrared luminosity density at $z \sim 1$, implying that the bulk of star formation is obscured by dust at high redshift.

LIRGs have typical star formation rates of between 10 and $100\,{\rm M}_{\odot}{\rm yr}^{-1}$ and ULIRGs have SFR$> 100\,{\rm M}_{\odot}{\rm yr}^{-1}$ which is extremely intense compared to the SFR of the Milky Way ($\sim 3{\rm M}_{\odot}{\rm yr}^{-1}$). LIRGs at $z \approx 0.5$ have been

found to contain a range of stellar masses typically between $10^{10} - 10^{12}\mathrm{M}_{\odot}$ (Kartaltepe et al. 2010). The star forming regions in LIRGS and ULIRGS are young with typical ages of $10^{7} - 10^{8}$yr (Genzel et al. 1998).

While LIRGs and ULIRGs are rare in the local Universe, their number density has been found to strongly increase with redshift (Soifer et al. 1989). A number of studies (Babbedge et al. 2006; Caputi et al. 2007; Magnelli et al. 2009, 2011) have characterised the evolution of the infrared galaxy population with redshift. They have consistently found strong positive luminosity evolution and there is also some evidence for density evolution. For example, Magnelli et al. (2009) found that LIRGs increase in number density by a factor of ~ 40 from $z = 0$ to $z \sim 1$ and that ULIRGs increase by a factor of ~ 100 over the same redshift range. Using *Spitzer* 24 μm data, Le Floc'h et al. (2005) found the density evolution of the infrared luminosity function of the LIRGs and ULIRGs to be less pronounced than the luminosity evolution, however there is considerable degeneracy between these scenarios.

At $z > 1$, LIRGs and ULIRGs represent the bulk of the observed star formation (e.g. Hughes et al. 1998) and have been found to contribute between $\sim 51 - 70$ per cent of the total co-moving energy density in the infrared at $z \sim 1$ (Le Floc'h et al. 2005; Magnelli et al. 2009; Rodighiero et al. 2010), i.e. they dominate the star formation rate at $z \sim 1$. This contribution increases to $\sim 66 - 93$ per cent at $z \sim 2$ (Caputi et al. 2007; Rodighiero et al. 2010; Magnelli et al. 2011).

At longer wavelengths, the Balloon-borne Large Aperture Submillimetre Telescope (BLAST; Scott et al. 2001) surveyed the sky at 250, 350 and 500μm as a precursor to *Herschel*. BLAST selected moderately-high star forming

galaxies out to $z \sim 1$, approximately $20 - 25$ per cent of which contain an AGN (Eales et al. 2009; Moncelsi et al. 2011). There is evidence for strong positive evolution in the population and also in the dust-mass function out to $z = 1$ (Eales et al. 2009). The population of galaxies at $z < 0.9$ detected by BLAST have median stellar mass of $\sim 10^{11} M_{\odot}$ and are typically spiral in morphology (Moncelsi et al. 2011). Studies of the star formation history with BLAST have confirmed that the majority of star formation out to $z \sim 1$ is dust obscured and increases steadily out to this epoch (Pascale et al. 2009).

With the recent launch of the *Herschel* space observatory, studies of luminous infrared galaxies can be extended to much greater depths. Elbaz et al. (2010) have shown that below $z = 1.5$, estimates of the total infrared luminosity based on mid-infrared data agree well with observations from *Herschel* at the far infrared and submillimetre wavelengths. Using the *Herschel* Multi-tiered Extragalactic Survey (HerMES) Vaccari et al. (2010) provided a measurement of the local ($0 < z < 0.2$) submillimetre luminosity function and determined the local luminosity density of far-infrared-selected galaxies to be $1.31^{+0.24}_{-0.21} \times 10^{8} L_{\odot}\,\mathrm{Mpc}^{-3}$. Using the wide-area *Herschel*-ATLAS (Eales et al. 2010a), Clements et al. (2010) found a sharp rise in the number counts of galaxies at the 250, 350 and 500 μm wavebands, indicating the increasing population of far-infrared selected galaxies towards higher redshift (see also Amblard et al. 2010) as the longer wavelength data samples the far-infrared peak out to higher redshift. Using the same data set, Dye et al. (2010) measured the 250μm luminosity function and found significant evolution in the population out to $z = 0.5$. While Eales et al. (2010b), using *Herschel*-HerMES, examined the evolution in the 250μm luminosity function

and found strong evolution out to $z = 1$ and little or no evolution between $1 < z < 2$.

1.4.3 Environments

Since the first indications that the extremely bright luminosities of infrared galaxies were due to star formation triggered by strong interactions and/or mergers, numerous studies have been conducted in order to characterise their environments.

A logical way to determine whether a galaxy is merging or not is to examine its optical morphology (See Figure 1.9). Wang et al. (2006) classified the morphological components of a sample of 159 local ($z < 0.1$) LIRGs from the Sloan Digital Sky Survey (SDSS) and found ≈ 48 per cent to be interacting galaxies or mergers and ≈ 40 per cent to be spiral galaxies. ULIRGs at low redshift ($z < 0.25$) have an even greater merger/disturbed fraction of > 91 per cent (Clements et al. 1996).

Estimates of the total major merger fraction out to $z = 1$ for both LIRGs and ULIRGs are a little lower, however there is evidence for an increasing merger rate with redshift (out to $z \sim 1$). Approximately $50 - 80$ per cent and $\approx 25 - 50$ per cent of ULIRGs and LIRGs respectively out to $z = 1$ show evidence of mergers or interactions (Shi et al. 2009; Kartaltepe et al. 2010). Beyond this redshift the rate of mergers seems to decrease to $30 - 40$ per cent for ULIRGs, however this should only be considered a lower limit due to the uncertainties and the difficulty of morphological classification at higher redshift (Kartaltepe et al. 2010).

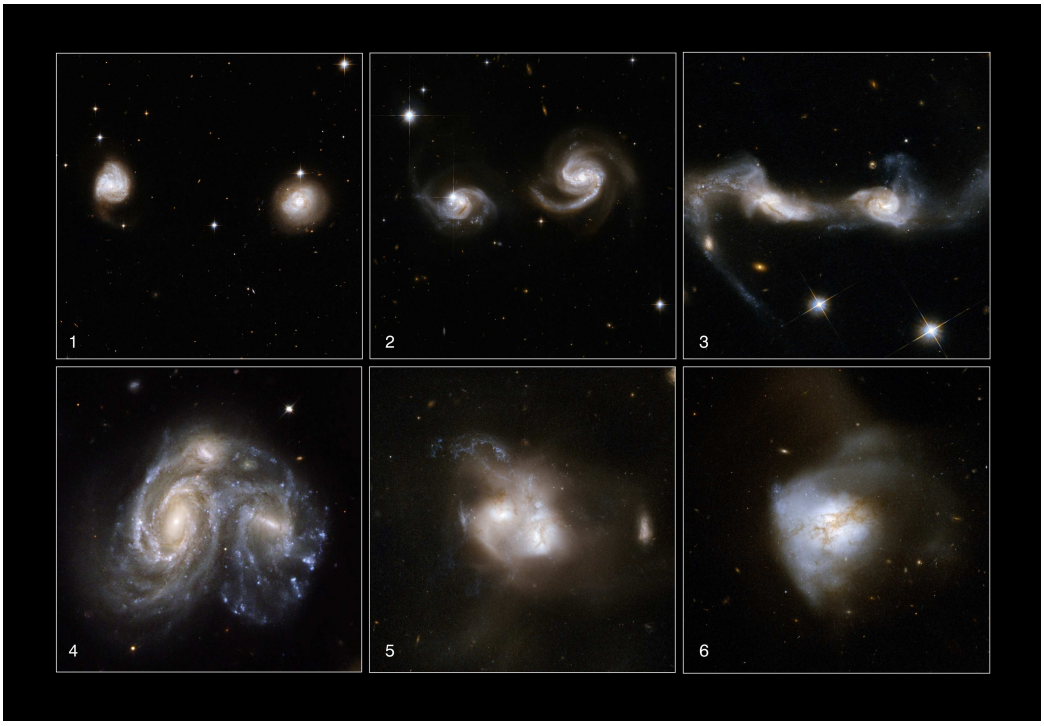

Figure 1.9: Panels: 1) The progenitors of ULIRGs are thought to be pairs of similarly sized gas rich galaxies. 2) As the galaxies begin to interact tidal streams will likely be created. 3) An early epoch of star formation may occur as the galaxies begin interacting. 4-5) As the merger progresses, and the nuclei coalesce, strong torques produce strong inflows towards the central regions fuelling star formation and possibly AGN. 6) (Arp 220) The resulting ULIRG may be highly disturbed, bearing the mark of its merging formation. Image credit: NASA, ESA, the Hubble Heritage Team (STScI/AURA)-ESA/Hubble Collaboration and A. Evans (University of Virginia, Charlottesville/NRAO/Stony Brook University), K. Noll (STScI), and J. Westphal (Caltech)

In a sample of 56 LIRGs, Ishida (2004) found all those with $L_{IR} > 10^{11.5} L_{\odot}$ to be strongly interacting merger systems. LIRGS with $L_{IR} < 10^{11.5}$ were found to typically be single galaxies not undergoing a merger but possibly a minor interaction, yet still rich in molecular gas and representing the high luminosity end of normal star-forming disk galaxies. These results do agree with the picture of an increasing number of interacting and/or merging galaxies out to $z = 1$.

A study of the IRAS 1Jy sample of ULIRGs with optical and near-infrared imaging (Kim et al. 2002) revealed none of the sources to be in the first pass stage of a merger. Interestingly though, 56 per cent were found to have a disturbed single nucleus indicating that they were in the later stages of a merger (Veilleux et al. 2002). Further support for a merger scenario comes from evidence of young stellar clusters $\approx 10^7 - 10^8$ yr in LIRGs and ULIRGs and a tendency for compact nuclei (Scoville et al. 2000). There is also evidence that LIRGs and ULIRGs may form from multiple mergers. Up to 20 per cent of ULIRGs have been found to display evidence of a multiple merger through identification of multiple nuclei in their cores (Borne et al. 2000).

Locally, LIRGs and ULIRGs do not preferentially occur in high density environments such as galaxy clusters, however they are dependent on the distance to their nearest neighbour and its morphology. The probability of a galaxy being a (U)LIRG increases as its neighbour approaches a late-type galaxy (Hwang et al. 2010). The infrared luminosity of a galaxy and consequentially its SFR, also increases with this effect. Up to $z = 1$ the number of (U)LIRGs decreases with increasing density [i.e. as the density of

an environment rises, the probability of finding a (U)LIRG there falls (Patel et al. 2009; Feruglio et al. 2010)].

Star formation in general, is also preferentially found in lower density regions in the local Universe (Dressler et al. 1997) and (U)LIRGs being highly star-forming objects follow this trend. Longer star formation timescales and lower SFRs are associated with higher density environments locally. However at $z = 1$ the total SFR appears to turn around and is actually higher in more dense environments (Elbaz et al. 2007). However it may be that the total SFR has increased but the specific SFR (the SFR divided by the stellar mass of the galaxy), may be similar to what is found locally (Cooper et al. 2008). The evidence showing higher rates of star formation in the past, in higher density regions may imply that the higher mass objects in the Universe formed the bulk of their stars earlier and the clusters are now virialised thereby not inducing mergers at lower redshift. Therefore the star formation activity will then be focused in the single gas-rich galaxies that will continue to form their stars down to a lower redshift.

1.4.4 Active Galactic Nuclei

As previously stated, LIRGs and ULIRGs are extremely important for characterising the star formation history of the Universe. Their extreme far infrared luminosities are indicative of dust obscured star formation, but could also be, in part, a product of AGN. Determining the relative contribution of AGN to the population is therefore necessary to gain a better understanding of the cosmic star formation history.

Warm colours, defined from the IRAS wavebands as $F_{25\mu m}/F_{60\mu m} \gtrsim 0.2$ are attributed to significant contribution from an AGN and have been used as such to identify active galaxies among infrared luminous galaxies (de Grijp et al. 1985). AGN have been found to contribute in 15-35 per cent of cool ULIRGs, however this fraction rises to 50-75 per cent in warm ULIRGs (Veilleux et al. 2009). A study of the far-infrared colours and SEDs of 51 nearby galaxies using Herschel SPIRE data has strengthened the assertion that AGN produce warmer colour temperatures compared to spiral galaxies whose luminosity is produced by star formation. Mid-infrared spectra have been used to discern the relative contributions of star formation and AGN to infrared luminosities of these types of galaxies. Tran et al. (2001) used this technique to find that at $L_{IR} > 10^{12.5} L_{\odot}$ AGN begin to dominate the infrared luminosity output.

The contribution from AGN is now widely believed to increase with increasing infrared luminosity (Goto et al. 2005; Alonso-Herrero et al. 2011). A recent study (Goto et al. 2011) with a large sample of (2357) local infrared galaxies from the AKARI all-sky survey, which covered 9, 18, 65, 90, 140 and 160μm, finds the contribution from AGN increases by $25 - 90$ per cent in the luminosity range of $L_{IR} = 10^{9} - 10^{12.5} L_{\odot}$. The AGN component is found to become dominant at $L_{IR} > 10^{11} L_{\odot}$. However, Symeonidis et al. (2010) found in a sample of 61 70μm selected galaxies (which more accurately traces star formation due to its sensitivity to cooler dust emission), that all were primarily powered by star formation with the fraction of starburst galaxies, LIRGs and ULIRGs containing AGN to be 0, 11 and 23 per cent respectively.

1.4.5 Evolutionary Paths

The dramatically increasing numbers of these bright infrared galaxies with redshift and therefore the lack of them at low redshift, in addition to the apparent lack of a post-ULIRG type object suggests that these objects transition in to another form within a short timescale.

The merging scenario offers an explanation for the extremely bright luminosities and high SFRs, as the probability of a galaxy showing signs of a merger (such as shells and tidal tails) increases with increasing total infrared luminosity (See Section 1.4.3). For a pictorial representation of a merging event with images from HST see Figure 1.9.

The progenitors of ULIRGs are most likely pairs of similarly sized gas-rich galaxies (Sanders, Scoville & Soifer 1991; Downes, Solomon & Radford 1993; Solomon et al. 1997; Veilleux et al. 2002). Many merging scenarios predict at least two epochs of star formation (e.g. Barnes & Hernquist 1996; Mihos & Hernquist 1996; Springel et al. 2005). The initial burst of star formation coincides with the first pass of a merger system as gas is syphoned to the central nuclear regions. As the merger progresses and the nuclei begin to coalesce, strong torques create inflows of gas towards the nucleus. These torques in the final stages of a merger can result in huge concentrations of gas in the cores and has been predicted with numerical simulations (e.g. Barnes & Hernquist 1996; Mihos & Hernquist 1996; Naab & Burkert 2003) and observed in the central kpc regions (Downes & Solomon 1998). These strong inflows in the final stage of a merger result in a later but often more intense epoch of star formation.

The compact and extremely bright nature of the nuclei in typical ULIRGs indicates they are associated with these late stages of a merger when the inflow of gas is peaking and therefore the nucleus of the merger has a huge reservoir of gas for star formation and/or an AGN.

It is also possible for a strong interaction to trigger star formation and ignite an AGN (Koulouridis et al. 2006; Sijacki et al. 2007; Di Matteo et al. 2008). As a nearby galaxy approaches, it can trigger the movement of molecular clouds to the centre of the galaxy simultaneously generating starburst activity in the nucleus and providing fuel for an AGN. In both cases, strong interactions and mergers may result in centrally concentrated star formation and an AGN. Widespread shocks due to late merging activity have been inferred from integral field spectroscopy of two local ULIRGs (Rich et al. 2011). Galactic superwinds are extremely common in infrared luminous galaxies that have $SFR > 10\mathrm{M}_{\odot}\mathrm{yr}^{-1}$, based on measurements of the Na I D interstellar absorption line and is also applicable to ULIRGs containing an AGN (Rupke et al. 2005). These shocks and winds may be a result of stellar winds from massive stars, supernovae and outflows from AGN. These strong galactic winds and the conversion of gas in to stars may eventually lead to a significant reduction in the star formation rate and also to the revelation of an unobscured AGN (i.e. visible in the optical).

There is significant support for the theory that some cool ULIRGs, as an AGN develops, may become warm ULIRGs, that appear similar to Seyferts (star-forming galaxies also containing a contribution from a low luminosity AGN) and eventually evolve in to a QSO (Sanders et al. 1988; Surace et al. 1998; Surace & Sanders 1999,2000;Veilleux et al. 2002, 2009). Although a

significant proportion of ULIRGs show no indication of Seyfert activity, other studies do not support the idea that cool ULIRGs evolve in to warm ones due to the little difference they find in the ages of the Young Stellar Populations (YSPs) in both types, indicating that the AGN has not ignited $> 100\,\mathrm{Myr}$ after the main epoch of star formation in the nuclei of cool ULIRGs. Models have also shown that it is possible for star formation alone to produce the warm colours (Younger et al. 2009).

However a number of possible transition objects between ULIRGs and QSOs have been identified. One such galaxy is IRAS F13308+5946. This object has features indicative of a Seyfert galaxy with star formation contributing $\sim$ 70 per cent to the infrared luminosity. Optical observations indicate the galaxy is in the late stage of a merger and extrapolations of the past infrared luminosity suggest a ULIRG phase (Meng et al 2010). A study by Kawakatu et al. (2006) examined ULIRGs containing a type 1 (unobscured) Seyfert nuclei and found that these objects could be in a transition stage between ULIRG and QSO.

Eventually the reservoir of the AGN itself may be depleted and the remaining star formation significantly reduced, this could result in an object similar to the present day elliptical galaxies. This is supported by typical central gas densities in ULIRGs being comparable to stellar mass densities in intermediate mass ellipticals (Kormendy & Sanders 1992). ULIRGs and L^* ellipticals lie near one another on the fundamental plane (Tacconi et al. 2002), and the brightness profiles of Seyferts, warm ULIRGs and those with $L_{IR} > 10^{12} L_{\odot}$ have comparable fits to an elliptical with an $R^{1/4}$ profile (Veilleux et al. 2002).

1.4.6 High-redshift Submillimetre Galaxies

The longer wavelengths of the CIB (the submillimetre emission) is generated from contributions of sources at higher redshift (i.e. the majority of the 500μm background was produced at $z > 1$). Submillimetre galaxies are massive star-forming galaxies at high redshift (typically $z \approx 2.2$ Smail et al. 2000; Chapman et al. 2005) analogous to more local ULIRGS but with SFR$\sim$ $1000\,\mathrm{M_{\odot}yr^{-1}}$ (Ivison et al. 2000; Alexander et al. 2005). Their extremely bright far-infrared emission has been shifted further in to the submillimetre wavelengths, but owing to the shifting of the far-infrared peak with redshift, positive k-corrections allow these galaxies in theory, to be observable out to high redshift ($z \sim 5$) at submillimetre wavelengths.

SCUBA (Holland et al. 1999) imaged the sky at 350, 450 and 850μm, revealing submillimetre galaxies and resolving ~ 30 per cent of the background at 850μm (Smail et al. 1997). The SCUBA HAlf Degree Extragalactic Survey (SHADES Mortier et al. 2005; Coppin et al. 2006), was designed to investigate submillimetre galaxies in the context of massive dust enshrouded star formation activity over cosmic time, examining clustering, AGN contribution, and to determine if they are the progenitors of present day massive ellipticals.

Mergers and interactions are important for triggering bursts of star formation in LIRGs and ULIRGs and it has been shown through optical morphologies that this mechanism remains important for submillimetre galaxies at high redshift (Smail et al. 1998). Typical SCUBA sources have been found to form significant fractions of their stellar mass in an early period of star

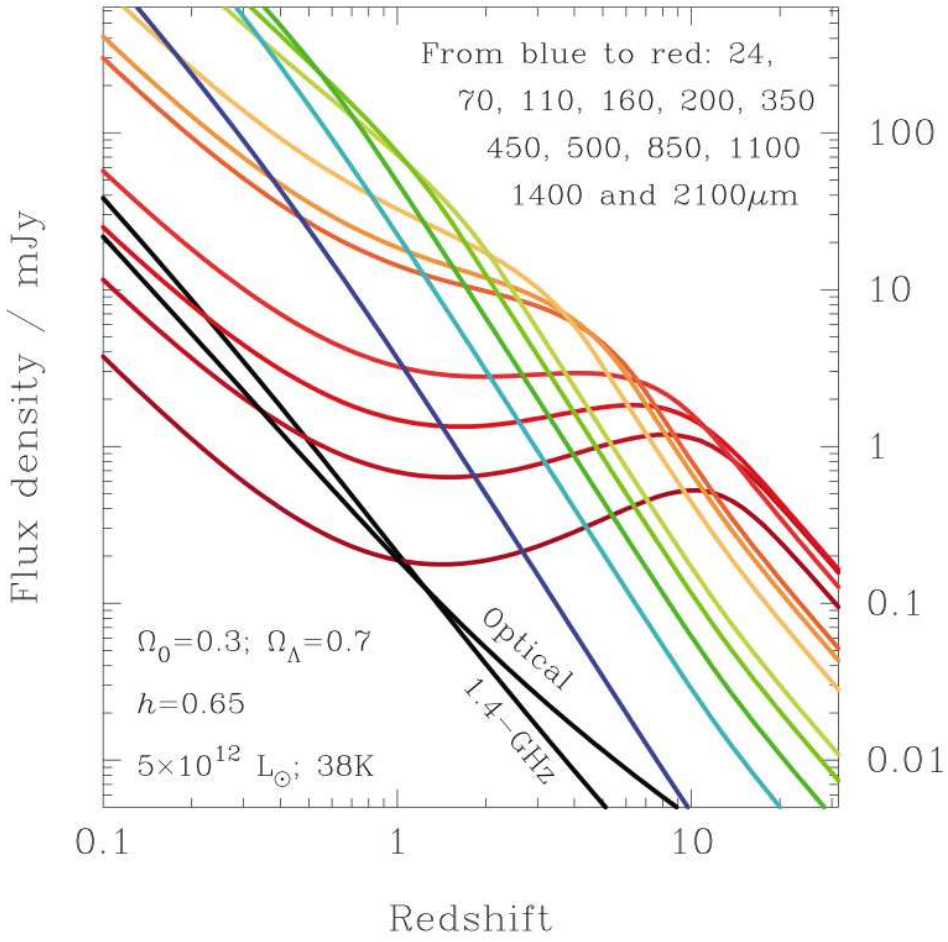

Figure 1.10: Figure taken from Blain et al. (2002) showing the positive k-correction with redshift for galaxies selected at multiple far-infrared to submillimetre wavelengths.

formation, and the remainder in a shorter more intense burst at later times (Dye et al. 2008), consistent with the merger formation theory proposed for LIRGs and ULIRGs (see Section 1.4.5). AGN are thought to be present in approximately 10 per cent of submillimetre galaxies, however they are not believed to contribute significantly to the bolometric luminosity (Clements et al. 2008), meaning that submillimetre galaxies are predominantly powered by star-formation with little to no contribution from AGN.

As ULIRGs are thought to evolve in to present day L^* ellipticals (see Section 1.4.5), their high redshift massive counterparts are thought to evolve in to present day massive ellipticals (Lilly et al. 1999; Scott et al. 2002; Dunne et al. 2003). The Sérsic index ($n \approx 2$) that fits the light profiles of submillimetre galaxies well, indicates that the stellar structure is similar to that of an elliptical galaxy (Swinbank et al. 2010; Targett et al. 2011). They also have stellar densities similar to or greater than local early-type galaxies. Submillimetre galaxies are also consistent with the picture of decreasing star formation activity occurring in higher density environments locally (see Section 1.4.3) reversing for $z \gtrsim 1$ (Serjeant et al. 2008). Luminous submillimetre galaxies contribute ≈ 20 per cent to the cosmic star formation rate density but $30-50$ per cent of the stellar mass density at $z = 2-4$ this makes them important, in terms of the build-up of stellar mass. Up to 80 per cent of the cosmic star formation at these redshifts took place in submillimetre galaxies brighter than $\sim 0.1\,\mathrm{mJy}$ (Michalowski et al. 2010).

1.5 In This Thesis

In this thesis, I consider obscured and unobscured star formation over a significant fraction of cosmic time. In Chapters 2 & 3, I discuss the data reduction of the Y-band HAWK-I science verification image and how I utilise it to search for Lyman-break galaxies at $z \gtrsim 6.5$ and place constraints on the luminosity function at this epoch at the end of reionisation. In Chapter 4, I discuss the selection of a sample of 70μm star-forming galaxies over the COSMOS field. In Chapter 5, I discuss how I use the aforementioned sample to construct the far-infrared luminosity function and measure its evolution out to $z \sim 1$. In Chapter 6, I determine the far-infrared–radio correlation for my sample of 70μm selected galaxies and examine its evolution with redshift. Chapter 7 is the summary and conclusions of this thesis and contains some prospects for continuing this work in the future.

Chapter 2

The HAWK-I Y-band Data

In this chapter, I will describe the data reduction techniques used to analyse the Y-band observations from the ESO/VLT archive, obtained as part of HAWK-I science verification program 60.A-9284(B) (Fontana et al. and Venemans et al. – "A deep infrared view on galaxies in the early Universe"). These observations will be used to probe Lyman Break Galaxies near the epoch of reionisation.The GOODS-South field was chosen due to the ample coverage of complementary multiwavelength data. Two areas within the field were imaged, with centres of 03:32:41.0 −27:51:45 (pointing 1) and 03:32:29.6 −27:44:37 (pointing 2, both in J2000).

2.1 The Observations

Infrared observations are hindered by water vapour and CO_2 molecules in the atmosphere absorbing infrared radiation thereby limiting the number of transmission windows available. The Y-band filter lies in one of these

transmission windows and is particularly useful because being in the near-infrared at $\sim 1\mu$m, it enables the detection of $z \sim 7$ Lyman-break galaxies (see Figure 2.1).

Observing in the infrared is further complicated by the brightness of the sky background being significantly greater than the sources being observed ($Y_{sky} \sim 18.5$ AB mag, High et al. 2010), therefore a good sky subtraction is vital. Effective removal of the sky background is facilitated by observations comprised of numerous short exposures, (to avoid saturation from the background), moved around in short dither patterns. This builds-up a good representation of the average sky magnitude. Individual exposure times for the HAWK-I Y-band observations were 30 seconds, with 10 such exposures averaged to form a single co-added frame of 300 seconds. A typical sequence was 12 exposures (1 hour), although sequences with between 6 and 13 exposures were used, with the telescope dithered by 5-10″ between exposures. There were 18 sequences around pointing 1 (comprising 195 frames in all, a total of 16.25 hours), and 14 around pointing 2 (comprising 138 frames, amounting to 11.5 hours), a full list of these observations can be found in Tables 2.1 & 2.2. The seeing in the Y-band was in the range $0.4'' - 0.7''$ (FWHM) in the individual exposures, with the stacked image having a seeing of $\approx 0.5''$.

The HAWK-I camera, and therefore each individual image, is comprised of 4 quadrants, each of 2048×2048 pixels with a scale $0.106''$ pixel^{-1}. These quadrants were separated in to individual images and reduced separately before final mosaicking. An example of a 10 x 30s co-added raw image from a single quadrant is shown in Figure 2.2.

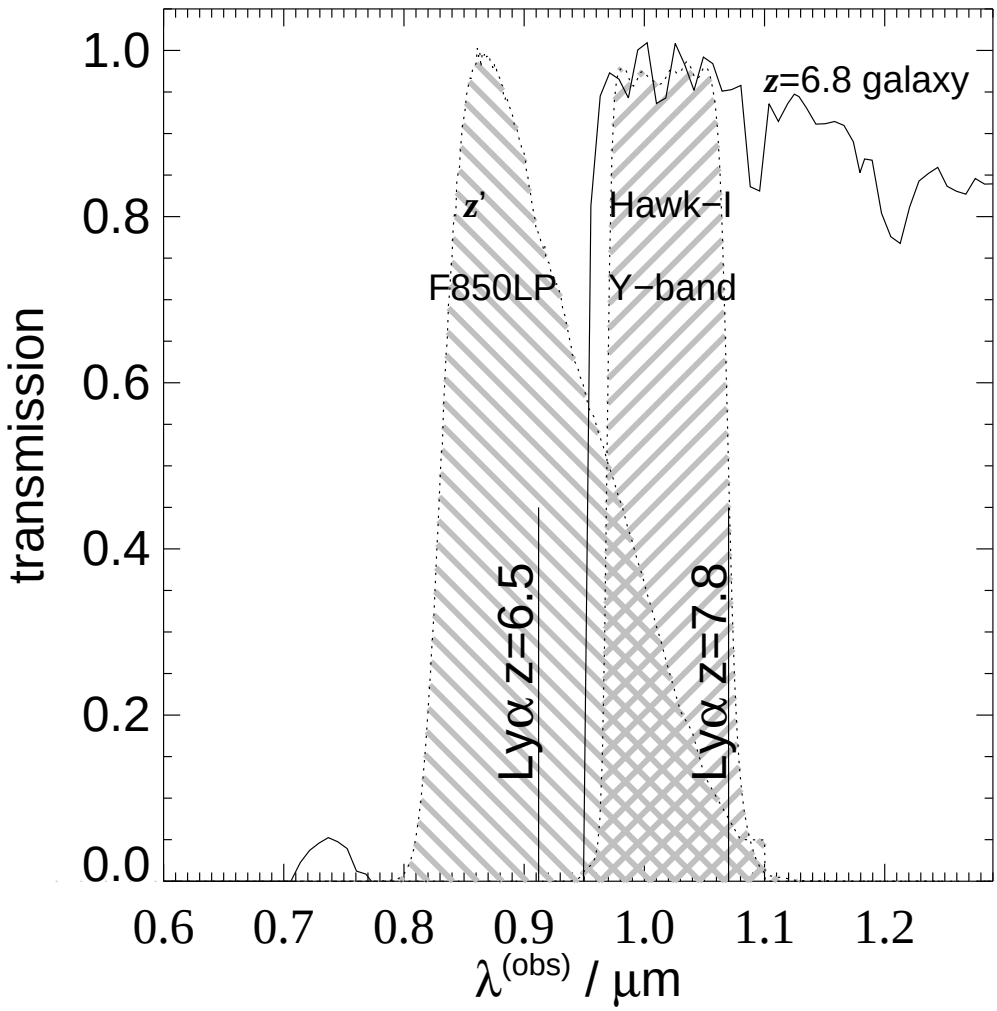

Figure 2.1: Figure showing the ACS z' and HAWK-I Y band passes over plotted on the spectrum of a $z = 6.8$ galaxy with 100 Myr of constant star formation and 0.2 solar metallicity (solid line), illustrating the utility of the two-filter technique for locating $z \approx 7$ sources. The filter transmission curves shown here do not include the effect of the quantum efficiency of the CCDs which in the case of the z'-band filter would result in a sharp cutoff at 0.97μm.

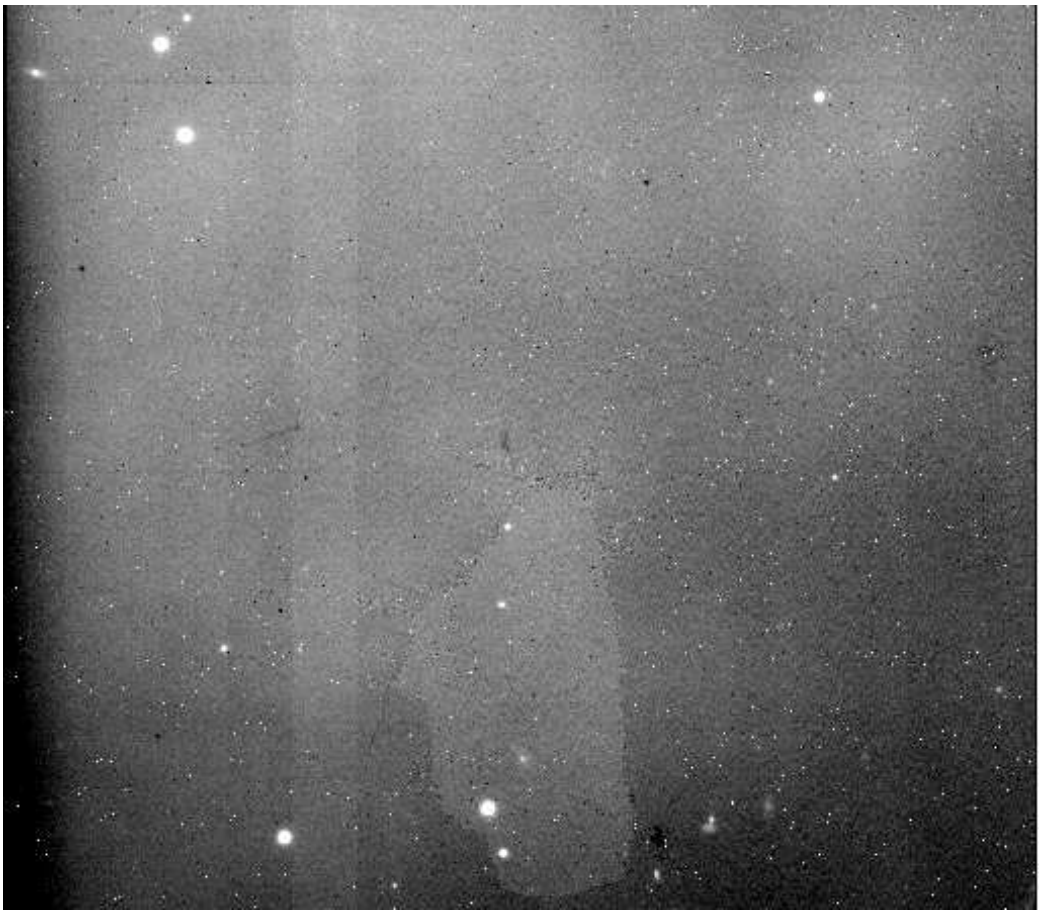

Figure 2.2: An example image of an unreduced co-added 10x30 second exposure from the first quadrant of pointing 1.

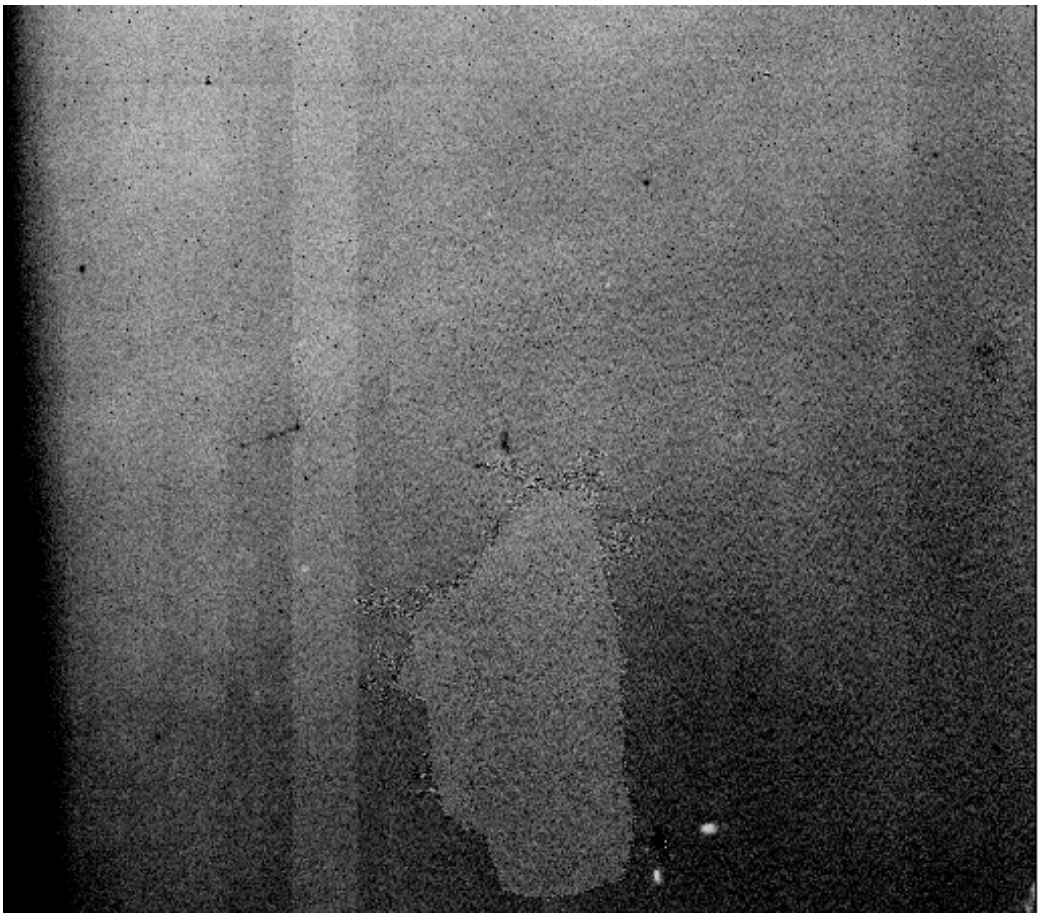

Figure 2.3: An example of one of the three averaged Y-band sky flats.

2.2 Data Reduction

The first step in the data reduction was to subtract the dark frame from the raw images. The dark frame is created by taking a typical exposure with the telescope but with no illuminating source. This dark current will therefore be present in every exposure and should be accounted for, by subtracting it from the raw data.

Another systematic effect that requires correction is the non-uniform response of different pixels in the detectors. This is accounted for with the

flatfield frame (see Figure 2.3) which is created by observing a bright, even patch of sky, preferably excluding any bright objects, typically at twilight or dawn. The flatfield frame can also account for any artifacts in the optics of a telescope. Due to this calibration frame being a measure of the response of the detectors, it should be divided out of the data.

The data was flat-fielded using the average of Y-band twilight sky flats from the ESO HAWK-I archive.

2.2.1 Sky Subtraction & Frame Addition

I used the `XDIMSUM` package within `IRAF` to further reduce the data. The `XDIMSUM` package was designed to accurately subtract sky from dithered infrared observations. The data were reduced in closely spaced time sequences, in order to minimise effects, such as a varying sky background. Combining the exposures in a given quadrant within hourly sequences required a knowledge of the exact shift between dithers. This knowledge was attained by interactively measuring a number of compact, bright but unsaturated sources, visible in all exposures, utilising the `xdshifts` task within `XDIMSUM`. The shifts were measured for the first quadrant in each of the ∼hourly sequences, and the same shifts were applied to the remaining quadrant members, as the offsets should be identical.

The data were further reduced and combined using the `xmosaic` task, which is comprised of an additional two tasks, `xfirstpass` and `xmaskpass`. The `xfirstpass` routine, was used to subtract the sky background for a sequence. The background was subtracted by median combining the 5 frames

before and 5 after the current working frame in the sequence. This meant that due to the dither pattern, all real sources in the image would move and, in the median combination, would disappear, leaving a good estimate of the sky background to be subtracted from the science images. If however, the dither pattern of the frames was not sufficient, bright sources may cover the same area in multiple frames and a median combination would result in dark halos, where bright objects had been subtracted out. This effect would also be produced if there were not a sufficient number of frames to include in the median combination (i.e. not enough information to determine an accurate sky median value). This lack of sufficient frames was only found to be an issue for a single sequence comprising an inadequate 3 frames. These were subsequently removed from the data.

The `xfirstpass` routine also removed cosmic rays through a median filter and used this to create the bad pixel mask. These processes were subsequently repeated by the `xmaskpass` task, where this time, the sky was subtracted while the objects were masked out. The sequences were then combined using the previously calculated image offsets. This resulted in 18 images in pointing 1 and 12 images in pointing 2. Exposure maps were also generated, these provided a measure of the observing time, and hence confidence in each region of sky. These maps can be used to assign weights to the confidence of detections.

Although `XDIMSUM`, through the median combination, rejected many of the cosmic rays present in the images, there were various electronic read-out artifacts visible which were pernicious and not removed. Hence the 14–18 final frames output by `XDIMSUM` were combined, once again using offsets de-

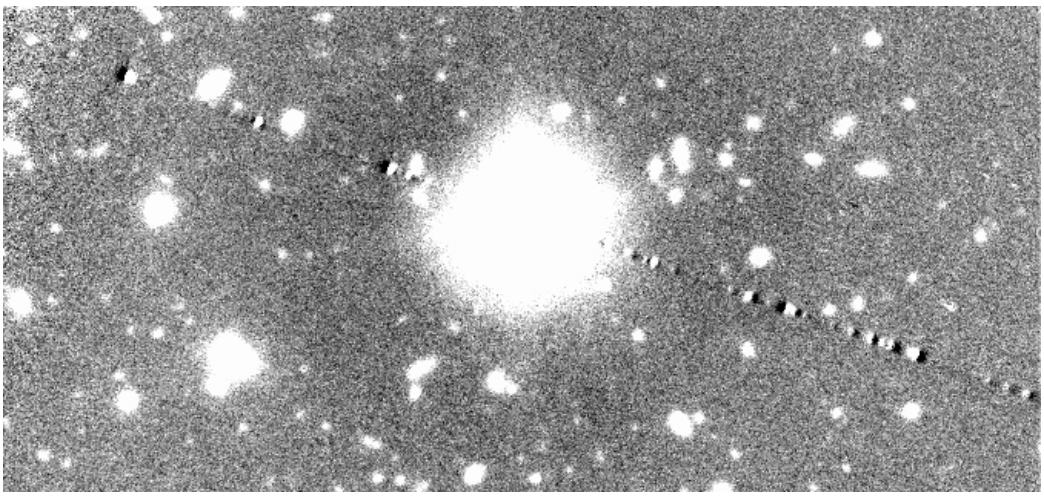

Figure 2.4: An example of the crosstalk effect that is visible as a diagonal line of black and white dots passing through the centre of the star.

termined from bright sources in the images using the `imcombine` task and the `ccdclip` rejection algorithm to reject cosmic rays, using the gain and readnoise properties of the detector and the Poisson noise of the sky background. The frames were weighted by the number of frames used to create the output image. The same routine was applied to the exposure maps. This resulted in 2 pointings, each with 4 quadrants, therefore a total of 8 frames.

A detector artefact which was not effectively eliminated by this rejection was a cross-talk effect (see Figure 2.4), whereby ghost images appeared in the same detector row as bright objects. As the apparent spatial position of the cross talk artifacts on the sky remains fixed with respect to the objects (i.e. it moves with the objects on the detector during the dithering pattern), this was not rejected in the co-addition. It was however, later eliminated through visual inspection and by masking detector rows affected by bright objects.

Table 2.1: Table of Observations for Pointing 1

Date	Time	No. of frames	Average seeing
2007-10-17	05:53-06:20	6	0.55
	07:45-08:13	6	0.70
2007-10-18	04:04-05:05	12	0.68
2007-10-19	02:27-03:37	13	0.48
	03:42-04:48	13	0.50
	04:53-05:55	12	0.33
	06:00-07:10	13	0.44
	07:15-07:59	9	0.45
2007-11-27	01:02-02:02	12	0.50
	02:09-02:48	8	0.45
	02:53-03:10	4	0.41
	04:38-05:38	12	0.43
	05:49-06:56	13	0.48
	07:01-08:14	14	0.55
2007-11-28	02:21-03:21	12	0.49
	04:17-05:17	10	0.48
	05:25-06:25	14	0.53
	06:34-07:34	12	0.56

Table 2.2: Table of Observations for Pointing 2 († denotes the sequence that was eliminated, due to lack of frames hindering a good sky subtraction)

Date	Time	No. of frames	Average seeing
2007-11-29	04:55-05:12	$3^{\dagger}$	0.37
	06:52-07:46	6	0.65
2007-11-30	01:13-02:13	12	0.58
	02:19-03:19	12	0.38
	04:29-05:29	12	0.33
	05:35-06:35	13	0.42
	06:47-07:42	11	0.59
2007-12-01	00:55-01:55	12	0.50
	02:02-03:01	12	0.48
	03:55-04:55	12	0.45
	06:16-07:16	12	0.53
	07:23-07:50	6	0.49
2007-12-02	05:08-06:08	12	0.59
	07:20-07:47	6	0.68

2.3 Astrometric Calibration

In order to combine the 8 quadrants in to a single $Y-$band image, it was necessary to determine an astrometric calibration as the information contained in the header is inaccurate, and there is no significant overlap between the quadrants, despite the dither pattern. An initial rough calibration was determined by identifying ~ 4 bright stars in each quadrant of the Y-band image and using their true RA and Dec, determined from the USNO-B catalogues (Monet et al. 2003), to inform the world coordinate system in the header file. The final Y-band image was intended for comparison with the HAWKI-I $J-$band data (Retzlaff et al. 2010) [1], in order to search for Y-drop candidates, therefore it is important that the two images are aligned accurately, for this reason the J-band image was used to astrometrically calibrate the $Y-$band. A list of the RA and Dec of bright but unsaturated sources in the J-band image were used to compare to the Y-band data. These RA and Dec coordinates were then transformed in to x and y pixel positions in the $Y-$band image. Due to the greater size of the $J-$band image, a catalogue for each quadrant was tailored to include only those sources that lay within the working quadrant, typically 60-100 bright sources. Then the `center` task in `IRAF` was used to find the true and x and y coordinates of the source in that image within a box of 40x40 pixels. A quadratic fit to the distortion produced residuals of $\sim 0.1''$ between the coordinates in the J- and Y-band images. This fit was then used to adjust the world coordinate system of the image using the `ccmap` routine and written to the header using the `setwcs`

[1] Version 2 was used here – available from
http://archive.eso.org/archive/adp/GOODS/ISAAC_imaging_v2.0

routine.

The $Y-$band quadrants were then mapped on to a larger $J-$band sized tile using the `wregister` routine and a constant background outside of the Y-band quadrant was adopted. This was undertaken in order to facilitate the combination of the quadrants and subsequently, straight forward comparison to the $J-$band image. The `wregister` task was used to compute the linear interpolation of the spatial transformation function required to map the Y-band data on to the J-band data pixel scale of $0.15''$, using the world coordinate system information in the headers of the files.

The exposure maps output by `XDIMSUM` were summed using the same measured shifts, creating a map of the total exposure time (see Figure 2.5) as a function of position on the sky, and correcting the astrometric distortions as described above. This was then used to inverse-variance weight the images when the four quadrants in both pointings were combined to form a final image mosaic. This weighting was done by taking the individual 8 frames output by `imcombine` and multiplying them by their corresponding exposure map. These images were then combined as were the exposure maps. The summed exposure map image for each quadrant was then used to divide the summed *science* x *exposure map* image resulting in an exposure map weighted science image. The 119 arcmin^2 of the final reduced Y-band image (see Figure 2.6) covered most of the ESO J-band and *HST* ACS GOODS images (97.5% of the HAWK-I Y-band image overlapped with the ESO J-band).

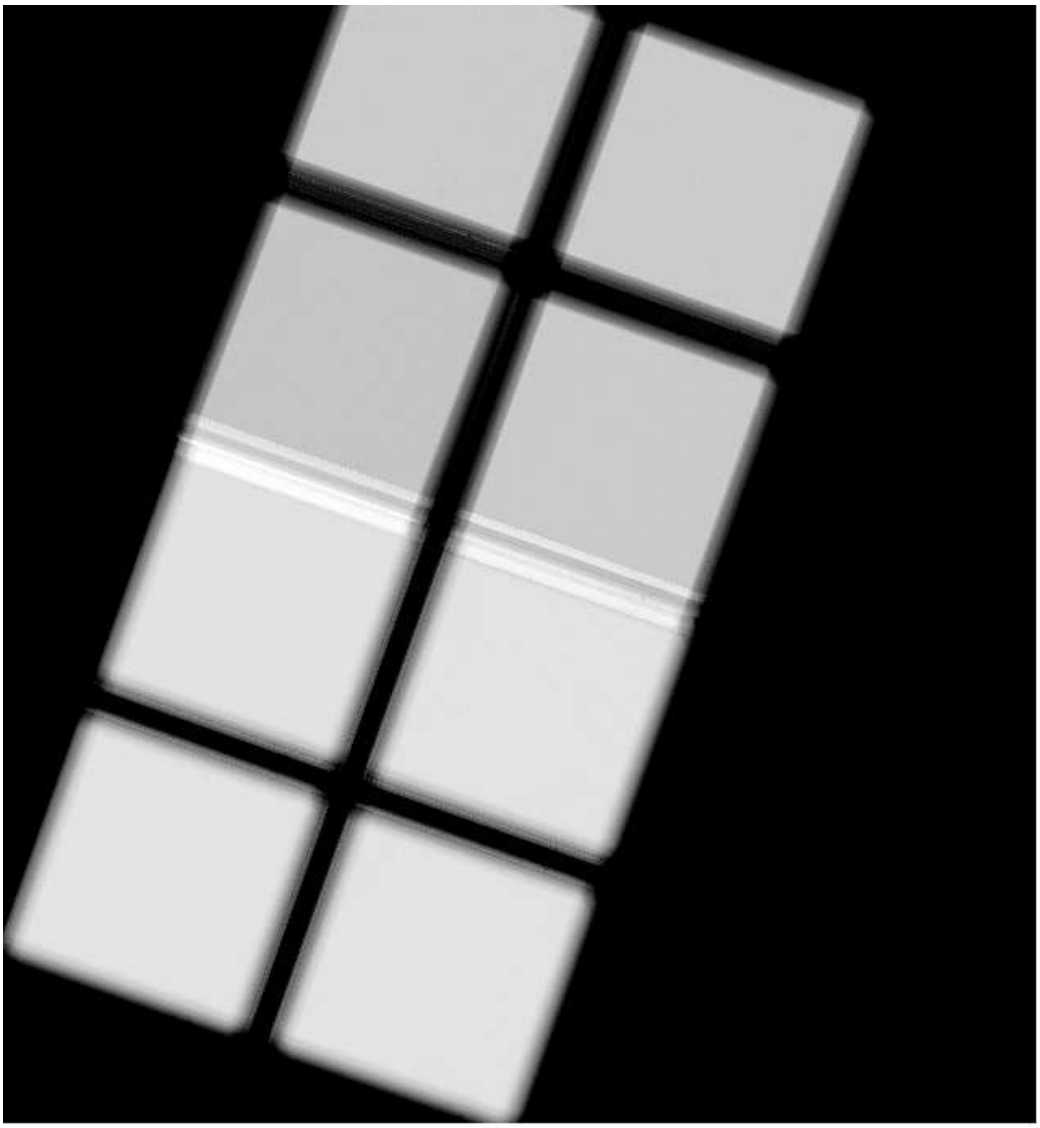

Figure 2.5: The combined exposure map image displayed with a linear grey-scale showing the greater exposure time in Pointing 1 (the lower half of the image) compared to Pointing 2 (the upper half of the image).

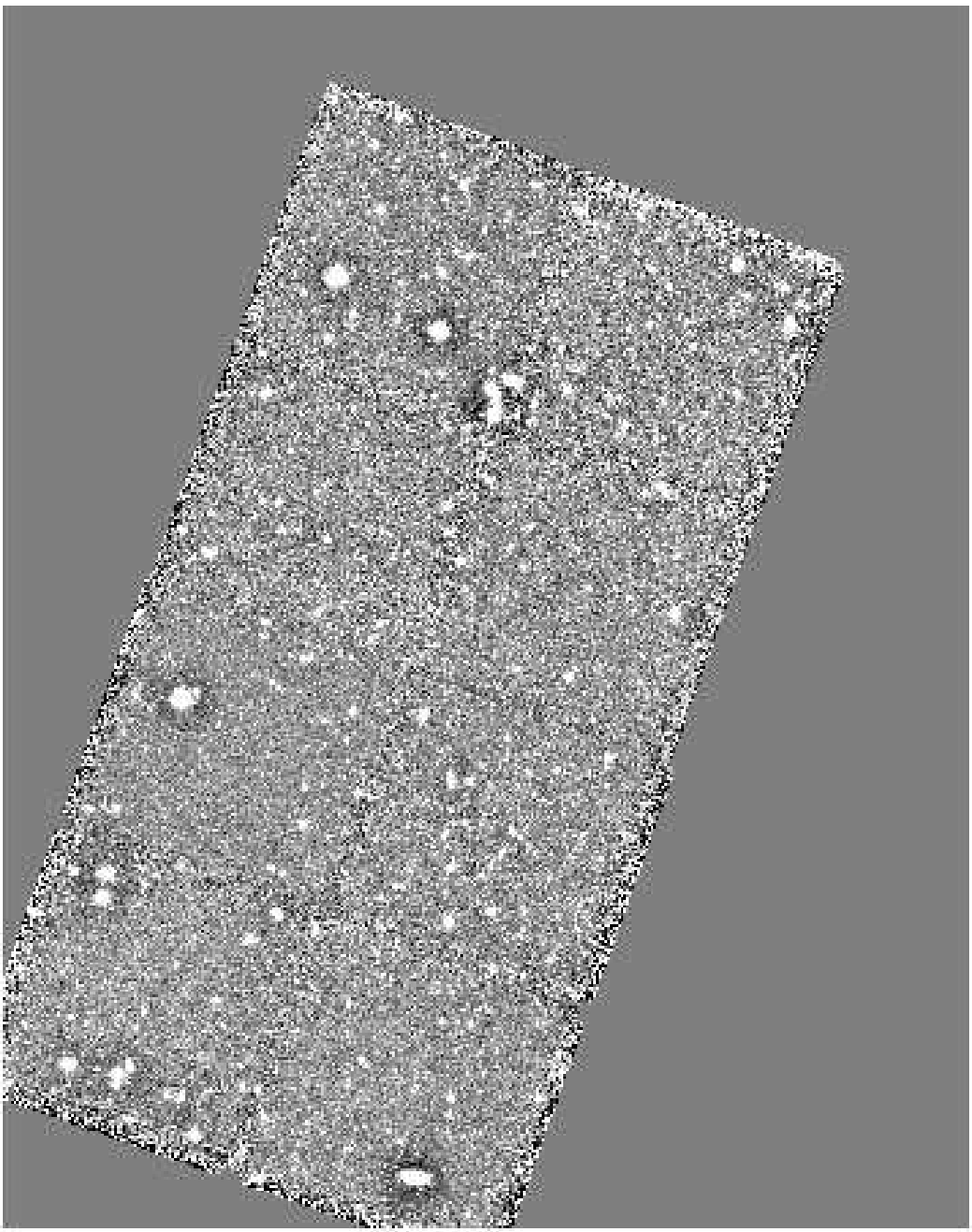

Figure 2.6: The final, reduced combined Y-band data image registered to the HAWK-I J-band image.

2.3.1 Y-band Zero Point and Aperture Correction

The zero point is the instrumental measure of one count per second on the magnitude scale and therefore allows the conversion between observed counts and flux or magnitude from a source. At the time of writing, the formal Y-band zero point for HAWK-I was not available, so the photometric zero point of the Y-band was determined by measuring the $Y - J$ colours of objects in identical apertures of 1 arcsec diameter, and setting the average AB colour of sources with flat spectra between the z' and J-band to be zero. The variation in the $z' - Y$ colours for those sources set to have $z' - J$ colours of zero was used to determine the error on the Y-band zero point. Figure 2.7 shows the binned $z' - Y$ colours. The solid line marks the Gaussian fit to the histogram and the 1σ error is 0.35.Using our computed zero point and error, the AB magnitude in the Y-band is given by

$$Y_{AB} = 26.77 \pm 0.35 - (\text{ap. corr.}) - 2.5 \log_{10}(\text{count rate}) \,,$$

where "ap corr" is the aperture correction in magnitudes, and "count rate" is the number of counts per second recorded. When measuring fluxes in apertures a correction is required to account for the flux estimated to fall outside of the aperture. The aperture correction was determined through comparison of 1 arcsec-diameter apertures with total magnitudes measured in `SExtractor` to be 0.4 mag for compact but unsaturated sources. This approach, for compact sources, is simpler and more reproducible than using the SExtractor curve-of-growth total magnitudes.

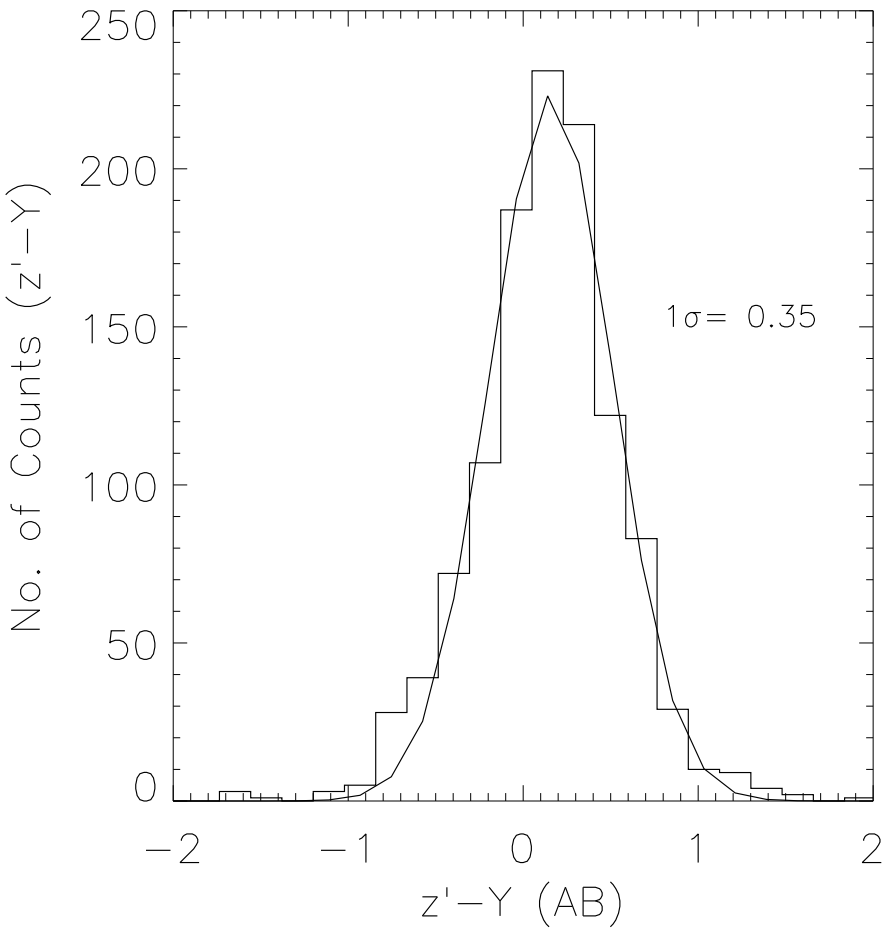

Figure 2.7: Histogram displaying the binned z'-Y colours for those sources with z'-J colours consistent with zero. The solid line shows the best fit Gaussian to the distribution and a 1σ error of 0.35.

2.3.2 5σ Limiting Magnitude

The 5σ limiting magnitude is the faintest source that can be observed in a set of observations with a 5σ confidence level. The 5σ limiting magnitude in the Y-band was originally measured from the standard deviation within a single aperture of $1''$. This produced a lower than true noise value because the Y-band frames were re-sampled on to a different pixel scale. This results in a correlation of the noise in a single aperture as the surrounding pixels were used to influence the central pixel value. In order to combat this effect, ~ 100 apertures were placed on regions of sky background and the counts were measured. These were then binned up for each aperture in to a histogram and a Gaussian was fit to the distribution (see Figure 2.8). The standard deviation was then taken from the Gaussian and used to compute the limiting magnitudes.

Applying the multiple aperture approach, the $5\,\sigma$ detection limit for a compact source in a 1 arcsec-diameter aperture is $Y_{AB} = 25.7$ mag, however pointing 1 is slightly deeper and reaches $Y_{AB} = 25.9$ mag (5σ). Figure 2.9 shows the greater depth and higher source count achieved by the Y-band image compared to the J-band. In all, the Y-band image covers 37.5 arcmin^2 to a maximum $5\,\sigma$ depth of $Y_{AB} \leq 25.9$, and an area of 90.6 arcmin^2 to $Y_{AB} \leq 25.7$. The total area surveyed to $Y_{AB} < 25.5$ was 115.6 arcmin^2.

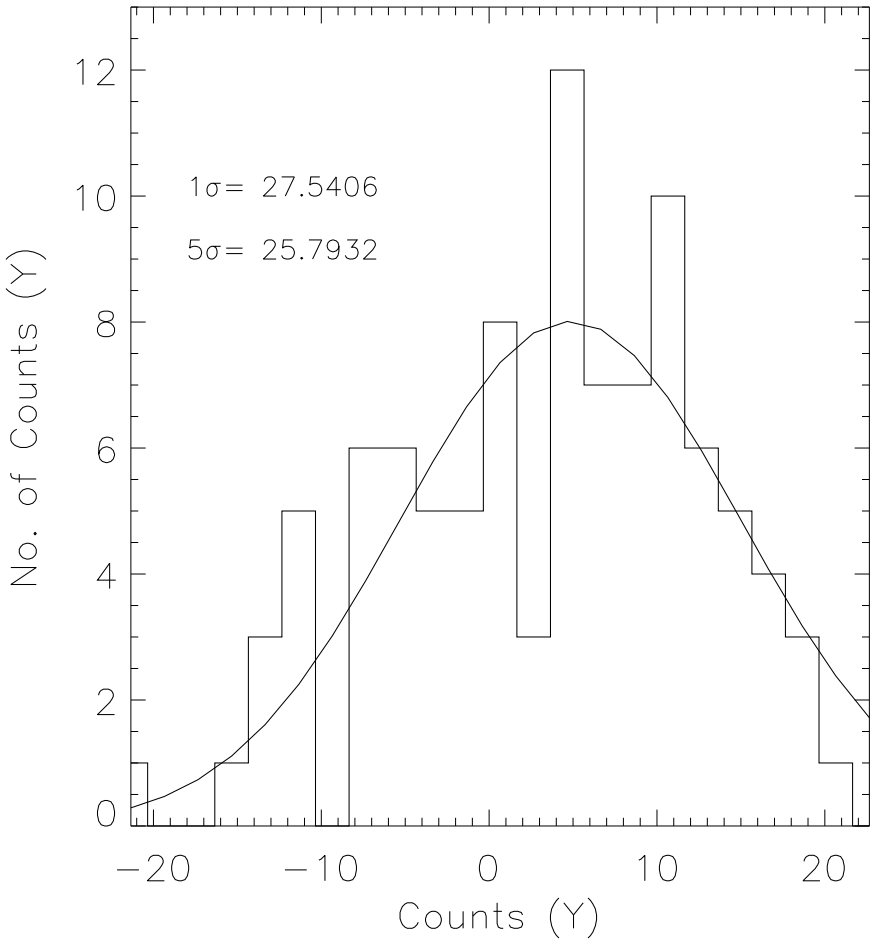

Figure 2.8: The binned up counts from 100 apertures placed in regions free from sources in the background-subtracted Y-band image. The standard deviation was determined from a Gaussian fit to the histogram.

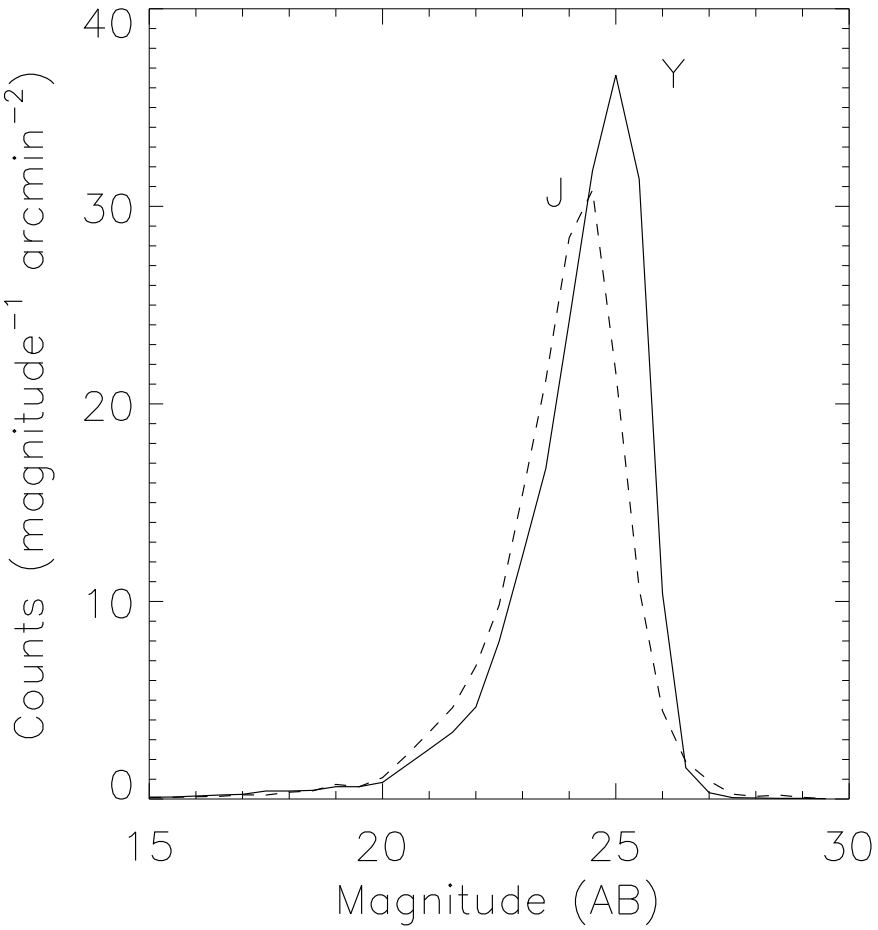

Figure 2.9: Number counts per magnitude per arcmin^2 of sources in the Y- and J-bands, including the 0.4 AB mag aperture correction for both wavebands.

Chapter 3

Constraints on star-forming Galaxies at $z \gtrsim 6.5$ from HAWK-I Y-band imaging of GOODS-South

The work described in this chapter was concluded in 2010 and published in Hickey et al. (2010), since then there have been many developments in the field, particularly with the arrival of WFC3 (Wide Field Camera 3) on HST (*The Hubble Space Telescope*). This new instrument with deep near-infrared capabilities has investigated the population of galaxies at $z \sim 7-8$ (e.g. McLure et al. 2010; Bouwens et al. 2010a & b; Wilkins et al. 2011) and facilitated the determination of the $z \sim 7$ luminosity function (e.g. Oesch et al. 2010). It has characterised the population of Lyman-break galaxies at $z > 7$ with indications of extremely blue UV spectral slopes (Bunker et

al. 2010; Bouwens et al. 2010b), see Chapter 1 for more details. In this chapter, I will describe how the VLT HAWK-I Y-band science verification data, described in Chapter 2, was used to search for z'- and Y-drops (objects where the Lyman-α break occurs in or just after the z' and Y-band filters) over the GOODS-South field. To explore the population of Lyman-Break Galaxies at $z \gtrsim 6.5$, we need a large sample of these galaxies. This has been hampered until now by a lack of sensitivity in the near infra-red and the small fields of view available. Now with HAWK-I, an instrument with a large field of view (7.5 x 7.5 arcmin^2) on the VLT, an 8-metre class telescope and critically with the Y-band filter, we can begin to increase the number of Lyman Break candidates at $z > 6.5$. The Y-band filter, centred on 1μm, is particularly useful as a discriminant of spectral breaks (a sharp cutoff), owing to its proximity to the z' filter's peak transmission wavelength of $\approx$ 0.9μm (see Figure 2.1). The proximity of the two filters makes discerning between a sharp cutoff, indicative of a spectral break and a more gradual slope, indicative of dust reddening, easier.

In order to identify Y-band ($7.5 \lesssim z \lesssim 9$) and z'-band ($6.5 \lesssim z \lesssim 7$) drop-outs through their extreme $(Y-J)$ or $(z'-Y)$ colours, the HAWK-I Y-band image is compared with the GOODS team J-band and z'-band images (taken with VLT-ISAAC and *HST*-ACS respectively).

The GOODS team reductions of the ACS images (Giavalisco et al. 2004), consisting of F450W B-band, F606W V-band, F775W i'-band and F850LP z'-band were utilised. The GOODS images had been drizzled from the original ACS pixel scale of 0.05″ on to a grid of 0.03″ pixels. Version 2.0 of the ACS

GOODS images[1] were used and the AB magnitude zeropoints re-determined for the v2 release were adopted.

I also made use of imaging over the GOODS-South field obtained with the Infrared Array Camera (IRAC; Fazio et al. 2004) on board the *Spitzer Space Telescope* which was conducted as part of the GOODS Legacy program (PID 194, PI Dickinson). The data were taken over two observing epochs, with the telescope roll angle differing by 180°, and I used the v2 and v3 reductions from the GOODS team, with the data drizzled onto a 0.6″ grid from the original 1.2″ pixels.

The 5σ limiting magnitudes were 24.76, and 24.87 for IRAC channels 1 and 2 respectively, measured in 2.4″ diameter apertures, and 22.77 and 22.81 for IRAC channels 3 & 4 measured in 3.0″ & 3.7″ diameter apertures respectively (these limits include aperture corrections of ~ 0.7 mag appropriate for unresolved sources, e.g. Eyles et al. 2005; 2007).

The $5\,\sigma$ limiting magnitudes in GOODS ACSv2 measured in 1.0″ diameter apertures are $B_{AB} = 27.20$, $V_{AB} = 26.90$, $i'_{AB} = 26.09$ and $z'_{AB} = 26.14$. The drizzled 0.03″ ACS pixels were block-averaged 5×5 to produce a z'-band frame which was registered to the VLT/ISAAC J-band pixel scale. The aperture corrected limiting magnitudes in 1.0″ apertures for the VLT-ISAAC images are $J = 25.2$ and $K_S = 24.7$ ($5\,\sigma$ AB magnitudes). These limits are corroborated by the median values found by Retzlaff et al. (2010) however they quote $5\,\sigma$ limiting magnitudes, for the entire VLT-ISAAC images, of $J = 25.0$ ABmag and $K_S = 24.4$ ABmag but due to the smaller region covered

[1]The GOODS ACS v2 images are available at `http://archive.stsci.edu/pub/hlsp/goods/v2/`

by the Y-band observations, we only utilise areas of good coverage in the J and Ks bands and therefore find the median values from Retzlaff et al. (2010) to be appropriate for this work.

3.1 Selection of z'-drop and Y-drop Candidates

3.1.1 Construction of Catalogues

Candidate selection for all objects in the field was performed using version 2.4.6 of the SExtractor photometry package (Bertin & Arnouts 1996). As I am searching specifically for objects which drop-out at short wavelengths through the Lyman-α forest absorption, I used SExtractor in dual-image mode, detecting objects in the longer-wavelength band and measuring the photometry within the same spatial apertures in the drop-out band(s). I produced separate catalogues for the Y-band drop outs (using the J-band as the detection image) and the z'-band drop-outs (using the Y-band as the detection image). To reduce the number of spurious sources in the noisy edge regions (where few frames overlap) the exposure maps were used as input weight maps for SExtractor. For object identification, I adopted a limit of at least 5 contiguous pixels above a threshold of 2σ per pixel (on the data drizzled to a scale of $0.15''$ pixel^{-1}). Spurious detections close to the noise limit were later eliminated through colour cuts and visual inspection. Although the weight map provided a good estimate of the confidence in different areas of the sky covered by the J-band image, it was found to be misleading in one

particular area (section 9) which had exceedingly deep coverage in comparison with the rest of the image (see Figure 3.1). This section was centred on RA=53.14 and Dec=27.7495 in the J-band weight image and gave rise to a number of spurious detections due to an over confidence of the weight map in this region. The SExtractor `BACKGROUND` algorithm creates a variance map based on the science image and this was used to weight section 9 alone. The J-band exposure map was used to weight the rest of the science image as it provides a significant advantage over background weighting particularly in regions with lower confidence due to less exposure time (e.g. regions towards the edge of an image).

As high redshift galaxies in the rest-UV are known to be compact (e.g., Ferguson et al. 2004; Bouwens et al. 2004), fixed circular apertures 1.0″ in diameter were used to select candidates. Corrected aperture magnitudes were used to approximate total magnitudes for each filter through an aperture correction, determined from bright compact sources. These were measured to be 0.07 mag in z'-band, 0.4 mag in Y-band and 0.4 mag in J-band.

3.1.2 Completeness

Towards fainter magnitudes, the ability to detect sources becomes increasingly dependent on the noise in the detection aperture. If a faint source lies in a positive region of the noise, this addition of source flux density + noise may be enough to raise the measured flux density above the detection limit, however were this source to lie in a region of negative noise, it would fall below the detection limit. This effect can be reduced with the use of a

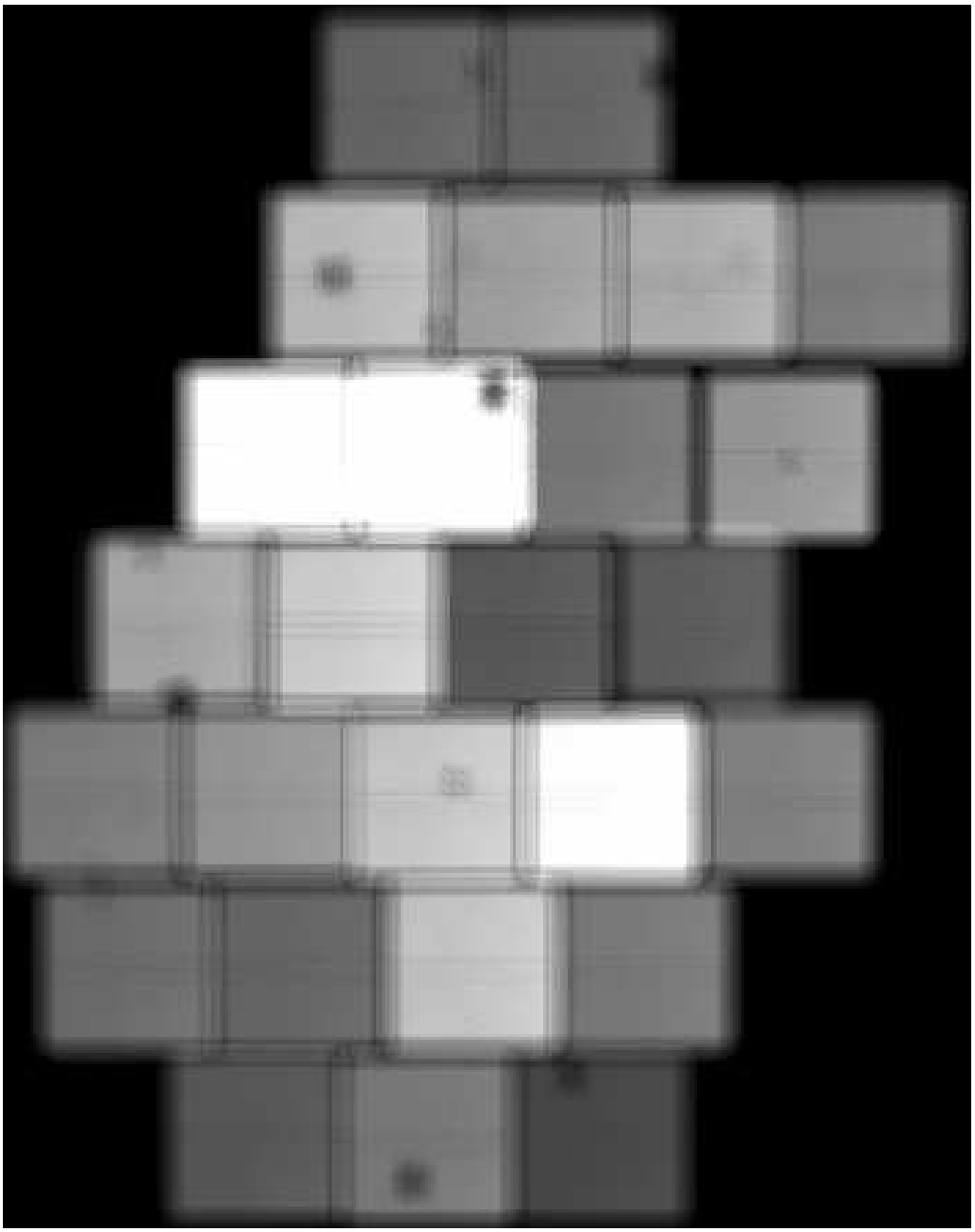

Figure 3.1: The J-band weight map image over GOODS-South (Retzlaff et al. 2010).

completeness correction. The completeness corrections for both the Y- and the J-band images were measured in the following way. Approximately 5000 artificial compact sources were created with diameters of 3 pixels and spanning magnitudes between 20 and 30. These objects were then convolved with the Point Spread Function (PSF) and added in to the original image. The new images (see Figure 3.2) were run through SExtractor again, using the same criteria that was employed to generate the object list. The resulting catalogues were compared with the list of input *'fake'* sources and a detection was considered to be made if a source was found within 5 pixels of its input position and had a magnitude correct to within a factor of 2 of the input flux. In order to determine the percentage recovery rate at different magnitudes, the number of detected sources was then compared to the number of input sources for each magnitude bin.

As described earlier, the Y-band image consisted of two individual pointings of unequal depth, to measure an accurate completeness limit, the calculations were determined for both pointings separately. The filled circles in Figure 3.3 show the Y-band image for Pointing 1 is ~ 95 per cent complete down to a magnitude of $Y_{AB} = 24.0$ and is 50 per cent complete at a magnitude of $Y_{AB} = 25.9$ over the deepest area. The Y-band image for Pointing 2 (denoted by open diamonds in figure 3.3) is ~ 95 per cent complete down to a magnitude of $Y_{AB} = 24.0$ and is 50 per cent complete at a magnitude of $Y_{AB} = 25.7$ over the deepest area in that pointing. The completeness of the J-band image is also estimated using a similar method. Figure 3.4 shows the J-band image is ~ 90 per cent complete to $J_{AB} = 24.0$ and is 50 per cent complete at $J_{AB} = 25.4$.

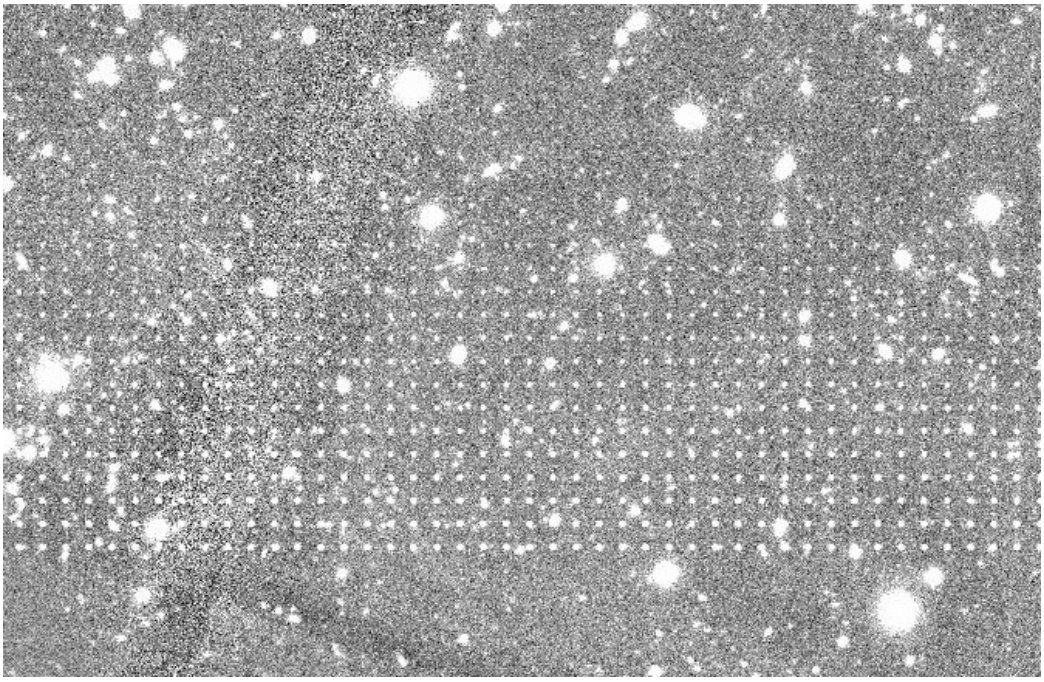

Figure 3.2: The Y-band image showing a section with '*fake*' sources added in.

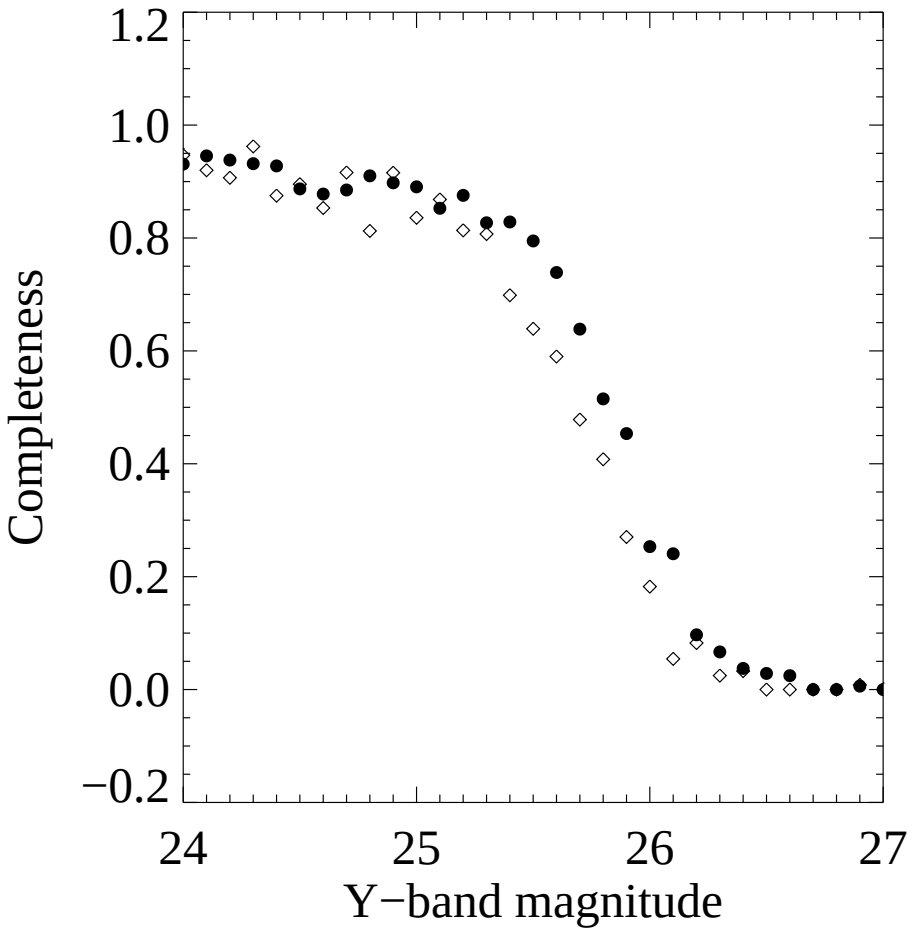

Figure 3.3: The Y-band completeness with SExtractor parameters of at least 5 pixels with $S/N > 2\sigma$. Pointing 1 is denoted by the filled circles and Pointing 2 by the open diamonds.

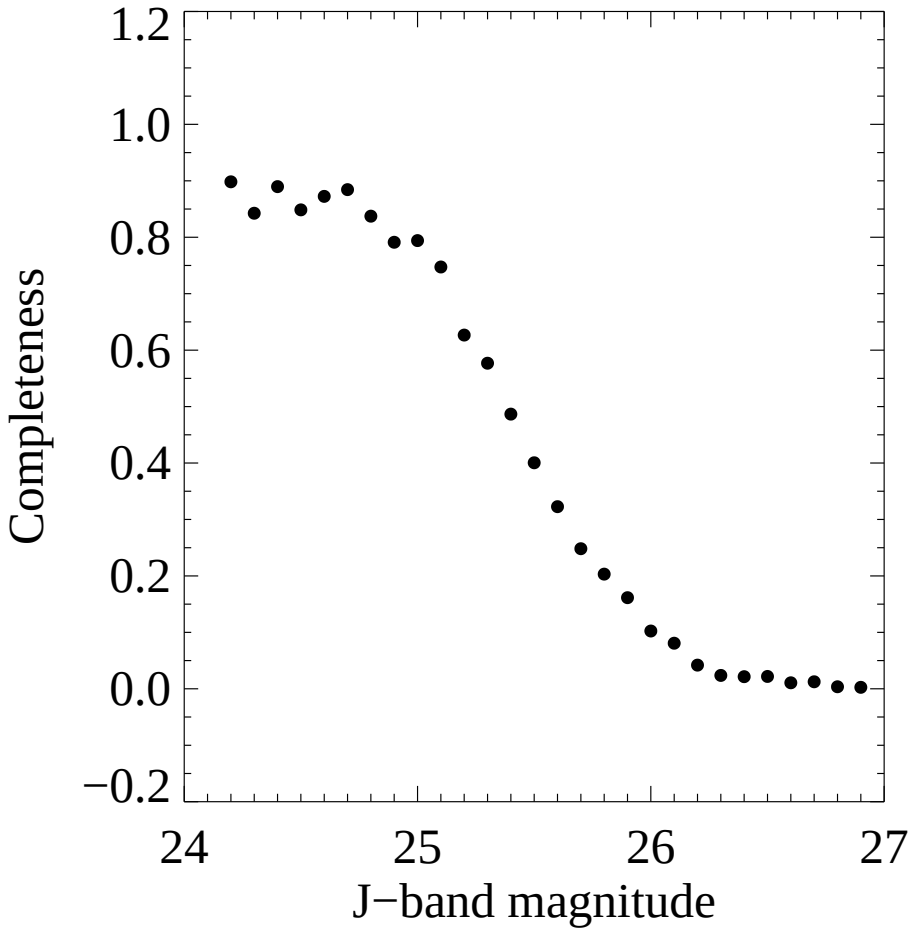

Figure 3.4: The J-band completeness with SExtractor parameters of at least 5 pixels with $S/N > 2\sigma$

The $5\,\sigma$ limit in the Y-band was found to be 25.9 in pointing 1 (see Section 2.3.2, which is similar to the 50 per cent completeness limit (Fig. 3.3). We tested the SExtractor parameters by reducing our detection thresholds and found they had little or no effect on our completeness implying that our original parameters of at least 5 pixels at $2\,\sigma$ or above were reasonable and did not eliminate credible sources from our selection. It is also worth noting that the completeness does not reach 100 per cent at bright magnitudes due to the fact that in creating the '*fake*' objects, existing real objects are not avoided. Thus the completeness correction described here is directly related to the ability to recover galaxies at all positions on the image and is not a true indicator of the depth.

3.1.3 z-drop Candidate Selection

A colour cut of $(z' - Y)_{AB} > 1\,\mathrm{mag}$ was chosen to select candidates because although it does not eliminate all of the low redshift interlopers it does omit a significant fraction without excluding potential candidates at $z > 6.5$ (see Figure 3.5). The distribution of $z' - Y$ colours for all of the detected objects is shown in Figure 3.6.

For the z'-drop selection, the SExtractor catalogues revealed 278 candidates with aperture corrected colours $(z' - Y)_{AB} > 1\,\mathrm{mag}$ and $S/N > 5$ in the Y band. It was expected that many of these candidates would be low-redshift interlopers such as low-mass stars or red galaxies at $z \sim 1.5$, which can produce large $(z' - Y)$ colours (in particular due to 4000 Å and Balmer breaks – see Figure 3.5). The Balmer break (3646 Å) is caused by

absorption from hydrogen in the atmospheres of B, but predominantly A stars and is therefore due to a relatively young star forming population. Between $1 \lesssim z \lesssim 2$, it would lie between $\sim 0.7 - 1.1\mu$m. The 4000 Å break is associated with cooler lower mass stars and is a result of an accumulation of metal absorption lines such as calcium and is therefore indicative of an older, more evolved stellar population. This break increases with age due to the buildup of metals. Between $1 \lesssim z \lesssim 2$, it would lie between $\sim 0.8 - 1.2\mu$m.

In order to eliminate obvious low-redshift contaminants, the list of z'-drop candidates was compared to the GOODS MUSIC catalogue (Grazian et al. 2006) with a matching radius of $0.36''$. This catalogue provides photometry from HST-ACS, *Spitzer*-IRAC, and ground-based U-band and VLT-ISAAC JHK_s imaging, with PSF-matching used to determine accurate colours. The GOODS-MUSIC catalogue includes photometric redshift estimates derived from the 14-band photometry, and the catalogue is a combination of a K_s-band and z'-band selection.

Of the 278 candidates, 101 appeared in the GOODS-MUSIC catalogue, mostly with photometric redshifts $z_{phot} = 1 - 2.5$, although there were two with $z_{phot} = 6.9$ which were identified by Mannucci et al. (2007) as brown dwarfs – these objects are discussed in Section 3.2.4.

There was also one other candidate with $z_{phot} > 5$ that was identified in our original search but was found to have a match to GOODS-MUSIC catalogue object 30046. It has detections in the i', z', Y, J, Ks and *Spitzer* bands (see Figure 3.7) with strong emission at the *Spitzer* wavelengths. Its photometric redshift of $z_{phot} = 5.14$, along with its detection in the i'-band coupled with its non-detection at the shorter ACS wavelengths, indicates its

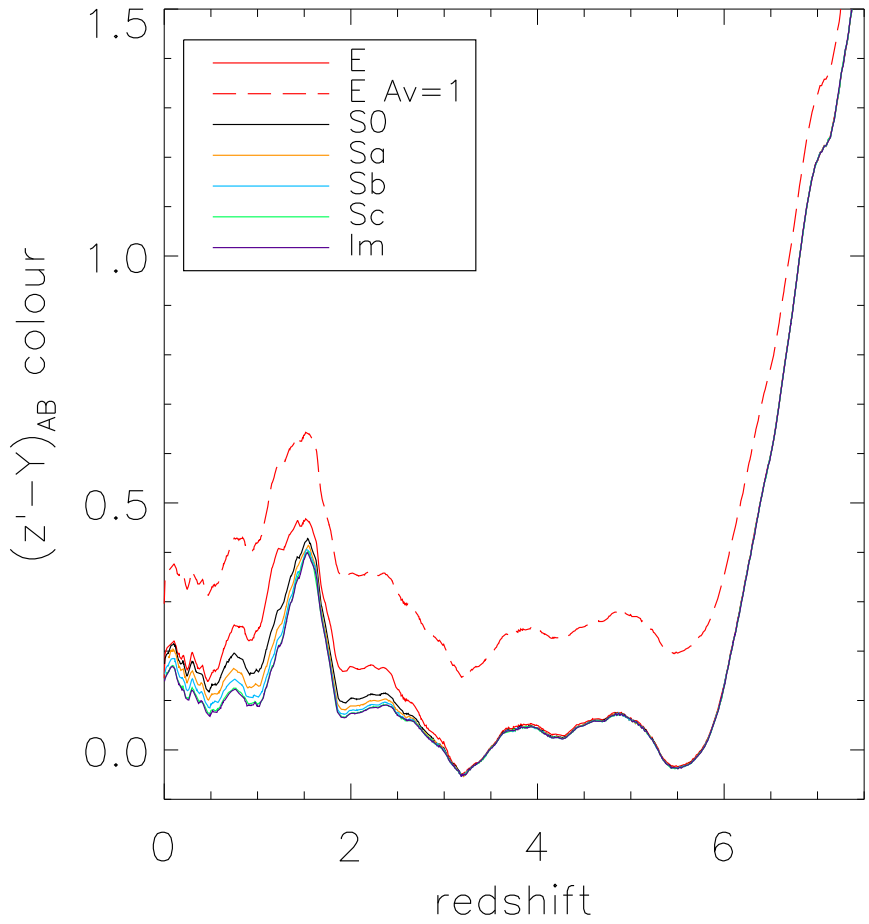

Figure 3.5: Model colour-redshift tracks for galaxies from Bruzual & Charlot (1993) template spectra. The contaminating 'hump' in the $(z' - Y)$ colour at $z \approx 1.5$ arises when the Balmer break and/or the 4000 Å break redshifts beyond the z'-filter. All galaxy types are represented with solid lines and are unreddened (i.e. Av=0 mag) except for the elliptical template which is shown with one magnitude of visual extinction by the dashed red line and without any visual extinction by the solid red line. This indicates that with increasing reddening and photometric scatter, it is plausible that some low redshift galaxies may contaminate our $z' - Y$ colour cut of 1 AB magnitude. It also shows that beyond $z = 6.5$ all galaxies should satisfy our $z' - Y$ colour cut.

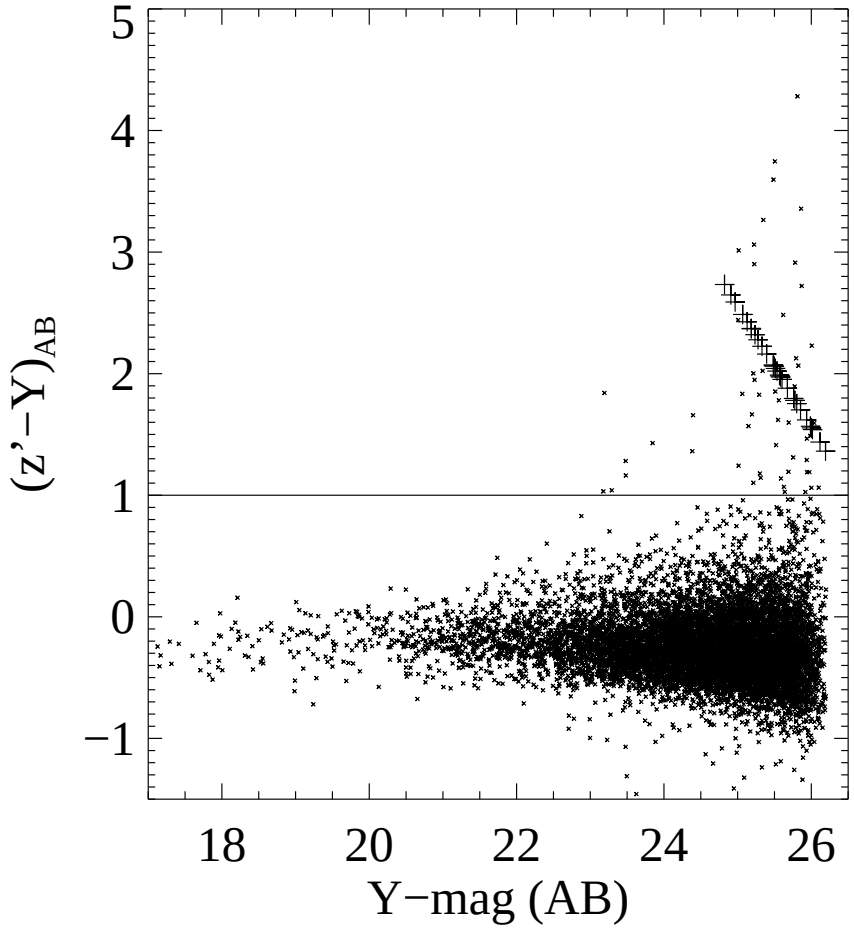

Figure 3.6: $z' - Y$ colours of all objects in the HAWK-I data. The plus signs are $2\,\sigma$ lower limits on the $(z' - Y)$ colour where objects are undetected in the z'-band. The horizontal line shows the colour cut imposed on the z'-drop candidates.

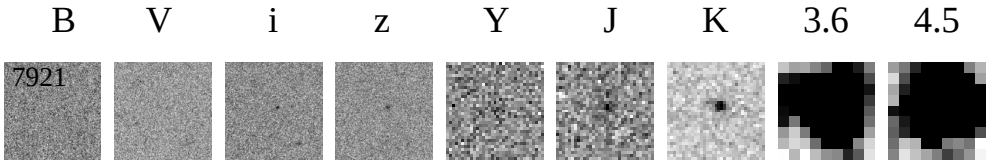

Figure 3.7: A possible V-drop candidate showing detections in i', z', Y, J, Ks, 3.6μm and 4.5μm wavebands, but has dropped out in the shorter wavelength B and V bands.

possible V-drop nature. It was therefore removed from the sample of z'-drop candidates.

I confirmed that all of the $z_{phot} < 5$ matches to GOODS-MUSIC had detections in one or more of the deep ACS B-, V- and i'-bands, ruling out high-redshift interpretations due to the absence of a break at Lyman-α. Figure 3.8 shows the $(z' - J)$ colours of the z'-drop candidates with GOODS-MUSIC matches over-plotted and the full GOODS-MUSIC catalogue (with a J-band threshold of $S/N > 3$). As can be seen, most of the sources have $(z'-J)_{\rm MUSIC} > 1.0$, as would be expected from the selection of $(z'-Y) > 1.0$, and the bulk lie at $z_{phot} \approx 2$ (as would be expected for the interloper populations – see Figure 3.5). The $z'-$drop candidates that do not lie at $z \sim 2$ or $z > 6$ or have $(z' - J)_{\rm MUSIC} > 1.0$ are largely attributable to the GOODS-MUSIC catalogue dealing with total magnitudes, whereas I used aperture magnitudes (more accurate for the expected compact nature of high-redshift galaxies), with large low-redshift galaxies having a greater aperture correction than was adopted. Also, colour gradients within galaxies mean that aperture photometry may select red regions of galaxies (e.g. spiral bulges) as z'-drop candidates; the HST-ACS z'-band has better resolution than the ground-based Y-band therefore the edges of large objects may be selected as

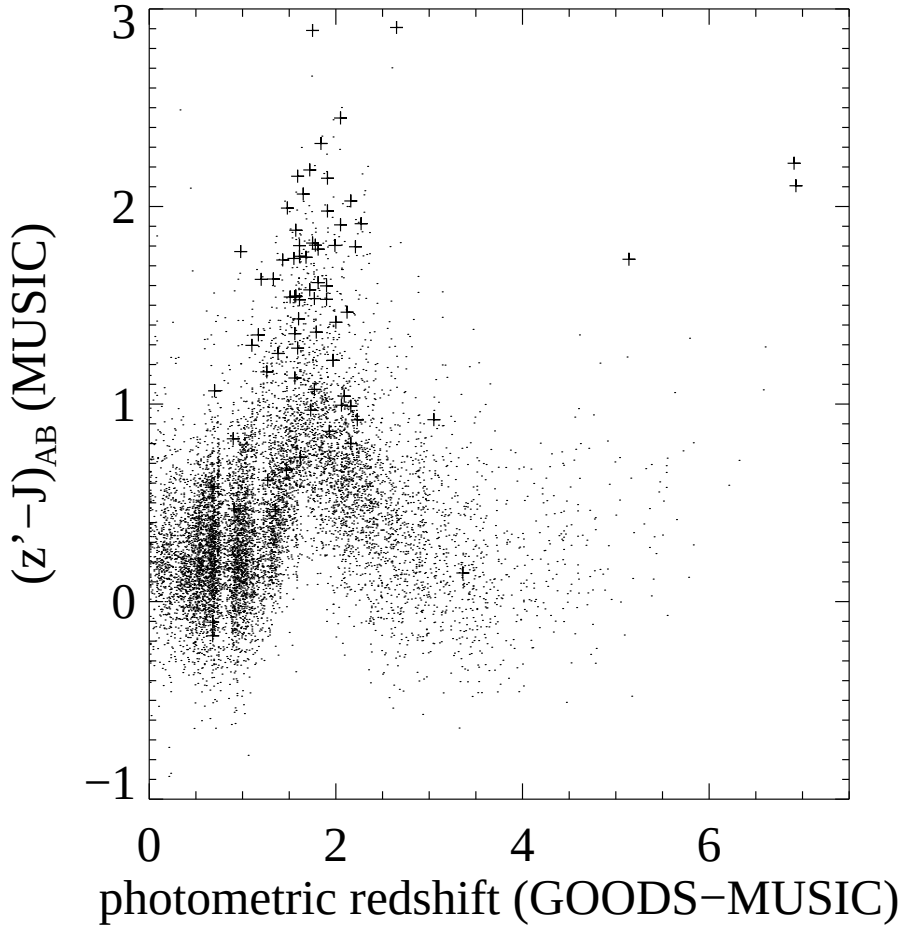

Figure 3.8: $z' - J$ colour versus the photometric redshift derived from the GOODS-MUSIC catalogue. The z'-drop out candidates that satisfy the colour selection criteria are marked with crosses. All of the sources in the GOODS-MUSIC catalogue with $S/N > 3$ in the J-band are denoted by dots.

spurious candidates.

For the 177 z'-drop candidates which did not lie within $0.36''$ of a GOODS-MUSIC source, all four HST-ACS wavebands were visually inspected, as well as the HAWK-I Y-band and the ISAAC J and K_s bands, to ascertain whether the Y-band detection was real, and if there was any detection at other wavelengths. Flux in the ACS B-, V- or i'-bands would be incompatible with the source being a z'-drop Lyman-break galaxy at $z > 6.5$. Approximately 17.5 per cent (31) of the remaining 177 candidates were detector artifacts (most frequently the cross-talk effect due to a bright object in the same detector row, manifesting a positive-negative dipole signal). Ghost image halos around bright stars accounted for another 14 per cent (25), and 14 per cent (25) again of the candidates were unreliable due to falling in regions of excess noise (despite using exposure weight maps to cut-down on spurious detections).

To verify the reality of the six remaining z'-drop candidates, the Y band data was split in to two halves (in time) and the first half and the second half of the data were combined separately. The Y-band magnitudes of the candidates were then measured in both halves of the data along with a reference star to check for consistency (in case the seeing or magnitude zeropoints differed over time). Two of the six remaining candidates were eliminated during this process as they were only visible in the second half of the data. These objects appeared bright in the Y-band and were undetected in all of the other bands. This prompted an examination of the individual images which revealed the two sources to be time variable (possibly supernovae). Each night's data was combined separately and the photometry on the individual

Table 3.1: Table of magnitudes for the transient sources. Where the objects were undetected, 2σ limiting magnitudes are quoted.

Date	Object ID 1321	Object ID 4806
	(Y_{ABmag})	(Y_{ABmag})
2007-10-17	>25.82	>25.74
2007-10-18	>25.65	>25.69
2007-10-19	>26.82	>26.81
2007-11-27	24.78 ± 0.08	24.77 ± 0.08
2007-11-28	24.88 ± 0.08	24.78 ± 0.07

nights were measured for each candidate.

Both candidates were found in pointing 1, which consisted of 5 nights of observations, in quadrants p1r1 (object ID 1321) and p1r4 (object ID 4806). The magnitude of bright reference stars was measured for each nights combined data and the offsets were found to be between ($\sim 0.007 - 0.311$ mag). These offsets in the magnitudes of bright stars between each night was used to correct the limiting magnitudes (see Table 3.1).

Both of the transient objects were undetected on 2007-10-17, 2007-10-18, and 2007-10-19 but were visible on 2007-11-27 and 2007-11-28 with magnitudes from $Y_{AB} = 24.77 - 24.88$ (see Table 3.1). The two transient objects have coordinates of $\alpha = 03^h32^m54.4^s$ $\delta = -27^d53^m35.7^s$ (Object ID 1321) and $\alpha = 03^h32^m33.5^s$ $\delta = -27^d49^m38.3^s$ (Object ID 4806).

After all of these checks I find that 46.7 per cent of the 177 z'-drop candidates without GOODS-MUSIC matches are spurious. A comparable fraction (50 per cent) had detections visible in the HST-ACS images; it is probable that they did not have corresponding GOODS-MUSIC matches because of the small matching radius we adopted ($0.36''$) to cut down on multiple matches. Small astrometric shifts in some regions, the z'-band and

K-band magnitude cuts in GOODS-MUSIC, and spatially extended galaxies with colour gradients account for these objects not having GOODS-MUSIC matches. Hence, from an initial colour selection resulting in 278 objects, 4 $z'-$drop candidates without GOODS-MUSIC matches remain. Table 3.2 contains the list of z'-drop candidates.

3.1.4 Photometric Scatter

Some of the z'-drop candidates may simply meet the selection criteria due to photometric scatter. To assess how significant this may be in the data set, the parent catalogue of Y-band detected sources was used over the 90.6 arcmin^2, which reaches a 5σ depth of $Y_{AB} = 25.7$ mag, and the magnitudes were randomly redistributed according to their corresponding uncertainties in both the z' and $Y-$bands and the new $z' - Y$ colour was calculated for each source. On average, nine objects may be due purely to photometric scatter in the parent catalogue. However, propagating this fraction through the subsequent cuts on the candidates through matching to the HST-ACS images etc., then approximately 0.2 sources are expected to be spurious in the final candidate list. Therefore, it is conceivable that one of the sources is a product of photometric scatter. Due to the lack of detection in any band other than the Y-band then Object 9266 is plausibly spurious.

3.1.5 Y-drop Candidate Selection

The Y-drop candidate selection was carried out in the same manner as the z'-drop selection. The criteria for the Y-drop candidates was a colour difference

Table 3.2: Properties of the 4 z'-drop candidates, magnitudes are listed with an aperture correction applied as described in the text. Where the candidate is undetected the 2σ limiting magnitudes are quoted. Object 2200 is probably a low redshift contaminant at $3.25 < z < 3.85$ as discussed in the text. Objects 9136 and 9697 are our most convincing z'-drop candidates.

Our ID	2200	9136	9266	9697
RA & Dec	03 32 25.3 -27 52 30.7	03 32 17.4 -27 43 43.0	03 32 19.2 -27 43 33.4	03 32 22.7 -27 43 00.8
z'_{AB}	26.87 ± 0.31	27.19 ± 0.38	>27.14	27.76 ± 0.65
Y_{AB}	25.70 ± 0.14	25.90 ± 0.18	25.94 ± 0.19	25.29 ± 0.10
J_{AB}	25.23 ± 0.16	24.98 ± 0.23	>26.18	26.0 ± 0.42
K_{AB}	23.8 ± 0.07	24.98 ± 0.32	> 25.42	>25.42
3.6_{AB}	21.4 ± 0.01	23.6 ± 0.054	>25.76	24.01 ± 0.07
4.5_{AB}	21.1 ± 0.01	23.55 ± 0.07	>25.87	24.35 ± 0.13
5.8_{AB}	20.53 ± 0.02	>23.77	>23.77	> 23.77
8.0_{AB}	20.46 ± 0.02	22.24 ± 0.28	>23.81	>23.81
$(z' - Y)_{AB}$	1.17 ± 0.34	1.29 ± 0.42	>1.20	2.47 ± 0.66

Table 3.3: Properties of the 4 Y-drop candidates, magnitudes are listed with an aperture correction applied as described in the text. Where the candidates are undetected in the Y-band the 2σ limiting magnitudes are quoted.

Our ID	2058	4551	5512	4532
RA & Dec	03 32 27.6 -27 51 04.1	03 32 16.2 -27 47 39.1	03 32 27.5 -27 46 14.7	03 32 48.3 -27 47 39.9
Y_{AB}	>26.6	>26.6	>26.6	27.47 ± 0.64
J_{AB}	25.37 ± 0.19	25.07 ± 0.19	25.05 ± 0.19	25.37 ± 0.19
K_{AB}	>25.42	>25.42	>25.42	>25.42
3.6_{AB}	>25.76	>25.76	>25.76	>25.76
4.5_{AB}	>25.87	>25.87	>25.87	>25.87
5.8_{AB}	>23.77	>23.77	>23.77	> 23.77
8.0_{AB}	>23.81	>23.81	>23.81	>23.81
$(Y-J)_{AB}$	>1.23	>1.53	>1.55	2.1 ± 0.67

of $(Y - J)_{AB} > 0.75$, a signal-to-noise ratio $S/N > 5$ in the J-band and a value in both the Y- and J-band exposure maps equivalent to a minimum of 2.5 hours of observation in the Y-band. This selection yielded a list of 133 possible Y-drop candidates. This list was then compared to the GOODS MUSIC catalogue to eliminate the low redshift interlopers from the selection. In all, 98 of the 133 objects had GOODS MUSIC matches to within $0.36''$ of a candidate. One of these objects had no detection in the bands B, V or i' so it was retained in the candidate list. This resulted in 37 Y-drop candidates. These remaining objects were inspected more closely with postage stamps in B, V, i', z', Y, J and K_s bands. Approximately 16 per cent (6) of the remaining candidates were found to be ghost image halos around bright stars, 27 per cent (10) were detections picked up on the edges of bright galaxies in the J-band. Another 3 per cent (1) fell on noisy regions of the Y-band image and 43 per cent (16) of the candidates had visible ACS detections. From the original list of 133 candidates only 4 possible Y-drops remain, and these are listed in Table 3.3.

3.2 Discussion

3.2.1 z'-drop Candidates

Four z'-drop candidates remain after eliminating artifacts and low-redshift interlopers. The candidates span a range $Y_{AB} = 25.3 - 26.0$ (after applying the aperture correction), two of which have $> 2\,\sigma$ detections in the z'-band. Three of the candidates have strong detections in the IRAC wavebands. I

determined photometric redshifts for these objects because the detection at the IRAC wavelengths increases the likelihood of the validity of a candidate and also improves the accuracy of the photometric redshift solutions. The publicly available software HYPERZ [2] (Bolzonella et al. 2000) was used to derive our photometric redshift estimates in the redshift range $0 < z < 9$. Visual extinction values between $A_V = 0 - 4$ were used and the Calzetti (1997) reddening law was assumed. Eight Bruzual & Charlot (2003) template spectra with solar metallicity were used, and the following 11 filters B, V, i', z', Y, J, K_s, and the four IRAC channels were included. Option 2 for the error treatment of an undetected source was implemented, which assumes that the flux in that filter and its 1σ error are equal to half the flux of the limiting magnitude (i.e. the error bar ranges from flux=0 to the 1σ limiting magnitude in that waveband).

Object 2200

This object displays a strong detection in the $Y-$, $J-$ and K_s-bands as well as a significant detection in the IRAC channels 1 and 2. There is some flux detected in the z'-band, however this is to be expected for some candidates as an examination of Figure 2.1 shows the z'- and Y-filter transmission curves do overlap significantly. This means as the Lyman break moves through the Y-band filter with increasing redshift its contribution to the z'-band flux will decrease but may not entirely disappear. The K_s-band source is slightly offset from the detection in the other wavebands for object 2200, this prompted a widening of the search area in the GOODS-MUSIC catalogue to a $1.0''$ radius. This larger radius yielded a match to an object

[2]Hyperz is available at http://webast.ast.obs-mip.fr/hyperz/

in GOODS-MUSIC with an ID 30199 and $z_{phot} = 2.73$. This object was also identified by Stanway et al. (2008) as a possible z'-drop. However, the detection by Stanway et al. is centred $0.8''$ from Object 2200 . Figure 3.9 shows the photometry of Object 2200 with a best fit SED of a dusty galaxy at $z_{phot} = 2.73$.

This object also has a reported MIPS 24 μm detection (source mip003485 in Alonso-Herrero et al. 2006), and coincides with a $0.5 - 2$ keV *Chandra* X-ray source, and hence probably has an AGN contribution. This object has also been presented in Dunlop et al. (2007), their object 2336, who derive a photometric redshift in the range $z = 3.25 - 3.85$. The photometry presented in Table 3.2 is for an object at the position of the $Y-$band source, this is offset from the K_s-band source and as such has a fainter magnitude than that given by Dunlop et al. (2007). The $Y-$band detection is probably associated with the K_s-band source, although this requires additional imaging and/or spectroscopy to confirm. The results from the probability distribution function (See Figure 3.10) output by *Hyperz* show multiple peaks, indicating the difficulty in pinning down a redshift for this source, however the most significant peak lies at $z \sim 2$.

Object 9136

This candidate displays a strong detection in the Y-band and is also detected in the J- and K_s-bands, and like object 2200 it is strongly detected at the IRAC wavelengths. In Figure 3.11 the photometric data points for this object are shown with the best fit galaxy template overlaid. The best fit solution from HYPERZ is $z_{phot} = 7.01$ with a secondary peak in the probability distribution at $z_{phot} = 7.23$ (Fig. 3.12). This best fit solution is for a

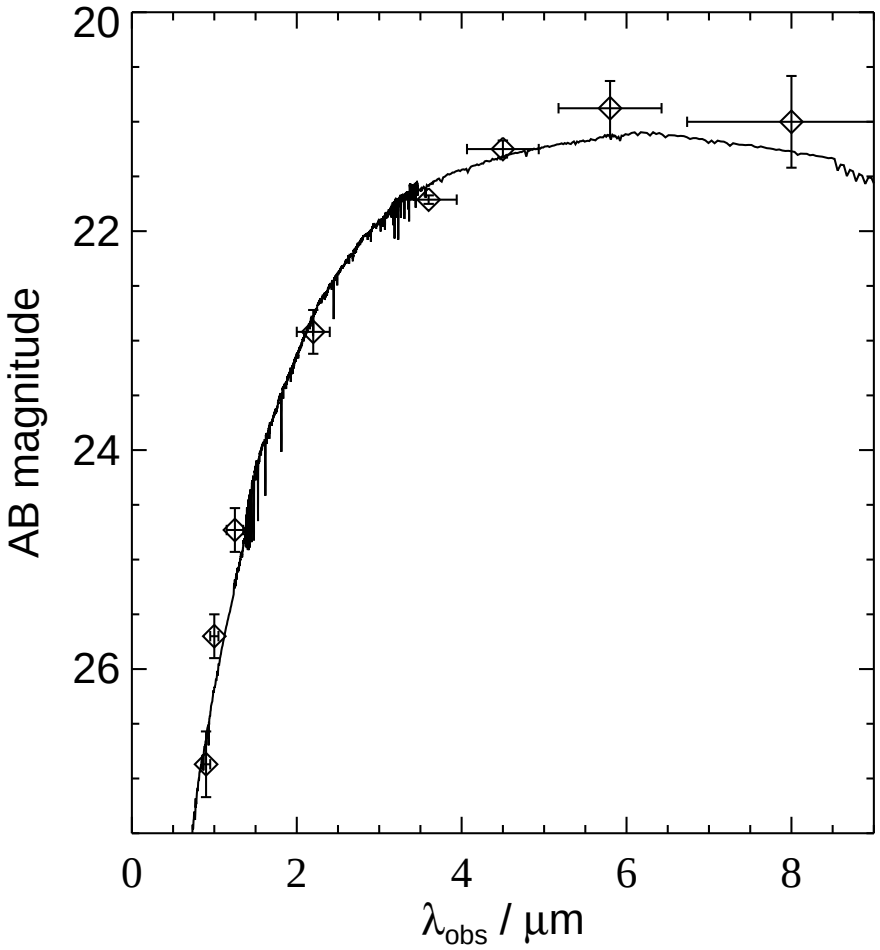

Figure 3.9: Photometry of Object 2200 with a best fit spectral energy distribution of a dusty galaxy at $z_{phot} = 2.73$

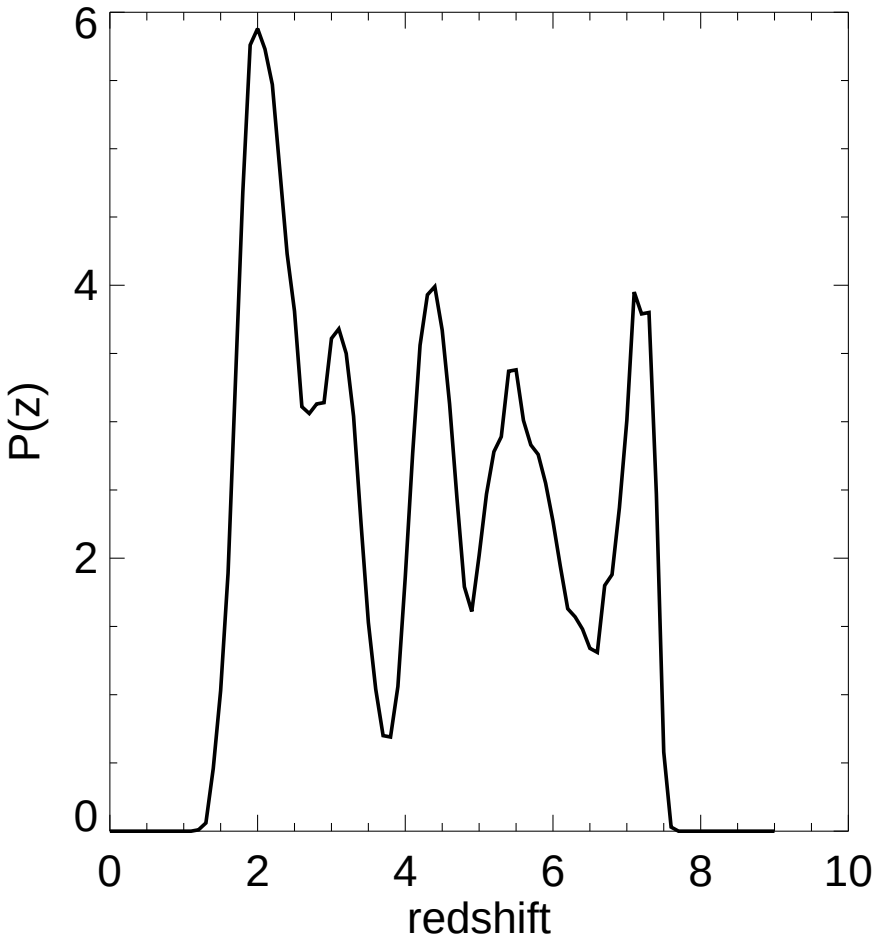

Figure 3.10: Redshift probability distribution function of Object 2200. The multiple peaks indicate probable redshift solutions and highlighting the difficulty in isolating a redshift for this source. However the lowest redshift peak at $z \sim 2$ is also the most likely.

starburst galaxy with $A_V = 0$. The star formation rate of the object 9136 was calculated based on the rest frame UV continuum at 1500 Å (see Bunker et al. 2004), and was found to have a star formation rate of ≈ 22 $M_\odot\,yr^{-1}$.

Object 9266

This object is detected in the Y-band, but not in the J- and K_s-bands. However the limits in these bands are fainter than the measured Y-band magnitude. This could indicate that the object is spurious or a result of line contamination in the Y-band filter, or simply that its continuum is fainter than the J- and K_s-band limits but bright enough to be detected in the Y-band. A photometric redshift was not fitted for this object due to its limited detections.

Object 9697

This object was previously identified as an i'-band drop-out in the GOODS ACSv1 data by Bouwens et al. (2006), and is #2226643007 in their catalogue, with $z'_{AB} = 27.54 \pm 0.18$, $(i' - z') > 1.3$ and infrared magnitudes $J_{AB} = 26.04$ and $K_{AB} > 25.4$. The source is detected in the Y- and J-bands and there is also a strong *Spitzer* detection. However there is a nearby source in the z'-band unconfirmed at the other wavelengths and another detection $\approx 0.7''$ to the east in the B and V bands which, while unassociated with the z'-band detection, may be at least partially responsible for the IRAC flux as it does fall within the IRAC aperture. However it would be a rather unusual object to be detected in B and V and the *Spitzer* bands and undetected in z', Y, J, and K_s. The $i'z'YJK_s$ colours appear consistent with a high-redshift interpretation. HYPERZ was also used to determine the photometric redshift for this object assuming the *Spitzer* flux was contributed by candidate 9697. In

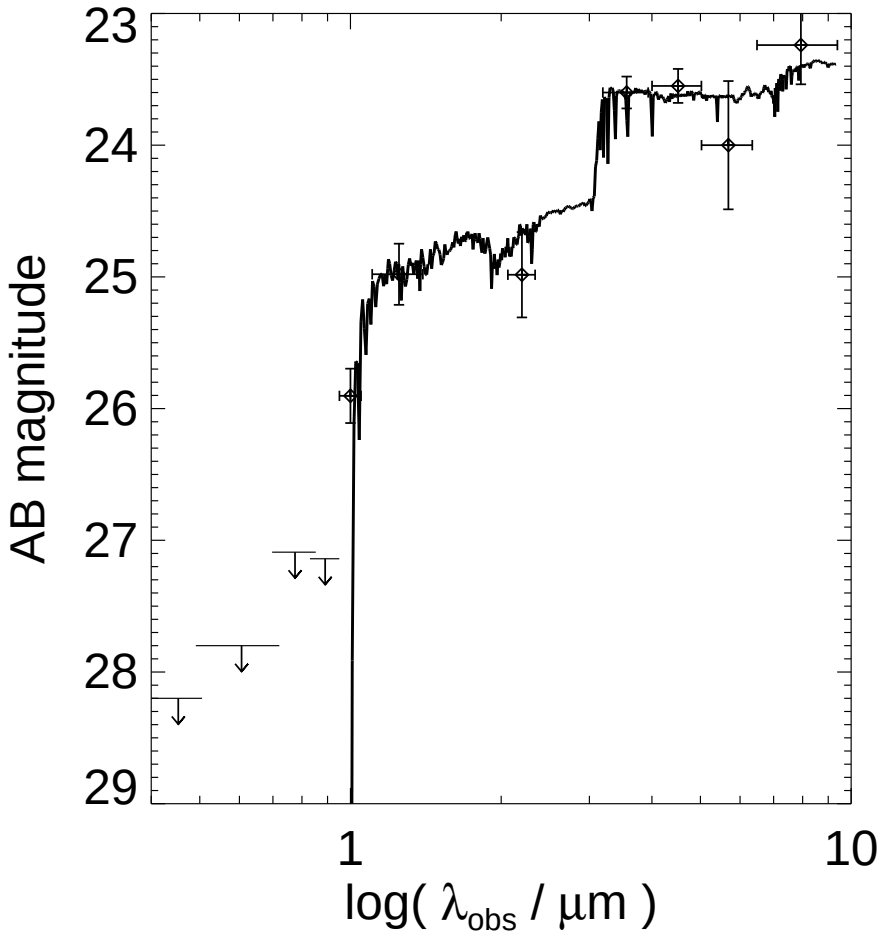

Figure 3.11: Best fit spectral energy distribution at $z_{phot} = 7.01$ to Object 9136 with photometry overlaid and 2σ upper limits denoted by down arrows

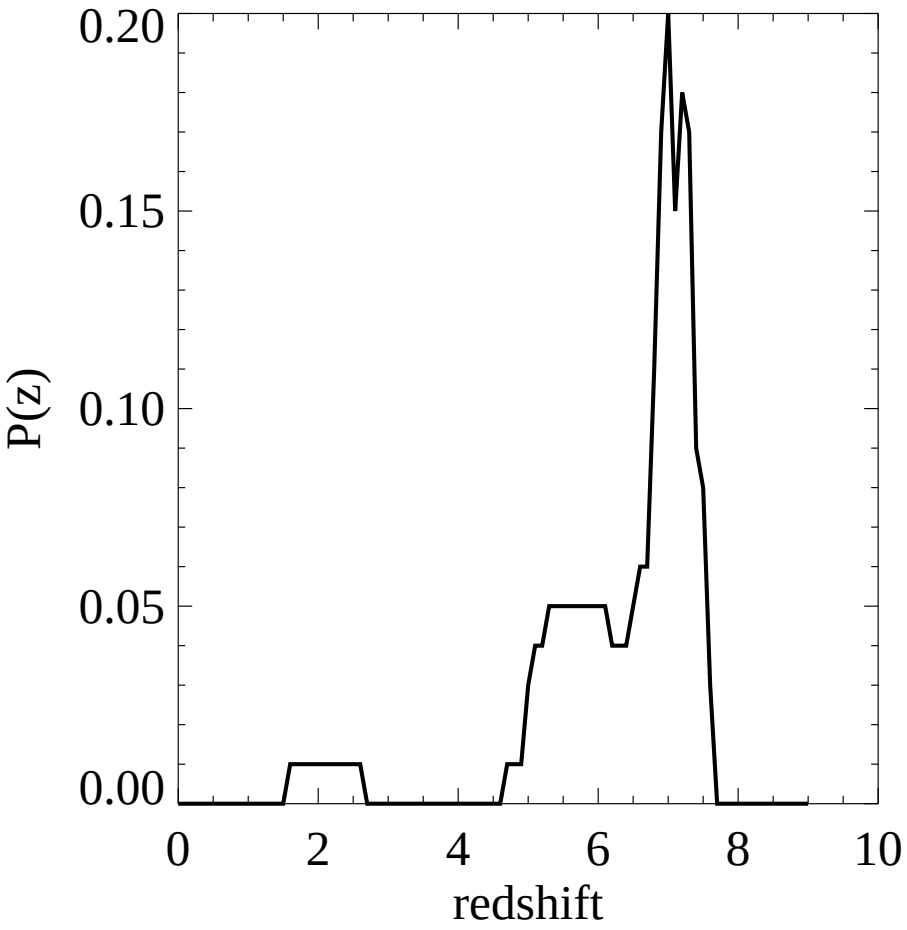

Figure 3.12: The redshift probability distribution for Object 9136, showing the best-fit photometric redshift of $z = 7.01$.

Figure 3.13 the photometry of this object is shown with the best-fit galaxy template overlaid. The best-fit solution was $z_{phot} = 6.92$ with a secondary peak in the probability distribution at $z_{phot} = 5.22$, see Figure 3.14. This best-fit solution is for an elliptical galaxy with $A_V = 0$. The star formation rate based on the UV continuum was calculated to be $\approx 25 M_{\odot}\,\mathrm{yr}^{-1}$.

Another possibility, other than a high redshift interpretation, is that the objects that are strongly detected in the IRAC bands, 9136, 9697 and 2200 may be similar to IRAC-selected extremely red objects (IEROs) see (Yan et al. 2004). But in the sample discussed by Yan et al. the sources had optical detections which the candidates described here, do not. At the high-redshifts estimated for these galaxies, if there was an old stellar population present, the 4000 Å break could fall between the K_s and the 3.6μm bands. This could explain some of the sources increasing in brightness at the IRAC wavelengths.

3.2.2 Brown Dwarf Contamination

The possibility that some or all of the remaining candidates could be brown dwarfs was also explored. Patten et al. (2006) presented observationally-derived colours for various spectral types of M, L and T dwarfs in the near-infrared and IRAC bands. In order to rule out the possibility of the candidates being brown dwarfs, their near-infrared colours were compared to the following three colour spaces: $[3.6 - 4.5]$; $[J - 4.5]$; and $[K_s - 4.5]$. The errors on the data points were combined to conservatively explore the colour space covered by the candidates, this colour space was then compared with

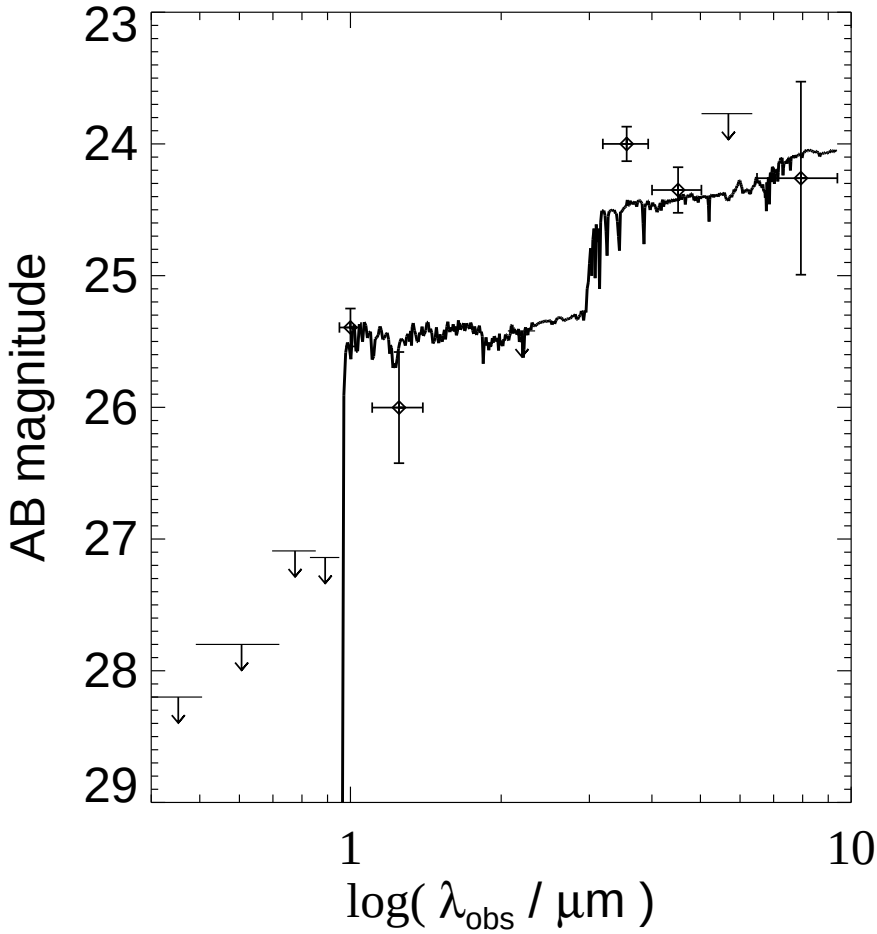

Figure 3.13: The best-fit spectral energy distribution at $z_{phot} = 6.92$ for Object 9697 with the multiband photometry overlaid. The 2σ upper limits are denoted by the down arrows

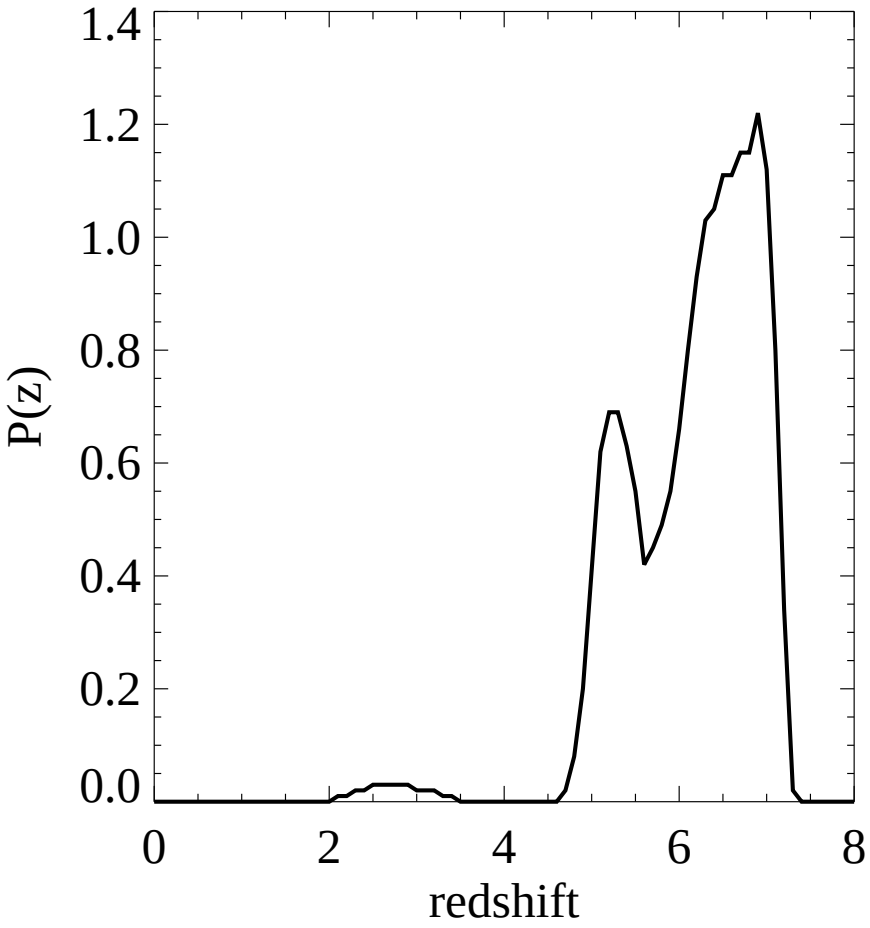

Figure 3.14: The redshift probability distribution for Object 9697, which shows the best-fit photometric redshift of $z = 6.92$.

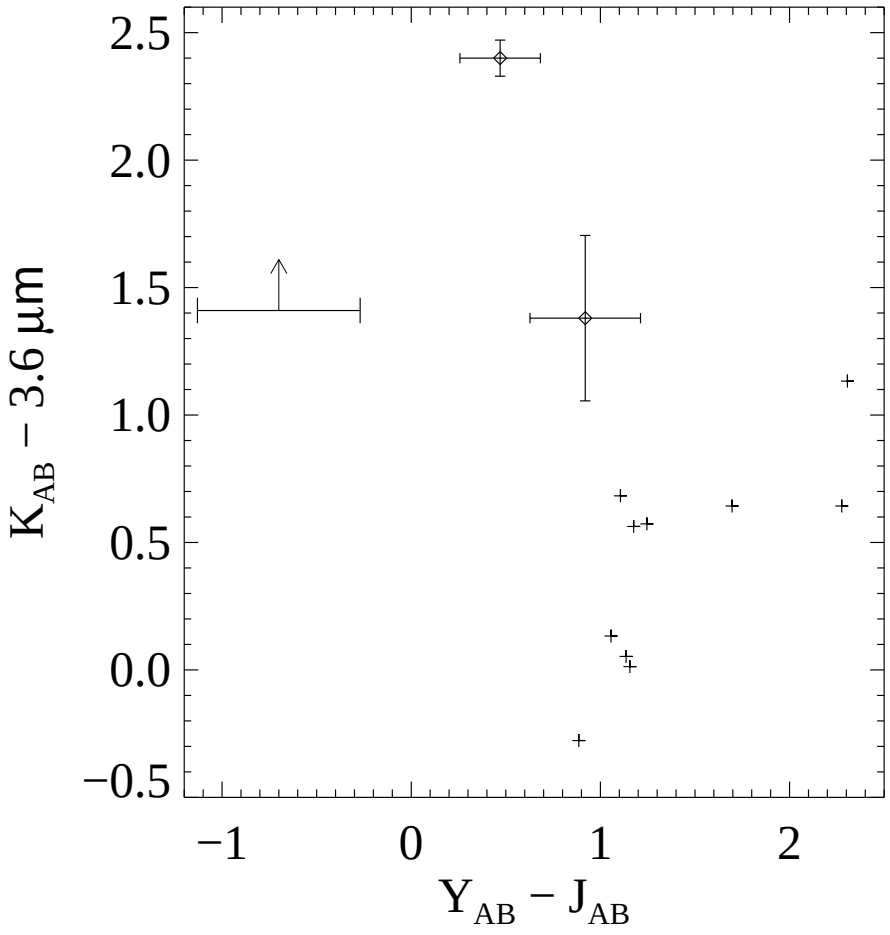

Figure 3.15: $Y - J$ vs. $K - 3.6$ colours for a sample of brown dwarfs (plus signs) from L1-T8. The open diamonds on the plot mark the three candidates, from left to right 9697, 2200 and 9136. Object 9266 is not shown as it is only detected in the Y-band. All 3 of these candidates lie away from the brown dwarfs marked by plus signs. Brown dwarf colours are taken from Leggett et al. (2000, 2001,2002), Kirkpatrick et al. (2000), Geballe et al. (2002), Knapp et al. (2004) and Hewett et al. (2006).

the expected brown dwarf colours. $[3.6 - 4.5]$ colours indicative of spectral types T2-5 were found for object 9136 but $[J - 4.5]$ colours indicative of an L8 dwarf and $[K_s - 4.5]$ colours of a T7 or T8 dwarf were also found. Each constraint contradicts the next, it therefore is unlikely that object 9136 is a brown dwarf.

Object 9697 has $[3.6 - 4.5]$ colours consistent with all M, L and T0-3 spectral types and $[Ks - 4.5]$ colours consistent with L5-8 and all T-dwarfs and (at the limit of its errors) $[J - 4.5]$ colours between 3.47 and 4.59. The plots provided by Patten et al. (2006) indicate that a brown dwarf of type M, L or T will have $[J-4.5]$ colours of < 3.5, so at the extreme of its errors, object 9697 has colours just consistent with an L8 brown dwarf. However when the typical $Y - J$ colours of brown dwarfs (Hewett et al. 2006) were compared with $K_s - 3.6\mu$m colours, see Figure 3.15, it was found that object 9136 lies significantly away from the typical low-mass star colours, again making it unlikely that the objects can be explained as brown dwarfs. A combination of resolution (in the near-infrared bands) and signal-to-noise ratio (in the $z'-$band) is insufficient to determine whether this object is unresolved, as would be expected for a brown dwarf.

3.2.3 Plausibility of Y-drop candidates

The final list of Y-drop candidates consists of 4 objects. They span a magnitude range of $J_{AB} = 25.0 - 25.4$ after applying aperture corrections.

Object 2058 is detected only in the J-band with no IRAC source associated.

Object 4551 is also only detected in the J-band but falls in a noisy region

of the Y-band image.

Object 5512 falls on the edge of the ACS images.

Object 4532 has a J-band detection which is possibly associated with the extended edge of a galaxy $1.2''$ away. This source is detected in all of the ACS bands and has a match to GOODS-MUSIC object 9610 with a spectroscopic redshift of $z = 0.347$. It is likely that the large apparent $(Y - J)$ colour recorded at the position of object 4532 is due to worse seeing in the J-band than the Y-band, or perhaps an intrinsic colour gradient in GOODS-MUSIC 9610. Given the proximity of this low-redshift source, it is extremely unlikely that object 4532 is a genuine Y-drop at $z > 8$.

No robust Y-drop candidates were found as all of the candidates only appear in the J-band image with no significant K_s-band detection which is unexpected as the J and K_s-bands probe similar depths. They also have no clear IRAC detection. This could indicate spurious detections in the J-band because they are unconfirmed in any other, or it could be the result of line contamination in the J-band filter from high equivalent width Lyman α emission. They could also be galaxies with extremely blue spectra indicating low metallicity and little or no dust.

In order to assess whether such blue colours could be plausible, two scenarios are considered, one of which has the colour difference produced by a blue spectral slope, the second assumes that the brightness in the J-band relative to K_S is attributable to a strong emission line (e.g. Lyman-α at $8.0 < z < 10.5$). The constraints on the spectral slope and Lyman-α equivalent width are compared with the known properties of Lyman-break galaxies at high redshift. If the limits fall outside the range observed in distant galax-

ies, then the J-band detections are probably spurious (i.e., inconsistent with these being Y-band drop-outs at $z > 8$).

A simple power law is assumed for the spectrum of $f_\lambda \propto \lambda^\beta$ (or equivalently $f_\nu \propto \lambda^{\beta+2}$, where $\beta = -2$ is a spectrum of constant AB magnitude, flat in f_ν). $2\,\sigma$ upper limits are placed on the spectral slope of $\beta < -2.44$ (for sources 4551 and 5512 with $J_{AB} = 25.0$) and $\beta < -2.06$ (for sources 2058 and 4532 with $J_{AB} = 25.4$); these limits are conservative, because if the Lyman-α break occurs in the J-band filter (i.e. $z > 8$) rather than short ward of $1.1\,\mu$m then the true spectral slope would be even bluer. The $2\,\sigma$ limits are consistent within the errors with the reported average for $z = 6$ i'-drop galaxies. Stanway et al. (2005) derive values of $\beta = -2.2 \pm 0.2$ from i'-drop galaxies at $z \approx 6$, with Bouwens et al. (2008) reporting $\beta = -2.0$.

As an alternative to the blue $(J - K_S)$ colour being due to a steep blue spectral slope, it is now considered whether the apparent flux excess in the J-band could be due to emission line contamination. To determine lower limits on the equivalent width of this putative line emission, a spectrum flat in f_ν is assumed (i.e., constant AB magnitude with wavelength) longward of Lyman-α; this is typical of a low-extinction star-forming galaxy. The $2\,\sigma$ upper limit for the flux density (f_ν) in the K_s-band is taken as the upper limit on the continuum level in the $J-$band filter, and the $> 1.4\times$ greater flux density (for objects 4551 and 5512) in the J-band ($2\,\sigma$ lower limit) is attributed to line emission. The J band has a width of 3000 Å, which sets a $2\,\sigma$ lower limit on the observed equivalent width of $EW_{obs} > 1205$ Å (for J-drops 4551 & 5512). This corresponds to a rest-frame equivalent width of $EW_{rest} > 133$ Å if the line is Lyman-α at $z = 8$, where it enters the J-band

(this limit is conservative because at larger redshifts, an increasing fraction of the J-band falls below the Lyman-α break, so the contribution of the continuum to the flux density would be even lower and hence the equivalent width higher). These equivalent widths are plausible for the Lyman-break and Lyman-α emitter populations at high redshift (e.g., Dawson et al. 2004). The lower redshift lines can be ruled out with higher confidence (e.g., Hα at $z \approx 0.9$ would have an implausibly high $EW_{rest} > 634\,\text{Å}$, and [O II] 3727 Å at $z \approx 2.3$ would have $EW_{rest} > 365\,\text{Å}$).

The marginal J-band detections are considered to be highly suspect, although they cannot be eliminated from the selection based on their blue spectral slopes or high equivalent width line emission falling in the J-band. They are unconfirmed in any other band studied here and may be the result of spurious detections. Deeper imaging in J, H and K and/or spectroscopy is required to confirm or disprove the nature of these candidates.

3.2.4 Discussion of Other Work

Before 2010, when this work was completed, there were a few authors who provided galaxy candidates at $z > 6.5$ using the Lyman Break technique. As mentioned before, one of the z'-drop candidates, object 2200 has also been identified by Stanway et al. (2008) but with a slight offset of 0.8″. Two other objects were also identified as possible high-redshift candidates in that paper, one of which would not be expected to be detected here because it does not lie within the field considered here and the other object has a signal-to-noise ratio of less than the cut of $S/N > 5$ in the Y-band employed here.

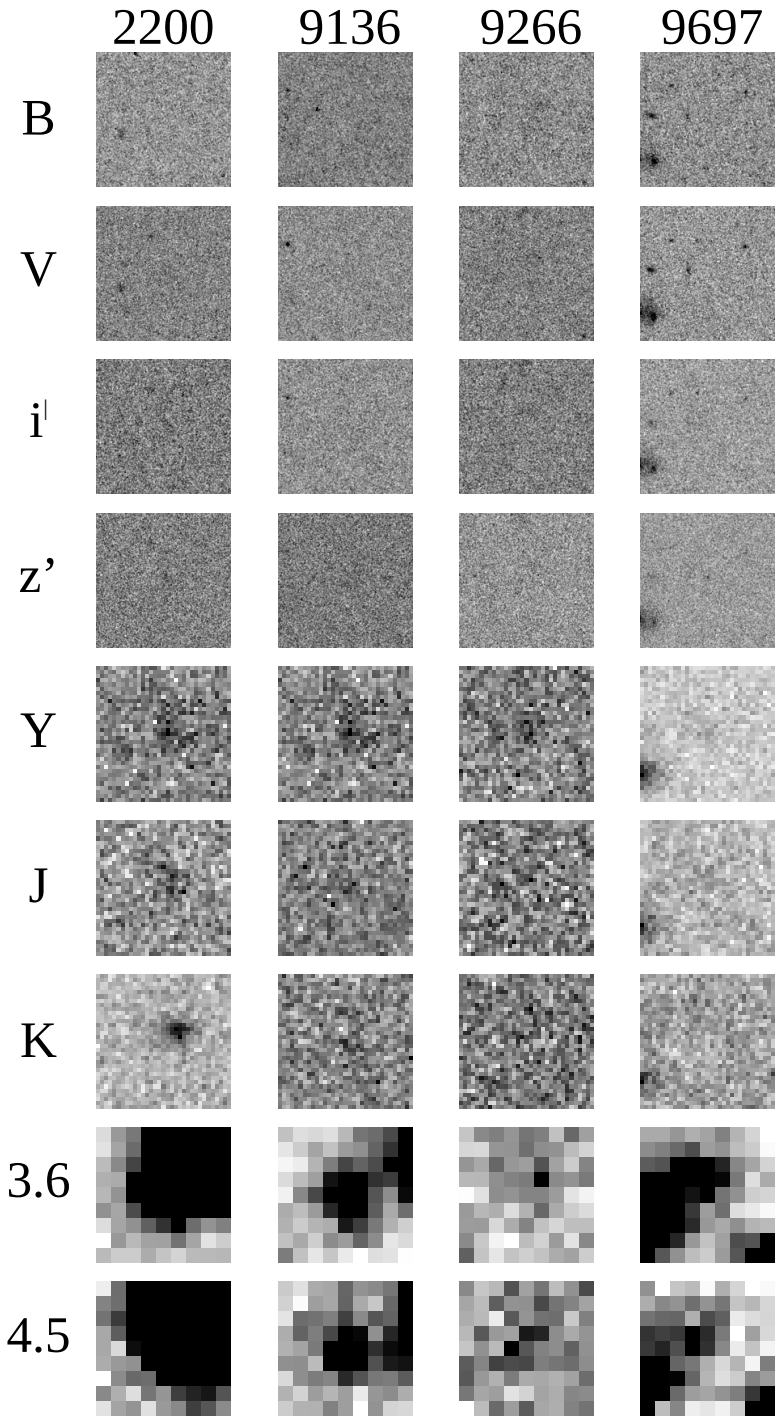

Figure 3.16: z'-band drop-out candidates. Each postage stamp is 5x5 arcsec in size. All candidates are undetected in the optical wavebands at the 2σ level but have $> 5\sigma$ detections in the Y-band. Objects 9136 and 9697 are detected in all of the longer wavelength filters, excluding the Ks-band for Object 9697, making these the most plausible candidates in this work.

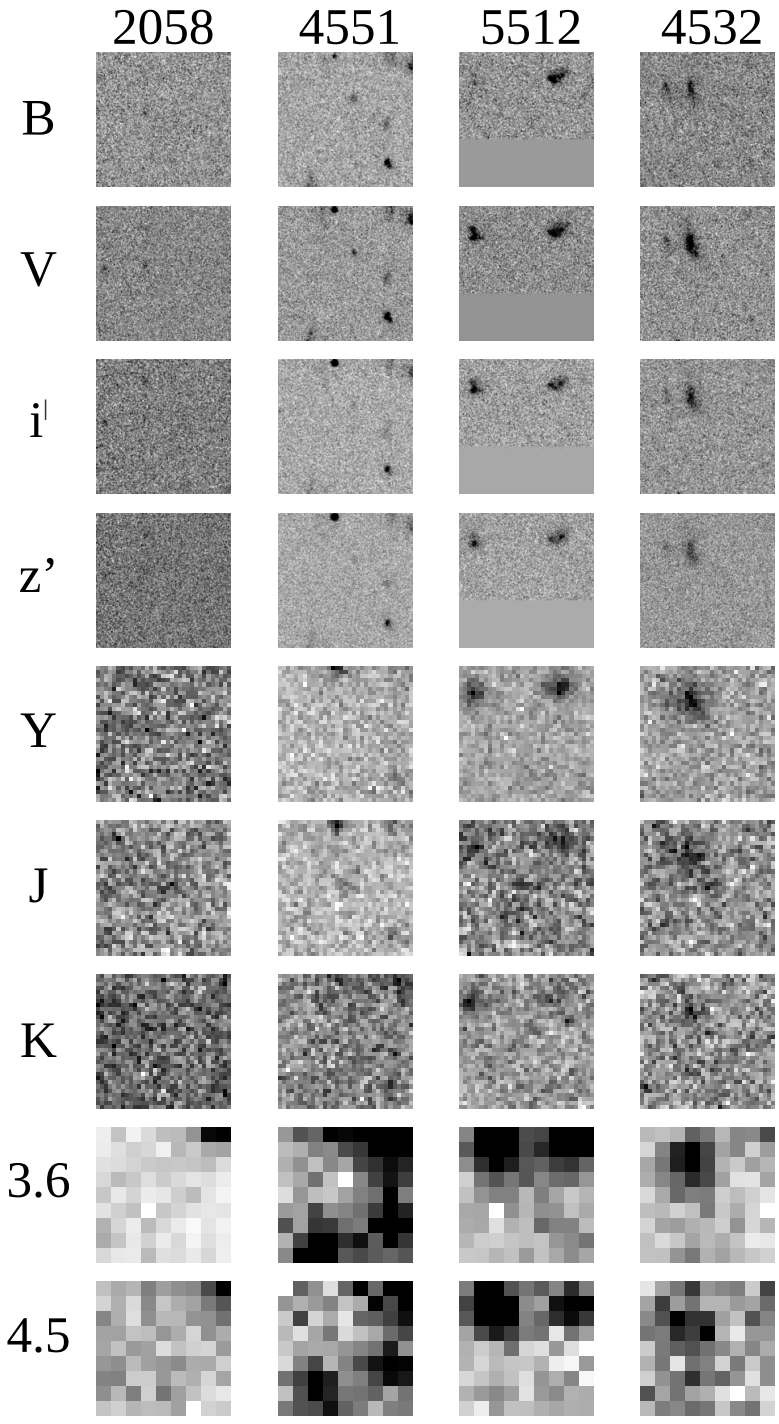

Figure 3.17: Y-band drop out candidates. Each postage stamp is 5x5 arcsec in size. The candidates are undetected in the optical wavebands down to the 2σ level. Each Y-drop candidate is detected in the J-band with $S/N > 5$ but have no clear detections in any of the longer wavelength bands.

Within the limits of their study, Stanway et al. found the luminosity function at $z = 7$ to be consistent with predictions of the luminosity function from Bouwens et al. (2007) and McLure et al. (2009) at $z \sim 6$. Two other objects within the GOODS-South field were originally flagged by Mannucci et al. (2007) as high-redshift candidates but were later dismissed as brown dwarfs based on their morphologies, *Spitzer* colours and spectroscopic information. These objects were included in the original catalogues compiled here as they do have the colours of high-redshift galaxies, and they were also identified in the GOODS-MUSIC catalogue with photometric redshifts of $z \approx 6.9$ (objects 11002 & 7004 in the GOODS-MUSIC catalogue). Based on the non-detection of any credible candidates Mannucci et al. placed constraints on the UV luminosity function at $z = 7$ and claimed strong evolution in the luminosity function from $z = 6$ to $z = 7$. Further evidence for the evolution of the luminosity function from $z = 3.8$ to $z = 6 \rightarrow 7$ is presented in Bouwens et al. (2004, 2005, 2008). No robust J-drops were presented but a number of z'-drop candidates were found. However the observations used in the Bouwens et al. (2008) study were much deeper than in other searches and some results even implied evolution from $z = 6$ to $z = 7$ and a potential luminosity function at $z = 7$ was derived while constraints were set on the luminosity function at $z = 9$ (the J-drop population).

3.2.5 Implications for the UV Luminosity Function

The number of robust candidates that are detected here, can constrain the UV luminosity functions at $z \gtrsim 7$. The number of galaxies expected to be

selected within the survey area for two luminosity functions, derived from lower-redshift samples is calculated. A significant discrepancy between the observed number counts and those predicted would argue for strong evolution in the star-forming population with redshift.

To model the predicted number counts, first a simple model spectrum of a star-forming galaxy is adopted, where the rest-UV spectrum is approximately flat in f_ν longward of Lyman-α (i.e. $\beta = -2$ where $f_\lambda \propto \lambda^\beta$, appropriate for star-forming galaxies at $z \approx 6$ – Stanway et al. 2005) and is severely attenuated below Lyman-α due to the opacity of the intervening neutral hydrogen absorbers (an absorption of $D_A = 0.99$ for $z > 6.5$ is adopted). The Y-band filter is sensitive to the UV continuum longward of Lyman-α at $6.6 < z < 7.7$, although at the higher redshifts the galaxies would have to be extremely luminous to appear in the magnitude-limited sample – not only is the luminosity distance greater, but also a smaller fraction of the filter band-pass lies above Lyman-α. This is modelled by considering small increments of redshift ($\Delta z = 0.1$) between $z = 6$ and $z = 8$, and for each redshift bin, the number of galaxies expected as a function of limiting apparent magnitude is calculated. The expected $z' - Y$ colours are also determined to assess whether the colour cut will select star-forming galaxies in that redshift bin. By summing over all the redshift bins, the expected surface density of z'-drop galaxies as a function of magnitude is obtained. Then the exposure maps are considered, and are used to compute the various areas of sky observed to different limiting magnitudes. For each area observed, the predicted number counts are corrected for the measured completeness as a function of magnitude (see Section 3.1.2). By summing the expected number of galaxies above

the colour cut ($z' - Y > 1.0$) and the significance threshold ($S/N > 5$ in the Y-band) for each area of the survey, the total number of z'-drop star-forming galaxies expected to be found, if the assumed luminosity function is appropriate at $z \approx 7$ is obtained.

The number of expected galaxies derived from models can be compared with the number actually detected. In this work two UV luminosity functions are compared, one derived by Steidel et al. (1999) for Lyman-break galaxies at $z = 3$ (the U-band dropouts), and the other by Bouwens et al. (2007) for the Lyman-break population at $z \approx 6$ (the i'-band dropouts). The Steidel et al. UV luminosity function at $z = 3$ has a faint end slope of $\alpha = -1.6$ and $L^*_{SFR} = 15.0\,M_\odot\,\mathrm{yr}^{-1}$ and $\Phi = 0.00138\,\mathrm{Mpc}^{-3}$, where L^* is derived from the rest-frame UV around 1500 Å and has been converted to an effective star formation rate using the relation $L_{UV} = 8{\times}10^{27}{\times}SFR$ $\mathrm{ergs\,s^{-1}\,Hz^{-1}}$ (Madau et al. 1998), appropriate for a Salpeter (1955) stellar initial mass function. At $z \approx 6$ the Bouwens et al. luminosity function shows strong evolution in L^* from $z \sim 3$, with $L^*_{SFR} = 8.6\,M_\odot\,\mathrm{yr}^{-1}$ (equivalent to $0.575\,L^*_{UV}$ at $z = 3$). The faint end slope is also steeper at $z \approx 6$ ($\alpha = -1.74$) and $\Phi = 0.001135\,\mathrm{Mpc}^{-3}$ (which is $0.82\,\phi^*_{z=3}$).

For the deepest region of this survey (pointing 1), a z'-drop surface density brighter than the 50 per cent completeness limit ($Y_{AB} < 25.9$) of $0.373\,\mathrm{arcmin}^{-2}$ and $0.066\,\mathrm{arcmin}^{-2}$ is expected for the Steidel et al. (1999) and Bouwens et al. (2007) luminosity functions respectively. Accounting for completeness and the different depths as a function of survey area, the total numbers expected are 29.5 ± 5.4 or 5.2 ± 2.3 if the $z = 3$ or $z = 6$ luminosity functions, respectively, are appropriate for the Lyman-break population at

$z \approx 7$ (Figure 3.18). Clearly, as only two z'-drop candidates (and at most three) are robust, a model where there is no evolution in the rest-frame UV luminosity function from $z = 7$ to $z = 3$ can be strongly ruled out, as the number of high-redshift galaxies is over-predicted by a factor of 10. There is some evidence for evolution from $z = 6$ to $z = 7$: it is likely that some or all of the z'-drop candidates are not at $z = 7$, and hence the observed number is at least a factor of two less than the prediction based on the $z = 6$ luminosity function, although the statistical significance of this is marginal given the small numbers.

The same models were applied for the Y-drop candidates. The 50 per cent completeness limit in the J-band is $J_{AB} = 25.4$, correcting for incompleteness means 10.5 ± 3.2 and 1.1 ± 1 Y-drops are expected to be found for the Steidel et al. and Bouwens et al. luminosity functions respectively (Figure 3.19). All four of the candidates lie very close to the $5\,\sigma$ J-band cut and object 4532 is possibly the edge of an extended object $\approx 1.2''$ away. They are also undetected in K_s-band which is of a similar depth to the J-band and hence the sources may be spurious or the result of line contamination in the J-band. Although not all of the Y-band candidates can be ruled out, they are not believed with a high degree of confidence. Thus the Steidel et al. luminosity function is inconsistent with the results found here, implying evolution in the UV luminosity function between $z = 8$ and $z = 3$. Within the errors, the Bouwens luminosity function at $z = 6$ is consistent with the findings presented here.

The limit of the survey described here, for z'-drops at $z \approx 7$, begins to probe the $z = 6$ Bouwens et al. luminosity function if there is little evo-

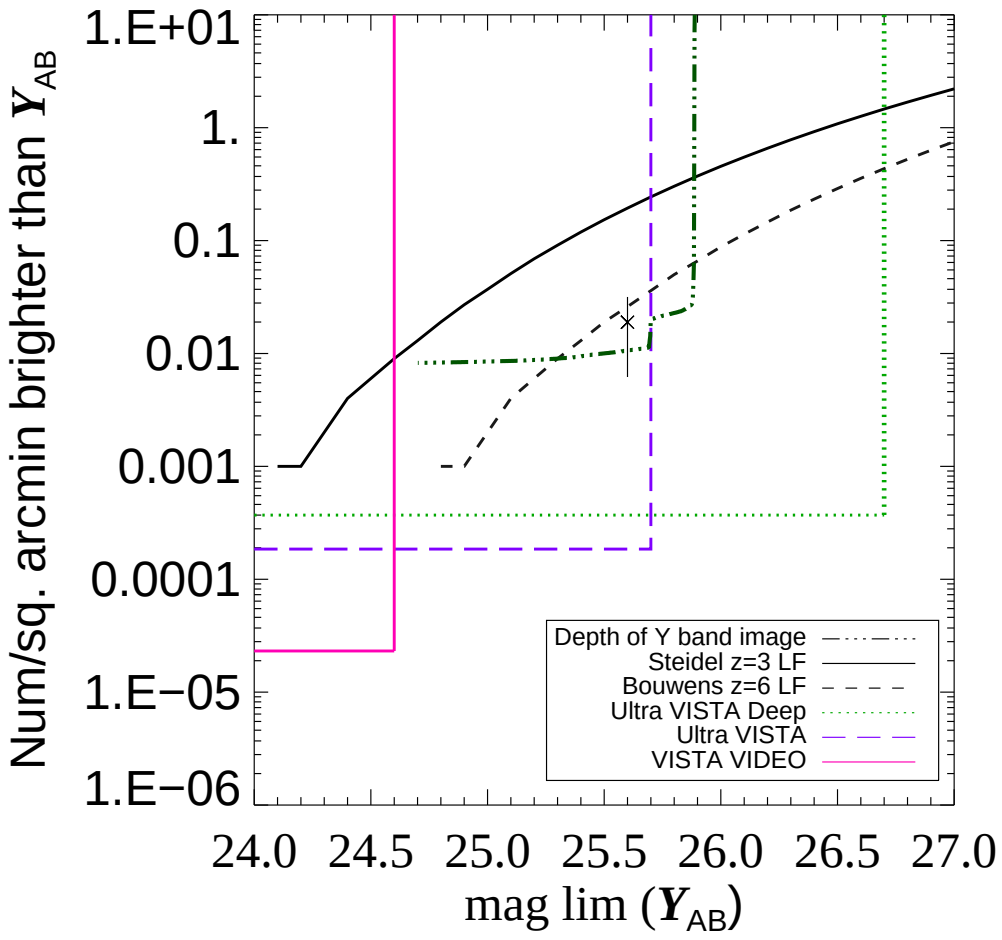

Figure 3.18: Expected number of z'-drops, with the solid (black) line assuming the $z = 3$ luminosity function from Steidel et al. (1996) and the dashed (black) line the $z = 6$ luminosity function from Bouwens et al. (2006). The dotted dashed (dark green) line marks the phase space probed by the Y-band data. If no candidates were found, the region above and to the left of the line would be excluded. The point denotes the two candidates we found. The dotted, hyphenated and solid lines mark the phase spaces that will be probed by the UltraVISTA Deep (light green), the UltraVISTA shallow (purple) and the VISTA VIDEO surveys (pink) respectively. The luminosity functions shown here are not constrained at the bright end but with the depth and area of the VISTA surveys we will be able to measure the form of the function at these bright magnitudes.

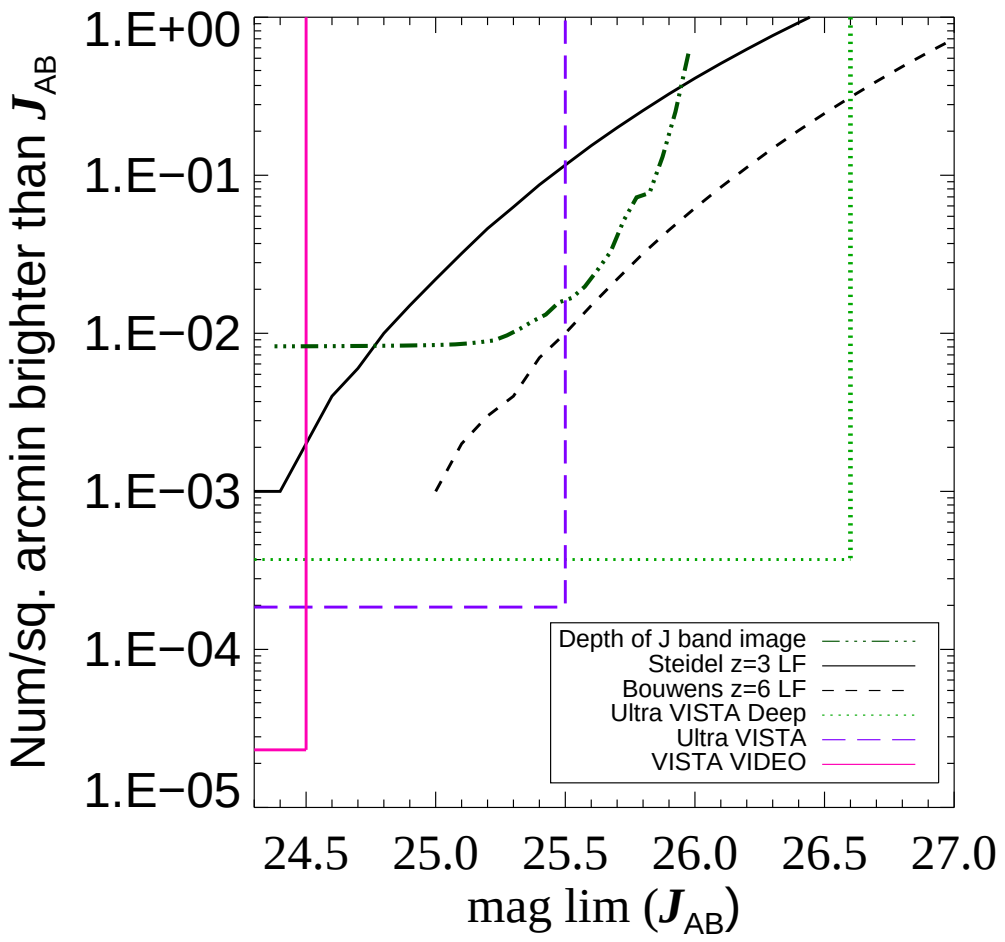

Figure 3.19: Expected number of Y-drops, the various lines are the same as those presented in figure 3.18 but using the J band as the long wavelength detection band.

lution, but in order to constrain the luminosity function more effectively, deeper and/or wider observations are needed. This is a possibility with the VISTA Deep Extragalactic Observations (VIDEO) and the UltraVISTA surveys (Arnaboldi et al. 2007; see also Figures 3.18 and 3.19). Due to its large area of ≈ 12 sq. degrees, VIDEO will be able to probe the bright end of the luminosity function and after five years will reach 5σ limiting magnitudes of $Y_{AB} = 24.6$ and $J_{AB} = 24.5$. UltraVISTA goes considerably deeper (to $Y_{AB} = 25.7$ and $J_{AB} = 25.5$ over 1.5 sq. degrees and $Y_{AB} = 26.7$ and $J_{AB} = 26.6$ over 0.75 sq. degrees) but over a smaller area than VIDEO, and hence UltraVISTA will be more effective at measuring the position of the break (i.e. the knee of the Schechter luminosity function) and the slope of the faint end of the luminosity function (see Figure 3.18).

3.3 Conclusion

I have searched for high-redshift drop-out galaxies in the GOODS-South field using the new HAWK-I Y-band data covering ~ 119 arcmin^2. This data has been complemented with VLT ISAAC J and K_s images in addition to HST-ACS images in B, V, i' and z' along with the deep *Spitzer* data in these fields. A selection criteria of $(Y - J)_{AB} > 0.75$ was employed for the Y-drops and $(z' - Y)_{AB} > 1.0$ was utilised for the z'-drops where both satisfied a $S/N > 5$ cut. These catalogues were matched to the GOODS-MUSIC catalogue to eliminate objects with optical detections from the candidate lists. Each remaining candidate was inspected by eye to eliminate remaining data artifacts, spurious sources and optical detections. A total of 4 Y-drop

candidates were found within the data. Due to the fact that all of the Y-drop candidates are close to our $S/N > 5$ cut and are only significantly detected in the J-band, they are not believed with a high degree of confidence. If none of the Y-band sources are indeed real, then this demands significant evolution in the UV luminosity function since $z = 3$ based on the predictions by Steidel et al. (1999).

A total of 4 possible z'-drop candidates were found, one of which, Object 2200, has a probable low redshift solution of $z_{phot} = 3.25 - 3.85$. Another of the candidates, Object 9266, is only detected in the Y-band. However 2 robust candidates remain, Objects 9136 and 9697, which have significant detections in the IRAC wavebands and photometric redshifts of $z_{phot} > 6.9$. These findings show evolution in the luminosity function since $z = 3$ but are, within the Poisson error, consistent with the Bouwens et al. (2007) $z = 6$ luminosity function although small number statistics preclude any strong statements on the evolution in the Lyman-Break population at $z > 6$ being made. In order to constrain the UV luminosity function at these high redshifts more effectively, searches over a wider and/or deeper area are required. This will be possible with the combination of surveys such as VIDEO and UltraVISTA (Arnaboldi et al. 2007).

Since I undertook my survey for Lyman-break galaxies using the HAWK-I Y-band data, there have been further searches over the GOODS-South field. Another group (Castellano et al. 2010) have also published an analysis of the same data set but search down to $Y = 26.7$ AB mag. They identify seven sources as potential $z \gtrsim 6.5$ galaxies. All but one of these sources lie below our 5σ Y-band limit of $Y = 25.7 - 25.9$ AB mag. The single candidate

above this threshold is designated G2_2370 and is identified in this work as object 9697. The second of my robust candidates (object 9136) was rejected by Castellano et al. (2010) due to a marginal i'-band detection, slightly above their threshold. They also eliminated objects 2200 and 9266 from their candidate list due to more significant detections at the shorter wavelengths. As expected, none of the 4 marginal Y-drop candidates is reproduced.

Seven relatively bright, potentially high redshift ($z \sim 7$), sources over the GOODS-South field were targeted by Fontana et al. (2010) for follow-up spectroscopy. Both of my robust candidates 9136 and 9697 were included in the target list, however no emission lines were detected and therefore they remain unconfirmed via spectroscopy. Five other $z \sim 6.5$ candidate galaxies were also targeted but only a single object, G2_1408, from Castellano et al. (2010) showed a weak emission line. This lack of confirmation led the authors to speculate that there is either a significant interloper population affecting the candidate lists or that some physical mechanism is quenching the Lyα emission at $z \sim 6.5$ possibly due to an increasingly neutral inter-galactic medium.

The GOODS-South field has subsequently been the target of deep *HST* imaging with WFC3, using the F105W Y-band filter over the *Hubble* Ultra Deep Field and flanking field regions, and the narrower F098M Y-band over the Early Release Science (ERS) extended region at the northern end of GOODS-South. Most of my candidates fall outside these regions. However, z'-drop 9697 does fall within the ERS and is confirmed as a good candidate in the high-quality HST images: it is ERS.z.46030 in Wilkins et al. (2010) and ERSz226543006 in Bouwens et al. (2011c) as part of their "possible $z \sim 7-8$

candidates" list with $Y_{AB} = 26.0$ in the narrower F098M filter.

Hence, deeper HST imaging has been able to confirm one of my z'-drops which fell within the WFC3 camera survey as being a robust candidate.

WFC3 has allowed the study of high redshift galaxies to be extended to even greater epochs (i.e. $z \sim 7 - 9$) and many authors have used this instrument to place constraints on the $z = 7$ luminosity function (e.g. Oesch et al. 2009; Ouchi et al. 2009; McLure et al. 2010; Bouwens et al. 2011). Significant evolution in the ultraviolet luminosity function has been found from $z \sim 6$ to $z \sim 7$ even discounting the effects of cosmic variance (Ouchi et al. 2009; Castellano et al. 2010). This is evidenced by the declining comoving number density of galaxies by a factor of 2-2.5 over this epoch (Oesch et al. 2009; McLure et al. 2010). This evolution of the luminosity function has led many authors to invoke a steep faint end slope for the luminosity function, a higher escape fraction of Lyα photons and/or lower metallicity in order for galaxies to be responsible for reionisation at $z \sim 7$ (e.g. Ouchi et al. 2009; Bunker et al. 2010; McLure et al. 2010; Grazian et al. 2011). Bouwens et al. (2011c) finds evidence for a steeper faint end slope with a value of $\alpha = -2.01 \pm 0.21$ for the $z = 7$ luminosity function compared to the -1.73 ± 0.05 for the $z = 4$ luminosity function. While this is evidence for a steep slope it is within the uncertainties of the slope at $z \sim 4$.

The parameters for a number of recently determined $z = 7$ luminosity functions are shown in Table 3.4. My 1 ± 1 remaining robust candidates 9136 and 9697 have best-fit photometric redshifts of $z_{\rm phot} = 7.01$ and $z_{\rm phot} = 6.92$ respectively. Due to the low number of candidates and therefore large uncertainties, I have shown in Section 3.2.5 that my candidates are consistent

Table 3.4: Determinations of the Best-fit Schecter Parameters for the Rest-frame UV luminosity functions at $z \sim 7$. Table taken from Bouwens et al. (2011c).

Reference	$M^*_{\rm UV}$	ϕ^* (10^{-3} Mpc^{-3}	α
Bouwens et al. (2011c)	-20.14 ± 0.26	$0.86^{+0.70}_{-0.39}$	-2.01 ± 0.21
Castellano et al. (2010)	-20.24 ± 0.45	$0.35^{+0.16}_{-0.11}$	-1.71 (fixed)
McLure et al. (2010)	-20.04	0.7	-1.71 (fixed)
Oesch et al. (2010)	-19.91 ± 0.09	1.4 (fixed)	-1.77 ± 0.20
Ouchi et al. (2009)	-20.1 ± 0.76	$0.69^{+2.62}_{-0.55}$	-1072 ± 0.65
Oesch et al. (2009)	-19.77 ± 0.30	1.4 (fixed)	-1.74 (fixed)
Bouwens et al. (2008)	-19.8 ± 0.4	$1.1^{+1.7}_{-0.7}$	-1.74 (fixed)

with the scenario of no evolution in the luminosity function since $z = 6$. However they are also consistent with the $z = 7$ luminosity functions shown in Table 3.4.

Chapter 4

Selection of COSMOS 70μm Sample

The COSMOS survey is a multiwavelength survey utilising X-ray (XMM and Chandra; Hasinger et al. 2007; Elvis et al. 2007), UV/optical (GALEX, HST, CFHT and Subaru; Scoville et al. 2007a; Capak et al. 2007; Taniguchi et al. 2007), infrared (UKIRT, UH2.2m, KPNO, Blanco, *Spitzer*; Capak et al. 2007; Sanders et al. 2007; Frayer et al. 2009), submillimetre (CSO and IRAM; Bertoldi et al. 2007) and radio wavelengths (VLA; Schinnerer et al 2010). For an overview of the COSMOS project and its associated data products, see Scoville et al. (2007b). It was focused on a 2 square degree equatorial field. The main aim of the project is to study large scale structure and the formation and evolution of galaxies over the majority of cosmic time (75 per cent). S-COSMOS is the branch of the COSMOS survey carried out with the *Spitzer* IRAC and MIPS instruments. MIPS (Multiband Imaging Photometer) was capable of observing in the mid-far infrared at wavelengths

of 24, 70 and 160μm.

The 70μm waveband samples close to the rest-frame far-infrared peak. Due to the fact that this peak arises as a result of obscured star formation heating dust, this makes 70μm flux a good tracer of star formation. This waveband was used to select a sample of low to intermediate redshift, highly star-forming galaxies.

The original selection of objects used in this Chapter and Chapters 5 & 6 was based on the second version (v2) of the MIPS 70μm catalogue. Later, with the release of the version 3 catalogue, the sample was reselected. In this chapter, I will describe the selection process from both of these catalogues and the optical spectroscopy obtained for a sub-sample of 70μm sources from the version 2 selection.

4.1 COSMOS 70μm Version 2 Catalogue

Version 2 of the 70μm catalogue was comprised of 168 objects over the COSMOS field (Scoville et al. 2007b). In order to obtain spectroscopy of these objects a refinement of the positional accuracy, above what is given in the 70μm catalogue, is required. Redshifts, preferably spectroscopic, are desired in order to determine the far-infrared luminosity function (see Chapter 5) and the far-infrared/radio correlation (see Chapter 6), therefore a sample of 70μm detected sources were selected for spectroscopy with AAOmega, which is a dual-beam fibre-fed multi-object spectrograph on the 3.9-m Anglo-Australian Telescope. The angular size of each fibre on AAOmega, in multiple object spectroscopy mode, is $\sim 2''$. However, the point response function of the

MIPS photometer at 70 μm is $\sim 18''$, thus the positional uncertainty of a source becomes an issue for positioning the fibres. In order to observe these objects with the AAT it is necessary to refine the position. To achieve this the 70μm fluxes were matched to successively shorter wavelength data with better positional accuracy. The matching was carried out in stages to maximise the probability of correctly associating the 70μm sources with their shorter wavelength counterparts. The matching radii were determined by taking in to account the positional uncertainty for both of the matching wavebands.

First, the 70μm sources were matched to the 24μm catalogue within a search radius of $10''$ and 153 objects were found to have matches. 13 of the 15 unmatched objects were not covered by the 24μm observations and of the remaining two one was faintly visible, while the other was undetected. Then using the 24μm positions, 153 sources were matched to the IRAC data, within $2''$ and 117 matches were found. The 36 sources that were unmatched fell outside of the IRAC data. Lastly, the remaining 117 sources were matched to the the COSMOS ACS catalogue [1] which is i-band selected ($i < 25AB_{mag}$) and covers 2 square degrees. Photometric redshifts were associated with the COSMOS ACS catalogue by Ilbert et al. (2009). To find matches to the COSMOS ACS catalogue, a search radius of $1''$ was utilised and 103 matches were found. The 14 sources that did not have matches were located in an area not covered by the ACS imaging. This resulted in the initial selection of 103 70 μm sources, from which, just over half (56) were randomly selected for spectroscopy. From this sample, 49 spectroscopic redshifts were obtained

[1]The COSMOS ACS data is available from http://vizier.cfa.harvard.edu/viz-bin/VizieR?-source=II/284

from the observations with AAOmega, the coordinates and redshifts of these objects are given in Table 4.1.

Table 4.1: Table of the spectroscopic redshifts of the 49 70μm sources obtained with AAOmega. MIPS-ID, IRAC-ID and ACS-ID are the ID numbers taken from the MIPS 70μm v2 catalogue, the IRAC catalogue and the ACS catalogue respectively. The RA and Dec are the positions from the COSMOS ACS catalogue. S_{70} and σ_{70} gives the 70μm flux and its associated error in mJy from the v3 70μm catalogue. The z_{phot} is the photometric redshift associated with the COSMOS ACS catalogue and determined by Ilbert et al. (2009). Fiber is the AAOmega fiber number used to observe the 70μm source. Obs-ID is the observing id used for AAOmega, derived from the MIPS ID number. z_{spec} is the spectroscopic redshift measured with AAOmega. q stands for quality and is a measure of the security of the spectroscopic redshift on a scale of 1-5 with 5 being a highly secure determination. The object with MIPS-ID 247 had no match to the ACS catalogue and so the RA and Dec is from the match to the IRAC catalogue.

MIPS-ID	IRAC-ID	ACS-ID	RA	Dec	S_{70}	σ_{70}	z_{phot}	Fiber	Obs-ID	q	z_{spec}
296	19931	79069	150.72162	1.52685	18.05	5.69	0.63	56	P70_296	4	0.62881
305	24286	73949	150.6134	1.546519	11.57	4.35	0.09	62	P70_305	5	0.10289
311	28141	108612	150.52022	1.56554	12.63	3.10	0.21	67	P70_311	5	0.09813
320	32667	287025	149.59378	1.584794	126.84	3.96	0.02	144	P70_320	5	0.02764
321	32903	252068	149.73014	1.586028	16.77	3.74	0.65	136	P70_321	3	0.62272

Continued on the next page

Table 4.1 – continued from previous page

MIPS-ID	IRAC-ID	ACS-ID	RA	Dec	S_{70}	σ_{70}	z_{phot}	Fiber	Obs-ID	q	z_{spec}
359	44756	513810	150.3316	1.642763	114.82	3.87	0.29	71	P70_359	4	0.36629
373	51694	547310	150.21341	1.674234	17.54	5.97	0.22	92	P70_373	5	0.16601
442	82433	989977	149.8907	1.818334	16.87	4.29	0.16	134	P70_442	5	0.13289
460	91692	784016	150.57438	1.856765	67.15	4.94	0.07	45	P70_460	5	0.06252
486	380627	740575	150.80633	1.895363	7.47	3.79	0.06	30	P70_486	5	0.04532
490	100723	894161	150.13791	1.903949	21.38	3.82	0.2	101	P70_490	4	0.21984
500	104470	851225	150.33157	1.921229	29.76	4.00	0.16	64	P70_500	4	0.09854
502	105643	850467	150.26559	1.92593	31.71	3.82	0.18	75	P70_502	5	0.16809
541	119393	1346471	149.88016	1.987962	29.35	3.66	0.07	140	P70_541	4	0.1084
566	124429	1419372	149.44795	2.010338	22.74	3.92	0.12	180	P70_566	3	0.53152
588	132474	1372394	149.68634	2.047093	6.58	3.66	0.18	175	P70_588	4	0.09261
610	137001	1327363	149.785	2.067674	13.56	3.88	0.14	172	P70_610	4	0.50051
653	148004	1277317	149.95115	2.117754	7.40	3.58	0.16	142	P70_653	3	0.46271

Continued on the next page

Table 4.1 – continued from previous page

MIPS-ID	IRAC-ID	ACS-ID	RA	Dec	S_{70}	σ_{70}	z_{phot}	Fiber	Obs-ID	q	z_{spec}
663	149570	1314264	149.79298	2.12563	29.05	4.03	0.38	163	P70_663	3	0.35321
676	152871	1560623	150.32905	2.139546	56.10	7.67	0.29	39	P70_676	5	0.16798
683	154936	1673063	149.93529	2.14962	17.76	3.80	0.3	145	P70_683	3	0.30879
699	159621	1704835	149.89171	2.169369	49.46	3.79	0.22	147	P70_699	5	0.18595
719	167281	1501445	150.59848	2.192379	40.35	7.61	0.17	396	P70_719	4	0.12229
733	168487	1659309	149.89456	2.208026	12.06	3.51	0.39	161	P70_733	4	0.34508
741	171477	1616073	150.09563	2.22017	23.92	3.98	0.06	114	P70_741	5	0.18589
774	179330	1687625	149.84102	2.254936	15.38	5.28	0.31	206	P70_774	4	0.34452
787	184609	1563881	150.25277	2.278139	15.08	3.21	0.21	6	P70_787	5	0.16596
793	186192	1561724	150.3748	2.284759	18.04	3.12	0.12	392	P70_793	5	0.07538
816	192262	1961157	150.07602	2.304862	146.44	3.38	0.25	353	P70_816	4	0.12296
818	190616	1922756	150.3355	2.304947	20.19	3.11	0.16	3	P70_818	5	0.12284
848	394841	1812045	150.74592	2.343078	18.68	6.08	0.03	390	P70_848	5	0.04421

Continued on the next page

Table 4.1 – continued from previous page

MIPS-ID	IRAC-ID	ACS-ID	RA	Dec	S_{70}	σ_{70}	z_{phot}	Fiber	Obs-ID	q	z_{spec}
893	207937	1899672	150.53263	2.380782	12.31	2.93	0.09	379	P70_893	5	0.17627
951	396322	1962614	150.11895	2.457178	54.11	3.05	0.31	389	P70_951	5	0.24789
976	231230	2310968	150.31458	2.482922	48.48	2.74	0.15	368	P70_976	4	0.07505
984	236453	2383625	150.02316	2.497129	9.23	2.77	0.11	231	P70_984	4	0.10847
1006	240012	2185127	150.79488	2.5231	29.24	5.44	0.19	375	P70_1006	4	0.19442
1007	240212	2301423	150.22856	2.523945	11.73	3.10	0.36	362	P70_1007	3	0.37567
1094	402652	2754649	149.77294	2.636147	8.93	2.48	0.04	247	P70_1094	4	0.07854
1107	267385	2593896	150.43734	2.643231	17.76	2.76	0.08	355	P70_1107	4	0.10472
1128	273793	2581931	150.60726	2.674518	23.41	3.26	0.1	356	P70_1128	5	0.09397
1131	275182	2581048	150.68933	2.680503	9.80	6.02	0.27	358	P70_1131	3	0.27471
1132	275665	2700037	150.19332	2.683072	14.92	3.40	0.32	335	P70_1132	5	0.31135
1158	282967	2731440	150.03859	2.71323	9.23	2.60	0.01	289	P70_1158	5	0.03241
1187	294402	2561816	150.59493	2.755317	12.05	2.70	0.07	347	P70_1187	5	0.07193

Continued on the next page

Table 4.1 – continued from previous page

MIPS-ID	IRAC-ID	ACS-ID	RA	Dec	S_{70}	σ_{70}	z_{phot}	Fiber	Obs-ID	q	z_{spec}
1218	300982	3026076	150.19578	2.794368	13.25	3.06	0.33	310	P70_1218	3	0.24977
1245	314902	3011457	150.28505	2.854104	13.54	2.62	0.16	326	P70_1245	4	0.10301
247	148004	1277317			63.21	2.57	0.16	104	P70_247	5	0.08261
253	158856	1708638	149.85029	2.166726	16.50	3.76	0.85	74	P70_253	5	0.08587
499	175128	1692169	149.77093	2.235695	16.41	1.53	1.02	176	P70_499	5	0.03201

4.2 AAOmega Observations

The observations of the 56 70μm selected sources from the COSMOS v2 catalogue (Frayer et al. 2009) are described below. The observations were undertaken in service mode, at the AAT on the night of 3 January 2008. The AAOmega spectrograph was used with the MOS fibre feed from the 2dF fibre positioner (Saunders 2004; Sharp 2006). The red and blue arms of AAOmega were used with the 580V and 385R VPH gratings centred and blazed at 4800Å and 7250Å, yielding spectral resolutions (3.4 pixels per resolution element) of R$\sim$8200 and R$\sim$7245. The goal of the observations was to measure the redshifts of the objects using absorption in the continuum of the spectra and/or using emission lines, therefore wavelength coverage was considered more important than the resolution of the spectra. The 5700Å AAOmega dichroic was used. Skies were clear with a seeing of approximately 1.7″.

Two fibre configurations were used. Each observing block consists of a flat-field frame (quartz-halogen lamp), an arc frame for wavelength calibration (CuAr, FeAr, He and Neon), a set of twilight sky flat-field frames (to normalise the relative fibre transmissions for sky subtraction) and a series of 1800sec science frames for each configuration. The total observing time was 3x1800sec.

4.2.1 Data Reduction

As is usual for AAOmega, the data were processed using the 2dfdr data reduction package. 2dfdr performs the standard reduction operations: overscan correction; fibre trace and extraction; flat fielding and wavelength calibration.

Twenty-five fibres in each configuration are given over to observation of blank sky regions in order to create an average sky spectrum during observations. Sky subtraction is performed using this sky spectrum. The relative intensity of sky to subtract is determined from observations of twilight flat-field frames taken at the end of the night. Science frames are combined using a single relative flux weighting derived from spectral intensities in each frame.

A cosmic ray rejection was also performed on the 2D science frames by 2dfdr prior to extraction, following the prescription of van Dokkum (2001).

Spectroscopic redshifts were determined by examining the spectra by eye, and using the runz program to 'guess' the emission/absorption line. This could then be verified by overlaying the positions of the spectral lines relative to the 'guessed' line. All of the spectra with typical emission lines overlaid are shown in Figure 4.1.

4.3 COSMOS 70μm Version 3 Catalogue

Frayer et al. (2009) released version three (v3) of the 70μm COSMOS catalogue. In order to take advantage of these new data the sample was re-selected. The selection was carried out in a similar manner to the original selection described in Section 4.1. First, a region was defined, covered by the MIPS 24μm and 70μm data as well as the IRAC and ACS. This region was limited to be between 149.51 and 150.75 degrees in right ascension, and between 1.51 and 2.89 degrees in declination, (see Figure 4.2) covering a total of 1.7 square degrees. 878 sources fell within this region. A flux-density limit of 10 mJy was imposed on the 70μm catalogue, corresponding to 100

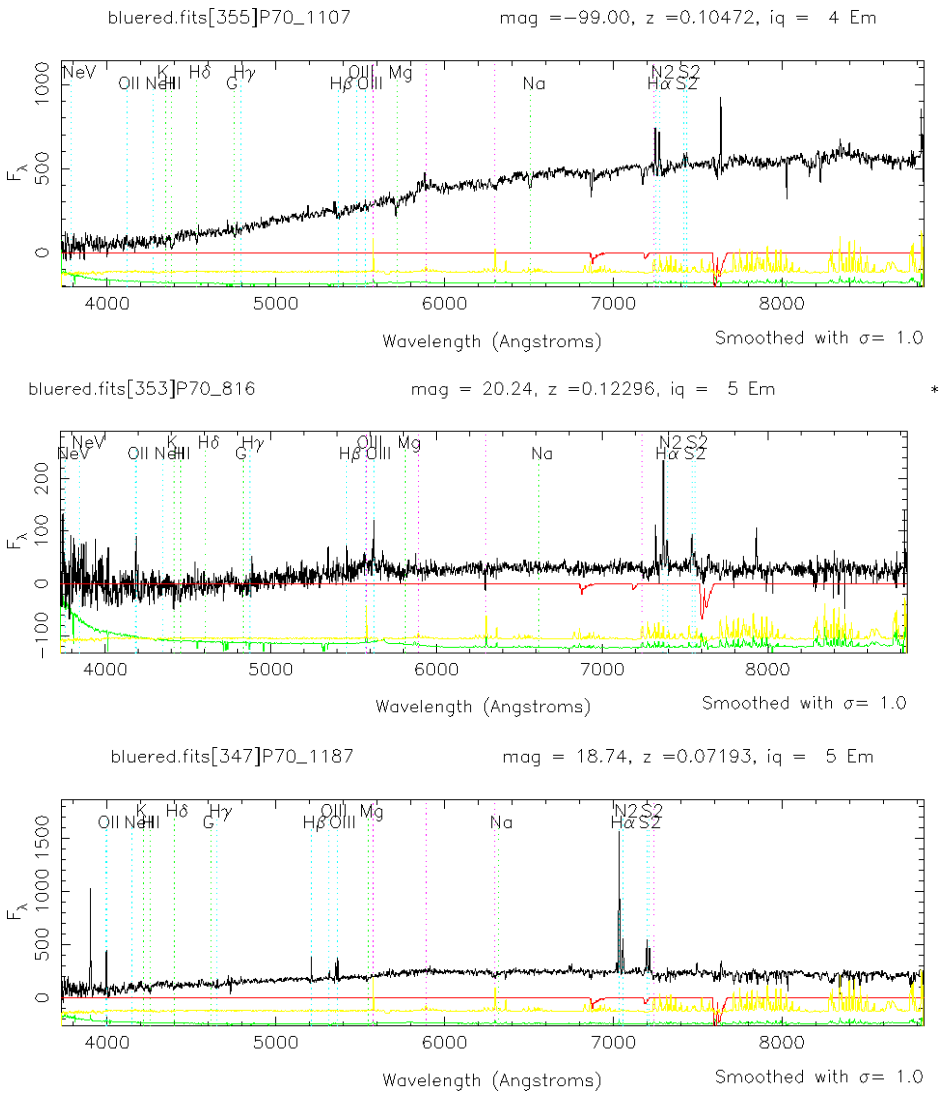

Figure 4.1: The optical spectroscopy taken with AAOmega for 70μm sources with the positions of potential emission and absorption lines overlaid in red and green respectively. The P70 ID number is the same 70μm ID number shown in Table 4.1 from v2 of the COSMOS catalogue and iq is the quality for each spectrum ranging from 1-5 with 5 being the most robust, also shown in Table 4.1. The yellow,red and green lines shown at the bottom of the plots represent the sky, atmospheric absorption and variance spectra respectively. The plots were generated using the 2dF redshift code runz created by W. Sutherland.

bluered.fits[326]P70_1245 mag =−99.00, z =0.10301, iq = 0 Manual

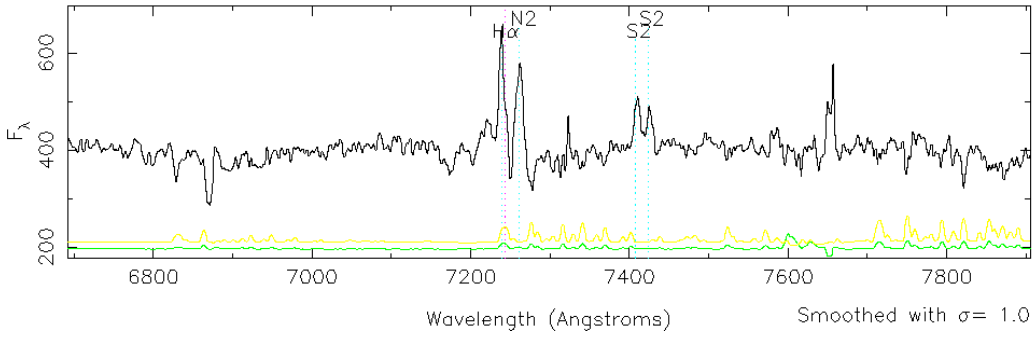

bluered.fits[310]P70_1218 mag = 19.83, z =0.24977, iq = 0 E/X Disc *

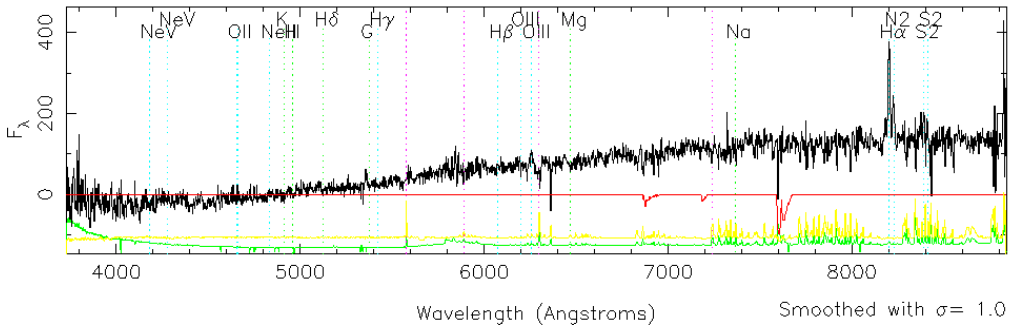

bluered.fits[289]P70_1158 mag =−99.00, z =0.03241, iq = 0 E/X Disc *

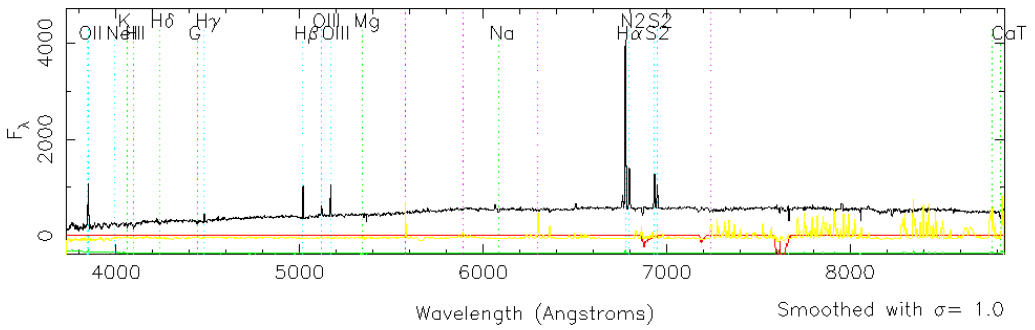

bluered.fits[247]P70_1094 mag =−99.00, z =0.07854, iq = 5 Em *

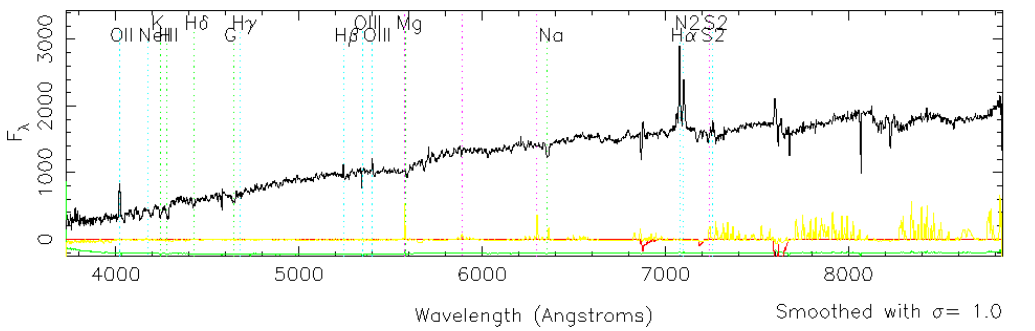

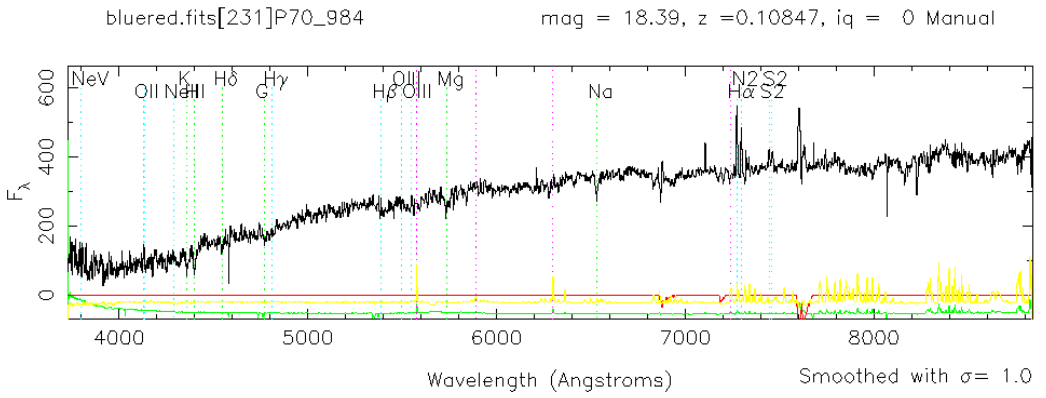
bluered.fits[231]P70_984
mag = 18.39, z =0.10847, iq = 0 Manual
NeV
OII NeIII
K
Hδ
G
Hγ
Hβ OIII
Mg
Na
N2 S2
Hα S2
Fλ
0
200
400
600
4000
5000
6000
7000
8000
Wavelength (Angstroms)
Smoothed with σ= 1.0

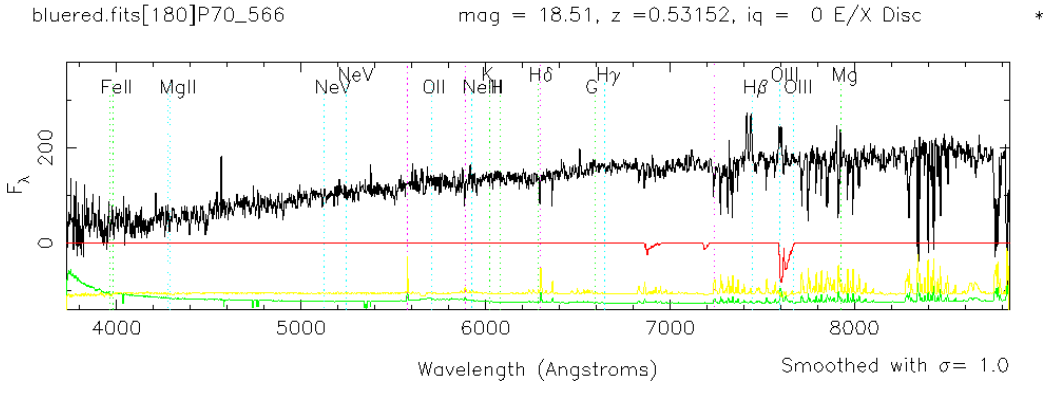
bluered.fits[180]P70_566
mag = 18.51, z =0.53152, iq = 0 E/X Disc
*
FeII
MgII
NeV
OII
NeIII
K
H
Hδ
G
Hγ
Hβ
OIII
Mg
Fλ
0
200
4000
5000
6000
7000
8000
Wavelength (Angstroms)
Smoothed with σ= 1.0

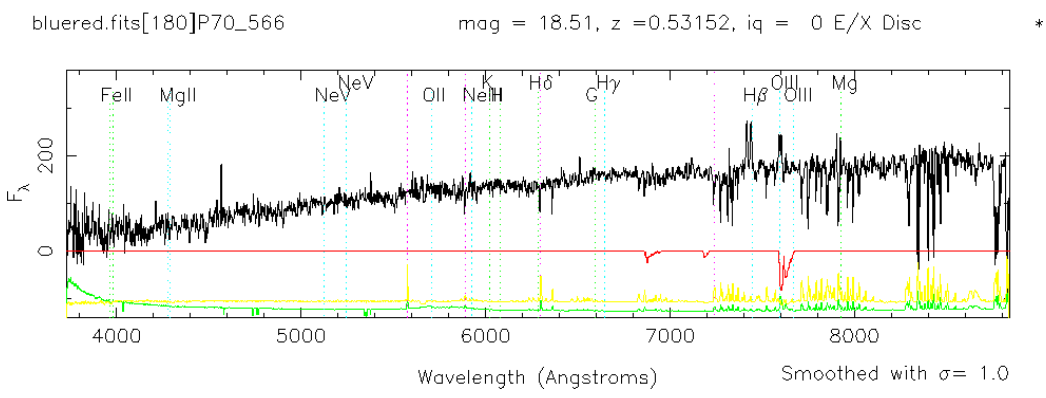
bluered.fits[180]P70_566
mag = 18.51, z =0.53152, iq = 0 E/X Disc
*
FeII
MgII
NeV
OII
NeIII
K
H
Hδ
G
Hγ
Hβ
OIII
Mg
Fλ
0
200
4000
5000
6000
7000
8000
Wavelength (Angstroms)
Smoothed with σ= 1.0

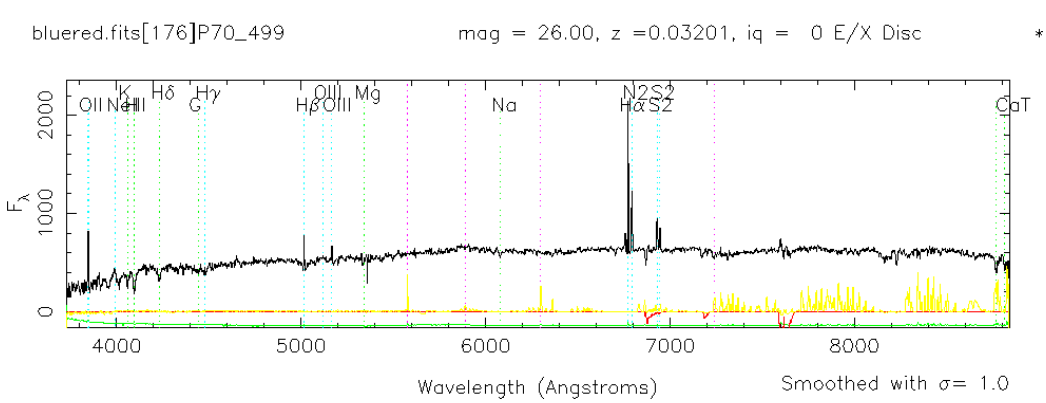
bluered.fits[176]P70_499
mag = 26.00, z =0.03201, iq = 0 E/X Disc
*
OII NeIII
K
Hδ
G
Hγ
Hβ OIII
OIII
Mg
Na
N2 S2
Hα S2
CaT
Fλ
0
1000
2000
4000
5000
6000
7000
8000
Wavelength (Angstroms)
Smoothed with σ= 1.0

bluered.fits[175]P70_588 mag =−99.00, z =0.09261, iq = 0 Manual

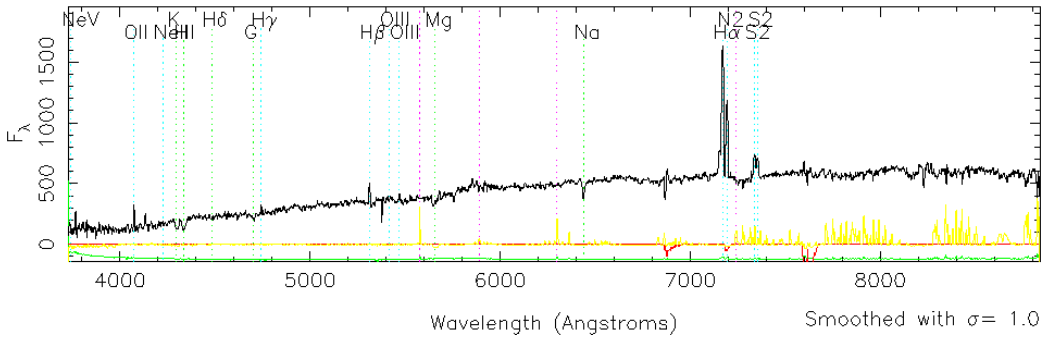

bluered.fits[172]P70_610 mag =−99.00, z =0.50051, iq = 0 E/X Disc

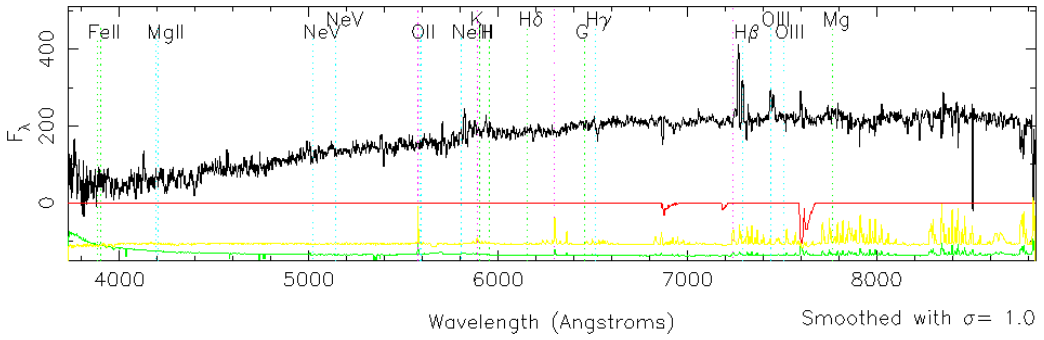

bluered.fits[163]P70_663 mag = 19.21, z =0.35321, iq = 0 E/X Disc *

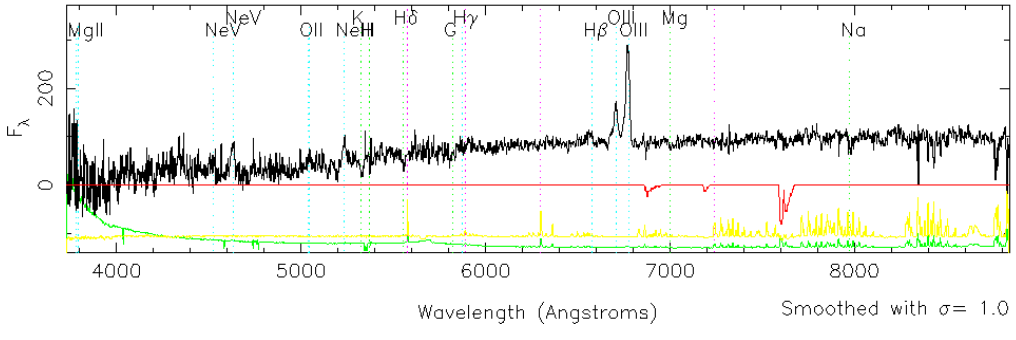

bluered.fits[161]P70_733 mag = 19.87, z =0.34508, iq = 0 Manual

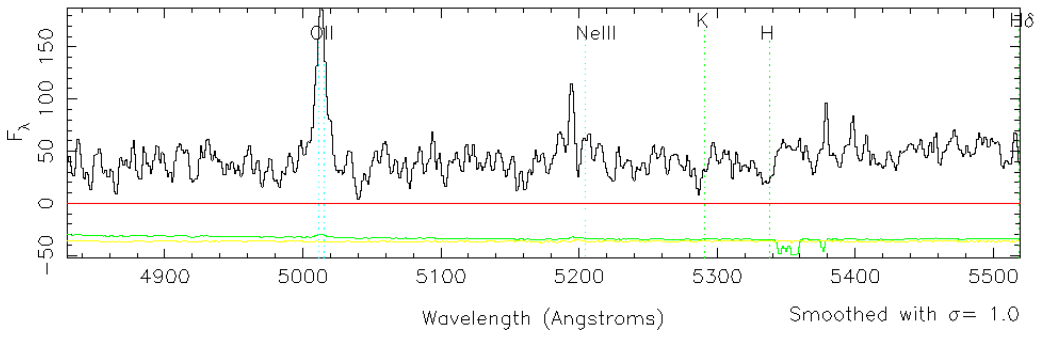

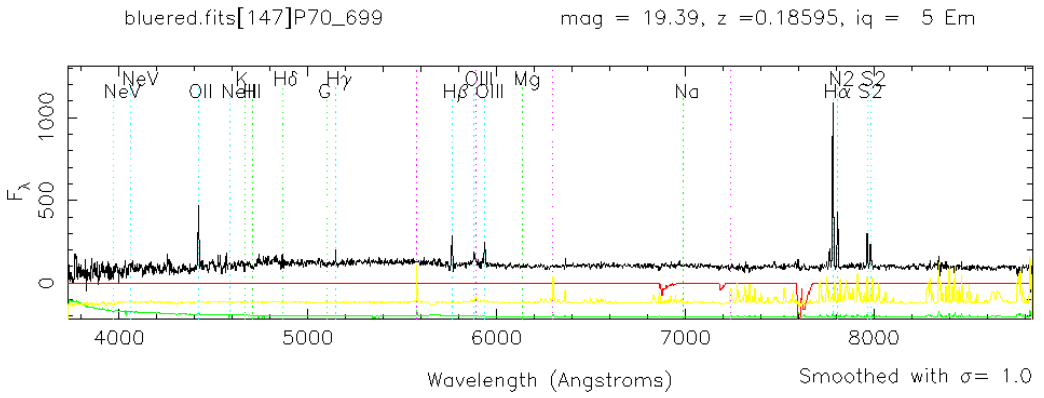
bluered.fits[147]P70_699
mag = 19.39, z =0.18595, iq = 5 Em
NeV
NeV
OII
NeIII
K
H
Hδ
G
Hγ
Hβ
OIII
OIII
Mg
Na
N2
Hα
S2
S2
Fλ
0
500
1000
4000
5000
6000
7000
8000
Wavelength (Angstroms)
Smoothed with σ= 1.0

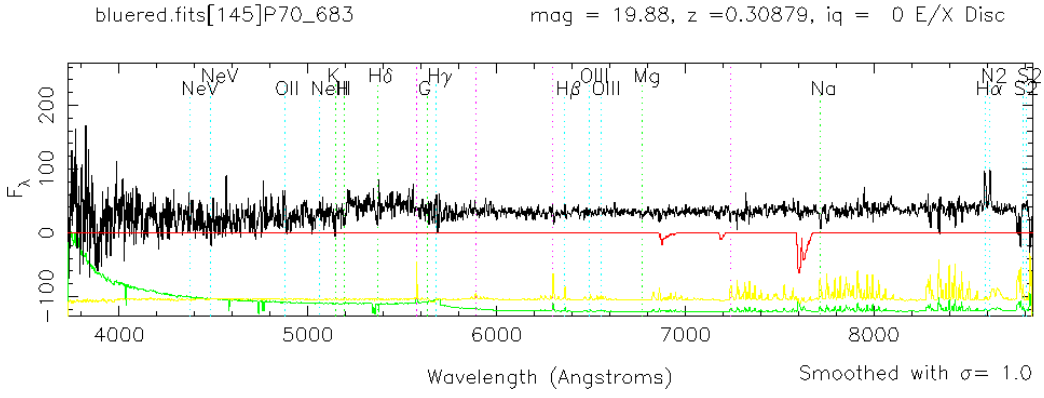
bluered.fits[145]P70_683
mag = 19.88, z =0.30879, iq = 0 E/X Disc
NeV
NeV
OII
NeIII
K
H
Hδ
G
Hγ
Hβ
OIII
OIII
Mg
Na
N2
Hα
S2
S2
Fλ
−100
0
100
200
4000
5000
6000
7000
8000
Wavelength (Angstroms)
Smoothed with σ= 1.0

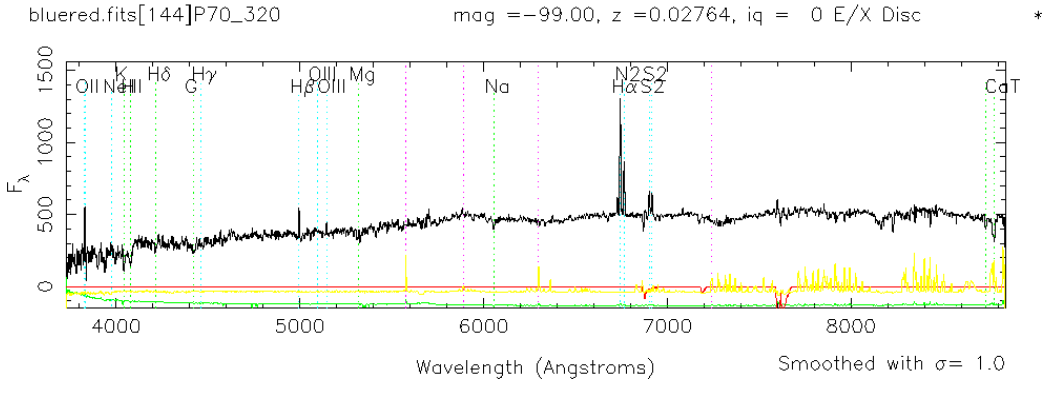
bluered.fits[144]P70_320
mag =−99.00, z =0.02764, iq = 0 E/X Disc
*
OII
NeIII
K
H
Hδ
G
Hγ
Hβ
OIII
OIII
Mg
Na
N2
Hα
S2
S2
CaT
Fλ
0
500
1000
1500
4000
5000
6000
7000
8000
Wavelength (Angstroms)
Smoothed with σ= 1.0

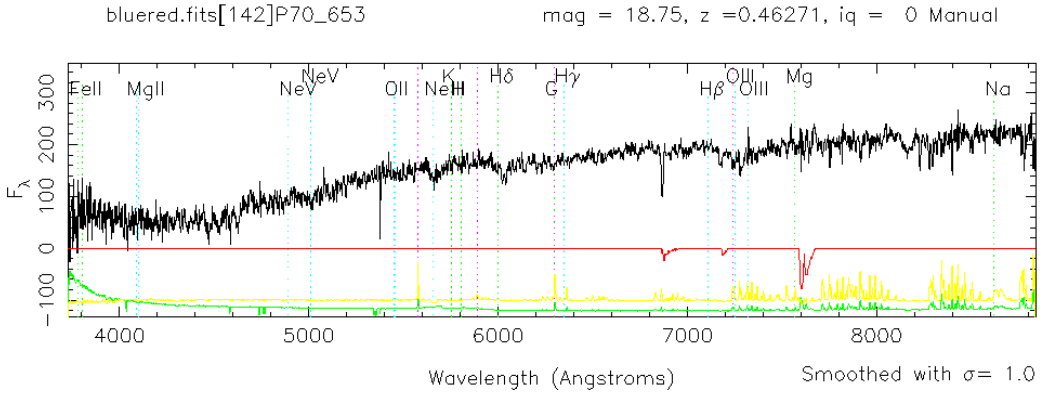
bluered.fits[142]P70_653
mag = 18.75, z =0.46271, iq = 0 Manual
FeII
MgII
NeV
NeV
OII
K
NeIII
H
Hδ
G
Hγ
Hβ
OIII
OIII
Mg
Na
Fλ
−100
0
100
200
300
4000
5000
6000
7000
8000
Wavelength (Angstroms)
Smoothed with σ= 1.0

bluered.fits[140]P70_541 mag = 19.09, z =0.10840, iq = 5 Em

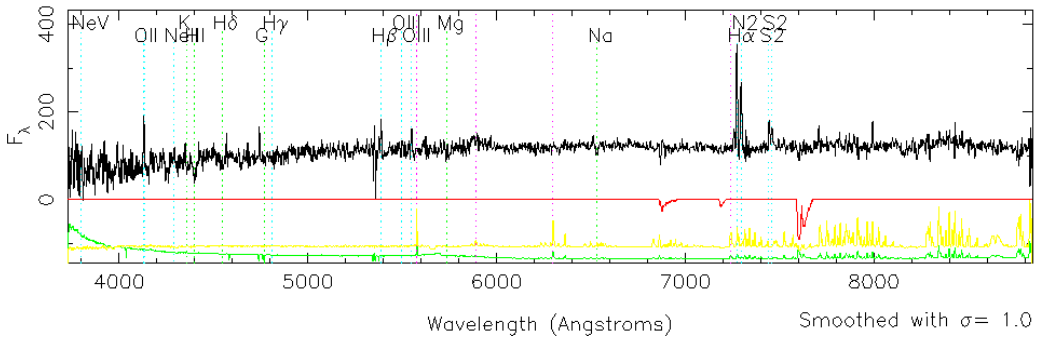

bluered.fits[136]P70_321 mag = 20.49, z =0.62272, iq = 0 E/X Disc *

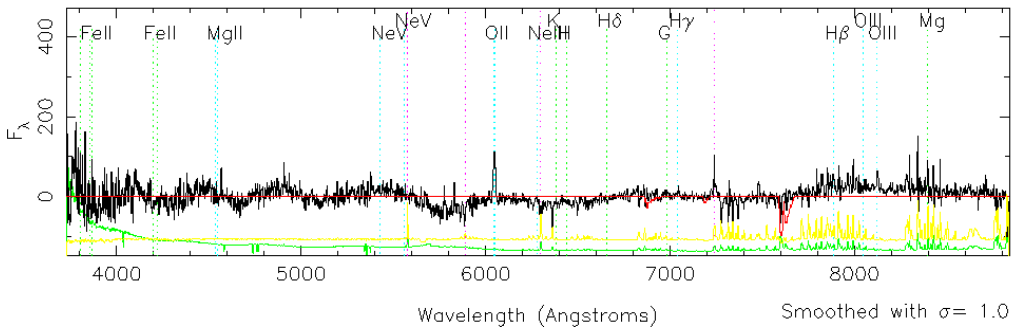

bluered.fits[134]P70_442 mag = 18.19, z =0.13289, iq = 5 Em *

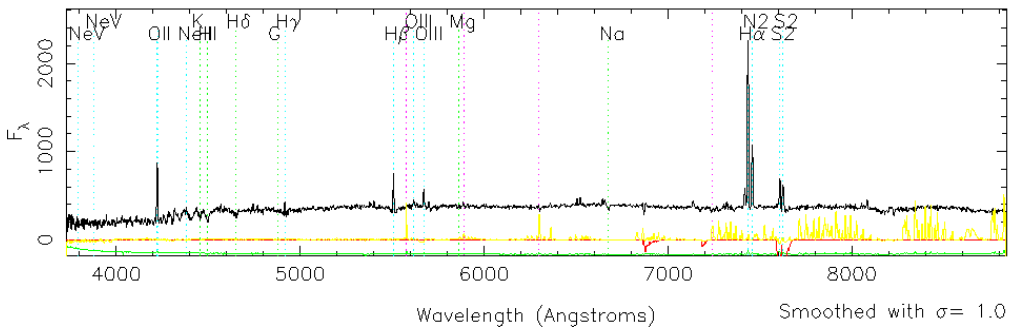

bluered.fits[114]P70_741 mag =−99.00, z =0.18589, iq = 5 Em

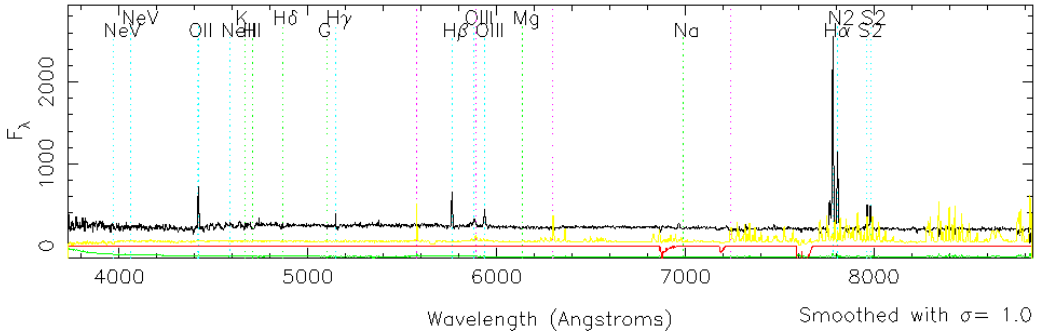

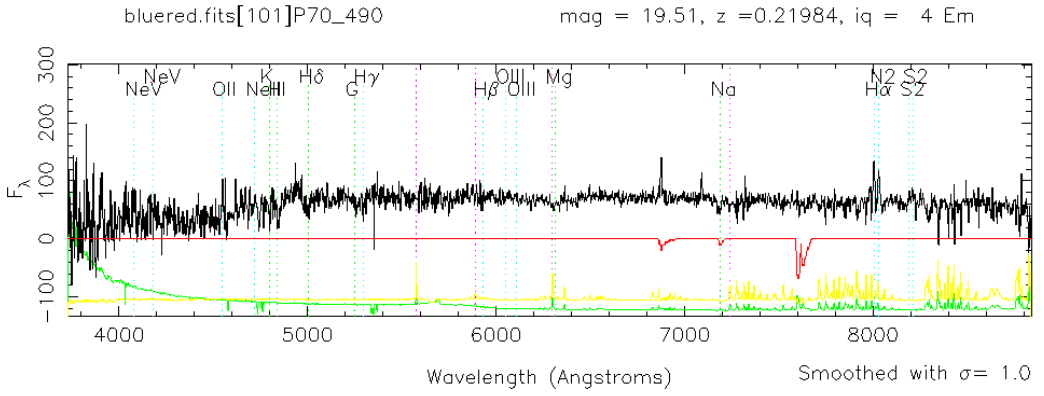
bluered.fits[101]P70_490
mag = 19.51, z =0.21984, iq = 4 Em
NeV
NeV
OII
NeIII
K
Hδ
G
Hγ
OIII
Hβ
OIII
Mg
Na
N2
S2
Hα
S2
F_λ
−100
0
100
200
300
4000
5000
6000
7000
8000
Wavelength (Angstroms)
Smoothed with σ= 1.0

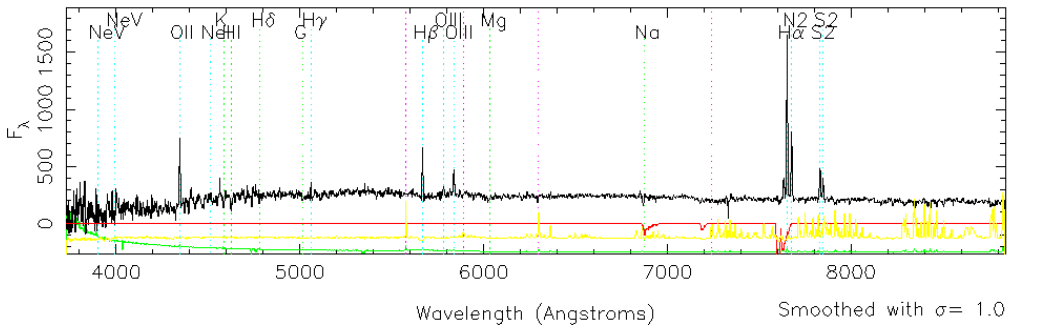
bluered.fits[092]P70_373
mag =−99.00, z =0.16601, iq = 0 E/X Disc
*
NeV
NeV
OII
NeIII
K
Hδ
G
Hγ
OIII
Hβ
OIII
Mg
Na
N2
S2
Hα
S2
F_λ
0
500
1000
1500
4000
5000
6000
7000
8000
Wavelength (Angstroms)
Smoothed with σ= 1.0

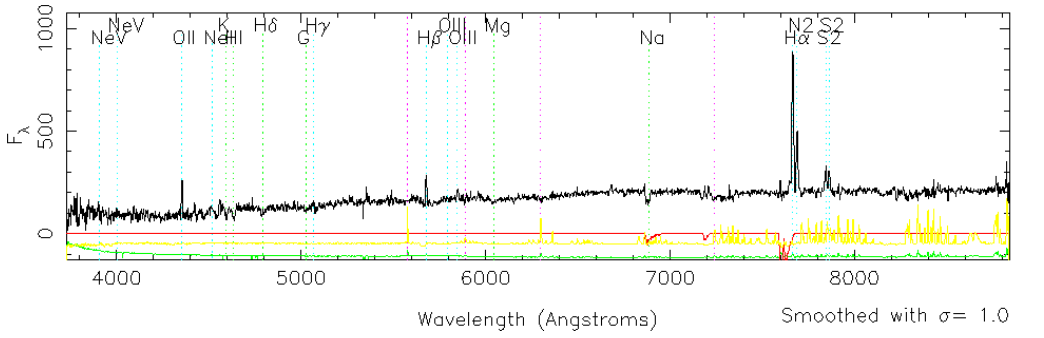
bluered.fits[075]P70_502
mag = 18.65, z =0.16809, iq = 0 E/X Disc
*
NeV
NeV
OII
NeIII
K
Hδ
G
Hγ
OIII
Hβ
OIII
Mg
Na
N2
S2
Hα
S2
F_λ
0
500
1000
4000
5000
6000
7000
8000
Wavelength (Angstroms)
Smoothed with σ= 1.0

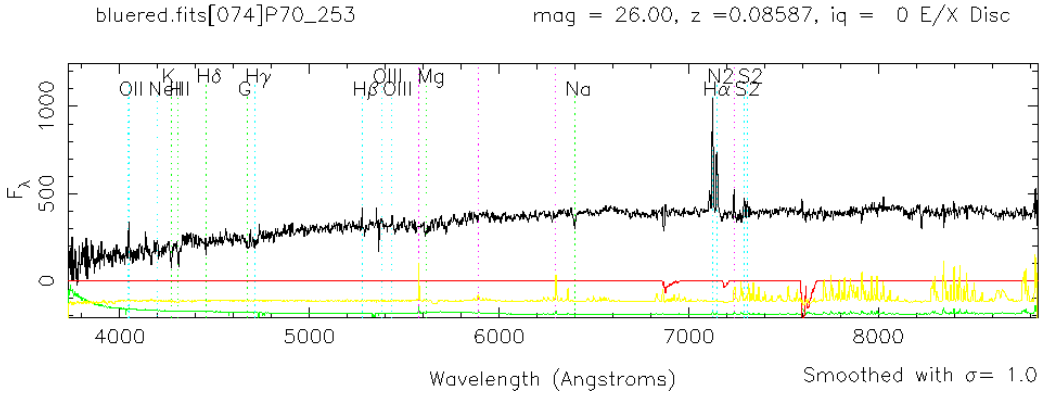
bluered.fits[074]P70_253
mag = 26.00, z =0.08587, iq = 0 E/X Disc
OII
NeIII
K
Hδ
G
Hγ
OIII
Hβ
OIII
Mg
Na
N2
S2
Hα
S2
F_λ
0
500
1000
4000
5000
6000
7000
8000
Wavelength (Angstroms)
Smoothed with σ= 1.0

bluered.fits[071]P70_359 mag = 19.72, z =0.36629, iq = 3 Manual

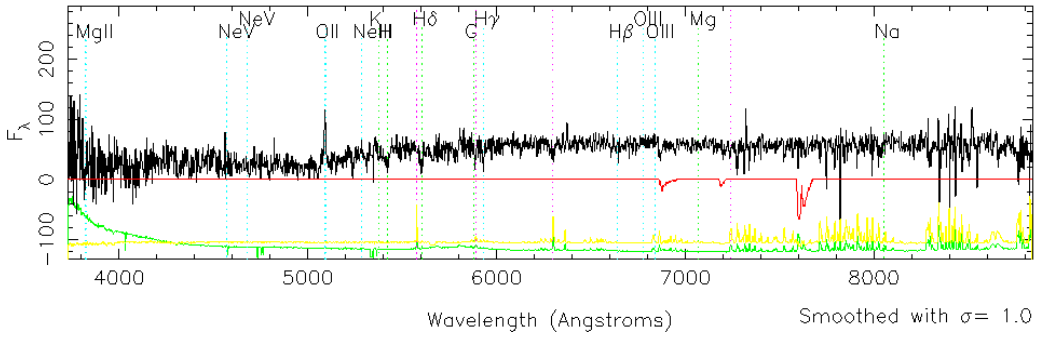

bluered.fits[067]P70_311 mag = 18.28, z =0.09813, iq = 0 E/X Disc

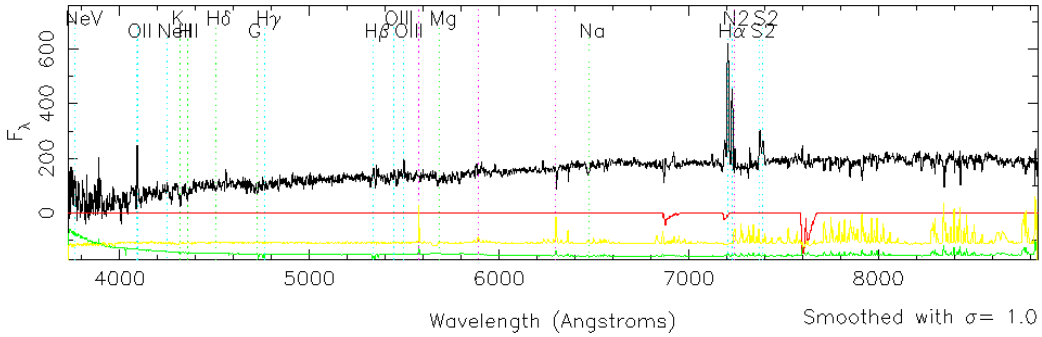

bluered.fits[062]P70_305 mag = 18.05, z =0.10289, iq = 5 Em

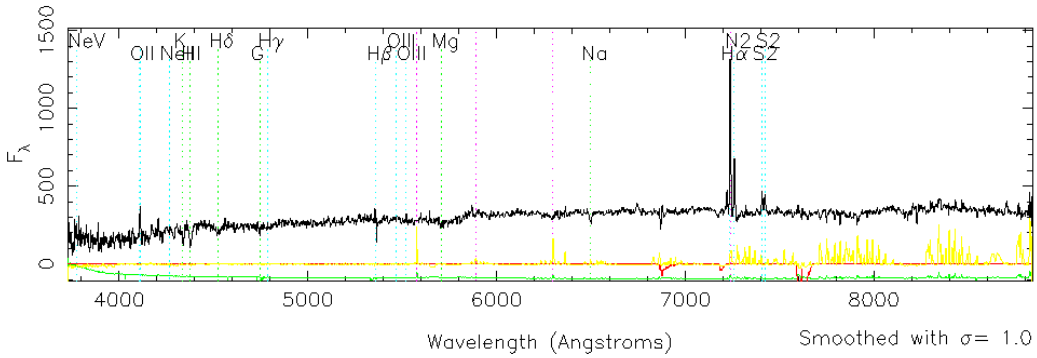

bluered.fits[056]P70_296 mag = 21.43, z =0.62881, iq = 0 E/X Disc *

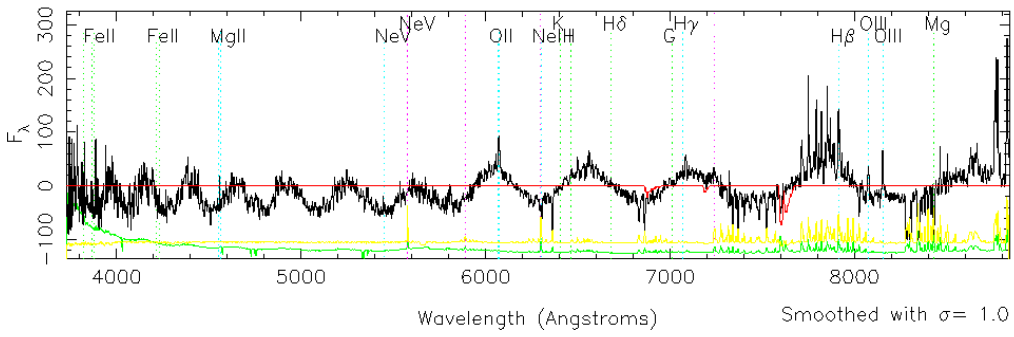

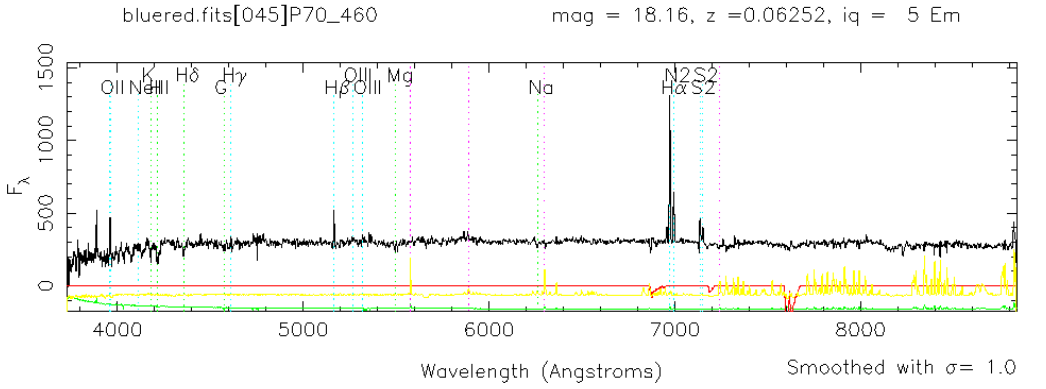
bluered.fits[045]P70_460
mag = 18.16, z =0.06252, iq = 5 Em
NeV
OII
NeIII
K
Hδ
G
Hγ
Hβ
OIII
Mg
Na
N2
Hα
S2
Fλ
0
500
1000
1500
4000
5000
6000
7000
8000
Wavelength (Angstroms)
Smoothed with σ= 1.0

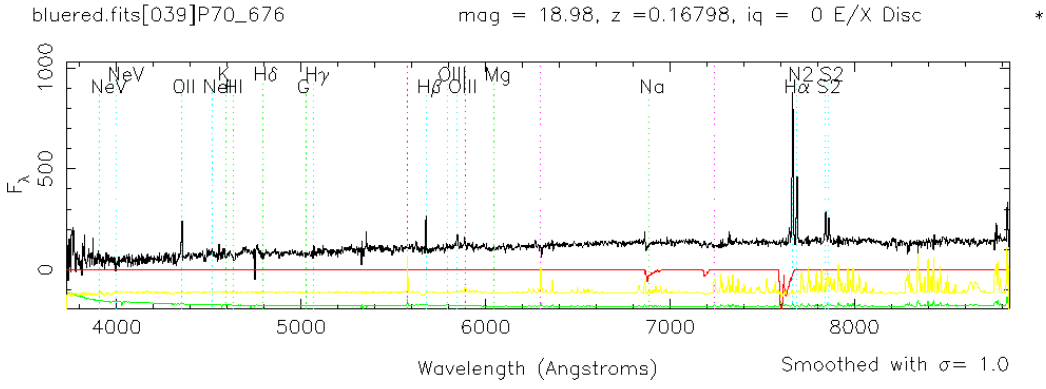
bluered.fits[039]P70_676
mag = 18.98, z =0.16798, iq = 0 E/X Disc
*
NeV
OII
NeIII
K
Hδ
G
Hγ
Hβ
OIII
Mg
Na
N2
Hα
S2
Fλ
0
500
1000
4000
5000
6000
7000
8000
Wavelength (Angstroms)
Smoothed with σ= 1.0

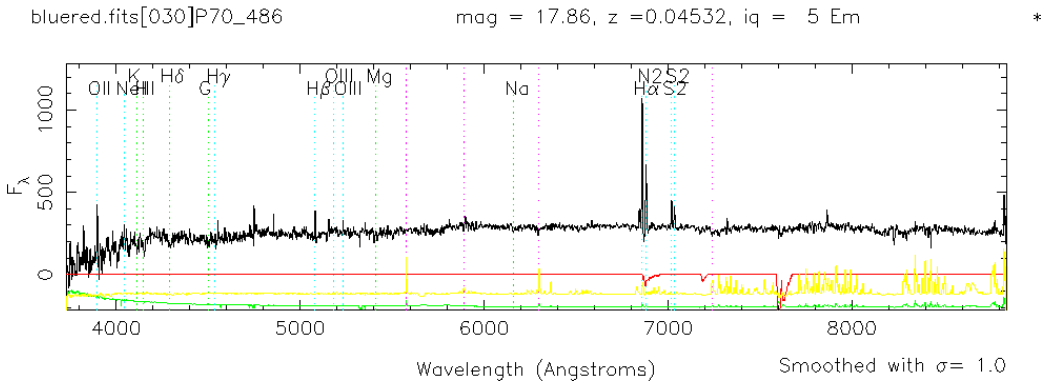
bluered.fits[030]P70_486
mag = 17.86, z =0.04532, iq = 5 Em
*
OII
NeIII
K
Hδ
G
Hγ
Hβ
OIII
Mg
Na
N2
Hα
S2
Fλ
0
500
1000
4000
5000
6000
7000
8000
Wavelength (Angstroms)
Smoothed with σ= 1.0

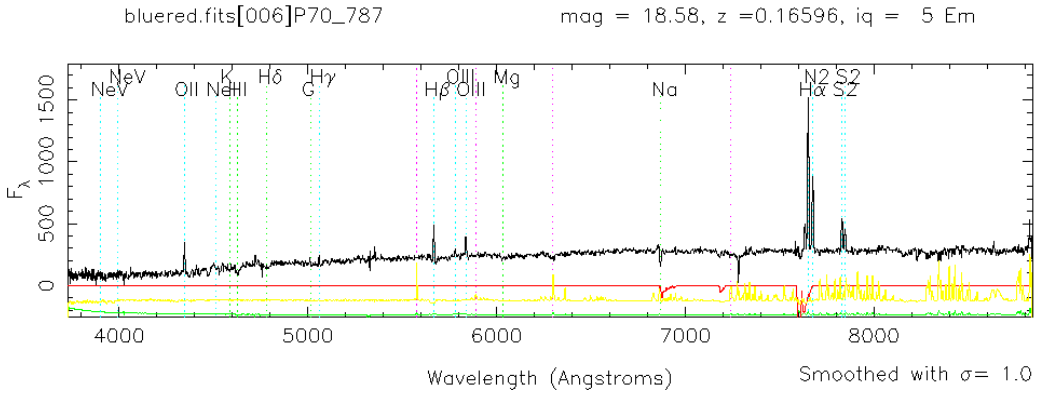
bluered.fits[006]P70_787
mag = 18.58, z =0.16596, iq = 5 Em
NeV
OII
NeIII
K
Hδ
G
Hγ
Hβ
OIII
Mg
Na
N2
Hα
S2
Fλ
0
500
1000
1500
4000
5000
6000
7000
8000
Wavelength (Angstroms)
Smoothed with σ= 1.0

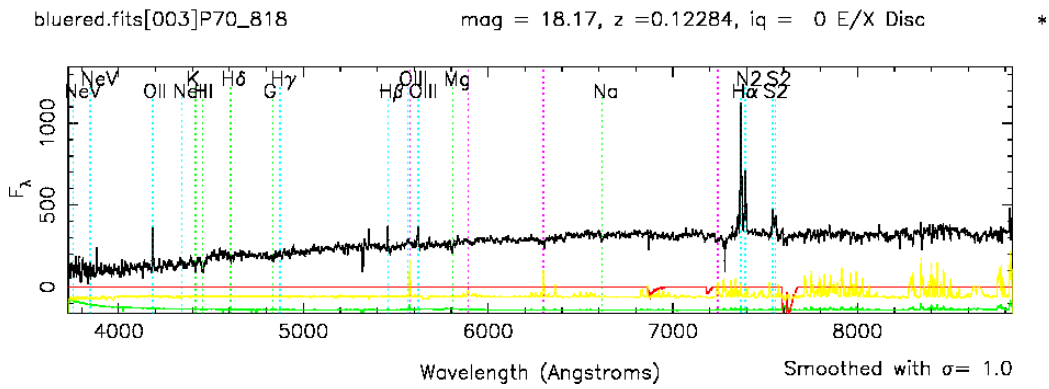
bluered.fits[003]P70_818
mag = 18.17, z =0.12284, iq = 0 E/X Disc
NeV
OII
NeIII
K
Hδ
G
Hγ
Hβ
OIII
Mg
Na
N2
Hα
S2
Fλ
Wavelength (Angstroms)
Smoothed with σ= 1.0

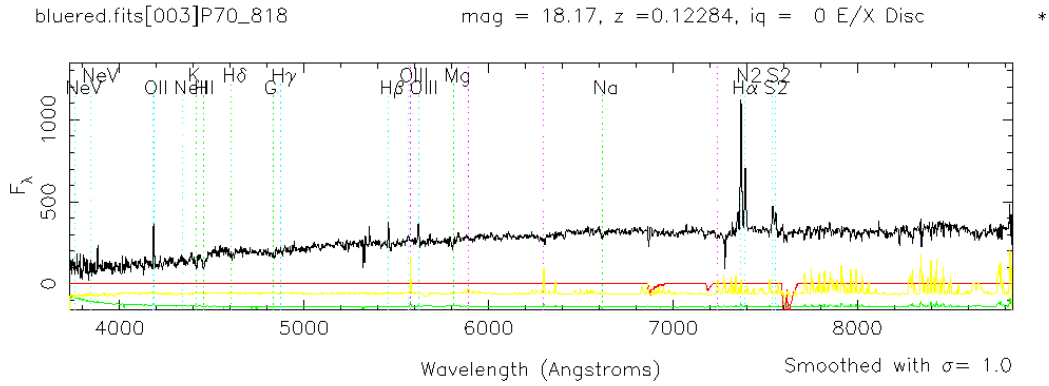
bluered.fits[003]P70_818
mag = 18.17, z =0.12284, iq = 0 E/X Disc
NeV
OII
NeIII
K
Hδ
G
Hγ
Hβ
OIII
Mg
Na
N2
Hα
S2
Fλ
Wavelength (Angstroms)
Smoothed with σ= 1.0

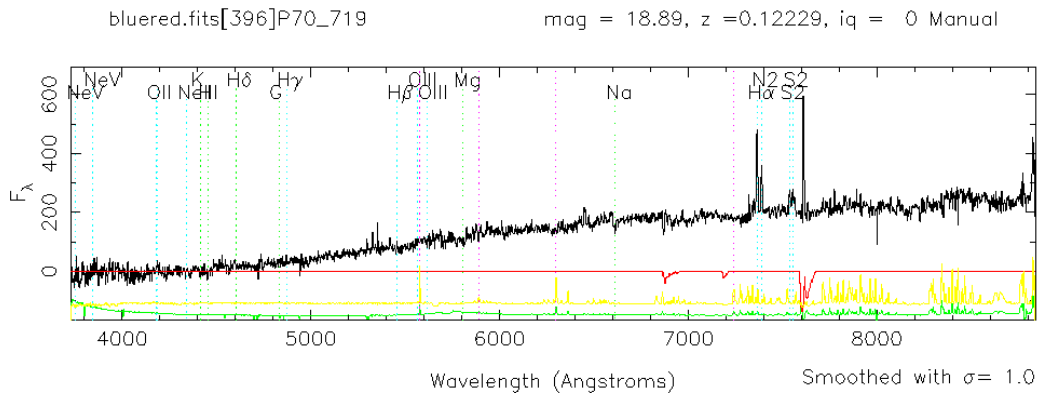
bluered.fits[396]P70_719
mag = 18.89, z =0.12229, iq = 0 Manual
NeV
OII
NeIII
K
Hδ
G
Hγ
Hβ
OIII
Mg
Na
N2
Hα
S2
Fλ
Wavelength (Angstroms)
Smoothed with σ= 1.0

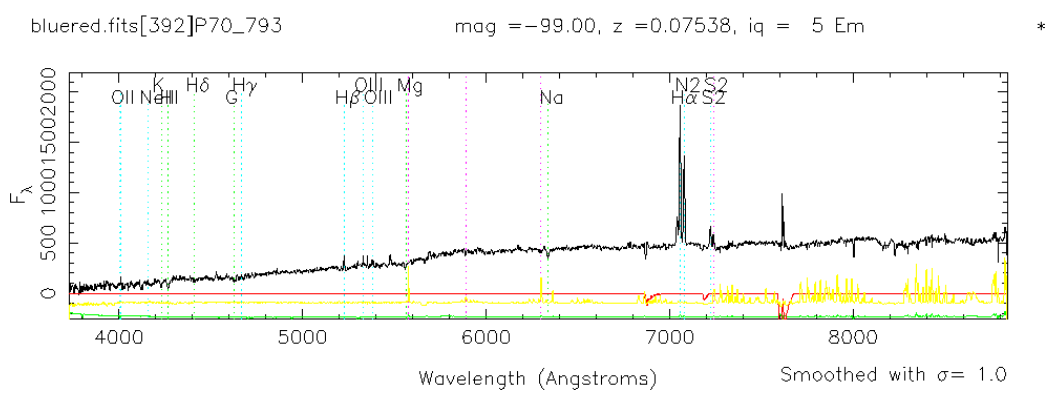
bluered.fits[392]P70_793
mag =−99.00, z =0.07538, iq = 5 Em
OII
NeIII
K
Hδ
G
Hγ
Hβ
OIII
Mg
Na
N2
Hα
S2
Fλ
Wavelength (Angstroms)
Smoothed with σ= 1.0

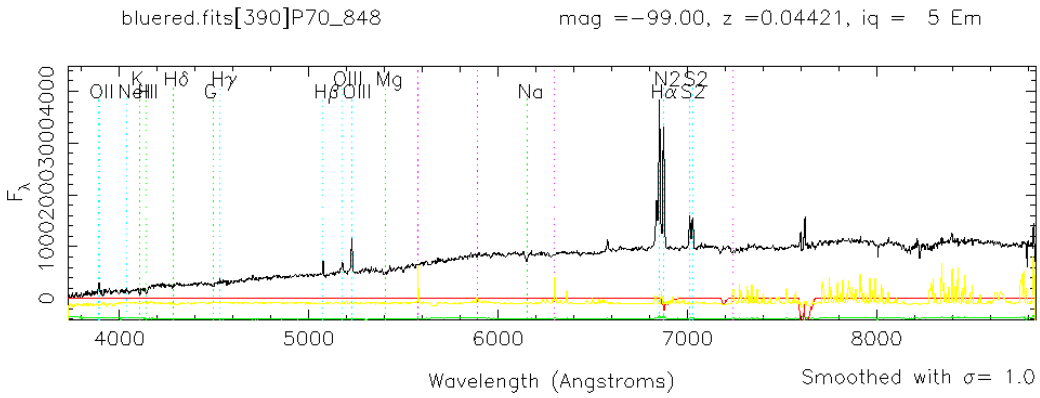
bluered.fits[390]P70_848
mag =−99.00, z =0.04421, iq = 5 Em
OII NeIII K Hδ G Hγ Hβ OIII OIII Mg Na N2 Hα S2
F_λ
0 1000 2000 3000 4000
4000 5000 6000 7000 8000
Wavelength (Angstroms)
Smoothed with σ= 1.0

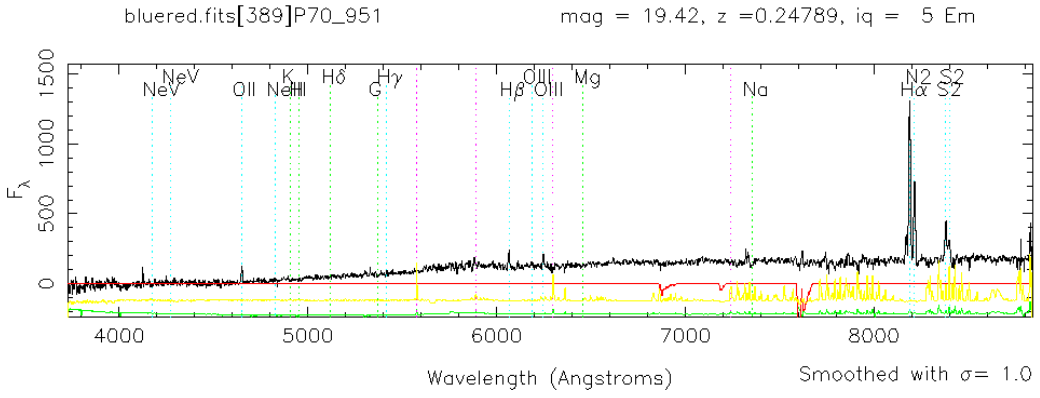
bluered.fits[389]P70_951
mag = 19.42, z =0.24789, iq = 5 Em
NeV NeV OII NeIII K Hδ G Hγ Hβ OIII OIII Mg Na N2 Hα S2
F_λ
0 500 1000 1500
4000 5000 6000 7000 8000
Wavelength (Angstroms)
Smoothed with σ= 1.0

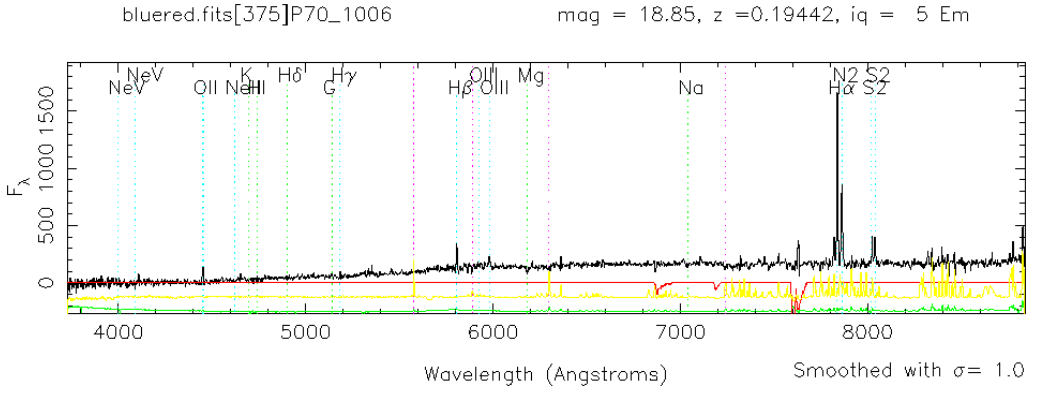
bluered.fits[375]P70_1006
mag = 18.85, z =0.19442, iq = 5 Em
NeV NeV OII NeIII K Hδ G Hγ Hβ OIII OIII Mg Na N2 Hα S2
F_λ
0 500 1000 1500
4000 5000 6000 7000 8000
Wavelength (Angstroms)
Smoothed with σ= 1.0

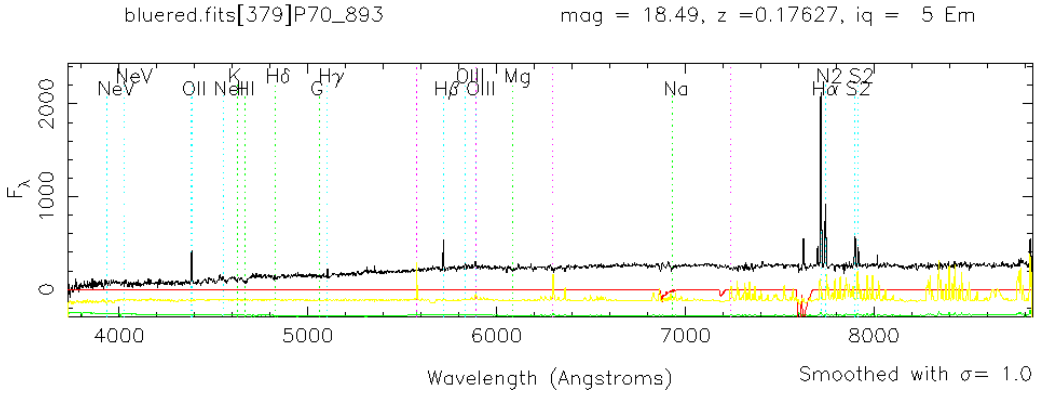
bluered.fits[379]P70_893
mag = 18.49, z =0.17627, iq = 5 Em
NeV NeV OII NeIII K Hδ G Hγ Hβ OIII OIII Mg Na N2 Hα S2
F_λ
0 1000 2000
4000 5000 6000 7000 8000
Wavelength (Angstroms)
Smoothed with σ= 1.0

bluered.fits[368]P70_976 mag = 18.19, z =0.07505, iq = 5 Em *

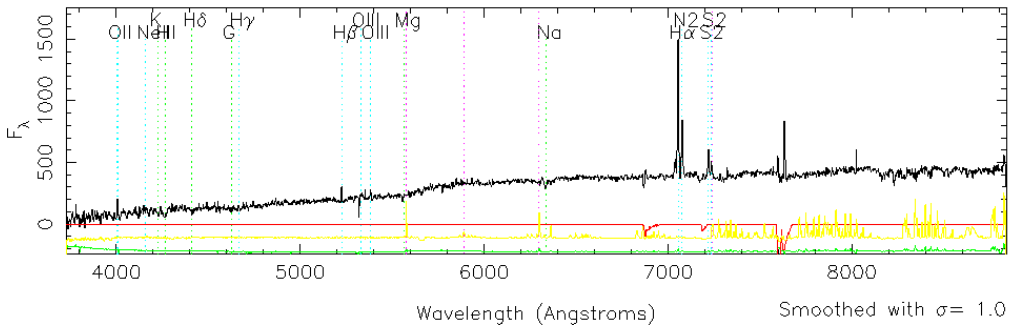

bluered.fits[362]P70_1007 mag = 19.95, z =0.37567, iq = 4 Manual

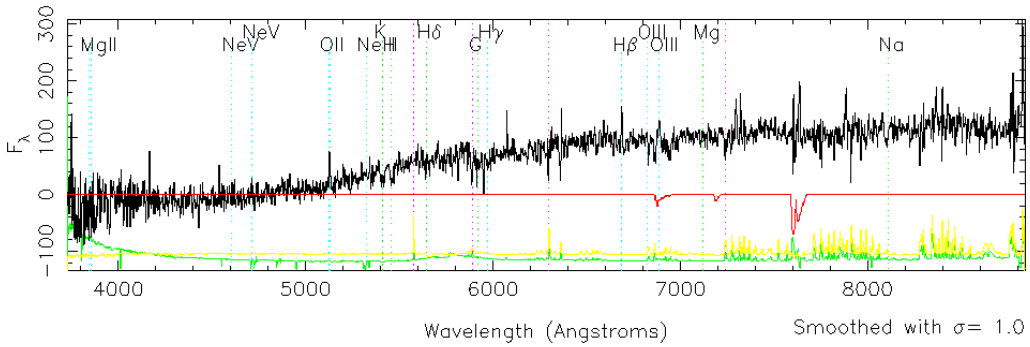

bluered.fits[358]P70_1131 mag = 20.31, z =0.27471, iq = 4 Em

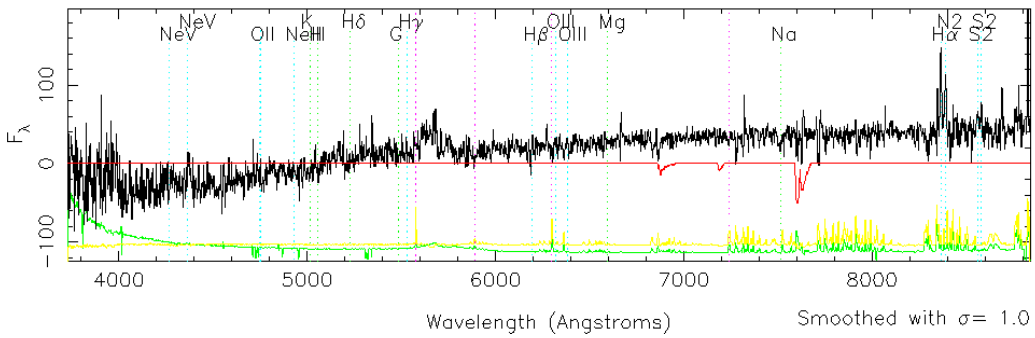

bluered.fits[356]P70_1128 mag = 18.13, z =0.09397, iq = 5 Manual

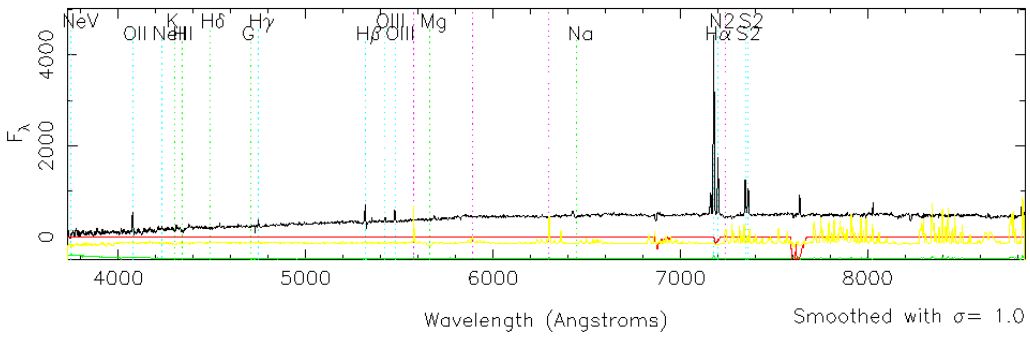

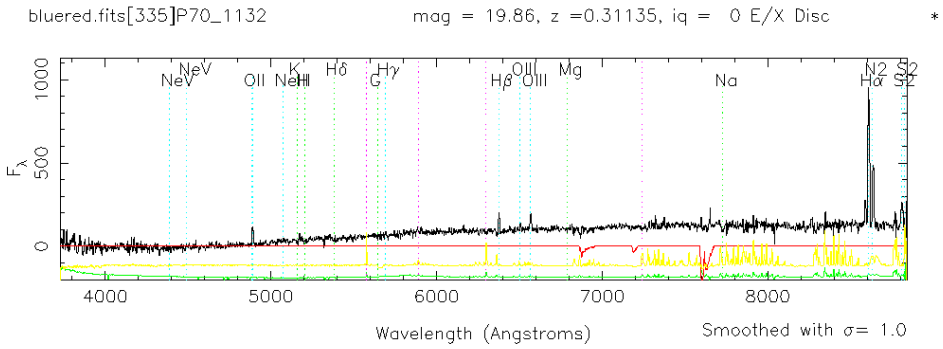

per cent completeness in the deep region (0.5×0.33 degrees^2) of the survey and at least 50 per cent completeness (i.e. corresponding to a signal-to-noise ratio of more than 5) in the shallow region which covers 1.75×1.97 degrees^2 (Frayer at al. 2009). This particular value was chosen, rather than using a fainter limit in order to ensure the sample did not suffer from significant incompleteness effects. Using the $S/N > 5$ cut resulted in a sample more than 65 per cent complete according to the completeness determined for the field by Frayer et al. (2009). All sources were corrected for completeness as determined by Frayer et al. (2009), however in the majority of cases this had very little effect owing to the fact that $\sim$ 86 per cent of the sample was $>$ 80 per cent complete. The 10 mJy flux-density limit imposed resulted in 763 70μm sources. Figure 4.3 shows the 70μm flux density versus completeness (as measured by Frayer et al. 2009), for all sources in the sample. It displays two different depths to the data corresponding to the deep and shallow region covered by the v3 70μm catalogue. The figure shows the deep data has attained $\sim$ 100 per cent completeness at the 10 mJy flux cut, while the shallower data is still more than 65 per cent complete at the same flux density cut.

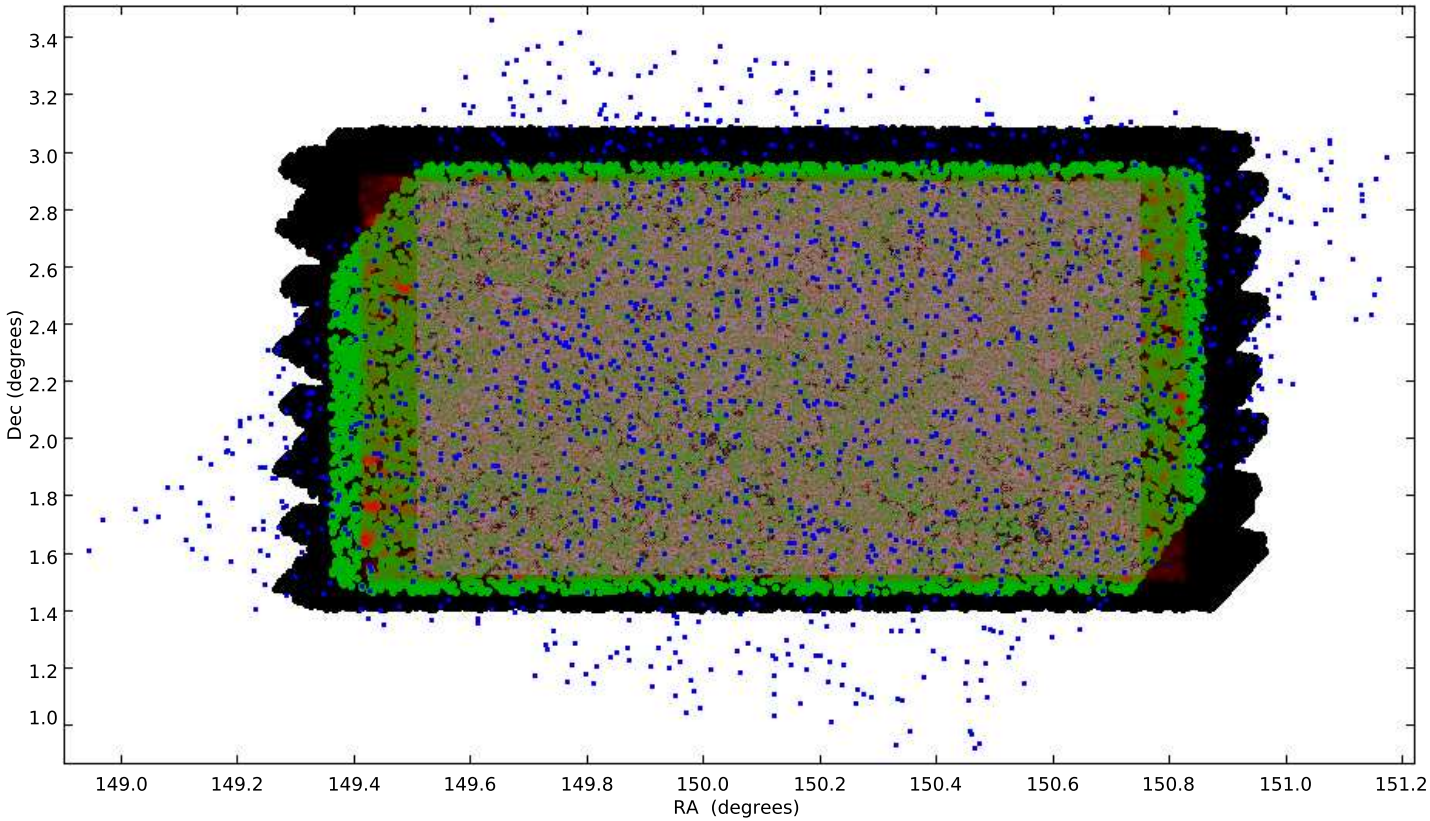

Figure 4.2: Figure showing the overlap of different wavelengths over the COSMOS field. The black region represents the area covered by the IRAC data. The green region represents the area covered by the 24μm data. The red region represents the area covered by the ACS data and the blue points represent the 70μm sources in the v3 Frayer et al. (2009) catalogue. The grey area shows the region with good coverage in all wavebands, within which the selection took place.

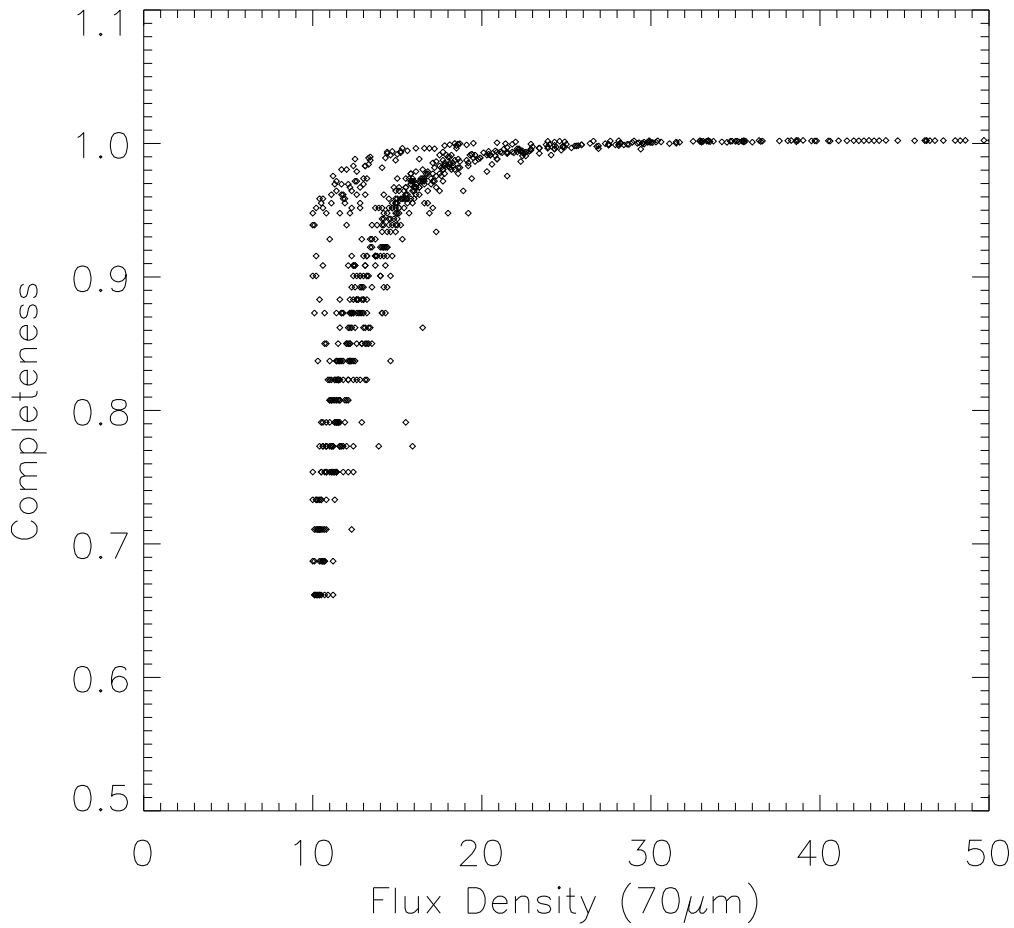

Figure 4.3: 70μm flux density versus completeness (Frayer et al. 2009) for all 736 sources in the sample displaying the different depths of the 70μm data. The plot shows, in the deep region $\sim$ 100 per cent completeness has been maintained and in the shallow region $>$ 65 per cent completeness has been attained due to our 10 mJy flux limit and matching procedure.

Matching to the MIPS 24μm waveband yielded 759 matches ($\sim$ 95.5 per cent) within 10$''$. Of these 759 matches, 229 ($\sim$ 30 per cent) had multiple matches. Owing to the manner in which likely counterparts are selected (i.e. by taking the closest match), the alternative matches were located further from the search position. Out of the 759 best matches 93 per cent were found within 4$''$, while 88 per cent of the alternative matches were located beyond 4$''$ of the search coordinates. Then matching to the IRAC data within 2$''$ produced 745 matches ($\sim$ 97.6 per cent). Lastly, a total of 736 matches ($\sim$ 96.5 per cent) to the ACS catalogue within 1$''$ were found. In all cases the closest match was used. In Figure 4.4, examples of both an ambiguous and a clear match are shown in the upper and lower panel respectively. The green circles mark the radii that counterparts were sought within, namely 10, 2 and 1$''$ for the 24, IRAC and ACS catalogues respectively. In the upper panel, where there are two potential matches, the yellow arrow marks the source closest to the search position and thus considered the best match.

The total 27 unmatched objects ($\sim$ 3.5 per cent) were either located on the edge of the field, close to a bright object or simply not detected at the shorter wavelengths. No significant biases are expected to be introduced by omitting these objects, due to their rejection being predominantly due to random aspects of the data and the survey area is scaled accordingly in the calculation of $V_{\rm max}$ in Chapter 5. Only a few of the sources are undetected at the shorter wavelengths and will not significantly alter the results in Chapters 5 & 6.

The 70μm sources were also matched to the 160μm catalogue (Frayer et al. 2009) and 227 matches ($\sim$ 31 per cent) were found within 20$''$. I sup-

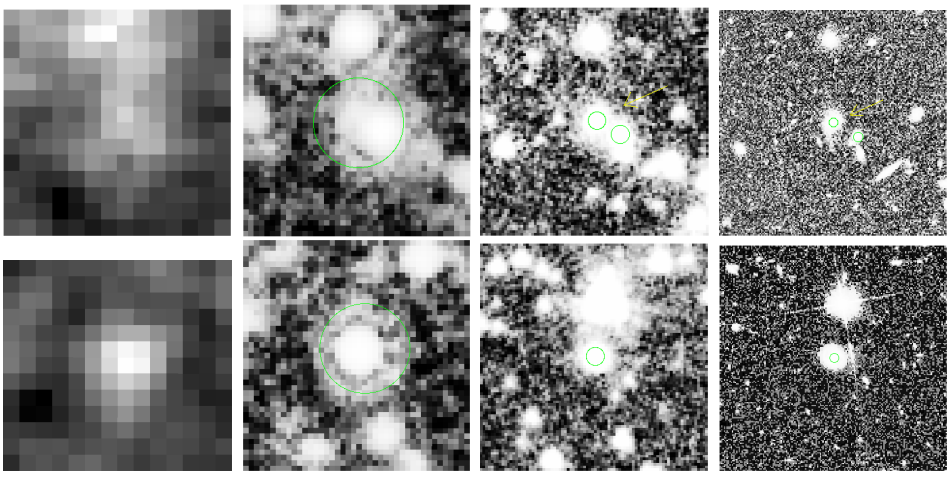

Figure 4.4: Figure shows both an example of an ambiguous and a clear match using the procedure described in the text by stepping through the successive wavebands. Each postage stamp has dimensions of $50 \times 50''$. From left to right, the cut outs represent the 70μm, 24μm, IRAC (3.6μm) and ACS (I-band) wavelengths. The green circles mark the radii that counterparts were sought within, namely 10, 2 and $1''$ for the 24, IRAC and ACS catalogues respectively. Where multiple matches are possible, the yellow arrow marks the counterpart included in our catalogue as the best match.

plemented these data with my own measurements of the 160μm flux density. Using the 70μm positions, list-driven source extraction was performed on the 160μm image with the IRAF/ APPHOT package, making it possible to go below the confusion limit estimated to be of the order of 40 mJy at 160μm (e.g. Dole, Lagache & Puget 2003). An aperture radius of 40″ (equivalent to the 160μm diffraction limit) and a sky annulus of $64 - 128''$ was used along with the aperture correction of a factor of 1.752 specified by the MIPS team[2]. The ~ 7.7 times larger area covered by the sky annulus was selected in order to minimise the background contribution in the source extraction aperture. The strong 70μm detection ($S_{70} > 10$ mJy) increased the likelihood of the presence of a 160μm source at the 70μm position. In addition to the 227 catalogue matches, a further 241 sources ($\sim$ 33 per cent) had 160μm detections above the 40 mJy limit and 180 sources ($\sim$ 24 per cent) had detections below 40 mJy from the list driven photometry. Therefore, a total of 648 sources ($\sim$ 88 per cent) had 160μm detections. For the remaining 88 sources ($\sim$ 12 per cent), a 1σ upper limit was used in the fitting of the spectral energy distribution. See Section 5.1.1 in Chapter 5 for a comparison of $L_{\rm IR}$ values determined by imposing the 40 mJy confusion limit cut at 160μm versus the $L_{\rm IR}$ determined using the actual measured flux densities at 160 μm.

4.4 Redshifts of 70μm Sources

In order to calculate total infrared luminosities and derive a luminosity function (see Chapter 5) and to investigate the far-infrared/radio correlation (see

[2]http://irsa.ipac.caltech.edu/data/SPITZER/docs/mips/mipsinstrumenthandbook/50/

Chapter 6) for the population of 70μm selected galaxies, redshift information is required. The data taken with AAOmega provide spectroscopic redshifts for 42 objects in the selected field, see Table 4.1. Although 49 spectroscopic redshifts were obtained with AAOmega derived from the v2 selection, only 42 had matches to our final catalogue using the v3 selection. These redshifts were supplemented with further spectroscopic redshifts from the zCOSMOS bright spectroscopic catalogue (Lilly et al. 2009). In the zCOSMOS catalogue, 183 70 μm sources were found. 13 objects were found in both our spectroscopy taken on the AAT and the zCOSMOS catalogue. All of the redshifts obtained with AAOmega and as part of zCOSMOS were consistent.

Confidence classes (1-4) were assigned, by the zCOSMOS team, on the basis of the reliability of the spectroscopic redshift (e.g. based on the signal to noise ratio of the spectrum). The classes were evaluated using a sub-sample of more than 600 sources with repeat spectroscopic observations. In the sub-sample, classes 3 and 4 had $>$ 99.5 per cent agreement with the subsequent spectroscopic observations indicating that these classes represent secure redshifts. Class 2 was considered a probable redshift with 92 per cent agreement with further spectroscopic observations. A decimal place value of 0.5 is added to the confidence class of those objects whose photometric redshift agreed within $0.08(1 + z)$ (for full details see Lilly et al. 2009). Of the 183 matches to the zCOSMOS catalogue, $\sim$ 98 per cent had confidence classes of $\geq$ 2.5. The three remaining objects however had matches to the Kartaltepe et al. (2010) catalogue and therefore, these secondary spectroscopic redshifts were used. In addition, a further 114 spectroscopic redshifts were obtained from the Kartaltepe et al. (2010) catalogue. This provides

us with a total of 326 spectroscopic redshifts for our sample of 736 galaxies ($>$ 44 per cent).

All of the 736 sources had photometric redshifts from the ACS COSMOS catalogue (Ilbert et al. 2009). For the remaining 410 galaxies, where no spectroscopic data were available these photometric redshifts instead were relied upon. The photometric redshifts were derived from the 30-band photometry available over the COSMOS field and have a dispersion of $\sigma_{(z_{spec}-z_{phot})/(1+z_{spec})} = 0.007$ for $i^{+}_{AB} < 24$. In Figure 4.5, spectroscopic versus photometric redshift for the objects where both were available are shown. Good agreement between the two estimates is found, with an rms scatter of 0.236. In Figure 4.6, the distribution of sources as a function of redshift is shown for the spectroscopic and photometric redshift samples.

Table 4.2 lists a sample of the fluxes and redshifts for all the sources defined in the sample, for the full list see Appendix A. A Kolmogorov-Smirnov test undertaken on the spectroscopic and photometric redshift distributions shown in Figure 4.6 determined that the null hypothesis (that the two distributions are drawn from the same sample) cannot be rejected at the 96 per cent level. This indicates that the spectroscopic sample is consistent with being a random subset of the photometric redshift distribution and is therefore not biased towards any particular redshift.

In the following Chapters, I use the v3 sample described here to determine the far-infrared luminosity function (Chapter 5) and to investigate the far-infrared–radio correlation (Chapter 6) out to $z \sim 2$.

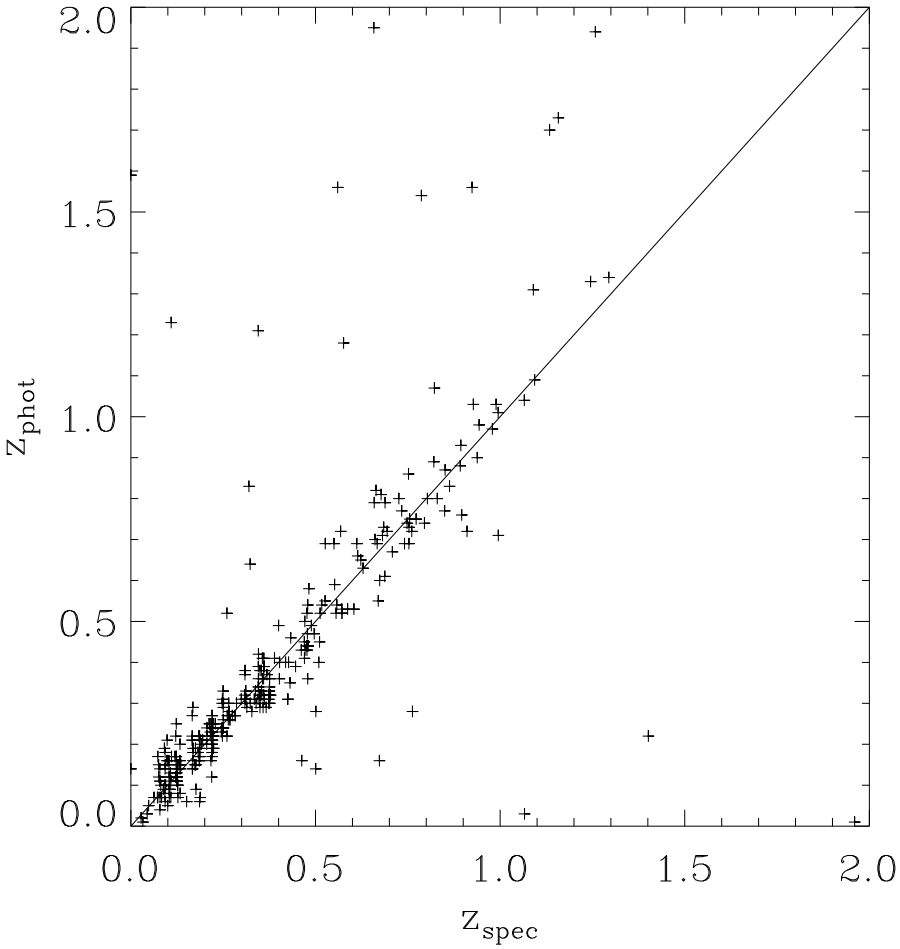

Figure 4.5: A comparison of spectroscopic redshifts obtained through time on AAOmega, the zCOSMOS catalogue and matches to the Kartaltepe et al. (2010) catalogue versus the photometric redshift estimates from the COSMOS ACS catalogue.

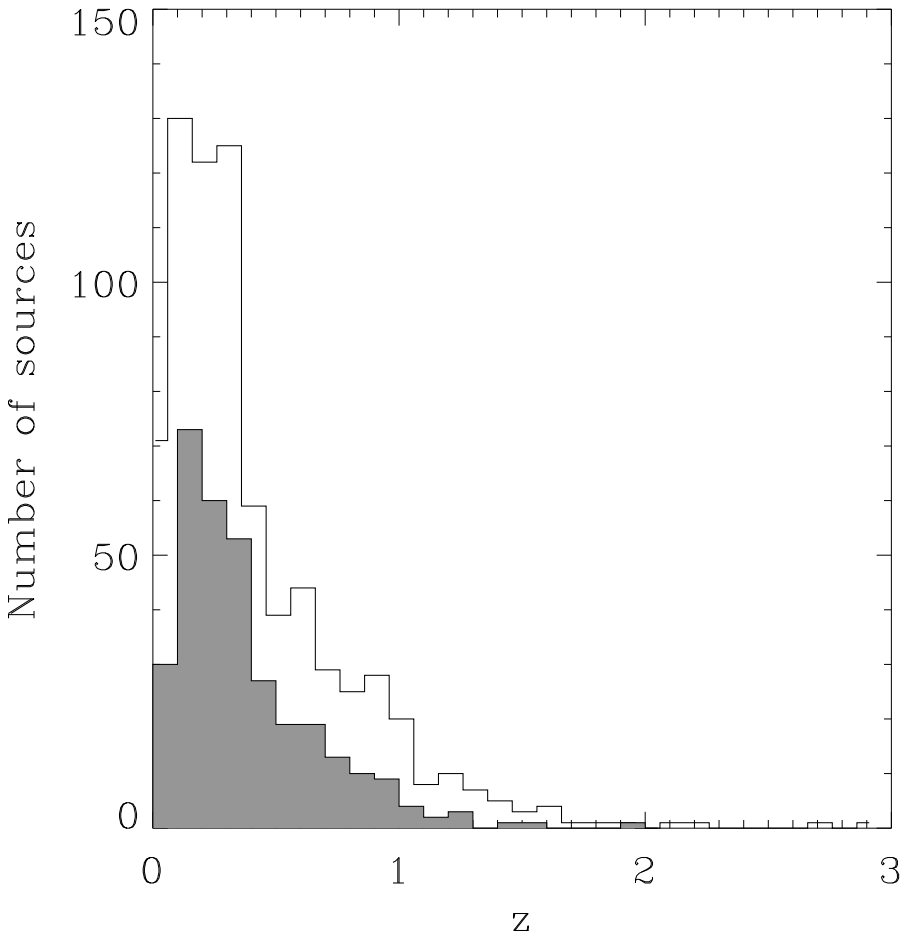

Figure 4.6: Histogram displaying the redshift distribution for all sources included in this study. The shaded region represents the distribution of sources with spectroscopic redshifts. For the photometric redshifts, the most likely redshift is shown (i.e. the peak of the probability distribution).

Table 4.2: Table showing a sample of the resulting 736 70μm sources (see Appendix A for the full version of the table). The ID corresponds to the v3 70μm catalogue (Frayer et al. 2009). The RA and Dec are supplied by the COSMOS ACS catalogue, as it provided the most accurate positional information. 8, 24, 70 and 160μm flux densities and associated errors are listed, all are given in mJy. The 160μm flag F/S denotes where the 160μm flux came from. F denotes the Frayer et al. (2009) catalogue and S denotes aperture measurements undertaken in this work. Both spectroscopic (z_{spec}) (where available) and photometric (z_{phot}) redshifts are listed. The flag denotes where the redshifts were obtained from, A denotes spectroscopic redshifts obtained through AAOmega, C denotes the zCOSMOS catalogue and K denotes the catalogue of Kartaltepe et al. (2010). Min and max, denote the 1σ errors on the photometric redshifts (Ilbert et al. 2009).

ID	RA	Dec	S_8	σ_8	S_{24}	σ_{24}	S_{70}	σ_{70}	S_{160}	σ_{160}	F/S	z_{phot}	min	max	z_{spec}	Flag
209	150.6457	1.59175	0.12	0.002	0.597	0.019	14.9	2.8	20.6	7.6	S	0.41	0.47	2.27		
231	150.7105	1.60540	0.04	0.002	0.454	0.02	13.1	2.6	41.0	5.9	S	0.68	0.6	0.68		
322	150.0120	1.65216	0.05	0.002	0.451	0.017	20.4	3.0	74.0	22.2	F	1.38	1.23	1.43		
498	150.5351	1.75739	0.16	0.002	0.77	0.016	11.0	2.4	<11.6	<11.6	S	0.15	0.1	0.19	0.173	CK
672	149.5164	1.87075	0.27	0.002	0.97	0.085	15.8	2.7	73.9	20.9	F	0.43	0.37	0.49		
769	150.4262	1.91365	0.23	0.002	0.734	0.019	11.6	2.6	33.6	5.9	S	0.31	0.28	0.34		
852	150.1100	1.95357	0.21	0.002	0.958	0.02	15.8	2.7	<11.6	<11.6	S	0.64	0.61	0.68	0.323	K
1014	149.8740	2.02713	0.03	0.002	0.449	0.016	10.4	1.9	61.0	7.0	S	0.73	0.69	0.77	0.685	C

Continued in Appendix A

Table 4.2 – continued from previous page

ID	RA	Dec	S_8	σ_8	S_{24}	σ_{24}	S_{70}	σ_{70}	S_{160}	σ_{160}	F/S	z_{phot}	min	max	z_{spec}	Flag
1129	150.6109	2.09471	0.20	0.002	0.313	0.017	12.3	2.5	44.2	6.5	S	0.91	0.87	0.96		
1142	149.6450	2.10180	0.16	0.002	0.844	0.019	10.8	2.0	<11.6	<11.6	S	0.25	0.21	0.32		
1167	149.9512	2.11775	0.42	0.002	0.809	0.017	30.4	3.2	91.8	23.4	F	0.16	0.15	0.19	0.463	A
1640	149.9658	2.32717	0.15	0.002	0.6	0.015	10.5	1.9	27.4	4.6	S	0.32	0.28	0.37	0.378	CK
1693	150.2984	2.34661	0.08	0.002	0.396	0.015	10.0	2.3	19.5	5.8	S	0.41	0.39	0.46	0.470	K
1730	150.4344	2.36838	0.02	0.002	0.436	0.017	13.0	2.6	33.0	6.1	S	1.18	1.13	1.22		
1883	150.7055	2.41793	0.13	0.002	0.438	0.014	13.1	2.8	<11.6	<11.6	S	0.37	0.3	0.42		
1900	150.6416	2.42346	0.04	0.002	0.4	0.019	16.1	2.8	71.8	21.1	F	0.72	0.7	0.8	0.568	K
1907	150.1754	2.42619	0.30	0.002	1.473	0.021	24.0	3.2	21.2	5.0	S	0.31	0.3	0.35	0.311	CK
2000	149.5486	2.47738	0.45	0.002	0.653	0.076	11.0	2.5	48.3	6.1	S	0.18	0.17	0.26	0.220	CK
2235	150.0548	2.56946	0.04	0.002	0.654	0.014	36.4	3.4	73.4	18.4	F	0.75	0.7	0.79	0.755	K
2642	150.3547	2.75182	0.04	0.002	0.797	0.019	11.7	2.6	54.5	7.8	S	0.97	0.93	1.02	0.978	CK
2680	149.6611	2.77783	0.24	0.002	0.646	0.223	15.0	2.9	95.2	7.5	S	0.25	0.23	0.3		
2739	150.3751	2.80926	0.25	0.002	0.934	0.018	12.1	2.7	96.0	8.8	S	0.24	0.21	0.28		
2794	149.6956	2.85078	0.12	0.002	0.835	0.016	16.5	2.7	70.8	7.4	S	0.27	1.54	1.86		
2825	150.2358	2.85822	0.10	0.002	0.747	0.014	11.2	2.6	11.9	5.8	S	0.45	0.41	0.52	0.511	K
2847	150.1896	2.87273	0.05	0.002	0.799	0.015	19.4	3.0	12.2	4.7	S	0.68	0.67	0.77		
2859	149.8764	2.88449	0.10	0.002	0.541	0.016	11.5	2.6	<11.6	<11.6	S	1.18	1.16	1.19		
3187	149.7692	1.52009	0.26	0.002	0.475	0.017	14.1	3.0	73.7	8.2	S	0.21	1.58	2.21		

Chapter 5

The Far-Infrared Luminosity Function

The work described in this Chapter is mostly drawn from Hickey et al. (2011 - submitted). In this Chapter, the luminosity function and the total infrared energy density are determined out to $z \sim 1$, for a sample of 70μm selected galaxies from the COSMOS field. These data will provide better constraints on the bright end of the luminosity function, as they are deep (10 mJy) but cover a wider area ($\sim$ 1.7 sq. degrees), than previous 70 μm selected studies, e.g. Huynh et al. (2007) which covered $\sim$ 180 arcmin^2 down to 2 mJy and Magnelli et al. (2009) which covered 0.4 sq. degrees down to 3 mJy. The 1.7 sq. degrees described here covers an area 4.5 and 34 times larger than the areas probed by Magnelli et al. (2009) and Huynh et al. (2007) respectively. The 70 μm waveband also has the advantage of being beyond the Polycyclic Aromatic Hydrocarbon (PAH) emission range which affects the MIPS 24 μm band over the redshift considered here. It also suffers less contamination

from AGN because it samples the cooler dust associated with star formation more effectively than the mid-infrared (Symeonidis et al. 2010). Infrared luminosities determined from fitting Spectral Energy Distributions (SEDs) to both mid-infrared and 70μm data have been shown to offer a significant improvement over mid-infrared data alone (Murphy et al. 2009).

5.1 Total Infrared Luminosities

Using the redshifts from the AAOmega spectroscopy and the ACS COSMOS, zCOSMOS, and Kartaltepe et al. (2010) catalogues (see Chapter 4), the total infrared luminosity ($L_{\rm IR}$) was determined for each galaxy. $L_{\rm IR}$ is defined as the integrated flux from $8-1000\mu$m, in the rest frame. In order to calculate $L_{\rm IR}$ values, it is necessary to assume an SED for each object. The SED library from Siebenmorgen & Krügel (2007) was used to provide the templates. This library is composed of more than 7000 SEDs, defined using the radiative transfer and dust model from Krügel (2003). They are determined assuming spherical geometry and a uniform distribution of galactic type dust. PAHs are also included in the models. The SEDs are defined by varying the following 5 parameters; the total luminosity ($10^{10}{\rm L}_{\odot}$ <$\rm L_{tot}$ < $10^{14}{\rm L}_{\odot}$); the nuclear radius (R= $0.35, 1$ and 3kpc); the visual extinction from the edge to the centre of the nucleus (2.2 <$\rm A_{\it v}$ < 120 mag); the ratio of the luminosity of OB stars to the total luminosity ($\rm L_{OB}/L_{tot}$ = $0.4, 0.6$ and 0.9) and the dust density in the hot spots. Unphysical combinations are omitted from the library.

The best fit template was determined, for each object using χ^2 minimi-

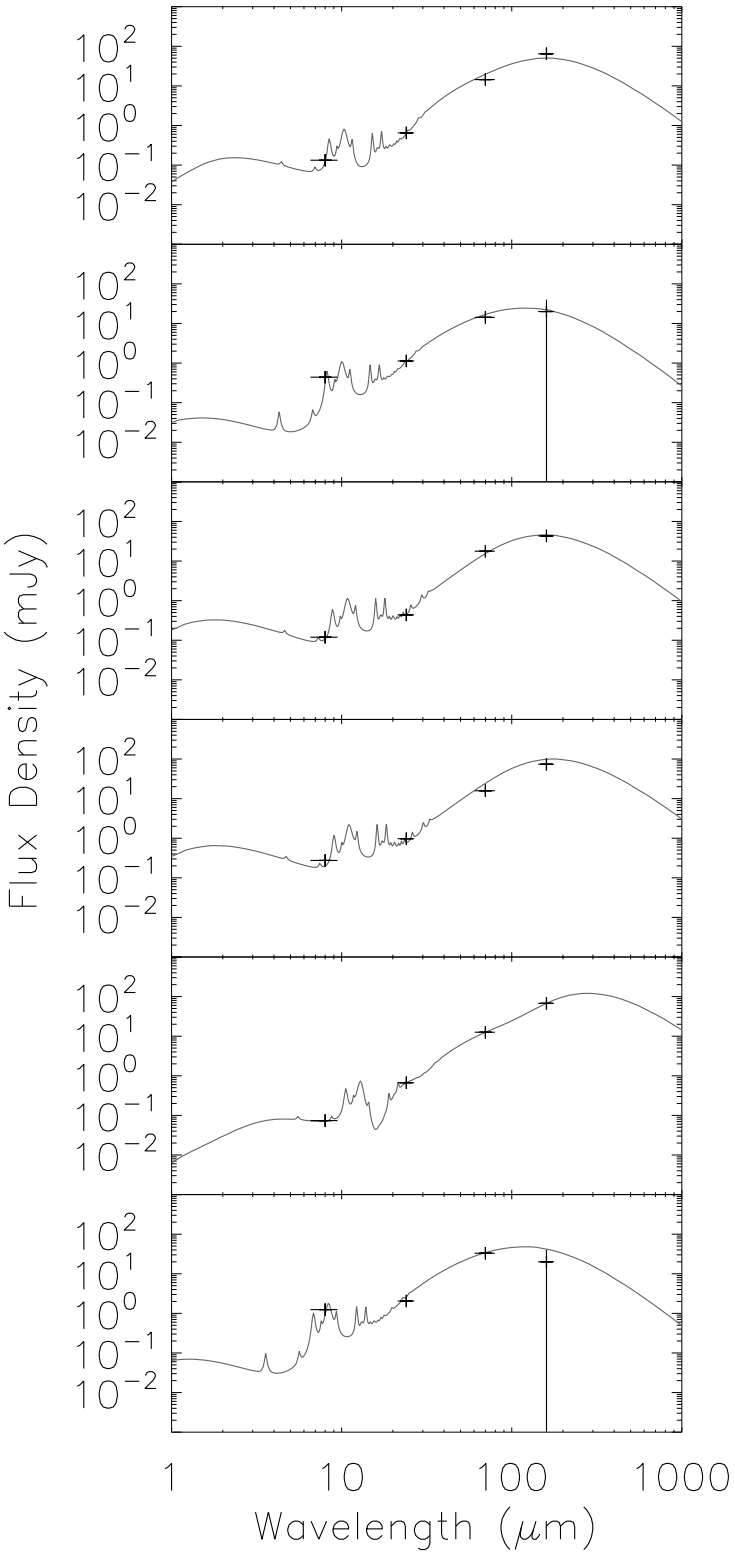

Figure 5.1: A sample of best fit SEDs to the observed 8, 24, 70 and 160μm photometry. The SEDs are from the Siebenmorgen and Krügel (2007) library.

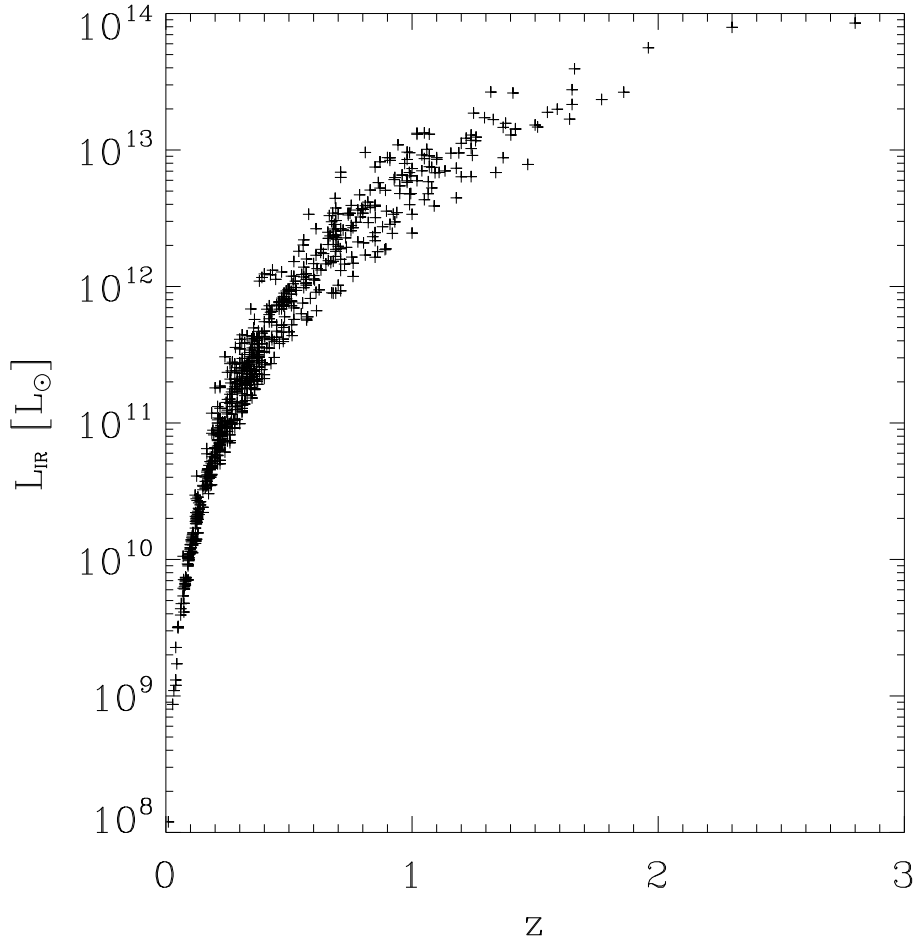

Figure 5.2: Far-infrared luminosity versus redshifts for the entire sample. The $L_{\rm IR}$ was calculated from the most likely redshift (i.e. the peak of the probability distribution) where spectroscopic redshifts were unavailable.

sation. 10 per cent uncertainty was added in quadrature to the error on the IRAC data, 4 per cent to the 24μm data, 7 per cent to the 70μm data and 12 per cent to the 160μm data due to the *Spitzer* calibration uncertainties [1]. It was found that it was not useful to use all four of the IRAC points in the fit as, for the majority of objects, they are dominated by stellar continuum emission which is poorly constrained in the models. The templates were fitted to the 8μm IRAC data in conjunction with the MIPS 24, 70 and 160μm data points. Similar values of L_{IR} were obtained with and without the use of the 8μm data point due to the longer wavelength data, particularly the 70 and 160μm data points, being far more influential in constraining the far-infrared peak. The templates were normalised to the 70μm flux density and then varied by a factor of 2 above and below this flux density for each template per object. A sample of best fit template spectra are shown in the Figure 5.1.

The values for L_{IR} were then calculated by integrating the flux under the SED from 8 to 1000μm. Figure 5.2 shows the luminosity distribution as a function of redshift for the entire sample based on the templates from Siebenmorgen & Krügel (2007). It should be noted that the choice of template does not affect the L_{IR} significantly for all reliable fits, (i.e. while the variety of templates do slightly improve the fits to the photometry, the resulting L_{IR} does not change considerably, see Figure 5.3) thus one can be confident that the calculated total infrared luminosities are robust. Furthermore, while a different choice of model may alter the physical properties of the galaxies

[1] http://irsa.ipac.caltech.edu/data/SPITZER/docs/mips/mipsinstrumenthandbook/49/

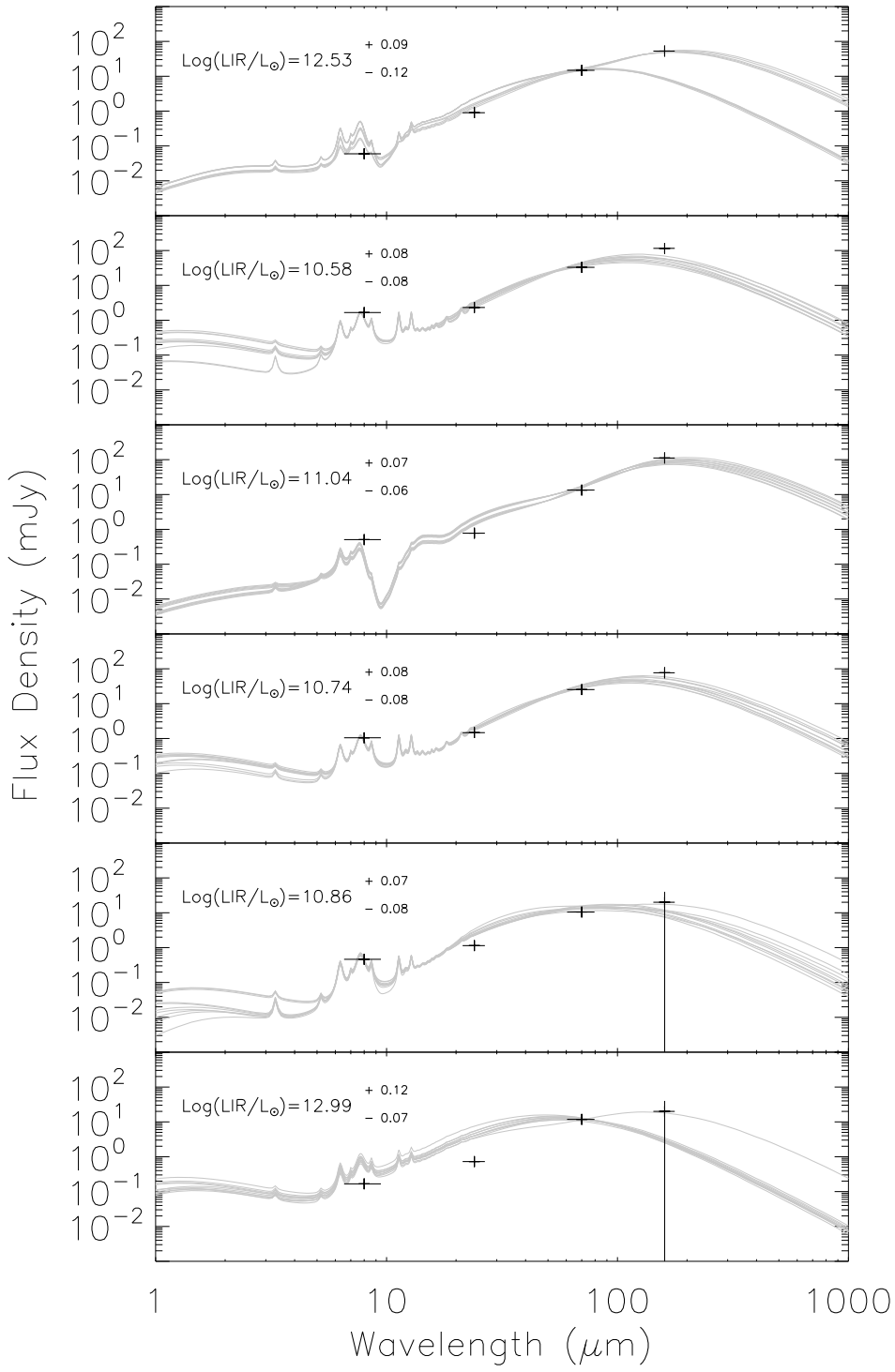

Figure 5.3: A comparison of 10 best fit Siebenmorgen & Krügel (2007) templates to a random sample of 6 sources. The corresponding mean $L_{\rm IR}$, minimum and maximum values are also shown.

(e.g. size, visual extinction), the far-infrared luminosities remain similar.

5.1.1 Comparison with Chary & Elbaz models (2001)

The Chary & Elbaz (2001) models consist of a library of 105 template SEDs of normal star-forming galaxies, starbursts, LIRGs and ULIRGs. To test whether the choice of model suite affects the values of $L_{\rm IR}$, I compared the $L_{\rm IR}$ determined from the Siebenmorgen & Krügel models with the $L_{\rm IR}$ determined using the models of Chary & Elbaz (2001). Figure 5.5 shows, for a random sample of 6 sources, the best fit template from Siebenmorgen & Krügel (2007) in the solid green line and the best fit Chary & Elbaz (2001) model over-plotted in the dashed blue line for comparison. Both the SED fits and the resulting χ^2 values indicate that the Siebenmorgen & Krügel models provide a better fit to the data. However, a reasonably good agreement between the two determinations was found (see Figure 5.6). The Siebenmorgen & Krügel (2007) templates tend to find larger values of $\rm L_{IR}$ compared to the determinations based on the Chary & Elbaz (2001) models. Approximately 88 per cent of the galaxies have larger values for their total infrared luminosity (i.e. they fall below the dotted line marking unity) when determined using the Siebenmorgen & Krügel (2007) models compared to the Chary & Elbaz (2001) models. The mean of the distribution in Figure 5.6 indicates that the Chary & Elbaz (2001) models typically find $\rm L_{IR}$ values 72 per cent of the luminosity of their counterparts determined using the Siebenmorgen & Krügel (2007) models. The blue crosses denote the mean of the distribution in bins of $\Delta L = 10^{0.4}$. While the scatter increases with increasing $\rm L_{IR}$, the

Chary & Elbaz models tend to find larger values for L_{IR} when compared to the determinations based on the Siebenmorgen & Krügel (2007) templates at the brighter end. At the highest luminosities considered here, ($\gtrsim 10^{13} L_{\odot}$), the Chary & Elbaz (2001) models switch to over-predicting the L_{IR} when compared to the Siebenmorgen & Krügel (2007) templates by approximately 30 per cent.

Owing to the difference in the L_{IR} determinations between the two model suites and the desire to include the Huynh et al. (2007) data points determined over the GOODS-North field using the Chary & Elbaz (2001) models and only the 70μm value, it is necessary to correct these determinations of the L_{IR}. In order to determine this correction, the L_{IR} values for all 736 galaxies were calculated using the method of Huynh et al. (2007) by fixing the galaxy model and calculating the normalisation using the 70μm flux density and the redshift of each object. These values were then compared to my previously described measurements of the L_{IR} using all four photometric points (8, 24, 70 and 160μm) and the Siebenmorgen & Krügel (2007) templates. Interestingly using the Chary & Elbaz (2001) models and the 70μm data point alone, versus all four photometric data points, more closely approximated the L_{IR} determined using all four photometric points and the Siebenmorgen & Krügel (2007) templates. This indicates that using the 70μm point alone leads to higher values of the L_{IR} than when the additional data points are used. The comparison of the L_{IR} values calculated using the method of Huynh et al. (2007) and the method described in this work was used to determine an offset to be applied to each luminosity bin in the Huynh et al. (2007) data set. This offset was applied in order to allow a direct comparison to the values

determined in this work.

The L_{IR} values derived by imposing the 40 mJy confusion limit and those found allowing values down to the 160μm 1σ limit were also compared for the two model libraries. The Siebenmorgen & Krügel (2007) templates and the Chary & Elbaz (2001) models had scatters of 0.07 dex and 0.035 dex respectively (see Figure 5.4). Neither gave indications that going below the 40 mJy confusion limit had any significant impact on the determinations of L_{IR}.

5.1.2 Removing the contribution of AGN

Le Floc'h et al. (2005) considered the contribution from AGN at $z < 1$ to be negligible at 24μm, and we would expect the contribution at 70μm to be even less, as it traces the FIR peak, associated with star formation, more effectively. We note that the incidence of AGN activity increases with increasing total infrared luminosity (Murphy et al. 2009; Bonfield et al. 2011; Alonso-Herrero et al. 2011). Murphy et al. (2011) estimated that AGN typically contribute < 18 per cent to the total infrared luminosity density between $0 < z < 2.35$. While a galaxy may host an AGN, it may also contain a greater contribution from star formation. Symeonidis et al. (2010) found in a sample of 61 70μm selected galaxies, that all were primarily powered by star formation with the fraction of star-burst galaxies, LIRGs and ULIRGs containing AGN to be 0, 11 and 23 per cent respectively. For those galaxies displaying an infrared excess, defined as emitting a greater infrared luminosity than would be predicted based on extinction corrected ultraviolet

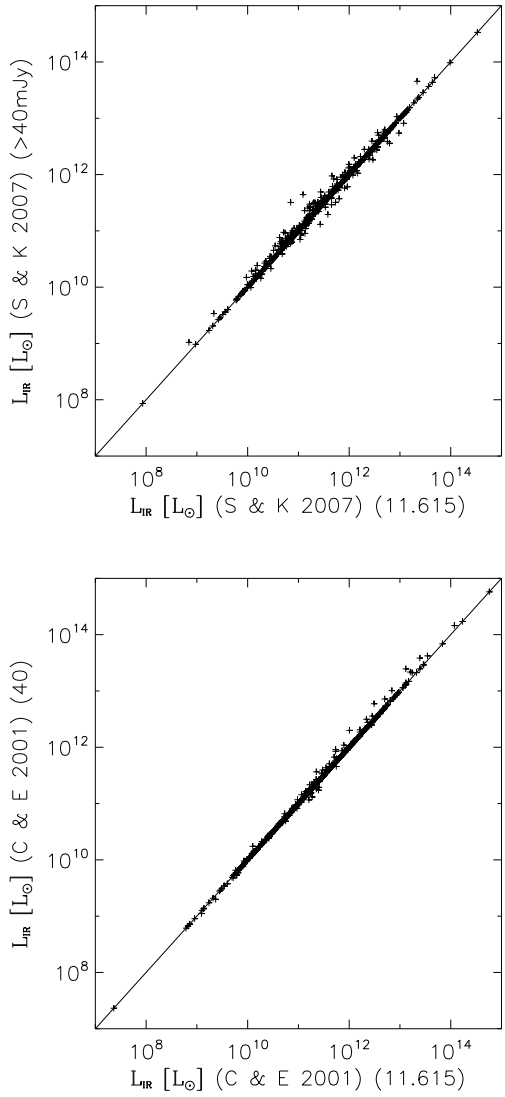

Figure 5.4: Top: A comparison of the L_{IR} values obtained from the Siebenmorgen & Krügel (2007) models using the 1σ limit on the 160μm flux density and the L_{IR} values measured imposing the 160μm 40 mJy confusion limit. The plot shows there is no offset between the two determination which have a scatter of 0.07 dex. Bottom: A comparison of the L_{IR} values obtained from the Chary & Elbaz (2001) models using the 1σ limit on the 160μm flux density and the L_{IR} values measured imposing the 160μm 40 mJy confusion limit. The plot shows there is no offset between the two determination, which have a scatter of 0.035 dex.

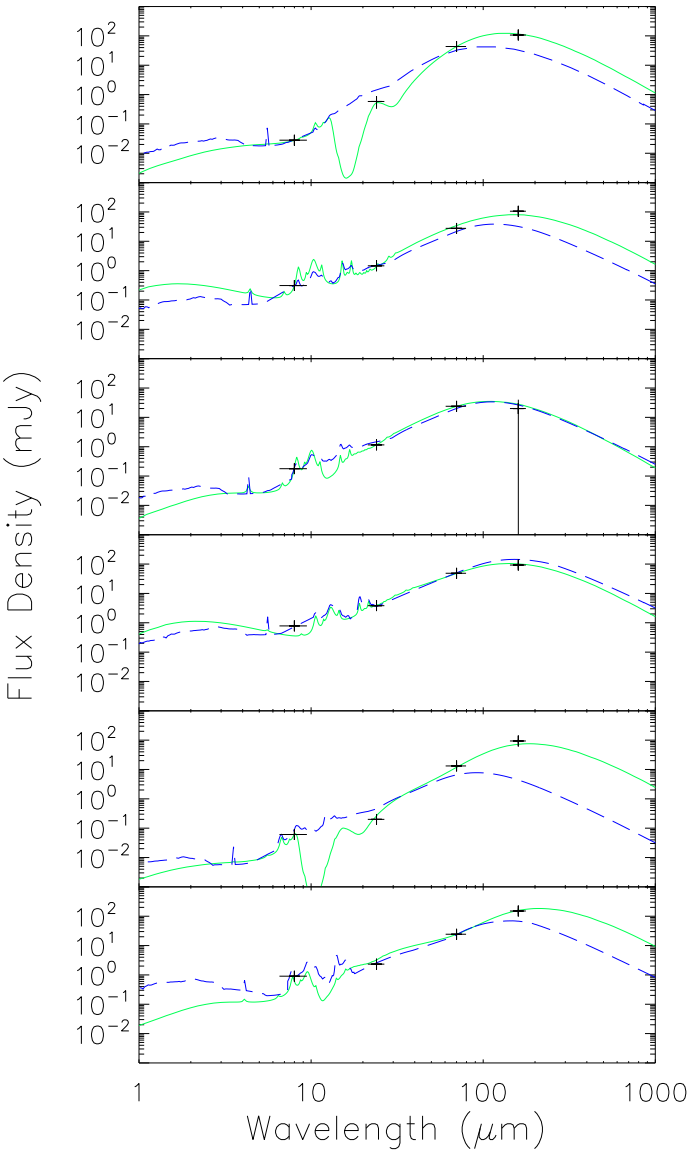

Figure 5.5: A random sample of sources with both the best fit Siebenmorgen & Krügel (2007) (green solid line) and Chary & Elbaz (2001) models (blue dashed line) over-plotted for comparison. These show that the Chary & Elbaz models tend to under predict the longer wavelength flux density. This is explored further in Chapter 6.

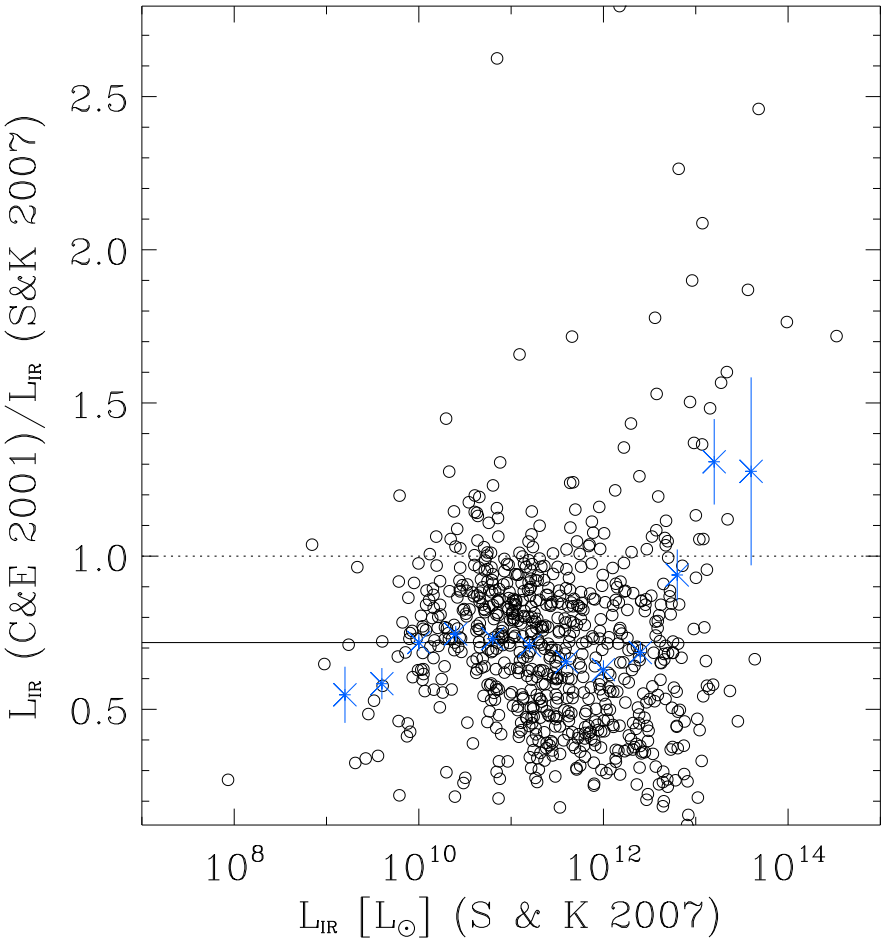

Figure 5.6: A comparison of the Siebenmorgen & Krügel (2007) templates (S & K 2007) and the Chary & Elbaz (2001) models (C & E 2001) showing that the Chary & Elbaz models typically find lower L_{IR} values compared to the Siebenmorgen & Krügel (2007) templates. The dotted line marks the limit over which the Chary & Elbaz models find higher values for the L_{IR} when compared to the Siebenmorgen & Krügel (2007) templates. The mean and the median of the distribution are indicated by the solid line on the plot and occur at ~ 0.72. The blue crosses denote the mean of the distribution in bins of $\Delta L = 10^{0.4}$. While the scatter increases with increasing L_{IR}, the Chary & Elbaz models tend to find larger values for the L_{IR} when compared to the determinations based on the Siebenmorgen & Krügel (2007) templates for increasing L_{IR}.

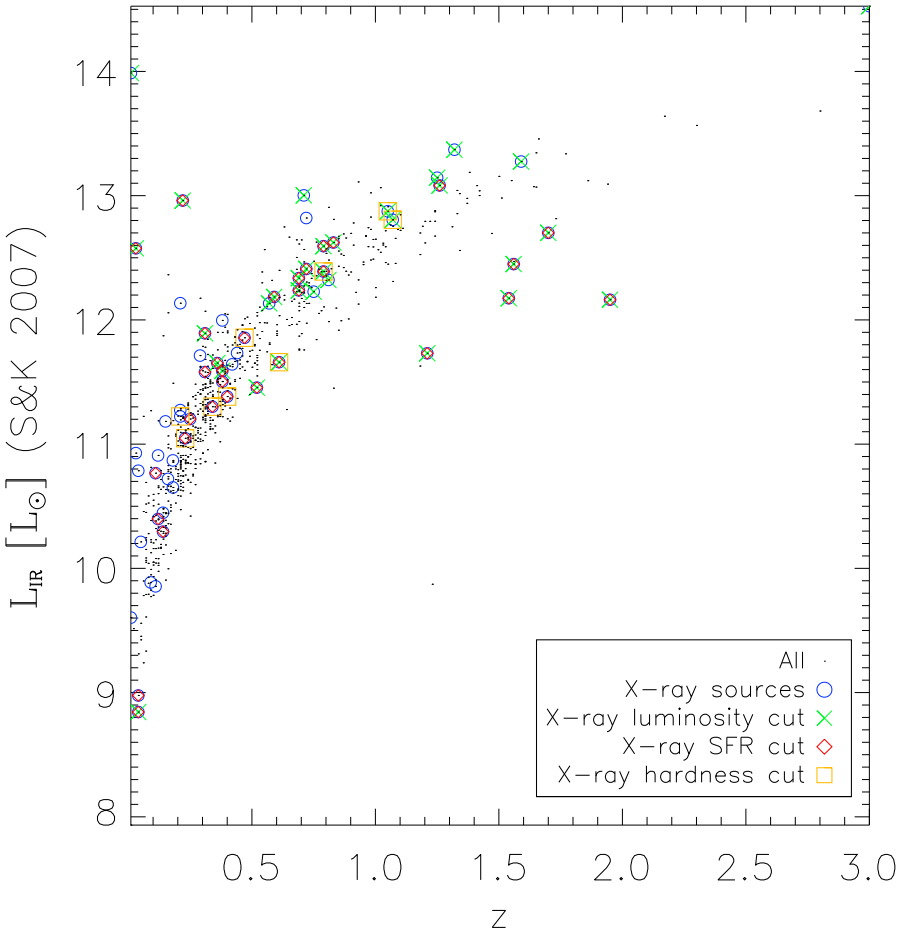

Figure 5.7: Figure showing the potential AGN in our sample with redshift versus total infrared luminosity. The black circles represent all of the 736 galaxies in our sample. The blue circles represent the 63 galaxies that have X-ray counterparts in the Brusa et al. (2010) catalogue. The green dots denotes the sources with $L_{2-10keV} > 10^{42} ergs\,s^{-1}$. The red dots denote those 32 galaxies with X-ray emission in excess of what would be expected based on the infrared determined star formation rate. Finally the yellow dots mark the 9 galaxies with a X-ray hardness ratio > 0.8.

luminosity determinations of the star formation rate, on average, only 35 per cent of this excess can be attributed to an AGN (Murphy et al. 2009). Without the ability to separate the emission, removing AGN from the sample also removes the star formation contribution of the host galaxy. However this increasing contribution from AGN with increasing infrared luminosity would have the greatest effect on the bright end of the luminosity function which is the main focus of this work. Therefore we endeavour to conservatively remove the contribution from AGN to our sample in order to minimise their effect on our determination of the bright end slope.

The multi-wavelength coverage of the COSMOS field makes the removal of galaxies potentially including an AGN possible. AGN removal was carried out using a number of indicators, the hard X-ray luminosity, the X-ray predicted star formation rate and the hardness ratio. All of these methods were used to identify galaxies with an excess in hard X-ray luminosity. Over the COSMOS field there are both *XMM-Newton* (Cappelluti et al. 2009) and *Chandra* (Elvis et al. 2009) data available. The *Chandra* data only cover approximately 53 per cent of the area studied in this survey whereas the *XMM-Newton* data, while less sensitive, cover the entire field. Despite the sensitivities of the respective surveys, they both detect the brightest X-ray sources which are the ones of interest as potential AGN, therefore the larger area covered by the *XMM-Newton* survey is better suited for this work. The catalogue of Brusa et al. (2010) provides optical counterparts for the X-ray sources over the COSMOS field in the *XMM-Newton* survey. A total of 63 out of the 736 sources had an X-ray counterpart in the Brusa et al. (2010) catalogue. The 63 matches are marked in large blue open circles in Figure

5.7.

A hard X-ray luminosity of $L_{2-10\mathrm{keV}} > 10^{42}\mathrm{ergs\,s^{-1}}$ from a source is often used as an indicator that an AGN is likely to be present (see Brandt & Hasinger 2005 for a review). Out of the 63 sources that had X-ray counterparts, 32 had hard X-ray luminosities in excess of this value and were therefore considered to be possible AGN contaminants and are marked in green crosses in Figure 5.7.

Ranalli et al. (2003) suggested that the hard X-ray emission is directly related to the star formation rate of nearby star forming galaxies. Therefore a comparison of star formation rates based on the infrared and X-ray emission should determine if the X-ray emission is attributable to star formation alone. The star formation rate of starbursts, LIRGs and ULIRGs is well approximated using the far-infrared emission. The following relation

$$SFR(\mathrm{M_\odot yr^{-1}}) = 4.5 \times 10^{-44} L_{\mathrm{FIR}}(\mathrm{ergs\,s^{-1}}), \tag{5.1}$$

from Kennicutt (1998b) was used to estimate the star formation rate of the galaxies. A relation for the X-ray determined star formation rate was proposed by Pereira-Santaella et al. (2011) and is given by

$$SFR(\mathrm{M_\odot yr^{-1}}) = 3.9 \times 10^{-40} L_{2-10\mathrm{keV}}(\mathrm{ergs\,s^{-1}}) \tag{5.2}$$

where the scatter on the relation is approximately 0.27 dex. Out of the 63 galaxies with X-ray counterparts, 32 had a hard X-ray luminosity in excess of that expected based on the far infrared determined star formation rate, even

allowing for the 0.27 dex of scatter on the relation and are marked in small red open circles in Figure 5.7. 21 of these 32 galaxies had both a hard X-ray luminosity in excess of $L_{2-10keV} > 10^{42} ergs\,s^{-1}$ and an X-ray based star formation rate in excess of that predicted using the far -infrared emission resulting in a total of 43 potential AGN contaminants.

The final indicator used to remove AGN from the sample was the hardness ratio. This ratio relates the hard and the soft X-ray emission and a value > 0.8 was used to identify potential AGN. 9 out of the 63 objects satisfied this criteria and are marked in Figure 5.7 in orange open squares. Eight of these are common with the luminosity cut and the star formation rate cut resulting in a single additional candidate making a total of 44 galaxies (approximately 6 per cent of the sample) identified as potentially containing an AGN. These 44 galaxies were removed from the sample in order to minimise the contamination from AGN.

5.2 The Far-Infrared Luminosity Function

5.2.1 The Monte Carlo Approach

The luminosity function was determined from the total $L_{\rm IR}$ and the redshifts of the galaxies. In order to account for the errors on the photometric redshifts, the whole probability distribution was considered by taking a Monte Carlo approach. The distributions were generated using an asymmetric Gaussian of width determined by the 1σ upper and lower redshift uncertainties (see Figure 5.8) in the photometric redshift catalogue. The

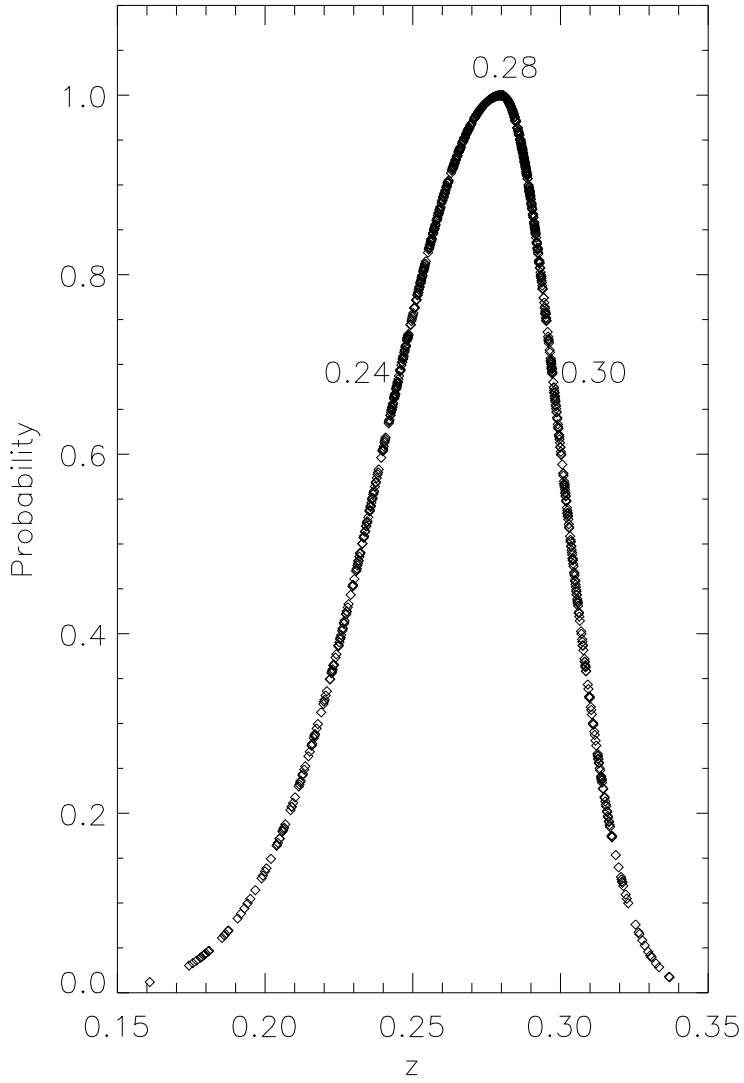

Figure 5.8: An example of 1000 random redshifts sampling the full probability distribution function of a single source. The peak redshift of 0.28 is given, as are the 1σ minimum and maximum limits of 0.24 and 0.30 respectively. Note the increasing density of points at the highest probability showing the source was most frequently sampled around the peak redshift.

lower bounds in redshift were also limited to $z > 0$. Where no error values in the COSMOS photometric catalogue were given, an error of $0.3(1 + z)$ was assumed. This value was determined by examining the dispersion of the photometric redshift for the cases where errors on the photometric redshifts were available. The mean $\sigma_{zphot}/(1 + z_{phot})$ was found to be < 0.1 and therefore a conservative value of 0.3 was chosen for the dispersion. The redshifts for each object were drawn 1000 times from the probability distribution (see Figure 5.8 for an example) and a corresponding $L_{\rm IR}$ was determined.

5.2.2 The 1/Vmax Method

The luminosity function was determined using the standard $1/V_{\rm max}$ technique described by Schmidt (1968). The galaxies from all realisations of the Monte Carlo simulation were sorted in to luminosity and redshift bins. Using their redshifts and best fitted SEDs, the maximum redshift they could be observed at and still remain above the flux density limit ($S_{70} = 10$ mJy) of the survey was determined. Then either this maximum redshift, or the maximum redshift of the bin the galaxy is located in (whichever is smaller) was used in the $1/V_{\rm max}$ calculation. This maximum redshift was converted to a maximum volume, using the distance based on the redshift. Then the volume corresponding to the minimum redshift of each bin was subtracted in order to determine $V_{\rm max}$. This $1/V_{\rm max}$ value is summed for all galaxies within a redshift and luminosity bin, given by

$$\rho = \sum_{i=0}^{n} [1/V_{\rm max}(i)] d\Omega, \tag{5.3}$$

where $d\Omega$ is the area of the survey in steradians. The area of the survey is usually accounted for after the summation of $V_{\rm max}$ value, however I have included it before the summation is carried out. This minor change does not effect the final determination of the $1/V_{\rm max}$ terms because these processes are distributive. The uncertainty on the $1/V_{\rm max}$ value is simply given by the Poisson statistics,

$$\sigma(\rho) = \sum_{i=0}^{n} [1/(V_{\rm max}(i))^2]^{1/2} d\Omega, \tag{5.4}$$

As a result of the 'artificial' increase in the number of objects due to the Monte Carlo realisations, although the Poisson error in each realisation will remain roughly constant, the total Poisson error would naturally decrease, however this can be corrected for with the $d\Omega$ term ($d\Omega_{eff}$=$d\Omega_{act}/\sqrt{N_{mc}}$, where N_{mc} is the number of Monte Carlo simulations, $d\Omega_{eff}$ is the effective area and $d\Omega_{act}$ is the actual or real area of the survey). The standard deviation of the $1/V_{max}$ points from all of the Monte Carlo simulations were added in quadrature to the Poisson uncertainty. The $1/V_{max}$ data points determined in this work are listed in Table 5.1.

5.2.3 The Fitting of the Far-Infrared Luminosity Function

The objects were divided in to luminosity bins of $\Delta \log_{10}(\mathrm{L}) = 0.4$ and sorted in redshift slices of $\Delta z \sim 0.2$. The five redshift bins were defined as follows: $0 < z \leq 0.2$, $0.2 < z \leq 0.4$, $0.4 < z \leq 0.6$, $0.6 < z \leq 0.9$ and $0.9 < z \leq 1.1$. These bins were selected to be the same as described in Huynh et al. (2007) in order to include their $1/V_{\rm max}$ data points determined over the GOODS-

Table 5.1: The $1/V_{\rm max}$ points determined in this study.

$\rm Log_{10}(L_{IR}/L_{\odot})$	$\rm Log_{10}(V_{max})$	$\rm Log_{10}(\sigma V_{max})$
$0 < z \leq 0.2$		
9.4	-2.142	-2.681
9.8	-2.478	-3.241
10.2	-2.581	-3.490
10.6	-2.886	-3.745
11.0	-3.446	-4.082
11.4	-3.888	-4.370
$0.2 < z \leq 0.4$		
10.6	-2.812	-3.273
11.0	-2.988	-3.886
11.4	-3.466	-4.407
11.8	-4.388	-4.927
$0.4 < z \leq 0.6$		
11.4	-3.685	-4.264
11.8	-3.959	-4.378
12.2	-4.830	-5.334
$0.6 < z \leq 0.9$		
11.8	-4.161	-4.580
12.2	-4.115	-4.711
12.6	-4.866	-5.472
$0.9 < z \leq 1.1$		
12.6	-4.574	-5.122
13.0	-5.415	-5.729

North field. The authors fixed the values of L^*, and the slopes (α) of the double power law to the local luminosity function from Sanders et al. (2003), and measured the evolution in different redshift slices. In my analysis, I am able to fit for all of these parameters rather than assume the local values due to the large area and depth of the S-COSMOS data.

In the fitting procedure, three types of evolution were considered; (1) Pure Luminosity Evolution (PLE; $q = 0$, see Equations 5.5 & 5.6), (2) Pure Density Evolution (PDE; $p = 0$) and (3) Luminosity Dependent Density Evolution (LDDE). The uncertainties on these fitted parameters were determined by marginalising over all values within 5σ of the best fit χ^2 value. The results of the best fits for each parameterisation are shown in Tables 5.2 & 5.3 and Figures 5.9, 5.10, 5.11, 5.12, 5.13 & 5.14. Solutions were searched for using both a Schechter function and double power law parameterisation.

Double Power Law

Using the same parameterisation as described in Huynh et al. (2007) for the double power law function:

$$\rho = \rho^*(1+z)^q \left[\frac{L}{L^*(1+z)^p}\right]^\alpha, \tag{5.5}$$

where q describes the density evolution, p the luminosity evolution and α is the slope of the luminosity function. For $L < L^*$, $\alpha = \alpha_1$ was used

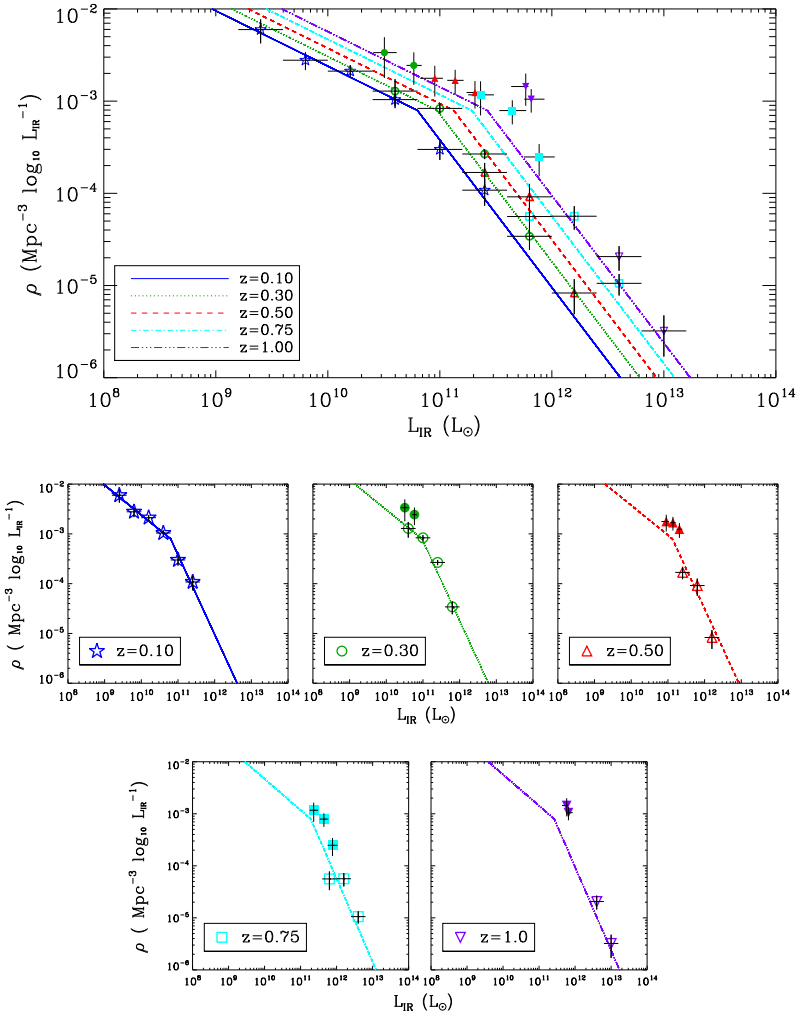

Figure 5.9: Top panel: The far-infrared luminosity function with pure luminosity evolution. The solid line and the stars corresponds to $z = 0.1$ (dark blue). The dotted line and the circles correspond to $z = 0.3$ (green). The dashed line and triangles correspond to $z = 0.5$ (red). The dot dashed line and the squares correspond to $z = 0.75$ (cyan). The dashed triple dotted line and the inverted triangles correspond to $z = 1$ (purple). The filled symbols represent the data from Huynh et al. (2007) and the open symbols represent this work. The Huynh et al. (2007) redshift $z = 1$ points lie beyond the luminosity function, this may be due to an overestimation of the L_{IR} by Huynh et al. (2007) and/or the use of the peak of the photometric redshift distribution. The best-fit values for the parameters governing the luminosity function are given in Table 5.2. Bottom panel: The far-infrared luminosity function separated into individual redshift slices.

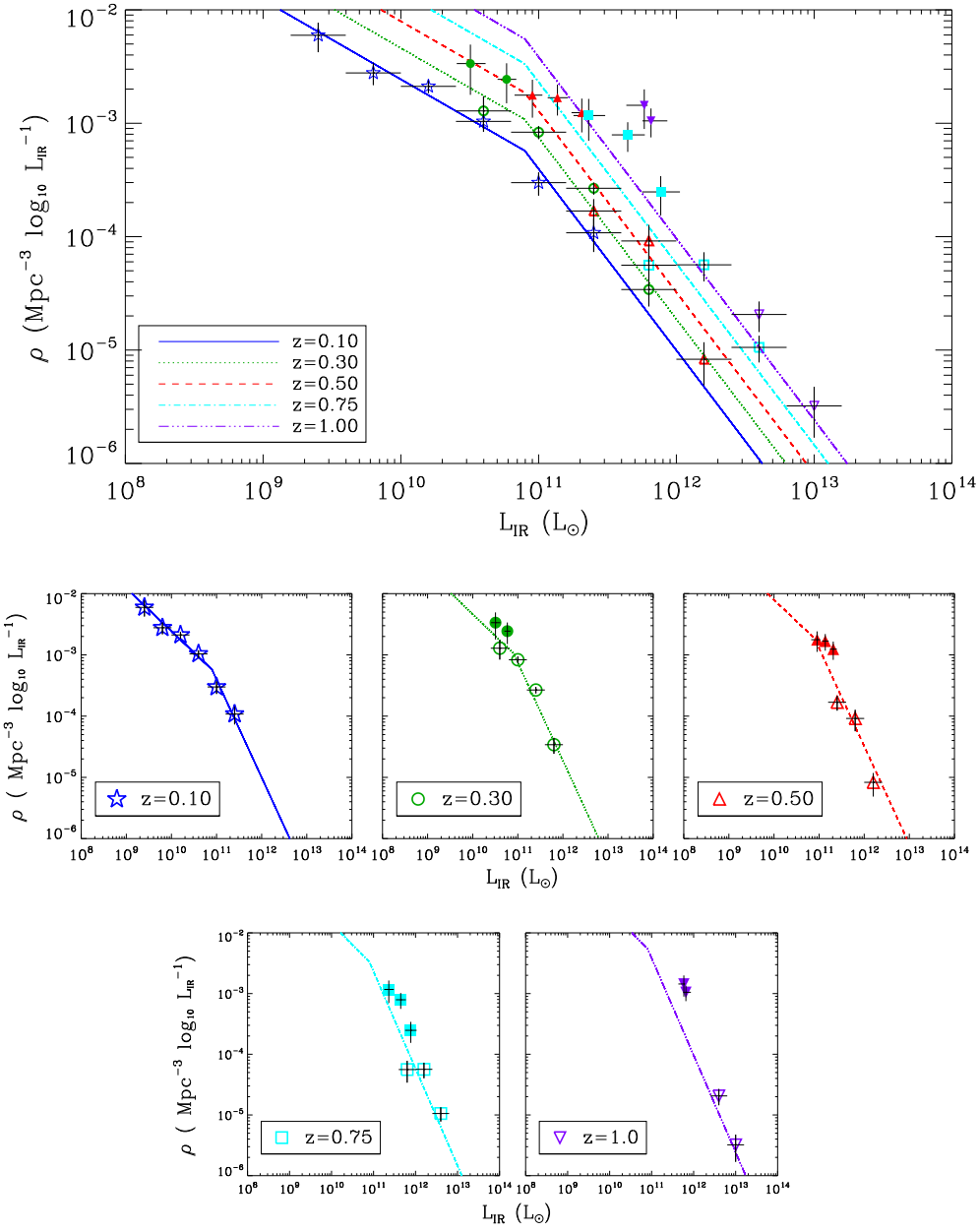

Figure 5.10: The symbols are the same as described in figure 5.9 but for the case of pure density evolution.

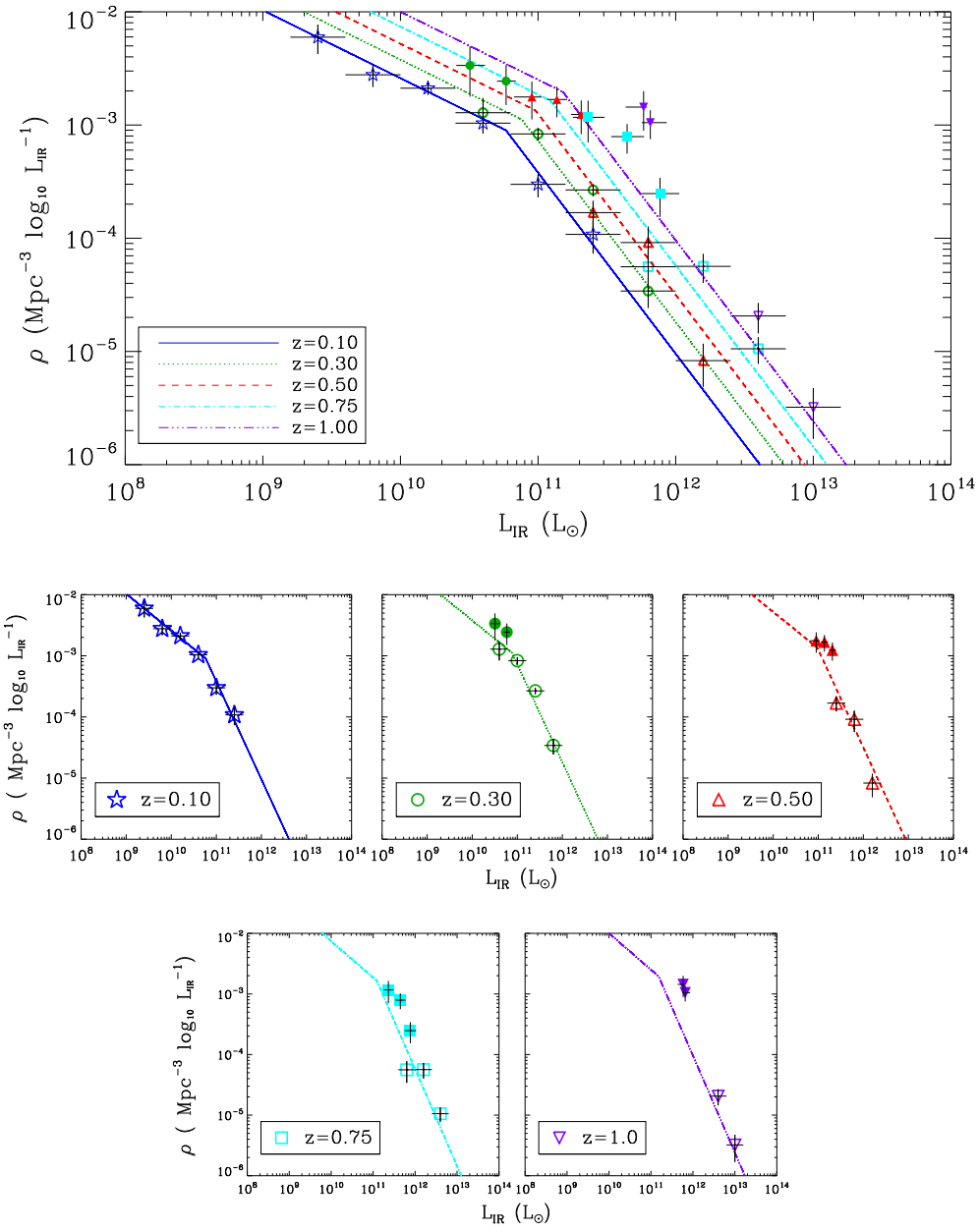

Figure 5.11: The symbols are the same as described in figure 5.9 but for the case of luminosity dependent density evolution.

Table 5.2: The best fit parameters to $1/V_{\rm max}$ for pure luminosity, pure density and luminosity dependent density evolution for the double power law parameterisation. The quoted uncertainties represent 1 σ error values based on the resultant χ^2.

Type of Evolution	α_1 (L<L*)	α_2 (L>L*)	$\log_{10}$L$^*(L_\odot)$	$\log_{10}\phi^*$	p	q	χ^2	Reduced χ^2
Pure Luminosity	$-0.6^{+0.2}_{-0.1}$	-1.6 ± 0.2	$10.7^{+0.1}_{0.3}$	$-3.1^{+0.3}_{-0.1}$	$2.4^{+0.6}_{-0.7}$	0.0	79.49	3.61
Pure Density	$-0.7^{+0.3}_{-0.1}$	-1.6 ± 0.2	$10.9^{+0.0}_{-0.2}$	$-3.4^{+0.3}_{-0.1}$	0.0	$3.8^{+1.0}_{-1.4}$	79.61	3.62
Luminosity dependent Density	-0.6 ± 0.2	-1.6 ± 0.2	$10.7^{+0.2}_{-0.3}$	$-3.1^{+0.3}_{-0.4}$	$1.6^{+1.4}_{-1.6}$	$1.3^{+3.4}_{-1.3}$	78.00	3.71

and for $L > L^*$, $\alpha = \alpha_2$ was used. Then all parameters (α_1, α_2, L^*, ρ^*, p and q) of the luminosity function were fitted for using Equation 5.5 to the aforementioned redshift slices, simultaneously measuring the evolution in luminosity and density up to a redshift of $z = 1.1$. The best fits for PLE, PDE and LDDE are shown in Figures 5.9, 5.10 and 5.11 respectively. The best fit values for all models are listed in Table 5.2.

Schechter Function

The Schechter function was fit in much the same way as the double power law with the following parameterisation:

$$\rho = \rho^*(1+z)^q \left[\frac{L}{L^*(1+z)^p}\right]^{\alpha} exp^{\left[\frac{-L}{L^*(1+z)^p}\right]}, \tag{5.6}$$

where q describes the density evolution, p the luminosity evolution and α is the slope of the faint end of the luminosity function and the bright end slope is governed by the exponent term. Then all parameters (α, L^*, ρ^*, p and q) of the luminosity function were fitted for using Equation 5.6 to the aforementioned redshift slices, simultaneously measuring the evolution in luminosity and density up to a redshift of $z = 1.1$.

The best fits for PLE, PDE and LDDE are shown in Figures 5.12, 5.13 and 5.14 respectively. The best fit values for all models are listed in Table 5.3. It should be noted that the best fit scenario for LDDE is the same as for PLE indicating that the luminosity evolution is the dominant form.

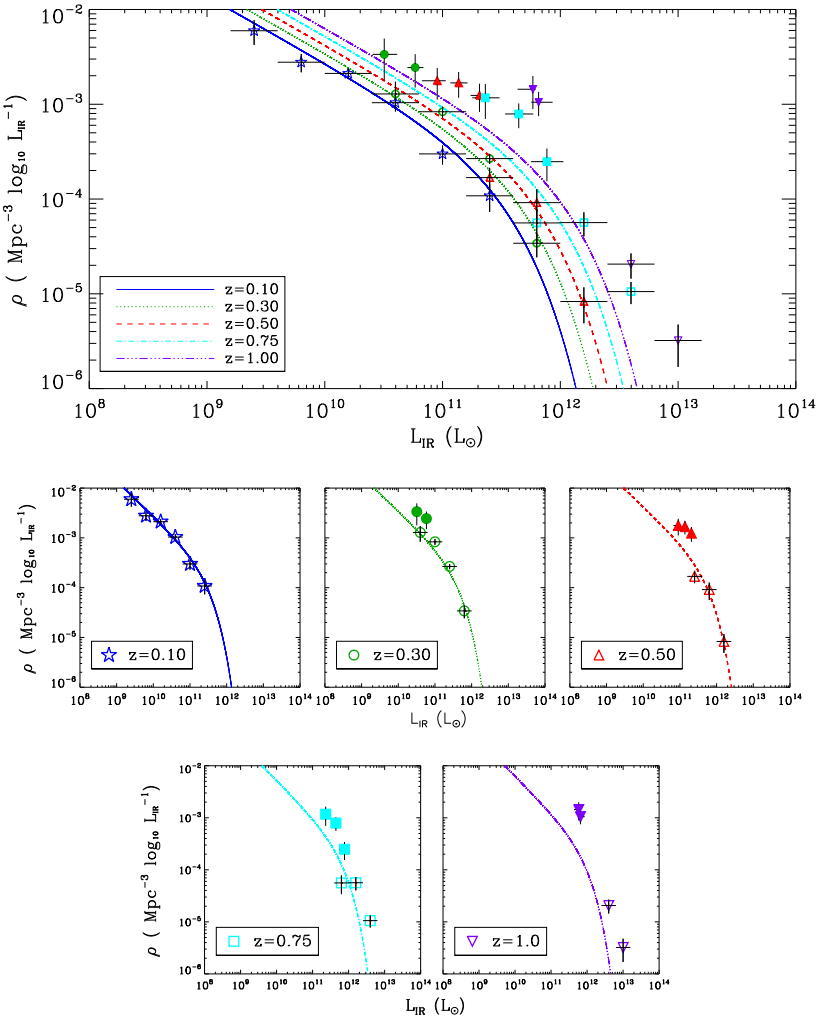

Figure 5.12: Top panel: The far-infrared luminosity function with pure luminosity evolution. The solid line and the stars corresponds to $z = 0.1$ (dark blue). The dotted line and the circles correspond to $z = 0.3$ (green). The dashed line and triangles correspond to $z = 0.5$ (red). The dot dashed line and the squares correspond to $z = 0.75$ (cyan). The dashed triple dotted line and the inverted triangles correspond to $z = 1$ (purple). The filled symbols represent the data from Huynh et al. (2007) and the open symbols represent this work. The Huynh et al. (2007) redshift $z = 1$ points lie beyond the luminosity function, this may be due to an overestimation of the L_{IR} by Huynh et al. (2007) and/or the use of the peak of the photometric redshift distribution. The best-fit values for the parameters governing the luminosity function are given in Table 5.3. Bottom panel: The far-infrared luminosity function separated into individual redshift slices

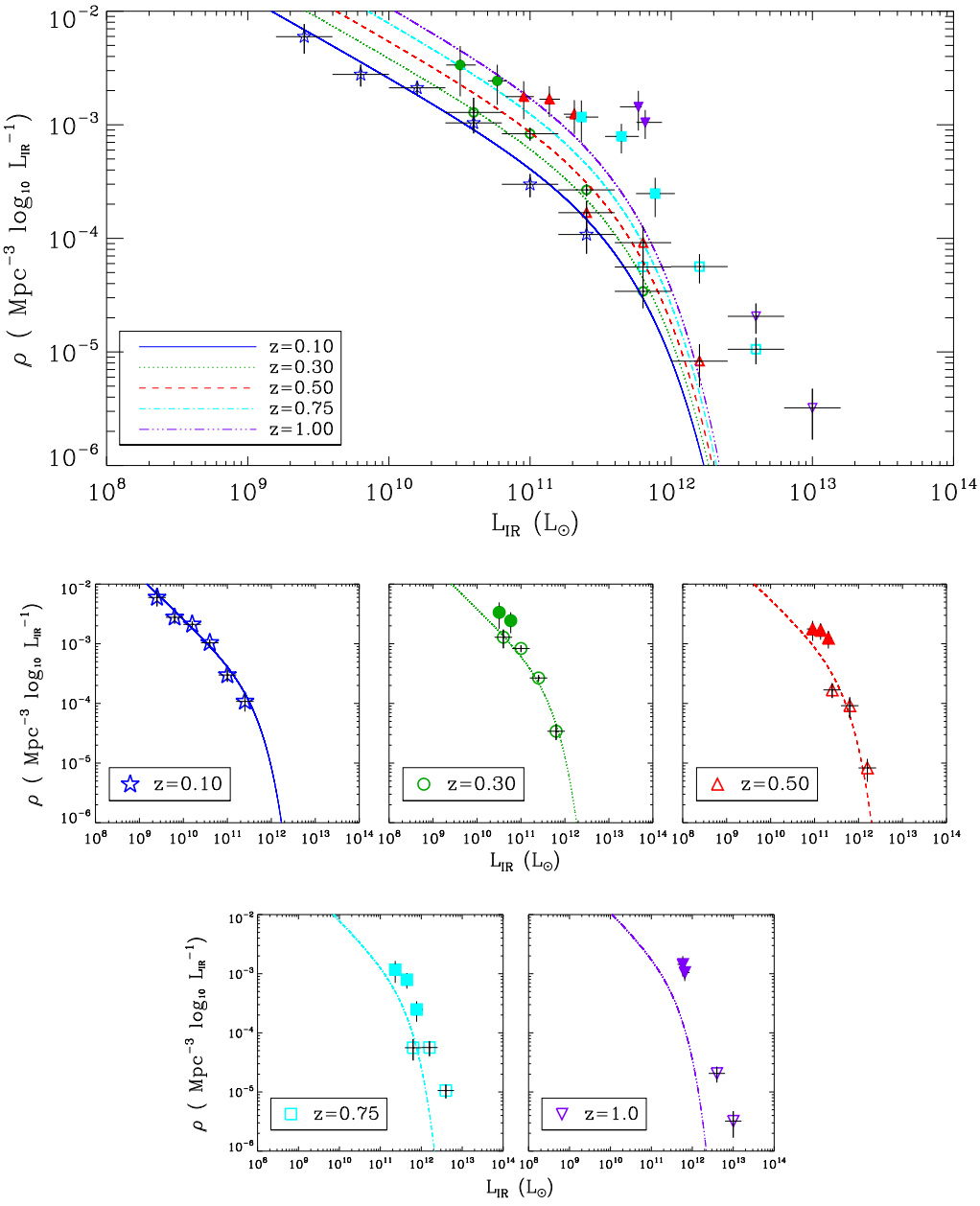

Figure 5.13: The symbols are the same as described in figure 5.12 but for the case of pure density evolution.

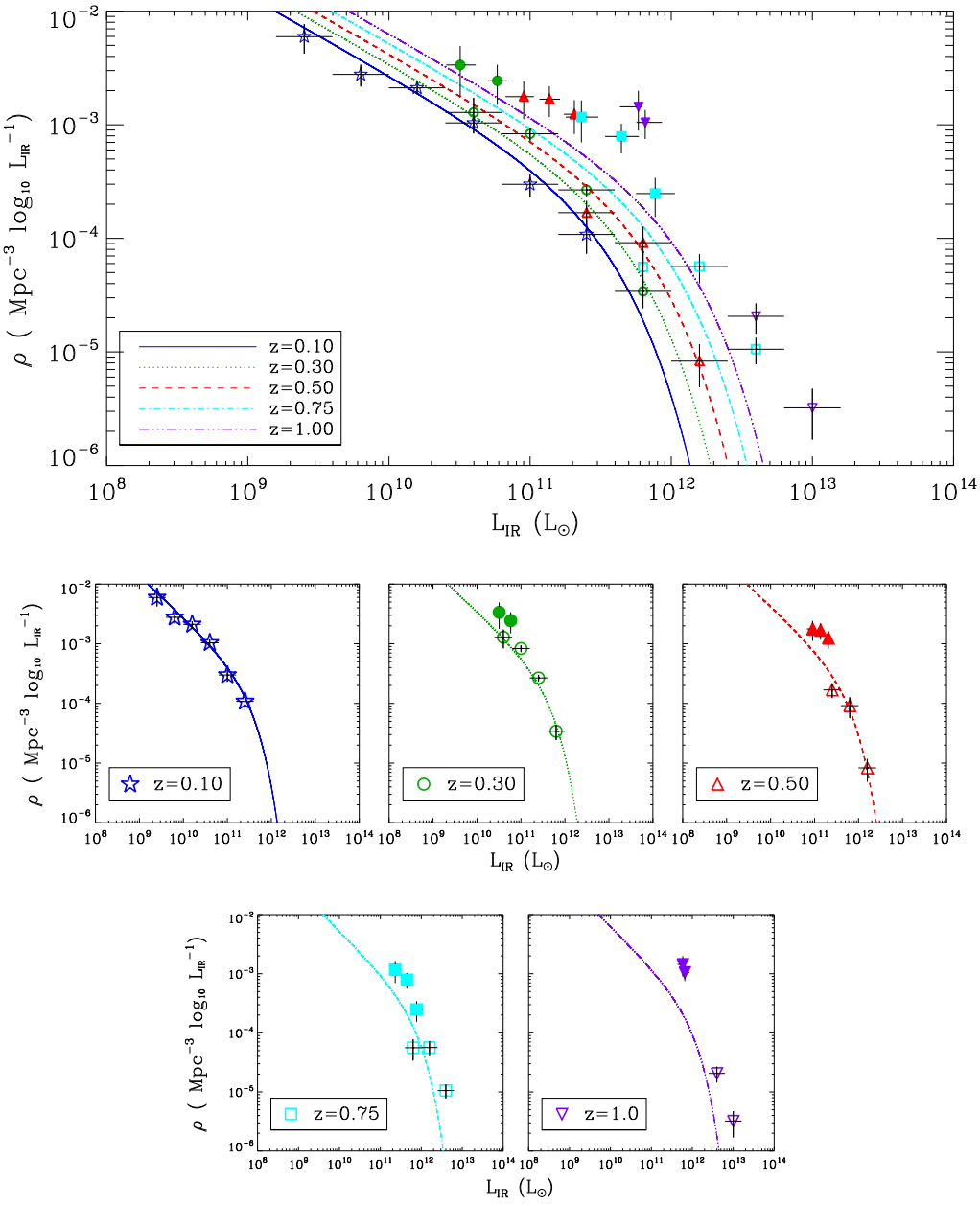

Figure 5.14: The symbols are the same as described in figure 5.12 but for the case of luminosity dependent density evolution.

Table 5.3: The best fit parameters to $1/V_{\rm max}$ for pure luminosity, pure density and luminosity dependent density evolution for the Schechter function parameterisation. The quoted uncertainties represent 1 σ error values based on the resultant χ^2.

Type of Evolution	α	$\log_{10}$L* (L$_\odot$)	$\log_{10}\phi^*$ (Mpc^{-3})	p	q	χ^2	Reduced χ^2
Pure Luminosity	-0.7 ± 0.1	$11.4^{+0.3}_{-0.2}$	$-3.6^{+0.3}_{-0.4}$	$2.0^{+0.9}_{-0.5}$	0.0	109.87	4.78
Pure Density	-0.7 ± 0.1	$11.6^{+0.2}_{-0.3}$	-3.8 ± 0.3	0.0	$2.4^{+1.7}_{-0.6}$	113.20	4.92
Luminosity dependent Density	-0.7 ± 0.2	$11.4^{+0.3}_{-0.2}$	$-3.6^{=0.4}_{-0.5}$	$2.0^{+0.9}_{-2.0}$	$0.0^{+3.9}_{-0.0}$	109.87	4.78

Comparison

For the three types of evolution, the Schechter function provided reduced χ^2 values of ~ 4.8 (see Section 5.2.3) while the double power law parameterisation provided reduced χ^2 values of ~ 3.6 (see Section 5.2.3). The Schechter function while adequately fitting the lower redshift points seemed to fail to produce a good fit towards the highest redshift bin. This is likely due to the data points from Huynh et al. (2007) which may not be accurate (see Section 5.3 for further details). Due to the better representation of the data by the double power law function, only this parameterisation was considered from this point onwards.

One can quickly see that for the double power law parameterisation, the reduced χ^2 for all the forms of evolution are similar, thus it is difficult to establish the exact form for the evolution. This is in large part due to a lack of faint sources beyond $z > 0.5$ making constraining the faint end slope and break of the luminosity function beyond this redshift problematic, leading to degeneracies between the different types of evolution. However, the best fit case (i.e. that with the lowest reduced χ^2 value) is PLE. In all cases there is strong positive evolution to higher redshifts.

5.3 Discussion and Comparison with Other Work

5.3.1 The Bright End Slope

Sanders et al. (2003) derived the local far-infrared luminosity function from a catalogue of 629 objects with $S_{60\mu\mathrm{m}} > 5.24$ Jy in the IRAS Revised Bright Galaxy Sample (RBGS). This sample covered nearly the entire sky and reached a maximum redshift of 0.0876. The parameters determined by Sanders et al. (2003) were $\alpha_1 = -0.6 \pm 0.1$, $\alpha_2 = -2.2$, $\log_{10} L^* = 10.5$ and $\log_{10} \Phi^* = -2.5$ and are in good agreement with our findings with the exception of the bright end slope (α_2) where they find $\alpha_2 = -2.2$. A shallower bright end slope would imply a higher number density of the most luminous galaxies and therefore a more significant contribution to the total infrared energy density from these luminous galaxies, than previously determined. No evidence for an increasing slope with redshift was found. Subsequent studies of the $\sim 70\mu$m selected luminous infrared galaxy population at $z \sim 1$ have typically fixed the slopes of the luminosity function to the local values determined by Sanders et al. (2003) and fit for the evolution (e.g. Huynh et al. 2007; Magnelli et al. 2009). These studies are deep ($S_{70\mu\mathrm{m}} > 2 - 3$ mJy) and are therefore effective at constraining the break in the luminosity function, however they do not reach the high total infrared luminosities attained here ($L_{\mathrm{IR}} \sim 10^{13} L_{\odot}$) due to the smaller field of view they probe. Therefore, this work can place better constraints on the bright end of the luminosity function. Magnelli et al. (2009) find no evidence for a change in slope of the

bright end of the luminosity function from the value of $\alpha_2 = -2.2$ (Sanders et al. 2003).

Figure 5.15 shows the luminosity function determined by Magnelli et al. (2009) for the $0.7 < z < 1.0$ epoch with the solid black line. The data utilised by Magnelli et al. (2009) to determine the luminosity function fit came from four fields the Extended Groth Strip (EGS), the Great Observatories Origin Deep Survey (GOODS) both northern and southern fields and the ECDFS-0, the $1/\mathrm{V_{max}}$ data points from these fields are marked in red, orange and blue open triangles respectively. Magnelli et al. (2009) also made use of stacking analysis to provide better constraints on the faint end of the luminosity function and these points for each field are marked in open squares. Also overplotted are my determinations of the $z \sim 0.75$ and $z \sim 1.0$ V_{max} points in open green squares and purple triangles respectively. The Huynh et al. (2007) data points are also marked in the same manner in filled symbols. The green and purple dashed lines show my determinations of the $z \sim 0.75$ and $z \sim 1.0$ luminosity functions respectively. The greatest discrepancy shown in Figure 5.15 between the two luminosity functions occurs at the faint end where this work has few constraints at this redshift. However, at the bright end, my luminosity function is consistent with the constraints provided by Magnelli et al. (2009) but with a shallower bright end slope.

This difference in bright end slope however, could be attributed to the choice of model suite. When determining the infrared luminosity function, the Chary & Elbaz (2001) models can produce a steeper bright end slope of $\alpha_2 = -2.2$. This is due to the increasing values for $\mathrm{L_{IR}}$ found using the Chary & Elbaz (2001) models when compared to the determinations using

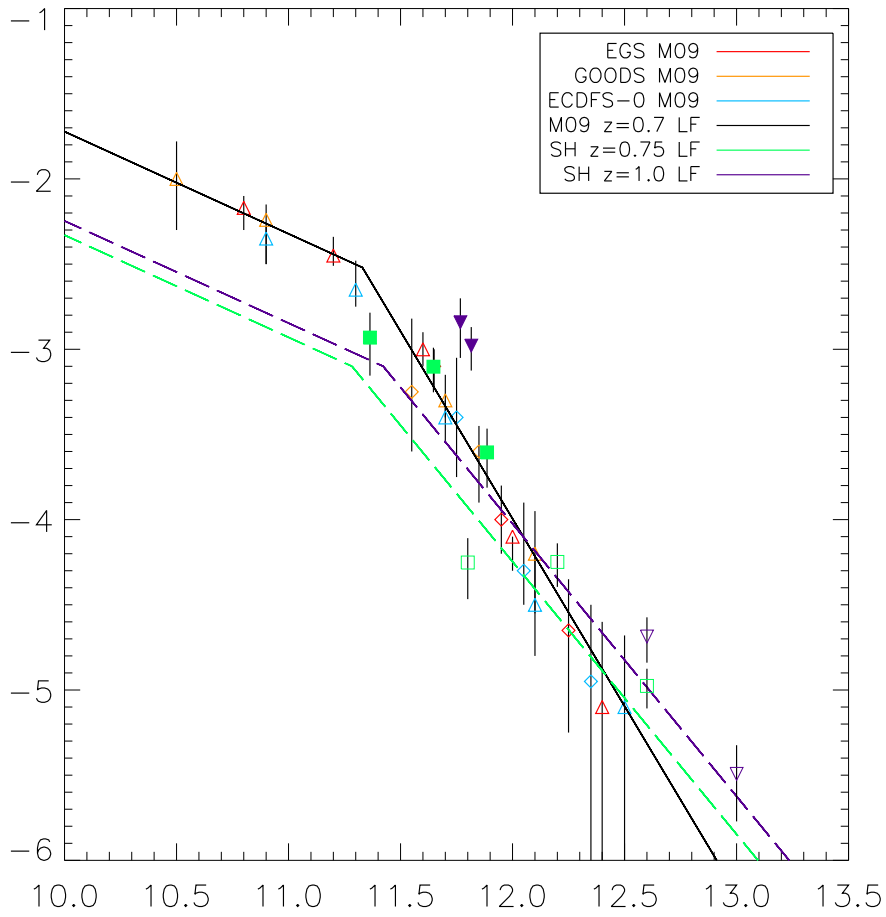

Figure 5.15: Plot showing both the $z \sim 0.7$ luminosity function of Magnelli et al. (2009) in the solid black line and my determinations of the $z \sim 0.75$ luminosity function in the green dashed line and my $z \sim 1.0$ luminosity function in the purple dashed line. The data points used by Magnelli in the luminosity function fit came from the EGS, GOODS and ECDFS-0 fields and are denoted by diamonds in red, orange and blue respectively. The results from the stacking of those fields are shown in the same colours but marked with an upward pointing triangle. My $z \sim 0.75$ and $z \sim 1.0$, $1/V_{\rm max}$ points are denoted by open green squares and open downward pointing purple triangles respectively. The Huynh data points for the same redshift epoch are marked in the same way but with filled symbols.

the Siebenmorgen & Krügel (2007) templates (see Section 5.1). Although the bright end slope changes significantly with the choice of template set, the parameters governing the evolution are consistent, within the uncertainties, regardless of template suite choice.

The Huynh et al. (2007) data points, although included in the fits, appear to disagree with the fitted luminosity function in the highest redshift bin. This may be in part due to the use of upper limits in the bins and the small number of objects used to define each bin. Another contribution to this discrepancy may arise from their use of just the best fit photometric redshifts, thereby not taking the full probability distribution function in to account. The accuracy of photometric redshifts generally decline with increasing redshift due to the increase in the photometric uncertainties for fainter galaxies. This would result in larger errors on the photometric redshifts in the highest redshift bins where the disagreement between the Huynh et al. (2007) data points and the luminosity function derived here is the most pronounced.

5.3.2 The Evolution of the Far-Infrared Luminosity Function

The solution with the lowest reduced χ^2 value is the pure luminosity evolution scenario (i.e. $q = 0$) where $p = 2.4^{+0.6}_{-0.7}$. This result is consistent with the evolution found by Huynh et al. (2007), where a value of $p = 2.8 \pm 0.3$ was found for the luminosity evolution. My result also agrees with the value of $p = 2.6 \pm 1.1$ from Pérez-González et al. (2005), derived using a 24μm selected sample from $z = 0$ to $z \sim 3$. Goto et al. (2010) measured the

8μm, 12μm and the total infrared luminosity function using *AKARI* between $0.15 < z < 2.2$. They found strong positive evolution in the populations towards higher redshift. Their value for the luminosity evolution is larger than the one found in this work ($p = 4.1 \pm 0.4$) for the total infrared luminosity function. Higher values for pure luminosity evolution of $p = 3.6 \pm 0.4$ and $p = 4.1^{+0.3}_{-0.2}$ out to $z \sim 1.3$ were found by Magnelli et al. (2009) and Gruppioni et al. (2010) respectively. However these all lie within $2 - 3\sigma$ of the best fit model, although for those studies with a fixed bright-end slope, we would expect a slightly higher degree of evolution compared to the fitted form. This greater evolution allows the bright-end slope to take on a shallower form and is therefore degenerate with the evolution term when the data only populate a small baseline in luminosity at any given redshift. It should be noted that the case of pure luminosity evolution proved only a marginally better fit than that of pure density evolution (i.e. $p = 0$) which yielded a value of $q = 3.8^{+1.0}_{-1.4}$.

The case of luminosity dependent density evolution yielded values of $p = 1.7^{+1.3}_{-1.7}$ and $q = 0.8^{+3.1}_{-0.8}$ for the luminosity and density terms respectively. These findings agree, within the uncertainties, with the evolution found by Le Floc'h et al. (2005) where $p = 3.2^{+0.7}_{-0.2}$ and $q = 0.7^{+0.2}_{-0.6}$. Pérez-González et al. (2005) find the best fit to their data to be from LDDE with values of $p = 3.0 \pm 0.3$ and $q = 1.0 \pm 0.3$. Rodighiero et al. (2010) from a sample of 24μm selected galaxies found evolution of $p = 2.7$ and $q = 1.1$ out to $z \sim 1$ and little or no evolution beyond this to $z \sim 2$ consistent with Magnelli et al. (2011) and Gruppioni et al. (2010). These also agree well with the findings of this work, where luminosity evolution appears to be the dominant mode.

The case of luminosity dependent density evolution provided the lowest χ^2 value, as would be expected due to the extra free parameter. However it allows for both pure luminosity and pure density evolution within the 1σ error, highlighting the degeneracy between these two parameters. The case of LDDE however, it is not statistically justified as the best case scenario, this is evidenced by an examination of the reduced chi squared statistic for all cases. Both PLE and PDE have lower values for the reduced chi squared owing to the similar fits found by both cases (reduced $\chi^2 \sim 3.6$) with one less free parameter. The case of PLE results in the lowest reduced χ^2 value, however there is little difference in this value for PLE and PDE, making it difficult to discern the specific type of evolution. Nevertheless it is clear that there is strong positive evolution in the 70μm population out to $z \sim 1$.

Due to the large reduced χ^2 values for all three cases $\chi^2 \sim 3.6$ it can be assumed that the errors on the $1/V_{\rm max}$ data points are underestimates of the true values. Based on this, the error bars of the points were scaled to result in a reduced $\chi^2 \lesssim 1$, which would indicate a good fit to the data. Re-determining the fits to the luminosity function does not effect the best fit value of each parameter, however it does effect the uncertainties on each parameter. The results of this re-scaling of the $1/V_{\rm max}$ uncertainties on the parameters governing the luminosity function are shown in Table 5.4.

5.4 Infrared Energy Density Evolution

Using the derived luminosity functions found in this work and following Le Floc'h et al. (2005) the values for the total infrared energy density were

Table 5.4: The best fit parameters to $1/V_{\rm max}$ for pure luminosity, pure density and luminosity dependent density evolution for the double power law parameterisation with uncertainties re-scaled to result in a reduced $\chi^2 \lesssim 1$. The quoted uncertainties represent 1 σ error values based on the resultant χ^2.

Type of Evolution	α_1 (L<L*)	α_2 (L>L*)	$\log_{10}$L$^*(L_\odot)$	$\log_{10}\phi^*$	p	q	χ^2
Pure Luminosity	$-0.6^{+0.5}_{-0.3}$	$-1.6^{+0.4}_{-0.3}$	$10.7^{+0.2}_{0.5}$	$-3.1^{+0.5}_{-0.3}$	$2.4^{+1.4}_{-1.7}$	0.0	19.87
Pure Density	$-0.7^{+0.6}_{-0.2}$	$-1.6^{+0.4}_{-0.3}$	$10.9^{+0.0}_{-0.6}$	$-3.4^{+0.7}_{-0.2}$	0.0	$3.8^{+1.1}_{-2.9}$	19.90
Luminosity dependent Density dependent Density	$-0.6^{+0.5}_{-0.3}$	$-1.6\pm^{+0.4}_{-0.3}$	$10.7^{+0.2}_{-0.5}$	$-3.1^{+0.5}_{-0.6}$	$1.6^{+2.7}_{-1.6}$	$1.3^{+3.6}_{-1.3}$	78.00

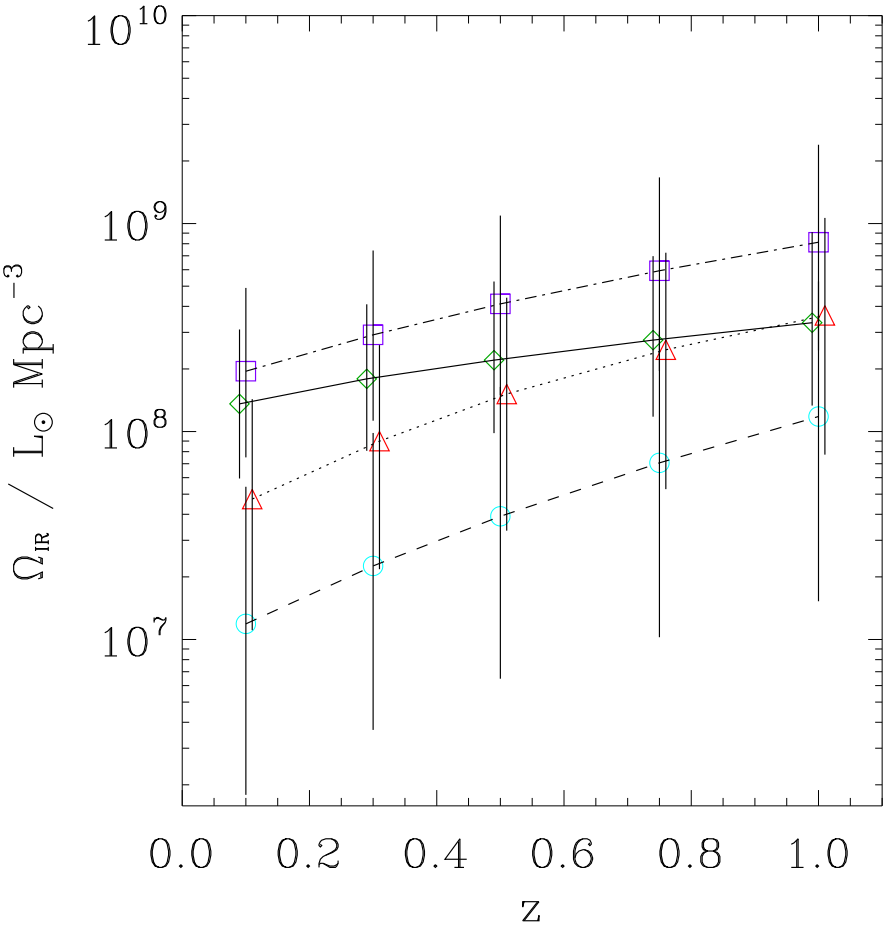

Figure 5.16: The infrared energy density for the case of pure luminosity evolution derived by integrating under the curves of the luminosity functions at the five redshift epochs. The green diamonds and the solid line mark the contribution from the the star forming galaxies (10^8 <$L/L_\odot$ < 10^{11}). The red triangles and the dotted line show the contribution from LIRGs (10^{11} <$L/L_\odot$ < 10^{12}), the blue circles and the dashed line show the contribution from the ULIRGs (10^{12} <$L/L_\odot$ < 10^{12}) and the purple squares and the dot-dashed line mark the total infrared energy density from the star forming galaxies, LIRGs and ULIRGs.

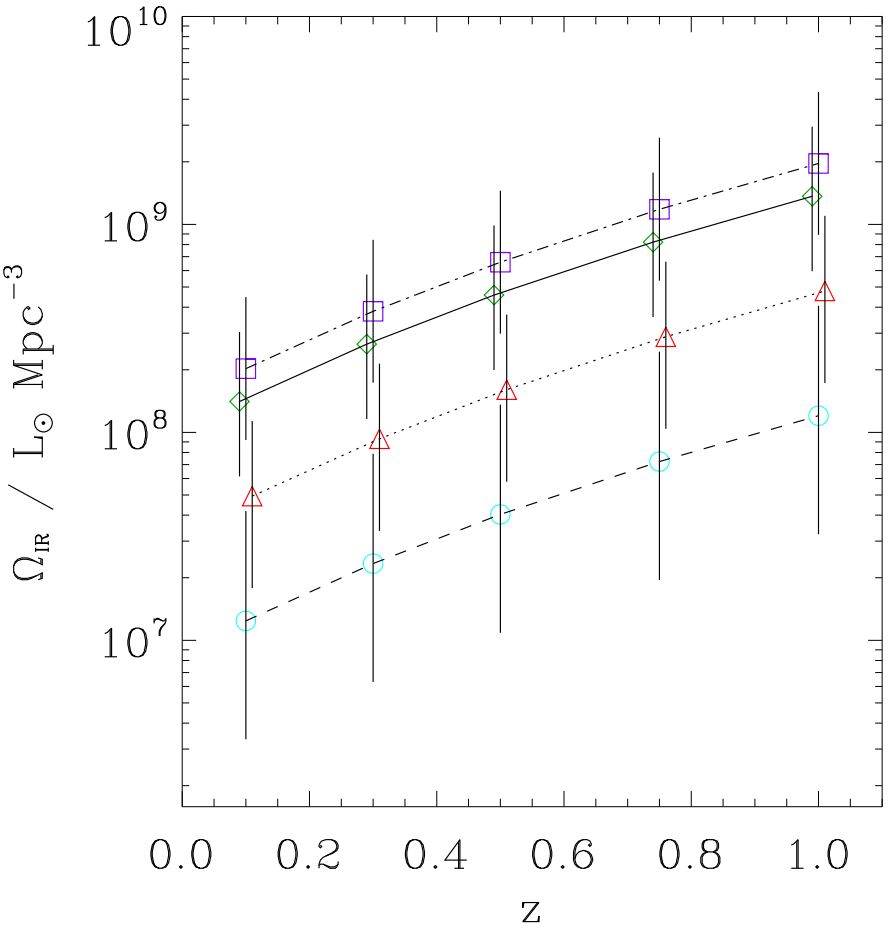

Figure 5.17: The symbols are the same as described in figure 5.16 but for the case of pure density evolution.

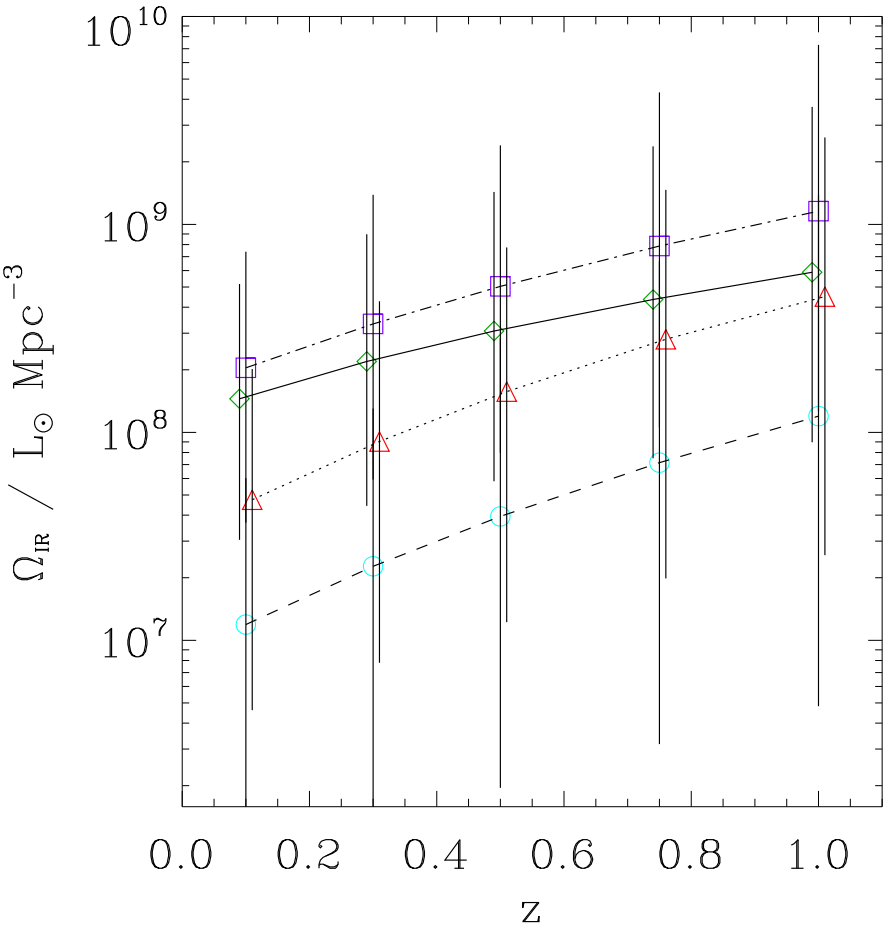

Figure 5.18: The symbols are the same as described in figure 5.16 but for the case of luminosity dependent density evolution.

determined from $0 < z < 1$, by integrating under the luminosity function. See Figures 5.16, 5.17 and 5.18 for the infrared energy densities for the cases of PLE, PDE and LDDE respectively. By modelling the entire luminosity function as a function of redshift, different populations constrain the luminosity function at different redshifts. The faint end slope and break of the luminosity function are constrained by the fainter galaxies, predominantly lying at $z < 0.5$. Assuming no change in the slope of the luminosity function with redshift, we extend the luminosity function fitting out to $z \sim 1$, allowing an examination of the evolution of the luminosity function. However we note that without constraints on the knee of the luminosity function out to high redshift, the cases of PLE, PDE and LDDE become degenerate. We also note that at high redshift ($z \sim 1$) we only directly constrain the ULIRG population.

In all cases, the most significant contribution to the infrared energy density in the lowest redshift bin ($z < 0.2$) is from the star-forming galaxies ($\mathrm{L/L_\odot} < 10^{11}$), agreeing well with the study of Le Floc'h et al. (2005), who used a sample of 24μm selected galaxies. The measurement of the total infrared energy density at $z < 0.2$ of $\Omega_{\mathrm{IR}} = 2.37^{+3.63}_{-1.41} \times 10^8 L_\odot\,\mathrm{Mpc}^{-3}$ is in good agreement with the study of Vaccari et al. (2010) who measured $\Omega_{\mathrm{IR}} = 1.31^{+0.24}_{-0.21} \times 10^8 L_\odot\,\mathrm{Mpc}^{-3}$ based on slightly longer wavelength observations (250μm) from *Herschel*. In the cases of PLE and LDDE, the contribution from the LIRGs ($10^{11} < \mathrm{L/L_\odot} < 10^{12}$) increases with redshift, and may be the more dominant population at $z > 1$ as found by Le Floc'h et al. (2005) and Magnelli et al. (2009). The contribution from the ULIRGs ($10^{12} < \mathrm{L/L_\odot} < 10^{13}$) is lower than that of the star-forming galaxies and

the LIRGs in the lowest redshift bins, but appears to increase strongly with redshift, in much the same way as the LIRGS. Other work (e.g. Caputi et al. 2007; Rodighiero et al. 2010) has shown the ULIRG population evolves faster than the LIRGs, however this evolution is not particularly apparent in Figure 5.16. This is due to the break in the luminosity function just beginning to effect the LIRG population at the highest redshift considered here (see Figure 5.9). A stronger evolution in the ULIRG population with respect to the LIRG population would likely become more evident towards higher redshift.

However, for the case of PDE, strong positive evolution results in an increase in the density in a comoving volume with redshift, and therefore no evolution in the population of sources defined by their luminosity will be evident. The contribution to the infrared energy density increases from all sources as a result of the increasing density.

Under the preferred scenario of this work (PLE), over the interval $0 < z < 1$, the contribution to the infrared energy density ($\Omega_{\rm IR}$) from LIRGs and ULIRGs increases by a factor of $7.4^{+19.2}_{-7.8}$ and $8.6^{+26.9}_{-10.8}$ respectively.

5.5 Conclusion

We have selected a sample of 736 galaxies detected ($> 5\sigma$) at 70μm from $\sim$ 1.7 square degrees within the COSMOS field where there is multiwavelength data available. This work was carried out with the aim of providing better constraints on the evolution of the far-infrared luminosity function. We have obtained spectroscopic redshifts of 42 of these sources using

AAOmega on the *AAT* and supplemented these redshifts with 170 and 114 redshifts from the zCOSMOS and Kartaltepe et al. (2010) catalogues respectively. Where no spectroscopic redshift was available we have used photometric redshifts from the COSMOS catalogue and accounted for the errors by sampling their full probability distributions using Monte Carlo simulations. We have calculated values of total infrared luminosity (L_{IR}) for each of our galaxies and used this in conjunction with their best fit SEDs from the Siebenmorgen & Krügel (2007) and the Chary & Elbaz (2001) libraries to calculate $1/V_{max}$ in luminosity bins of $\Delta L = 10^{0.4} L_{\odot}$ from $10^{7} L_{\odot}$ to $10^{13} L_{\odot}$, and redshift slices of $0 < z \leq 0.2$, $0.2 < z \leq 0.4$, $0.4 < z \leq 0.6$, $0.6 < z \leq 0.9$ and $0.9 < z \leq 1.1$. We have supplemented our $1/V_{max}$ values with those of Huynh et al. (2007) after correcting for their choice of models in the L_{IR} determination. We have found evidence for strong positive evolution where the best fit scenario is the case of pure luminosity evolution with $p = 2.4^{+0.6}_{-0.7}$. Our findings for the luminosity function and the infrared energy density agree with other values from the literature (e.g. Le Floc'h et al. 2005). The shallower value of the bright end slope derived here ($\alpha_2 = -1.6$) using the Siebenmorgen & Krügel (2007) templates, as compared with the previous measurement from Sanders et al. (2003: $\alpha_2 = -2.2$), implies a higher number density of the most luminous objects, however the bright end slope is found to be dependent on the choice of model suite. Other studies using this steeper slope may have underestimated the contribution from ULIRGs to the total infrared energy density.

In all cases the infrared energy density is dominated by L^* galaxies, which is similar to the break in the double power law luminosity function. In the

case of PLE, at $z \sim 1$, the L* population is dominated by LIRGs. ULIRGS have been found to increase their contribution to the infrared energy density with redshift (Magnelli et al. 2011; Gruppioni et al. 2010; Rodighiero et al. 2010) and even potentially dominate at $z \sim 2$ (Caputi et al. 2007). From $z \sim 1$ to $z \sim 0$, the value of L* shifts to lower values. This is consistent with downsizing (Cowie et al. 1996), where the LIRGS (and ULIRGS) form the bulk of their stars at a high star-formation rate at an earlier time than the less luminous star-forming galaxies, which form the bulk of their stars at a slower rate at lower redshift. This would ensure that the most massive, systems that formed their stars in a short intense period of star formation, would dominate the source population at high redshift, whilst resulting in a decrease in the characteristic luminosity to lower redshift.

Using the present MIPS-70μm observations of the COSMOS field, it is difficult to determine whether galaxies are intrinsically less numerous (PDE) at lower redshift, or whether their luminosity has evolved (PLE) to be below the flux density cut of the survey.Deeper observations such as The H-ATLAS and HerMES surveys being conducted with the *Herschel Space Observatory* will be able to better constrain the evolution of these IR luminous galaxies. The dramatically larger area covered by H-ATLAS (550 sq. deg) should constrain the evolution of galaxies spanning the break of the luminosity function out to $z = 1$, enabling us to discriminate between PLE or PDE models, or possibly showing that LDDE may be the preferred form of any evolution with redshift. The narrower (70 sq. deg) but greater depth probed by HerMES will allow measurements of the luminosity function out to $z = 2$, providing the necessary data to determine which sources dominate the overall FIR

energy density out to the highest redshifts.

Chapter 6

The Far-Infrared–Radio Correlation

The far-infrared–radio correlation (FIRC) is thought to arise due to the common link powering both types of emission, namely star formation. The far-infrared emission is produced by dust reprocessing the UV and optical light from massive stars and the radio emission arises from the supernovae produced by the same short-lived massive stars accelerating electrons to relativistic velocities causing synchrotron radiation. The FIRC has shown remarkable uniformity over a wide range of galaxy luminosities (Yun, Reddy & Condon 2001) and a range of redshifts (e.g. Jarvis et al. 2010; Michalowski et al. 2010; Sargent et al. 2010). Here, the FIRC is examined for the sample of 736 70μm-selected star-forming galaxies over the COSMOS field that has been discussed in Chapters 4 & 5.

6.1 Radio Flux Densities

As described in Section 5.1, estimates of the total infrared luminosity have been derived for all 736 galaxies in the sample, based on SED fitting of templates from the Siebenmorgen & Krügel library (2007). Due to the multi-wavelength coverage over the COSMOS field, there are also 1.4GHz VLA data available from the joint catalogue (Schinnerer et al. 2010). The radio joint catalogue combines both the deep and the large area data over the COSMOS field. The catalogue was created by searching for 4σ sources where $1\sigma = 12\mu$Jy beam^{-1}, however only 5σ sources were retained in the catalogue.

Matches to this catalogue were searched for within $2''$ of the matched ACS position due to the $2.5''$ resolution of the radio data. 442 matches (~ 60 per cent) were found within the $2''$ matching radius. The number of matches did not increase significantly for larger matching radii. The COSMOS VLA data covered the entirety of the 1.7 square degree region in which the initial selection took place (see Section 4.3), therefore any non-matches are likely due to data artifacts, noise in the image, proximity to a bright source or simply falling below the 5σ flux density cut of the catalogue. For the 294 sources not found in the joint catalogue, flux densities at 1.4 GHz were measured by taking the flux density in the pixel at the location of its right ascension and declination. This was then compared to a local background measurement, which was determined, as recommended by Schinnerer et al. (2010), in boxes of $17.5'' \times 17.5''$ around the source position. Any pixels with values greater than 3σ were eliminated from the background box in order to reduce the contribution of real sources to the local background measurement. The stan-

dard deviation within the box was measured. Mean values for the background were approximately $\sim 20\mu$Jy beam^{-1}, comparable to, but higher than the $1\sigma = 12\mu$Jy beam^{-1} found in the deep region. However this is to be expected, as the nature of the non-matches to the catalogue would imply, on average, that the sources fall in noisier regions of the image. All sources with 1.4 GHz flux densities greater than the 2σ local background level were added to the catalogue of detections. This resulted in a further 192 sources (26 per cent) being added to the catalogue providing a total of 634 radio detections ($\sim$ 86 per cent). The errors on the detections were taken as the 1σ background fluctuations. 2σ upper limits for the remaining 102 non-detections ($\sim$ 14 per cent) were measured and retained for the investigation of the FIRC.

All of the 736 sources had photometric redshifts from the ACS COSMOS catalogue and a subset of 348 (47 per cent) had spectroscopic measurements from AAT spectroscopy, the zCOSMOS catalogue or the Kartaltepe et al. (2010) catalogue (see Section 4.4 for full details). Spectroscopic redshifts were used where available, and photometric redshifts were used for the remainder of the sample. Figure 6.1 shows the total infrared luminosity versus the rest-frame 1.4GHz luminosity, with the 2σ upper limits over-plotted in green.

6.2 The Total Far-Infrared–Radio Correlation, $q_{\rm IR}$

The FIRC is defined by the following expression:

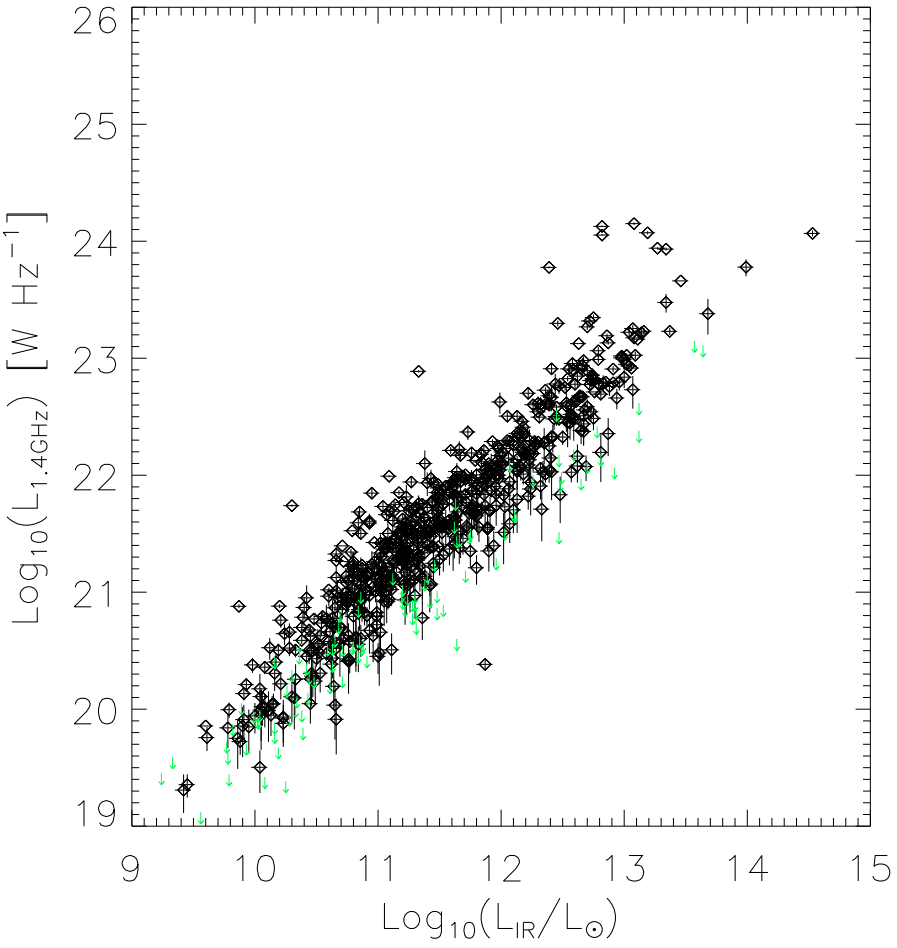

Figure 6.1: Total far-infrared luminosity versus 1.4 GHz luminosity. The black diamonds represent the detections. The green down arrows mark the 2σ upper limits for the radio non-detections. L_{IR} values were determined using the Siebenmorgen & Krügel models.

$$q_{\rm IR} = \log_{10}\left[\frac{S_{\rm IR}/3.75\times10^{12}}{S_{\rm 1.4GHz}}\right], \tag{6.1}$$

where, $S_{\rm IR}$ is the total integrated infrared flux ($\rm Wm^{-2}$) between $8-1000\mu$m in the rest-frame. $S_{\rm IR}$ errors of 15 per cent were assumed based on the range of far-infrared luminosities measured using the 10 best fit Siebenmorgen & Krügel templates to the 8, 24, 70 and 160μm flux densities (See Section 5.1). The factor of 3.75×10^{12} Hz is the normalising frequency (Helou et al. 1985) and $S_{\rm 1.4GHz}$ is the k-corrected 1.4 GHz flux density in units of $\rm Wm^{-2}Hz^{-1}$. The radio fluxes were k-corrected assuming a power law of $S_\nu \propto \nu^{-\alpha}$, where α is the radio spectral index and is assumed to be equal to 0.8.

Using the above relation (see Equation 6.1), the $q_{\rm IR}$ for all sources were determined and are shown in Figure 6.2. The mean of the distribution is 2.82 ± 0.01 and the median is 2.82 ± 0.01. The values found here, are on average higher than those found in other studies e.g. Yun, Reddy & Condon (2001) who found $q_{\rm IR} = 2.65 \pm 0.02$ when corrected for the conversion from $\rm L_{FIR}$ to $\rm L_{TIR}$ defined as the total luminosity between 8 and 1000μm (Sergeant et al. 2010) for a sample of 60μm selected local galaxies. Jarvis et al. (2010) find a mean value of $q_{\rm IR} = 2.52\pm0.03$ for a sample of 250μm selected galaxies, while Bourne et al. (2011) find a slightly larger value of $q_{\rm IR} = 2.65 \pm 0.12$ for their near infrared (2μm selected) sample. Sargent et al. (2010) who studied a sample of infrared and radio selected samples over the COSMOS field found $q_{\rm IR} \sim 2.5 - 2.7$.

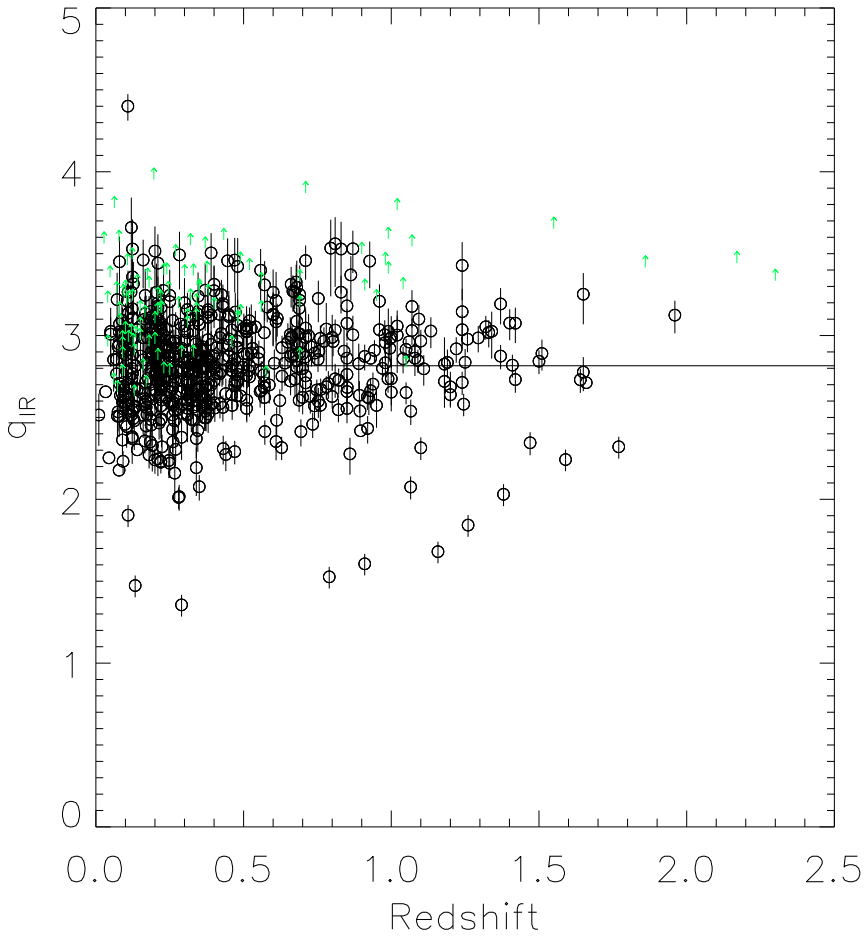

Figure 6.2: Redshift versus $q_{\rm IR}$, where $q_{\rm IR}$ was calculated using the Siebenmogen & Krügel models to determine $L_{\rm IR}$. The black circles represent the detections. The green up arrows mark the 2σ lower limits for the radio non-detections. The horizontal line shows the mean of the distribution (not including limits).

6.3 Evolution with Redshift

If the FIRC evolves with redshift, it could have implications for using either far-infrared or radio emission as a star formation rate indicator towards high redshift. While a number of authors have found no evidence for evolution (e.g. Jarvis et al. 2010; Sargent et al. 2010), there has been some evidence for evolution with redshift. Ivison et al. (2010a), from a sample of 250μm and radio selected galaxies found evidence for evolution in $q_{\rm IR}$ with redshift $\propto (1+z)^{-0.15\pm0.03}$, (i.e. decreasing towards higher redshift). They attribute this evidence for evolution to the possibility that they are seeing a rise in radio emission in normal star-forming galaxies.

The data points in this work were binned in order to more clearly see a correlation, if present (see Figure 6.3). The data were separated in to 4 redshift bins of $0 < z \leq 0.25$, $0.25 < z \leq 0.5$, $0.5 < z \leq 1.0$ and $1.0 < z \leq 2.0$. The bins were selected in order to include a significant number of sources in each bin, therefore the bins get progressively larger with redshift with, 213, 212, 153 and 54 sources contributing to the first, second, third and fourth bins respectively. The weighted mean was computed for each bin and the errors are represented by $\sigma/\sqrt{(N)}$ where N is the number of objects per bin. The mean value of $q_{\rm IR}$ is over-plotted in Figure 6.2 for comparison. No correlation with redshift is apparent. In order to determine if there is any evolution with redshift in the sample under investigation here, the `coxhazard` statistic in IRAF was used. The `coxhazard` statistic computes the probability that there is no correlation, in the presence of a single type of limit (in this case, lower limits). The result of the `coxhazard` statistic

indicates that the null hypothesis (i.e. that there is no correlation) can not be ruled out at the 78 per cent level (1σ lower limits on $q_{\rm IR}$ were used for the `coxhazard` test).

6.4 The Monochromatic Far-Infrared–Radio Correlation, q_{70}

q_{70} is the monochromatic comparison of the k-corrected 70μm and 1.4 GHz flux densities. Some authors have found evidence of evolution in the FIRC when examining this parameter (e.g. Seymour et al. 2009; Bourne et al. 2011). I calculate q_{70} for the entire sample. The rest-frame 70μm flux density should be better constrained than the total infrared flux density as, out to $z \sim 2$ it only requires the SED to be well constrained short-ward of the 70μm data point, for which the 24, 70 and 160μm data points are available. Therefore q_{70} does not suffer from significant extrapolations of the spectral energy distribution where the peak is uncertain, which may have a greater effect on $q_{\rm IR}$. Due the fact that q_{70} is a comparison of the monochromatic 70μm and 1.4GHz flux densities, no normalising frequency is required and the relation is given by the following equation;

$$q_{70} = \log_{10}\left[\frac{S_{70}}{S_{1.4\rm GHz}}\right]. \tag{6.2}$$

The rest-frame 70μm flux densities were calculated, using the best fit template from the Siebenmorgen & Krügel library and the spectroscopic redshift (or peak photometric redshift if spectroscopic was unavailable). The

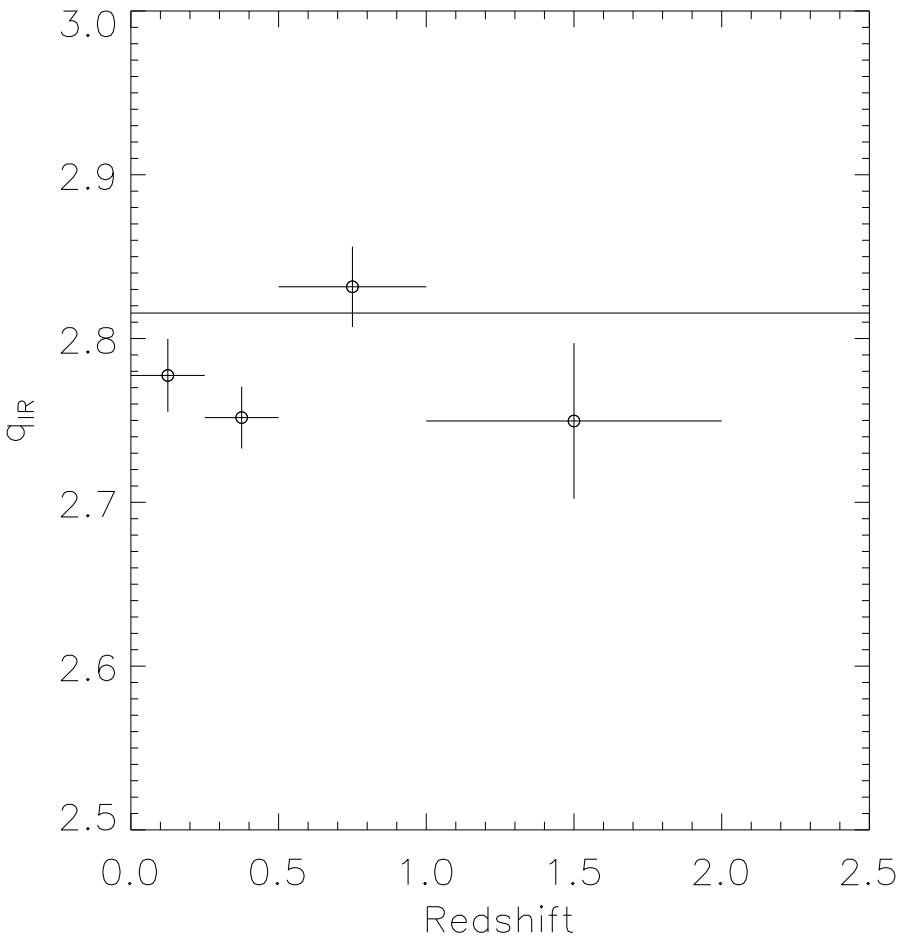

Figure 6.3: Redshift versus the weighted mean of $q_{\rm IR}$. The data points represent the weighted mean of $q_{\rm IR}$ for each of the four redshift bins $0 < z \leq 0.25$, $0.25 < z \leq 0.5$, $0.5 < z \leq 1.0$ and $1.0 < z \leq 2.0$. The mean value for $q_{\rm IR}$ is over plotted for comparison as the horizontal line. Total infrared luminosities ($L_{\rm IR}$) were determined using the Siebenmorgen & Krügel models.

q_{70} distribution with redshift is shown in Figure 6.4 with the mean over plotted as the horizontal line. The mean of the q_{70} distribution is 2.56 ± 0.02 and the median is 2.58 ± 0.03.

The q_{70} distribution was also examined to determine if there was any change in the correlation with redshift. Figure 6.5 shows the weighted mean points for the q_{70} distribution determined in the same manner described in Section 6.4. The error on the rest-frame 70μm flux density was assumed to be comparable to the observed 70μm flux density error. Once again, there appears to be no significant correlation with redshift and this assertion is strengthened by the `coxhazard` statistic returning a probability of ~ 12 per cent that the null hypothesis can not be rejected.

Appleton et al. (2004) examined a sample of 24 and 70μm selected galaxies and found no evolution in the q_{70} parameter out to $z \sim 1$ with a mean value of $q_{70} = 2.15 \pm 0.16$. My value is larger again than that found by Appleton et al. (2004). Seymour et al. (2009) examined q_{70} for a sample of radio selected galaxies and found a decrease in q_{70} towards higher redshift ($z \sim 1$). They attribute this evolution as evidence for a change in the spectral energy distribution for ULIRGs between $0 < z < 1$. Bourne et al. (2011) also found evidence for evolution in the q_{70} parameter for a near-infrared selected sample. They found a decrease with redshift from $q_{70} \approx 2.2 - 2.4$ at $z \sim 0.2$ to $q_{70} \approx 1.5 - 1.9$ at $z \sim 1.6$ depending on the spectral energy distribution template used. However the authors found no evidence for a similar evolution in $q_{\rm IR}$ or in q_{24} or q_{160} and so (in agreement with Seymour et al. 2009) attribute this decline in q_{70} to a change in the spectral energy distribution with redshift.

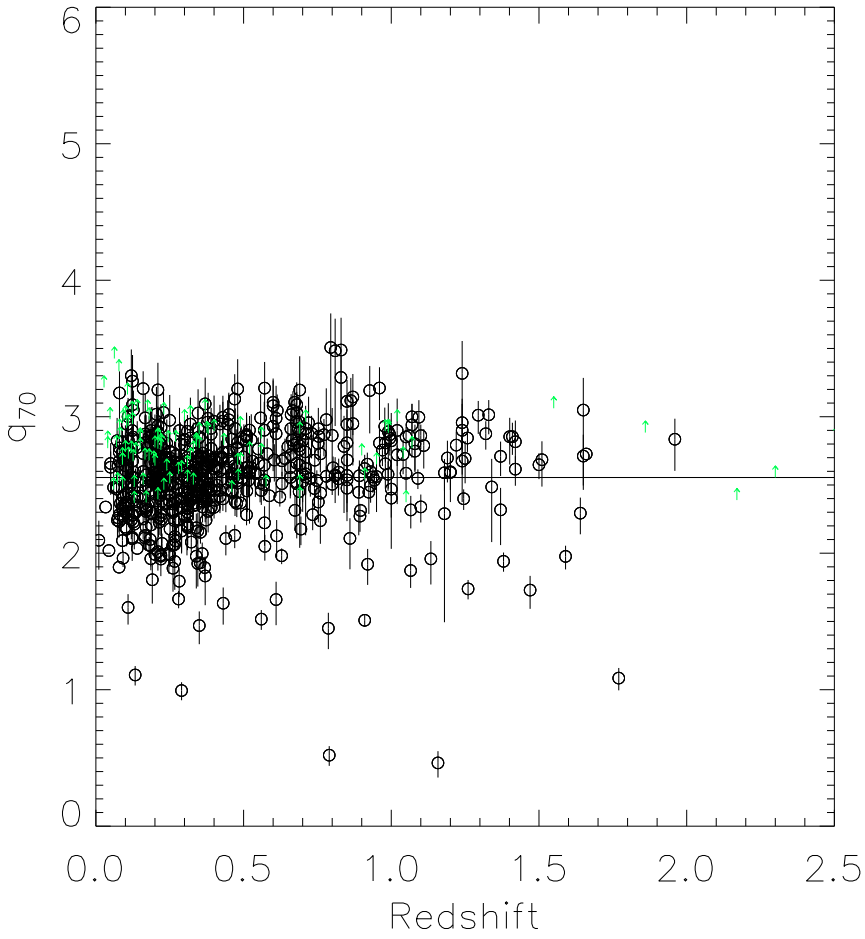

Figure 6.4: Redshift versus q_{70}, where q_{70} was calculated using the Siebenmogen & Krügel models to determine $L_{\rm IR}$. The black circles represent the detections. The green up arrows mark the 2σ lower limits for the radio non-detections. The horizontal line shows the mean value for the sample.

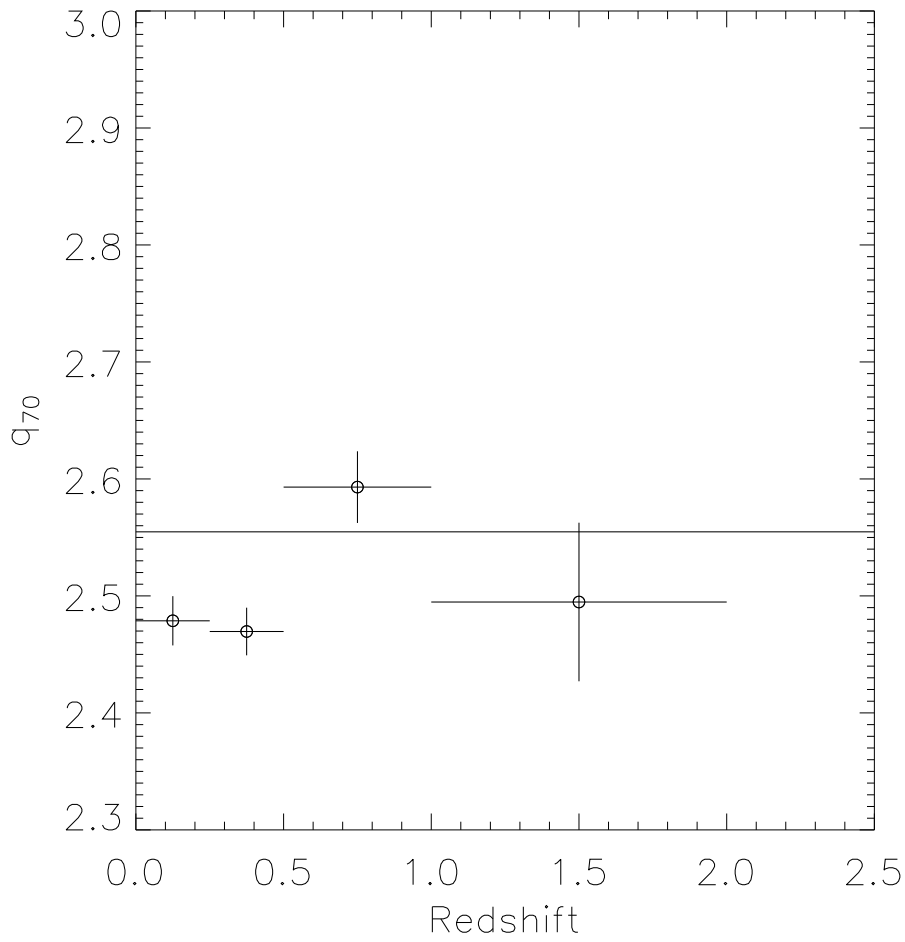

Figure 6.5: Redshift versus the weighted mean of q_{70}. The data points represent the weighted mean of q_{70} for each of the four redshift bins $0 < z \leq 0.25$, $0.25 < z \leq 0.5$, $0.5 < z \leq 1.0$ and $1.0 < z \leq 2.0$. The mean value for q_{70} is over plotted for comparison as the horizontal line. The Siebenmorgen & Krügel models were used to determine q_{70}.

6.5 Comparison with Chary and Elbaz (2001) Models

The same calculations for $q_{\rm IR}$ and q_{70} were repeated, using the Chary & Elbaz (2001) models instead of the Siebenmorgen & Krügel (2007) templates, in order to determine if the choice of template set produced differing results. This is to be expected as the values of $\rm L_{IR}$ were systematically lower for the Chary & Elbaz models compared to the Siebenmorgen & Krügel templates (see Section 5.1)

The mean value for $q_{\rm IR}$ determined using the Chary & Elbaz models is found to be 2.65 ± 0.01 (see Figure 6.6) with a median value of 2.66 ± 0.01. These values are indeed slightly lower than those derived using the Siebenmorgen & Krügel templates.It should be noted however, that the lower value of $q_{\rm IR}$ determined using the Chary & Elbaz models agrees well with a number of other findings (e.g. Yun, Reddy & Condon 2001, Sargent et al. 2010 and Bourne et al. 2011) discussed in Section 6.2. This is likely due to the fact that the values of $q_{\rm IR}$ determined by others (e.g. Yun, Reddy & Condon 2001; Sargent et al. 2010; Bourne et al. 2011) were determined using the models of Chary & Elbaz (2001) or other locally defined spectral energy distributions defined in much the same manner.

Again, the FIRC was tested for any evolution using the templates of Chary & Elbaz (2001). No evidence for evolution with redshift is present (see Figure 6.7) based on the `coxhazard` test finding that the null hypothesis can not be rejected at the 47 per cent level indicative of no correlation. This is understandable as the Chary & Elbaz models predict lower total $L_{\rm IR}$

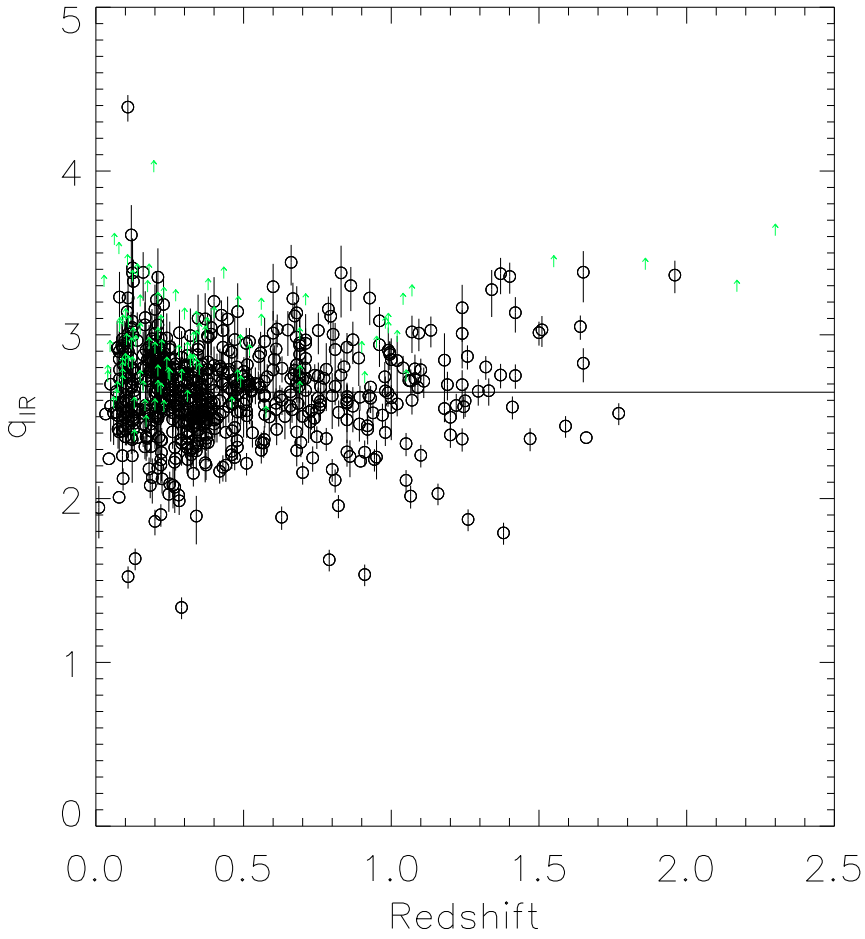

Figure 6.6: Redshift versus $q_{\rm IR}$ calculated using the Chary & Elbaz models to determine $L_{\rm IR}$. The black circles represent the detections. The green up arrows mark the 2σ lower limits for the radio non-detections. The horizontal line shows the mean value.

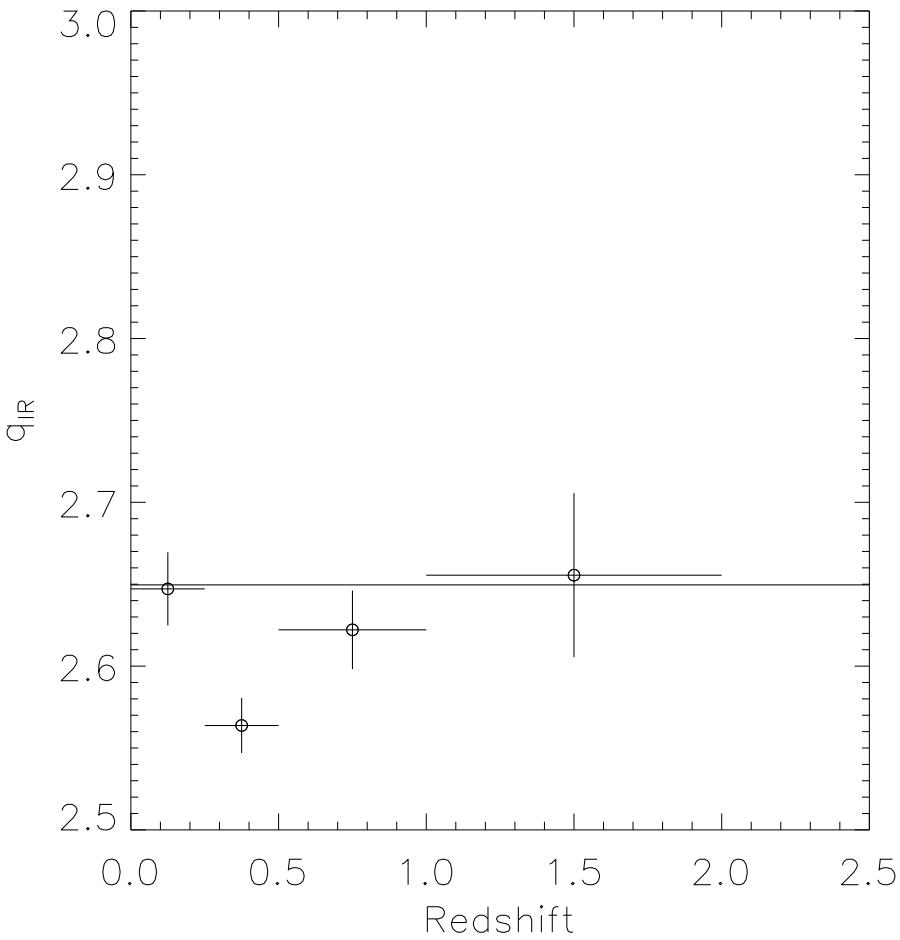

Figure 6.7: Redshift versus the weighted mean of $q_{\rm IR}$. The data points represent the weighted mean of $q_{\rm IR}$ for each of the four redshift bins $0 < z \leq 0.25$, $0.25 < z \leq 0.5$, $0.5 < z \leq 1.0$ and $1.0 < z \leq 2.0$. The mean value for $q_{\rm IR}$ is over-plotted for comparison as the horizontal line. $q_{\rm IR}$ was determined using the Chary & Elbaz models.

uniformly (i.e. without any redshift dependence).

q_{70} is also determined for the Chary & Elbaz models and the mean is found to be 2.45 ± 0.01 (See Figure 6.8) with a median of 2.47 ± 0.01. Once again these values are lower than those found using the Siebenmorgen & Krügel models. However Figure 6.9 shows an increasing value of q_{70} with redshift. This is verified by the `coxhazard` test finding that the null hypothesis can not be rejected at the 0.27 per cent level. This indicates a positive correlation of ~ 0.2 dex at a 3σ level of significance over the redshift range $0 < z \leq 2$.

The fact that the $q_{\rm IR}$ distributions for both the Siebenmorgen & Krügel and the Chary & Elbaz models show no correlation with redshift, but the q_{70} distribution for the Chary & Elbaz models do, suggests a difference in the spectral energy distributions of the two models around the 70μm region. As discussed in Section 6.4, both Seymour et al. (2009) and Bourne et al. (2011) find evolution in q_{70} with redshift and attribute their observed decrease to a change in the spectral energy distributions of ULIRGs with redshift.

Figure 6.10 shows a comparison of the $\rm L_{70\mu m}/L_{IR}$ ratios determined using the Chary & Elbaz (2001) models and the Siebenmorgen & Krügel (2007) templates. The data are divided in to four redshift bins of $0 < z < 0.25$ (blue), $0.25 < z < 0.5$ (pink), $0.5 < z < 1.0$ (green) and $1.0 < z < 2.0$ (purple). Reasonably good agreement between the two ratios is evident, however there is a tendency for larger values from the Chary & Elbaz (2001) models compared to the Siebenmorgen & Krügel (2007) templates with increasing redshift. This would explain the apparent evolution in the $\rm q_{70}$ parameter found when using the Chary & Elbaz (2001) models. Owing to the generally lower values of $\rm L_{IR}$ and thus $\rm q_{IR}$ found using the Chary & Elbaz (2001)

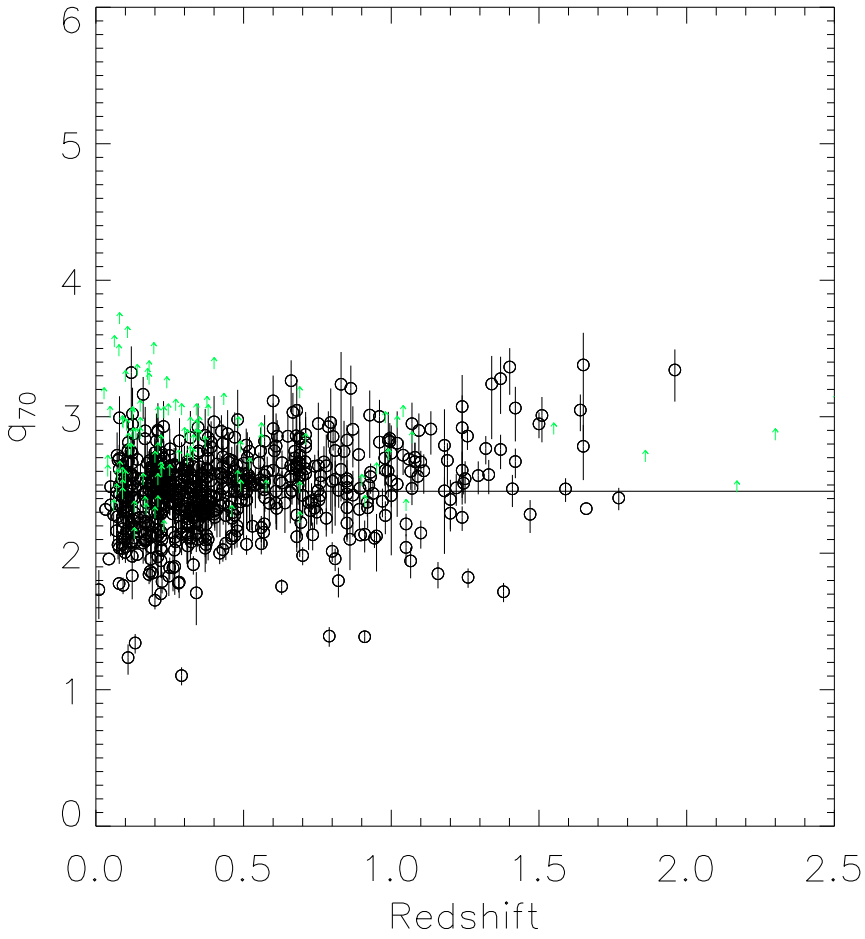

Figure 6.8: Redshift versus q_{70} found using the Chary & Elbaz models. The black circles represent the detections. The green up arrows mark the 2σ lower limits for the radio non-detections. The horizontal line shows the mean value over-plotted for comparison.

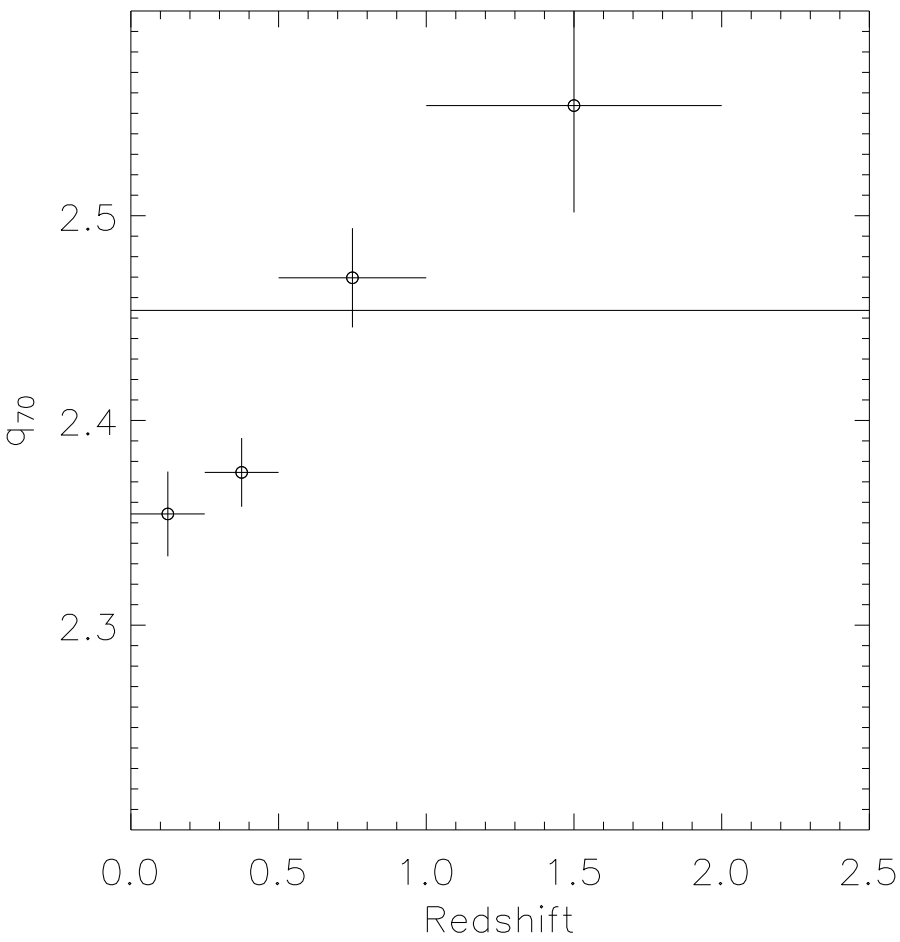

Figure 6.9: Redshift versus the weighted mean of q_{70}. The data points represent the weighted mean of q_{70} for each of the four redshift bins $0 < z \leq 0.25$, $0.25 < z \leq 0.5$, $0.5 < z \leq 1.0$ and $1.0 < z \leq 2.0$. The mean value for q_{70} is over-plotted for comparison shown by the horizontal line. q_{70} was determined using the Chary & Elbaz models.

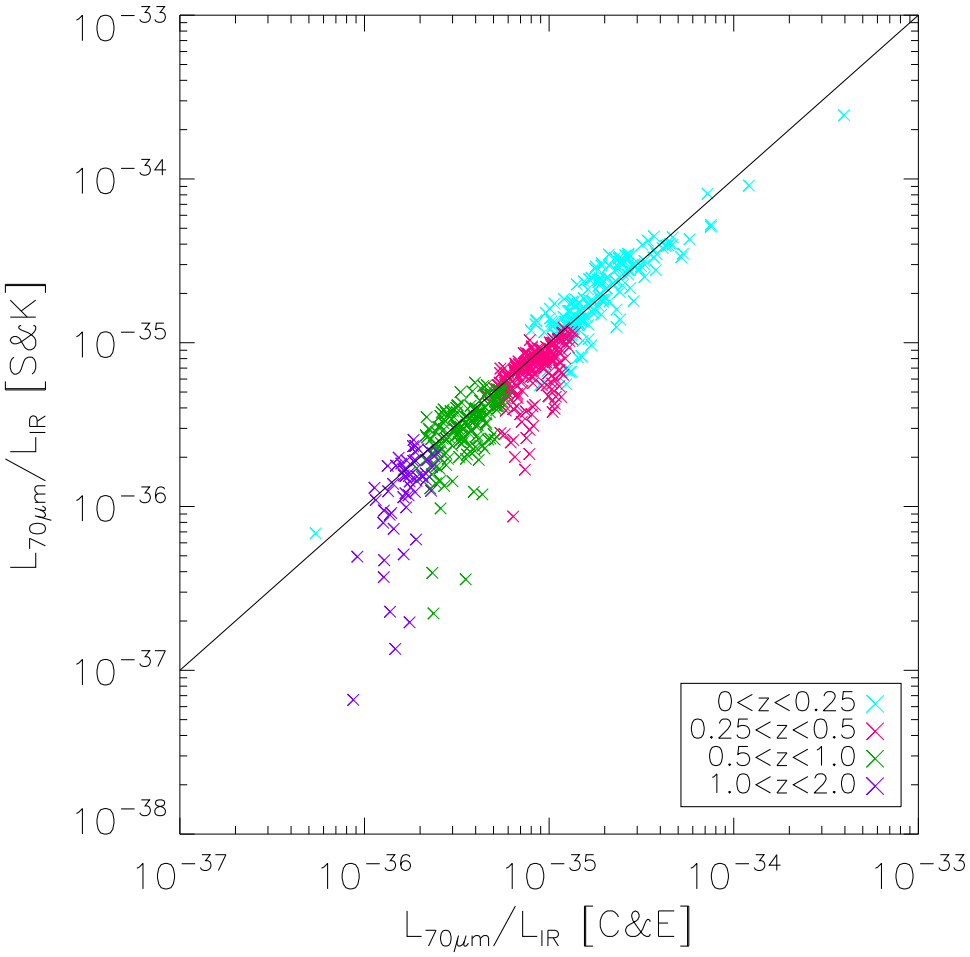

Figure 6.10: Figure showing the $L_{70\mu m}/L_{IR}$ ratio for both the Chary & Elbaz (2001) models and the Siebenmorgen & Krügel (2007) templates. The data are divided in to four redshift bins of $0 < z < 0.25$ (blue), $0.25 < z < 0.5$ (pink), $0.5 < z < 1.0$ (green) and $1.0 < z < 2.0$ (purple). The line of unity is marked in black. The figure shows reasonably good agreement between the two ratios with a tendency for greater $L_{70\mu m}/L_{IR}$ values determined using the Chary & Elbaz (2001) models compared to the Siebenmorgen & Krügel (2007) templates for increasing redshift.

models, one would also expect lower values of q_{70}. This is borne out in the lower redshift bins in Figure 6.9. However the increasing values with redshift in q_{70} but not q_{IR} implies that the Chary & Elbaz (2001) models used in the fits must be different at high redshift.

Sargent et al. (2010) measure q_{IR} over the COSMOS field and calculate total L_{IR} values using the Chary & Elbaz (2001) spectral energy distributions. Their uncorrected data displays positive evolution with redshift of the order of 0.3 dex out to $z \sim 2$. However after correcting for the scatter in the L_{IR} determinations increasing to higher redshift, they are consistent with no evolution. This bias correction can easily account for the $\sim$0.2 dex increase found here, using the same models, although it should be evident in all the determinations of q_{IR} and q_{70}.

A possible reason for the difference in L_{IR} and q_{70} determinations for the Chary & Elbaz (2001) and the Siebenmorgen & Krügel (2007) models may arise from the predisposition to higher temperatures in the Chary & Elbaz (2001) spectral energy distributions. The Chary & Elbaz templates are derived by initially employing the Silva et al. (1998) models to reproduce the spectral energy distributions of 4 typical galaxies, namely Arp220 (ULIRG), NGC6090 (LIRG), M82 (starburst) and M51 ('normal' galaxy).

Arp220 is a bright ULIRG with a hot dust temperature which may be due to a contribution from an AGN and may therefore, not be representative of ULIRGs powered predominantly by star formation with a large cold dust component. Further constraints are placed on the mid-infrared portion of the Chary & Elbaz spectral energy distributions from ISOCAM CVF observations of the 4 prototypical galaxies. However this only places constraints on

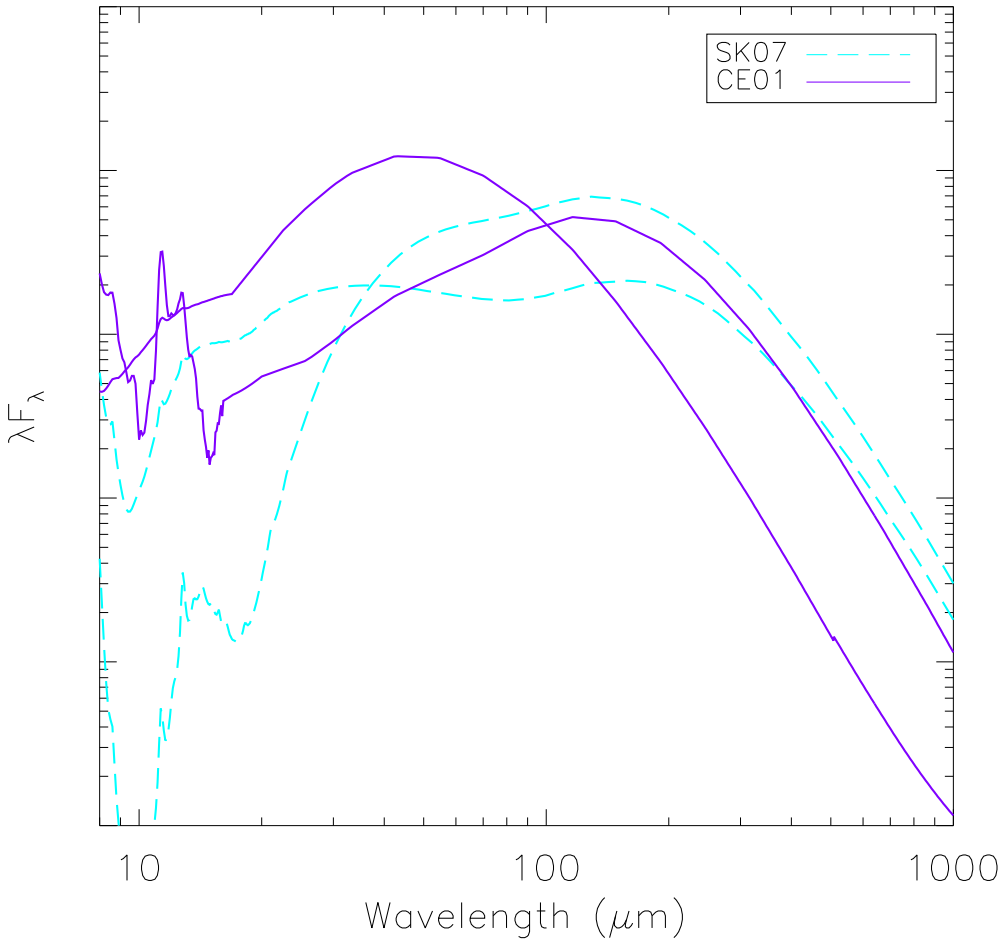

Figure 6.11: Figure showing the models with the shallowest and steepest spectral slopes between 24 and 70μm (rest-frame) from the Siebenmorgen & Krügel (SK07 - blue dashed line) template fits used in the analysis. Also shown are the models with the steepest and shallowest slopes from the 105 Chary & Elbaz (CE01 - purple solid line) library, showing the range of slopes available. The flux is represented with an arbitrary normalisation.

the 3-18μm range of the spectral energy distribution. Templates from Dale et al. (2001) are included to supplement the far-infrared templates, however these templates were derived for 'normal' type galaxies. The Chary & Elbaz templates place strong constraints on the mid-infrared part of the spectral energy distribution which is dominated by warm dust, however they may not provide as effective a fit to the colder dust component dominating in the far-infrared. Figure 5.5 and Chapter 5 demonstrate the Chary & Elbaz templates systematically fail to match the 160μm flux density, thereby finding lower $L_{\rm IR}$ values. However these lower values, are in some cases mitigated by the shallower mid-infrared slope provided by the template (see Figure 5.5 & 6.11) compared to the Siebenmorgen & Krügel models. Figure 6.11 shows the spectral energy distributions that exhibit the steepest and shallowest slopes defined between rest-frame 24 and 70μm achieved by the Siebenmorgen & Krügel templates (blue dashed line) from the fits to the sample of 736 galaxies. Over-plotted (purple solid line) are spectral energy distributions that exhibit the the most extreme slopes (again defined between 24 and 70μm in the rest-frame) from the entire Chary & Elbaz library of models. Figure 6.11 shows that the Siebenmorgen & Krügel templates provide a much wider range of mid-infrared slopes and allows for a noticeably steeper mid-infrared slope. This difference in mid-infrared slope would increase the disparity in k-corrected 70μm flux density towards higher redshift (i.e. the k-corrected 70μm flux density from the Chary & Elbaz models would become comparatively larger than the k-corrected 70μm flux density from the Siebenmorgen & Krügel models). This could result in the observed increase in q_{70} with redshift for the Chary & Elbaz models.

6.6 Conclusions

The FIRC has been examined for a sample of 736 70μm selected galaxies over the COSMOS field (Schinnerer et al. 2010). 1.4 GHz radio flux densities were obtained by matching to the VLA joint catalogue. For sources below 5σ and therefore not included in the 1.4 GHz catalogue, flux densities were measured down to 2σ, and where no detections were found, 2σ upper limits determined from the local background were used. The FIRC determined using the Siebenmorgen & Krügel (2007) models was found to have a mean value of $q_{\rm IR} = 2.82 \pm 0.01$ which is larger than other values found in the literature. However when $q_{\rm IR}$ was determined using the $\rm L_{IR}$ determinations based on the Chary & Elbaz (2001) models a lower value of $q_{\rm IR} = 2.65 \pm 0.01$ was found and this is consistent with the other findings in the literature indicating that the determinations of $q_{\rm IR}$ are dependent on the choice of model suite. No evidence for evolution with redshift was found in $q_{\rm IR}$ using either the Siebenmorgen & Krügel (2007) or Chary & Elbaz (2001) models.

The monochromatic q_{70} correlation was also evaluated and was found to have a mean value of $q_{70} = 2.56 \pm 0.01$ for the Siebenmorgen & Krügel (2007) models. Again, no evidence for evolution in redshift was found for this correlation. A small evolution in q_{70} of 0.2 dex was found when using the Chary & Elbaz (2001) models, however this can be accounted for within the bias determined over the COSMOS field (Sargent et al. 2010). It may also be a result of the Chary & Elbaz (2001) models typically finding higher $\rm L_{70}/L_{IR}$ ratios compared to the Siebenmorgen & Krügel (2007) templates for increasing values of redshift possibly due to the higher temperatures preferred

by these models.

Chapter 7

Summary, Conclusions & Future Work

In this thesis, I have studied unobscured star formation at high redshift by searching for Lyman-break galaxies. I have placed constraints on the luminosity function at $z \sim 6.5$ at the end of the epoch of reionisation. I have also studied obscured star formation in LIRGs and ULIRGs which contribute significantly to the cosmic infrared background and I have determined the far-infrared luminosity function of 70μm selected star-forming galaxies out to $z \sim 1$.

7.1 Lyman-Break Galaxies

In Chapters 2 & 3, I describe the data reduction of HAWK-I Y-band science verification data over GOODS-South and its use in searching for high redshift Lyman-break galaxies. The search utilised the multi-wavelength coverage of

the field, particularly optical data from ACS coverage over the field in addition to the near infrared data from VLT HAWK-I Y-band science verification data and the VLT ISAAC J- and K-band data, and *Spitzer* IRAC data. z'-drops ($6.5 \lesssim z \lesssim 7$) were searched for by employing the Lyman-break technique of searching for a significant flux decrement between two filters, in this case the z'- and Y-band filters. A selection criteria of $(z' - Y)_{AB} > 1.0$ was imposed and a $S/N > 5$ cut. Potential contaminants in the sample were eliminated through comparisons with the GOODS MUSIC optical catalogue, and removing those sources with optical detections short-ward of the z'-band as this would be inconsistent with the Lyman-break occurring between the z'- and Y-band filters. Each remaining candidate was inspected by eye to eliminate remaining data artifacts, spurious sources and optical detections. Two transient objects were identified in the data when the validity of candidates was examined by splitting the Y-band data in to individual nights. Four potential z'-drop candidates were identified, with two of these considered robust. Contamination of these two candidates by brown dwarfs was considered and determined unlikely on the basis of colour comparisons with typical brown dwarf colours. The implications of the number density of robust candidates found were examined and compared to predictions based on two luminosity functions. The case of no evolution in the luminosity since $z = 3$ (Steidel et al. 1999) was ruled out due to the large number of galaxies predicted by this scenario compared to the four robust candidates that were found. The case of no evolution since $z = 6$ (Bouwens et al 2007) was also examined and found to be consistent with the two robust candidates found within the ~ 119 arcmin^2 HAWK-I Y-band data.

Y-drops ($7.5 \lesssim z \lesssim 9$) were also searched for in much the same manner as the z'-drops. The J-band data was utilised in combination with the Y-band in order to bracket the Lyman-break. Colour and signal to noise cuts of $(Y - J)_{AB} > 0.75$ and $S/N > 5$ were the selection criterion imposed to identify potential Y-drops. Four possible candidates were identified however they were not determined to be robust as they were only detected in the J-band data, and not in any of the shorter or longer wavelength filters. Possibilities of the detections being due to blue spectral slopes or high Lyα equivalent widths were considered but could not be rejected as they are not implausibly large compared to the known Lyman-break galaxy population at similar redshift. Although no robust Y-drop candidates were found, constraints were placed on the two luminosity functions scenarios by considering the area and depth probed by the HAWK-I Y-band data. If none of the Y-band sources are indeed real, then this demands significant evolution in the UV luminosity function since $z = 3$ based on the predictions by Steidel et al. (1999). It was also found that the case of no evolution in the luminosity function since $z = 6$ was consistent with the lack of candidates found in the area and depth probed by the HAWK-I Y-band data. The work on Lyman-break galaxies in this thesis pre-dated the WFC3 data over the H-UDF which is now placing good constraints to the luminosity function at $z \gtrsim 6.5$, and this deeper HST imaging has been able to confirm one of my z'-drops (9697), which fell within the WFC3 camera survey as being a robust candidate.

This work could be extended by obtaining infrared spectroscopy of the four z'-drop candidates in order to confirm if they are indeed Lyman-break galaxies at $z \sim 6.5$. However two of my candidates, Objects 9136 and 9697,

have already been targetted for spectroscopy without sucess (Fontana et al. 2010). Infrared spectroscopy could provide emission lines from which the star formation rate can be determined and compared to the estimates from the UV continuum. The search for high redshift Lyman-break galaxies using WFC3 over the H-UDF could be complemented by utilising surveys such as VIDEO and UltraVISTA (Arnaboldi et al. 2007). The significantly larger area probed by VIDEO compared to the area studied here would be extremely useful in placing constraints on the bright end of the luminosity function at $z > 6$. UltraVISTA on the other hand, owing to its depth could be pivotal in constraining the break and faint end of the luminosity function at $z > 6$.

7.2 The 70μm Selected Star-Forming Population

In Chapters 4 & 5, the selection of 736 70μm selected galaxies is described and used to determine the far-infrared luminosity function and its evolution over the COSMOS field. Sources were selected from within a 1.7 square degree region that had good coverage at other infrared and optical wavelengths. Sources were required to satisfy a 10 mJy flux cut corresponding to $> 5\sigma$ in order to ensure > 50 per cent completeness. The sources were then matched to the 160μm, 24μm, IRAC then ACS catalogue within progressively smaller search radii in order to maximise accurate associations. This resulted in a sample of 736 sources. 326 of these had spectroscopic redshifts from AAT spectroscopy, the zCOSMOS catalogue, or the Kartaltepe et al. (2010) cat-

alogue. For the remaining 410 sources, photometric redshifts from the ACS COSMOS catalogue were used. The errors on the photometric redshift estimates were taken into account, by sampling the full probability distribution in 1000 Monte Carlo simulations. Total infrared luminosities were calculated for each source by fitting the 8, 24, 70 and 160μm flux densities to spectral energy distribution templates from the Siebenmorgen & Krügel (2007) library. For comparison, total infrared luminosities were also determined using the Chary & Elbaz (2001) spectral energy distributions and comparable but consistently lower values were found. Using the redshift information in conjunction with the total infrared luminosities, $1/V_{\rm max}$ values were calculated for each source and then binned in luminosity and redshift slices of ΔLog(L)= 0.4 and $\Delta z \sim 0.2$ respectively.

Using these $1/V_{\rm max}$ points the luminosity function and its evolution were determined through χ^2 minimisation. Both a double power law and Schechter function parameterisation were considered, however the double power law function was found to provide a better fit in all cases. Three forms of evolution were considered, pure luminosity, pure density and luminosity dependent density, with all forms showing strong positive evolution. The best fit case was that of pure luminosity evolution where $p = 2.4^{+0.6}_{-0.7}$, which is consistent with other values in the literature. The infrared energy density corresponding to the derived luminosity functions were examined showing an increasing contribution from LIRGs and ULIRGs out to $z \sim 1$. The shallower value of the bright end slope found in this work of $\alpha = -1.6 \pm 0.2$, when compared to previous work in the local Universe by Sanders et al. (2003), implies a higher number density of the most luminous objects and a corresponding greater

contribution to the infrared energy density. However the bright end slope is found to be dependent on the choice of model suite.

In Chapter 6, the far-infrared–radio correlation (FIRC) has been examined for the sample of 736 70μm selected galaxies over the COSMOS field described in Chapter 4. 1.4 GHz radio flux densities have been matched to the sources from the joint catalogue of VLA observations over the COSMOS field (Schinnerer et al. 2010). Where no matches to the catalogue were found, 1.4 GHz flux densities were measured down to 2σ. The local background for undetected sources was also measured. The total infrared luminosities and the 1.4 GHz flux densities were compared out to $z \sim 2$ to determine if there was any evolution in the FIRC out to this epoch. The FIRC was also examined when using total infrared luminosities determined from Chary & Elbaz templates and compared to those found using the Siebenmorgen and Krügel templates. No evidence for evolution in either case was found. The k-corrected 70μm flux density was also compared to the 1.4 GHz flux density in order to examine any evolution in this monochromatic FIRC. The values from both sets of templates were compared and while no evidence for evolution was found when using the Siebenmorgen and Krügel templates, ~ 0.2 dex of positive evolution was found when using the Chary & Elbaz models. This increase may be attributable to the bias in the COSMOS field found by Sargent et al. (2010) or additionally it may be due to the warmer temperatures (or shallower mid-infrared slopes) forced by the Chary & Elbaz templates.

The work described here, struggled to differentiate between the exact form of the evolution in the far-infrared luminosity function, however this work

could be extended in the future with deeper observations, reaching faint flux densities over a large enough area to constrain the break in the luminosity function out to high redshift. These data will be available with the H-ATLAS (Eales et al. 2010a) and HerMES (Oliver et al. 2010) surveys. The ability of *Herschel* to sample the far-infrared peak, through measurements at 250, 350 and 500μm, will provide more robust measurements of the total infrared luminosities (L_{IR}). The dramatically larger area covered by H-ATLAS (550 sq. deg) should constrain the evolution of galaxies spanning the break of the luminosity function out to $z = 1$, enabling discrimination between pure luminosity evolution or pure density evolution models, or possibly showing that luminosity dependent density evolution may be the preferred form of evolution with redshift. The narrower (70 sq. deg) but greater depth probed by HerMES will allow measurements of the luminosity function out to $z = 2$, providing the necessary data to determine which sources dominate the overall FIR energy density out to the highest redshifts.

Bibliography

Ajiki, M., Taniguchi, Y., Fujita, S. S., et al. 2003, AJ, 126, 2091

Alexander, D. M., Bauer, F. E., Chapman, S. C., et al. 2005, ApJ, 632, 736

Alonso-Herrero, A., et al. 2006, ApJ, 640, 167

Alonso-Herrero, A., Pereira-Santaella, M., Rieke, G. H., & Rigopoulou, D. 2011, arXiv:1109.1372

Amblard, A., et al. 2010, A&A, 518, L9

Appleton, P. N., Fadda, D. T., Marleau, F. R., et al. 2004, ApJS, 154, 147

Arnaboldi, M., Neeser, M. J., Parker, L. C., Rosati, P., Lombardi, M., Dietrich, J. P., & Hummel, W. 2007, The Messenger, 127, 28

Babbedge, T. S. R., et al. 2006, MNRAS, 370, 1159

Barnes, J. E., & Hernquist, L. 1996, ApJ, 471, 115

Blain, A. W., Smail, I., Ivison, R. J., Kneib, J.-P., & Frayer, D. T. 2002, Phys. Rep., 369, 111

Becker, R. H., et al. 2001, AJ, 122, 2850

Beckwith, S. V. W., Stiavelli, M., Koekemoer, A. M., et al. 2006, AJ, 132, 1729

Bertin, E., & Arnouts, S. 1996, A&AS, 117, 393

Bertoldi, F., Carilli, C., Aravena, M., et al. 2007, ApJS, 172, 132

Bolzonella, M., Miralles, J.-M., & Pelló, R. 2000, A&A, 363, 476

Bonfield, D. G., Jarvis, M. J., Hardcastle, M. J., et al. 2011, MNRAS, 416, 13

Borne, K. D., Bushouse, H., Lucas, R. A., & Colina, L. 2000, ApJ, 529, L77

Bothwell, M. S., Kenicutt, R. C., Johnson, B. D., et al. 2011, MNRAS, 415, 1815

Bourne, N., Dunne, L., Ivison, R. J., et al. 2011, MNRAS, 410, 1155

Bouwens, R. J., Illingworth, G. D., Blakeslee, J. P., Broadhurst, T. J., & Franx, M. 2004, ApJ, 611, L1

Bouwens, R. J., Illingworth, G. D., Thompson, R. I., & Franx, M. 2005, ApJ, 624, L5

Bouwens, R. J., Illingworth, G. D., Blakeslee, J. P., & Franx, M. 2006, ApJ, 653, 53

Bouwens, R. J., Illingworth, G. D., Franx, M., & Ford, H. 2007, ApJ, 670, 928

Bouwens, R. J., Illingworth, G. D., Franx, M., & Ford, H. 2008, ApJ, 686, 230

Bouwens, R. J., Illingworth, G. D., Oesch, P. A., et al. 2010a, ApJ, 709, L133

Bouwens, R. J., Illingworth, G. D., González, V., et al. 2010b, ApJ, 725, 1587

Bouwens, R. J., Illingworth, G. D., Oesch, P. A., et al. 2011a, arXiv:1105.2038

Bouwens, R. J., Illingworth, G. D., Oesch, P. A., et al. 2011b, arXiv:1109.0994

Bouwens, R. J., Illingworth, G. D., Oesch, P. A., et al. 2011c, ApJ, 737, 90

Bridle, A. H. 1967, MNRAS, 136, 219

Bruzual A., G., & Charlot, S. 1993, ApJ, 405, 538

Bruzual, G., & Charlot, S. 2003, MNRAS, 344, 1000

Buat, V., Giovannoli, E., Burgarella, D., et al. 2010, MNRAS, 409, L1

Bunker, A. J., Stanway, E. R., Ellis, R. S., McMahon, R. G., & McCarthy, P. J. 2003, MNRAS, 342, L47

Bunker, A. J., Stanway, E. R., Ellis, R. S., & McMahon, R. G. 2004, MNRAS, 355, 374

Bunker, A. J., Wilkins, S., Ellis, R. S., et al. 2010, MNRAS, 409, 855

Calzetti, D., Kinney, A. L., & Storchi-Bergmann, T. 1994, ApJ, 429, 582

Calzetti, D. 1997, AJ, 113, 162

Calzetti, D. 2011, EAS Publications Series, 46, 133

Capak, P., et al. 2007, ApJS, 172, 99

Capak, P., Mobasher, B., Scoville, N. Z., et al. 2011, ApJ, 730, 68

Caputi, K. I., et al. 2007, ApJ, 660, 97

Casali et al., 2006, SPIE 6269, 29

Castellano, M., Fontana, A., Boutsia, K., et al. 2010, A&A, 511, A20

Chabrier, G. 2003, PASP, 115, 763

Chapman, S. C., Blain, A., Ivison, R., & Smail, I. 2005, Multiwavelength Mapping of Galaxy Formation and Evolution, 119

Chary, R., & Elbaz, D. 2001, ApJ, 556, 562

Clements, D. L., Sutherland, W. J., McMahon, R. G., & Saunders, W. 1996, MNRAS, 279, 477

Clements, D. L., Vaccari, M., Babbedge, T., et al. 2008, MNRAS, 387, 247

Clements, D. L., et al. 2010, A&A, 518, L8

Coleman, G. D., Wu, C.-C., & Weedman, D. W. 1980, ApJS, 43, 393

Condon, J. J., Cotton, W. D., & Broderick, J. J. 2002, AJ, 124, 675

Cooper, M. C., Newman, J. A., Weiner, B. J., et al. 2008, MNRAS, 383, 1058

Coppin, K., Chapin, E. L., Mortier, A. M. J., et al. 2006, MNRAS, 372, 1621

Cowie, L. L., Songaila, A., Hu, E. M., & Cohen, J. G. 1996, AJ, 112, 839

Cowie, L. L., & Hu, E. M. 1998, AJ, 115, 1319

da Cunha, E., Charmandaris, V., Díaz-Santos, T., et al. 2010, A&A, 523, A78

Dale, D. A., Helou, G., Contursi, A., Silbermann, N. A., & Kolhatkar, S. 2001, ApJ, 549, 215

Dawson, S., et al. 2004, ApJ, 617, 707

de Grijp, M. H. K., Miley, G. K., Lub, J., & de Jong, T. 1985, Nature, 314, 240

de Jong, T., Klein, U., Wielebinski, R., & Wunderlich, E. 1985, A&A, 147, L6

Dijkstra, M., Haiman, Z., & Loeb, A. 2004, ApJ, 613, 646

Di Matteo, T., Colberg, J., Springel, V., Hernquist, L., & Sijacki, D. 2008, ApJ, 676, 33

Djorgovski, S., Spinrad, H., McCarthy, P., & Strauss, M. A. 1985, ApJ, 299, L1

Dole, H., Lagache, G., & Puget, J.-L. 2003, ApJ, 585, 617

Dole, H., Lagache, G., Puget, J.-L., et al. 2006, A&A, 451, 417

Downes, D., Solomon, P. M., & Radford, S. J. E. 1993, ApJ, 414, L13

Downes, D., & Solomon, P. M. 1998, ApJ, 507, 615

Dressler, A., Oemler, A., Jr., Couch, W. J., et al. 1997, ApJ, 490, 577

Dunkley, J., et al. 2009, ApJS, 180, 306

Dunlop, J. S., Cirasuolo, M., & McLure, R. J. 2007, MNRAS, 376, 1054

Dunne, L., Eales, S. A., & Edmunds, M. G. 2003, MNRAS, 341, 589

Dye, S., Eales, S. A., Aretxaga, I., et al. 2008, MNRAS, 386, 1107

Dye, S., et al. 2010, A&A, 518, L10

Eales, S., Chapin, E. L., Devlin, M. J., et al. 2009, ApJ, 707, 1779

Eales, S., et al. 2010a, PASP, 122, 499

Eales, S. A., et al. 2010b, A&A, 518, L23

Elbaz, D., Daddi, E., Le Borgne, D., et al. 2007, A&A, 468, 33

Elbaz, D., et al. 2010, A&A, 518, L29

Elvis, M., & Chandra-COSMOS Team 2007, Bulletin of the American Astronomical Society, 38, 899

Eyles, L. P., Bunker, A. J., Stanway, E. R., Lacy, M., Ellis, R. S., & Doherty, M. 2005, MNRAS, 364, 443

Eyles, L. P., Bunker, A. J., Ellis, R. S., Lacy, M., Stanway, E. R., Stark, D. P., & Chiu, K. 2007, MNRAS, 374, 910

Fabian, A. C., & Barcons, X. 1992, ARA&A, 30, 429

Fan, X., Narayanan, V. K., Strauss, M. A., White, R. L., Becker, R. H., Pentericci, L., & Rix, H.-W. 2002, AJ, 123, 1247

Fazio, G. G., et al. 2004, ApJS, 154, 10

Ferguson, H. C., et al. 2004, ApJ, 600, L107

Finkelstein, S. L., Papovich, C., Giavalisco, M., et al. 2010, ApJ, 719, 1250

Fontana, A., Vanzella, E., Pentericci, L., et al. 2010, ApJ, 725, L205

Frayer, D. T., et al. 2009, AJ, 138, 1261

Geballe, T. R., et al. 2002, ApJ, 564, 466

Genzel, R., Lutz, D., Sturm, E., et al. 1998, ApJ, 498, 579

Genzel, R., & Cesarsky, C. J. 2000, ARA&A, 38, 761

Giavalisco, M. 2002, ARA&A, 40, 579

Giavalisco, M., et al. 2004, ApJ, 600, L93

Goto, T. 2005, MNRAS, 360, 322

Goto, T., et al. 2010, A&A, 514, A6

Goto, T., Arnouts, S., Malkan, M., et al. 2011, MNRAS, 414, 1903

Grazian, A., et al. 2006, A&A, 449, 951

Gruppioni, C., Pozzi, F., Andreani, P., et al. 2010, A&A, 518, L27

Guhathakurta, P., Tyson, J. A., & Majewski, S. R. 1990, ApJ, 357, L9

Hasinger, G., Cappelluti, N., Brunner, H., et al. 2007, ApJS, 172, 29

Hauser, M. G., & Dwek, E. 2001, ARA&A, 39, 249

Helou, G., Soifer, B. T., & Rowan-Robinson, M. 1985, ApJ, 298, L7

Hewett, P. C., Warren, S. J., Leggett, S. K., & Hodgkin, S. T. 2006, MNRAS, 367, 454

Hickey, S., Bunker, A., Jarvis, M. J., Chiu, K., & Bonfield, D. 2010, MNRAS, 404, 212

High, F. W., Stubbs, C. W., Stalder, B., Gilmore, D. K., & Tonry, J. L. 2010, PASP, 122, 722

Holland, W. S., Robson, E. I., Gear, W. K., et al. 1999, MNRAS, 303, 659

Hu, E. M., & Cowie, L. L. 1987, ApJ, 317, L7

Hu, E. M., Cowie, L. L., McMahon, R. G., et al. 2002, ApJ, 568, L75

Hughes, D. H., et al. 1998, Nature, 394, 241

Huynh, M. T., Frayer, D. T., Mobasher, B., Dickinson, M., Chary, R.-R., & Morrison, G. 2007, ApJ, 667, L9

Hwang, H. S., Elbaz, D., Lee, J. C., et al. 2010, A&A, 522, A33

Ilbert, O., et al. 2009, ApJ, 690, 1236

Ishida, C. M. 2004, Ph.D. Thesis,

Ivison, R. J., Smail, I., Barger, A. J., et al. 2000, MNRAS, 315, 209

Ivison, R. J., Alexander, D. M., Biggs, A. D., et al. 2010, MNRAS, 402, 245

Ivison, R. J., Magnelli, B., Ibar, E., et al. 2010, A&A, 518, L31

Iye, M., et al. 2006, Nature, 443, 186

Jarvis, M. J., Smith, D. J. B., Bonfield, D. G., Hardcastle, M. J., Falder, J. T., et al. 2010, MNRAS, 409, 92

Kartaltepe, J. S., et al. 2010, ApJ, 721, 98

Kashikawa, N., Shimasaku, K., Matsuda, Y., et al. 2011, ApJ, 734, 119

Kawakatu, N., Anabuki, N., Nagao, T., Umemura, M., & Nakagawa, T. 2006, ApJ, 637, 104

Kennicutt, R. C., Jr. 1998, ApJ, 498, 541

Kennicutt, R. C., Jr. 1998, ARA&A, 36, 189

Kennicutt, R. C., Jr., Hao, C.-N., Calzetti, D., et al. 2009, ApJ, 703, 1672

Kessler, M. F., Steinz, J. A., Anderegg, M. E., et al. 1996, A&A, 315, L27

Kewley, L. J., Geller, M. J., & Jansen, R. A. 2004, AJ, 127, 2002

Kim, D.-C., Veilleux, S., & Sanders, D. B. 2002, ApJS, 143, 277

Kirkpatrick, J. D., et al. 2000, AJ, 120, 447

Knapp, G. R., et al. 2004, AJ, 127, 3553

Kogut, A., et al. 2003, ApJS, 148, 161

Koulouridis, E., Chavushyan, V., Plionis, M., Krongold, Y., & Dultzin-Hacyan, D. 2006, ApJ, 651, 93

Kleinmann, D. E., & Low, F. J. 1970, ApJ, 159, L165

Kleinmann, D. E., & Low, F. J. 1970, ApJ, 161, L203

Kormendy, J., & Sanders, D. B. 1992, ApJ, 390, L53

Kroupa, P., Tout, C. A., & Gilmore, G. 1990, MNRAS, 244, 76

Kruegel, E. 2003, The physics of interstellar dust, by Endrik Kruegel. IoP Series in astronomy and astrophysics, ISBN 0750308613. Bristol, UK: The Institute of Physics, 2003.,

Labbé, I., González, V., Bouwens, R. J., et al. 2010, ApJ, 716, L103

Lacki, B. C., Thompson, T. A., & Quataert, E. 2010, ApJ, 717, 1

Lagache, G., Puget, J.-L., & Dole, H. 2005, ARA&A, 43, 727

Larson, R. B., & Tinsley, B. M. 1978, ApJ, 219, 46

Lawrence, A., et al. 2007, MNRAS, 379, 1599

Le Floc'h, E., et al. 2005, ApJ, 632, 169

Leggett, S. K., et al. 2000, ApJ, 536, L35

Leggett, S. K., Allard, F., Geballe, T. R., Hauschildt, P. H., & Schweitzer, A. 2001, ApJ, 548, 908

Leggett, S. K., et al. 2002, ApJ, 564, 452

Lilly, S. J., Le Fevre, O., Hammer, F., & Crampton, D. 1996, ApJ, 460, L1

Lilly, S. J., Eales, S. A., Gear, W. K. P., et al. 1999, ApJ, 518, 641

Lilly, S. J., et al. 2007, ApJS, 172, 70

Lilly, S. J., et al. 2009, ApJS, 184, 218

Lorenzoni, S., Bunker, A. J., Wilkins, S. M., et al. 2011, MNRAS, 414, 1455

Low, F. J., & Tucker, W. H. 1968, Physical Review Letters, 21, 1538

Madau, P., Ferguson, H. C., Dickinson, M. E., et al. 1996, MNRAS, 283, 1388

Madau, P., Pozzetti, L., & Dickinson, M. 1998, ApJ, 498, 106

Magnelli, B., Elbaz, D., Chary, R. R., Dickinson, M., Le Borgne, D., Frayer, D. T., & Willmer, C. N. A. 2009, A&A, 496, 57

Magnelli, B., Elbaz, D., Chary, R. R., et al. 2011, A&A, 528, A35

Malhotra, S., & Rhoads, J. E. 2002, ApJ, 565, L71

Mannucci, F., Buttery, H., Maiolino, R., Marconi, A., & Pozzetti, L. 2007, A&A, 461, 423

McLure, R. J., Cirasuolo, M., Dunlop, J. S., Foucaud, S., & Almaini, O. 2009, MNRAS, 395, 2196

McLure, R. J., Dunlop, J. S., Cirasuolo, M., et al. 2010, MNRAS, 403, 960

McLure, R. J., Dunlop, J. S., de Ravel, L., et al. 2011, arXiv:1102.4881

Meier, D. L. 1976, ApJ, 203, L103

Meier, D. L. 1976, ApJ, 207, 343

Meng, X.-M., Wu, H., Gu, Q.-S., Wang, J., & Cao, C. 2010, ApJ, 718, 928

Michałowski, M. J., Watson, D., & Hjorth, J. 2010, ApJ, 712, 942

Mihos, J. C., & Hernquist, L. 1996, ApJ, 464, 641

Moncelsi, L., Ade, P. A. R., Chapin, E. L., et al. 2011, ApJ, 727, 83

Monet, D. G., Levine, S. E., Canzian, B., et al. 2003, AJ, 125, 984

Mortier, A. M. J., Serjeant, S., Dunlop, J. S., et al. 2005, MNRAS, 363, 563

Moustakas, J., Kennicutt, R. C., Jr., & Tremonti, C. A. 2006, ApJ, 642, 77

Murphy, E. J., Chary, R.-R., Alexander, D. M., et al. 2009, ApJ, 698, 1380

Naab, T., & Burkert, A. 2003, ApJ, 597, 893

Neugebauer, G., et al. 1984, ApJ, 278, L1

Oesch, P. A., Carollo, C. M., Stiavelli, M., et al. 2009, ApJ, 690, 1350

Oesch, P. A., Bouwens, R. J., Carollo, C. M., et al. 2010, ApJ, 709, L21

Oke, J. B., & Gunn, J. E. 1983, ApJ, 266, 713

Ota, K., et al. 2008, ApJ, 677, 12

Ouchi, M., Mobasher, B., Shimasaku, K., et al. 2009, ApJ, 706, 1136

Ouchi, M., Shimasaku, K., Furusawa, H., et al. 2010, ApJ, 723, 869

Oliver, S. J., Wang, L., Smith, A. J., et al. 2010, A&A, 518, L21

Papovich, C., Dickinson, M., & Ferguson, H. C. 2001, ApJ, 559, 620

Patten, B. M., et al. 2006, ApJ, 651, 502

Penzias, A. A., & Wilson, R. W. 1965, ApJ, 142, 419

Pérez-González, P. G., et al. 2005, ApJ, 630, 82

Pilbratt, G. L., Riedinger, J. R., Passvogel, T., et al. 2010, A&A, 518, L1

Pirard et al., 2004, SPIE 5492, 510

Puget, J.-L., Abergel, A., Bernard, J.-P., et al. 1996, A&A, 308, L5

Retzlaff, J., Rosati, P., Dickinson, M., et al. 2010, A&A, 511, A50

Rhoads, J. E., Malhotra, S., Dey, A., et al. 2000, ApJ, 545, L85

Rich, J. A., Kewley, L. J., & Dopita, M. A. 2011, ApJ, 734, 87

Rieke, G. H., & Lebofsky, M. J. 1978, ApJ, 220, L37

Rieke, G. H., et al. 2004, ApJS, 154, 25

Rodighiero, G., Vaccari, M., Franceschini, A., et al. 2010, A&A, 515, A8

Rupke, D. S., Veilleux, S., & Sanders, D. B. 2005, ApJS, 160, 115

Salpeter, E. E. 1955, ApJ, 121, 161

Sanders, D. B., Scoville, N. Z., & Soifer, B. T. 1991, ApJ, 370, 158

Sanders, D. B., Soifer, B. T., Elias, J. H., Neugebauer, G., & Matthews, K. 1988, ApJ, 328, L35

Sanders, D. B., Mazzarella, J. M., Kim, D.-C., Surace, J. A., & Soifer, B. T. 2003, AJ, 126, 1607

Sanders, D. B., Salvato, M., Aussel, H., et al. 2007, ApJS, 172, 86

Sargent, M. T., Schinnerer, E., Murphy, E., et al. 2010, ApJ, 714, L190

Scalo, J. M. 1986, Fund. Cosmic Phys., 11, 1

Schiminovich, D., Ilbert, O., Arnouts, S., et al. 2005, ApJ, 619, L47

Schlegel, D. J., Finkbeiner, D. P., & Davis, M. 1998, ApJ, 500, 525

Schmidt, M. 1959, ApJ, 129, 243

Schmidt, M. 1968, ApJ, 151, 393

Schinnerer, E., Sargent, M. T., Bondi, M., et al. 2010, ApJS, 188, 384

Scott, D., Ade, P., Bock, J. J., et al. 2001, The Promise of the Herschel Space Observatory, 460, 305

Scott, S. E., Fox, M. J., Dunlop, J. S., et al. 2002, MNRAS, 331, 817

Scoville, N. Z., Young, J. S., & Lucy, L. 1982, BAAS, 14, 617

Scoville, N. Z. 2000, Dynamics of Galaxies: from the Early Universe to the Present, 197, 301

Scoville, N., et al. 2007a, ApJS, 172, 38

Scoville, N., et al. 2007b, ApJS, 172, 1

Searle, L., Sargent, W. L. W., & Bagnuolo, W. G. 1973, ApJ, 179, 427

Serjeant, S., Dye, S., Mortier, A., et al. 2008, MNRAS, 386, 1907

Seymour, N., Huynh, M., Dwelly, T., et al. 2009, MNRAS, 398, 1573

Shapley, A. E., Steidel, C. C., Adelberger, K. L., et al. 2001, ApJ, 562, 95

Shi, Y., Rieke, G., Lotz, J., & Perez-Gonzalez, P. G. 2009, The Starburst-AGN Connection, 408, 468

Shimasaku, K., Kashikawa, N., Doi, M., et al. 2006, PASJ, 58, 313

Siebenmorgen, R., & Krügel, E. 2007, A&A, 461, 445

Sijacki, D., Springel, V., Di Matteo, T., & Hernquist, L. 2007, MNRAS, 380, 877

Silva, L., Danese, L., Granato, G. L., Bressan, A., & Franceschini, A. 1998, The Young Universe: Galaxy Formation and Evolution at Intermediate and High Redshift, 146, 334

Smail, I., Ivison, R. J., & Blain, A. W. 1997, ApJ, 490, L5

Smail, I., Ivison, R. J., Blain, A. W., & Kneib, J.-P. 1998, ApJ, 507, L21

Smail, I., Ivison, R. J., Owen, F. N., Blain, A. W., & Kneib, J.-P. 2000, ApJ, 528, 612

Smoot, G. F., Bennett, C. L., Kogut, A., et al. 1992, ApJ, 396, L1

Soifer, B. T., Rowan-Robinson, M., Houck, J. R., et al. 1984, ApJ, 278, L71

Soifer, B. T., Sanders, D. B., Madore, B. F., Neugebauer, G., Danielson, G. E., Elias, J. H., Lonsdale, C. J., & Rice, W. L. 1987a, ApJ, 320, 238

Soifer, B. T., Neugebauer, G., & Houck, J. R. 1987b, ARA&A, 25, 187

Soifer, B. T., Boehmer, L., Neugebauer, G., & Sanders, D. B. 1989, AJ, 98, 766

Soifer, B. T., Helou, G., & Werner, M. 2008, ARA&A, 46, 201

Solomon, P. M., Downes, D., Radford, S. J. E., & Barrett, J. W. 1997, ApJ, 478, 144

Springel, V., & Hernquist, L. 2005, ApJ, 622, L9

Sreekumar, P., Bertsch, D. L., Dingus, B. L., et al. 1998, ApJ, 494, 523

Stanway, E. R., Bunker, A. J., & McMahon, R. G. 2003, MNRAS, 342, 439

Stanway, E. R., Bunker, A. J., McMahon, R. G., et al. 2004, ApJ, 607, 70

Stanway, E. R., McMahon, R. G., & Bunker, A. J. 2005, MNRAS, 359, 1184

Stanway, E. R., et al. 2007, MNRAS, 376, 727

Stanway, E. R., Bremer, M. N., Squitieri, V., Douglas, L. S., & Lehnert, M. D. 2008, MNRAS, 386, 370 4

Steidel, C. C., Sargent, W. L. W., & Dickinson, M. 1991, AJ, 101, 1187

Steidel, C. C., Pettini, M., & Hamilton, D. 1995, AJ, 110, 2519

Steidel, C. C., Giavalisco, M., Dickinson, M., & Adelberger, K. L. 1996, AJ, 112, 352

Steidel, C. C., Adelberger, K. L., Giavalisco, M., Dickinson, M., & Pettini, M. 1999, ApJ, 519, 1

Surace, J. A., Sanders, D. B., Vacca, W. D., Veilleux, S., & Mazzarella, J. M. 1998, ApJ, 492, 116

Surace, J. A., & Sanders, D. B. 1999, ApJ, 512, 162

Surace, J. A., Sanders, D. B., & Evans, A. S. 2000, ApJ, 529, 170

Swinbank, A. M., Smail, I., Longmore, S., et al. 2010, Nature, 464, 733

Symeonidis, M., et al. 2007, ApJ, 660, L73

Symeonidis, M., Rosario, D., Georgakakis, A., Harker, J., Laird, E. S., Page, M. J., & Willmer, C. N. A. 2010, MNRAS, 403, 1474

Tacconi, L. J., Genzel, R., Lutz, D., et al. 2002, ApJ, 580, 73

Taniguchi, Y., Scoville, N., Murayama, T., et al. 2007, ApJS, 172, 9

Tanvir, N. R., et al. 2009, arXiv:0906.1577

Targett, T. A., Dunlop, J. S., McLure, R. J., et al. 2011, MNRAS, 412, 295

Telesco, C. M., & Harper, D. A. 1980, ApJ, 235, 392

Tran, Q. D., et al. 2001, ApJ, 552, 527

Vaccari, M., et al. 2010, A&A, 518, L20

van Dokkum, P. G. 2001, PASP, 113, 1420

Vanzella, E., Pentericci, L., Fontana, A., et al. 2011, ApJ, 730, L35

Veilleux, S., Kim, D.-C., & Sanders, D. B. 2002, ApJS, 143, 315

Veilleux, S., Rupke, D. S. N., Kim, D.-C., et al. 2009, ApJS, 182, 628

Venemans, B. P., McMahon, R. G., Warren, S. J., Gonzalez-Solares, E. A., Hewett, P. C., Mortlock, D. J., Dye, S., & Sharp, R. G. 2007, MNRAS, 376, L76

Verma, A., Lehnert, M. D., Förster Schreiber, N. M., Bremer, M. N., & Douglas, L. 2007, MNRAS, 377, 1024

Völk, H. J. 1989, A&A, 218, 67

Wang, J. L., Xia, X. Y., Mao, S., et al. 2006, ApJ, 649, 722

Werner, M. W., et al. 2004, ApJS, 154, 1

Wilkins, S. M., Bunker, A. J., Ellis, R. S., et al. 2010, MNRAS, 403, 938

Willott, C. J., Delfosse, X., Forveille, T., Delorme, P., & Gwyn, S. D. J. 2005, ApJ, 633, 630

Wu, X., Hamilton, T., Helfand, D. J., & Wang, Q. 1991, ApJ, 379, 564

Yan, H., et al. 2004, ApJ, 616, 63

Yan, H., Yan, L., Zamojski, M. A., et al. 2011, ApJ, 728, L22

Younger, J. D., Omont, A., Fiolet, N., et al. 2009, MNRAS, 394, 1685

Yun, M. S., Reddy, N. A., & Condon, J. J. 2001, ApJ, 554, 803

Appendix A

Flux Table

Table A.1: Table of the resulting 736 70μm sources. The ID is the ID from the v3 70μm catalogue (Frayer et al. 2009). The RA and Dec are taken from the COSMOS ACS catalogue, as it provided the most accurate positional information. 8, 24, 70 and 160μm flux densities and associated errors are listed, all are given in mJy. The 160μm flag F/S denotes where the 160μm flux came from. F denotes the Frayer et al. (2009) catalogue and S denotes aperture measurements undertaken in this work. Both spectroscopic (z_{spec}) (where available) and photometric (z_{phot}) redshifts are listed. The flag denotes where the redshifts were obtained from, A denotes spectroscopic redshifts obtained through AAOmega, C denotes the zCOSMOS catalogue and K denotes the catalogue of Kartaltepe et al. (2010). min and max, denote the 1σ errors on the photometric redshifts (Ilbert et al. 2009).

ID	RA	Dec	S_8	σ_8	S_{24}	σ_{24}	S_{70}	σ_{70}	S_{160}	σ_{160}	F/S	z_{phot}	min	max	z_{spec}	Flag
209	150.6457	1.59175	0.12	0.002	0.597	0.019	14.9	2.8	20.6	7.6	S	0.41	0.47	2.27		
231	150.7105	1.60540	0.04	0.002	0.454	0.02	13.1	2.6	41.0	5.9	S	0.68	0.6	0.68		
322	150.0120	1.65216	0.05	0.002	0.451	0.017	20.4	3.0	74.0	22.2	F	1.38	1.23	1.43		
498	150.5351	1.75739	0.16	0.002	0.77	0.016	11.0	2.4	<11.6	<11.6	S	0.15	0.1	0.19	0.173	CK
672	149.5164	1.87075	0.27	0.002	0.97	0.085	15.8	2.7	73.9	20.9	F	0.43	0.37	0.49		
769	150.4262	1.91365	0.23	0.002	0.734	0.019	11.6	2.6	33.6	5.9	S	0.31	0.28	0.34		
852	150.1100	1.95357	0.21	0.002	0.958	0.02	15.8	2.7	<11.6	<11.6	S	0.64	0.61	0.68	0.323	K
1014	149.8740	2.02713	0.03	0.002	0.449	0.016	10.4	1.9	61.0	7.0	S	0.73	0.69	0.77	0.685	C
1129	150.6109	2.09471	0.20	0.002	0.313	0.017	12.3	2.5	44.2	6.5	S	0.91	0.87	0.96		
1142	149.6450	2.10180	0.16	0.002	0.844	0.019	10.8	2.0	<11.6	<11.6	S	0.25	0.21	0.32		
1167	149.9512	2.11775	0.42	0.002	0.809	0.017	30.4	3.2	91.8	23.4	F	0.16	0.15	0.19	0.463	A
1640	149.9658	2.32717	0.15	0.002	0.6	0.015	10.5	1.9	27.4	4.6	S	0.32	0.28	0.37	0.378	CK
1693	150.2984	2.34661	0.08	0.002	0.396	0.015	10.0	2.3	19.5	5.8	S	0.41	0.39	0.46	0.470	K
1730	150.4344	2.36838	0.02	0.002	0.436	0.017	13.0	2.6	33.0	6.1	S	1.18	1.13	1.22		
1883	150.7055	2.41793	0.13	0.002	0.438	0.014	13.1	2.8	<11.6	<11.6	S	0.37	0.3	0.42		
1900	150.6416	2.42346	0.04	0.002	0.4	0.019	16.1	2.8	71.8	21.1	F	0.72	0.7	0.8	0.568	K

Continued on next page

Table A.1 – continued from previous page

ID	RA	Dec	S_8	σ_8	S_{24}	σ_{24}	S_{70}	σ_{70}	S_{160}	σ_{160}	F/S	z_{phot}	min	max	z_{spec}	Flag
1907	150.1754	2.42619	0.30	0.002	1.473	0.021	24.0	3.2	21.2	5.0	S	0.31	0.3	0.35	0.311	CK
2000	149.5486	2.47738	0.45	0.002	0.653	0.076	11.0	2.5	48.3	6.1	S	0.18	0.17	0.26	0.220	CK
2235	150.0548	2.56946	0.04	0.002	0.654	0.014	36.4	3.4	73.4	18.4	F	0.75	0.7	0.79	0.755	K
2642	150.3547	2.75182	0.04	0.002	0.797	0.019	11.7	2.6	54.5	7.8	S	0.97	0.93	1.02	0.978	CK
2680	149.6611	2.77783	0.24	0.002	0.646	0.223	15.0	2.9	95.2	7.5	S	0.25	0.23	0.3		
2739	150.3751	2.80926	0.25	0.002	0.934	0.018	12.1	2.7	96.0	8.8	S	0.24	0.21	0.28		
2794	149.6956	2.85078	0.12	0.002	0.835	0.016	16.5	2.7	70.8	7.4	S	0.27	1.54	1.86		
2825	150.2358	2.85822	0.10	0.002	0.747	0.014	11.2	2.6	11.9	5.8	S	0.45	0.41	0.52	0.511	K
2847	150.1896	2.87273	0.05	0.002	0.799	0.015	19.4	3.0	12.2	4.7	S	0.68	0.67	0.77		
2859	149.8764	2.88449	0.10	0.002	0.541	0.016	11.5	2.6	<11.6	<11.6	S	1.18	1.16	1.19		
3187	149.7692	1.52009	0.26	0.002	0.475	0.017	14.1	3.0	73.7	8.2	S	0.21	1.58	2.21		
3515	150.6353	1.65253	0.06	0.002	0.246	0.028	12.2	2.7	43.1	6.0	S	0.48	0.44	0.59		
3556	150.5874	1.66877	0.08	0.002	0.511	0.016	14.7	2.7	66.7	20.7	F	1.42	1.37	1.46		
3637	150.1709	1.69093	0.33	0.002	0.833	0.027	12.4	2.7	59.8	8.0	S	0.21	0.19	0.25		
3649	149.5375	1.69200	0.21	0.002	0.764	0.022	11.1	2.6	<11.6	<11.6	S	0.37	0.32	0.39	0.309	K
3682	149.8452	1.70981	0.03	0.002	0.499	0.016	13.8	2.7	12.8	6.2	S	0.7	0.67	0.76		
3758	150.4282	1.73607	0.10	0.002	0.41	0.017	14.3	2.9	123.4	8.2	S	0.32	0.28	0.37		
3786	149.8089	1.74639	0.02	0.002	0.375	0.016	10.6	2.5	14.4	5.2	S	1.0	0.94	1.06		
3855	150.0740	1.77263	0.02	0.002	0.409	0.014	11.1	2.6	<11.6	<11.6	S	0.71	0.67	0.75		
3891	150.1483	1.78122	0.04	0.002	0.357	0.016	11.0	2.5	50.6	6.7	S	1.2	1.15	1.36		
3909	150.7424	1.79512	0.03	0.002	0.362	0.021	12.7	2.6	56.1	6.0	S	0.64	0.6	0.66		
4121	149.6798	1.86700	0.15	0.002	0.594	0.015	12.1	2.6	47.7	6.4	S	0.33	0.29	0.4		

Continued on next page

Table A.1 – continued from previous page

ID	RA	Dec	S_8	σ_8	S_{24}	σ_{24}	S_{70}	σ_{70}	S_{160}	σ_{160}	F/S	z_{phot}	min	max	z_{spec}	Flag
4202	150.3948	1.88891	0.41	0.002	0.629	0.02	11.4	2.5	<11.6	<11.6	S	0.14	0.08	0.17		
4206	149.9383	1.89177	0.18	0.002	0.542	0.015	14.5	2.6	29.1	5.8	S	0.22	0.16	0.27	0.220	C
4216	149.6456	1.89677	0.21	0.002	0.536	0.016	15.6	2.9	53.9	6.6	S	0.31	0.28	0.32	0.311	CK
4263	150.5454	1.90827	0.03	0.002	0.284	0.015	12.6	2.7	15.5	6.2	S	0.53	0.47	0.59	0.587	K
4276	150.7457	1.91333	0.09	0.002	0.543	0.017	11.4	2.6	62.4	19.2	F	0.9	0.87	0.97		
4366	149.7588	1.94358	0.22	0.002	0.451	0.014	11.6	2.4	<11.6	<11.6	S	0.22	0.18	0.27	0.260	C
4423	150.2414	1.97207	0.02	0.002	0.164	0.015	10.1	2.5	57.1	18.4	F	1.23	1.13	1.38	0.109	K
4477	149.7711	1.99034	0.06	0.002	0.736	0.019	17.7	2.6	67.2	20.0	F	1.1	1.01	1.13		
4725	149.8325	2.06602	0.03	0.002	0.201	0.016	12.0	2.0	41.2	5.4	S	1.24	1.21	1.39		
4752	150.0369	2.07514	0.08	0.002	0.334	0.015	14.9	2.9	20.5	5.4	S	0.43	0.4	0.49	0.461	C
4775	150.1255	2.08704	0.05	0.002	0.553	0.016	14.9	2.7	<11.6	<11.6	S	0.93	0.9	0.97	0.894	CK
4778	149.9188	2.07781	0.04	0.002	0.204	0.017	10.6	2.0	39.8	6.4	S	1.22	1.16	1.37		
4954	150.0521	2.12671	0.07	0.002	0.888	0.017	17.5	3.1	142.1	8.4	S	0.82	0.71	0.83	0.664	CK
4998	149.5146	2.14364	0.02	0.002	0.178	0.016	10.6	2.6	<11.6	<11.6	S	1.0	0.92	1.05		
5031	150.0113	2.15669	0.11	0.002	0.567	0.016	21.8	2.9	89.0	22.6	F	0.36	0.33	0.42	0.479	CK
5081	150.7434	2.17054	0.25	0.002	1.582	0.392	19.4	3.0	66.0	6.7	S	1.26	2.29	2.71		
5084	149.6436	2.17112	0.01	0.002	0.187	0.016	10.3	2.3	<11.6	<11.6	S	0.85	0.8	1.0		
5099	149.7798	2.17772	0.23	0.002	0.631	0.017	10.6	1.9	52.1	7.4	S	0.19	0.11	0.22	0.168	CK
5152	150.3118	2.19611	0.03	0.002	0.287	0.027	29.6	3.6	34.2	5.5	S	1.31	1.18	1.39	1.090	K
5315	149.6000	2.23212	0.03	0.002	0.389	0.016	11.5	2.5	<11.6	<11.6	S	0.69	0.58	0.72		
5333	150.3069	2.23825	0.34	0.002	0.892	0.016	11.7	2.5	17.0	4.9	S	0.22	0.2	0.28	0.248	CK
5353	150.2016	2.24842	0.47	0.002	0.656	0.017	12.3	2.6	30.3	5.6	S	0.15	0.09	0.18	0.093	CK

Continued on next page

Table A.1 – continued from previous page

ID	RA	Dec	S_8	σ_8	S_{24}	σ_{24}	S_{70}	σ_{70}	S_{160}	σ_{160}	F/S	z_{phot}	min	max	z_{spec}	Flag
5392	150.3284	2.25482	0.01	0.002	0.193	0.016	10.7	2.6	<11.6	<11.6	S	1.47	1.05	1.51		
5447	150.1611	2.27871	0.15	0.002	0.798	0.018	11.1	2.5	<11.6	<11.6	S	0.4	0.35	0.44	0.427	K
5499	149.6431	2.29777	0.29	0.002	0.861	0.048	14.6	2.8	91.5	7.8	S	0.28	0.25	0.33	0.328	CK
5522	149.8722	2.28967	0.06	0.002	0.781	0.014	13.1	2.1	61.1	19.2	F	0.78	0.73	0.8		
5687	150.2401	2.35324	0.04	0.002	0.157	0.075	10.4	2.5	67.7	6.9	S	1.41	1.37	1.44		
5703	149.7733	2.33988	0.16	0.002	0.627	0.106	13.0	2.3	<11.6	<11.6	S	0.36	0.32	0.39		
5722	149.9113	2.34858	0.05	0.002	0.266	0.014	14.4	2.1	33.4	5.6	S	0.45	0.38	0.48		
5961	149.5288	2.42024	0.11	0.002	0.618	0.04	13.0	2.7	32.6	6.0	S	0.45	0.39	0.49		
6096	150.4177	2.46000	0.39	0.002	0.79	0.016	29.3	3.6	44.8	6.4	S	0.17	0.16	0.24		
6176	150.1595	2.47434	0.05	0.002	0.79	0.019	12.2	2.3	74.0	6.5	S	0.66	0.58	0.69		
6187	149.7526	2.47589	0.15	0.002	0.779	0.017	14.0	2.8	94.5	7.9	S	0.44	0.38	0.49	0.478	CK
6412	149.6286	2.54949	0.10	0.002	1.029	0.02	17.5	3.0	21.1	4.8	S	0.47	0.36	0.5		
6425	150.4216	2.54743	0.03	0.002	0.285	0.016	11.2	2.8	36.5	7.4	S	0.57	0.5	0.61		
6428	150.4770	2.54882	0.07	0.002	0.152	0.083	10.8	2.5	24.2	5.9	S	0.3	0.22	0.38	0.373	K
6442	150.3218	2.55233	0.07	0.002	0.647	0.102	11.8	2.8	<11.6	<11.6	S	0.69	0.58	0.71	0.612	CK
6524	150.3419	2.56825	0.02	0.002	0.206	0.015	11.9	2.7	61.0	7.1	S	0.89	0.85	0.93	0.821	CK
6748	149.5738	2.63114	0.21	0.002	0.584	0.03	13.7	2.7	73.0	7.2	S	0.3	0.24	0.32	0.286	C
6788	150.0440	2.64391	0.07	0.002	1.172	0.017	13.2	2.3	86.5	7.4	S	0.69	0.64	0.7		
6947	150.2373	2.68925	0.17	0.002	0.728	0.016	11.8	2.1	23.9	5.6	S	1.51	0.93	1.56		
7010	149.7585	2.71004	0.11	0.002	0.378	0.021	11.7	2.7	<11.6	<11.6	S	0.37	0.36	0.82		
7216	150.1269	2.76538	0.04	0.002	0.457	0.014	12.2	2.2	24.9	4.7	S	0.77	0.73	0.8	0.734	CK
7254	150.3917	2.77900	0.16	0.002	0.523	0.018	11.8	2.6	31.7	8.2	S	0.31	0.29	0.33		

Continued on next page

Table A.1 – continued from previous page

ID	RA	Dec	S_8	σ_8	S_{24}	σ_{24}	S_{70}	σ_{70}	S_{160}	σ_{160}	F/S	z_{phot}	min	max	z_{spec}	Flag
7316	150.3994	2.79420	0.08	0.002	0.565	0.016	22.1	3.2	80.0	8.8	S	0.8	0.74	0.83		
7448	149.8809	2.83728	0.14	0.002	0.509	0.016	11.3	2.6	<11.6	<11.6	S	0.31	0.28	0.38		
7484	150.4464	2.84699	0.01	0.002	0.169	0.018	14.8	2.6	57.7	6.4	S	1.18	1.17	1.19	0.576	K
7513	149.9616	2.86227	0.08	0.002	0.696	0.033	16.6	2.9	62.0	19.2	F	1.11	1.08	1.19		
7801	150.6755	1.56848	0.02	0.002	0.334	0.107	10.2	2.4	78.0	7.5	S	0.69	0.66	0.72		
7807	150.4106	1.60268	0.25	0.002	0.638	0.163	11.5	2.6	35.8	5.3	S	0.2	0.16	0.27		
7810	149.6628	1.60950	0.06	0.002	0.386	0.035	13.2	2.7	54.7	7.5	S	0.51	0.49	0.59		
7815	149.9107	1.66256	0.07	0.002	0.75	0.024	10.8	2.5	30.3	5.9	S	0.56	0.54	0.69		
7829	150.6172	1.75579	0.35	0.002	1.072	0.019	14.6	2.8	64.5	20.0	F	0.3	0.29	0.35		
7831	149.6725	1.75591	0.02	0.002	0.167	0.072	15.1	2.7	39.7	6.0	S	0.6	0.57	0.64		
7850	150.6381	1.87833	0.03	0.002	0.44	0.017	18.1	2.9	119.8	26.9	F	0.81	0.78	0.91		
7851	150.4607	1.87602	0.05	0.002	0.34	0.016	10.2	2.6	37.9	6.5	S	0.51	0.42	0.54		
7889	150.4704	2.02046	0.58	0.002	1.686	0.019	29.6	3.9	62.1	19.7	F	0.27	0.25	0.29	0.220	K
7950	150.5614	2.34566	0.21	0.002	0.942	0.059	10.3	2.5	22.1	5.7	S	1.65	1.57	1.94		
7962	150.4577	2.41064	0.09	0.002	0.315	0.097	12.9	2.8	54.7	6.9	S	0.25	0.21	0.29		
8038	150.3099	2.86389	0.04	0.002	0.808	0.04	14.4	2.8	48.2	6.4	S	0.69	0.64	0.73		
8147	149.5641	1.52368	0.02	0.002	0.182	0.018	12.9	2.9	59.2	7.8	S	0.01	0.0	0.41		
8163	150.0947	1.53237	0.20	0.002	0.202	0.055	10.8	2.5	34.9	6.2	S	0.17	0.38	2.03		
8205	150.2872	1.56675	0.29	0.002	0.935	0.042	15.4	2.8	75.4	21.8	F	0.33	1.4	2.22		
8217	150.2213	1.57800	0.07	0.002	0.462	0.018	11.6	2.7	68.3	6.6	S	0.52	0.46	0.53		
8228	149.8927	1.57196	0.16	0.002	0.78	0.017	21.2	3.2	73.8	22.2	F	0.46	0.44	0.49		
8254	149.5317	1.59026	0.11	0.002	0.364	0.048	38.6	4.6	57.0	9.3	S	0.33	0.27	0.38		

Continued on next page

Table A.1 – continued from previous page

ID	RA	Dec	S_8	σ_8	S_{24}	σ_{24}	S_{70}	σ_{70}	S_{160}	σ_{160}	F/S	z_{phot}	min	max	z_{spec}	Flag
8294	149.7653	1.61702	0.17	0.002	1.081	0.019	18.4	2.9	63.4	20.4	F	0.54	0.44	0.56	0.517	K
8306	150.2868	1.62143	0.18	0.002	0.547	0.054	10.6	2.6	61.5	7.0	S	0.38	0.35	0.39		
8322	150.6594	1.62964	0.34	0.002	1.009	0.021	10.4	2.6	<11.6	<11.6	S	0.04	0.03	0.04	2.506	K
8366	150.6854	1.66109	0.07	0.002	0.965	0.153	17.1	2.8	32.6	5.2	S	0.71	0.68	0.75		
8386	150.1146	1.67305	0.04	0.002	0.36	0.014	11.4	2.6	40.2	7.0	S	0.5	0.47	0.52		
8436	150.1874	1.70899	0.35	0.002	0.531	0.016	12.1	2.6	20.9	8.2	S	0.12	0.07	0.18		
8500	149.8854	1.75349	0.07	0.002	0.266	0.016	18.1	2.9	65.7	7.3	S	0.05	0.01	0.13		
8649	149.7187	1.84988	0.07	0.002	0.85	0.038	15.3	2.8	<11.6	<11.6	S	0.6	0.57	0.67	0.674	CK
8723	149.6389	1.90171	0.11	0.002	0.598	0.018	10.8	2.5	70.5	6.7	S	0.4	0.37	0.45		
8773	150.5394	1.92363	0.17	0.002	0.928	0.043	13.2	2.7	15.5	5.6	S	0.71	0.7	0.71		
8865	150.6876	1.97093	0.03	0.002	0.509	0.019	14.5	2.7	57.4	6.1	S	0.73	0.69	0.78		
8873	150.0004	1.97863	0.46	0.002	0.892	0.06	16.3	2.9	61.2	7.1	S	0.08	0.03	0.13		
8947	149.8137	2.02333	0.11	0.002	0.97	0.029	24.6	2.8	55.8	5.7	S	0.76	0.71	0.88	0.896	K
8966	149.5939	2.04146	0.03	0.002	0.338	0.017	11.7	2.5	26.1	5.7	S	0.78	0.7	0.83		
9020	149.7685	2.05932	0.05	0.002	0.652	0.133	13.4	2.1	20.8	5.1	S	0.93	0.89	0.96		
9035	149.7376	2.06521	0.07	0.002	0.669	0.054	12.6	2.1	67.5	6.7	S	0.81	0.78	0.83	0.678	CK
9131	150.2174	2.11408	0.03	0.002	0.282	0.017	19.2	3.1	70.2	21.5	F	1.07	1.07	1.34		
9145	150.2107	2.11728	0.10	0.002	0.652	0.018	10.7	2.6	109.4	7.8	S	1.05	0.99	1.07		
9157	150.5162	2.12328	0.22	0.002	0.691	0.018	10.7	2.6	42.0	6.8	S	0.33	0.29	0.37	0.338	CK
9164	150.1731	2.12696	0.05	0.002	0.46	0.017	11.6	2.7	34.5	6.4	S	1.37	1.32	1.46		
9167	150.4519	2.12792	0.02	0.002	0.432	0.031	11.3	2.6	13.5	5.1	S	0.81	0.77	0.86		
9219	150.5318	2.14780	0.10	0.002	0.523	0.017	13.5	2.8	30.8	5.7	S	0.33	0.26	0.36		

Continued on next page

Table A.1 – continued from previous page

ID	RA	Dec	S_8	σ_8	S_{24}	σ_{24}	S_{70}	σ_{70}	S_{160}	σ_{160}	F/S	z_{phot}	min	max	z_{spec}	Flag
9244	149.7859	2.17295	0.16	0.002	0.695	0.03	11.3	2.0	37.9	7.4	S	0.32	0.28	0.37	0.355	CK
9285	150.2130	2.19380	0.24	0.002	0.35	0.021	14.2	2.7	72.0	6.6	S	0.12	0.05	0.16	0.123	CK
9494	149.5282	2.29189	0.05	0.002	0.877	0.017	16.1	2.9	107.8	25.4	F	0.97	0.91	1.0		
9501	149.9162	2.28392	0.38	0.002	0.606	0.015	11.9	2.2	21.2	5.7	S	0.1	0.06	0.19		
9528	149.6462	2.29095	0.53	0.002	0.682	0.016	15.0	2.8	77.0	21.2	F	0.15	0.08	0.17		
9569	150.2102	2.31171	0.07	0.002	0.868	0.024	15.8	2.7	71.0	6.9	S	0.74	0.68	0.78	0.748	K
9627	149.7608	2.33037	0.30	0.002	0.353	0.059	10.4	2.2	69.6	7.4	S	0.17	0.11	0.21		
9630	150.5691	2.33303	0.09	0.002	0.96	0.029	14.9	2.7	34.0	5.7	S	0.4	0.28	0.42	0.509	K
9667	150.4115	2.35746	0.14	0.002	1.028	0.02	14.0	2.8	<11.6	<11.6	S	0.32	0.28	0.37	0.373	C
9737	149.7446	2.38859	0.07	0.002	0.439	0.015	11.3	2.5	17.4	5.9	S	0.11	0.06	0.12		
9738	149.7866	2.38753	0.04	0.002	0.277	0.014	13.3	2.2	66.9	18.4	F	1.33	1.13	1.47		
9908	150.6386	2.46682	0.22	0.002	0.262	0.079	11.5	2.6	16.7	5.4	S	0.15	0.06	0.19		
9913	150.5489	2.46907	0.84	0.002	1.229	0.02	35.6	4.0	49.8	6.2	S	0.18	0.13	0.2		
9917	149.7524	2.47081	0.04	0.002	0.171	0.016	10.3	2.6	56.1	17.8	F	0.49	0.42	0.54	0.489	CK
10135	150.6454	2.59059	0.16	0.002	0.379	0.027	10.3	2.5	44.9	7.6	S	0.2	0.18	0.26		
10170	149.9147	2.60134	0.10	0.002	0.211	0.013	10.0	2.0	42.2	6.2	S	0.23	0.2	0.29	0.245	K
10171	149.8570	2.60272	0.18	0.002	1.013	0.018	12.8	2.4	31.8	5.0	S	0.45	0.41	0.47	0.470	CK
10314	150.5988	2.67438	0.06	0.002	0.2	0.043	13.2	2.9	93.7	7.2	S	0.07	0.02	0.13		
10316	150.5180	2.68438	0.09	0.003	0.392	0.028	12.1	2.7	30.2	6.8	S	0.31	0.27	0.36	0.362	C
10357	149.8311	2.69138	0.28	0.002	0.747	0.033	14.1	3.0	75.8	7.8	S	0.3	0.23	0.35		
10375	150.5043	2.70360	0.76	0.003	0.857	0.016	29.5	3.7	76.0	22.8	F	0.19	0.17	0.22	0.224	K
10376	149.7166	2.70568	0.04	0.002	0.588	0.017	11.5	2.6	113.8	8.3	S	0.98	0.89	0.99		

Continued on next page

Table A.1 – continued from previous page

ID	RA	Dec	S_8	σ_8	S_{24}	σ_{24}	S_{70}	σ_{70}	S_{160}	σ_{160}	F/S	z_{phot}	min	max	z_{spec}	Flag
10379	149.8126	2.71498	0.01	0.002	0.271	0.068	11.4	2.6	53.6	7.9	S	0.69	0.6	0.71		
10398	150.6654	2.71866	0.08	0.003	0.736	0.016	18.3	3.0	<11.6	<11.6	S	0.35	0.29	0.42		
10497	150.5841	2.77492	0.20	0.002	0.881	0.018	13.1	2.9	66.7	7.3	S	0.21	0.04	0.21		
10503	150.4087	2.77726	0.02	0.002	0.343	0.016	12.8	2.7	104.9	9.1	S	0.85	0.8	0.9		
10504	149.7371	2.78241	0.28	0.002	0.672	0.044	12.9	2.5	<11.6	<11.6	S	0.25	0.2	0.28		
10587	150.0398	2.81351	0.10	0.002	0.762	0.022	11.9	2.2	58.0	7.9	S	0.33	0.25	0.38		
10668	150.0381	2.86272	0.17	0.002	0.444	0.038	10.7	2.3	63.6	6.5	S	0.31	0.29	0.37		
10690	150.5702	2.87372	0.53	0.002	0.848	0.058	15.5	3.6	36.2	6.9	S	0.09	0.04	0.11		
10721	150.0238	2.88252	0.08	0.002	0.591	0.019	16.1	2.7	22.0	5.4	S	0.52	0.48	0.56		
10968	150.2021	1.60204	0.07	0.002	0.407	0.016	13.4	2.9	43.9	6.9	S	0.48	0.46	0.56		
11140	150.0098	1.73681	0.40	0.002	0.647	0.103	12.9	2.7	<11.6	<11.6	S	0.26	0.21	0.27		
11152	150.4830	1.74797	0.08	0.002	0.458	0.018	21.9	3.3	63.4	20.1	F	0.51	0.47	0.55		
11164	150.5043	1.75301	0.06	0.002	0.438	0.018	12.8	2.9	29.7	5.9	S	0.51	0.48	0.57		
11171	150.2488	1.76145	0.04	0.002	0.323	0.016	22.4	3.4	81.0	22.7	F	0.53	0.51	0.6		
11217	150.0761	1.80854	0.03	0.002	0.293	0.05	10.5	2.5	24.9	6.0	S	1.08	0.93	1.44		
11218	150.5035	1.81186	0.10	0.002	0.341	0.016	19.3	3.0	73.2	20.2	F	1.05	0.96	1.11		
11220	149.7170	1.81491	0.12	0.002	0.434	0.017	20.4	3.1	122.2	8.8	S	0.4	0.33	0.45	0.419	K
11227	150.4715	1.82080	0.53	0.002	0.669	0.066	12.2	2.6	36.1	6.1	S	0.07	0.05	0.12		
11294	150.6487	1.87451	0.19	0.002	0.98	0.019	16.3	2.9	80.2	22.9	F	0.38	0.3	0.42		
11296	149.6490	1.87534	0.04	0.002	0.15	0.024	11.3	2.5	42.2	7.0	S	0.35	0.29	0.41		
11392	150.1469	1.95722	0.31	0.002	1.029	0.018	15.5	2.7	<11.6	<11.6	S	0.39	0.35	0.4	0.361	CK
11421	150.3511	1.98700	0.02	0.002	0.304	0.027	11.1	2.6	66.0	7.2	S	0.8	0.72	0.86	0.830	C

Continued on next page

Table A.1 – continued from previous page

ID	RA	Dec	S_8	σ_8	S_{24}	σ_{24}	S_{70}	σ_{70}	S_{160}	σ_{160}	F/S	z_{phot}	min	max	z_{spec}	Flag
11448	150.2588	1.98877	0.06	0.002	0.659	0.093	28.9	3.6	51.1	6.5	S	0.8	0.75	0.84	0.726	CK
11469	150.3931	2.00046	0.04	0.002	0.418	0.019	11.8	2.7	64.8	8.3	S	0.51	0.45	0.57		
11520	150.5733	2.02859	0.04	0.002	0.357	0.149	10.7	2.5	19.9	6.2	S	0.84	0.8	0.86		
11595	150.4577	2.06246	0.08	0.002	0.331	0.175	16.6	2.9	12.4	5.8	S	0.04	0.0	0.06		
11603	150.4125	2.07343	0.03	0.002	0.213	0.04	14.2	2.9	80.2	8.1	S	0.81	0.73	0.85		
11689	150.1955	2.12404	2.07	0.003	7.197	0.058	12.9	2.8	47.3	6.6	S	1.73	1.45	1.78	1.158	CK
11735	150.3459	2.14756	0.11	0.002	0.611	0.155	21.5	3.2	64.5	20.0	F	1.94	1.88	2.23	1.258	C
11778	150.0760	2.19054	0.31	0.002	0.819	0.016	14.4	3.0	43.1	8.2	S	0.25	0.17	0.29	0.223	CK
11861	150.0676	2.23324	0.38	0.002	1.082	0.028	14.6	3.0	22.5	10.3	S	0.16	0.12	0.21	0.186	CK
11893	150.5261	2.25611	0.52	0.002	1.322	0.019	14.5	2.7	38.5	6.4	S	0.2	0.18	0.22		
11966	149.6839	2.31888	0.01	0.002	0.178	0.023	10.4	2.4	24.2	6.1	S	1.86	1.63	1.98		
12056	150.5303	2.37387	0.04	0.002	0.422	0.017	28.1	3.8	174.2	9.6	S	0.7	0.66	0.78		
12096	149.7092	2.40308	0.05	0.002	0.206	0.018	17.0	2.9	58.1	7.3	S	0.37	0.32	0.42		
12106	149.6553	2.40180	0.21	0.002	0.449	0.014	11.6	2.7	85.6	7.3	S	0.21	0.13	0.23		
12120	149.9386	2.41388	0.03	0.002	0.524	0.017	10.0	1.9	<11.6	<11.6	S	0.89	0.85	0.91		
12134	149.8687	2.41880	0.08	0.002	0.678	0.016	22.0	2.6	<11.6	<11.6	S	0.49	0.43	0.5	0.400	K
12215	150.4415	2.48162	0.15	0.002	1.632	0.018	10.1	2.5	15.6	5.4	S	1.64	1.51	1.72		
12313	149.9330	2.55897	0.08	0.002	0.727	0.036	17.8	2.4	109.2	23.7	F	0.98	0.92	1.02	0.943	K
12321	150.7146	2.56801	0.66	0.003	2.112	0.024	29.8	3.7	63.7	9.4	S	0.21	0.18	0.22		
12336	149.7338	2.57495	0.08	0.002	0.814	0.051	15.9	2.7	39.8	6.0	S	0.67	0.64	0.7	0.708	CK
12339	150.2308	2.57818	0.30	0.003	1.392	0.02	11.4	2.4	19.1	6.9	S	0.22	0.02	2.31	1.401	CK
12384	150.4811	2.61115	0.59	0.002	0.529	0.17	13.7	2.7	18.0	6.3	S	0.16	0.08	0.18		

Continued on next page

Table A.1 – continued from previous page

ID	RA	Dec	S_8	σ_8	S_{24}	σ_{24}	S_{70}	σ_{70}	S_{160}	σ_{160}	F/S	z_{phot}	min	max	z_{spec}	Flag
12409	150.5916	2.63270	0.19	0.002	1.154	0.024	13.7	2.7	<11.6	<11.6	S	0.29	0.23	0.31		
12410	150.2797	2.63016	0.22	0.002	0.657	0.018	12.5	2.7	38.5	6.1	S	0.33	0.3	0.34	0.375	CK
12450	150.4271	2.65644	0.08	0.002	0.921	0.041	34.2	4.1	64.0	20.1	F	0.69	0.51	0.69	0.550	K
12466	150.2652	2.66813	0.04	0.002	0.314	0.015	12.8	2.4	78.1	20.7	F	1.24	1.14	1.34		
12473	150.7099	2.66770	0.04	0.002	0.651	0.018	13.1	2.8	37.5	6.8	S	0.69	0.59	0.7		
12517	150.4305	2.71508	0.34	0.003	0.503	0.019	12.4	2.6	28.2	5.9	S	0.09	0.04	0.14		
12524	150.3541	2.71530	0.08	0.002	0.448	0.028	14.7	2.8	76.3	22.2	F	0.3	0.23	0.37		
12530	150.5052	2.71576	0.17	0.002	0.984	0.074	13.0	2.8	<11.6	<11.6	S	0.21	0.03	0.21		
12588	150.7319	2.76129	0.30	0.002	0.791	0.034	14.6	3.2	40.1	7.0	S	0.23	0.19	0.25		
12606	150.5165	2.77613	0.21	0.003	0.235	0.044	12.2	2.6	62.1	6.7	S	0.21	0.16	0.24		
12617	149.6580	2.78562	0.28	0.002	0.749	0.026	22.2	3.2	74.1	21.0	F	0.83	0.81	0.85	0.320	CK
12621	149.8888	2.79712	0.34	0.002	0.294	0.058	10.1	2.5	30.8	7.1	S	0.06	0.02	0.13		
12643	150.4729	2.81084	0.05	0.002	0.184	0.015	14.1	2.7	27.6	5.8	S	1.2	1.08	1.3		
12647	150.3804	2.81742	0.20	0.002	0.78	0.052	14.0	2.8	93.2	25.7	F	0.34	0.31	0.37		
12653	150.6104	2.81862	0.02	0.002	0.343	0.02	13.9	3.2	<11.6	<11.6	S	0.86	0.79	0.9		
12709	150.3803	2.86635	0.01	0.002	0.166	0.054	12.3	3.0	190.4	10.3	S	2.17	1.67	2.29		
12723	150.0808	2.87542	0.13	0.002	0.46	0.027	10.4	2.5	84.1	7.8	S	0.13	0.07	0.17		
12726	149.5891	2.88305	0.43	0.002	1.742	0.02	15.4	2.9	43.7	5.7	S	0.31	0.36	2.5		
12844	149.7901	1.58414	0.10	0.002	1.313	0.019	13.5	2.7	56.3	6.4	S	0.29	1.48	1.92		
12865	150.6546	1.65128	0.18	0.002	0.817	0.02	13.8	2.6	<11.6	<11.6	S	0.39	0.36	0.42		
12929	149.5909	1.79005	0.21	0.002	0.861	0.032	30.6	3.7	62.7	19.2	F	0.43	0.42	0.52		
12956	149.6924	1.85934	0.43	0.002	0.7	0.021	14.1	2.7	24.4	5.3	S	0.13	0.07	0.17		

Continued on next page

Table A.1 – continued from previous page

ID	RA	Dec	S_8	σ_8	S_{24}	σ_{24}	S_{70}	σ_{70}	S_{160}	σ_{160}	F/S	z_{phot}	min	max	z_{spec}	Flag
12979	150.0307	1.91324	0.11	0.002	0.317	0.133	11.4	2.5	12.5	5.8	S	0.15	0.08	0.19	0.174	CK
12998	150.2340	1.94515	0.28	0.002	1.036	0.02	15.3	2.8	21.8	5.8	S	0.41	0.36	0.43	0.360	K
13008	150.0518	1.96124	0.18	0.002	0.566	0.117	10.0	2.4	<11.6	<11.6	S	0.41	0.38	0.42	0.356	CK
13050	150.1476	2.06368	0.02	0.002	0.33	0.054	10.4	2.6	65.2	6.5	S	0.71	0.61	0.77		
13051	149.6288	2.05950	0.05	0.002	0.677	0.02	12.6	2.3	58.0	18.6	F	0.56	0.54	0.64		
13077	150.4634	2.12085	0.14	0.002	0.627	0.019	18.1	2.8	56.9	6.8	S	0.39	0.35	0.44		
13097	150.6163	2.16800	0.04	0.002	0.387	0.015	12.5	2.7	81.4	22.5	F	1.66	1.48	1.72		
13107	150.3701	2.19653	0.03	0.002	0.47	0.05	17.7	3.1	37.8	6.3	S	0.88	0.82	0.94	0.919	K
13152	149.9353	2.29998	0.03	0.002	0.273	0.02	11.0	2.2	71.1	18.0	F	0.99	0.91	1.02		
13164	150.6312	2.32704	0.35	0.002	1.087	0.026	22.1	3.3	56.4	6.4	S	0.22	0.19	0.23	0.184	K
13167	149.8983	2.33070	0.07	0.002	0.999	0.03	12.6	2.2	47.8	15.4	F	1.08	0.92	1.1		
13186	150.5395	2.36422	0.11	0.002	0.839	0.047	19.4	3.3	61.0	6.7	S	0.28	0.2	0.36	0.501	K
13194	150.5939	2.38414	0.30	0.002	1.443	0.018	20.5	3.1	55.6	5.9	S	0.25	0.2	0.26		
13253	149.9485	2.47968	0.34	0.002	0.976	0.017	11.4	2.0	54.4	5.8	S	0.24	0.2	0.3	0.247	K
13321	150.7406	2.65490	0.09	0.002	0.45	0.016	10.5	2.5	58.5	18.4	F	0.46	0.42	0.52		
13331	149.5288	2.67216	0.02	0.002	0.309	0.015	10.1	2.5	42.6	6.8	S	0.72	0.67	0.82		
13342	150.2232	2.69025	0.04	0.002	0.242	0.042	11.8	2.1	64.8	18.0	F	1.34	1.28	1.39	1.294	C
13350	149.7162	2.71095	0.02	0.002	0.25	0.134	10.8	2.5	82.9	22.9	F	1.07	0.99	1.11		
13485	150.7216	1.52685	0.16	0.002	1.886	0.03	62.0	5.7	162.3	36.9	F	0.63	0.61	0.64	0.629	A
13502	150.6051	1.52393	0.03	0.002	0.258	0.061	11.3	2.7	41.0	6.3	S	0.95	0.91	1.0		
13508	150.3632	1.52979	0.07	0.002	0.352	0.015	13.2	2.6	72.4	22.0	F	0.49	2.34	2.84		
13549	149.6641	1.55973	0.07	0.002	1.203	0.023	23.4	3.5	82.0	8.5	S	0.56	0.28	0.35		

Continued on next page

Table A.1 – continued from previous page

ID	RA	Dec	S_8	σ_8	S_{24}	σ_{24}	S_{70}	σ_{70}	S_{160}	σ_{160}	F/S	z_{phot}	min	max	z_{spec}	Flag
13561	150.3358	1.56515	0.76	0.003	0.613	0.039	15.6	2.8	108.8	27.4	F	0.09	0.2	0.29		
13603	150.3891	1.59655	0.09	0.002	0.751	0.038	10.8	2.5	37.3	6.1	S	0.21	0.2	0.23		
13619	150.6325	1.61188	0.27	0.002	1.692	0.024	35.5	4.3	51.5	7.0	S	0.85	0.74	0.98		
13632	150.0448	1.61927	0.08	0.002	0.958	0.017	22.9	3.3	43.0	6.0	S	0.52	0.48	0.55		
13645	150.3516	1.63455	0.76	0.002	0.577	0.062	17.8	3.0	53.8	7.4	S	0.1	0.06	0.16	0.081	K
13672	150.2069	1.68029	0.42	0.002	0.591	0.078	17.3	3.3	85.8	9.3	S	1.32	1.28	1.38		
13685	150.1624	1.71450	0.02	0.002	0.493	0.017	11.0	2.5	90.6	7.9	S	0.61	0.58	0.68		
13707	150.5704	1.72144	0.06	0.002	0.925	0.024	18.2	2.8	58.8	18.7	F	1.5	1.46	1.54		
13708	149.9904	1.72104	0.13	0.002	0.815	0.038	14.2	2.6	33.6	5.9	S	0.37	0.32	0.41		
13730	149.5924	1.75676	2.31	0.003	12.822	0.144	34.8	3.9	82.7	22.8	F	0.01	0.0	0.01	1.960	K
13735	149.5864	1.76932	1.06	0.002	5.02	0.04	11.9	2.7	58.8	6.4	S	1.54	1.5	1.58	0.787	CK
13752	149.8518	1.78107	0.39	0.002	0.752	0.019	22.2	3.2	78.7	22.3	F	0.1	0.07	0.14	0.127	CK
13773	150.0415	1.80126	0.24	0.002	0.704	0.019	12.6	2.6	24.5	5.8	S	0.27	0.25	0.29	0.267	K
13803	150.3712	1.84906	0.08	0.002	0.329	0.026	12.5	2.5	56.8	6.5	S	0.46	0.38	0.5		
13813	150.4547	1.84666	0.07	0.002	0.475	0.016	10.4	2.5	<11.6	<11.6	S	1.34	1.24	1.43		
13820	150.6740	1.85340	0.07	0.002	0.669	0.018	12.6	2.6	<11.6	<11.6	S	0.52	0.47	0.56	0.512	C
13834	150.6602	1.86351	0.03	0.002	1.049	0.02	13.4	2.6	33.5	6.0	S	0.65	0.64	0.65		
13841	150.3328	1.86820	0.01	0.002	0.213	0.017	10.2	2.4	41.9	6.8	S	1.55	1.46	1.66		
13845	150.2304	1.87190	0.01	0.002	0.195	0.086	12.4	2.5	63.0	6.7	S	0.74	0.61	0.79	0.795	K
13864	150.7263	1.89342	0.03	0.002	0.346	0.027	12.2	2.7	46.8	6.7	S	0.69	0.64	0.71		
13881	149.6082	1.90173	0.12	0.002	0.708	0.083	10.6	2.4	<11.6	<11.6	S	0.43	0.4	0.51	0.477	K
13891	149.5487	1.91969	0.08	0.002	0.289	0.044	13.2	2.6	62.3	6.9	S	0.22	0.06	0.22		

Continued on next page

Table A.1 – continued from previous page

ID	RA	Dec	S_8	σ_8	S_{24}	σ_{24}	S_{70}	σ_{70}	S_{160}	σ_{160}	F/S	z_{phot}	min	max	z_{spec}	Flag
13903	150.7417	1.91765	0.06	0.002	0.964	0.022	15.1	2.8	48.6	6.5	S	0.7	0.69	1.01		
13956	150.2778	1.96767	0.07	0.002	0.86	0.019	11.3	2.6	24.1	5.5	S	0.38	0.31	0.42		
13989	149.5691	2.00635	0.27	0.002	0.358	0.063	11.5	2.5	59.7	8.1	S	0.22	0.19	0.26	0.223	CK
13990	149.9993	2.00599	0.13	0.002	1.424	0.021	26.8	3.7	23.4	6.1	S	0.72	0.68	0.78	0.761	CK
14047	150.2984	2.05397	0.03	0.002	0.358	0.114	10.4	2.5	<11.6	<11.6	S	0.76	0.75	1.47		
14115	150.3066	2.11494	0.24	0.002	1.921	0.025	23.9	3.4	<11.6	<11.6	S	0.28	0.26	0.31		
14225	150.0566	2.20855	1.09	0.003	6.892	0.077	157.0	10.9	187.4	37.4	F	0.18	0.12	0.18	0.182	K
14266	150.4084	2.23075	0.43	0.002	0.46	0.127	11.5	2.6	42.4	6.0	S	0.23	0.21	0.26		
14289	149.7237	2.24308	0.06	0.002	0.393	0.041	10.6	2.1	67.3	20.0	F	0.54	0.49	0.57	0.558	C
14290	150.0676	2.24300	0.23	0.002	0.95	0.021	10.4	2.5	<11.6	<11.6	S	0.34	0.3	0.39	0.345	CK
14323	150.7022	2.26580	0.21	0.002	0.908	0.019	18.7	3.0	<11.6	<11.6	S	0.3	0.29	0.36		
14330	150.0075	2.27426	0.07	0.002	0.344	0.019	13.1	2.1	71.3	19.3	F	0.43	0.36	0.45	0.472	CK
14352	149.7322	2.29642	0.65	0.002	1.182	0.019	19.1	2.6	<11.6	<11.6	S	0.15	0.1	0.19	0.130	CK
14386	150.3190	2.32231	0.03	0.002	0.185	0.017	10.5	2.6	62.6	19.4	F	0.14	0.06	0.16	0.166	C
14398	149.7527	2.33176	0.17	0.002	0.682	0.041	10.7	2.3	63.5	7.8	S	0.31	0.29	0.38	0.334	CK
14513	149.6462	2.43805	0.01	0.002	0.281	0.018	13.7	2.7	40.2	7.2	S	0.99	0.93	1.03		
14530	150.4525	2.45038	0.43	0.002	1.747	0.022	30.0	3.7	<11.6	<11.6	S	0.24	0.17	0.28		
14543	149.9757	2.46148	0.21	0.002	0.864	0.029	11.2	1.9	42.3	5.6	S	0.34	0.27	0.41	0.346	CK
14552	149.7746	2.47117	0.04	0.002	0.49	0.019	16.5	2.9	55.6	7.0	S	0.76	0.67	0.79		
14560	150.1502	2.47520	0.78	0.002	3.822	0.031	48.6	4.1	92.7	21.7	F	0.79	0.73	0.8	0.688	CK
14567	149.6837	2.47888	0.18	0.002	0.738	0.041	17.5	2.9	85.7	9.8	S	0.31	0.01	0.33		
14573	149.5828	2.48433	0.96	0.002	3.614	0.029	13.7	2.5	<11.6	<11.6	S	1.21	1.19	1.28	0.345	K

Continued on next page

Table A.1 – continued from previous page

ID	RA	Dec	S_8	σ_8	S_{24}	σ_{24}	S_{70}	σ_{70}	S_{160}	σ_{160}	F/S	z_{phot}	min	max	z_{spec}	Flag
14633	150.2937	2.54064	0.31	0.002	1.465	0.021	42.0	4.3	84.5	24.1	F	0.32	0.26	0.36	0.376	K
14636	150.6852	2.54292	0.03	0.002	0.487	0.016	10.6	2.6	74.8	23.2	F	0.87	0.77	0.97		
14652	150.6814	2.56167	0.33	0.003	1.19	0.021	27.5	3.7	85.6	25.2	F	0.32	0.29	0.36	0.351	C
14659	150.4144	2.56432	0.44	0.002	1.109	0.027	21.5	3.2	90.2	9.0	S	0.25	0.22	0.26	0.213	CK
14686	150.6973	2.60841	0.52	0.003	0.802	0.022	15.1	2.7	26.5	5.9	S	0.1	0.06	0.15		
14728	149.7247	2.64566	0.40	0.003	1.324	0.021	10.8	2.6	<11.6	<11.6	S	0.35	0.32	0.41		
14735	150.1599	2.65436	0.07	0.002	0.807	0.068	19.5	2.5	72.9	18.4	F	0.85	0.81	0.88		
14815	149.9660	2.72424	0.39	0.002	1.214	0.021	15.6	2.3	33.6	4.9	S	0.06	0.04	0.16	0.151	K
14921	149.9417	2.79545	0.96	0.003	3.763	0.024	12.4	2.6	<11.6	<11.6	S	0.03	0.01	0.03	1.066	K
14938	150.4010	2.81059	0.20	0.002	0.712	0.018	11.4	2.7	62.7	8.1	S	0.32	0.25	0.36		
14947	149.9451	2.82042	0.61	0.002	0.775	0.02	16.6	3.0	24.0	5.6	S	0.12	0.07	0.14	0.104	K
15097	150.0673	1.59524	0.19	0.002	1.224	0.022	23.4	3.3	28.9	5.2	S	0.32	0.28	0.35		
15138	150.2283	1.76731	0.30	0.002	1.928	0.022	28.7	3.8	47.3	6.5	S	0.31	0.29	0.35	0.350	CK
15157	149.7256	1.81087	0.06	0.002	1.227	0.022	28.2	3.6	110.2	25.5	F	0.86	0.8	0.88	0.752	CK
15196	150.1962	1.94821	0.06	0.002	0.653	0.051	12.6	2.6	<11.6	<11.6	S	0.4	0.3	0.45		
15224	149.9676	2.09832	0.48	0.002	0.513	0.016	12.8	2.3	71.9	20.7	F	0.28	0.26	0.29		
15240	150.3227	2.12390	1.01	0.002	1.613	0.036	24.8	3.5	33.5	6.1	S	0.19	0.17	0.21	0.187	CK
15263	150.1595	2.19148	0.06	0.002	0.563	0.158	17.1	3.0	49.3	6.4	S	1.56	1.51	1.61	0.924	K
15271	150.7132	2.20944	0.14	0.002	0.65	0.084	11.6	2.5	54.3	6.5	S	0.28	0.22	0.33		
15277	150.0956	2.22017	1.62	0.003	8.203	0.066	75.9	6.4	57.8	7.5	S	0.06	0.05	0.08	0.186	ACK
15278	149.5250	2.22394	0.37	0.002	1.202	0.025	15.5	2.8	<11.6	<11.6	S	0.09	0.04	0.15		
15340	150.0221	2.42105	0.02	0.002	0.26	0.02	10.1	1.9	50.1	14.8	F	0.98	0.85	1.06		

Continued on next page

Table A.1 – continued from previous page

ID	RA	Dec	S_8	σ_8	S_{24}	σ_{24}	S_{70}	σ_{70}	S_{160}	σ_{160}	F/S	z_{phot}	min	max	z_{spec}	Flag
15341	150.3835	2.42081	0.20	0.002	1.02	0.021	17.3	3.1	79.5	23.2	F	0.47	0.42	0.5	0.478	K
15349	149.6962	2.43930	0.13	0.002	0.712	0.041	14.4	2.8	99.9	10.4	S	0.45	0.36	0.5		
15359	149.6751	2.47548	0.04	0.002	0.592	0.075	15.5	2.7	87.3	9.4	S	0.96	0.9	0.99		
15396	150.3744	2.58530	0.36	0.002	0.505	0.054	14.0	2.8	57.5	7.1	S	0.18	0.13	0.22		
15414	150.5079	2.67563	0.04	0.002	0.457	0.021	13.2	2.9	21.4	6.6	S	1.24	1.1	1.31		
15436	150.6452	2.71480	0.45	0.002	1.239	0.022	10.6	2.6	44.5	5.6	S	0.42	0.4	0.43	0.196	K
15522	150.3630	1.62933	0.12	0.002	0.792	0.028	19.6	3.1	64.9	7.0	S	0.55	0.51	0.59	0.526	K
15551	150.2887	1.91007	0.39	0.002	0.699	0.019	13.0	2.7	78.2	6.8	S	0.16	0.14	0.22	0.673	K
15600	149.9403	2.27153	0.17	0.002	0.466	0.069	11.7	1.9	22.2	5.9	S	0.38	0.3	0.41	0.350	C
15607	149.9937	2.30407	0.57	0.002	0.653	0.02	14.7	2.2	19.7	5.0	S	0.06	0.03	0.15	0.093	CK
15609	150.3780	2.31825	0.09	0.002	1.263	0.02	13.4	2.6	63.0	6.4	S	1.59	1.54	1.8		
15615	149.5789	2.37072	0.07	0.002	0.845	0.055	13.1	2.6	16.4	5.1	S	2.8	0.2	0.3		
15652	150.4874	2.62046	0.36	0.002	0.778	0.022	12.0	2.7	<11.6	<11.6	S	0.12	0.09	0.17		
15661	149.7341	2.69112	0.19	0.002	1.712	0.027	48.0	4.7	92.5	24.1	F	0.72	0.71	0.82	0.910	CK
15668	150.2198	2.72573	0.21	0.002	1.501	0.019	12.3	2.3	<11.6	<11.6	S	0.21	0.1	0.22		
15695	149.9102	2.89149	0.80	0.002	1.966	0.022	60.8	5.5	115.1	27.0	F	0.2	0.17	2.91		
15732	150.4325	1.54994	0.06	0.002	0.53	0.02	10.8	2.3	33.8	5.7	S	0.95	0.92	1.03		
15733	149.6761	1.55077	0.15	0.002	1.64	0.021	20.3	3.4	93.5	28.4	F	0.68	2.16	2.49		
15736	150.0164	1.56469	0.06	0.002	0.899	0.019	14.8	2.8	52.7	6.3	S	0.85	0.82	0.87		
15749	150.1732	1.61631	0.26	0.002	1.686	0.024	31.5	4.0	97.9	25.0	F	0.71	0.69	0.71	0.995	K
15759	150.1823	1.70083	0.52	0.002	1.791	0.023	17.0	3.0	71.3	8.9	S	0.69	0.63	0.73	0.741	K
15770	149.6390	1.75080	0.10	0.002	0.44	0.024	12.5	2.6	29.3	7.3	S	0.38	0.36	0.43		

Continued on next page

Table A.1 – continued from previous page

ID	RA	Dec	S_8	σ_8	S_{24}	σ_{24}	S_{70}	σ_{70}	S_{160}	σ_{160}	F/S	z_{phot}	min	max	z_{spec}	Flag
15788	150.6525	1.81004	0.31	0.002	0.646	0.031	19.2	3.1	78.6	22.5	F	0.04	0.03	0.18		
15797	149.9996	1.87113	0.43	0.002	0.681	0.019	13.5	2.6	34.6	6.3	S	0.31	0.29	0.32		
15800	150.6522	1.87725	0.15	0.002	0.581	0.016	13.7	2.8	81.5	7.8	S	0.37	0.32	0.39		
15808	150.1379	1.90395	0.87	0.002	3.505	0.028	53.3	5.0	18.7	5.2	S	0.2	0.18	0.21	0.220	ACK
15826	149.5499	1.93961	0.06	0.002	0.881	0.017	12.3	2.6	63.5	7.7	S	0.71	0.68	0.73		
15851	150.1764	2.01397	0.06	0.002	0.929	0.021	15.4	2.8	<11.6	<11.6	S	0.52	0.44	0.55	0.572	K
15859	150.0249	2.03941	0.20	0.002	0.984	0.024	12.7	2.7	57.0	7.1	S	0.31	0.29	0.31		
15864	149.5286	2.06650	0.06	0.002	0.708	0.02	16.6	2.9	79.6	7.0	S	0.53	0.47	0.56	0.571	C
15885	150.0295	2.12420	0.35	0.002	0.718	0.02	11.2	2.6	14.7	5.5	S	0.23	0.15	0.25		
15889	149.5280	2.12726	0.11	0.002	1.415	0.02	81.3	6.5	109.3	26.8	F	0.54	0.51	0.57	0.479	K
15899	149.8152	2.14910	0.85	0.002	2.805	0.027	24.9	2.9	45.6	6.9	S	0.16	0.14	0.2	0.168	K
15902	150.5129	2.15207	0.08	0.002	0.72	0.02	14.2	2.8	25.3	5.4	S	0.52	0.43	0.54	0.556	CK
15933	149.7928	2.28592	0.13	0.002	1.319	0.021	15.0	2.3	70.7	21.2	F	0.46	0.43	0.52		
15939	150.0940	2.29913	0.05	0.002	0.869	0.019	12.0	2.3	111.2	8.3	S	0.61	0.55	0.67	0.688	CK
15946	149.7086	2.33490	0.86	0.002	0.811	0.053	17.8	2.9	75.4	22.2	F	0.19	0.18	0.23	0.175	CK
15954	149.7570	2.37740	0.77	0.003	1.464	0.028	16.3	2.6	54.2	7.3	S	0.23	0.2	0.25		
15984	150.3223	2.50444	0.33	0.002	0.71	0.022	10.8	2.6	31.3	7.1	S	0.21	0.15	0.24	0.221	C
15997	150.5521	2.53885	0.27	0.002	0.707	0.019	11.6	2.6	18.3	5.9	S	0.22	0.16	0.25		
16004	150.2526	2.55148	0.03	0.002	0.473	0.019	12.8	2.6	26.3	7.2	S	0.66	0.55	0.7		
16006	150.4280	2.55865	0.25	0.002	0.835	0.036	13.3	2.9	99.5	25.6	F	1.25	1.22	1.31		
16015	150.1233	2.60378	0.07	0.002	1.026	0.021	16.9	2.4	70.0	18.1	F	0.71	0.68	0.73	0.681	CK
16032	150.6073	2.67452	2.06	0.003	4.341	0.042	67.0	5.8	102.6	25.3	F	0.1	0.07	0.18	0.094	AK

Continued on next page

Table A.1 – continued from previous page

ID	RA	Dec	S_8	σ_8	S_{24}	σ_{24}	S_{70}	σ_{70}	S_{160}	σ_{160}	F/S	z_{phot}	min	max	z_{spec}	Flag
16035	150.1080	2.69560	0.25	0.002	1.183	0.019	26.6	3.0	91.1	21.0	F	0.29	0.27	0.31	0.349	CK
16059	150.6931	2.76935	0.39	0.002	2.329	0.026	18.9	3.4	21.6	6.4	S	0.21	0.16	0.22		
16087	149.6734	2.87812	0.33	0.002	1.429	0.037	17.2	2.8	67.0	20.3	F	0.3	0.26	0.31		
16092	150.0686	2.87922	0.06	0.002	0.408	0.018	16.4	2.8	54.2	7.1	S	2.3	2.07	2.44		
16094	149.8484	2.88930	0.10	0.002	0.767	0.02	18.7	3.1	88.1	7.6	S	0.42	0.74	2.55		
16146	150.3223	1.61070	0.13	0.002	0.65	0.02	14.4	2.9	64.6	8.5	S	0.34	0.29	0.41		
16147	150.1549	1.62622	0.28	0.002	0.524	0.021	12.1	2.8	52.0	7.9	S	0.2	0.16	0.26		
16151	149.7912	1.62994	0.08	0.002	0.376	0.017	15.7	2.7	47.9	7.4	S	0.69	0.65	0.7	0.526	CK
16167	149.8962	1.76097	0.19	0.002	0.565	0.019	10.0	2.5	34.9	7.1	S	0.43	0.41	0.52		
16169	149.8869	1.76976	0.45	0.002	1.004	0.059	17.2	3.0	<11.6	<11.6	S	0.12	0.06	0.14		
16172	149.9145	1.78335	0.12	0.002	0.337	0.017	10.7	2.7	99.2	8.1	S	0.21	0.17	0.26		
16173	150.0545	1.78720	0.12	0.002	0.436	0.017	17.7	2.8	43.0	6.5	S	0.36	0.29	0.4	0.402	CK
16180	149.5547	1.81882	1.34	0.002	3.236	0.036	40.5	4.3	44.9	5.7	S	0.1	0.06	0.17	0.127	K
16188	150.4326	1.89033	0.06	0.002	0.78	0.022	11.6	2.7	19.0	5.0	S	1.04	0.99	1.06	1.066	C
16191	150.7284	1.90034	0.09	0.002	0.39	0.019	11.0	2.6	36.1	6.6	S	0.57	0.49	0.57		
16199	150.4815	2.01365	0.06	0.002	0.677	0.064	43.2	4.5	171.1	35.4	F	0.68	0.65	0.7		
16205	150.7496	2.04710	0.16	0.002	1.768	0.025	27.3	3.5	81.5	23.1	F	0.57	0.54	0.59		
16212	150.2279	2.11381	0.03	0.002	0.231	0.02	10.4	2.6	41.9	6.4	S	1.24	1.21	1.37		
16250	150.3991	2.42118	1.05	0.003	1.469	0.04	25.3	3.6	76.9	23.1	F	0.16	0.07	0.21		
16278	150.6339	2.59370	0.64	0.002	2.163	0.024	13.2	2.8	<11.6	<11.6	S	1.95	1.88	2.03	0.658	K
16298	149.7852	2.74782	0.09	0.002	0.512	0.056	12.9	2.7	65.5	19.7	F	0.8	0.74	0.83		
16318	150.5163	2.87506	0.62	0.003	4.454	0.029	59.4	6.3	95.8	29.1	F	0.21	0.65	2.55		

Continued on next page

Table A.1 – continued from previous page

ID	RA	Dec	S_8	σ_8	S_{24}	σ_{24}	S_{70}	σ_{70}	S_{160}	σ_{160}	F/S	z_{phot}	min	max	z_{spec}	Flag
16336	150.0507	1.56904	0.20	0.002	1.062	0.027	16.7	2.8	29.4	5.3	S	0.36	0.33	0.37		
16338	150.6204	1.59563	0.22	0.002	1.734	0.033	22.6	3.5	52.9	6.9	S	0.57	0.46	0.56		
16360	150.6807	2.22639	0.01	0.002	0.166	0.017	12.4	2.9	82.8	8.2	S	1.02	0.76	1.02		
16363	150.6676	2.24732	0.36	0.002	2.466	0.028	143.4	10.3	239.9	43.9	F	0.29	0.27	0.32	0.358	K
16398	150.6088	2.85953	0.05	0.002	0.68	0.02	16.5	3.5	82.6	8.0	S	0.91	0.87	0.97		
16413	149.9980	1.53096	0.09	0.002	1.314	0.025	15.8	2.8	66.9	21.0	F	0.98	0.96	1.05		
16417	150.0773	1.54572	0.20	0.002	0.931	0.021	15.0	2.7	<11.6	<11.6	S	0.26	1.27	1.85		
16431	150.3316	1.64276	0.18	0.002	1.98	0.029	47.3	4.7	67.4	21.1	F	0.29	0.26	0.32	0.368	ACK
16433	150.7098	1.64319	0.06	0.002	0.478	0.022	11.6	2.6	52.4	5.7	S	0.61	0.57	0.67		
16437	149.8128	1.70534	0.12	0.002	1.067	0.027	15.8	2.8	92.7	7.1	S	0.39	0.35	0.42	0.446	K
16444	149.5110	1.90544	0.13	0.002	0.495	0.018	13.5	2.6	19.9	4.8	S	0.33	0.3	0.83		
16447	149.8944	1.94756	0.04	0.002	0.626	0.062	12.3	2.2	43.0	5.7	S	0.75	0.7	0.79	0.772	CK
16449	150.3010	1.97846	0.14	0.002	0.692	0.063	10.9	2.4	<11.6	<11.6	S	0.41	0.33	0.41	0.389	K
16475	149.7468	2.18849	0.98	0.002	1.91	0.034	29.0	3.1	78.8	22.1	F	0.2	0.11	0.22		
16477	149.5411	2.21043	0.24	0.002	0.587	0.017	10.2	2.5	<11.6	<11.6	S	0.27	0.19	0.3		
16480	149.8467	2.26530	1.30	0.003	2.908	0.037	33.4	3.3	32.1	5.6	S	0.09	0.06	0.11		
16481	150.4129	2.27910	0.47	0.002	1.896	0.024	37.6	4.1	54.1	8.1	S	0.29	0.27	0.31		
16488	149.7897	2.30243	0.03	0.002	1.063	0.019	14.1	2.3	44.7	6.6	S	0.6	0.54	0.69		
16491	150.2344	2.33707	0.05	0.002	0.854	0.071	10.4	2.5	68.3	21.2	F	0.87	0.82	0.95		
16525	149.5736	2.81511	0.26	0.002	1.145	0.027	11.5	2.6	27.3	5.6	S	0.29	0.27	0.37		
16556	150.6328	1.99072	0.04	0.002	2.314	0.026	33.4	3.8	46.6	6.5	S	0.8	0.71	0.87	0.803	K
16568	149.9056	2.31831	0.41	0.002	2.155	0.017	10.1	2.1	52.5	6.3	S	1.03	0.98	1.06	0.927	CK

Continued on next page

Table A.1 – continued from previous page

ID	RA	Dec	S_8	σ_8	S_{24}	σ_{24}	S_{70}	σ_{70}	S_{160}	σ_{160}	F/S	z_{phot}	min	max	z_{spec}	Flag
16570	150.0950	2.42519	0.29	0.002	1.17	0.037	14.4	2.2	28.2	5.8	S	0.32	0.28	0.33	0.348	CK
16571	150.2286	2.43988	0.11	0.002	0.543	0.021	12.6	2.8	58.7	6.3	S	0.42	0.4	0.5		
16574	149.9106	2.55468	0.12	0.002	1.031	0.023	10.0	1.9	50.1	15.9	F	0.69	0.66	0.71	0.753	CK
16578	150.3490	2.65952	1.06	0.003	2.224	0.025	46.3	4.7	105.1	25.5	F	0.24	0.18	0.25	0.221	CK
16579	149.6929	2.66389	0.48	0.002	1.073	0.024	13.9	2.6	38.6	6.6	S	0.15	0.11	0.21		
16582	149.6813	2.68112	0.07	0.002	1.187	0.019	21.5	3.0	51.9	6.3	S	0.63	0.56	0.65		
16583	150.4892	2.73026	0.30	0.002	0.685	0.063	16.8	2.8	40.7	6.3	S	0.21	0.15	0.25		
16627	150.3726	1.60938	1.52	0.002	4.345	0.042	35.4	4.0	61.3	19.3	F	0.12	0.04	0.17	0.104	K
16628	149.7678	1.63394	0.76	0.002	1.641	0.026	21.3	3.1	62.4	7.4	S	0.22	0.17	0.25	0.206	K
16629	150.3198	1.65606	0.22	0.002	1.125	0.027	19.1	3.0	73.3	21.8	F	0.3	0.25	0.34		
16635	150.6953	1.74044	0.31	0.002	1.204	0.023	31.5	3.8	95.6	23.9	F	0.4	0.37	0.41		
16637	150.1930	1.75240	0.46	0.002	1.14	0.031	10.5	2.5	18.4	5.4	S	0.27	0.24	0.29	0.266	CK
16640	149.8107	1.84479	0.30	0.002	1.316	0.019	14.2	2.7	13.2	6.7	S	0.21	0.09	0.23	0.166	CK
16642	150.0679	1.85134	0.22	0.002	1.661	0.032	12.2	2.6	<11.6	<11.6	S	1.7	1.66	1.76	1.134	K
16644	149.7510	1.85476	0.27	0.002	1.818	0.023	13.2	2.7	<11.6	<11.6	S	1.37	1.12	1.42		
16656	150.2710	2.05002	0.40	0.002	0.865	0.019	14.4	2.8	49.3	6.5	S	0.05	0.04	0.11		
16666	149.7404	2.17823	0.31	0.002	1.463	0.023	27.6	3.0	106.1	7.7	S	0.34	0.32	0.38		
16668	150.2502	2.21459	0.21	0.002	1.105	0.018	11.8	2.6	68.4	6.7	S	0.47	0.45	0.52	0.496	CK
16670	149.7439	2.24975	0.68	0.002	2.681	0.026	14.9	2.4	29.8	6.0	S	0.14	0.1	0.2	0.133	CK
16676	149.7688	2.31281	0.37	0.002	1.693	0.022	32.9	3.3	81.7	22.7	F	0.31	0.29	0.34		
16677	150.4895	2.32665	0.18	0.002	0.857	0.022	13.7	2.7	<11.6	<11.6	S	0.36	0.33	0.38		
16686	150.0923	2.48203	0.48	0.002	1.261	0.03	18.6	2.4	53.6	15.2	F	0.24	0.21	0.27	0.250	K

Continued on next page

Table A.1 – continued from previous page

ID	RA	Dec	S_8	σ_8	S_{24}	σ_{24}	S_{70}	σ_{70}	S_{160}	σ_{160}	F/S	z_{phot}	min	max	z_{spec}	Flag
16691	149.8090	2.52643	0.07	0.002	0.475	0.018	12.1	2.4	<11.6	<11.6	S	0.44	0.41	0.53		
16702	150.4259	2.72520	1.12	0.002	4.742	0.038	15.5	2.7	22.1	5.5	S	1.77	1.7	1.83		
16706	149.8226	2.79693	0.85	0.002	2.097	0.034	27.5	3.7	83.7	22.7	F	0.2	0.15	0.23		
16711	150.5379	2.86264	0.67	0.002	1.498	0.022	19.2	3.6	103.8	10.1	S	0.06	0.32	2.55		
16723	150.1984	1.67184	0.84	0.002	1.709	0.046	24.7	3.6	85.6	24.0	F	0.31	0.28	0.33		
16724	149.5723	1.73705	0.25	0.002	1.726	0.025	20.1	3.0	15.0	4.3	S	0.52	0.47	0.54	0.477	K
16726	149.7685	1.80341	0.18	0.002	0.881	0.025	12.8	2.6	26.6	6.5	S	0.44	0.41	0.52	0.480	C
16729	149.9977	1.87531	0.32	0.002	0.55	0.046	11.3	2.5	23.8	6.0	S	0.17	0.16	0.21	0.187	CK
16730	149.8954	1.87809	0.68	0.002	2.348	0.026	24.8	3.4	72.6	7.5	S	0.08	0.07	0.18	0.134	CK
16734	150.5304	2.07727	0.70	0.002	0.826	0.026	15.5	2.8	18.2	5.7	S	0.2	0.18	0.21		
16743	150.6638	2.51810	0.28	0.002	1.053	0.024	18.3	2.9	22.7	5.8	S	0.4	0.37	0.41	0.403	C
16744	150.2202	2.52456	0.05	0.002	0.634	0.022	13.0	2.6	57.2	6.7	S	0.3	0.25	0.35	0.376	CK
16745	150.4930	2.58476	0.06	0.002	0.635	0.02	11.1	2.6	38.8	6.9	S	1.19	0.8	1.21		
16746	149.9079	2.60894	0.44	0.002	1.128	0.029	14.3	2.2	29.7	5.3	S	0.3	0.28	0.33	0.265	K
16774	149.5094	2.23190	0.39	0.002	0.996	0.033	12.4	2.5	12.2	5.5	S	0.27	0.25	0.32	0.282	CK
16784	149.6794	2.43304	0.29	0.002	1.031	0.023	15.9	2.9	68.4	10.1	S	0.3	0.26	0.31		
16788	150.3768	2.71566	0.25	0.002	2.932	0.028	15.1	2.8	51.4	7.2	S	0.96	0.9	1.01		
16795	150.1660	2.15589	0.74	0.002	1.06	0.029	17.8	2.9	71.6	6.5	S	0.09	0.06	0.14	0.106	CK
16812	150.6251	1.80292	1.26	0.003	3.039	0.029	32.9	3.8	77.3	22.1	F	3.0	2.99	3.0		
16813	149.5120	2.68915	0.42	0.002	1.183	0.023	14.5	2.8	18.2	6.0	S	0.23	0.2	0.27		
16815	150.3653	1.98716	0.58	0.002	0.722	0.018	14.7	2.9	63.3	7.4	S	0.21	0.15	0.21		
16816	149.7301	1.58603	0.39	0.002	5.861	0.047	98.2	7.6	122.2	30.2	F	0.65	0.64	0.67	0.623	A

Continued on next page

Table A.1 – continued from previous page

ID	RA	Dec	S_8	σ_8	S_{24}	σ_{24}	S_{70}	σ_{70}	S_{160}	σ_{160}	F/S	z_{phot}	min	max	z_{spec}	Flag
16818	149.9337	1.58983	0.64	0.002	1.252	0.032	14.9	2.7	53.1	6.1	S	0.25	0.33	0.7		
16819	149.8501	2.77711	1.71	0.003	1.848	0.038	36.5	4.2	113.3	28.0	F	0.14	0.13	0.18		
16850	149.7450	1.52115	0.15	0.002	1.032	0.098	20.6	3.4	52.8	8.0	S	0.4	0.45	0.6		
16857	150.5121	1.53030	0.18	0.002	1.022	0.104	18.0	2.8	28.5	7.3	S	0.99	0.97	1.05		
16858	150.2233	1.53694	0.64	0.002	1.419	0.448	16.0	2.8	50.8	6.1	S	0.22	0.19	0.26		
16862	150.4418	1.54742	0.15	0.002	0.836	0.38	12.9	2.7	47.9	6.1	S	0.69	0.65	0.7		
16865	150.6134	1.54652	3.08	0.003	6.347	0.853	90.8	7.1	304.2	55.5	F	0.09	0.02	0.06	0.103	A
16866	149.8873	1.55709	0.25	0.002	0.738	0.257	10.5	2.5	26.7	5.2	S	0.2	2.35	2.69		
16867	149.5280	1.56463	0.06	0.002	0.575	0.253	21.5	3.7	54.8	8.1	S	0.45	0.33	0.55		
16868	149.5891	1.55632	0.19	0.002	1.522	0.329	24.1	3.7	32.6	6.8	S	0.44	1.4	1.82		
16872	150.5202	1.56554	7.76	0.005	11.702	0.096	233.3	15.6	413.5	70.2	F	0.21	0.0	0.06	0.098	A
16877	150.2812	1.57914	0.09	0.002	0.653	0.094	10.9	2.7	65.9	7.4	S	0.32	0.28	2.77		
16879	150.2947	1.58763	0.74	0.002	1.551	0.05	20.8	3.2	17.3	7.2	S	0.2	0.46	0.54		
16882	150.2240	1.58863	0.67	0.002	2.232	0.451	33.0	3.8	92.1	7.4	S	0.07	0.02	0.1		
16884	149.5938	1.58479	1.41	0.002	4.009	0.298	75.4	6.4	183.2	46.5	F	0.02	0.01	0.14	0.028	A
16885	150.5700	1.59308	0.39	0.002	1.639	0.522	26.4	3.4	71.8	21.1	F	0.11	0.97	1.12		
16886	150.1426	1.59531	0.44	0.002	1.076	0.287	16.1	2.8	35.5	6.3	S	0.22	0.15	0.23		
16887	149.6514	1.59557	0.08	0.002	1.105	0.079	12.0	2.6	<11.6	<11.6	S	0.92	0.89	0.95		
16890	150.3269	1.60138	0.41	0.002	0.672	0.22	16.8	3.0	60.6	7.6	S	0.12	0.03	0.15	0.104	K
16891	150.1732	1.59798	0.28	0.002	1.617	0.349	22.3	3.6	18.0	6.7	S	0.31	0.3	0.35		
16894	150.2900	1.60815	0.43	0.002	1.928	0.146	26.9	3.7	20.5	6.5	S	0.36	0.32	0.38		
16895	150.6741	1.59724	0.15	0.002	1.67	0.135	11.3	2.7	<11.6	<11.6	S	0.61	0.58	0.66		

Continued on next page

Table A.1 – continued from previous page

ID	RA	Dec	S_8	σ_8	S_{24}	σ_{24}	S_{70}	σ_{70}	S_{160}	σ_{160}	F/S	z_{phot}	min	max	z_{spec}	Flag
16898	150.7199	1.61174	0.35	0.002	1.862	0.36	19.5	3.1	58.2	6.6	S	0.29	0.28	0.35		
16899	150.5060	1.61209	0.51	0.002	1.265	0.228	17.8	2.9	49.4	7.2	S	0.24	0.28	1.86	0.206	C
16902	149.7170	1.62026	0.82	0.002	1.476	0.078	23.8	3.2	108.9	26.9	F	0.05	0.02	0.12	0.100	CK
16903	150.1476	1.63224	0.30	0.002	1.022	0.226	16.9	3.2	23.7	7.0	S	0.21	0.18	0.23		
16906	150.0604	1.63268	0.41	0.002	3.542	1.243	24.4	3.4	43.6	6.8	S	0.49	0.44	0.55		
16911	150.1887	1.64661	0.90	0.002	2.332	0.358	24.3	3.5	150.6	31.8	F	0.24	0.21	0.29	0.220	K
16912	150.7036	1.64867	0.60	0.002	4.668	0.316	17.7	2.9	43.6	5.5	S	0.72	0.66	0.72	0.694	K
16915	150.1886	1.65499	0.25	0.002	1.509	0.058	22.5	3.4	173.8	10.2	S	0.54	0.51	0.56		
16916	150.1738	1.66017	0.25	0.002	2.431	1.414	28.4	3.8	25.5	7.1	S	0.39	0.3	0.39		
16918	149.6901	1.67114	0.32	0.002	0.924	0.157	14.4	2.7	76.9	20.7	F	0.38	0.36	0.4		
16919	149.5220	1.67106	0.43	0.002	0.963	0.137	11.1	2.5	25.0	6.1	S	0.11	0.06	0.16		
16923	150.2372	1.67725	0.32	0.002	0.702	0.127	12.2	2.7	<11.6	<11.6	S	0.17	0.1	0.18	0.185	CK
16925	150.3831	1.67993	0.23	0.002	1.016	0.149	15.0	2.7	44.0	6.0	S	0.31	0.27	0.38		
16927	150.2780	1.67363	0.17	0.002	1.913	1.202	11.8	2.5	48.6	6.4	S	1.04	1.01	1.07		
16931	150.2134	1.67423	2.08	0.003	7.732	1.288	83.1	6.9	126.9	30.7	F	0.22	0.11	0.23	0.166	AK
16932	149.8146	1.69174	0.27	0.002	0.839	0.198	12.6	2.7	65.7	6.8	S	0.31	0.29	0.41	0.299	K
16935	150.5818	1.68065	0.23	0.002	1.745	0.042	10.3	2.5	43.6	6.7	S	1.0	0.99	1.15		
16937	149.5510	1.70103	0.09	0.002	0.46	0.088	10.4	2.5	17.0	4.4	S	0.29	0.27	0.38		
16939	150.2264	1.69802	0.61	0.002	1.285	0.375	16.4	2.8	<11.6	<11.6	S	0.16	0.13	0.22	0.185	CK
16945	150.0447	1.70711	0.31	0.002	1.001	0.356	18.2	3.0	55.3	6.5	S	0.38	0.34	0.39		
16946	150.0332	1.70352	1.06	0.002	1.881	0.104	25.0	3.3	50.5	5.9	S	0.1	0.05	0.15	0.092	K
16947	149.7901	1.71191	0.03	0.002	1.059	0.172	14.9	2.7	76.1	21.6	F	1.65	1.55	1.71		

Continued on next page

Table A.1 – continued from previous page

ID	RA	Dec	S_8	σ_8	S_{24}	σ_{24}	S_{70}	σ_{70}	S_{160}	σ_{160}	F/S	z_{phot}	min	max	z_{spec}	Flag
16950	150.6479	1.71424	0.37	0.002	1.034	0.12	18.6	2.9	51.7	6.0	S	0.34	0.32	0.36		
16954	150.4212	1.73178	0.10	0.002	0.881	0.124	11.2	2.6	117.9	8.5	S	0.58	0.53	0.61		
16955	150.4318	1.72875	0.73	0.002	2.995	0.461	46.3	4.6	114.2	27.4	F	0.4	0.34	0.41		
16956	150.1812	1.74077	0.16	0.002	0.828	0.124	11.1	2.5	<11.6	<11.6	S	0.32	0.28	0.39		
16959	150.4190	1.73618	0.15	0.002	0.856	0.192	13.3	2.7	79.2	7.4	S	0.39	0.35	0.4		
16960	149.9314	1.73543	0.26	0.002	1.697	0.056	12.2	2.5	47.4	6.5	S	1.07	1.07	1.35		
16962	149.7778	1.73629	0.17	0.002	0.929	0.179	10.5	2.6	<11.6	<11.6	S	0.35	0.32	0.41	0.431	CK
16967	150.1484	1.75073	0.16	0.002	0.721	0.267	11.4	2.5	18.3	5.3	S	0.34	0.29	0.39		
16968	150.6140	1.75093	0.72	0.002	0.897	0.16	17.6	2.9	80.0	7.1	S	0.21	0.14	0.22		
16977	149.5763	1.76796	0.07	0.002	0.647	0.214	12.3	2.7	44.3	6.4	S	0.6	0.54	0.64		
16981	149.9258	1.77768	0.20	0.002	1.729	0.491	32.5	3.7	77.5	24.1	F	0.34	0.25	0.35	0.376	CK
16982	149.5178	1.78358	0.03	0.002	0.582	0.254	43.5	4.4	107.0	26.8	F	0.68	0.67	0.8		
16984	150.4832	1.77822	0.60	0.002	1.597	0.23	17.6	3.0	50.4	6.3	S	0.25	0.21	0.29	0.229	CK
16986	149.9040	1.78332	0.46	0.002	1.382	0.148	21.1	3.1	48.1	7.9	S	0.26	0.23	0.3	0.267	CK
16999	150.0908	1.82116	0.04	0.002	1.001	0.092	14.2	2.8	39.9	6.0	S	1.01	0.82	1.03	0.995	CK
17000	149.9409	1.82838	0.22	0.002	0.838	0.31	10.5	2.4	29.7	6.1	S	0.4	0.34	0.44		
17001	150.3531	1.82620	0.75	0.002	0.793	0.211	15.0	2.6	27.2	5.3	S	0.16	0.08	0.17	0.098	K
17002	149.8942	1.82350	1.33	0.002	1.954	0.28	42.3	4.4	277.3	11.2	S	0.2	0.16	0.2	0.133	CK
17004	149.6918	1.82850	0.28	0.002	1.27	0.321	16.1	2.8	33.5	5.4	S	0.5	0.47	0.51	0.471	K
17005	149.9856	1.82994	0.97	0.002	2.389	0.118	39.5	4.3	143.3	33.4	F	0.27	0.25	0.28	0.267	CK
17006	149.8907	1.81833	3.23	0.003	5.325	0.524	92.5	7.2	251.3	45.7	F	0.16	0.11	0.21	0.133	AC
17008	150.1383	1.84405	0.06	0.002	0.73	0.144	11.2	2.5	<11.6	<11.6	S	0.52	0.51	0.58	0.571	CK

Continued on next page

Table A.1 – continued from previous page

ID	RA	Dec	S_8	σ_8	S_{24}	σ_{24}	S_{70}	σ_{70}	S_{160}	σ_{160}	F/S	z_{phot}	min	max	z_{spec}	Flag
17014	149.9178	1.85604	0.12	0.002	3.056	0.354	11.5	2.5	<11.6	<11.6	S	0.24	0.23	0.24	0.251	CK
17015	150.5744	1.85676	1.94	0.003	3.866	0.185	70.7	6.0	254.7	48.3	F	0.07	0.02	0.14	0.063	A
17025	149.7826	1.88639	0.19	0.002	0.653	0.252	16.0	2.8	18.7	5.6	S	0.28	0.25	0.34	0.328	CK
17037	150.2034	1.90264	0.61	0.002	2.585	0.051	15.2	2.8	35.6	5.4	S	0.73	0.7	0.75	0.753	CK
17039	150.2794	1.90452	1.09	0.002	1.978	0.229	29.9	3.6	119.1	27.1	F	0.11	0.05	0.13	0.078	K
17045	149.5755	1.92362	0.43	0.002	1.515	0.418	20.5	3.1	117.7	8.0	S	0.32	0.29	0.4	0.308	C
17046	150.3316	1.92123	4.96	0.004	8.798	0.458	153.1	10.9	354.2	60.9	F	0.16	0.14	0.2	0.099	AK
17048	150.0258	1.92642	0.54	0.002	2.378	0.079	11.6	2.5	58.7	7.2	S	0.7	0.64	0.73	0.661	CK
17049	149.5728	1.92995	0.87	0.002	1.272	0.416	22.9	3.4	99.3	25.0	F	0.09	0.03	0.11	0.088	K
17052	149.9484	1.93217	0.30	0.002	1.766	0.293	30.3	3.7	64.8	7.2	S	0.33	0.29	0.35		
17054	150.1781	1.93587	0.17	0.002	0.94	0.093	11.4	2.7	23.7	5.3	S	0.38	0.33	0.43		
17055	150.2656	1.92593	2.24	0.003	3.754	0.283	72.3	6.2	110.0	26.2	F	0.18	0.11	0.21	0.169	AC
17058	150.1514	1.93599	0.55	0.002	1.984	0.213	33.0	4.0	68.1	20.9	F	0.3	0.27	0.33	0.323	CK
17061	150.3754	1.93932	0.45	0.002	1.47	0.231	17.7	2.9	86.0	23.9	F	0.39	0.37	0.46	0.361	CK
17075	150.4181	1.97675	0.18	0.002	1.967	0.157	14.9	2.8	65.6	7.4	S	0.83	0.77	0.95	0.863	K
17077	149.9995	1.98705	1.47	0.003	5.817	0.959	45.6	4.7	72.2	7.2	S	0.12	0.05	0.16		
17080	149.8802	1.98796	0.65	0.002	1.828	0.464	20.9	2.6	<11.6	<11.6	S	0.07	0.06	0.13	0.109	AC
17081	149.5896	1.99871	0.36	0.002	0.908	0.153	12.0	2.6	88.1	8.2	S	0.26	0.22	0.28		
17082	150.6802	1.99591	0.14	0.002	0.985	0.118	10.8	2.5	<11.6	<11.6	S	1.05	1.0	1.11		
17084	150.3989	2.00501	0.04	0.002	0.58	0.236	10.3	2.6	93.8	8.6	S	0.47	0.45	0.59		
17086	149.5385	1.99740	0.14	0.002	2.355	0.511	24.3	3.3	15.8	6.8	S	0.38	0.29	0.39		
17089	150.1622	1.99161	1.60	0.003	2.652	0.258	36.6	4.0	168.4	34.5	F	0.13	0.08	0.17	0.124	CK

Continued on next page

Table A.1 – continued from previous page

ID	RA	Dec	S_8	σ_8	S_{24}	σ_{24}	S_{70}	σ_{70}	S_{160}	σ_{160}	F/S	z_{phot}	min	max	z_{spec}	Flag
17093	150.0605	2.00675	1.88	0.003	2.669	0.349	46.2	4.6	202.8	40.5	F	0.14	0.08	0.15	0.079	CK
17095	149.9771	2.00487	0.82	0.002	1.047	0.273	30.1	3.7	115.5	27.8	F	0.08	0.04	0.12		
17096	150.3996	2.01426	0.12	0.002	0.974	0.414	16.3	2.8	73.2	23.0	F	0.63	0.61	0.72		
17100	150.2801	2.02101	0.40	0.002	0.728	0.168	12.3	2.6	53.1	6.4	S	0.3	0.27	0.31	0.247	K
17105	150.0221	2.02653	0.19	0.002	1.64	0.169	11.5	2.6	29.9	6.4	S	0.33	0.26	0.35	0.311	CK
17106	150.7067	2.03118	0.18	0.002	0.882	0.132	12.8	2.6	54.8	6.0	S	0.45	0.37	0.49		
17116	149.7205	2.04259	0.58	0.002	2.247	0.038	38.3	3.7	88.0	23.1	F	0.24	0.2	0.27	0.220	CK
17117	150.7221	2.03960	0.91	0.003	4.638	0.077	38.1	4.0	91.4	22.6	F	0.93	0.9	0.96		
17121	149.6863	2.04709	4.02	0.004	8.071	1.109	144.3	9.8	223.3	42.5	F	0.18	0.05	0.2	0.092	ACK
17126	150.5032	2.05879	0.46	0.003	2.019	0.388	17.3	2.9	<11.6	<11.6	S	0.37	0.31	0.38	0.368	C
17129	149.7850	2.06767	0.64	0.002	1.1	0.407	28.1	3.0	25.1	5.0	S	0.14	0.1	0.2	0.108	AC
17133	150.4250	2.06622	0.88	0.002	3.593	0.426	29.2	3.7	141.0	31.9	F	0.11	0.07	0.13	0.125	K
17141	150.4183	2.08515	0.30	0.002	1.657	0.095	14.3	3.0	97.7	8.1	S	0.31	0.3	0.39	0.425	CK
17143	150.3969	2.08599	0.84	0.002	1.334	0.407	18.1	3.0	28.7	7.7	S	0.17	0.07	0.18		
17144	150.4302	2.08690	0.17	0.002	2.063	0.048	50.3	5.0	99.7	25.3	F	0.55	0.54	0.6	0.670	K
17145	150.5653	2.09109	0.32	0.002	0.828	0.194	14.2	2.7	39.1	7.0	S	0.21	0.12	0.23		
17147	150.5578	2.08747	0.76	0.002	0.867	0.194	11.0	2.5	49.5	7.1	S	0.18	0.12	0.19		
17148	150.6802	2.08940	1.47	0.002	2.934	0.318	51.6	4.9	97.9	25.4	F	0.25	0.23	0.26	0.214	K
17149	150.0098	2.09554	0.88	0.002	0.934	0.189	21.5	3.2	70.8	6.6	S	0.19	0.18	0.22	0.091	CK
17150	149.7847	2.09465	1.69	0.002	2.982	1.965	59.3	4.7	93.1	25.7	F	0.14	0.08	0.17	0.093	CK
17158	150.4747	2.09409	1.23	0.002	4.568	0.093	19.9	3.1	22.0	6.5	S	1.56	1.5	1.62	0.560	K
17159	149.7675	2.11742	0.08	0.002	0.972	0.296	10.2	2.0	85.2	24.1	F	0.71	0.68	0.75		

Continued on next page

Table A.1 – continued from previous page

ID	RA	Dec	S_8	σ_8	S_{24}	σ_{24}	S_{70}	σ_{70}	S_{160}	σ_{160}	F/S	z_{phot}	min	max	z_{spec}	Flag
17160	150.1798	2.11038	0.42	0.002	2.033	0.478	16.0	2.9	46.7	6.4	S	0.38	0.36	0.39	0.360	CK
17162	150.1912	2.11407	0.39	0.002	1.098	0.098	11.4	2.7	68.3	7.1	S	0.23	0.21	0.27	0.220	CK
17165	150.6855	2.12429	0.03	0.002	0.322	0.14	11.5	2.6	51.4	6.7	S	1.04	0.96	1.08		
17167	150.0954	2.11695	0.47	0.002	2.418	0.047	17.1	2.9	47.3	6.4	S	0.21	0.19	0.23	0.195	CK
17168	149.9655	2.12349	0.11	0.002	0.778	0.138	12.1	2.1	17.7	5.5	S	0.9	0.81	0.98	0.938	K
17172	150.0787	2.12303	0.99	0.002	1.593	0.3	22.4	3.3	60.7	7.4	S	0.14	0.1	0.17	0.123	CK
17174	150.0455	2.12356	0.58	0.002	2.01	0.311	33.5	3.9	131.2	29.4	F	0.3	0.27	0.31	0.339	CK
17175	149.7930	2.12563	4.64	0.004	28.114	0.229	50.5	4.3	<11.6	<11.6	S	0.38	0.36	0.42	0.353	AK
17183	150.3290	2.13955	1.97	0.003	2.953	0.484	52.5	5.1	103.2	25.3	F	0.29	0.16	0.29	0.168	ACK
17184	149.7996	2.14010	0.36	0.002	1.772	0.055	21.4	2.8	90.8	23.9	F	0.33	0.31	0.35	0.354	K
17193	149.9353	2.14962	0.18	0.002	1.153	0.308	23.9	2.7	27.9	5.8	S	0.3	0.23	0.32	0.309	AK
17195	149.9622	2.15961	0.15	0.002	1.255	0.21	29.9	3.0	37.7	5.9	S	0.36	0.29	0.4	0.359	CK
17196	149.8408	2.16709	0.33	0.002	0.71	0.163	12.5	2.2	33.4	6.7	S	0.27	0.22	0.28	0.220	CK
17199	149.8917	2.16937	0.59	0.002	1.044	0.238	17.2	2.5	97.8	7.3	S	0.22	0.12	0.24	0.186	AK
17202	149.9091	2.16829	0.29	0.002	0.972	0.151	11.7	2.1	22.9	5.5	S	0.24	0.21	0.25	0.221	K
17205	149.6270	2.16752	0.46	0.002	1.262	0.165	12.2	2.6	33.8	7.2	S	0.27	0.23	0.31		
17207	150.5067	2.16554	0.28	0.002	1.59	0.109	12.2	2.7	14.6	5.0	S	0.16	0.11	0.22	0.217	CK
17208	149.9549	2.17240	0.12	0.002	0.788	0.113	11.1	2.0	<11.6	<11.6	S	0.31	0.27	0.35	0.310	C
17211	150.3467	2.17039	0.06	0.002	1.192	0.256	20.8	3.1	33.9	6.0	S	0.77	0.72	0.81	0.850	CK
17212	149.7495	2.17554	0.12	0.002	0.555	0.15	10.2	2.1	92.7	7.2	S	0.39	0.29	0.4		
17213	149.8865	2.17752	1.15	0.002	3.801	0.389	35.5	3.5	105.3	25.4	F	0.21	0.18	0.23	0.186	CK
17217	149.5645	2.19320	0.38	0.002	1.511	0.531	12.3	2.6	35.7	5.6	S	0.28	0.26	0.42		

Continued on next page

Table A.1 – continued from previous page

ID	RA	Dec	S_8	σ_8	S_{24}	σ_{24}	S_{70}	σ_{70}	S_{160}	σ_{160}	F/S	z_{phot}	min	max	z_{spec}	Flag
17219	150.5985	2.19238	2.21	0.003	2.886	0.249	61.9	5.5	181.2	35.8	F	0.17	0.16	0.21	0.123	AK
17224	150.2446	2.19435	1.41	0.003	5.188	0.393	61.6	5.3	114.0	27.6	F	0.17	0.09	0.17	0.110	CK
17227	149.6794	2.20803	0.22	0.002	1.023	0.174	18.5	2.6	93.2	24.0	F	1.02	0.99	1.05		
17228	149.8117	2.21236	0.24	0.002	0.919	0.196	15.2	2.3	30.6	5.2	S	1.33	1.25	1.36	1.245	K
17231	150.6813	2.20625	0.91	0.002	1.504	0.335	25.9	3.5	76.6	21.9	F	0.17	0.07	0.18	0.123	K
17234	149.8946	2.20803	0.50	0.002	3.127	0.044	124.3	8.4	133.9	30.4	F	0.39	0.35	0.4	0.345	ACK
17235	150.0669	2.21040	1.56	0.002	2.889	0.659	53.9	5.4	168.4	35.9	F	0.21	0.19	0.26	0.187	CK
17237	150.6737	2.22633	0.42	0.002	1.147	0.133	22.8	3.4	70.2	20.1	F	0.21	0.19	0.28		
17238	149.7884	2.22712	0.33	0.002	0.826	0.173	11.4	2.0	77.6	6.9	S	0.27	0.23	0.31	0.283	CK
17240	149.6420	2.23569	0.50	0.002	0.949	0.299	12.5	2.5	40.7	6.4	S	0.2	0.17	0.25	0.205	CK
17243	149.7320	2.23064	0.34	0.002	0.982	0.225	11.6	2.2	34.5	6.4	S	0.14	0.09	0.16		
17247	149.8538	2.24573	0.24	0.002	0.993	0.127	13.3	2.1	13.5	4.8	S	0.42	0.31	0.44	0.345	CK
17255	150.0352	2.25605	0.37	0.002	2.927	0.28	38.6	3.6	63.9	19.0	F	0.3	0.28	0.32	0.251	CK
17256	149.8410	2.25494	0.21	0.002	1.558	0.043	18.5	2.5	37.3	5.6	S	0.31	0.29	0.34	0.345	ACK
17259	149.6958	2.26452	0.36	0.002	1.598	0.083	22.9	3.0	108.3	8.3	S	0.59	0.57	0.65	0.552	C
17266	149.5724	2.26272	0.63	0.002	7.116	0.05	17.3	2.8	<11.6	<11.6	S	0.79	0.76	0.82		
17268	150.2528	2.27814	2.28	0.003	6.637	0.439	63.6	5.7	140.2	30.7	F	0.21	0.15	0.23	0.166	AK
17270	149.5229	2.28281	0.15	0.002	1.377	0.291	19.8	3.1	77.3	7.7	S	0.31	0.3	0.38	0.425	K
17278	150.3197	2.28664	0.77	0.003	0.83	0.08	18.6	3.1	126.9	28.1	F	0.14	0.1	0.15		C
17279	150.4308	2.29767	0.35	0.003	1.311	0.13	16.8	3.1	89.0	25.4	F	0.46	0.22	0.27		
17281	150.3748	2.28476	2.62	0.003	16.033	0.517	131.0	9.4	165.3	33.8	F	0.12	0.05	0.16	0.075	ACK
17282	150.0760	2.30486	0.73	0.002	0.973	0.177	24.3	2.9	82.2	21.6	F	0.25	0.22	0.25	0.123	AK

Continued on next page

Table A.1 – continued from previous page

ID	RA	Dec	S_8	σ_8	S_{24}	σ_{24}	S_{70}	σ_{70}	S_{160}	σ_{160}	F/S	z_{phot}	min	max	z_{spec}	Flag
17283	149.9100	2.30788	1.36	0.003	2.268	0.337	42.9	4.0	122.3	25.6	F	0.09	0.06	0.11		
17285	150.3355	2.30495	2.00	0.003	3.311	0.626	46.8	4.8	135.8	29.7	F	0.16	0.11	0.19	0.123	ACK
17286	149.5623	2.30513	0.77	0.002	1.061	0.145	15.9	2.8	<11.6	<11.6	S	0.11	0.08	0.15	0.124	K
17287	149.9054	2.30960	1.20	0.002	2.328	1.117	38.7	3.7	87.7	7.7	S	0.24	0.22	0.25		
17288	149.6555	2.31064	0.30	0.002	1.623	0.245	16.1	2.8	46.8	7.2	S	0.26	0.21	0.3		
17292	150.6327	2.30802	1.59	0.003	4.243	0.04	44.6	4.6	31.0	5.6	S	0.17	0.11	0.18	0.073	K
17302	149.5776	2.33068	0.38	0.002	1.309	0.105	15.9	2.8	63.4	20.4	F	0.32	0.26	0.36		
17306	150.5110	2.33052	0.30	0.002	4.336	0.053	14.9	2.8	<11.6	<11.6	S	0.08	0.04	0.12		
17311	149.7308	2.34374	0.42	0.002	2.392	0.413	15.9	2.8	38.3	8.1	S	0.36	0.3	0.4		
17312	149.7473	2.34574	0.63	0.002	2.566	0.162	64.2	5.2	149.6	32.7	F	0.31	0.26	0.32	0.373	C
17313	150.5390	2.34781	1.66	0.003	2.319	0.162	33.0	4.0	115.7	28.0	F	0.15	0.1	0.2	0.127	CK
17317	149.7282	2.35810	0.51	0.003	0.863	0.212	15.0	2.8	60.7	7.9	S	0.22	0.19	0.26		
17323	150.1757	2.35873	0.71	0.002	1.488	0.132	23.4	3.3	70.8	20.0	F	0.24	0.19	0.25		
17327	150.2096	2.35529	1.19	0.002	1.421	0.216	28.2	3.6	104.1	24.1	F	0.27	0.25	0.28	0.166	CK
17330	150.0348	2.37910	0.04	0.002	0.573	0.179	16.1	2.3	44.2	14.2	F	1.09	1.06	1.31	1.093	C
17335	150.6901	2.38101	0.12	0.002	0.93	0.092	14.3	2.8	21.4	5.2	S	0.43	0.4	0.47		
17336	150.5326	2.38078	2.20	0.003	4.218	0.646	70.7	6.2	198.5	38.6	F	0.09	0.09	0.21	0.176	AK
17337	150.0954	2.38475	0.42	0.002	1.003	0.298	15.3	2.2	69.7	17.5	F	0.28	0.24	0.29	0.266	CK
17338	150.3580	2.38354	0.63	0.002	1.277	0.198	22.6	3.4	97.9	24.0	F	0.19	0.15	0.23	0.222	CK
17342	150.7452	2.38805	0.59	0.002	1.175	0.292	19.9	3.1	<11.6	<11.6	S	0.15	0.07	0.19		
17349	150.2897	2.40002	0.05	0.002	0.711	0.175	15.7	2.9	51.3	6.6	S	0.66	0.59	0.68	0.614	CK
17351	149.6618	2.39693	0.64	0.002	2.657	0.625	18.4	3.1	72.4	7.7	S	0.36	0.32	0.39	0.356	CK

Continued on next page

Table A.1 – continued from previous page

ID	RA	Dec	S_8	σ_8	S_{24}	σ_{24}	S_{70}	σ_{70}	S_{160}	σ_{160}	F/S	z_{phot}	min	max	z_{spec}	Flag
17358	150.3466	2.40415	0.93	0.002	1.287	0.135	20.5	3.1	101.2	24.5	F	0.07	0.06	0.12	0.127	CK
17360	150.4720	2.41023	0.24	0.002	1.12	0.074	10.2	2.5	71.0	7.2	S	0.69	0.68	0.69	0.667	K
17362	149.6019	2.40768	0.61	0.003	1.924	0.311	24.3	3.5	68.2	21.9	F	0.14	0.08	0.19	0.167	C
17364	150.7165	2.41397	0.21	0.002	1.904	0.085	23.9	3.3	26.0	5.5	S	0.31	0.3	0.34		
17367	150.4651	2.41915	1.08	0.003	1.971	0.289	28.2	3.6	97.3	24.5	F	0.23	0.22	0.27	0.215	K
17374	150.2798	2.42211	0.87	0.003	5.283	2.175	39.8	4.3	76.3	21.2	F	0.22	0.19	0.25	0.122	C
17376	149.9388	2.43336	0.13	0.002	0.988	0.282	10.2	1.9	36.5	5.1	S	0.29	0.23	0.3	0.314	K
17378	149.6922	2.43199	0.60	0.002	1.62	0.491	25.7	3.5	106.1	26.9	F	0.26	0.24	0.29	0.264	CK
17383	150.2360	2.44321	0.43	0.002	1.661	0.21	25.6	3.5	47.1	6.0	S	0.31	0.3	0.37		
17384	150.6104	2.44296	0.87	0.002	1.759	0.292	27.5	3.6	<11.6	<11.6	S	0.12	0.07	0.15	0.122	K
17385	150.5973	2.44520	0.14	0.002	1.07	0.41	16.8	2.8	26.7	6.1	S	0.33	0.28	0.39		
17387	149.7918	2.44561	0.55	0.002	1.067	0.184	13.0	2.2	66.7	17.7	F	0.27	0.23	0.28	0.261	K
17388	150.2759	2.45197	0.24	0.002	1.146	0.113	13.0	2.7	<11.6	<11.6	S	0.21	0.12	0.24		
17399	149.5192	2.45996	0.11	0.002	1.679	0.266	12.4	2.6	57.5	6.8	S	0.41	0.28	0.41		
17400	150.3191	2.45774	0.80	0.002	2.191	0.486	31.1	4.0	127.0	30.4	F	0.22	0.2	0.27	0.217	CK
17404	150.1190	2.45718	1.28	0.003	6.564	0.045	102.5	7.1	160.0	31.1	F	0.31	0.27	0.31	0.248	A
17414	150.7105	2.47742	0.32	0.002	2.134	0.138	16.5	2.8	61.4	18.8	F	0.32	0.3	0.38	0.360	CK
17415	149.7381	2.48007	0.22	0.002	1.16	0.217	14.7	2.7	110.9	25.4	F	0.52	0.47	0.54		
17417	150.3146	2.48292	2.19	0.003	3.359	0.247	60.4	5.5	166.2	35.1	F	0.15	0.11	0.16	0.075	AK
17419	149.7965	2.49740	0.29	0.002	0.948	0.191	12.3	2.5	36.3	5.5	S	0.24	0.19	0.27		
17420	149.5618	2.49420	0.32	0.002	4.29	0.181	12.4	2.5	<11.6	<11.6	S	0.58	0.53	0.58	0.482	CK
17421	150.0232	2.49713	0.80	0.002	0.691	0.203	18.4	2.4	94.1	20.8	F	0.11	0.09	0.17	0.109	AK

Continued on next page

Table A.1 – continued from previous page

ID	RA	Dec	S_8	σ_8	S_{24}	σ_{24}	S_{70}	σ_{70}	S_{160}	σ_{160}	F/S	z_{phot}	min	max	z_{spec}	Flag
17424	150.0300	2.50411	0.51	0.002	0.778	0.205	13.4	2.1	111.4	8.0	S	0.2	0.16	0.22		
17426	150.3340	2.51330	0.44	0.002	0.945	0.201	11.2	2.7	<11.6	<11.6	S	0.15	0.12	0.22	0.176	K
17427	150.3968	2.51913	0.54	0.002	1.554	0.327	42.6	4.5	76.5	8.1	S	0.12	0.1	0.23	0.219	C
17429	150.4039	2.50892	1.19	0.002	2.337	0.193	35.2	4.2	182.4	38.3	F	0.12	0.06	0.16	0.124	CK
17433	150.2654	2.51479	1.69	0.003	2.301	0.836	41.6	4.3	124.0	27.7	F	0.13	0.11	0.19		
17436	150.2286	2.52394	0.26	0.002	1.823	0.21	35.4	3.9	81.4	22.3	F	0.36	0.31	0.38	0.376	A
17437	150.5225	2.52608	0.08	0.002	0.726	0.128	15.1	2.8	25.0	5.4	S	0.34	0.29	0.39		
17438	150.2591	2.52812	0.20	0.002	0.954	0.242	18.6	3.1	82.4	22.4	F	0.46	0.41	0.48		
17439	150.4227	2.53256	0.45	0.002	0.812	0.245	34.5	4.2	71.2	22.6	F	0.17	0.14	0.2	0.220	K
17440	149.9746	2.53514	0.31	0.002	0.849	0.194	12.4	2.0	<11.6	<11.6	S	0.21	0.16	0.27	0.219	CK
17441	150.3559	2.52922	2.23	0.003	5.354	0.426	82.6	6.8	143.3	31.6	F	0.12	0.09	0.17	0.121	K
17442	149.6338	2.53802	0.26	0.002	0.971	0.278	14.7	2.7	63.8	6.1	S	0.36	0.29	0.37	0.345	CK
17448	150.6211	2.54613	0.62	0.002	1.044	0.138	15.6	2.8	80.2	23.1	F	0.24	0.16	0.25		
17449	149.8176	2.55314	0.57	0.002	0.784	0.195	14.1	2.6	51.8	16.6	F	0.12	0.06	0.17	0.126	CK
17451	150.1939	2.55127	0.76	0.003	0.89	0.249	16.6	2.4	78.2	20.0	F	0.13	0.07	0.17	0.107	K
17455	150.0312	2.56876	0.13	0.002	0.894	0.103	15.2	2.3	59.9	7.6	S	0.34	0.25	0.37		
17456	150.3729	2.56480	0.70	0.002	1.487	0.191	25.5	3.5	<11.6	<11.6	S	0.25	0.21	0.28	0.220	CK
17460	149.8777	2.57644	0.07	0.002	0.819	0.071	11.1	2.0	60.5	17.1	F	1.42	1.38	1.46		
17461	150.6262	2.57559	0.55	0.002	0.766	0.134	15.8	2.9	39.2	7.6	S	0.07	0.04	0.15	0.104	K
17465	150.3000	2.57838	0.09	0.002	0.903	0.176	12.6	2.6	25.2	5.9	S	0.53	0.48	0.58	0.604	K
17466	149.9686	2.58325	0.28	0.002	0.953	0.109	18.7	2.4	78.7	19.1	F	0.38	0.34	0.4	0.309	CK
17468	150.4229	2.58326	0.05	0.002	0.685	0.218	14.2	2.8	42.4	7.9	S	1.07	0.84	1.09	0.822	K

Continued on next page

Table A.1 – continued from previous page

ID	RA	Dec	S_8	σ_8	S_{24}	σ_{24}	S_{70}	σ_{70}	S_{160}	σ_{160}	F/S	z_{phot}	min	max	z_{spec}	Flag
17471	150.3387	2.59326	0.06	0.002	0.94	0.252	20.9	3.3	70.7	20.8	F	0.87	0.82	0.89	0.851	K
17478	150.1493	2.59556	0.04	0.002	0.842	0.272	18.6	2.4	89.7	20.9	F	0.88	0.82	0.92	0.892	K
17479	149.7760	2.60547	0.48	0.002	0.947	0.253	10.5	2.5	23.0	6.8	S	0.23	0.17	0.25		
17484	150.2826	2.61010	0.42	0.003	0.995	0.149	14.1	2.7	59.0	7.3	S	0.2	0.17	0.26	0.220	C
17485	149.7405	2.60527	0.72	0.002	2.045	0.266	25.9	3.5	32.9	6.3	S	0.23	0.19	0.25		
17491	150.4338	2.62347	0.84	0.003	2.645	0.538	27.9	3.7	50.0	8.4	S	0.11	0.08	0.16		
17497	150.0459	2.63234	1.09	0.003	4.523	0.188	50.1	4.2	129.3	25.7	F	0.16	0.11	0.16		
17498	150.5473	2.63558	1.16	0.003	1.757	0.204	33.7	3.8	100.4	8.0	S	0.17	0.11	0.18		
17504	150.3330	2.64896	0.50	0.002	0.795	0.299	21.8	3.3	41.5	6.2	S	0.27	0.25	0.28		
17507	150.4373	2.64323	1.49	0.003	3.484	0.269	46.5	4.8	165.2	34.7	F	0.08	0.03	0.12	0.105	AK
17508	150.6910	2.64705	0.18	0.003	1.597	0.038	22.3	3.3	35.9	6.4	S	0.34	0.29	0.37		
17509	150.2270	2.65147	0.29	0.002	0.898	0.236	18.1	2.4	45.2	5.8	S	0.26	0.2	0.31	0.269	K
17510	149.7729	2.63615	4.83	0.005	10.89	0.706	179.4	12.3	563.9	92.9	F	0.04	0.01	0.13	0.079	A
17511	149.8796	2.66352	0.12	0.002	0.845	0.26	17.5	2.7	73.2	18.7	F	0.44	0.36	0.46	0.475	CK
17513	150.4585	2.66870	0.53	0.002	0.813	0.077	12.0	2.8	78.7	22.5	F	0.3	0.28	0.31		
17518	149.9359	2.66686	0.18	0.002	0.951	0.078	14.6	2.2	12.4	5.3	S	0.42	0.39	0.47		
17522	150.0228	2.66734	0.49	0.002	1.273	0.207	12.5	2.0	<11.6	<11.6	S	0.24	0.21	0.29	0.220	CK
17523	149.7874	2.67224	1.90	0.003	7.249	0.856	107.2	8.2	159.2	34.7	F	0.07	0.04	0.13	0.079	K
17525	150.6602	2.68563	0.09	0.002	0.754	0.251	12.3	2.6	26.6	4.9	S	0.33	0.26	0.4		
17528	150.1918	2.68494	0.77	0.003	1.568	0.363	49.7	4.2	137.6	27.7	F	0.29	0.27	0.3	0.250	C
17531	150.6893	2.68050	0.26	0.003	2.063	0.068	50.6	4.9	99.3	25.5	F	0.27	0.21	0.28	0.274	AK
17532	149.8387	2.67510	1.10	0.002	4.28	0.506	29.5	3.8	125.6	27.0	F	0.52	0.51	0.53	0.260	K

Continued on next page

Table A.1 – continued from previous page

ID	RA	Dec	S_8	σ_8	S_{24}	σ_{24}	S_{70}	σ_{70}	S_{160}	σ_{160}	F/S	z_{phot}	min	max	z_{spec}	Flag
17537	150.4894	2.68829	0.06	0.002	0.757	0.252	13.0	2.8	47.5	7.1	S	0.79	0.71	0.81	0.659	CK
17539	149.9398	2.68836	0.09	0.002	1.22	0.088	11.7	2.1	63.4	18.0	F	1.03	0.95	1.05	0.989	K
17544	149.6743	2.69444	0.58	0.002	0.965	0.278	15.5	2.8	25.2	5.5	S	0.07	0.06	0.16	0.188	CK
17545	150.4436	2.69191	0.63	0.003	1.506	0.249	24.9	3.5	37.2	6.2	S	0.24	0.19	0.28	0.219	C
17546	150.7154	2.69369	1.31	0.003	2.101	0.413	31.7	3.9	68.8	20.7	F	0.15	0.07	0.17	0.135	K
17547	149.8467	2.69385	0.73	0.002	0.705	0.106	20.9	3.3	108.9	25.1	F	0.05	0.01	0.1	0.048	K
17550	150.3995	2.68842	0.76	0.003	2.427	0.401	15.2	2.9	64.3	20.7	F	0.27	0.25	0.29		
17552	150.6947	2.70770	0.60	0.003	0.707	0.272	11.0	2.6	<11.6	<11.6	S	0.13	0.03	0.18		
17553	150.3682	2.70885	0.78	0.003	1.031	0.307	13.3	2.8	37.6	6.5	S	0.09	0.05	0.12		
17560	150.0339	2.71878	1.40	0.003	1.691	0.097	39.0	3.6	177.3	9.3	S	0.1	0.07	0.14		
17562	150.5455	2.71164	0.95	0.003	2.286	0.315	34.7	4.0	101.1	25.0	F	0.29	0.25	0.29		
17565	150.5919	2.72039	1.24	0.003	2.055	0.502	33.1	3.7	34.2	5.8	S	0.07	0.04	0.14	0.083	CK
17567	150.0702	2.72432	0.61	0.002	3.023	0.203	58.6	4.8	82.0	22.1	F	0.26	0.23	0.28	0.250	CK
17568	150.0386	2.71323	2.25	0.003	4.109	0.521	73.9	5.6	170.6	32.8	F	0.01	0.0	0.09	0.033	AK
17571	150.0928	2.73446	0.30	0.002	1.474	0.239	13.1	2.4	80.3	20.2	F	0.46	0.37	0.48	0.433	K
17573	149.8975	2.73309	0.93	0.002	1.54	0.239	16.3	2.9	86.1	22.1	F	0.14	0.1	0.18	0.124	K
17577	149.5506	2.74342	0.67	0.002	1.649	0.304	33.3	3.7	46.8	5.9	S	0.26	0.23	0.27		
17578	150.2780	2.74481	0.45	0.002	1.095	0.221	17.9	2.7	65.5	18.2	F	0.22	0.16	0.26		
17581	150.1955	2.74785	0.87	0.003	2.545	0.238	43.9	4.0	26.4	5.7	S	0.12	0.1	0.16	0.124	CK
17584	150.5949	2.75532	0.87	0.003	1.798	0.28	48.3	4.9	139.5	30.5	F	0.07	0.04	0.13	0.072	A
17585	150.5820	2.76189	0.44	0.002	0.875	0.259	13.5	2.9	64.0	20.1	F	0.1	0.02	0.16		
17586	149.6790	2.76426	0.05	0.002	0.718	0.082	12.2	2.6	70.9	20.7	F	1.1	1.06	1.18		

Continued on next page

Table A.1 – continued from previous page

ID	RA	Dec	S_8	σ_8	S_{24}	σ_{24}	S_{70}	σ_{70}	S_{160}	σ_{160}	F/S	z_{phot}	min	max	z_{spec}	Flag
17592	149.8450	2.76629	0.95	0.003	1.377	0.173	17.1	3.2	117.7	28.9	F	0.08	0.06	0.17		
17596	149.7108	2.77249	0.37	0.002	1.034	0.34	18.0	2.9	56.9	6.6	S	0.11	0.07	0.14	0.079	K
17600	150.4157	2.77695	0.27	0.002	0.924	0.265	16.0	2.9	69.4	8.4	S	0.43	0.38	0.45		
17604	150.0338	2.76516	7.80	0.007	40.21	1.83	374.6	22.6	560.7	85.8	F	0.21	0.0	0.22		
17605	150.3384	2.78739	0.13	0.002	0.542	0.212	10.8	2.5	<11.6	<11.6	S	0.07	0.02	0.14	0.073	CK
17610	150.0104	2.79315	0.77	0.002	1.616	0.277	50.2	4.3	145.9	29.4	F	0.29	0.27	0.3		
17611	150.6580	2.78351	2.21	0.003	14.665	0.123	22.4	3.5	32.2	6.9	S	0.25	0.21	0.26	0.212	K
17612	149.7913	2.79445	0.24	0.002	1.463	0.421	16.6	2.9	34.9	6.5	S	0.23	0.22	0.25		
17614	150.1958	2.79437	0.81	0.003	3.206	0.04	69.1	5.9	119.1	24.7	F	0.33	0.31	0.33	0.250	A
17615	149.5091	2.80358	0.48	0.002	1.16	0.244	12.4	2.9	66.1	21.0	F	0.28	0.24	0.3		
17616	149.8525	2.80338	0.70	0.002	0.867	0.177	14.1	2.8	21.5	8.4	S	0.1	0.05	0.13		
17619	149.5907	2.80582	0.29	0.002	1.802	0.044	35.0	4.0	82.8	22.3	F	0.31	0.28	0.35		
17621	149.8339	2.81345	2.03	0.003	2.859	0.582	52.6	4.9	118.8	27.1	F	0.13	0.06	0.18		
17625	149.9585	2.81648	0.70	0.003	1.189	0.188	19.6	3.0	61.8	17.7	F	0.1	0.03	0.14		
17628	150.1509	2.82469	0.23	0.002	1.625	0.035	23.0	3.2	25.7	4.8	S	0.38	0.34	0.4		
17634	149.7016	2.83645	0.06	0.002	0.645	0.208	11.6	2.5	75.2	22.8	F	1.06	1.03	1.23		
17635	149.7684	2.83272	1.11	0.003	3.995	0.494	41.1	4.3	102.4	24.7	F	0.17	0.11	0.18	0.119	K
17640	149.7589	2.85290	0.04	0.002	0.676	0.078	12.1	2.7	35.4	6.2	S	1.02	0.95	1.05		
17641	149.9250	2.84691	0.25	0.002	1.456	0.103	28.1	3.7	34.0	7.0	S	0.34	0.32	0.41		
17648	150.2850	2.85410	3.42	0.004	4.291	0.334	93.6	7.2	268.5	45.6	F	0.16	1.08	1.72	0.103	A
17649	150.5469	2.85658	0.11	0.002	0.647	0.353	29.4	4.2	114.4	28.6	F	0.48	0.42	0.5		
17650	150.5207	2.86092	0.50	0.002	0.762	0.182	15.9	3.7	108.9	10.5	S	0.19	0.14	0.23		

Continued on next page

Table A.1 – continued from previous page

ID	RA	Dec	S_8	σ_8	S_{24}	σ_{24}	S_{70}	σ_{70}	S_{160}	σ_{160}	F/S	z_{phot}	min	max	z_{spec}	Flag
17651	150.1520	2.86013	0.31	0.002	1.445	0.081	12.1	2.7	56.2	15.6	F	0.26	0.23	0.3		
17653	149.8764	2.86187	0.98	0.002	1.38	0.233	20.3	3.1	76.2	21.2	F	0.14	0.1	0.19	0.126	K
17654	149.7731	2.86253	0.29	0.002	3.929	0.688	12.4	2.7	<11.6	<11.6	S	0.37	0.27	0.43		
17655	150.3758	2.86126	1.02	0.002	1.035	0.171	40.6	4.5	206.6	39.0	F	0.08	0.04	0.14	0.092	K
17656	150.5008	2.86219	6.89	0.005	17.39	0.963	252.2	17.6	432.6	74.5	F	0.15	0.08	0.2	0.103	K
17658	150.1995	2.86955	0.02	0.002	1.559	0.234	10.6	2.5	55.8	6.4	S	0.74	0.71	2.37		
17666	150.2427	2.87819	0.59	0.002	0.881	0.114	15.3	3.0	79.3	20.0	F	0.16	0.28	2.31		
17668	149.9292	2.87107	0.90	0.002	1.392	0.184	28.6	3.8	135.9	28.8	F	0.11	0.02	0.12		
17670	149.6314	2.86822	0.36	0.002	3.761	0.475	20.9	3.1	60.4	6.8	S	0.29	0.42	0.53		
17672	150.1070	2.88147	0.27	0.002	0.801	0.188	11.2	2.6	<11.6	<11.6	S	0.16	0.08	0.17		
17673	150.3935	2.87162	0.59	0.002	1.708	0.269	26.9	3.9	68.8	8.3	S	0.23	0.15	0.23		
17676	149.8499	2.88137	0.56	0.002	2.333	0.621	39.7	4.3	104.2	25.0	F	0.22	0.04	2.5		
17678	150.4750	2.88589	0.34	0.002	1.862	0.035	18.0	3.4	<11.6	<11.6	S	0.18	0.17	0.22		
17691	150.3826	2.88924	1.34	0.003	3.014	0.619	36.0	4.4	91.4	24.8	F	0.2	0.14	0.24	0.191	K
17703	150.2535	2.88891	0.08	0.002	1.501	0.335	35.1	3.9	133.6	26.7	F	0.83	0.99	1.37		
17711	150.7459	2.34308	8.70	0.008	126.516	9.05	934.5	59.3	1349.2	214.4	F	0.03	0.02	0.23	0.044	A

Appendix B

Spectral Energy Distribution Fits

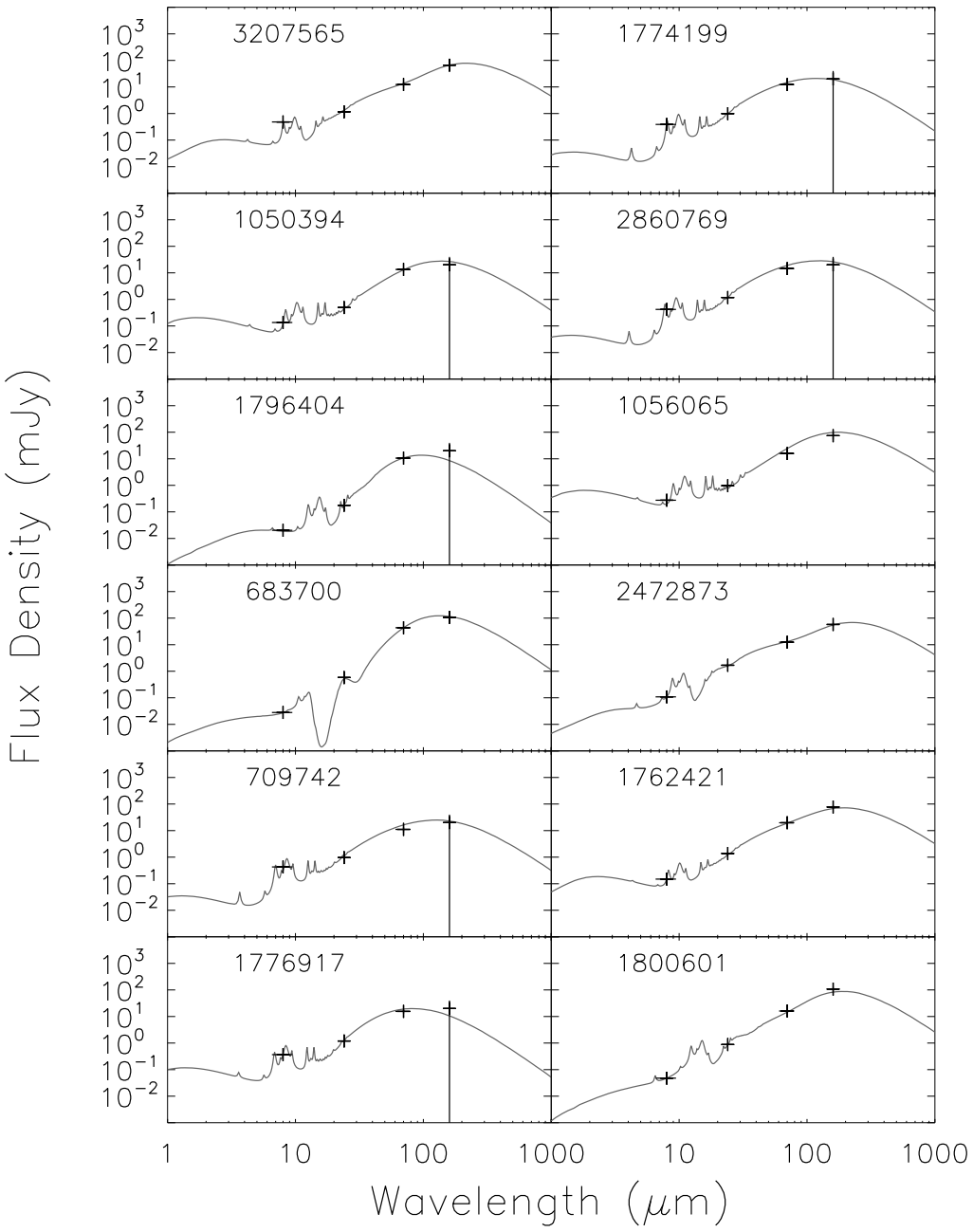

Figure B.1: Spectral energy distribution fits from the Siebenmorgen & Krügel (2007) library to the sample of 736 70μm selected galaxies. The points mark the measured 8, 24, 70 and 160μm flux densities.

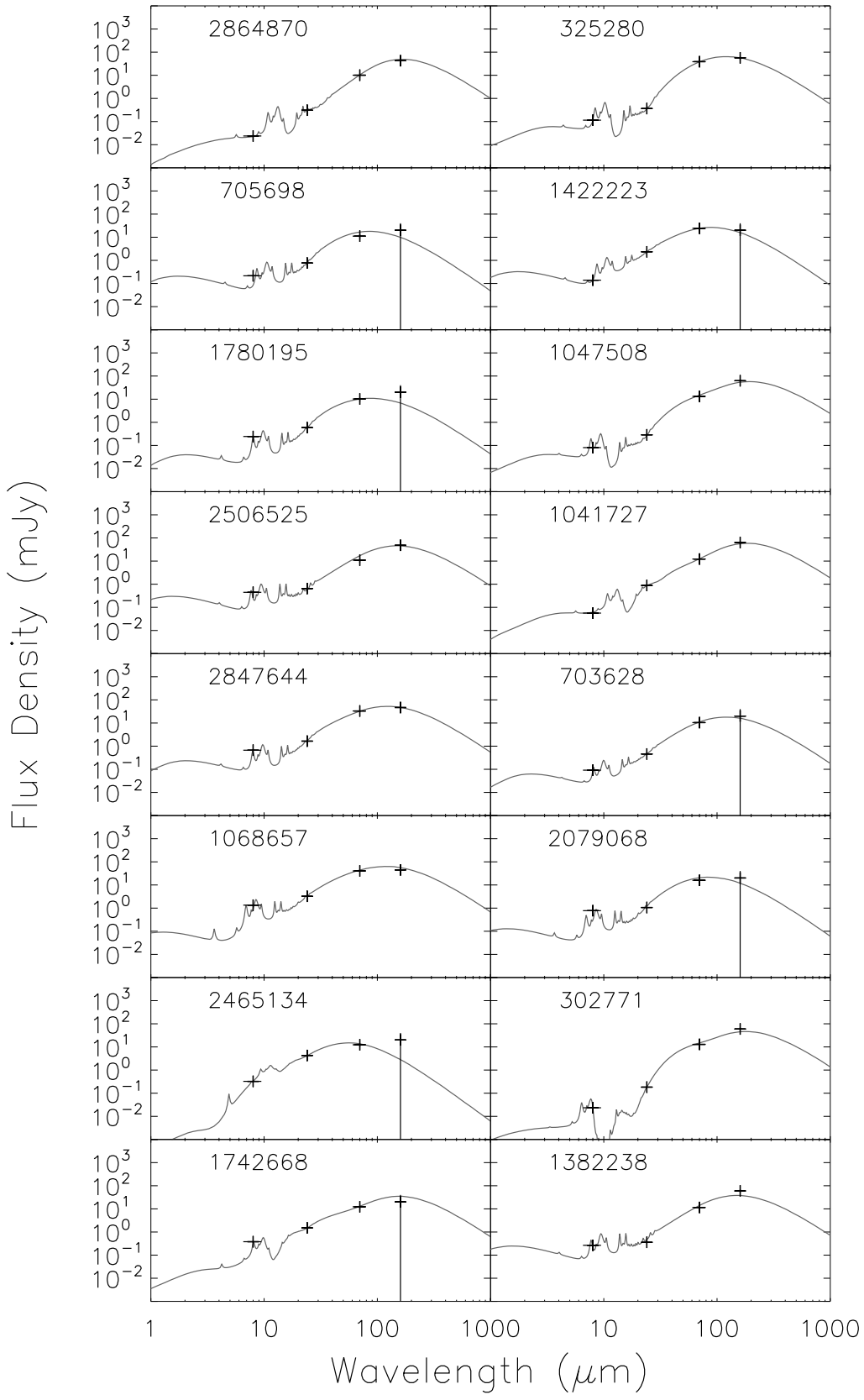
2864870
325280
705698
1422223
1780195
1047508
2506525
1041727
2847644
703628
1068657
2079068
2465134
302771
1742668
1382238
Flux Density (mJy)
Wavelength (μm)
1
10
100
1000

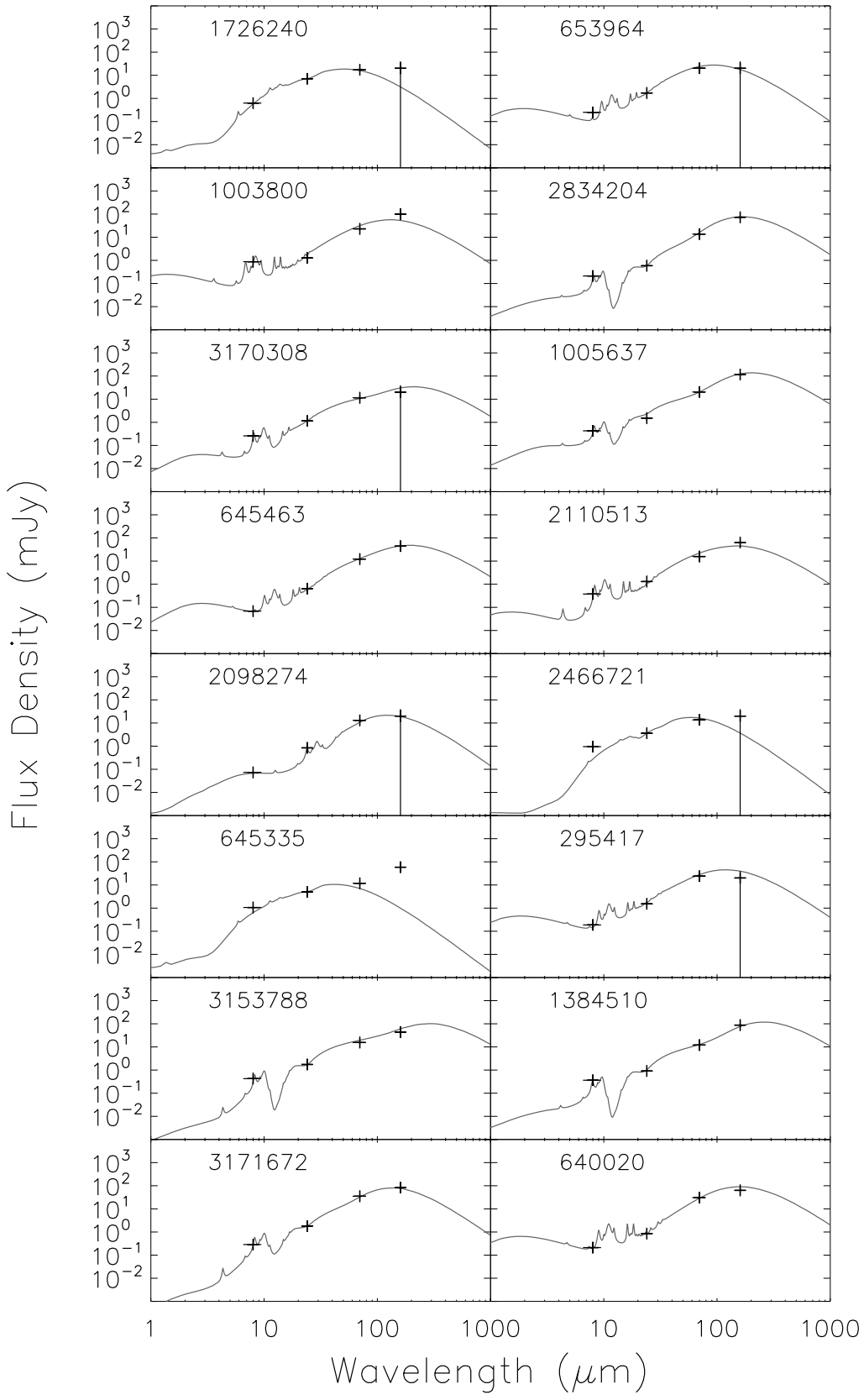
1726240
653964
1003800
2834204
3170308
1005637
645463
2110513
2098274
2466721
645335
295417
3153788
1384510
3171672
640020
Flux Density (mJy)
Wavelength (μm)
1
10
100
1000

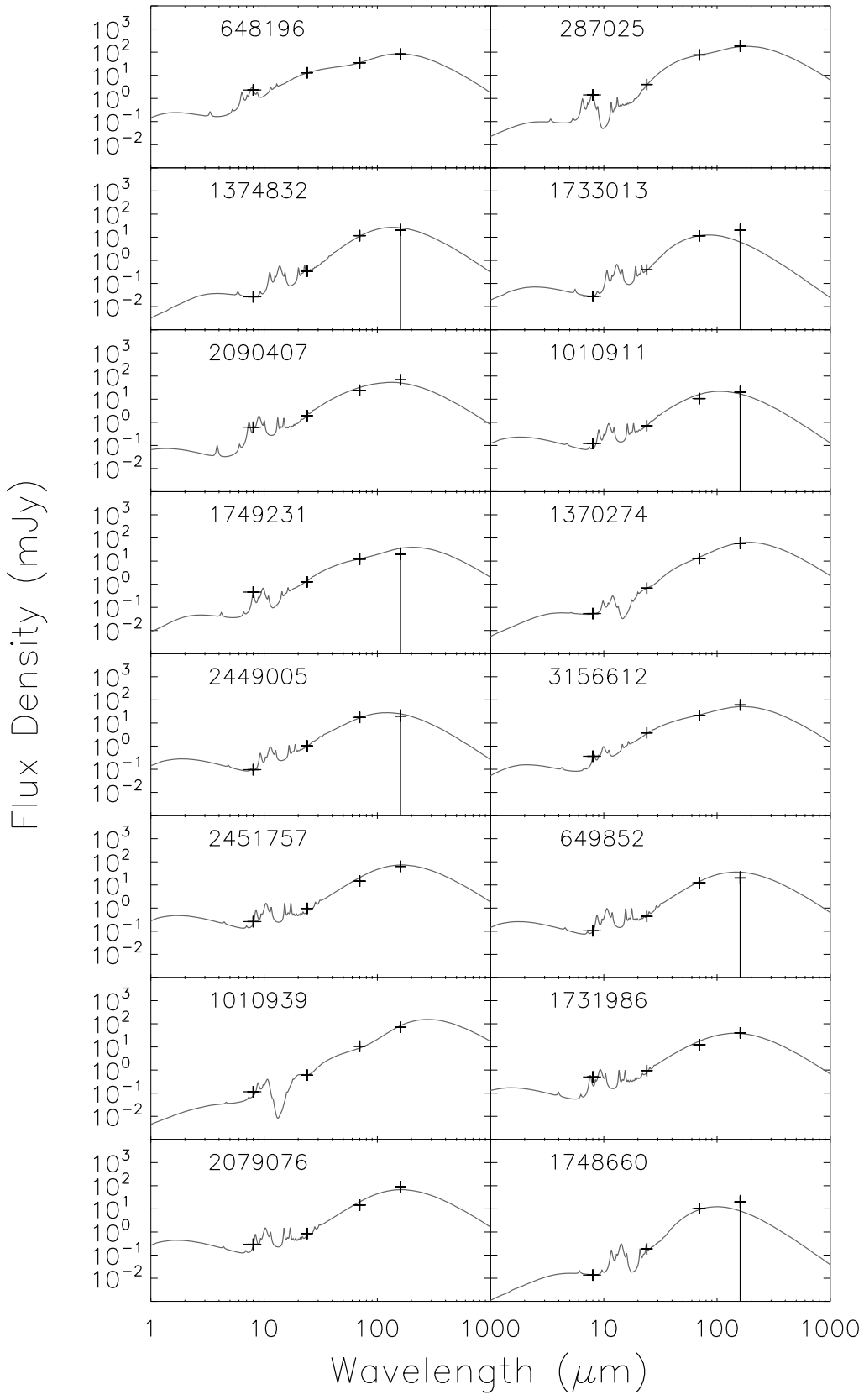
648196
287025
1374832
1733013
2090407
1010911
1749231
1370274
2449005
3156612
2451757
649852
1010939
1731986
2079076
1748660
Flux Density (mJy)
Wavelength (μm)
1
10
100
1000

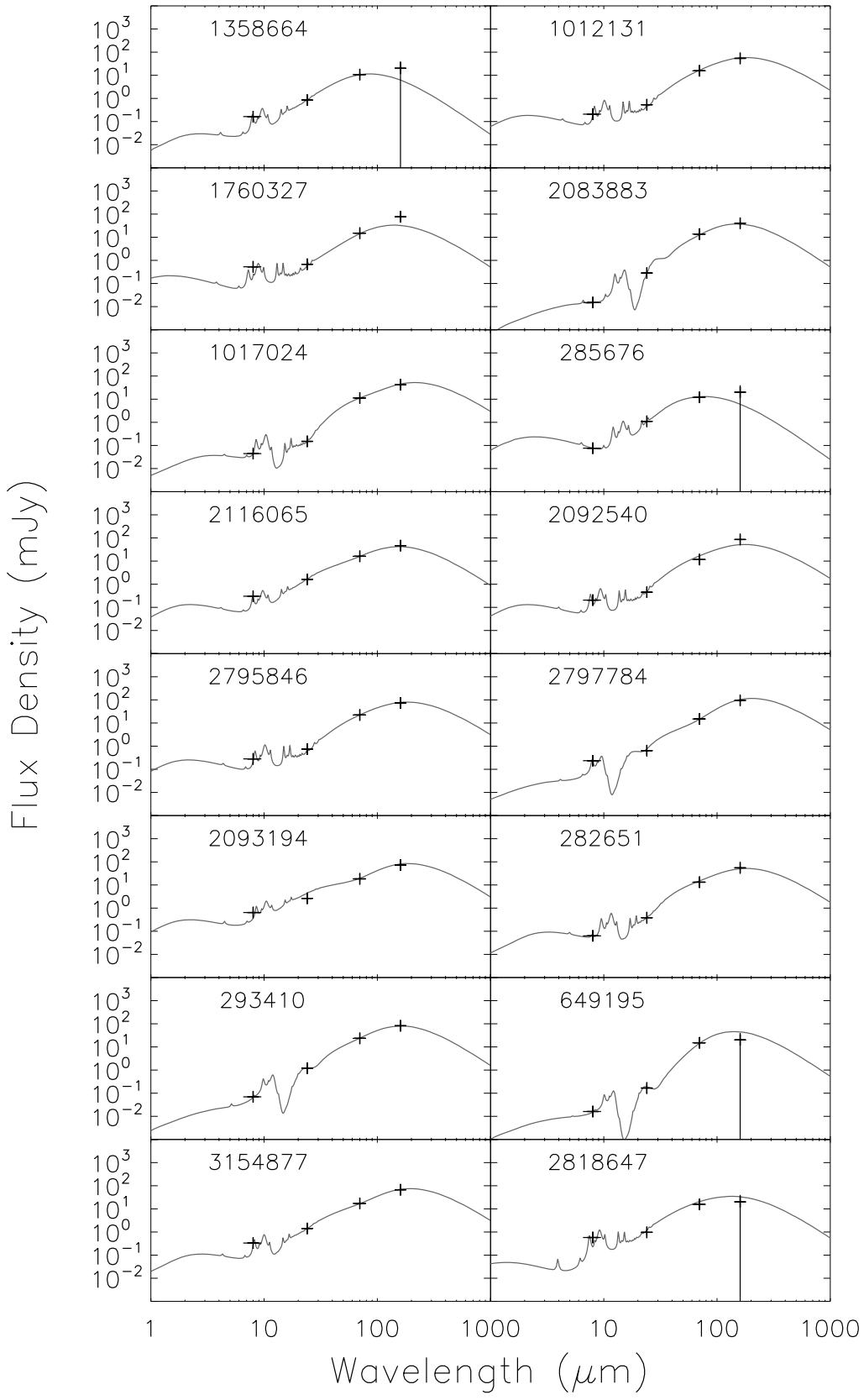
1358664
1012131
1760327
2083883
1017024
285676
2116065
2092540
2795846
2797784
2093194
282651
293410
649195
3154877
2818647
Flux Density (mJy)
Wavelength (μm)
1
10
100
1000

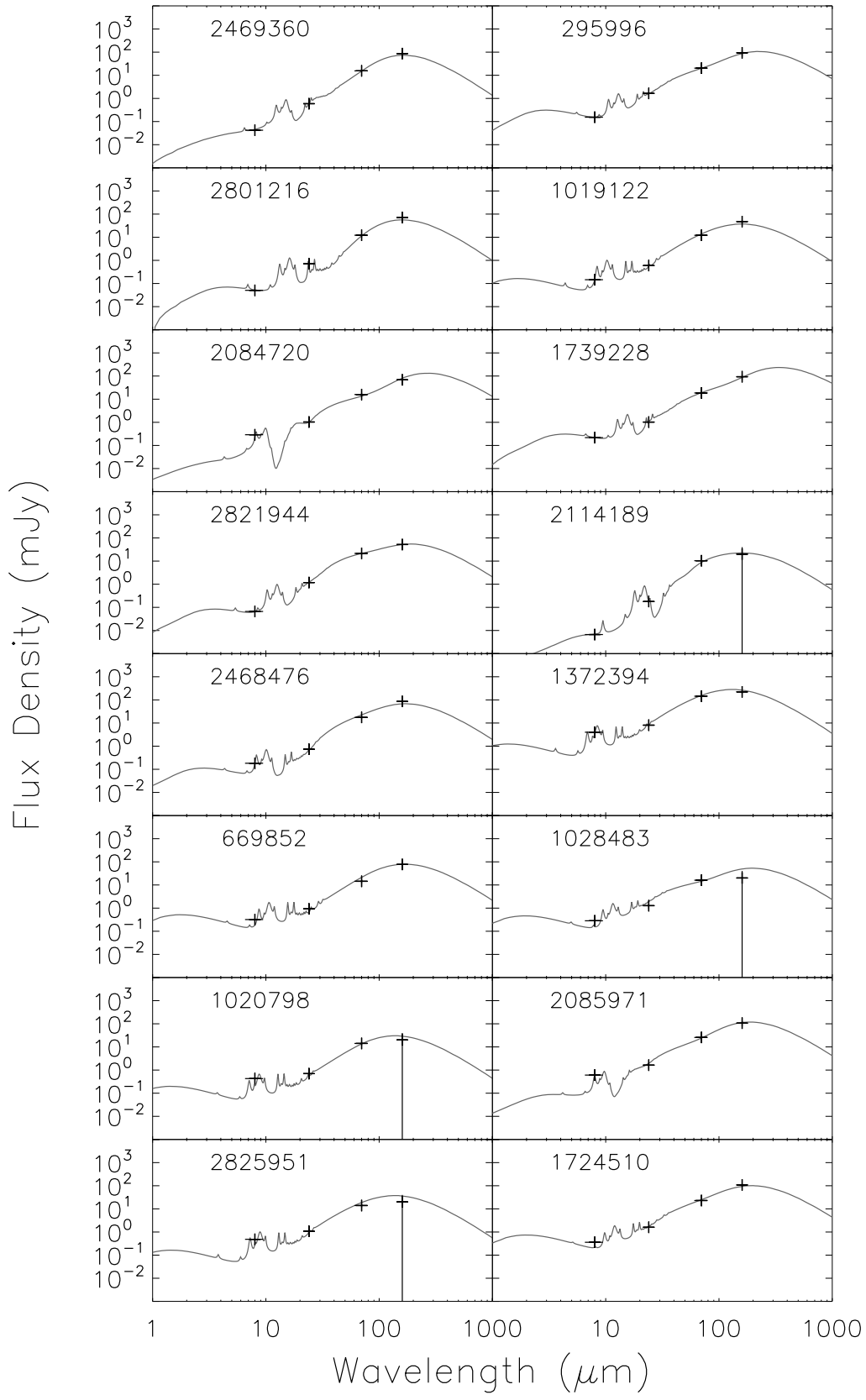
2469360
295996
2801216
1019122
2084720
1739228
2821944
2114189
2468476
1372394
669852
1028483
1020798
2085971
2825951
1724510
Flux Density (mJy)
Wavelength (μm)
1
10
100
1000

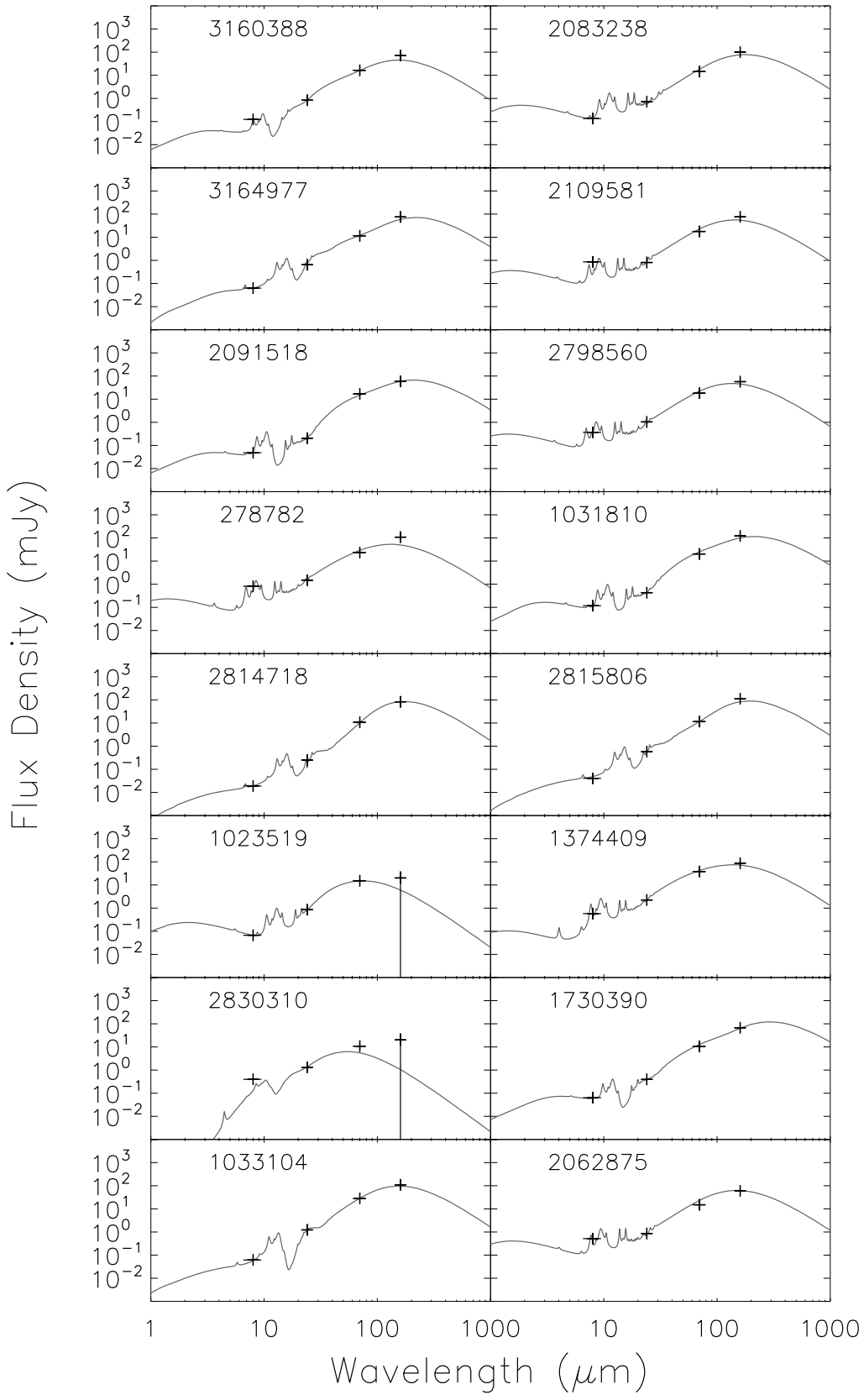
3160388
2083238
3164977
2109581
2091518
2798560
278782
1031810
2814718
2815806
1023519
1374409
2830310
1730390
1033104
2062875
Flux Density (mJy)
Wavelength (μm)
1
10
100
1000

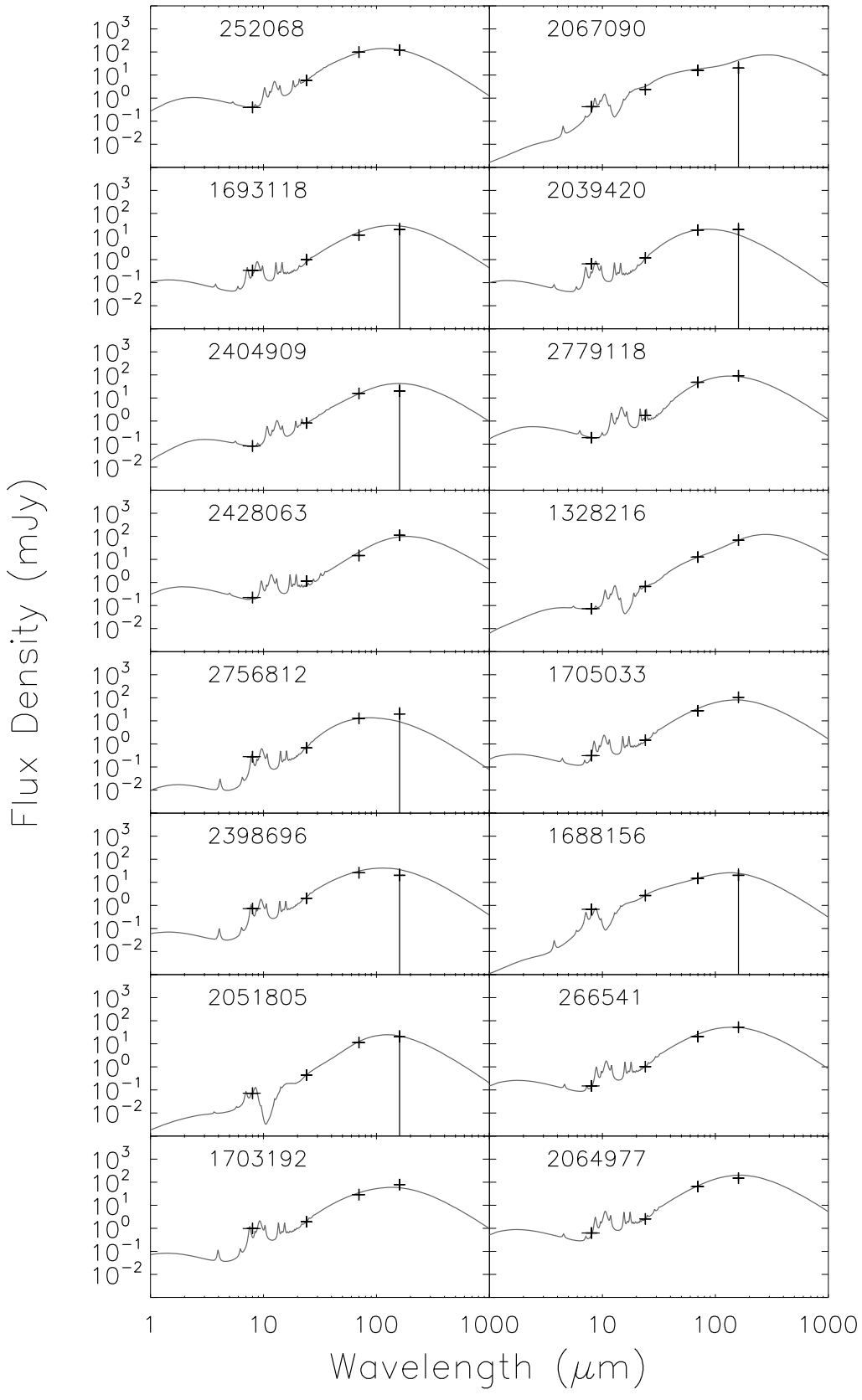
252068
2067090
1693118
2039420
2404909
2779118
2428063
1328216
2756812
1705033
2398696
1688156
2051805
266541
1703192
2064977
Flux Density (mJy)
Wavelength (μm)
1
10
100
1000

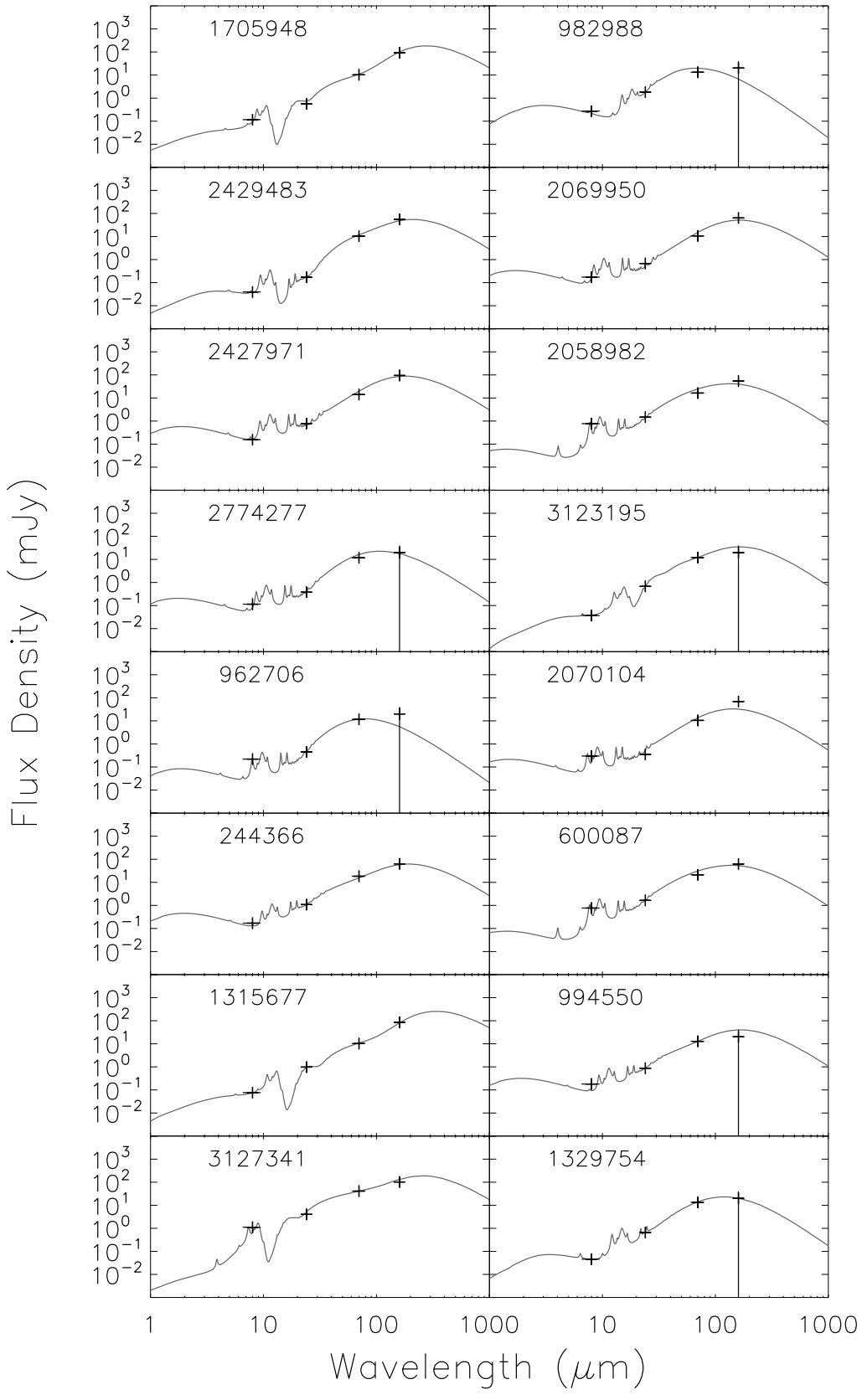
1705948
982988
2429483
2069950
2427971
2058982
2774277
3123195
962706
2070104
244366
600087
1315677
994550
3127341
1329754
Flux Density (mJy)
Wavelength (μm)
1
10
100
1000

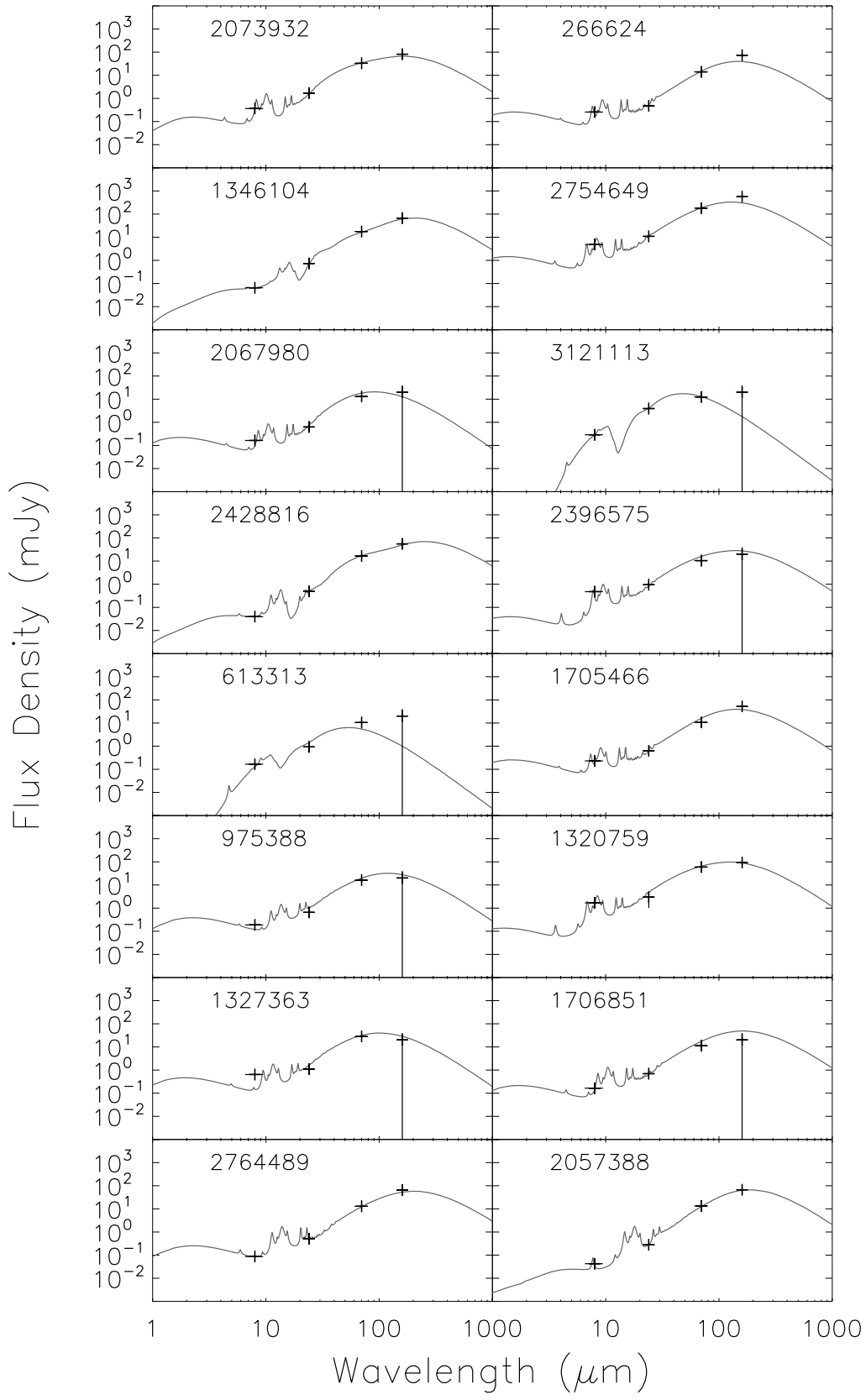
2073932
266624
1346104
2754649
2067980
3121113
2428816
2396575
613313
1705466
975388
1320759
1327363
1706851
2764489
2057388
Flux Density (mJy)
Wavelength (μm)
1
10
100
1000

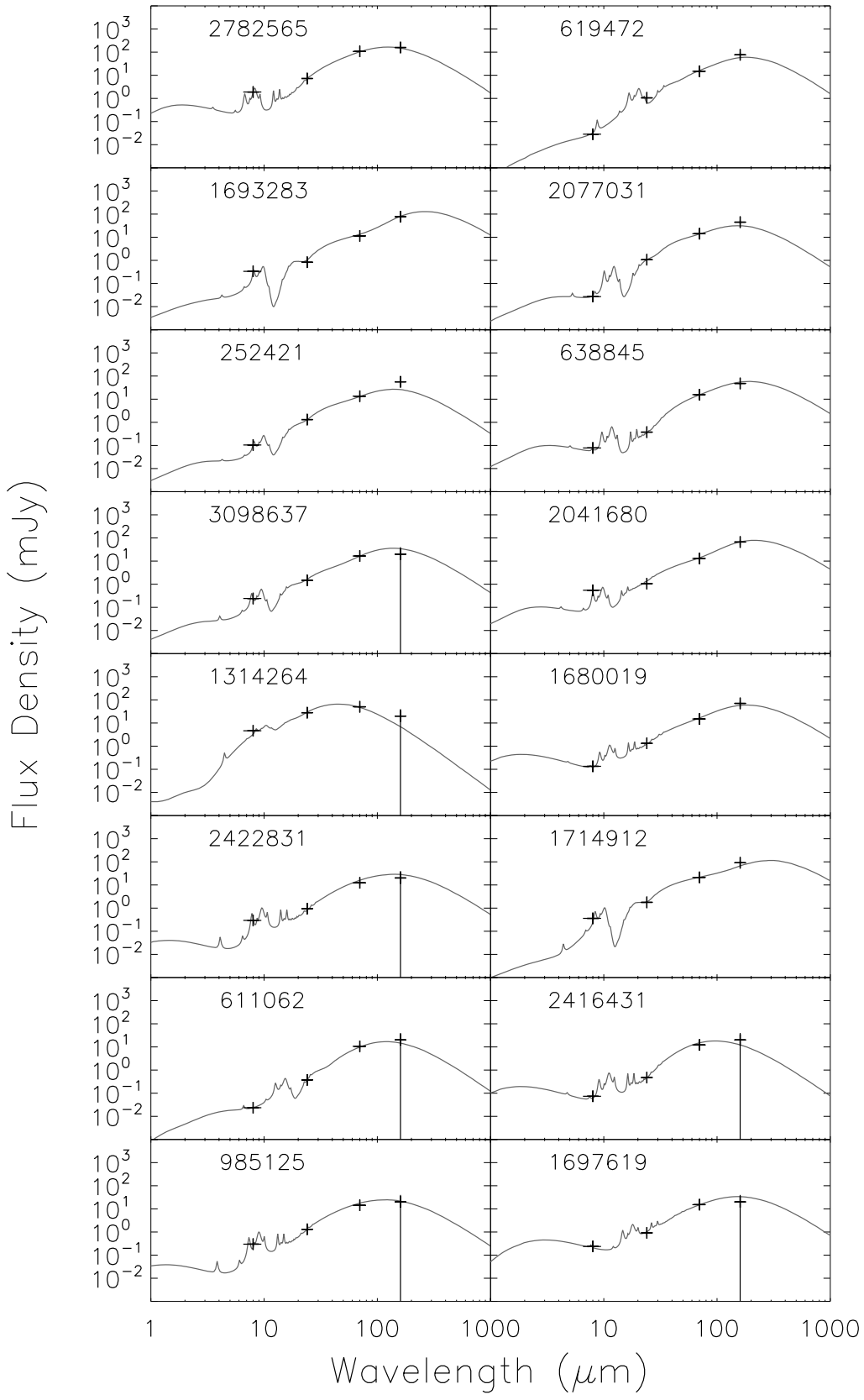
2782565
619472
1693283
2077031
252421
638845
3098637
2041680
1314264
1680019
2422831
1714912
611062
2416431
985125
1697619
Flux Density (mJy)
Wavelength (μm)
1
10
100
1000

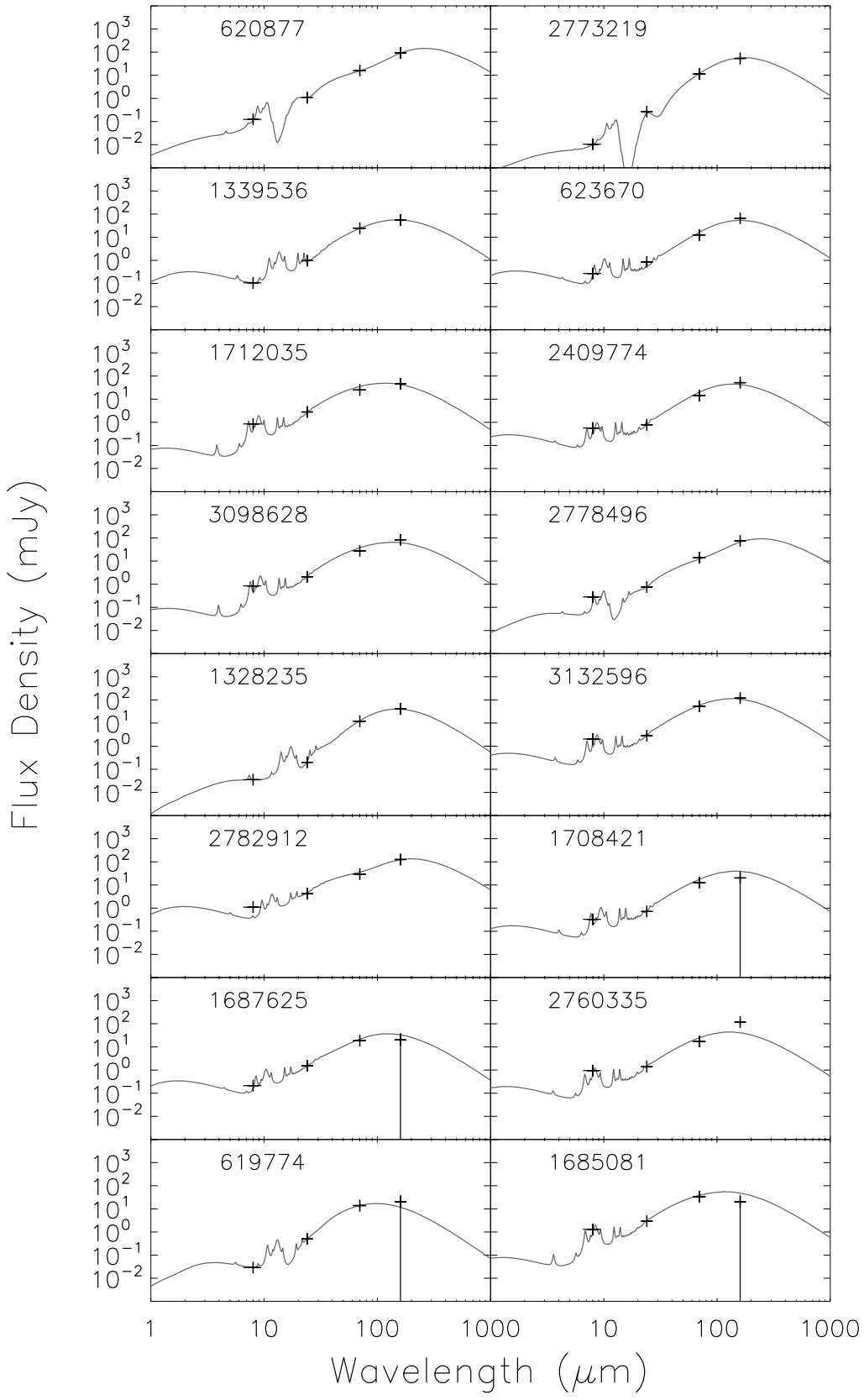
620877
2773219
1339536
623670
1712035
2409774
3098628
2778496
1328235
3132596
2782912
1708421
1687625
2760335
619774
1685081
Flux Density (mJy)
Wavelength (μm)
1
10
100
1000

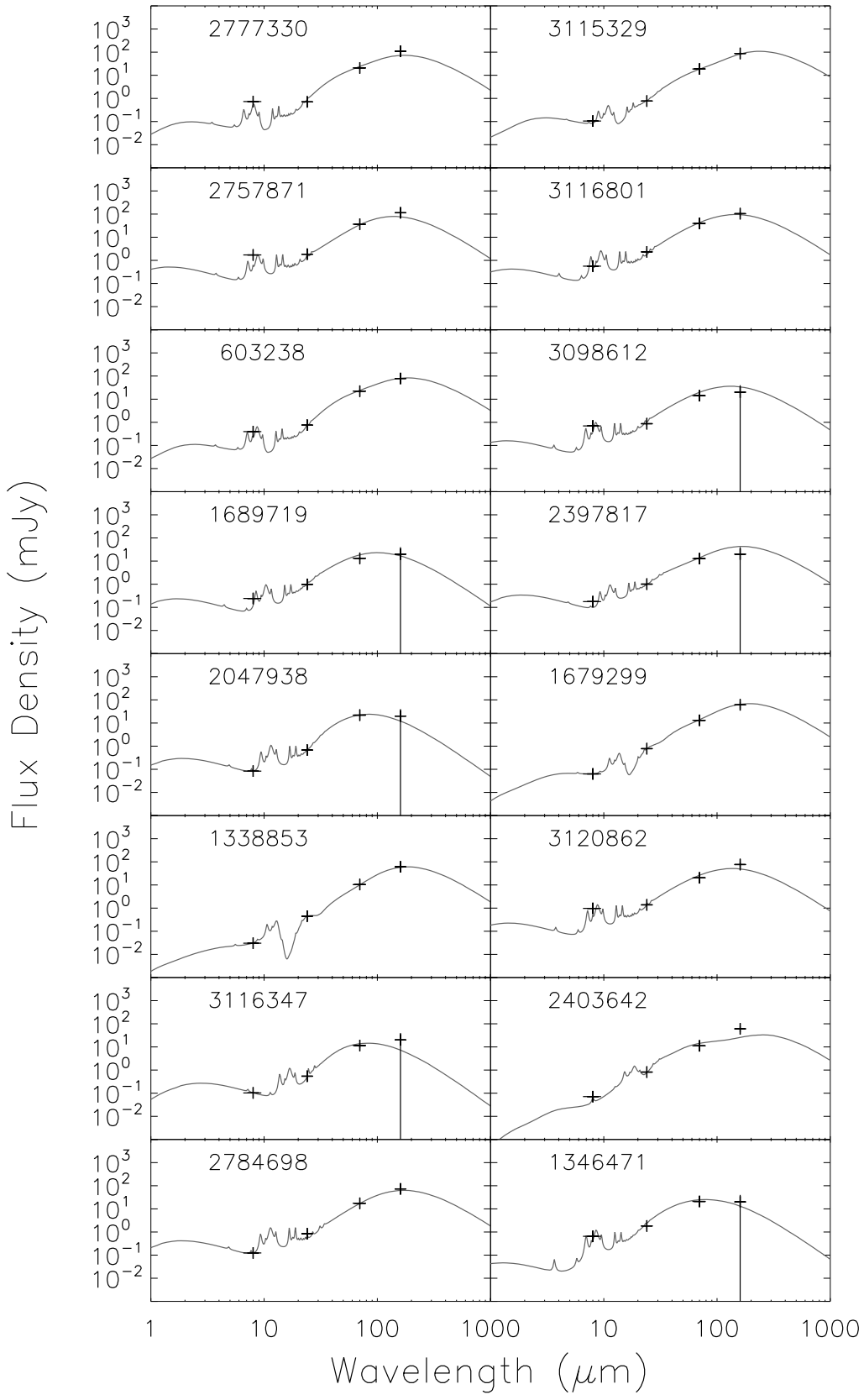
2777330
3115329
2757871
3116801
603238
3098612
1689719
2397817
2047938
1679299
1338853
3120862
3116347
2403642
2784698
1346471
Flux Density (mJy)
Wavelength (μm)
1
10
100
1000

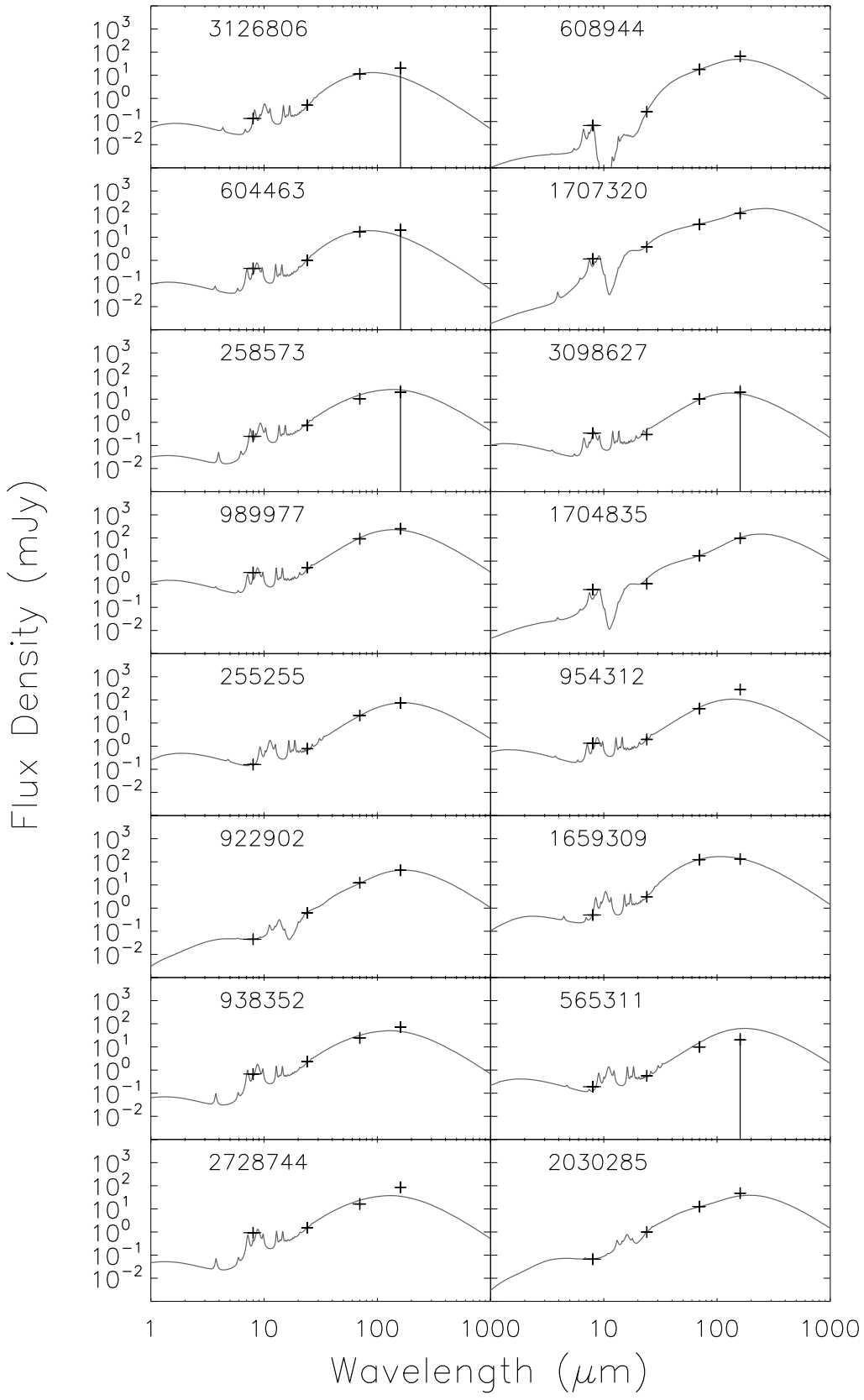
3126806
608944
604463
1707320
258573
3098627
989977
1704835
255255
954312
922902
1659309
938352
565311
2728744
2030285
Flux Density (mJy)
Wavelength (μm)
1
10
100
1000

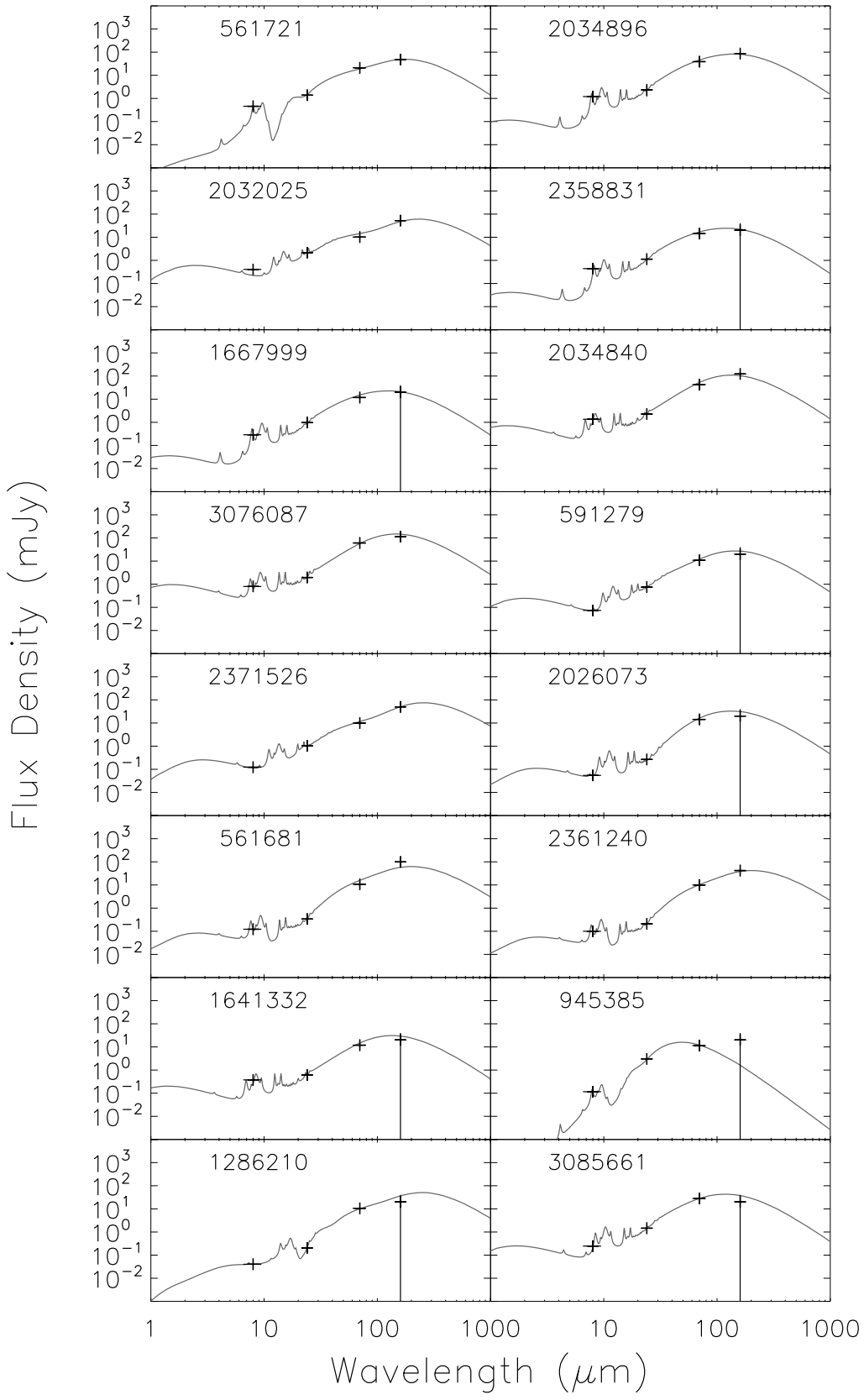
561721
2034896
2032025
2358831
1667999
2034840
3076087
591279
2371526
2026073
561681
2361240
1641332
945385
1286210
3085661
Flux Density (mJy)
Wavelength (μm)
1
10
100
1000

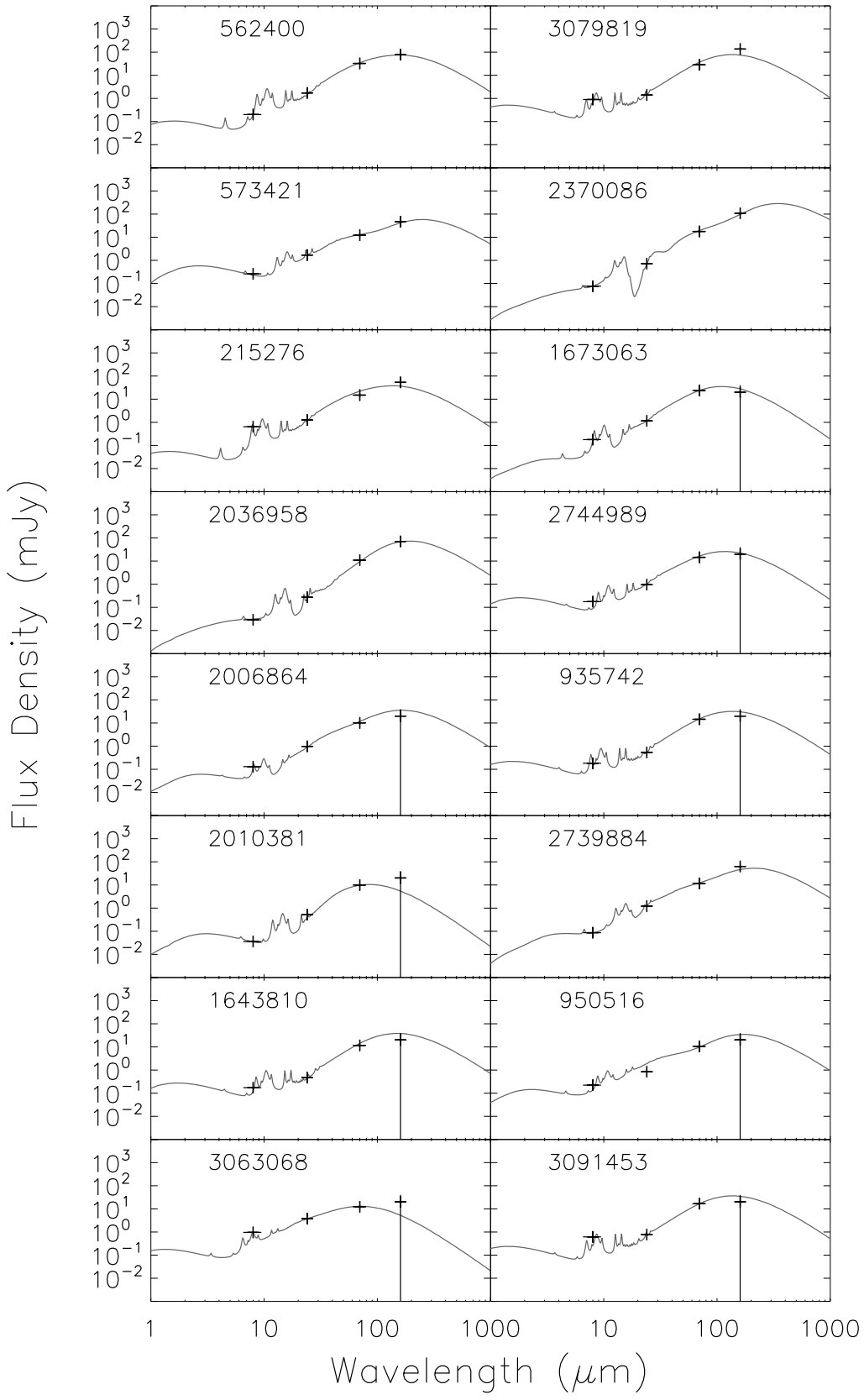
562400
3079819
573421
2370086
215276
1673063
2036958
2744989
2006864
935742
2010381
2739884
1643810
950516
3063068
3091453
Flux Density (mJy)
Wavelength (μm)
1
10
100
1000

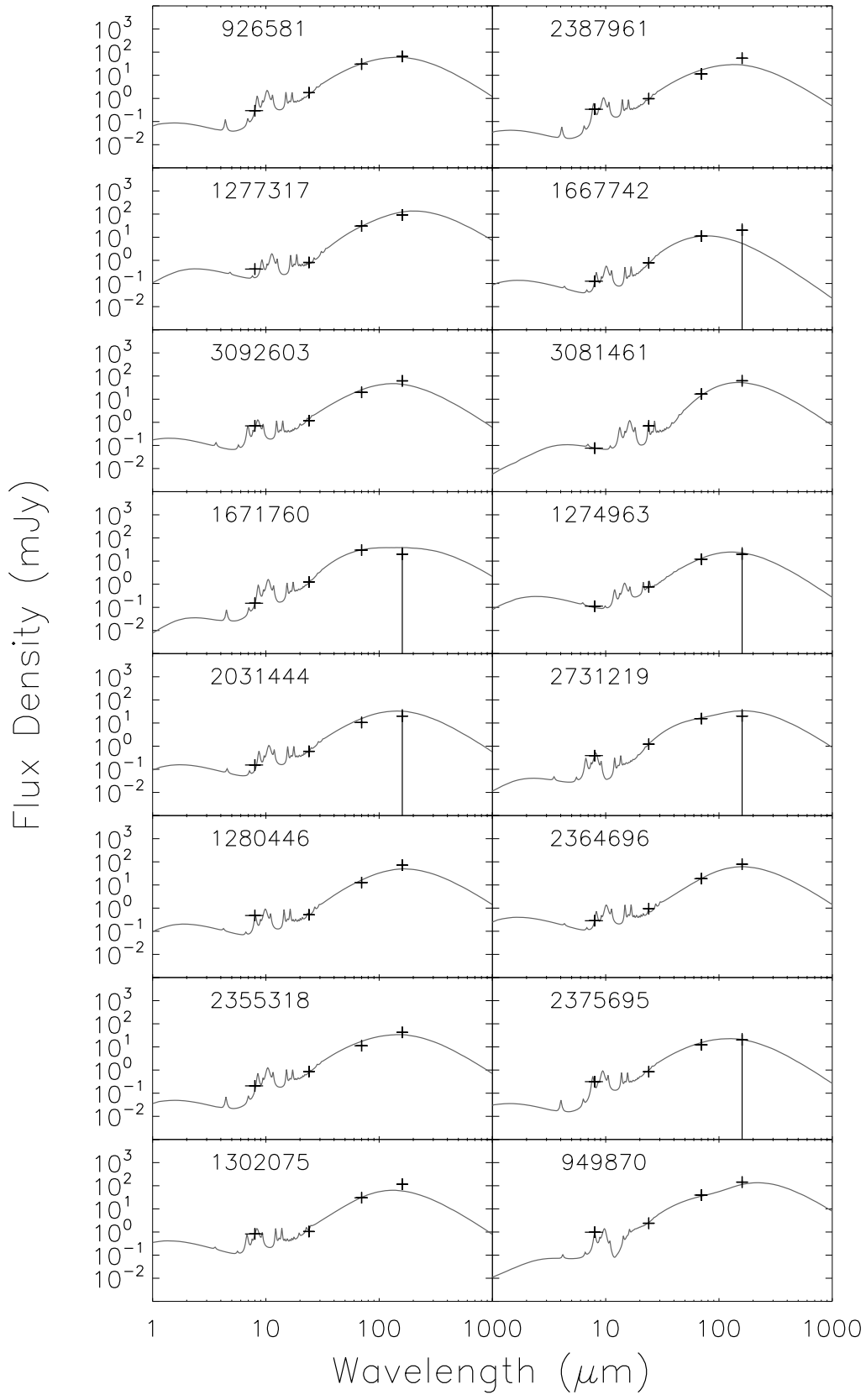
926581
2387961
1277317
1667742
3092603
3081461
1671760
1274963
2031444
2731219
1280446
2364696
2355318
2375695
1302075
949870
Flux Density (mJy)
Wavelength (μm)
1
10
100
1000

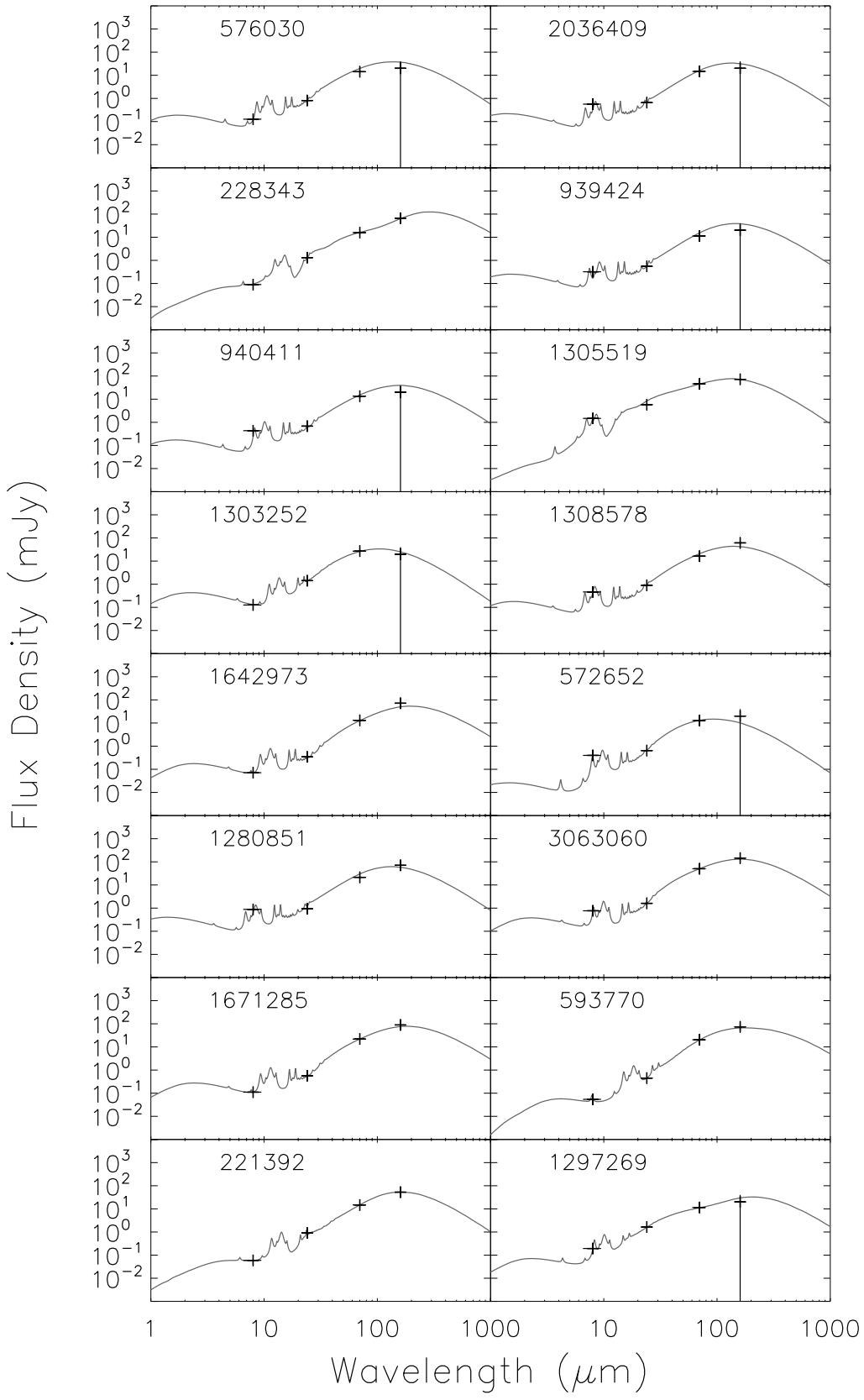
576030
2036409
228343
939424
940411
1305519
1303252
1308578
1642973
572652
1280851
3063060
1671285
593770
221392
1297269
Flux Density (mJy)
Wavelength (μm)
1
10
100
1000

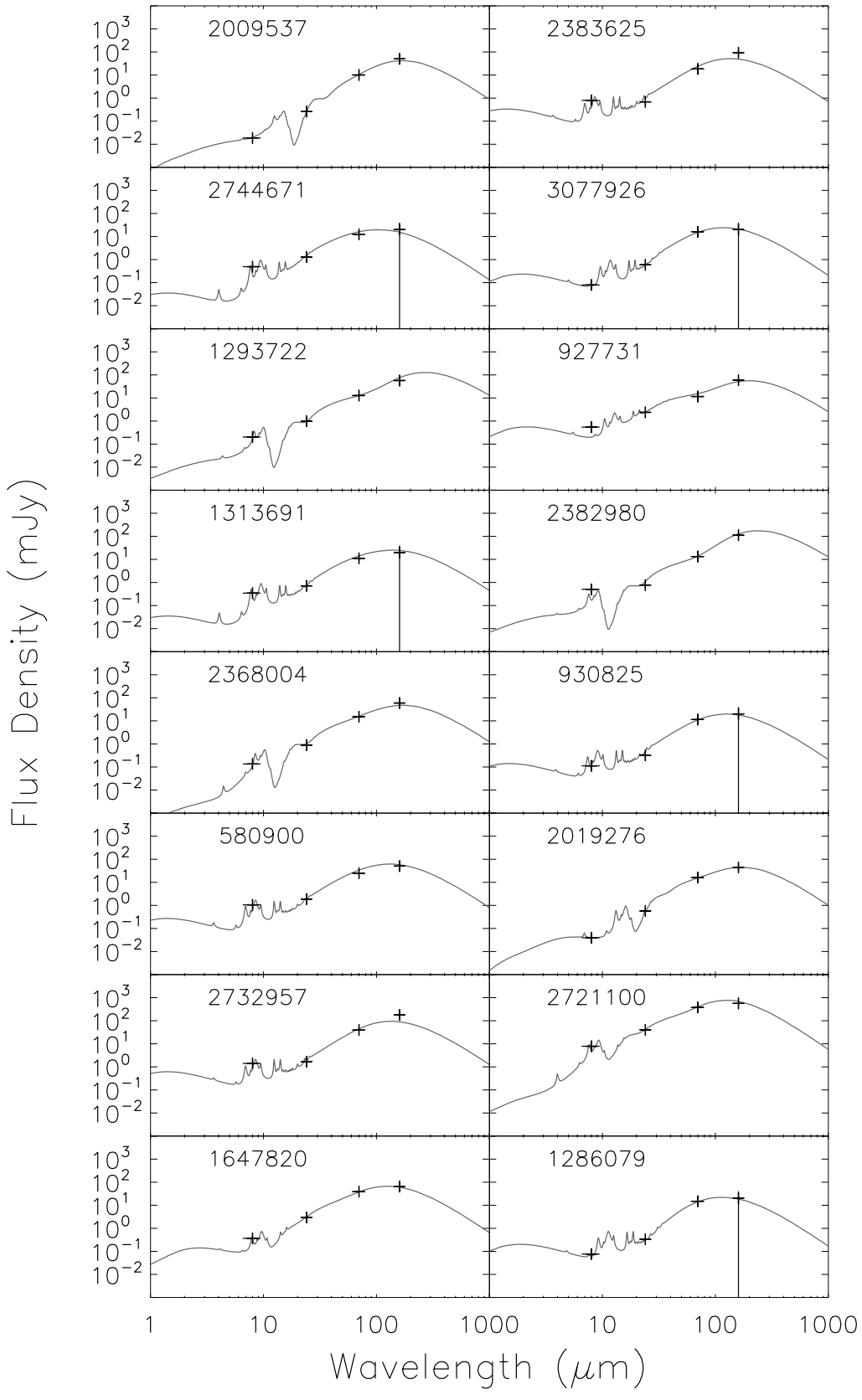
2009537
2383625
2744671
3077926
1293722
927731
1313691
2382980
2368004
930825
580900
2019276
2732957
2721100
1647820
1286079
Flux Density (mJy)
Wavelength (μm)
1
10
100
1000

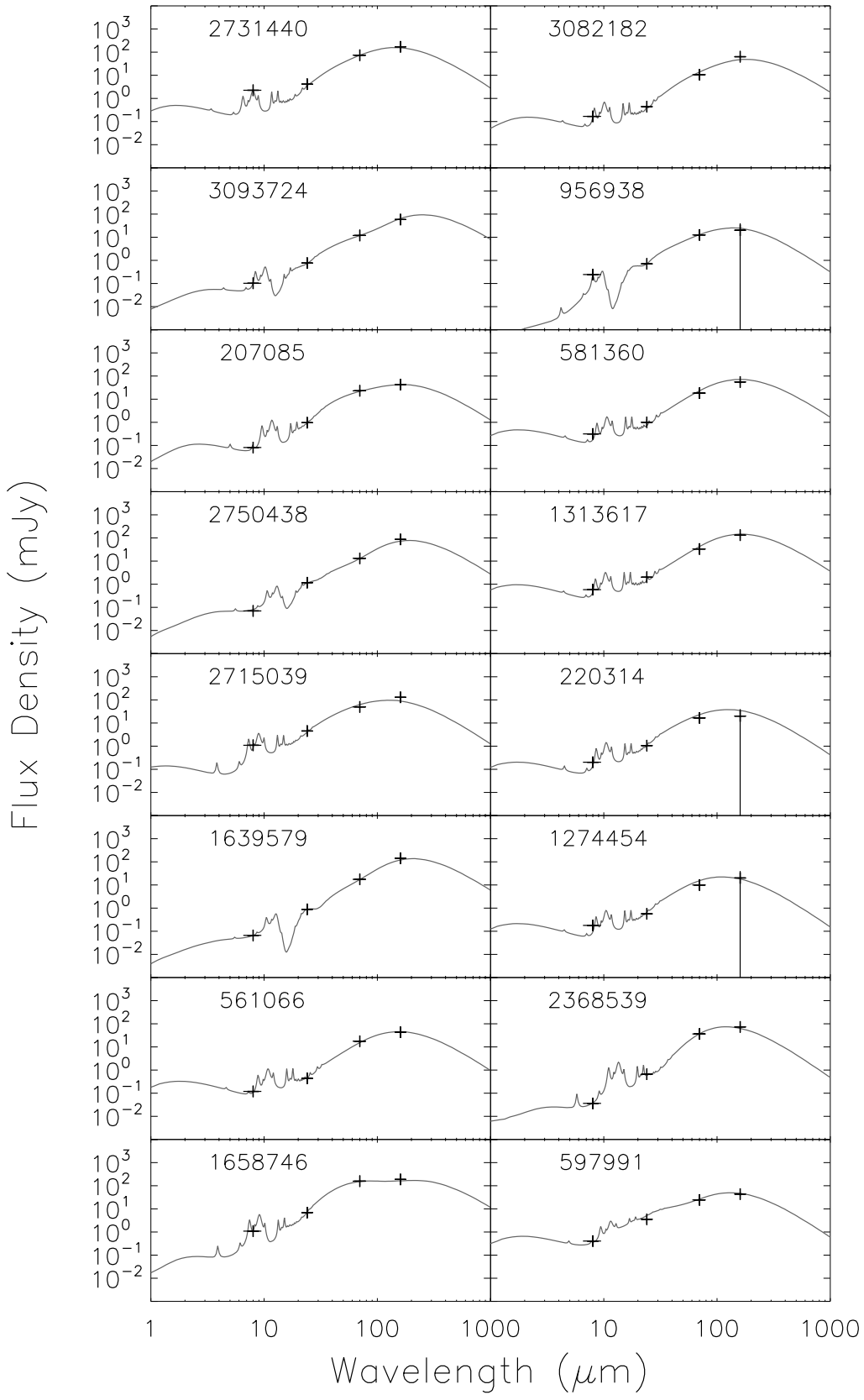
2731440
3082182
3093724
956938
207085
581360
2750438
1313617
2715039
220314
1639579
1274454
561066
2368539
1658746
597991
Flux Density (mJy)
Wavelength (μm)
1
10
100
1000

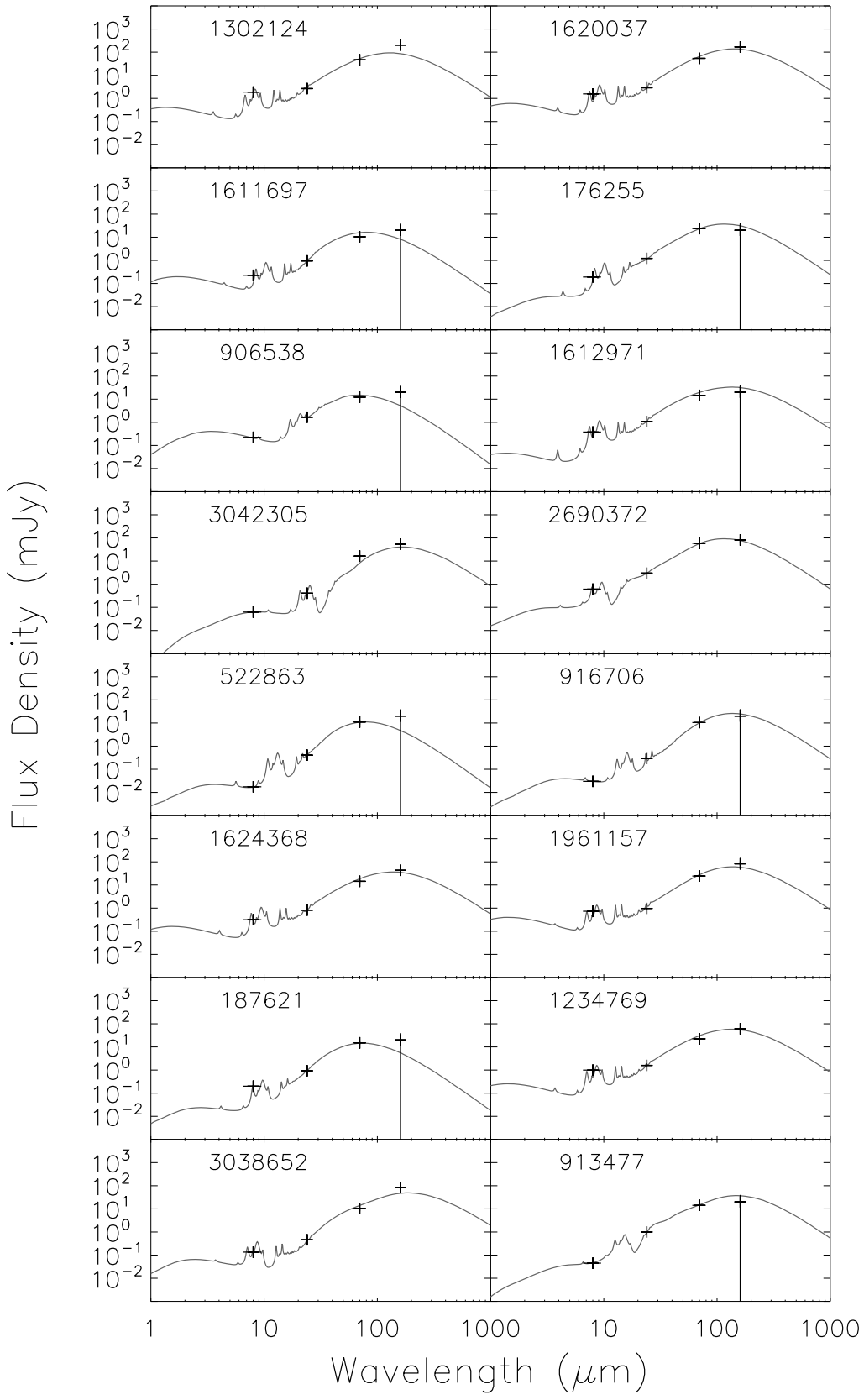
1302124
1620037
1611697
176255
906538
1612971
3042305
2690372
522863
916706
1624368
1961157
187621
1234769
3038652
913477
Flux Density (mJy)
Wavelength (μm)
1
10
100
1000

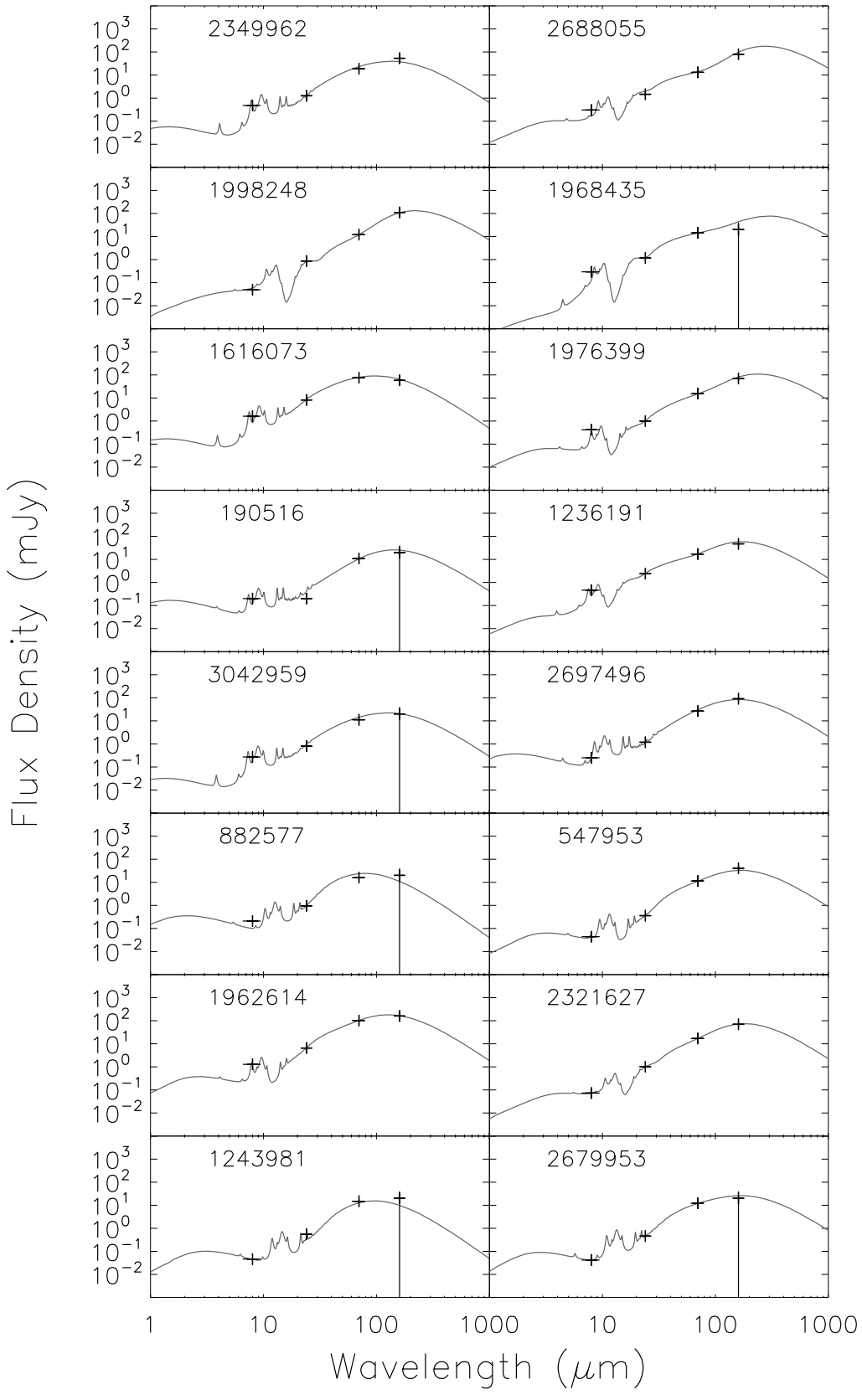
2349962
2688055
1998248
1968435
1616073
1976399
190516
1236191
3042959
2697496
882577
547953
1962614
2321627
1243981
2679953
Flux Density (mJy)
Wavelength (μm)
1
10
100
1000

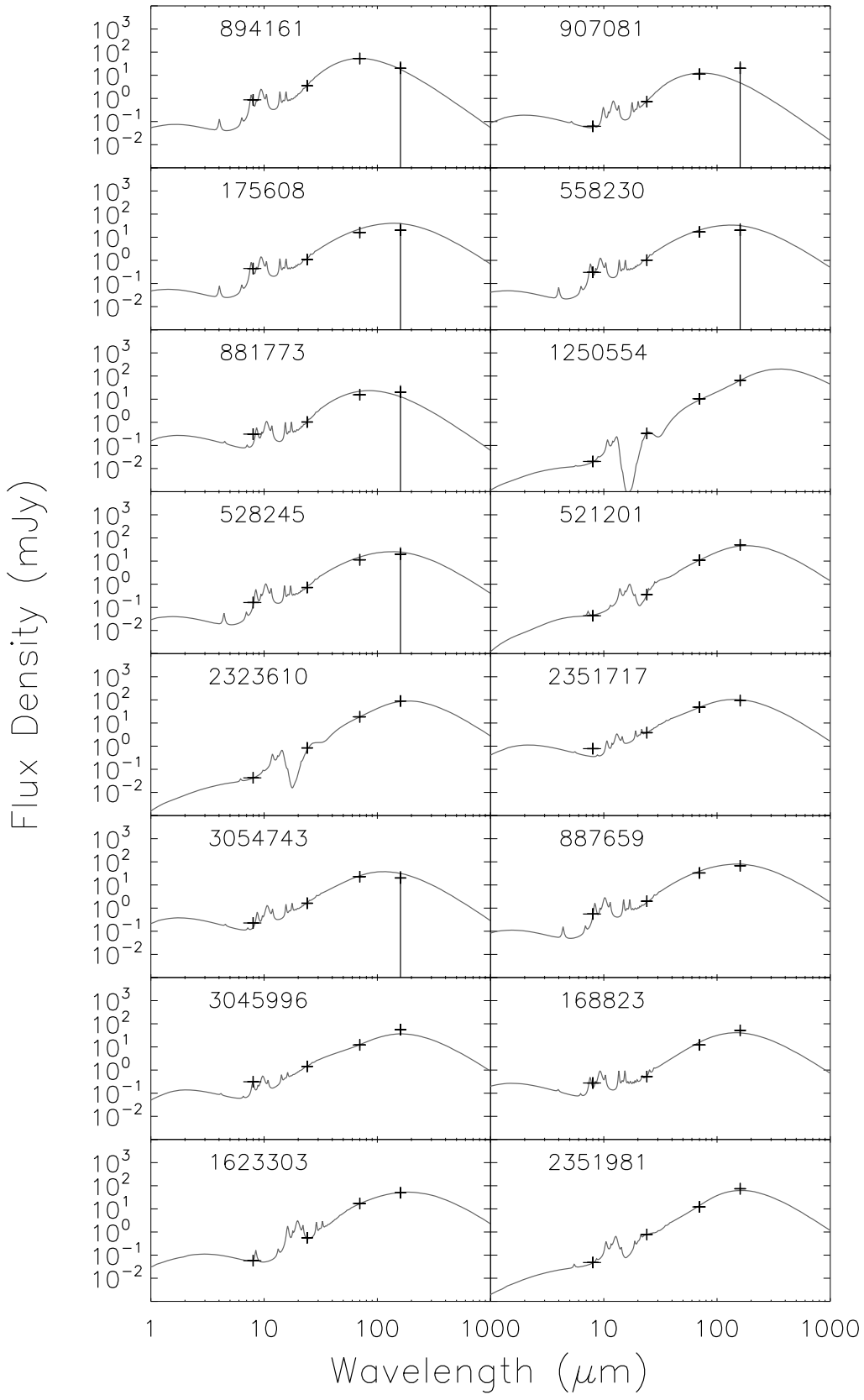
894161
907081
175608
558230
881773
1250554
528245
521201
2323610
2351717
3054743
887659
3045996
168823
1623303
2351981
Flux Density (mJy)
Wavelength (μm)
1
10
100
1000

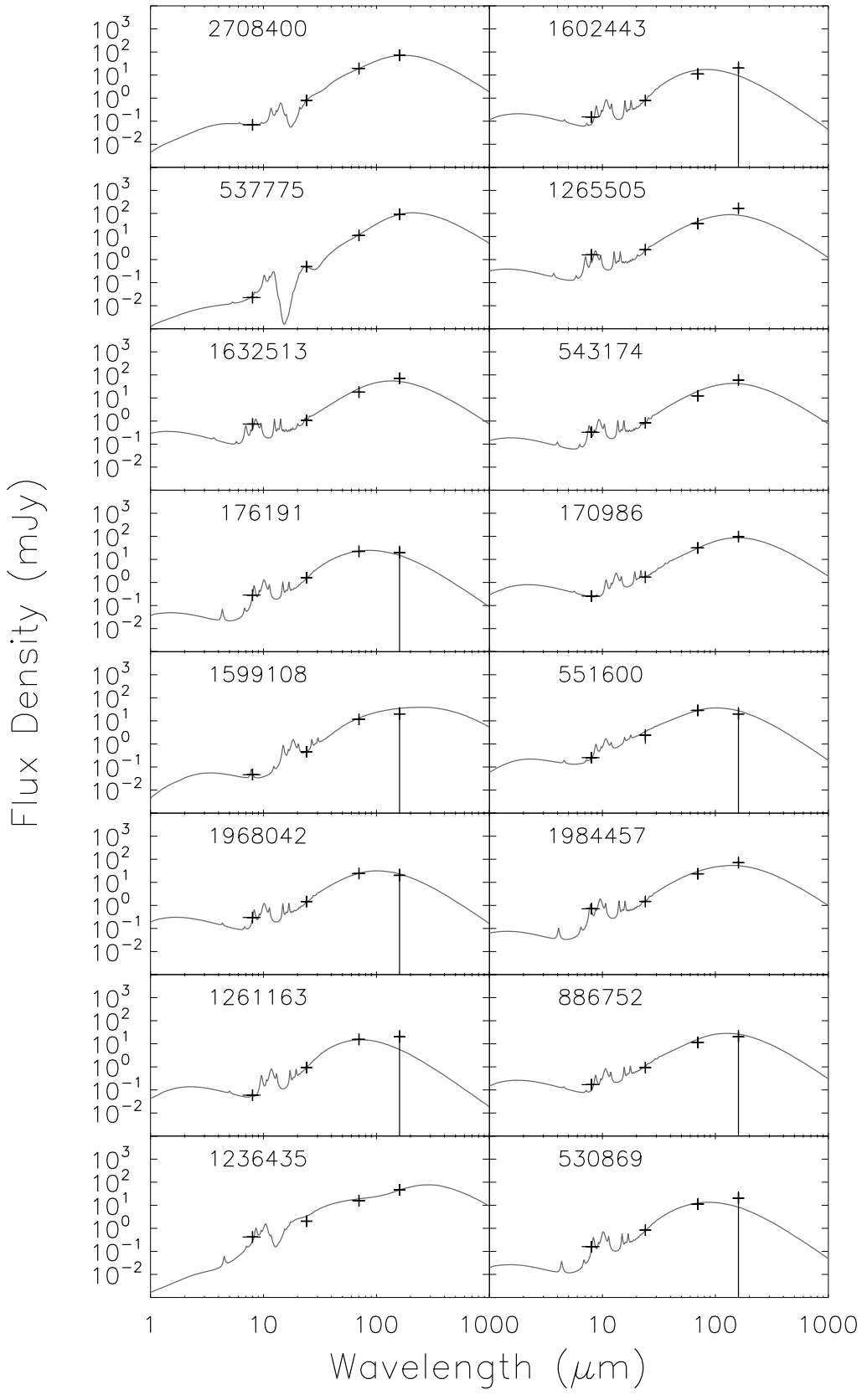
2708400
1602443
537775
1265505
1632513
543174
176191
170986
1599108
551600
1968042
1984457
1261163
886752
1236435
530869
Flux Density (mJy)
Wavelength (μm)
1
10
100
1000

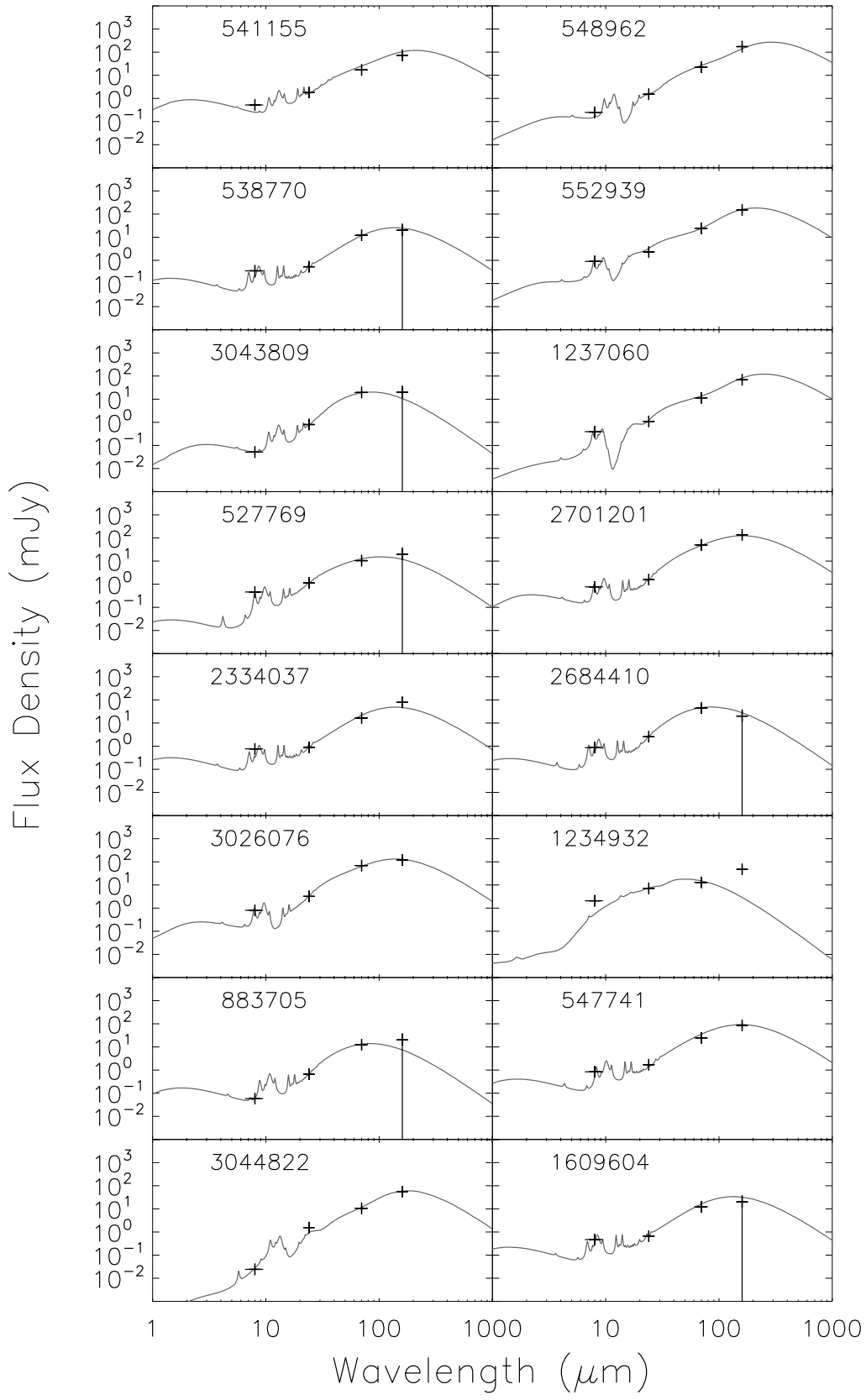
541155
548962
538770
552939
3043809
1237060
527769
2701201
2334037
2684410
3026076
1234932
883705
547741
3044822
1609604
Flux Density (mJy)
Wavelength (μm)
1
10
100
1000

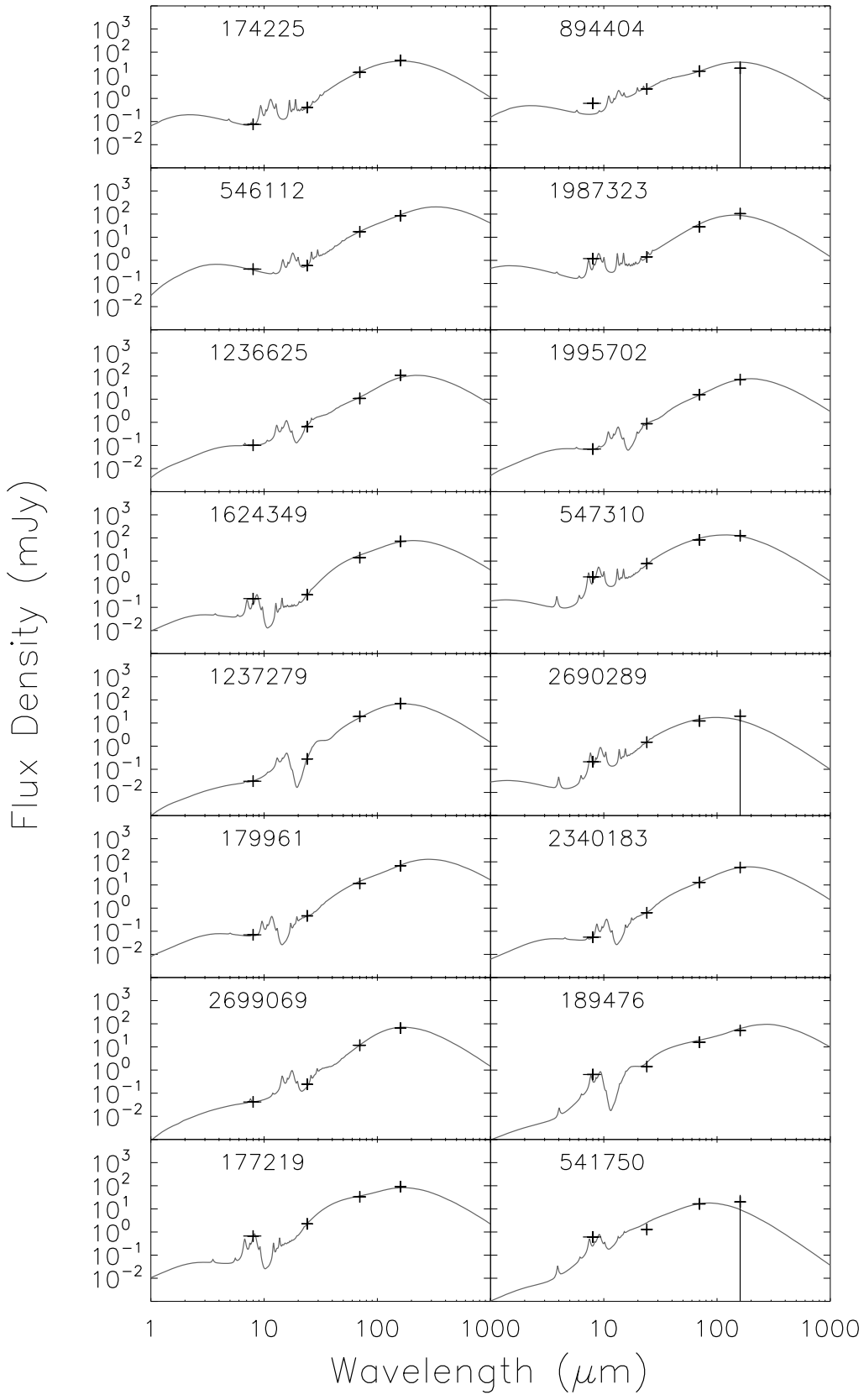
174225
894404
546112
1987323
1236625
1995702
1624349
547310
1237279
2690289
179961
2340183
2699069
189476
177219
541750
Flux Density (mJy)
Wavelength (μm)
1
10
100
1000

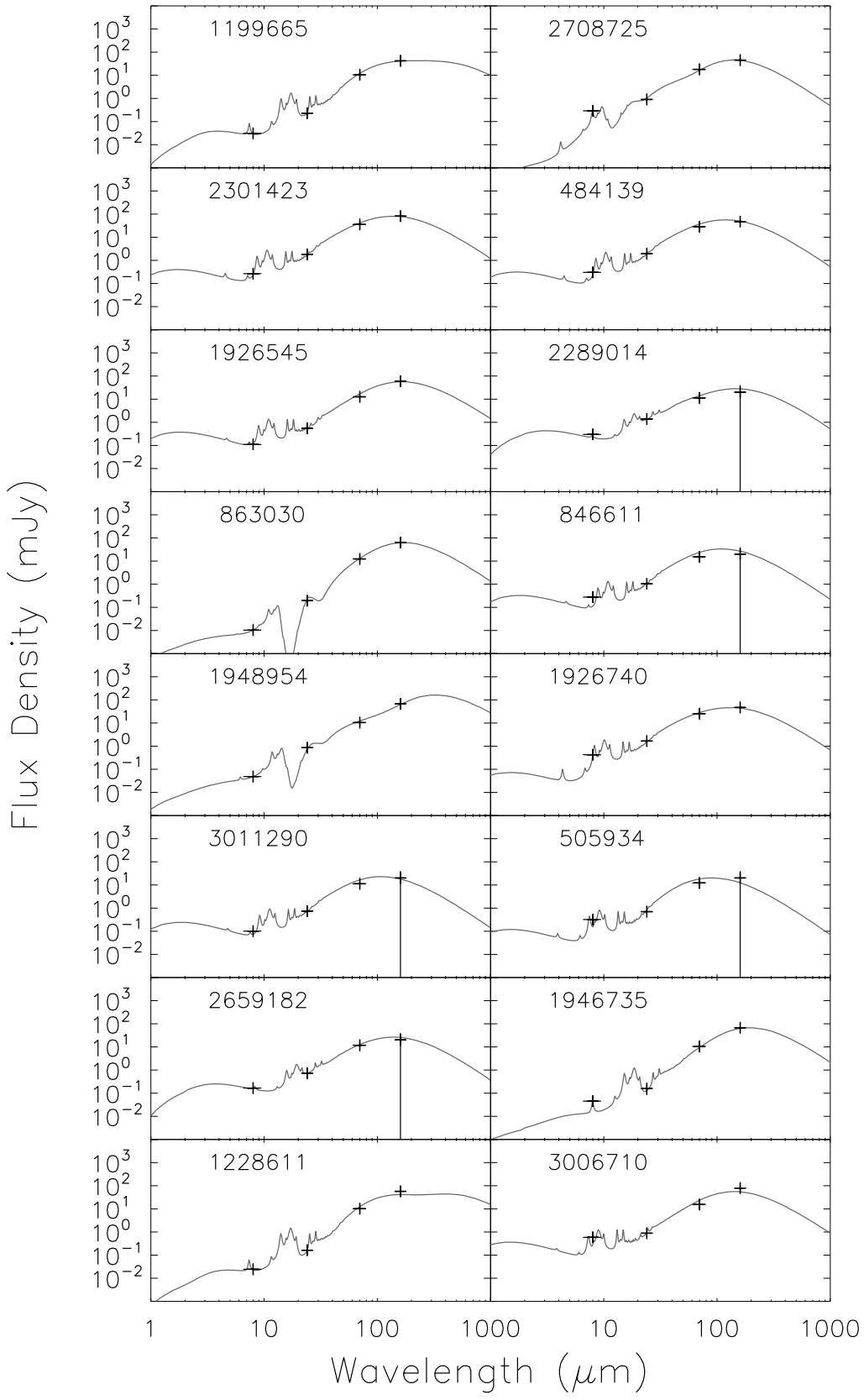
1199665
2708725
2301423
484139
1926545
2289014
863030
846611
1948954
1926740
3011290
505934
2659182
1946735
1228611
3006710
Flux Density (mJy)
Wavelength (μm)
1
10
100
1000

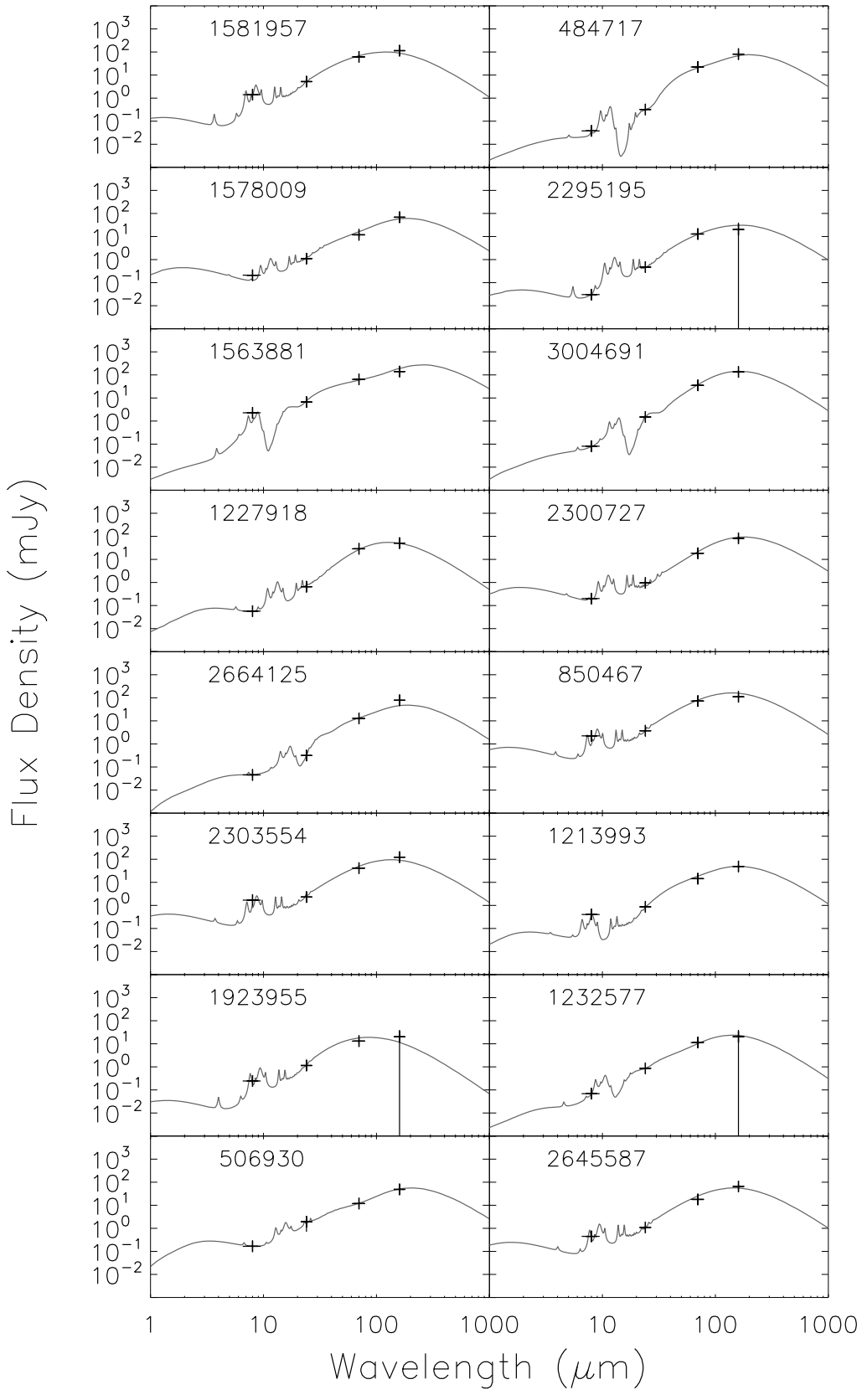
1581957
484717
1578009
2295195
1563881
3004691
1227918
2300727
2664125
850467
2303554
1213993
1923955
1232577
506930
2645587
Flux Density (mJy)
Wavelength (μm)
1
10
100
1000

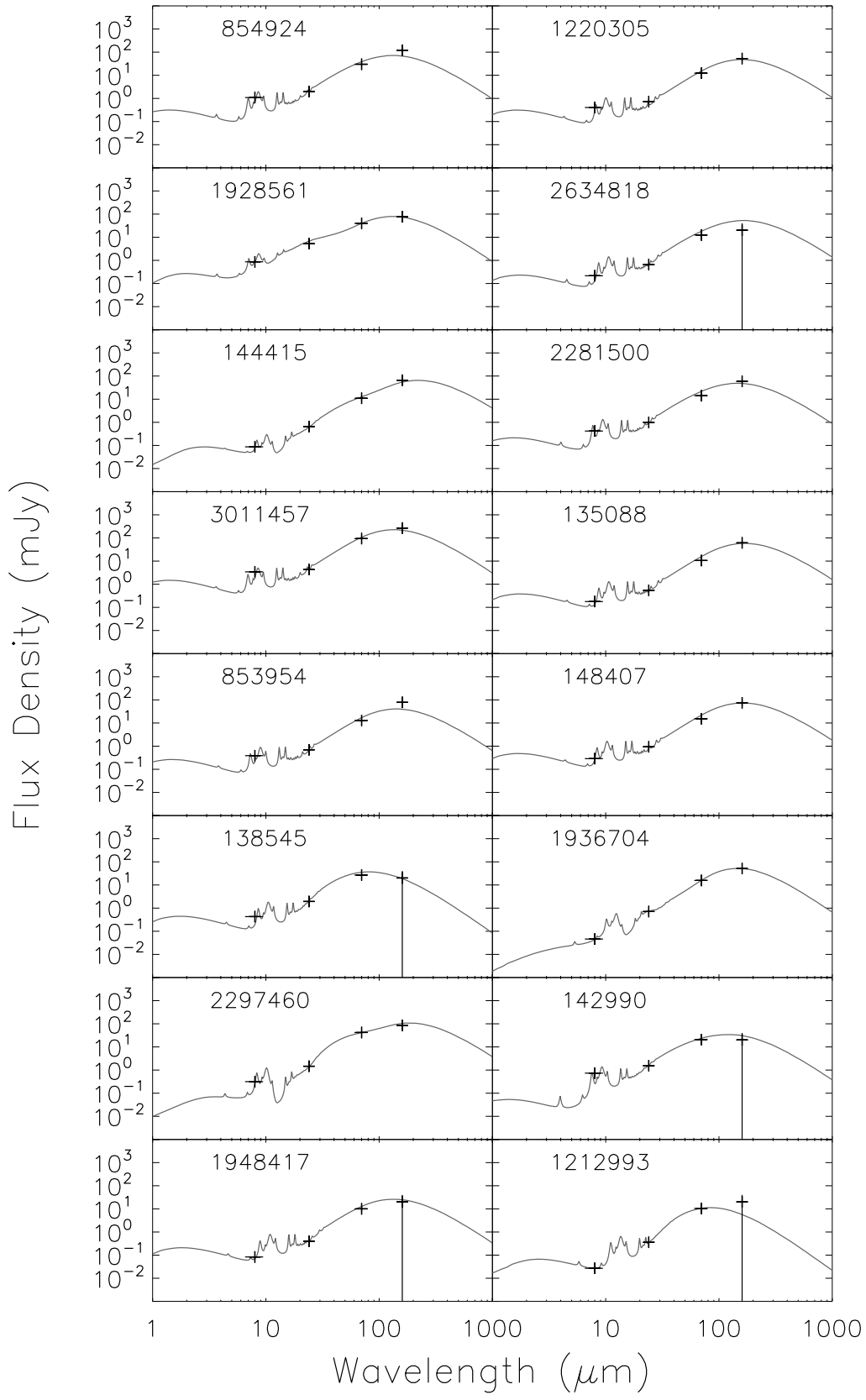
854924
1220305
1928561
2634818
144415
2281500
3011457
135088
853954
148407
138545
1936704
2297460
142990
1948417
1212993
Flux Density (mJy)
Wavelength (μm)
1
10
100
1000

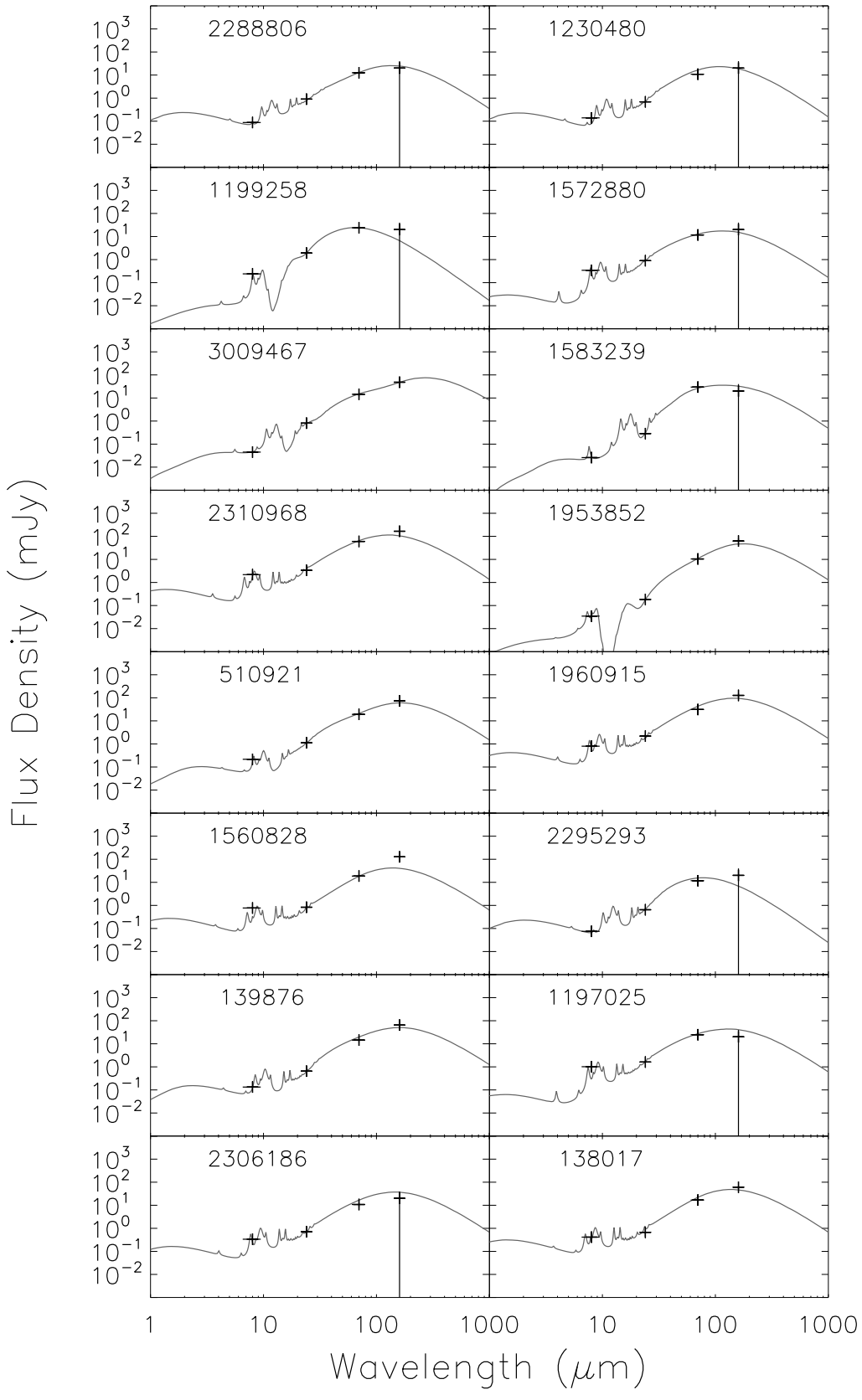
2288806
1230480
1199258
1572880
3009467
1583239
2310968
1953852
510921
1960915
1560828
2295293
139876
1197025
2306186
138017
Flux Density (mJy)
Wavelength (μm)
1
10
100
1000

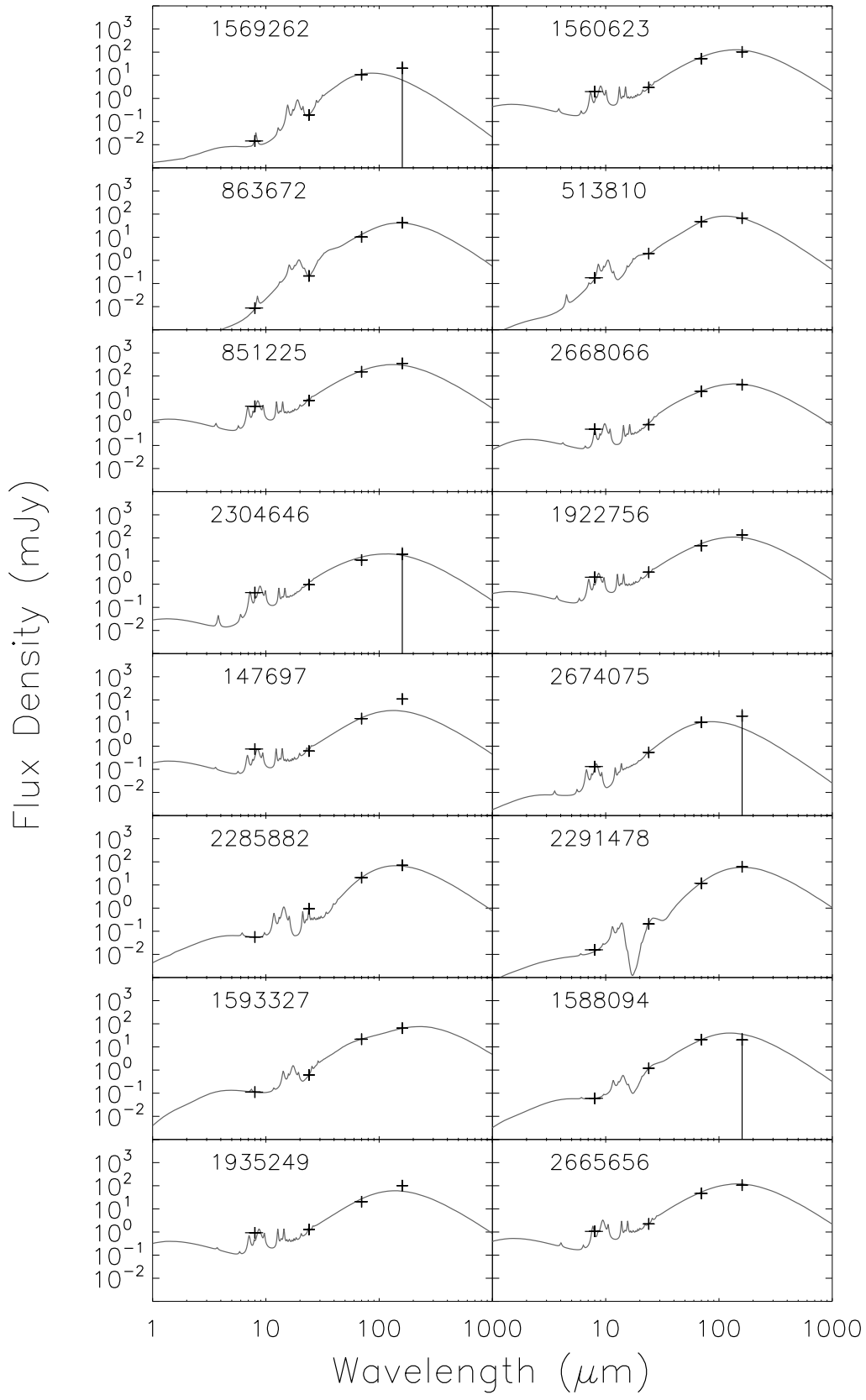
1569262
1560623
863672
513810
851225
2668066
2304646
1922756
147697
2674075
2285882
2291478
1593327
1588094
1935249
2665656
Flux Density (mJy)
Wavelength (μm)
1
10
100
1000

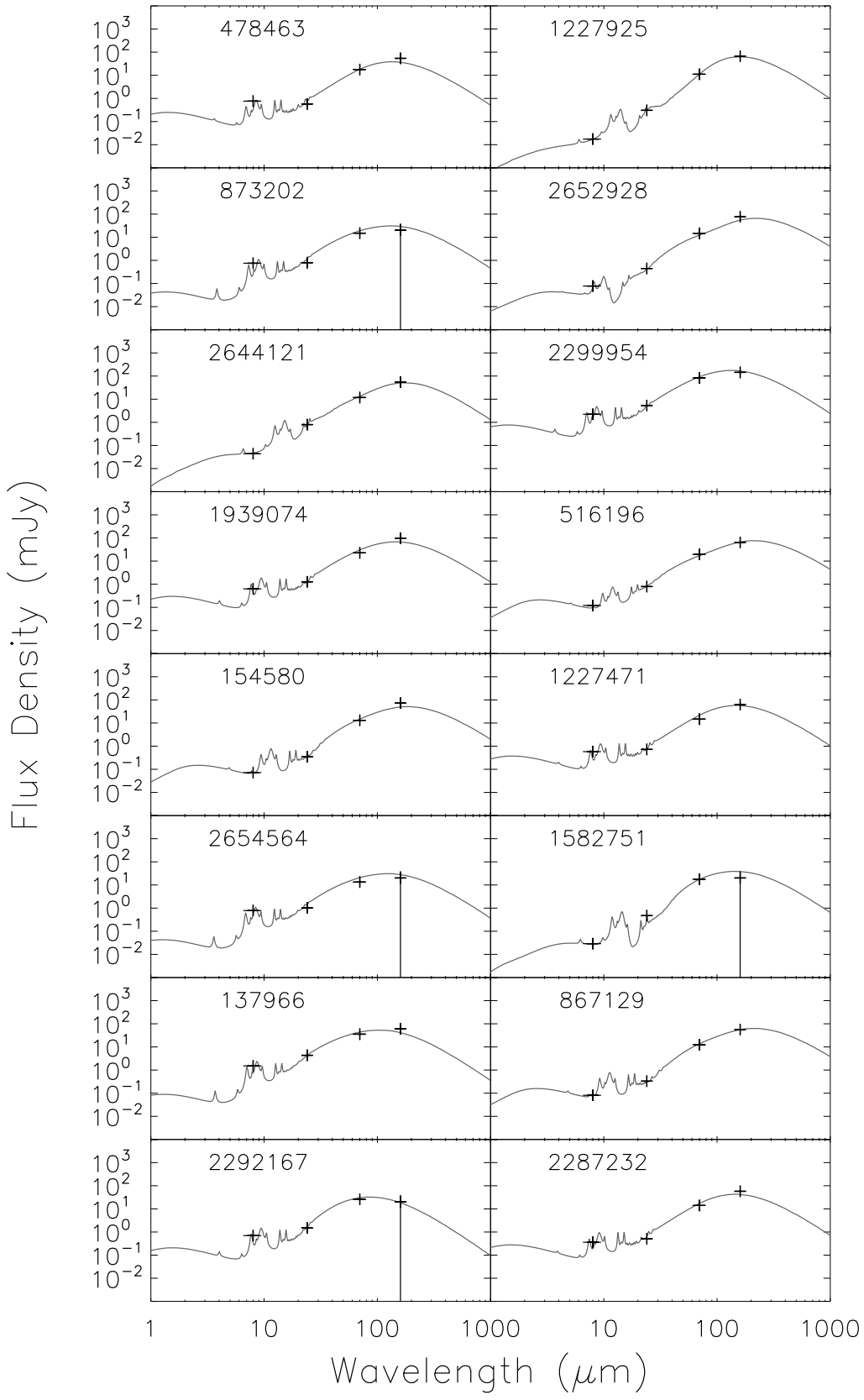
478463
1227925
873202
2652928
2644121
2299954
1939074
516196
154580
1227471
2654564
1582751
137966
867129
2292167
2287232
Flux Density (mJy)
Wavelength (μm)
1
10
100
1000

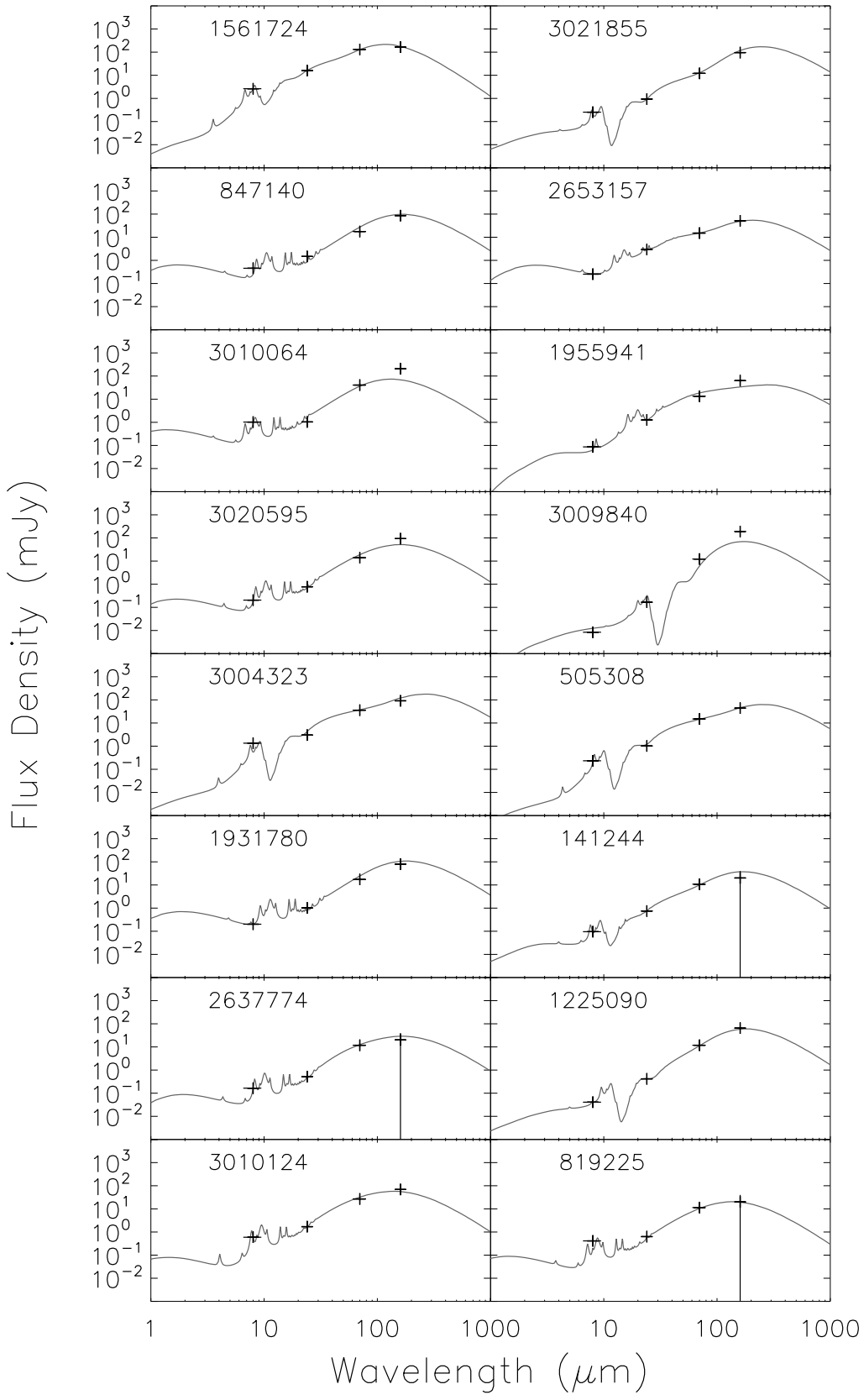
1561724
3021855
847140
2653157
3010064
1955941
3020595
3009840
3004323
505308
1931780
141244
2637774
1225090
3010124
819225
Flux Density (mJy)
Wavelength (μm)
1
10
100
1000

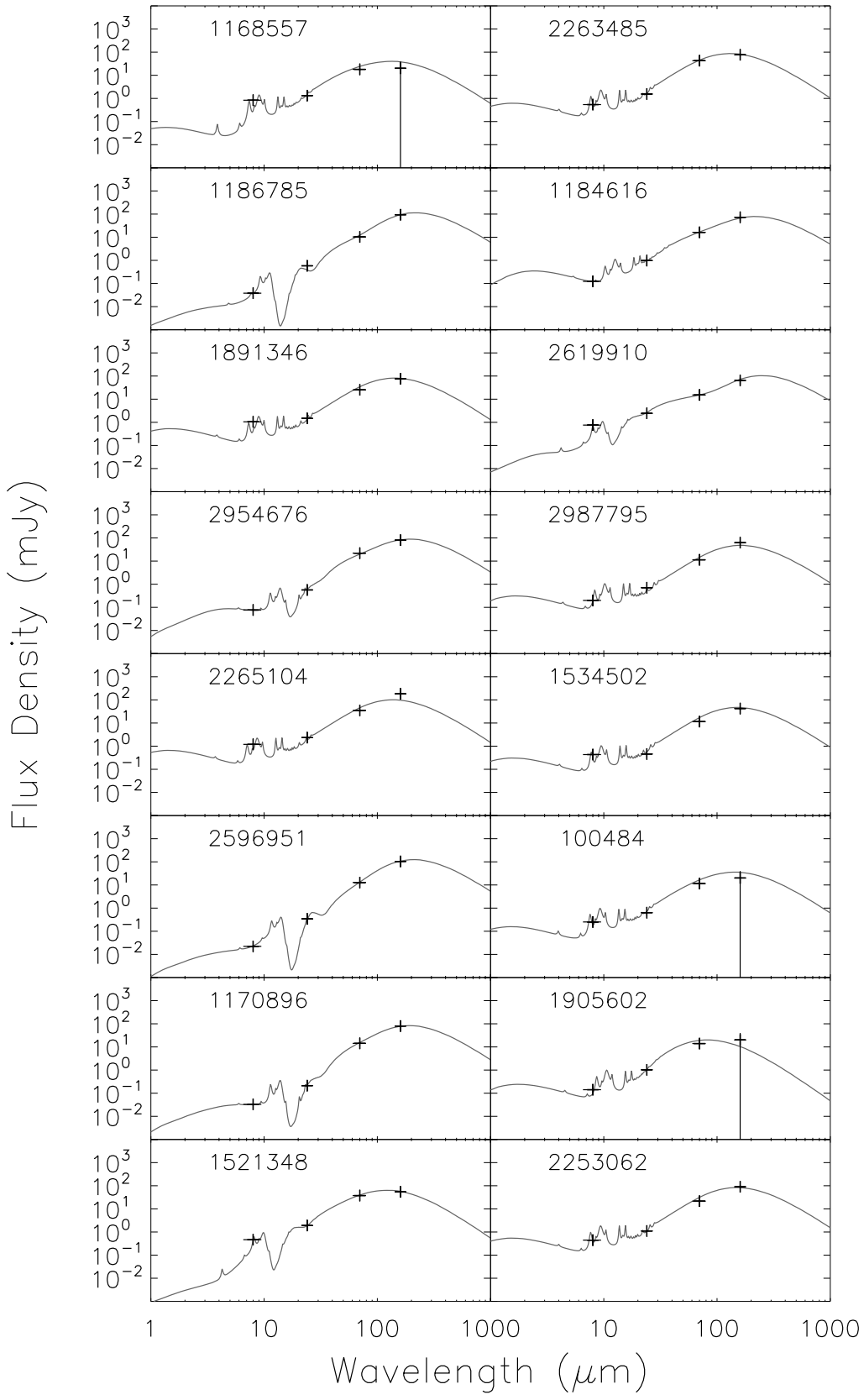
1168557
2263485
1186785
1184616
1891346
2619910
2954676
2987795
2265104
1534502
2596951
100484
1170896
1905602
1521348
2253062
Flux Density (mJy)
Wavelength (μm)
1
10
100
1000

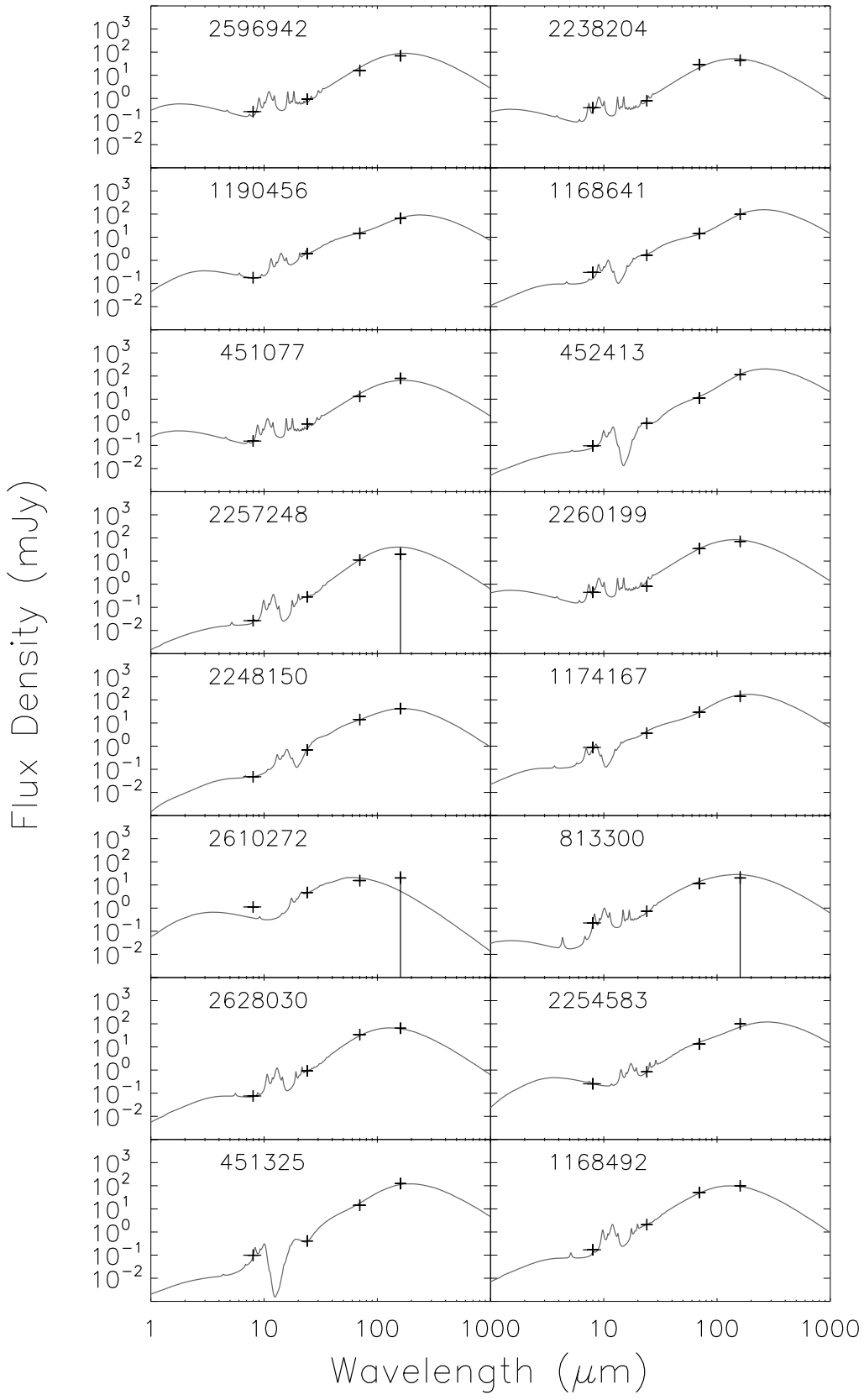
2596942
2238204
1190456
1168641
451077
452413
2257248
2260199
2248150
1174167
2610272
813300
2628030
2254583
451325
1168492
Flux Density (mJy)
Wavelength (μm)
1
10
100
1000

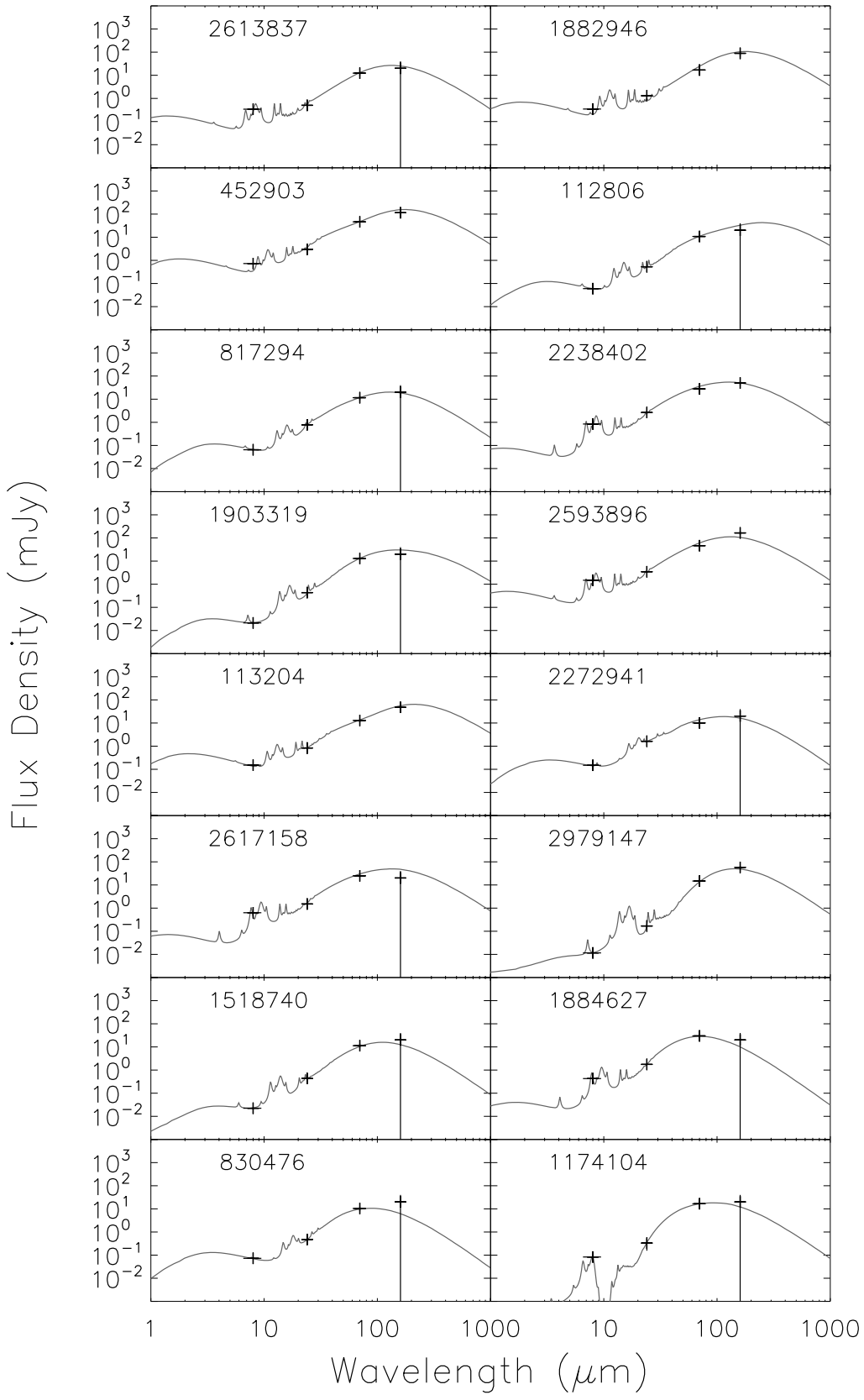
2613837
1882946
452903
112806
817294
2238402
1903319
2593896
113204
2272941
2617158
2979147
1518740
1884627
830476
1174104
Flux Density (mJy)
Wavelength (μm)
1
10
100
1000

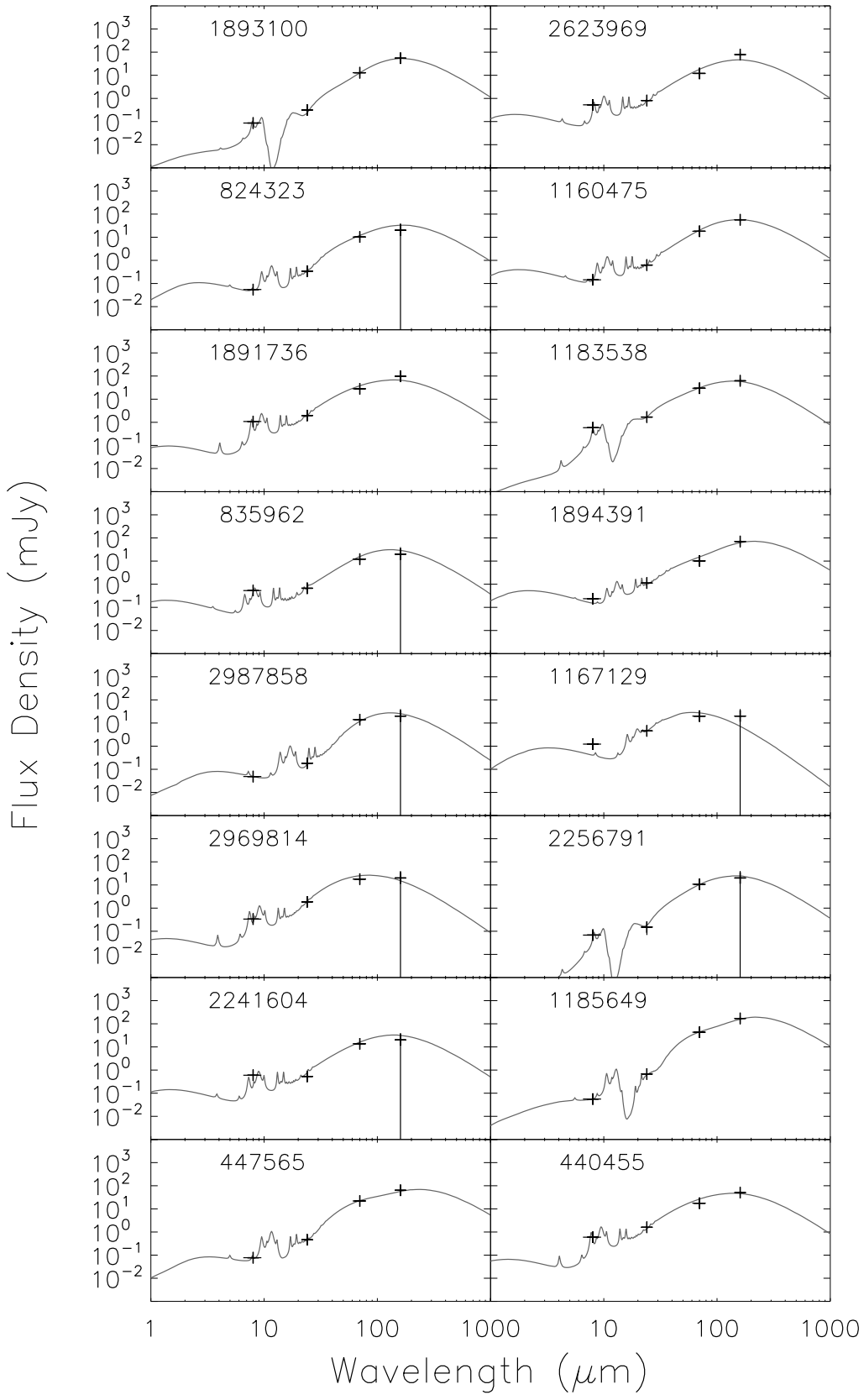
1893100
2623969
824323
1160475
1891736
1183538
835962
1894391
2987858
1167129
2969814
2256791
2241604
1185649
447565
440455
Flux Density (mJy)
Wavelength (μm)
1
10
100
1000

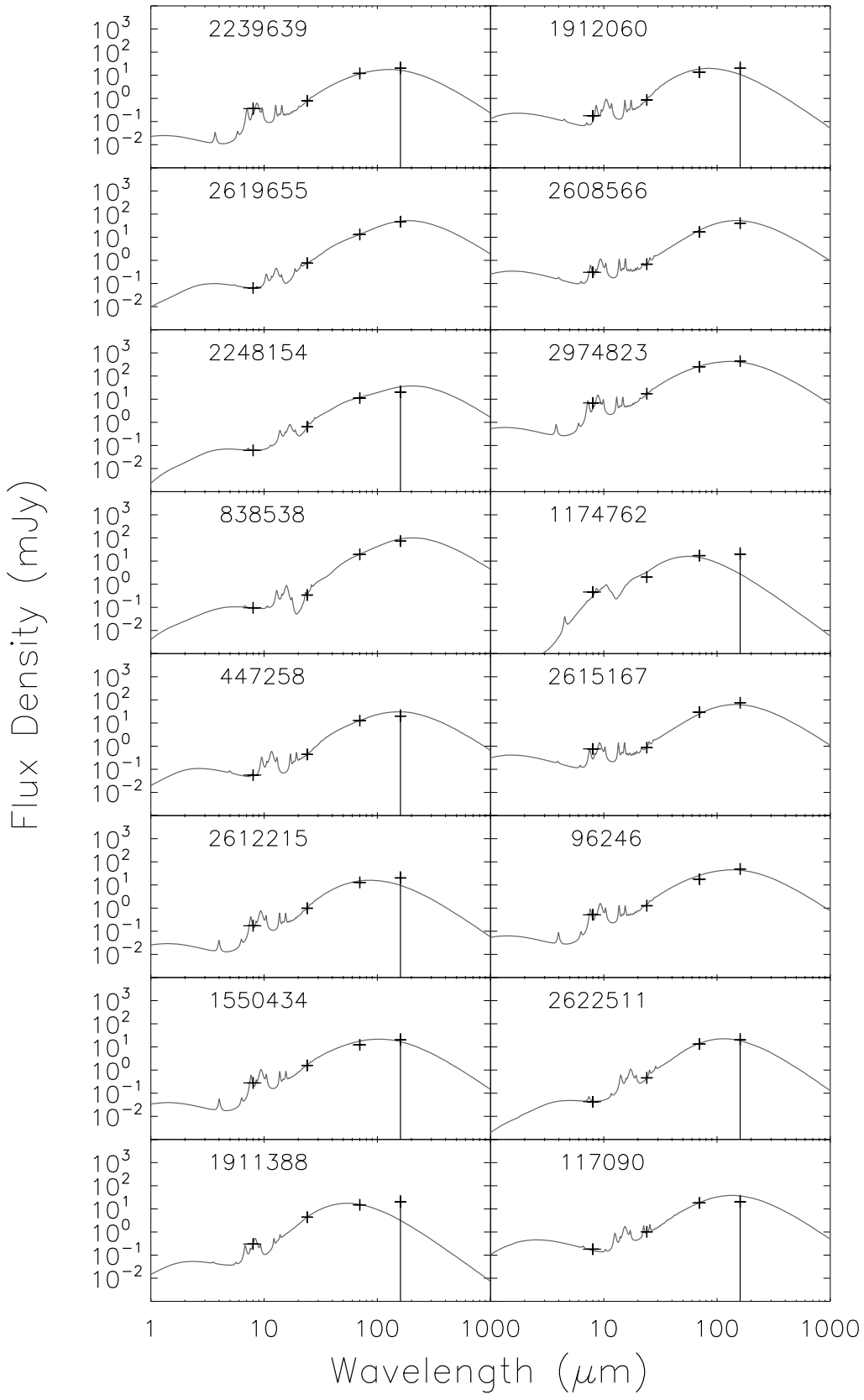
2239639
1912060
2619655
2608566
2248154
2974823
838538
1174762
447258
2615167
2612215
96246
1550434
2622511
1911388
117090
Flux Density (mJy)
Wavelength (μm)
1
10
100
1000

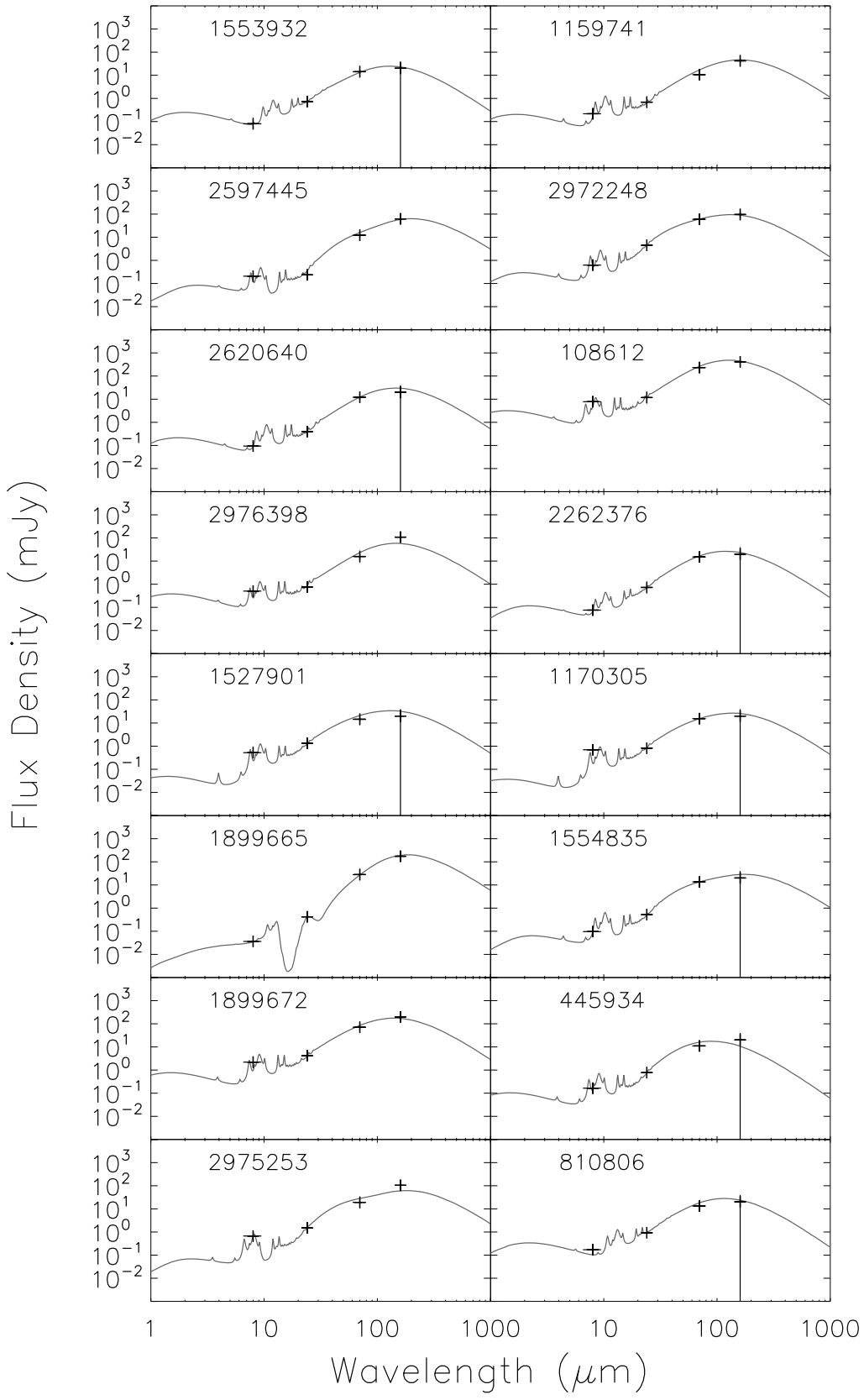
1553932
1159741
2597445
2972248
2620640
108612
2976398
2262376
1527901
1170305
1899665
1554835
1899672
445934
2975253
810806
Flux Density (mJy)
Wavelength (μm)
1
10
100
1000

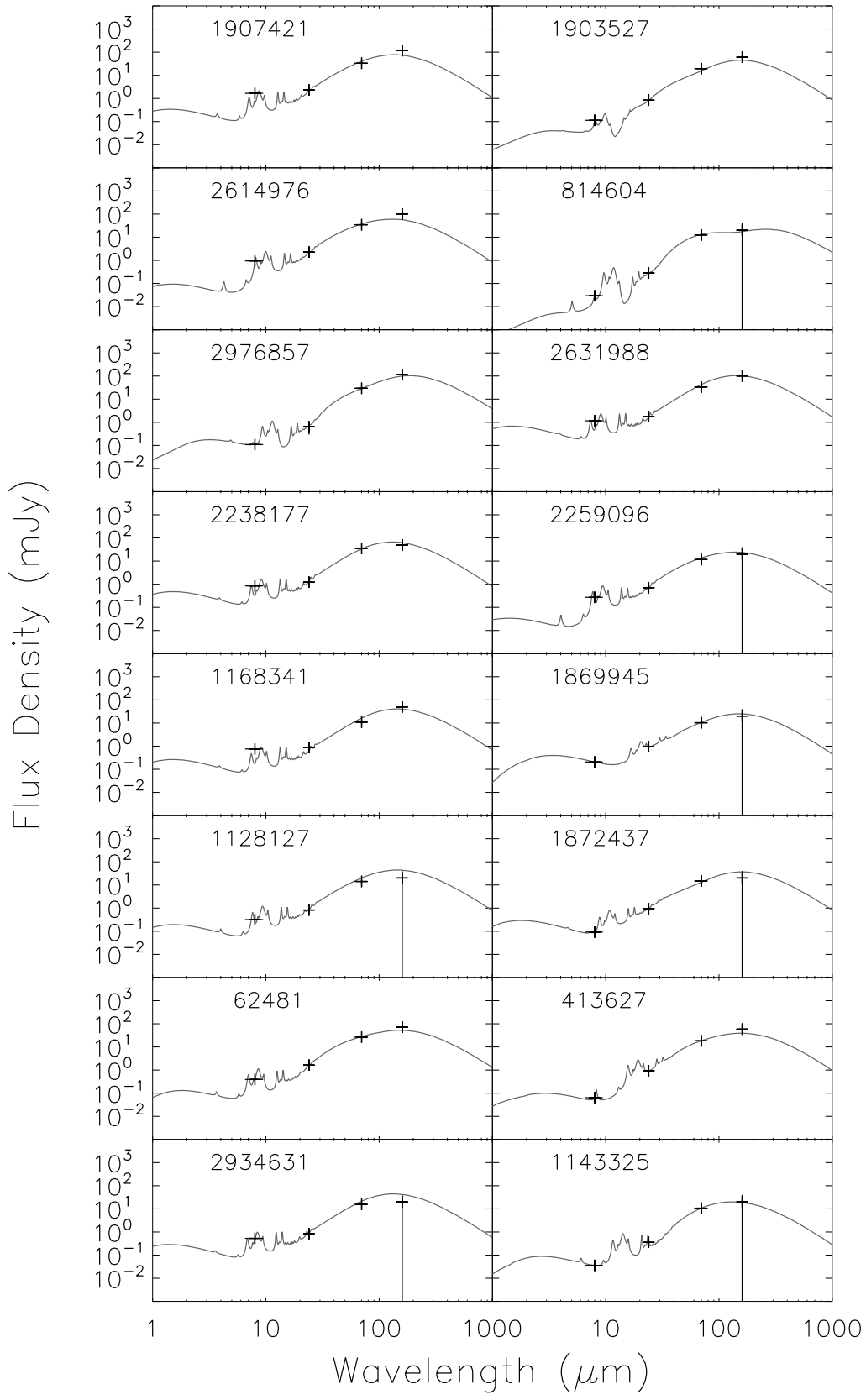
1907421
1903527
2614976
814604
2976857
2631988
2238177
2259096
1168341
1869945
1128127
1872437
62481
413627
2934631
1143325
Flux Density (mJy)
Wavelength (μm)
1
10
100
1000

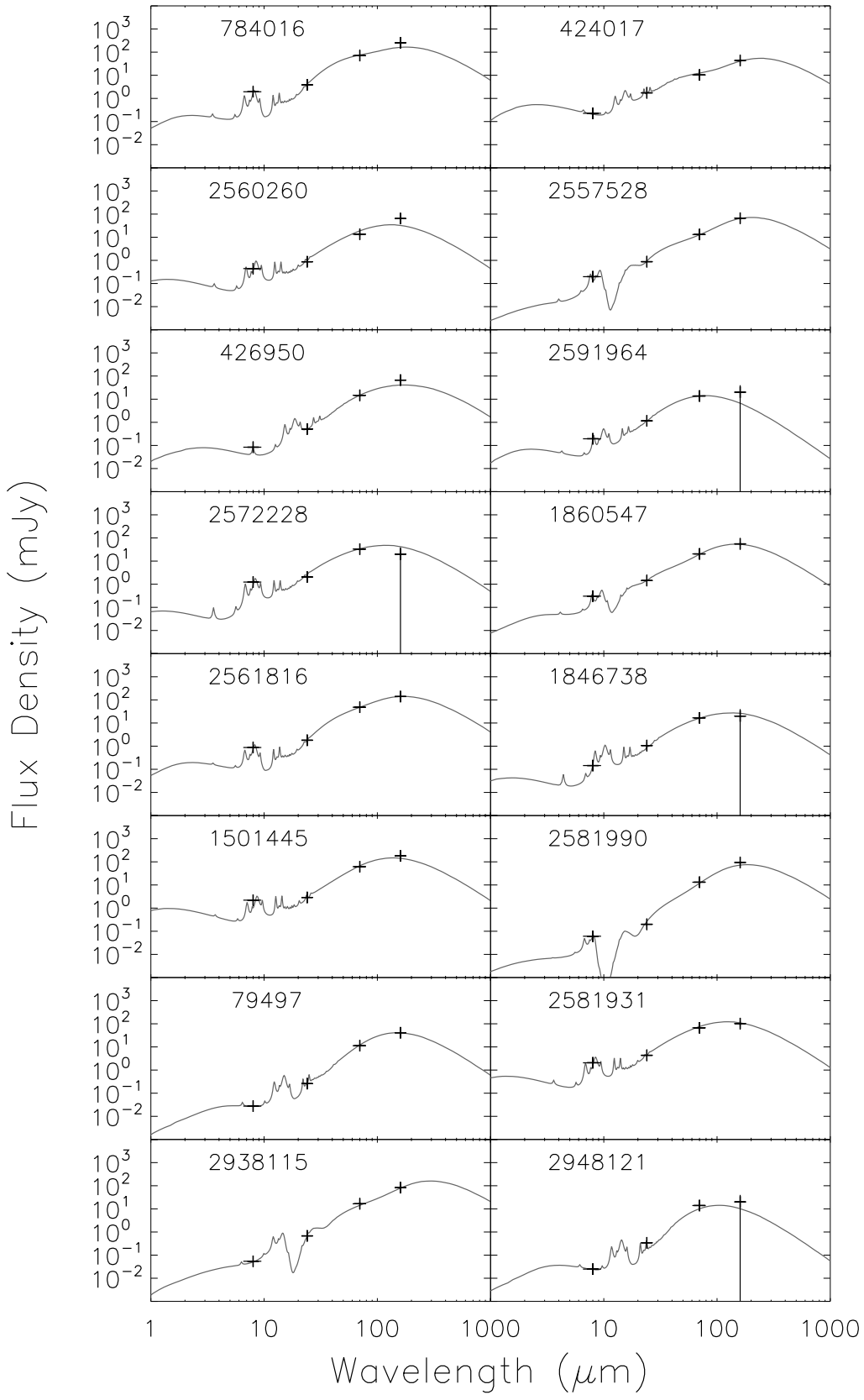
784016
424017
2560260
2557528
426950
2591964
2572228
1860547
2561816
1846738
1501445
2581990
79497
2581931
2938115
2948121
Flux Density (mJy)
Wavelength (μm)
1
10
100
1000

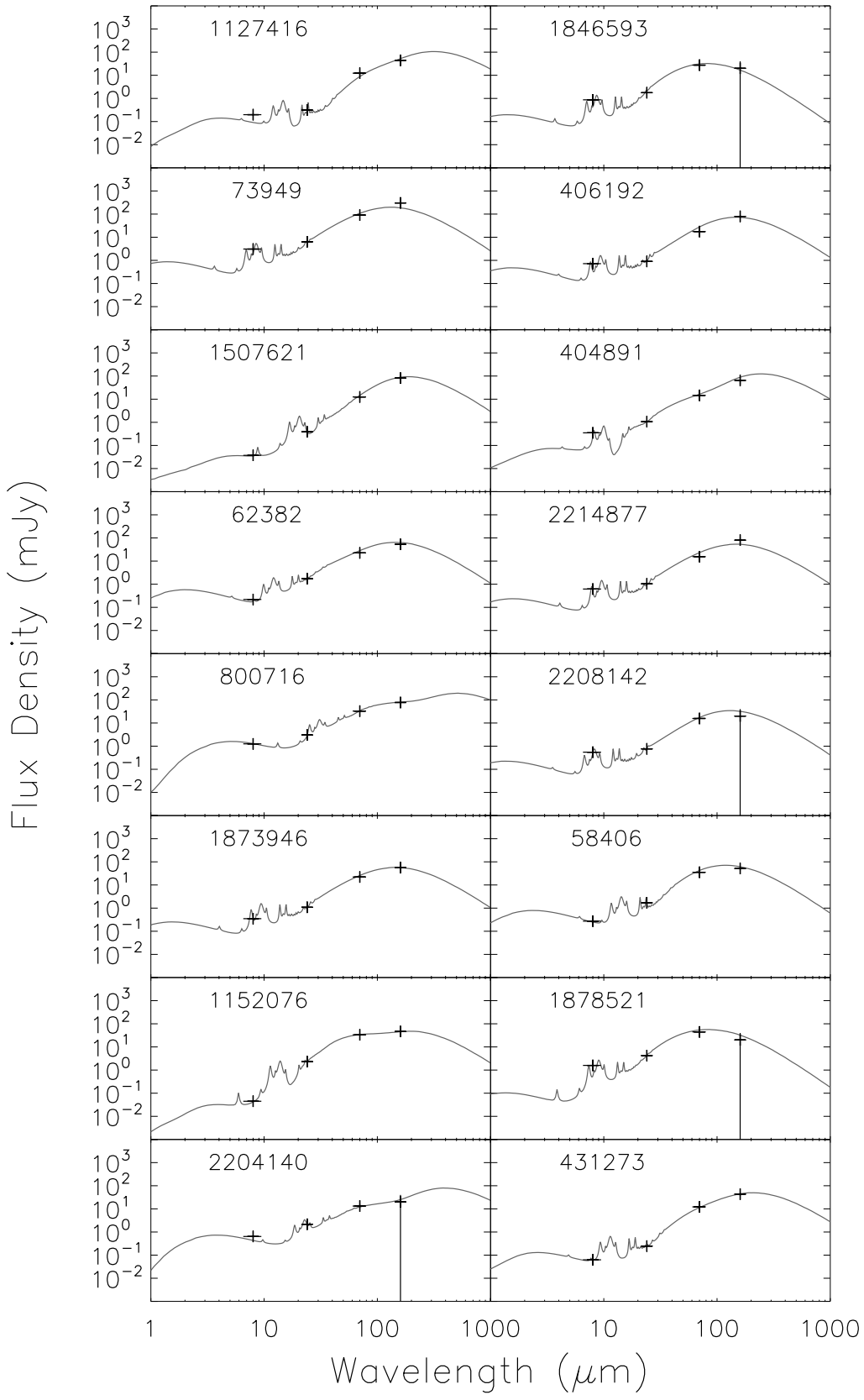
1127416
1846593
73949
406192
1507621
404891
62382
2214877
800716
2208142
1873946
58406
1152076
1878521
2204140
431273
Flux Density (mJy)
Wavelength (μm)
1
10
100
1000

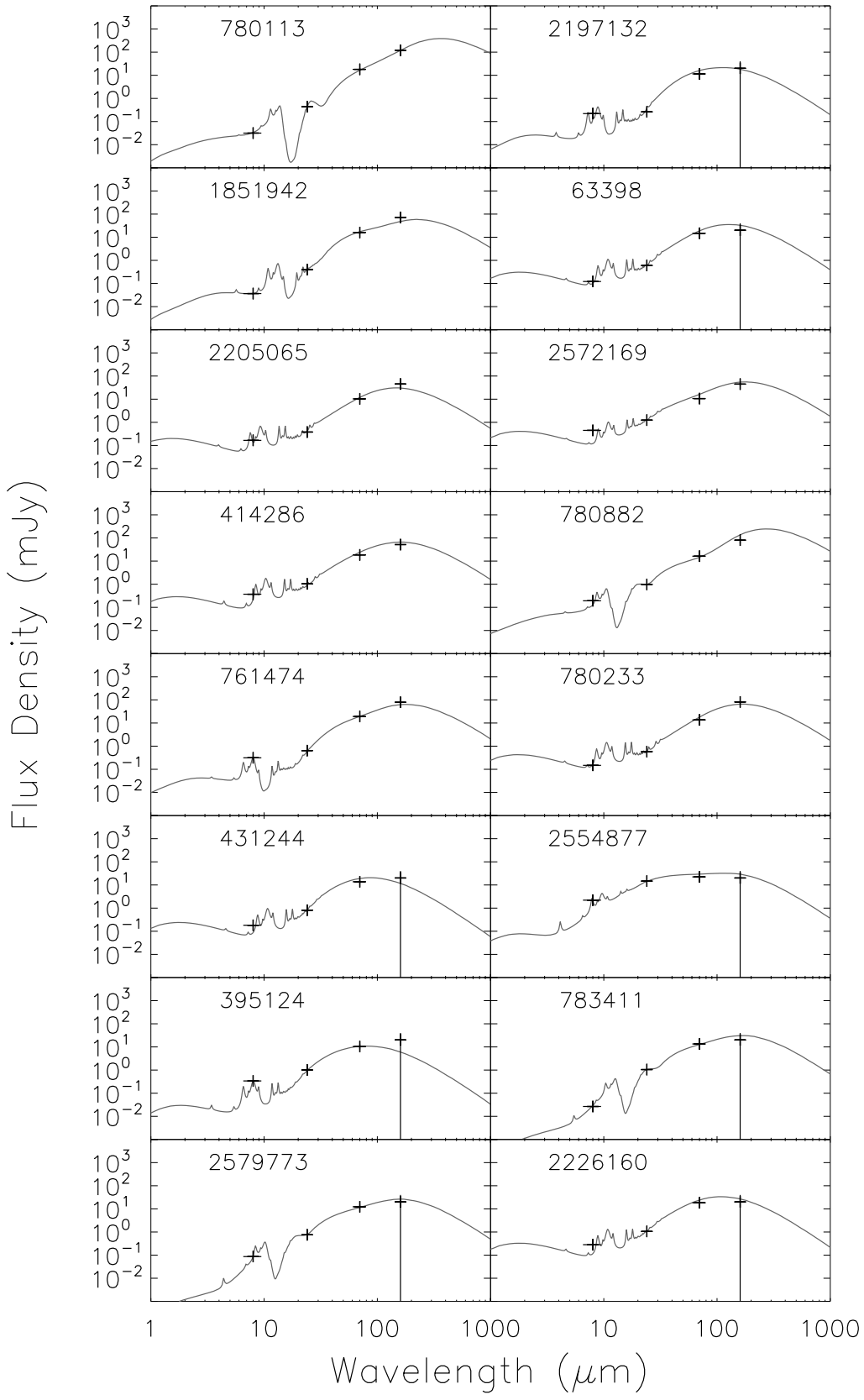
780113
2197132
1851942
63398
2205065
2572169
414286
780882
761474
780233
431244
2554877
395124
783411
2579773
2226160
Flux Density (mJy)
Wavelength (μm)
1
10
100
1000

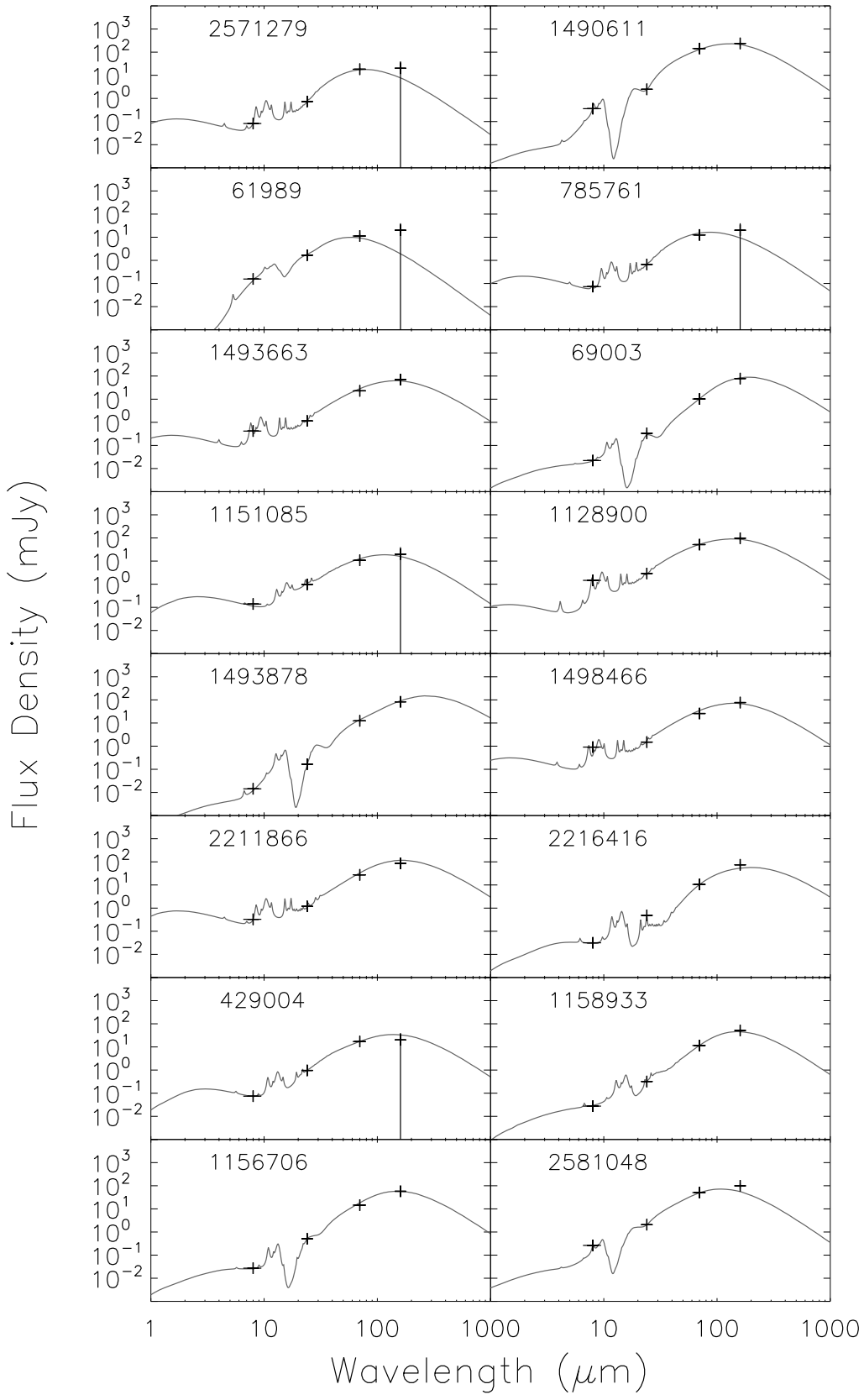
2571279
1490611
61989
785761
1493663
69003
1151085
1128900
1493878
1498466
2211866
2216416
429004
1158933
1156706
2581048
Flux Density (mJy)
Wavelength (μm)
1
10
100
1000

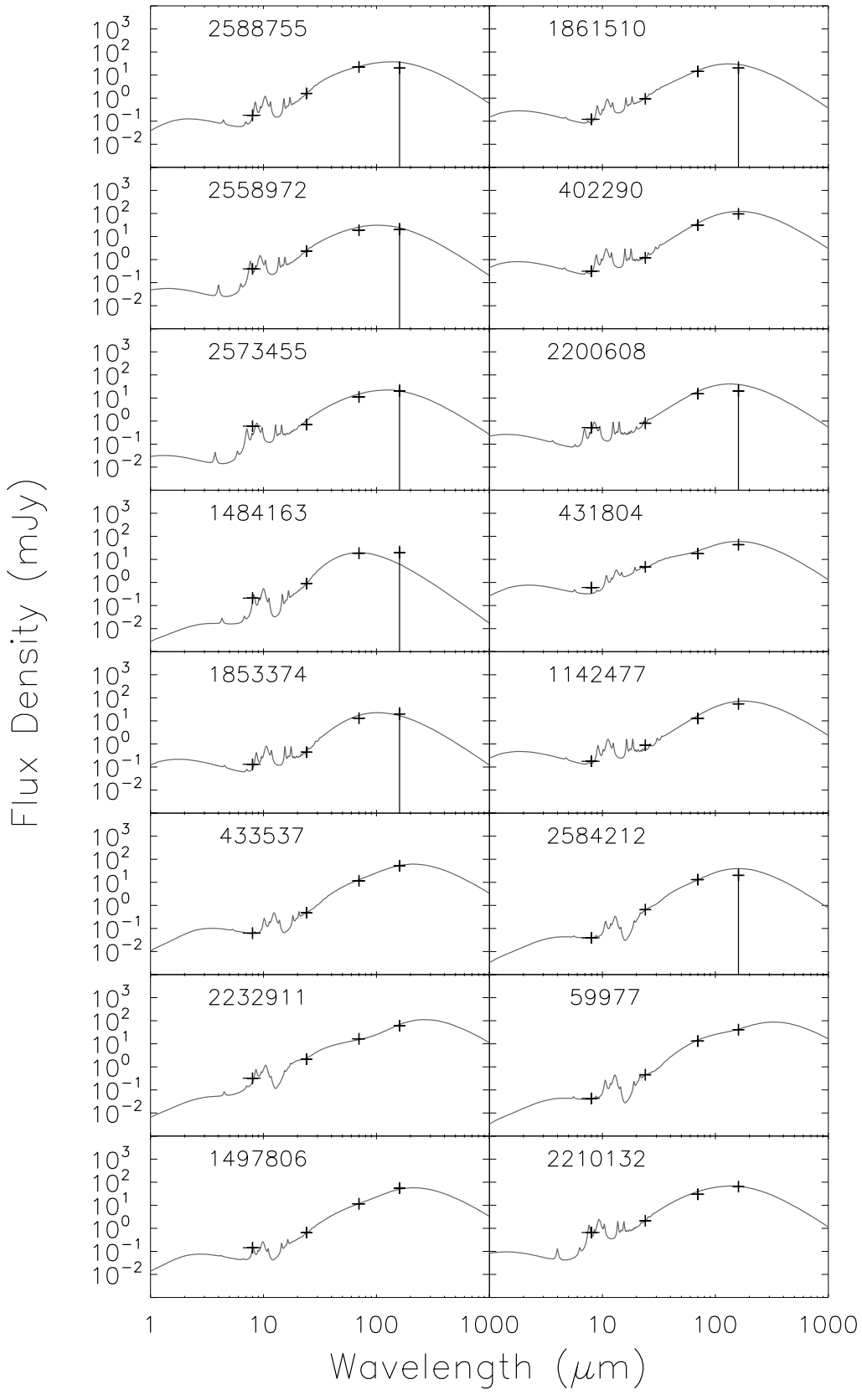
2588755
1861510
2558972
402290
2573455
2200608
1484163
431804
1853374
1142477
433537
2584212
2232911
59977
1497806
2210132
Flux Density (mJy)
Wavelength (μm)
1
10
100
1000

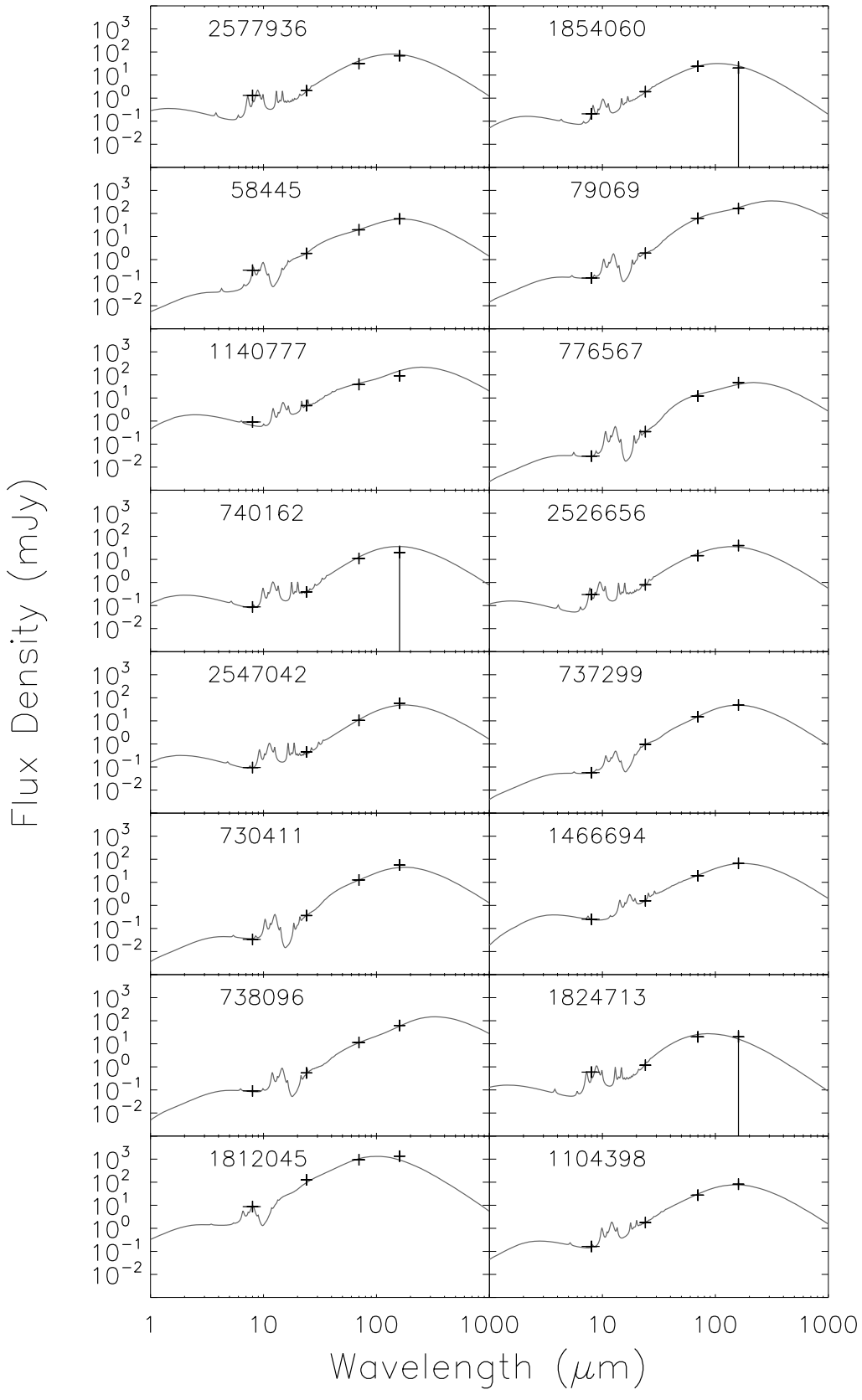
2577936
1854060
58445
79069
1140777
776567
740162
2526656
2547042
737299
730411
1466694
738096
1824713
1812045
1104398
Flux Density (mJy)
Wavelength (μm)
1
10
100
1000

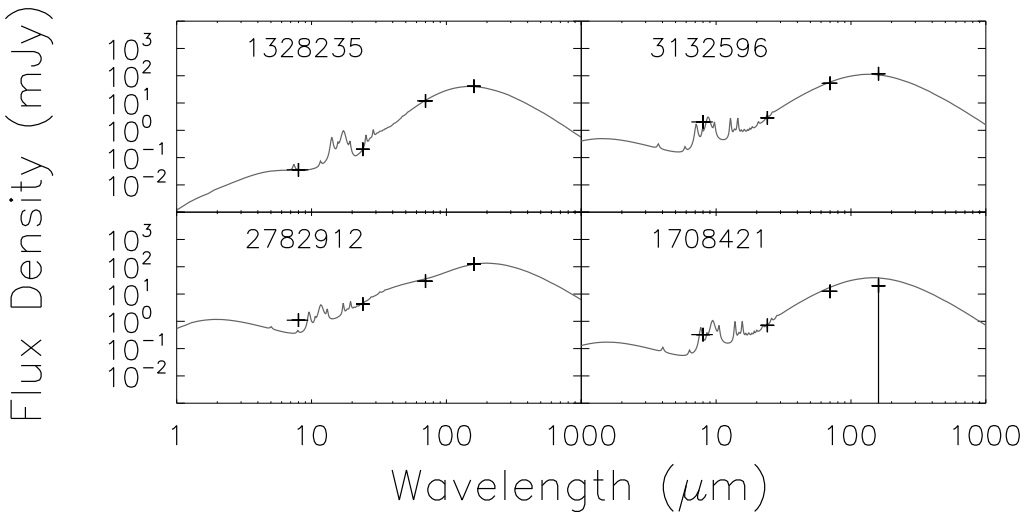
1328235
3132596
2782912
1708421
Flux Density (mJy)
Wavelength (μm)
10^3
10^2
10^1
10^0
10^-1
10^-2
1
10
100
1000

Appendix C

LIR

Table C.1

ACS ID	$\mathrm{Log}_{10}(L_{\mathrm{IR}}/L_{\odot})$ SK07	χ^2 SK07	$\mathrm{Log}_{10}(L_{\mathrm{IR}}/L_{\odot})$ CE01	χ^2 CE01
3207565	11.24	0.0	10.94	5.0
1774199	10.95	2.0	10.92	1.0
1050394	11.12	3.0	10.86	8.0
2860769	10.85	9.0	10.78	1.0
1796404	12.18	0.0	12.0	37.0
1056065	11.86	21.0	11.62	3.0
683700	12.5	0.0	12.23	26.0
2472873	11.63	0.0	11.49	14.0
709742	10.04	15.0	9.88	1.0
1762421	11.78	1.0	11.56	21.0
1776917	9.82	2.0	9.72	1.0
1800601	12.74	1.0	12.45	29.0

Continued on next page

Table C.1 – continued from previous page

ACS ID	$\mathrm{Log}_{10}(L_{\mathrm{IR}}/L_{\odot})$ SK07	χ^2 SK07	$\mathrm{Log}_{10}(L_{\mathrm{IR}}/L_{\odot})$ CE01	χ^2 CE01
331326	11.74	0.0	11.55	16.0
1760549	12.3	1.0	11.9	160.0
2128445	11.61	4.0	11.4	6.0
1408090	12.1	0.0	11.75	27.0
2864870	12.13	0.0	11.66	32.0
325280	11.49	0.0	11.16	87.0
705698	11.02	44.0	10.92	3.0
1422223	11.45	0.0	11.46	9.0
1780195	10.67	0.0	10.64	1.0
1047508	10.88	1.0	10.31	46.0
2506525	10.85	30.0	10.76	2.0
1041727	12.22	1.0	12.03	9.0
2847644	11.21	0.0	11.19	4.0
703628	10.84	0.0	10.69	4.0
1068657	10.6	10.0	10.53	7.0
2079068	10.16	43.0	10.1	13.0
2465134	11.64	0.0	11.73	173.0
302771	7.93	2.0	7.36	200.0
1742668	11.05	0.0	10.97	6.0
1382238	10.79	8.0	10.55	18.0
1726240	12.39	0.0	12.49	176.0
653964	11.7	26.0	11.76	46.0

Continued on next page

Table C.1 – continued from previous page

ACS ID	$\mathrm{Log}_{10}(L_{\mathrm{IR}}/L_{\odot})$ SK07	χ^2 SK07	$\mathrm{Log}_{10}(L_{\mathrm{IR}}/L_{\odot})$ CE01	χ^2 CE01
1003800	10.13	15.0	9.97	9.0
2834204	11.26	3.0	10.71	35.0
3170308	11.04	0.0	10.97	2.0
1005637	11.58	6.0	11.27	28.0
645463	11.96	0.0	11.84	4.0
2110513	11.33	8.0	11.18	3.0
2098274	13.68	2.0	14.07	51.0
2466721	11.73	53.0	11.35	23.0
645335	12.17	56.0	12.62	133.0
295417	11.73	6.0	11.66	1.0
3153788	11.46	16.0	11.25	7.0
1384510	11.24	1.0	10.81	29.0
3171672	11.48	0.0	11.3	10.0
640020	11.86	2.0	11.49	30.0
648196	13.99	0.0	14.23	138.0
287025	9.51	0.0	9.24	18.0
1374832	12.07	0.0	11.82	36.0
1733013	11.76	0.0	11.69	18.0
2090407	10.76	12.0	10.62	3.0
1010911	11.52	23.0	11.4	3.0
1749231	11.03	1.0	10.93	4.0
1370274	11.98	0.0	11.61	6.0

Continued on next page

Table C.1 – continued from previous page

ACS ID	$\mathrm{Log}_{10}(L_{\mathrm{IR}}/L_{\odot})$ SK07	χ^2 SK07	$\mathrm{Log}_{10}(L_{\mathrm{IR}}/L_{\odot})$ CE01	χ^2 CE01
2449005	11.59	0.0	11.55	3.0
3156612	11.33	1.0	11.31	19.0
2451757	11.5	10.0	11.28	15.0
649852	11.36	1.0	10.99	10.0
1010939	11.75	15.0	11.25	20.0
1731986	10.76	36.0	10.71	1.0
2079076	11.42	13.0	11.1	27.0
1748660	11.92	0.0	11.74	23.0
1358664	10.61	0.0	10.66	1.0
1012131	11.28	0.0	10.82	28.0
1760327	10.34	31.0	10.37	7.0
2083883	12.49	0.0	12.12	30.0
1017024	11.3	0.0	10.78	123.0
285676	12.22	0.0	12.21	14.0
2116065	11.05	0.0	10.98	9.0
2092540	10.84	18.0	10.48	48.0
2795846	11.45	0.0	10.99	20.0
2797784	11.23	1.0	10.83	34.0
2093194	11.65	26.0	11.58	0.0
282651	11.8	0.0	11.43	22.0
293410	12.11	0.0	11.85	18.0
649195	11.91	0.0	11.57	36.0

Continued on next page

Table C.1 – continued from previous page

ACS ID	$\mathrm{Log}_{10}(L_{\mathrm{IR}}/L_{\odot})$ SK07	χ^2 SK07	$\mathrm{Log}_{10}(L_{\mathrm{IR}}/L_{\odot})$ CE01	χ^2 CE01
3154877	11.34	0.0	11.11	4.0
2818647	10.69	42.0	10.62	2.0
2469360	12.67	1.0	12.4	46.0
295996	12.41	0.0	12.25	1.0
2801216	12.72	0.0	12.67	45.0
1019122	11.21	2.0	10.92	18.0
2084720	11.43	1.0	11.03	13.0
1739228	13.06	0.0	12.58	21.0
2821944	12.16	0.0	12.01	6.0
2114189	13.12	0.0	13.1	9.0
2468476	11.38	5.0	10.95	30.0
1372394	10.87	5.0	10.73	19.0
669852	11.64	27.0	11.46	2.0
1028483	11.76	26.0	11.66	0.0
1020798	10.17	27.0	10.03	5.0
2085971	11.38	0.0	11.12	8.0
2825951	10.44	8.0	10.31	3.0
1724510	12.18	13.0	12.15	2.0
3160388	11.07	5.0	10.78	32.0
2083238	11.8	7.0	11.49	23.0
3164977	12.76	0.0	12.52	9.0
2109581	10.71	54.0	10.63	9.0

Continued on next page

Table C.1 – continued from previous page

ACS ID	$\mathrm{Log}_{10}(L_{\mathrm{IR}}/L_{\odot})$ SK07	χ^2 SK07	$\mathrm{Log}_{10}(L_{\mathrm{IR}}/L_{\odot})$ CE01	χ^2 CE01
2091518	11.48	1.0	10.93	13.0
2798560	9.86	3.0	9.69	22.0
278782	10.21	14.0	10.06	13.0
1031810	11.9	5.0	11.3	126.0
2814718	12.81	0.0	12.5	18.0
2815806	12.73	6.0	12.3	60.0
1023519	11.87	0.0	11.92	19.0
1374409	11.18	1.0	11.0	10.0
2830310	10.85	51.0	11.27	21.0
1730390	12.07	0.0	11.56	9.0
1033104	12.53	0.0	12.29	22.0
2062875	10.99	24.0	10.84	5.0
252068	12.67	0.0	12.69	17.0
2067090	11.58	17.0	11.41	6.0
1693118	10.28	6.0	10.15	4.0
2039420	10.19	37.0	10.22	13.0
2404909	12.17	0.0	12.1	4.0
2779118	12.82	0.0	12.75	72.0
2428063	12.06	8.0	11.93	4.0
1328216	12.32	0.0	11.98	14.0
2756812	10.69	0.0	10.65	2.0
1705033	11.61	7.0	11.34	30.0

Continued on next page

Table C.1 – continued from previous page

ACS ID	$\mathrm{Log}_{10}(L_{\mathrm{IR}}/L_{\odot})$ SK07	χ^2 SK07	$\mathrm{Log}_{10}(L_{\mathrm{IR}}/L_{\odot})$ CE01	χ^2 CE01
2398696	11.05	10.0	11.02	1.0
1688156	10.3	23.0	10.46	57.0
2051805	9.91	0.0	9.54	8.0
266541	11.64	4.0	11.5	6.0
1703192	10.99	41.0	10.89	9.0
2064977	12.07	8.0	11.77	28.0
1705948	11.8	5.0	11.34	26.0
982988	12.94	9.0	13.12	37.0
2429483	11.71	0.0	11.2	66.0
2069950	11.32	8.0	10.99	20.0
2427971	11.92	11.0	11.62	20.0
2058982	10.98	34.0	10.93	1.0
2774277	11.22	17.0	10.9	10.0
3123195	12.54	0.0	12.38	7.0
962706	10.65	0.0	10.51	4.0
2070104	10.46	47.0	10.3	21.0
244366	11.91	2.0	11.84	2.0
600087	10.98	31.0	10.83	5.0
1315677	12.57	0.0	12.06	4.0
994550	11.67	27.0	11.59	0.0
3127341	10.77	25.0	10.54	4.0
1329754	12.32	0.0	12.27	15.0

Continued on next page

Table C.1 – continued from previous page

ACS ID	$\mathrm{Log}_{10}(L_{\mathrm{IR}}/L_{\odot})$ SK07	χ^2 SK07	$\mathrm{Log}_{10}(L_{\mathrm{IR}}/L_{\odot})$ CE01	χ^2 CE01
2073932	11.49	0.0	11.29	10.0
266624	10.75	17.0	10.51	30.0
1346104	12.85	0.0	12.67	55.0
2754649	10.79	9.0	10.62	35.0
2067980	11.22	22.0	11.1	5.0
3121113	11.34	0.0	11.22	24.0
2428816	12.35	0.0	11.94	52.0
2396575	10.8	21.0	10.73	0.0
613313	11.09	17.0	11.31	5.0
1705466	10.53	15.0	10.19	19.0
975388	11.02	19.0	10.73	9.0
1320759	10.48	3.0	10.39	4.0
1327363	11.87	60.0	11.86	22.0
1706851	11.4	12.0	11.09	6.0
2764489	12.35	0.0	11.99	13.0
2057388	13.04	0.0	12.68	43.0
2782565	10.52	0.0	10.47	6.0
619472	13.34	6.0	13.39	4.0
1693283	11.36	4.0	10.88	28.0
2077031	11.89	3.0	11.92	4.0
252421	11.02	12.0	10.96	19.0
638845	11.87	0.0	11.48	33.0

Continued on next page

Table C.1 – continued from previous page

ACS ID	$\mathrm{Log}_{10}(L_{\mathrm{IR}}/L_{\odot})$ SK07	χ^2 SK07	$\mathrm{Log}_{10}(L_{\mathrm{IR}}/L_{\odot})$ CE01	χ^2 CE01
3098637	10.87	0.0	10.82	3.0
2041680	11.13	4.0	10.86	7.0
1314264	12.0	10.0	11.73	70.0
1680019	11.77	1.0	11.62	4.0
2422831	10.85	3.0	10.71	7.0
1714912	11.67	13.0	11.42	5.0
611062	12.26	0.0	12.12	20.0
2416431	11.37	5.0	11.13	8.0
985125	10.47	6.0	10.43	1.0
1697619	12.86	0.0	12.84	17.0
620877	11.94	0.0	11.58	22.0
2773219	12.13	0.0	11.65	23.0
1339536	12.63	0.0	12.44	30.0
623670	11.22	4.0	11.0	20.0
1712035	10.78	31.0	10.79	8.0
2409774	10.3	28.0	10.19	3.0
3098628	11.03	35.0	10.89	5.0
2778496	11.32	4.0	10.87	28.0
1328235	12.79	0.0	12.44	75.0
3132596	10.79	32.0	10.77	3.0
2782912	11.45	42.0	11.43	16.0
1708421	10.84	13.0	10.64	6.0

Continued on next page

Table C.1 – continued from previous page

ACS ID	$\mathrm{Log}_{10}(L_{\mathrm{IR}}/L_{\odot})$ SK07	χ^2 SK07	$\mathrm{Log}_{10}(L_{\mathrm{IR}}/L_{\odot})$ CE01	χ^2 CE01
1687625	11.36	4.0	11.35	2.0
2760335	9.93	23.0	9.81	9.0
619774	11.89	0.0	11.82	13.0
1685081	10.21	18.0	10.11	8.0
2777330	9.56	16.0	9.1	32.0
3115329	11.8	4.0	11.41	30.0
2757871	10.66	43.0	10.73	1.0
3116801	11.22	1.0	11.09	7.0
603238	10.5	20.0	9.94	65.0
3098612	10.05	23.0	9.93	1.0
1689719	11.22	35.0	11.14	1.0
2397817	11.68	22.0	11.55	0.0
2047938	11.4	1.0	11.29	25.0
1679299	12.39	0.0	12.07	9.0
1338853	12.13	0.0	11.7	27.0
3120862	10.42	31.0	10.45	1.0
3116347	12.53	0.0	12.55	21.0
2403642	13.0	6.0	13.06	15.0
2784698	11.8	1.0	11.69	4.0
1346471	10.15	19.0	10.1	7.0
3126806	10.86	0.0	10.73	3.0
608944	9.42	2.0	8.96	27.0

Continued on next page

Table C.1 – continued from previous page

ACS ID	$\mathrm{Log}_{10}(L_{\mathrm{IR}}/L_{\odot})$ SK07	χ^2 SK07	$\mathrm{Log}_{10}(L_{\mathrm{IR}}/L_{\odot})$ CE01	χ^2 CE01
604463	10.08	24.0	9.96	11.0
1707320	11.2	30.0	11.03	1.0
258573	10.63	13.0	10.43	4.0
3098627	9.24	10.0	9.09	17.0
989977	11.07	29.0	11.04	12.0
1704835	11.01	45.0	10.75	13.0
255255	11.84	0.0	11.49	13.0
954312	10.74	52.0	10.72	38.0
922902	12.23	0.0	12.0	13.0
1659309	12.05	0.0	11.72	146.0
938352	10.53	13.0	10.48	18.0
565311	11.66	31.0	11.39	1.0
2728744	10.33	36.0	10.44	3.0
2030285	12.66	0.0	12.49	39.0
561721	11.15	0.0	11.06	5.0
2034896	11.31	13.0	11.31	5.0
2032025	12.62	25.0	12.39	7.0
2358831	10.93	2.0	10.91	2.0
1667999	10.72	3.0	10.63	1.0
2034840	10.38	10.0	10.23	20.0
3076087	11.27	5.0	10.89	54.0
591279	11.74	1.0	11.75	1.0

Continued on next page

Table C.1 – continued from previous page

ACS ID	$\mathrm{Log}_{10}(L_{\mathrm{IR}}/L_{\odot})$ SK07	χ^2 SK07	$\mathrm{Log}_{10}(L_{\mathrm{IR}}/L_{\odot})$ CE01	χ^2 CE01
2371526	12.34	1.0	12.14	1.0
2026073	11.53	1.0	11.08	118.0
561681	10.86	10.0	10.18	50.0
2361240	10.84	0.0	10.31	101.0
1641332	9.93	8.0	9.72	5.0
945385	10.85	0.0	10.91	20.0
1286210	12.79	0.0	12.44	74.0
3085661	11.43	0.0	11.35	4.0
562400	11.72	0.0	11.64	1.0
3079819	10.43	21.0	10.27	17.0
573421	12.75	2.0	12.59	8.0
2370086	13.02	1.0	12.35	67.0
215276	11.03	13.0	10.92	5.0
1673063	11.21	0.0	11.18	3.0
2036958	12.65	0.0	12.12	59.0
2744989	11.44	30.0	11.37	4.0
2006864	11.13	0.0	10.95	11.0
935742	10.74	0.0	10.4	16.0
2010381	12.01	0.0	12.04	34.0
2739884	12.6	1.0	12.51	2.0
1643810	11.28	18.0	11.02	6.0
950516	11.43	26.0	11.36	1.0

Continued on next page

Table C.1 – continued from previous page

ACS ID	$\mathrm{Log}_{10}(L_{\mathrm{IR}}/L_{\odot})$ SK07	χ^2 SK07	$\mathrm{Log}_{10}(L_{\mathrm{IR}}/L_{\odot})$ CE01	χ^2 CE01
3063068	12.58	0.0	12.76	78.0
3091453	10.04	37.0	9.93	9.0
926581	11.5	1.0	11.43	5.0
2387961	10.9	20.0	10.78	12.0
1277317	12.06	35.0	11.81	54.0
1667742	10.86	0.0	10.91	2.0
3092603	10.16	10.0	9.98	7.0
3081461	12.74	0.0	12.66	62.0
1671760	11.53	0.0	11.47	6.0
1274963	12.39	3.0	12.21	10.0
2031444	11.36	23.0	11.21	3.0
2731219	10.46	0.0	10.32	12.0
1280446	11.13	3.0	10.86	24.0
2364696	11.32	2.0	11.12	13.0
2355318	11.3	30.0	11.16	9.0
2375695	10.71	24.0	10.62	3.0
1302075	10.04	6.0	9.82	28.0
949870	11.48	2.0	11.25	12.0
576030	11.42	5.0	11.24	6.0
2036409	9.9	25.0	9.76	10.0
228343	12.83	0.0	12.53	6.0
939424	10.62	29.0	10.41	3.0

Continued on next page

Table C.1 – continued from previous page

ACS ID	$\mathrm{Log}_{10}(L_{\mathrm{IR}}/L_{\odot})$ SK07	χ^2 SK07	$\mathrm{Log}_{10}(L_{\mathrm{IR}}/L_{\odot})$ CE01	χ^2 CE01
940411	11.17	21.0	10.96	9.0
1305519	10.66	14.0	10.61	2.0
1303252	12.3	0.0	12.31	24.0
1308578	9.88	7.0	9.54	27.0
1642973	11.69	1.0	11.26	32.0
572652	10.74	0.0	10.71	2.0
1280851	10.14	21.0	10.05	8.0
3063060	11.62	0.0	11.4	31.0
1671285	11.9	0.0	11.5	38.0
593770	13.19	0.0	12.95	32.0
221392	12.43	0.0	12.17	14.0
1297269	11.14	0.0	11.13	10.0
2009537	12.48	0.0	12.08	30.0
2383625	10.23	39.0	10.19	11.0
2744671	10.71	41.0	10.72	16.0
3077926	11.64	0.0	11.59	4.0
1293722	11.45	4.0	11.04	14.0
927731	12.22	43.0	12.35	80.0
1313691	10.75	11.0	10.59	3.0
2382980	11.11	48.0	10.75	19.0
2368004	11.35	2.0	11.15	15.0
930825	10.33	2.0	10.19	4.0

Continued on next page

Table C.1 – continued from previous page

ACS ID	$\mathrm{Log}_{10}(L_{\mathrm{IR}}/L_{\odot})$ SK07	χ^2 SK07	$\mathrm{Log}_{10}(L_{\mathrm{IR}}/L_{\odot})$ CE01	χ^2 CE01
580900	10.2	18.0	10.09	2.0
2019276	12.73	0.0	12.64	24.0
2732957	10.42	32.0	10.35	34.0
2721100	12.13	15.0	12.09	12.0
1647820	11.27	0.0	11.23	1.0
1286079	11.44	4.0	11.28	43.0
2731440	9.6	0.0	9.46	23.0
3082182	11.2	4.0	10.74	33.0
3093724	11.42	0.0	11.0	16.0
956938	10.84	0.0	10.75	5.0
207085	11.88	0.0	11.75	11.0
581360	11.62	25.0	11.54	1.0
2750438	12.27	3.0	12.11	12.0
1313617	11.79	6.0	11.53	8.0
2715039	11.0	15.0	10.92	10.0
220314	11.42	11.0	11.25	1.0
1639579	12.41	1.0	11.96	38.0
1274454	11.19	31.0	10.98	2.0
561066	11.5	1.0	11.17	62.0
2368539	12.47	0.0	12.12	85.0
1658746	11.49	0.0	11.33	23.0
597991	11.97	3.0	11.87	2.0

Continued on next page

Table C.1 – continued from previous page

ACS ID	$\mathrm{Log}_{10}(L_{\mathrm{IR}}/L_{\odot})$ SK07	χ^2 SK07	$\mathrm{Log}_{10}(L_{\mathrm{IR}}/L_{\odot})$ CE01	χ^2 CE01
1302124	10.24	18.0	10.14	21.0
1620037	11.22	35.0	11.13	9.0
1611697	11.12	40.0	11.12	5.0
176255	11.26	0.0	11.16	4.0
906538	12.7	1.0	12.7	102.0
1612971	10.66	22.0	10.51	2.0
3042305	13.57	10.0	13.84	15.0
2690372	11.38	0.0	11.32	6.0
522863	11.76	0.0	11.74	5.0
916706	12.45	0.0	12.38	41.0
1624368	10.84	2.0	10.59	10.0
1961157	10.42	24.0	10.3	16.0
187621	10.76	0.0	10.8	3.0
1234769	10.45	32.0	10.39	1.0
3038652	10.3	11.0	9.77	39.0
913477	12.56	0.0	12.46	4.0
2349962	11.04	6.0	10.91	6.0
2688055	11.96	26.0	11.72	1.0
1998248	12.4	3.0	11.98	27.0
1968435	11.45	36.0	11.23	0.0
1616073	11.22	23.0	11.28	27.0
1976399	11.27	0.0	10.91	8.0

Continued on next page

Table C.1 – continued from previous page

ACS ID	$\mathrm{Log}_{10}(L_{\mathrm{IR}}/L_{\odot})$ SK07	χ^2 SK07	$\mathrm{Log}_{10}(L_{\mathrm{IR}}/L_{\odot})$ CE01	χ^2 CE01
190516	10.36	34.0	10.11	19.0
1236191	10.85	19.0	10.78	23.0
3042959	10.36	16.0	10.22	1.0
2697496	11.63	0.0	11.29	19.0
882577	11.28	35.0	11.06	26.0
547953	11.62	0.0	11.31	14.0
1962614	11.68	0.0	11.62	2.0
2321627	12.27	0.0	12.04	8.0
1243981	12.13	1.0	12.21	53.0
2679953	12.05	0.0	11.84	11.0
894161	11.16	17.0	11.14	36.0
907081	11.6	0.0	11.61	8.0
175608	10.91	16.0	10.78	3.0
558230	10.8	4.0	10.64	1.0
881773	11.31	42.0	11.24	8.0
1250554	12.47	0.0	11.78	31.0
528245	11.19	4.0	11.05	0.0
521201	12.79	1.0	12.54	44.0
2323610	12.66	0.0	12.48	12.0
2351717	12.59	30.0	12.67	6.0
3054743	11.5	15.0	11.49	3.0
887659	11.59	13.0	11.43	2.0

Continued on next page

Table C.1 – continued from previous page

ACS ID	$\mathrm{Log}_{10}(L_{\mathrm{IR}}/L_{\odot})$ SK07	χ^2 SK07	$\mathrm{Log}_{10}(L_{\mathrm{IR}}/L_{\odot})$ CE01	χ^2 CE01
3045996	10.97	1.0	10.91	9.0
168823	10.71	17.0	10.52	17.0
1623303	12.47	0.0	12.48	4.0
2351981	12.15	1.0	11.9	19.0
2708400	12.55	0.0	12.28	42.0
1602443	11.38	31.0	11.31	4.0
537775	12.18	3.0	11.64	32.0
1265505	10.64	40.0	10.66	5.0
1632513	10.23	29.0	10.16	6.0
543174	10.82	13.0	10.55	15.0
176191	11.19	0.0	11.21	2.0
170986	13.0	0.0	12.97	1.0
1599108	12.98	0.0	12.86	4.0
551600	11.6	0.0	11.58	5.0
1968042	11.23	1.0	11.22	2.0
1984457	11.12	10.0	10.99	8.0
1261163	11.67	0.0	11.77	12.0
886752	11.35	22.0	11.23	0.0
1236435	11.59	19.0	11.48	3.0
530869	10.95	0.0	10.94	2.0
541155	12.61	41.0	12.47	7.0
548962	12.39	9.0	12.04	21.0

Continued on next page

Table C.1 – continued from previous page

ACS ID	$\mathrm{Log}_{10}(L_{\mathrm{IR}}/L_{\odot})$ SK07	χ^2 SK07	$\mathrm{Log}_{10}(L_{\mathrm{IR}}/L_{\odot})$ CE01	χ^2 CE01
538770	10.02	25.0	9.93	4.0
552939	11.33	23.0	11.05	7.0
3043809	11.96	0.0	11.97	25.0
1237060	11.09	29.0	10.72	13.0
527769	10.8	2.0	10.89	2.0
2701201	11.44	0.0	11.28	27.0
2334037	10.19	40.0	10.18	3.0
2684410	10.52	9.0	10.42	12.0
3026076	11.52	0.0	11.34	17.0
1234932	12.82	80.0	13.17	41.0
883705	11.2	0.0	11.14	4.0
547741	11.55	21.0	11.33	5.0
3044822	12.26	7.0	12.18	14.0
1609604	9.91	13.0	9.78	3.0
174225	11.66	0.0	11.29	23.0
894404	12.3	43.0	12.45	66.0
546112	13.37	0.0	13.12	9.0
1987323	10.87	40.0	10.81	2.0
1236625	12.87	3.0	12.33	59.0
1995702	12.37	0.0	12.08	18.0
1624349	10.39	23.0	9.72	126.0
547310	11.21	16.0	11.17	3.0

Continued on next page

Table C.1 – continued from previous page

ACS ID	$\mathrm{Log}_{10}(L_{\mathrm{IR}}/L_{\odot})$ SK07	χ^2 SK07	$\mathrm{Log}_{10}(L_{\mathrm{IR}}/L_{\odot})$ CE01	χ^2 CE01
1237279	12.81	0.0	12.38	94.0
2690289	10.63	3.0	10.69	10.0
179961	12.03	1.0	11.5	25.0
2340183	11.48	0.0	11.13	20.0
2699069	13.02	1.0	12.69	40.0
189476	11.09	32.0	10.89	1.0
177219	10.05	1.0	9.85	26.0
541750	10.54	44.0	10.61	15.0
1199665	12.87	0.0	12.45	44.0
2708725	11.07	0.0	10.97	11.0
2301423	11.76	4.0	11.68	4.0
484139	11.58	8.0	11.48	5.0
1926545	11.62	3.0	11.3	20.0
2289014	12.96	2.0	13.24	127.0
863030	12.33	0.0	11.91	35.0
846611	11.37	41.0	11.26	0.0
1948954	12.69	0.0	12.13	7.0
1926740	11.36	0.0	11.32	2.0
3011290	11.64	12.0	11.54	2.0
505934	10.51	33.0	10.42	6.0
2659182	12.98	0.0	13.12	18.0
1946735	13.08	0.0	12.82	18.0

Continued on next page

Table C.1 – continued from previous page

ACS ID	$\mathrm{Log}_{10}(L_{\mathrm{IR}}/L_{\odot})$ SK07	χ^2 SK07	$\mathrm{Log}_{10}(L_{\mathrm{IR}}/L_{\odot})$ CE01	χ^2 CE01
1228611	9.87	1.0	9.49	47.0
3006710	10.63	32.0	10.52	5.0
1581957	10.66	3.0	10.55	5.0
484717	11.98	0.0	11.46	160.0
1578009	11.86	17.0	11.8	1.0
2295195	11.96	0.0	11.72	12.0
1563881	11.27	35.0	11.16	0.0
3004691	12.81	0.0	12.66	12.0
1227918	12.32	0.0	12.16	41.0
2300727	11.91	2.0	11.71	6.0
2664125	12.88	2.0	12.54	50.0
850467	11.19	41.0	11.15	8.0
2303554	10.71	34.0	10.69	3.0
1213993	9.45	2.0	9.14	24.0
1923955	10.66	8.0	10.6	3.0
1232577	11.22	0.0	11.25	1.0
506930	12.72	0.0	12.66	0.0
2645587	10.99	13.0	10.79	7.0
854924	10.08	24.0	10.0	10.0
1220305	10.93	2.0	10.72	16.0
1928561	10.62	0.0	10.5	3.0
2634818	11.49	25.0	11.27	3.0

Continued on next page

Table C.1 – continued from previous page

ACS ID	$\mathrm{Log}_{10}(L_{\mathrm{IR}}/L_{\odot})$ SK07	χ^2 SK07	$\mathrm{Log}_{10}(L_{\mathrm{IR}}/L_{\odot})$ CE01	χ^2 CE01
144415	11.3	1.0	10.9	24.0
2281500	10.93	18.0	10.74	11.0
3011457	10.83	18.0	10.78	25.0
135088	11.5	10.0	11.23	13.0
853954	12.36	32.0	12.21	27.0
148407	11.46	10.0	11.14	6.0
138545	11.52	32.0	11.47	7.0
1936704	12.02	0.0	11.95	8.0
2297460	11.84	0.0	11.47	28.0
142990	10.79	46.0	10.76	11.0
1948417	11.48	3.0	11.22	5.0
1212993	11.84	0.0	11.86	11.0
2288806	11.85	0.0	11.87	0.0
1230480	11.29	26.0	11.15	3.0
1199258	11.09	0.0	11.1	10.0
1572880	10.74	0.0	10.75	0.0
3009467	12.24	0.0	11.96	8.0
1583239	12.75	1.0	12.58	86.0
2310968	10.28	9.0	10.17	23.0
1953852	10.48	0.0	9.9	88.0
510921	11.31	0.0	11.04	7.0
1960915	11.21	17.0	11.05	8.0

Continued on next page

Table C.1 – continued from previous page

ACS ID	$\mathrm{Log}_{10}(L_{\mathrm{IR}}/L_{\odot})$ SK07	χ^2 SK07	$\mathrm{Log}_{10}(L_{\mathrm{IR}}/L_{\odot})$ CE01	χ^2 CE01
1560828	10.38	47.0	10.44	9.0
2295293	11.76	2.0	11.7	9.0
139876	11.38	3.0	10.98	22.0
1197025	10.8	51.0	10.76	6.0
2306186	10.81	17.0	10.56	4.0
138017	10.16	11.0	9.91	17.0
1569262	12.7	0.0	12.72	14.0
1560623	11.08	46.0	11.05	1.0
863672	13.12	2.0	12.88	6.0
513810	11.71	0.0	11.6	15.0
851225	10.97	10.0	10.89	24.0
2668066	11.14	0.0	11.08	10.0
2304646	10.45	16.0	10.43	6.0
1922756	10.72	35.0	10.71	2.0
147697	9.89	44.0	9.82	21.0
2674075	9.33	0.0	9.32	0.0
2285882	12.52	0.0	12.46	15.0
2291478	12.36	0.0	11.77	58.0
1593327	13.09	0.0	12.98	15.0
1588094	12.41	0.0	12.34	11.0
1935249	10.45	39.0	10.46	4.0
2665656	11.32	13.0	11.21	25.0

Continued on next page

Table C.1 – continued from previous page

ACS ID	$\mathrm{Log}_{10}(L_{\mathrm{IR}}/L_{\odot})$ SK07	χ^2 SK07	$\mathrm{Log}_{10}(L_{\mathrm{IR}}/L_{\odot})$ CE01	χ^2 CE01
478463	9.78	39.0	9.75	20.0
1227925	12.39	0.0	11.88	44.0
873202	10.0	47.0	9.99	2.0
2652928	11.22	6.0	10.71	24.0
2644121	12.59	1.0	12.33	11.0
2299954	10.91	14.0	10.79	19.0
1939074	11.08	8.0	10.87	12.0
516196	11.98	1.0	11.75	12.0
154580	11.75	1.0	11.31	25.0
1227471	10.91	32.0	10.77	6.0
2654564	9.95	26.0	9.91	0.0
1582751	12.39	0.0	12.21	37.0
137966	10.4	32.0	10.41	0.0
867129	11.71	1.0	11.19	35.0
2292167	10.92	39.0	10.87	22.0
2287232	10.63	30.0	10.45	13.0
1561724	10.6	0.0	10.59	9.0
3021855	11.28	7.0	10.7	31.0
847140	11.67	33.0	11.57	0.0
2653157	12.68	0.0	12.73	6.0
3010064	10.28	22.0	10.09	61.0
1955941	13.27	18.0	13.47	13.0

Continued on next page

Table C.1 – continued from previous page

ACS ID	$\mathrm{Log}_{10}(L_{\mathrm{IR}}/L_{\odot})$ SK07	χ^2 SK07	$\mathrm{Log}_{10}(L_{\mathrm{IR}}/L_{\odot})$ CE01	χ^2 CE01
3020595	11.38	4.0	11.08	9.0
3009840	13.64	38.0	13.46	56.0
3004323	11.23	40.0	11.03	1.0
505308	11.3	3.0	11.09	8.0
1931780	12.01	11.0	11.64	5.0
141244	10.68	0.0	10.48	11.0
2637774	11.07	0.0	10.77	9.0
1225090	11.79	0.0	11.37	23.0
3010124	11.11	2.0	11.0	9.0
819225	10.11	32.0	10.04	5.0
1168557	10.66	50.0	10.59	1.0
2263485	11.19	0.0	11.09	20.0
1186785	11.9	1.0	11.41	29.0
1184616	12.2	0.0	12.07	1.0
1891346	10.8	38.0	10.74	1.0
2619910	11.31	0.0	11.03	10.0
2954676	12.54	0.0	12.09	97.0
2987795	11.24	8.0	10.92	20.0
2265104	10.65	29.0	10.53	14.0
1534502	10.91	15.0	10.76	3.0
2596951	12.65	0.0	11.95	64.0
100484	10.7	11.0	10.44	10.0

Continued on next page

Table C.1 – continued from previous page

ACS ID	$\mathrm{Log}_{10}(L_{\mathrm{IR}}/L_{\odot})$ SK07	χ^2 SK07	$\mathrm{Log}_{10}(L_{\mathrm{IR}}/L_{\odot})$ CE01	χ^2 CE01
1170896	12.48	0.0	11.83	93.0
1905602	11.29	15.0	11.26	7.0
1521348	11.4	0.0	11.26	9.0
2253062	11.08	8.0	10.7	29.0
2596942	11.82	17.0	11.67	3.0
2238204	10.66	24.0	10.54	55.0
1190456	12.62	0.0	12.55	0.0
1168641	11.89	25.0	11.76	4.0
451077	11.58	6.0	11.46	12.0
452413	12.32	1.0	11.89	27.0
2257248	11.8	0.0	11.45	32.0
2260199	11.17	7.0	10.84	22.0
2248150	12.31	0.0	12.11	11.0
1174167	10.77	11.0	10.46	13.0
2610272	13.34	57.0	13.54	25.0
813300	11.1	1.0	10.92	7.0
2628030	11.99	1.0	11.83	47.0
2254583	13.14	2.0	12.9	5.0
451325	11.53	2.0	10.78	65.0
1168492	12.57	0.0	12.44	20.0
2613837	9.77	9.0	9.6	8.0
1882946	11.96	29.0	11.82	0.0

Continued on next page

Table C.1 – continued from previous page

ACS ID	$\mathrm{Log}_{10}(L_{\mathrm{IR}}/L_{\odot})$ SK07	χ^2 SK07	$\mathrm{Log}_{10}(L_{\mathrm{IR}}/L_{\odot})$ CE01	χ^2 CE01
452903	12.04	31.0	11.9	1.0
112806	12.47	0.0	12.18	38.0
817294	12.46	0.0	12.4	23.0
2238402	10.38	9.0	10.27	2.0
1903319	12.7	0.0	12.53	8.0
2593896	10.58	20.0	10.4	14.0
113204	12.23	1.0	12.17	1.0
2272941	13.07	2.0	13.39	170.0
2617158	11.01	19.0	10.92	4.0
2979147	11.63	1.0	11.38	61.0
1518740	11.99	0.0	11.94	10.0
1884627	10.97	2.0	10.96	18.0
830476	12.56	0.0	12.81	32.0
1174104	8.98	0.0	8.79	35.0
1893100	10.96	0.0	10.48	31.0
2623969	11.21	7.0	10.96	8.0
824323	11.65	0.0	11.34	15.0
1160475	11.57	1.0	11.17	28.0
1891736	11.11	22.0	11.07	4.0
1183538	11.03	0.0	10.9	5.0
835962	9.61	3.0	9.37	12.0
1894391	12.24	18.0	12.19	0.0

Continued on next page

Table C.1 – continued from previous page

ACS ID	$\mathrm{Log}_{10}(L_{\mathrm{IR}}/L_{\odot})$ SK07	χ^2 SK07	$\mathrm{Log}_{10}(L_{\mathrm{IR}}/L_{\odot})$ CE01	χ^2 CE01
2987858	12.62	0.0	12.43	97.0
1167129	12.45	54.0	12.01	207.0
2969814	10.65	14.0	10.63	11.0
2256791	11.2	0.0	10.85	19.0
2241604	10.44	48.0	10.39	3.0
1185649	12.64	0.0	12.06	96.0
447565	11.93	0.0	11.59	67.0
440455	11.02	13.0	10.93	1.0
2239639	9.98	25.0	9.84	5.0
1912060	11.23	20.0	11.13	5.0
2619655	12.1	0.0	12.03	3.0
2608566	10.87	5.0	10.55	22.0
2248154	12.75	0.0	12.61	4.0
2974823	11.18	5.0	11.13	6.0
838538	12.91	0.0	12.33	104.0
1174762	11.31	25.0	11.35	20.0
447258	11.65	0.0	11.43	7.0
2615167	11.07	43.0	10.87	21.0
2612215	10.58	1.0	10.53	1.0
96246	10.9	19.0	10.77	4.0
1550434	10.74	8.0	10.74	6.0
2622511	12.67	0.0	12.69	22.0

Continued on next page

Table C.1 – continued from previous page

ACS ID	$\mathrm{Log}_{10}(L_{\mathrm{IR}}/L_{\odot})$ SK07	χ^2 SK07	$\mathrm{Log}_{10}(L_{\mathrm{IR}}/L_{\odot})$ CE01	χ^2 CE01
1911388	9.79	0.0	9.87	43.0
117090	12.59	2.0	12.47	16.0
1553932	11.71	0.0	11.73	0.0
1159741	11.33	7.0	11.04	9.0
2597445	10.87	24.0	10.39	39.0
2972248	11.29	0.0	11.25	2.0
2620640	11.23	0.0	10.89	13.0
108612	11.14	16.0	11.04	31.0
2976398	10.82	38.0	10.68	16.0
2262376	11.19	0.0	11.05	5.0
1527901	10.76	40.0	10.68	0.0
1170305	10.64	57.0	10.69	8.0
1899665	12.64	0.0	11.91	163.0
1554835	11.16	0.0	10.84	14.0
1899672	11.27	38.0	11.2	9.0
445934	10.39	7.0	10.24	0.0
2975253	9.78	14.0	9.45	31.0
810806	12.1	21.0	12.08	11.0
1907421	10.6	43.0	10.6	3.0
1903527	11.84	7.0	11.57	35.0
2614976	11.4	3.0	11.36	5.0
814604	11.76	0.0	11.56	39.0

Continued on next page

Table C.1 – continued from previous page

ACS ID	$\mathrm{Log}_{10}(L_{\mathrm{IR}}/L_{\odot})$ SK07	χ^2 SK07	$\mathrm{Log}_{10}(L_{\mathrm{IR}}/L_{\odot})$ CE01	χ^2 CE01
2976857	12.02	0.0	11.74	16.0
2631988	10.96	40.0	10.88	5.0
2238177	10.86	39.0	10.77	14.0
2259096	10.69	12.0	10.52	3.0
1168341	10.61	65.0	10.68	1.0
1869945	13.07	0.0	13.2	16.0
1128127	10.84	7.0	10.6	7.0
1872437	11.78	0.0	11.7	1.0
62481	10.32	1.0	10.19	6.0
413627	13.16	1.0	13.33	1.0
2934631	9.99	7.0	9.79	4.0
1143325	12.1	0.0	12.0	8.0
784016	10.25	6.0	10.02	33.0
424017	12.65	2.0	12.61	1.0
2560260	10.03	6.0	9.83	7.0
2557528	10.89	9.0	10.51	25.0
426950	13.04	1.0	13.06	1.0
2591964	10.88	0.0	11.0	6.0
2572228	10.08	7.0	10.03	4.0
1860547	11.07	0.0	10.97	11.0
2561816	10.23	0.0	9.93	26.0
1846738	11.19	0.0	11.19	0.0

Continued on next page

Table C.1 – continued from previous page

ACS ID	$\mathrm{Log}_{10}(L_{\mathrm{IR}}/L_{\odot})$ SK07	χ^2 SK07	$\mathrm{Log}_{10}(L_{\mathrm{IR}}/L_{\odot})$ CE01	χ^2 CE01
1501445	10.8	32.0	10.77	18.0
2581990	9.79	4.0	9.13	112.0
79497	12.44	0.0	12.12	43.0
2581931	10.55	8.0	10.47	18.0
2938115	12.78	0.0	12.21	66.0
2948121	11.99	2.0	11.97	34.0
1127416	12.6	33.0	12.01	113.0
1846593	10.33	33.0	10.28	20.0
73949	10.81	16.0	10.71	18.0
406192	11.01	35.0	10.92	4.0
1507621	13.46	0.0	13.12	13.0
404891	11.45	2.0	11.01	5.0
62382	12.13	5.0	12.07	0.0
2214877	11.05	21.0	10.99	4.0
800716	14.53	0.0	14.76	23.0
2208142	10.06	1.0	9.81	13.0
1873946	10.78	1.0	10.51	21.0
58406	12.67	4.0	12.52	50.0
1152076	12.57	0.0	12.61	11.0
1878521	10.12	49.0	10.12	28.0
2204140	12.16	21.0	11.72	74.0
431273	11.67	0.0	11.25	42.0

Continued on next page

Table C.1 – continued from previous page

ACS ID	$\mathrm{Log}_{10}(L_{\mathrm{IR}}/L_{\odot})$ SK07	χ^2 SK07	$\mathrm{Log}_{10}(L_{\mathrm{IR}}/L_{\odot})$ CE01	χ^2 CE01
780113	12.91	0.0	11.99	59.0
2197132	10.26	12.0	10.0	12.0
1851942	11.97	1.0	11.55	56.0
63398	11.49	5.0	11.21	4.0
2205065	10.59	8.0	10.18	27.0
2572169	11.64	59.0	11.68	9.0
414286	11.49	14.0	11.27	9.0
780882	11.9	16.0	11.31	6.0
761474	9.31	0.0	8.82	20.0
780233	11.53	3.0	11.18	26.0
431244	11.33	29.0	11.22	6.0
2554877	11.2	4.0	11.15	162.0
395124	8.84	0.0	8.86	0.0
783411	11.95	0.0	12.02	1.0
2579773	11.12	0.0	11.06	2.0
2226160	11.52	39.0	11.39	2.0
2571279	11.15	0.0	11.05	9.0
1490611	12.17	10.0	11.82	142.0
61989	11.66	2.0	11.89	44.0
785761	11.55	1.0	11.48	7.0
1493663	10.99	3.0	10.73	9.0
69003	12.26	0.0	11.83	29.0

Continued on next page

Table C.1 – continued from previous page

ACS ID	$\mathrm{Log}_{10}(L_{\mathrm{IR}}/L_{\odot})$ SK07	χ^2 SK07	$\mathrm{Log}_{10}(L_{\mathrm{IR}}/L_{\odot})$ CE01	χ^2 CE01
1151085	12.45	7.0	12.36	14.0
1128900	11.25	0.0	11.16	4.0
1493878	12.92	1.0	12.11	77.0
1498466	10.49	39.0	10.41	2.0
2211866	11.72	3.0	11.33	10.0
2216416	12.42	1.0	11.98	34.0
429004	12.15	0.0	12.1	3.0
1158933	12.59	0.0	12.49	18.0
1156706	12.28	1.0	11.89	29.0
2581048	11.39	4.0	11.18	39.0
2588755	11.4	0.0	11.34	0.0
1861510	11.5	8.0	11.41	0.0
2558972	10.86	7.0	10.89	8.0
402290	11.91	8.0	11.49	21.0
2573455	10.16	44.0	10.08	6.0
2200608	10.05	12.0	9.84	4.0
1484163	11.03	0.0	10.96	7.0
431804	12.41	30.0	12.34	85.0
1853374	11.24	20.0	10.95	11.0
1142477	11.77	14.0	11.6	3.0
433537	12.03	0.0	11.73	14.0
2584212	12.07	0.0	11.86	7.0

Continued on next page

Table C.1 – continued from previous page

ACS ID	$\mathrm{Log}_{10}(L_{\mathrm{IR}}/L_{\odot})$ SK07	χ^2 SK07	$\mathrm{Log}_{10}(L_{\mathrm{IR}}/L_{\odot})$ CE01	χ^2 CE01
2232911	11.63	12.0	11.59	1.0
59977	12.23	0.0	11.79	18.0
1497806	11.11	1.0	10.77	21.0
2210132	11.09	9.0	10.93	6.0
2577936	10.63	19.0	10.57	1.0
1854060	11.24	0.0	11.25	2.0
58445	11.28	0.0	11.18	10.0
79069	12.75	0.0	12.32	48.0
1140777	13.11	14.0	12.93	9.0
776567	12.11	1.0	11.75	38.0
740162	11.81	0.0	11.51	10.0
2526656	10.86	1.0	10.62	10.0
2547042	11.62	0.0	11.24	8.0
737299	12.17	0.0	12.05	5.0
730411	12.0	2.0	11.67	35.0
1466694	13.08	0.0	13.11	3.0
738096	12.7	0.0	12.09	76.0
1824713	10.44	16.0	10.4	8.0
1812045	10.93	15.0	10.92	15.0
1104398	12.18	0.0	12.07	2.0